ENVIRONMENTAL HYDRAULICS

PROCEEDINGS OF THE INTERNATIONAL WORKSHOP ON ENVIRONMENTAL HYDRAULICS, IWEH09, VALENCIA, SPAIN, 29–30 OCTOBER 2009

# Environmental Hydraulics

## Theoretical, Experimental and Computational Solutions

*Editors*

P.A. López-Jiménez, V.S. Fuertes-Miquel, P.L. Iglesias-Rey,
G. López-Patiño, F.J. Martínez-Solano, G. Palau-Salvador
*Universidad Politécnica de Valencia, Valencia, Spain*

CRC Press
Taylor & Francis Group
Boca Raton London New York Leiden

CRC Press is an imprint of the
Taylor & Francis Group, an **informa** business
A BALKEMA BOOK


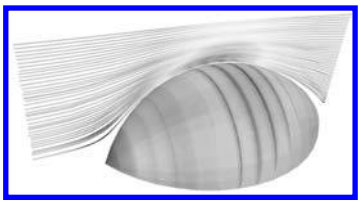






*Taylor & Francis is an imprint of the Taylor & Francis Group, an informa business*



Typeset by Macmillan Publishing Solutions, Chennai, India
Printed and bound in Great Britain by Antony Rowe (A CPI Group Company), Chippenham, Wiltshire



Published by: CRC Press/Balkema
P.O. Box 447, 2300 AK Leiden, The Netherlands
e-mail: Pub.NL@taylorandfrancis.com
www.crcpress.com – www.taylorandfrancis.co.uk – www.balkema.nl

ISBN: 978-0-415-56697-1 (Hardback)
ISBN: 978-0-203-85696-3 (eBook)

*Environmental Hydraulics – López-Jiménez et al (eds)*
*© 2010 Taylor & Francis Group, London, ISBN 978-0-415-56697-1*

# Table of Contents

*Water and environmental engineering and hydroinformatics*

*Environmental Hydraulics – López-Jiménez et al (eds)*
*© 2010 Taylor & Francis Group, London, ISBN 978-0-415-56697-1*

# Acknowledgements

For many years I have thought that, as hydraulic and environmental scientists and technicians, we need forums to share our experiences, our knowledge and skills. It is my wish to create a climate of cooperation among all my colleagues. This is what prompted me to share my ideas with colleagues and to engage them in this enthralling and wonderful IWEH09 project. First of all, I would like to express my gratitude to those good friends and colleagues who supported me from the very beginning of this adventure, especially Guillermo Palau and Carlo Gualtieri, who were the first and most enthusiastic supporters of this idea.

Secondly, we are most grateful to Professors Gerhard Jirka, Wolfgang Rodi, Hubert Chanson and Vladimir Nikora for their kind support in preparing this workshop. Their assistance and advice, as Senior Lecturers, has been crucial in this endeavour.

I would like to mention as well our sponsors: Ministerio de Ciencia y Tecnologia de España and Generalitat Valenciana. Our special acknowledgement to the Universidad Politécnica de Valencia and all the extraordinary people who made this event possible. Finally, of course also thanks to the International Societies supporting our Workshop: IAHR and IEMSS.

I would also like to take this opportunity to express my sincere appreciation to the members of my research group: Multidisciplinary Center of Fluid Modeling, who have been active collaborators in this project, especially Francisco García, Daniel Mora and Jesús Mora. Their contribution, together with that of the members of the Local Organization Committee has been invaluable.

Hopefully this will not only be the first International Workshop on Environmental Hydraulics, but the first of many workshops of its kind.

On behalf of the Local Organizing Committee.
Petra A. López-Jiménez
IWEH09 Chair

*Environmental Hydraulics – López-Jiménez et al (eds)*
*© 2010 Taylor & Francis Group, London, ISBN 978-0-415-56697-1*

# IWEH 09 committees

***Chair***
Petra Amparo López Jiménez

***Local Organizing Committee***
Vicente S. Fuertes Miquel
Maria Gasque Albalate
Josep R. González Castro
Pablo González Altozano
Pedro Luís Iglesias Rey
Gonzalo López Patiño
Francisco J. Martínez Solano
Guillermo Palau Salvador
Rafael Pérez García

***International Scientific Committee***
Hubert Chanson
Peter B. Cheung
Didia Covas
Guadalupe Estrada Gutiérrez
Manuel García Villalba
Nahun H. García Villanueva
Carlo Gualtieri
Anthony Jakeman
Bill James
Gerhard Jirka
Benjamín Lara Ledesma
Frédéric Moulin
Vladimir Nikora
Heber Pimentel Gomes
Guelfo Pulci Doria
Helena Ramos
Gian Marco Revel
Luisa Fernanda Ribeiro Reis
Wolfgang Rodi
Nils Rüther
Rita Ugarelli

*Environmental Hydraulics – López-Jiménez et al (eds)*
*© 2010 Taylor & Francis Group, London, ISBN 978-0-415-56697-1*

# Preface

It is a great pleasure to endorse on behalf of the International Association of Hydraulic Engineering and Research (IAHR) this "International Workshop on Environmental Hydraulics 2009" organized by the Universidad Politécnica de Valencia. Since its foundation some 25 years ago IAHR has continuously fostered and supported the organization of conferences and symposia on new and emerging themes in hydraulics and water science and engineering. Many of these have become over the years highly regarded continuing symposia series that are attended not only by hydraulic researchers, but by colleagues from other science and engineering communities. The regular symposia in "Stratified Flow", on "Gas Transfer at Water Surfaces", or on "Shallow Flows" all endorsed by the IAHR Committee on Fluid Mechanics are excellent examples in that regard.

The colleagues from UPV are to be congratulated on this new initiative for launching the IWEH 09. It promises to bring together not only the Spanish community of researchers concerned with this specialty, but will also have special appeal to scientists from the Mediterranean area and from Europe and Latin America. "Environmental hydraulics" with its focus on the flow-associated mass and heat transport processes and on the flow interaction with the biological and ecological components of our water systems transcends the traditional hydraulic approach. It promises to obtain new understanding on the functioning of our aquatic ecosystems and to develop new tools for its appropriate engineering management in order to provide optimal environmental quality and socio-economic well-being for our future generations.

Prof. Gerhard H. Jirka
University of Karlsruhe
Vice-President IAHR

*Invited lectures*

*Environmental Hydraulics – López-Jiménez et al (eds)*
*© 2010 Taylor & Francis Group, London, ISBN 978-0-415-56697-1*

# Environmental, ecological and cultural impacts of tidal bores, burros and bonos

Hubert Chanson
*School of Civil Engineering, The University of Queensland, Brisbane, Australia*

ABSTRACT: A tidal bore is a series of waves propagating upstream as the tidal flow turns to rising. It forms during the spring tide conditions when the tidal range exceeds 4 to 6 m and the flood tide is confined to a narrow funnelled estuary with low freshwater levels. Tidal bores are locally called mascaret, pororoca, burro, bono, benak and aegir. A tidal bore is associated with a massive mixing of the estuarine waters that stirs the organic matter and creates some rich fishing grounds. Its occurrence is essential to many ecological processes and the survival of unique eco-systems. The tidal bores are also part of the cultural heritage in many regions: the Qiantang River bore in China, the Severn River bore in UK, the Dordogne River in France. In this contribution, the environmental, ecological and cultural impacts of tidal bores are detailed and discussed.

*Keywords*: Tidal bores, turbulence, turbulent mixing, theory, observation, environmental impact, ecological impact, cultural heritage, burro, bono.

## 1 INTRODUCTION

A tidal bore is a surge of waters propagating upstream as the tidal flow turns to rising and the flood tide rushes into a funnel shaped river mouth (Fig. 1). The bore forms during the spring tides when the tidal range exceeds 4 to 6 m and the rising tide waters are confined to the narrow funnelled estuary with low freshwater levels. It is estimated worldwide that over 400 estuaries are affected by a tidal bore, on all continents but Antarctica. A bore is a discontinuity of the water depth and it represents a hydrodynamic shock. The tidal bores have a significant impact on the environmental system and the ecology of the river mouth. Recent studies demonstrated in particular the significant impact of small tidal bores and of non-breaking undular surges on natural channels[13,14,15]. Surprisingly, the tidal bore remains a challenging research topic to theoreticians, and many hydrodynamic features remain unexplained.

The existence of a tidal bore is based upon a fragile hydrodynamic balance between the tidal flow range, the freshwater river flow conditions and the channel bathymetry. Some simple theoretical considerations show that this balance may be too easily disturbed by changes in boundary conditions and freshwater inflow. For examples, a number of tidal bores disappeared because of river training, dredging and damming. Man-made interventions led to the loss of several bores with often adverse impacts onto the eco-system: e.g., the mascaret of the Seine River (France) no longer exists after extensive training works and dredging; the Colorado River bore (Mexico) is drastically smaller after dredging. Although the fluvial traffic gained in safety in some case, the ecology of estuarine zones were adversely affected. The tidal bores of the Colorado (Mexico), Couesnon (France) and Petitcodiac (Canada) Rivers almost disappeared after construction of upstream barrage(s). At Petitcodiac, this yielded the elimination of several native fish species. The proposed construction of the Severn Barrage in UK is a major threat to one of the best documented tidal bores: the Severn River bore. The tidal bores do have a significant effect on the natural channels and their ecology. The tidal bore affected estuaries are the natural habitats of several fish species, for example in the Severn, Petitcodiac and Rokan Rivers, as well as the feeding grounds of larger predators. The tidal bores can be some major tourism attractions like in Canada, China, France and UK. Several tidal bores are regularly surfed by kayakers and surfers in Brazil, France and UK. The surfers' aim is the distance and duration of the ride: how long can we ride the bore? But some bores are dangerous and have had a sinister reputation although they contribute to our cultural heritage.

The tidal bores were studied by hydraulic engineers and applied mathematicians for a couple of centuries. Major contributions included the works of Bazin[2], Barré de Saint Venant[1], Boussinesq[4], Benjamin And Lighthill[3], and Peregrine[22]. For example, in his milestone paper, Adhémar Jean Claude Barré de Saint Venant (1797–1886) applied his famous equations to the tidal bore of the Seine River[1].

The origin of the word 'bore' is believed to derive from the Icelandic 'bara' ('billow") indicating a potentially dangerous phenomenon: i.e., a tidal bore with a breaking roller[8]. The French name is 'mascaret' and other local names of tidal bores include 'le montant' (Garonne River, France), 'la barre' (Seine River, France), 'le mascarin' (Vilaine, France), the 'pororoca' (Amazon River, Brazil), the 'burro' (Colorado River, Mexico), the 'bono' (Rokan River, Indonesia).

In this keynote, the author aims to share his enthusiasm and passion for the tidal bore. Some basic theoretical considerations are developed. Then the turbulence and turbulent mixing induced by a tidal bore are documented. The rumble noise of tidal bores is discussed based upon field observations, before the interactions between tidal bores and mankind are discussed.

## 2 THEORETICAL CONSIDERATIONS

### 2.1 *Basic principles*

A tidal bore may occur when the tidal range exceeds 4 to 6 m and the funnel shape of the river mouth amplifies the tidal wave. The driving process is the large tidal amplitude. The tides are forced oscillations generated by the attractions of the Moon

(A) Tidal bore ('pororoca') of the Rio Mearim (Brazil) in 205 (Courtesy of Antony Colas)

(B) Tidal bore ('bono') of the Kampar River (Indonesia) - Note the boats riding the bore front

Figure 1. Photographs of tidal bores.

and Sun, and have the same periods as the motion of the Sun and Moon relative to the Earth. Every fourteenth day at full moon or new moon, the attraction forces of the Sun and Moon reinforce one another, and these conditions give the spring tide conditions. The tidal range may be locally amplified further by a number of factors including when the natural resonance of the bay and estuary is close to the tidal period[7,21]. This coincidence implies that the general sloshing of the waters around the inlet or bay becomes synchronised with the lunar tides and amplify their effect, yielding often the best tidal bores a couple of days after the date of the maximum tidal range.

When the sea level rises with time during the flood tide, the tidal wave becomes steeper and steeper, until it forms an abrupt front: the tidal bore. After the formation of the tidal bore, there is an abrupt rise in water depth at the bore front and the flow singularity may be analysed as a hydraulic jump in translation[18,5]. The inception and development of a tidal bore may be predicted using the Saint-Venant equations and the method of characteristics. The flow properties immediately upstream and downstream of the tidal bore front must satisfy the continuity and momentum principles[24,12]. Considering a tidal bore travelling in a river section, the bore front propagates upstream with a celerity U (Fig. 2). Yet the same tidal bore is seen by an observer running alongside the bore at a speed U as a quasi-steady flow situation called a hydraulic jump in translation. The integral equations of conservation of mass and momentum give a series of relationships between the flow properties in front of and behind the bore front:

$$(V_1 + U) \times d_1 = (V_2 + U) \times d_1 \tag{1}$$

$$\frac{1}{2} \times \rho \times g \times ({d_2}^2 - {d_1}^2) = \rho \times (V_1 + U) \times d_1 \times (\beta_1 \times (V_1 + U) - \beta_2 \times (V_2 + U)) \tag{2}$$

where $\rho$ is the water density, g is the gravity acceleration, V is the flow velocity positive downstream towards the river mouth, d is the water depth, $\beta$ is a momentum correction coefficient, the subscript 1 refers to the initial flow conditions and the subscript 2 refers to the new flow conditions (Fig. 2). Herein $d_1$ and $d_2$ are respectively the flow depths immediately before and after the tidal bore passage. Note that Equation (2) is based the assumption of hydrostatic pressure distribution in front of and behind

(C) Tidal bore ('mascaret') of the Garonne River (France) 2 September 2008

(D) Small tidal bore ('burro') in the Colorado River estuary in 1904 (after Sykes 1937)

Figure 1. (*continued*)

the bore front, and the friction losses are neglected. The combination of Equations (1) and (2) yields the classical result:

$$\frac{d_2}{d_1} = \frac{1}{2}\left(\sqrt{1 + 8 \times Fr_1^{\,2}} - 1\right) \tag{3}$$

where $Fr_1$ is the tidal bore Froude number:

$$Fr_1 = \frac{V_1 + U}{\sqrt{g \times d_1}} \tag{4}$$

The tidal bore Froude number $Fr_1$ is always greater than unity and it is a measure of the strength of the bore. If the Froude number $Fr_1$ is less than unity, the tidal wave cannot become a tidal bore. Equations (1) and (2) form a system of two equations with five variables ($d_1$, $d_2$, $V_1$, $V_2$, U). Typically the upstream conditions ($V_1$, $d_1$) are known and one more boundary condition is required[12].

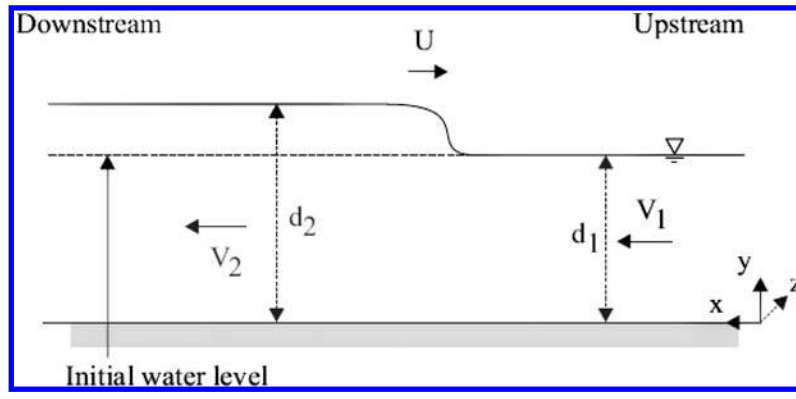


Figure 2. Definition sketch of a tidal bore propagating upstream.

Figure 3. Undular tidal bore of the Dordogne River (France) on 27 September 2008 – The surfer is riding in front of the third wave crest.

### 2.2 *Undular tidal bores*

The shape of the tidal bore is directly linked with its Froude number $Fr_1$. An undular tidal bore is observed for a bore Froude number between 1 and 1.5 to 1.8. For larger Froude numbers, a breaking bore takes place. Practically the very large majority of tidal bore occurrences have an undular shape: i.e., the leading wave followed by a train of well-developed undulations called whelps (Fig. 3). For example, the Equipe Cousteau photographed the 'pororoca' 10 nautical miles before it reached the river mouth[20]. There were more than 30 waves, each 2–3 m high with 20–30 m between crests, and extending behind the horizon with an estimated visibility of 20 nautical miles. Figure 3 shows show an example of an undular tidal bore. Immediately behind the bore front, the wave train presents a pseudo-periodic, undular profile, although the observations show also the development of "semi-chaotic" patterns with increasing time. The field observations indicate also the long-lasting effects of the wave motion, sometimes more than 20 to 30 minutes after the tidal bore passage. This aspect is well-known to surfers and kayakers who can experience some difficulties to come back ashore after surfing.

Considering an undular bore in the system of co-ordinates in translation with the bore front, the flow is quasi-steady and the free-surface profile is stationary. For a two-dimensional incompressible flow, the differential form of the equation of conservation of mass is:

$$\frac{\partial V_x}{\partial x} + \frac{\partial V_y}{\partial x} = 0 \tag{5}$$

where $V_x$ is the longitudinal velocity component positive downstream and $V_y$ is the vertical velocity component positive upwards. Since the fluid is incompressible, the stream function $\psi$ exists and the velocity components equal $V_x = -\partial\psi/\partial y$ and $V_y = \partial\psi/\partial x$. The condition of irrotational flow motion is a Laplace equation in terms of the stream function: $\Delta\psi = 0$, and the boundary conditions are: (a) $\psi(y = 0) = 0$ at the channel bed, (b) $\psi(y = d) = -q$ at the water free-surface where $q = (V_1 + U) \times d_1$ is the water flow rate per unit width in the quasi-steady flow analogy system of co-ordinates (Eq. (1)), and (c) the Bernoulli principle:

$$\frac{(V_x^2 + V_y^2)}{2} + g \times y + \frac{P}{\rho} = \text{cons tan t}$$

with y the vertical elevation ($y = 0$ at the bed), P the local pressure and $\rho$ the fluid density. With the sign convention that is selected, the flux q is positive for a tidal bore propagating upstream. Using the continuity equation, the Navier-Stokes equation

for an ideal fluid in the y-direction yields:

$$V_x^2 \times \frac{\partial (V_y / V_x)}{\partial x} = -\frac{1}{\rho} \times \frac{\partial P}{\partial y} - g \tag{6}$$

When the streamline curvature is non negligible, the pressure gradient departs from the hydrostatic pressure gradient ($\partial P/\partial y = -\rho \times g$) and Equation (6) gives an expression for the pressure deviation caused by the free-surface curvature[19]. Let us assume a linear vertical velocity distribution:

$$\frac{V_y(y=d)}{V_x(y=d)} = \frac{\partial d}{\partial x} \tag{7}$$

After re-arranging, the variation of pressure field in response to the surface curvature gives a differential equation in terms of the flow depth d and depth-averaged longitudinal velocity. For an ideal fluid in a horizontal channel, it yields:

$$\frac{\partial}{\partial x}\left(\overline{V}^2 \times d + \frac{1}{2} \times g \times d^2 + \frac{1}{3} \times \overline{V}^2 \times d \times \left(d \times \frac{\partial^2 d}{\partial x^2} - \left(\frac{\partial d}{\partial x}\right)^2\right)\right) = 0 \tag{8}$$

Note that a velocity correction coefficient was dropped in the uppermost left term for clarity. In the system of co-ordinates of the quasi-steady flow analogy, the integration of Equation (8) has a solution:

$$\left(\frac{\partial d}{\partial x}\right)^2 = 6 \times g \times \left(-M \times d - \frac{1}{3} \times d^3 + \frac{q}{g} - E \times d^2\right) = 0 \tag{9}$$

where M and E are respectively the momentum function and the specific energy. The M- and E-functions must be defined herein for the general case of a non hydrostatic pressure distribution and non-uniform velocity profile:

$$M = \int_0^d \left(\frac{P}{\rho \times g} + \frac{V_x^2}{2 \times g}\right) \times dy \tag{10}$$

$$E = \frac{1}{d} \times \int_0^d \left(y + \frac{P}{\rho \times g} + \frac{V_x^2 + V_y^2}{2 \times g}\right) \times dy \tag{11}$$

The periodic wave solution of Equation (9) is called a cnoidal wave function because it takes the form of the square of the Jacobian elliptic function cn[10,11,25]. Some typical free-surface profiles are presented in Figures 4 and 5. Figure 4 shows the water depth as a function of the time at a fixed location, while Figure 5 presents the water elevation as a function of the longitudinal distance at a given time. The measurements highlight the pseudo-periodic shape of the free-surface undulations. In Figures 4 and 5, the data are compared with a sinusoidal curve and cnoidal wave function. Herein, each function was fitted for each half-wave length between a crest/trough and the adjacent trough/crest. Altogether there is a reasonable agreement between the data and mathematical functions, although neither the linear wave theory nor the Boussinesq equations capture the asymmetrical wave shape nor the fine details of the free-surface profile shape. The findings are consistent with an earlier study of relatively large amplitude shallow water waves[16].

Noteworthy, the agreement between the free-surface data and cnoidal function is best achieved using the parameter of the elliptic function $m > 0.5$ between a wave crest and trough, while $m < 0.5$ between a wave trough and crest. For $m = 0$, the cnoidal wave function equals the sinusoidal profile and more generally the nonlinearity causes little departure from the linear wave theory for small values of m. As m increases, the crest becomes more peaky and the trough shallower. The experimental observations highlight the asymmetry of the free-surface undulations, with some differences in wave shape between a crest and trough, and between a trough and the next wave crest. The undulation asymmetry was already noted in the stationary undular hydraulic jumps in terms of both the free-surface profile and the vertical distributions of pressure and velocity[9].

## 3 IMPACT OF TIDAL BORES

A tidal bore is a hydrodynamic shock with a sudden rise in water elevation. The flow singularity progresses upstream and may travel dozens of kilometres inland before vanishing. The development and advance of a tidal bore may be predicted by some simple theoretical considerations. The presence of a tidal bore indicates some macro-tidal conditions associated with an asymmetrical tide. The flood tide is usually shorter than the ebb tide period and the flood flow is much faster. Worldwide, it is believed that over 400 estuaries are affected by a tidal bore on all continents but Antarctica, and that number is likely an underestimate because it does not include the numerous tidal bores in small inlets, creeks and drainage canals in shallow-water bays (e.g. Baie du Mont Saint Michel, Bristol Channel) nor the small tributaries of large rivers (e.g., Seine, Hooghly, Garonne).

Limited quantitative information is available on the turbulence and mixing induced by the tidal bore because the field observations are difficult and most studies did not use a fine instrumentation under well-defined flow conditions. Some recent laboratory investigations provide some much needed details. The results demonstrate unequivocally that a tidal bore acts like a ‘gigantic’ mixer that stirs the matters and sediments, and advects upstream the suspended materials into the upper estuarine

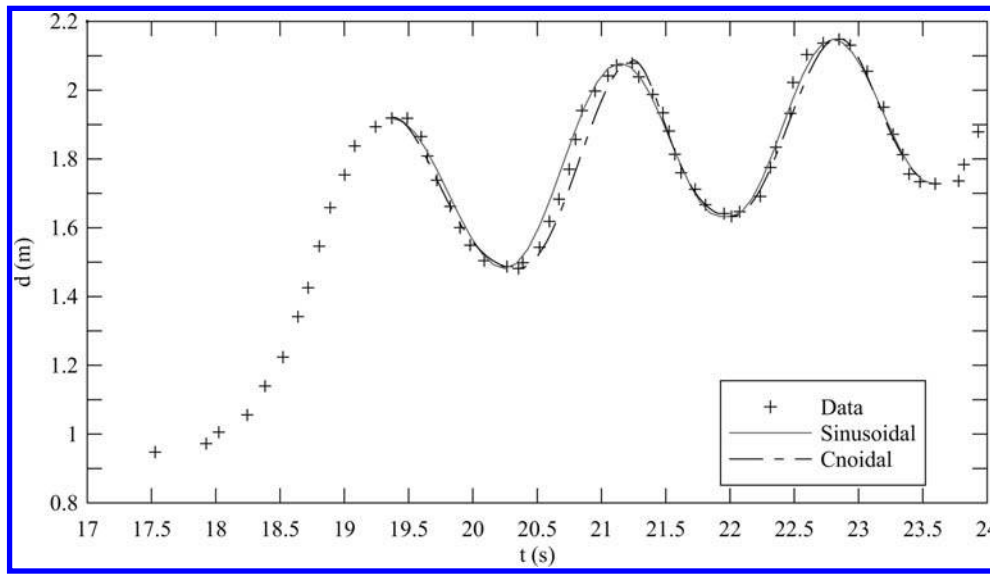


Figure 4. Free-surface profile of an undular tidal bore: time-variation of the flow depth for the Dee River tidal bore on 22 September 1972 (Data: Lewis 1972) – Comparison with the linear wave theory (sinusoidal) and Boussinesq equation solution (cnoidal).

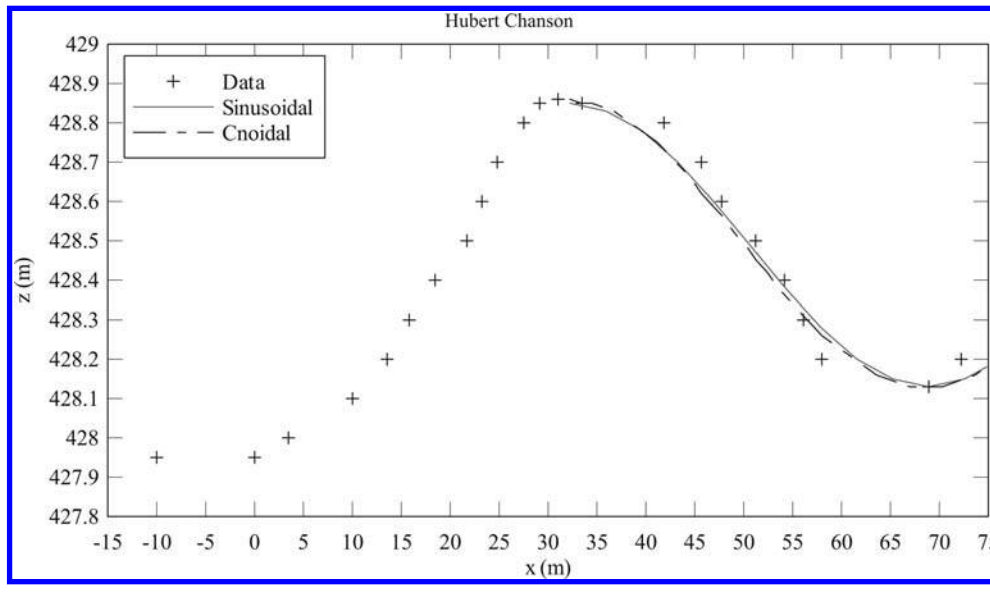


Figure 5. Free-surface profile of an undular tidal bore: longitudinal variation of the water elevation in an undular positive surge in the Oraison power plant intake channel (Data: Ponsy and Carbonnell 1966) – Comparison with the linear wave theory (sinusoidal) and Boussinesq equation solution (cnoidal).

regions. All the observations show further the significant impact of small tidal bores and of non-breaking undular bores. A key feature of a tidal bore is its rumble noise that can be heard from far away. Some detailed measurements show that the sounds generated by a breaking bore have a low-pitch comparable to the sounds generated by bass drums and locomotive trains, and the dominant source of the rumble noise is the collective oscillations of the bubble clouds entrained in the tidal bore roller[6].

The tidal bores do have a significant effect on the natural channels and their ecology. The tidal bore affected estuaries are the natural habitats of several fish species, as well as the feeding grounds of larger predators like sharks, crocodiles, seals and whales. A tidal bore is the result of delicate balance between the tidal conditions, the freshwater conditions and the estuarine bathymetry. This fragile balance can be easily disturbed: e.g., by a change in freshwater discharge or some variation in bathymetry (dredging, river training). Man-made interventions led to the disappearance of several tidal bores with often adverse impacts onto the eco-systems. The interactions between tidal bores and Mankind are complicated. The tidal bores can be some major tourism attractions like in Canada, China, France and UK. Several tidal bores are regularly surfed by kayakers and surfers in Brazil, France and UK. The surfers' aim is the distance and duration of the ride: how long can we ride the bore? But some bores are dangerous and have had a sinister reputation (Qiantang River, Seine River, Bamu and Fly Rivers) while hindering the local development and transportation. A tidal bore is an integral part of our environment and cultural heritage like in China where the tidal bore attracts half million of tourists during the Moon festival. But it is an endangered phenomenon that can be too easily affected adversely by human interventions.

REFERENCES


[1] Barré de Saint Venant, A.J.C. (1871). "Théorie et Equations Générales du Mouvement Non Permanent des Eaux Courantes." ('Theory and General Equations of Unsteady Open Channel Flow Motion.') *Comptes Rendus des séances de l'Académie des Sciences*, Paris, France, Séance 17 July 1871, Vol. 73, pp. 147–154 (in French).

[2] Bazin, H. (1865). "Recherches Expérimentales sur la Propagation des Ondes." ('Experimental Research on Wave Propagation.') *Mémoires présentés par divers savants à l'Académie des Sciences*, Paris, France, Vol. 19, pp. 495–644 (in French).

[3] Benjamin, T.B., and Lighthill, M.J. (1954). "On Cnoidal Waves and Bores." *Proc. Royal Soc. of London, Series A, Math. & Phys. Sc.*, Vol. 224, No. 1159, pp. 448–460.

[4] Boussinesq, J.V. (1877). "Essai sur la Théorie des Eaux Courantes." ('Essay on the Theory of Water Flow.') *Mémoires présentés par divers savants à l'Académie des Sciences*, Paris, France, Vol. 23, Série 3, No. 1, supplément 24, pp. 1–680 (in French).

[5] Chanson, H. (2009). "Current Knowledge In Hydraulic Jumps And Related Phenomena. A Survey of Experimental Results." *European Journal of Mechanics B/Fluids*, Vol. 28, No. 2, pp. 191–210 (DOI: 10.1016/j.euromechflu.2008.06.004).

[6] Chanson, H. (2009b). "The Rumble Sound Generated by a Tidal Bore Event in the Baie du Mont Saint Michel." *Journal of Acoustical Society of America*, Vol. 125, No. 6, pp. 3561–3568 (DOI: 10.1121/1.3124781).

[7] Clancy, E.P. (1968). "The Tides Pulses of the Earth." *Anchor Books*, New York, USA, 228 pages.

[8] Coates, R. (2007). "The Genealogy of *Eagre* 'Tidal Surge in the River Trent'." *English Language and Linguistics*, Vol. 11, No. 3, pp. 507–523.

[9] Donnelly, C., and Chanson, H. (2005). "Environmental Impact of Undular Tidal Bores in Tropical Rivers." *Environmental Fluid Mechanics*, Vol. 5, No. 5, pp. 481–494 (DOI: 10.1007/s10652-005-0711-0).

[10] Fenton, J.D. (1979). "A High-Order Cnoidal Wave Theory." *Jl of Fluid Mech.*, Vol. 94, Part I, pp. 129–161.

[11] Fenton, J.D. (1998). "The Cnoidal Theory of Water Waves." in "Developments in Offshore Engineering: Wave Phenomena and Offshore Topics (Handbook of Coastal & Ocean Engineering)", Ed. J.B. Herbich, *Gulf Professional Publishing*, Houston, USA, pp. 55–101.

[12] Henderson, F.M. (1966). "Open Channel Flow." *MacMillan Company*, New York, USA.

[13] Hornung, H.G., Willert, C., and Turner, S. (1995). "The Flow Field Downsteam of a Hydraulic Jump." *Jl of Fluid Mech.*, Vol. 287, pp. 299–316.

[14] Koch, C., and Chanson, H. (2008). "Turbulent Mixing beneath an Undular Bore Front." *Journal of Coastal Research*, Vol. 24, No. 4, pp. 999–1007 (DOI: 10.2112/06-0688.1).

[15] Koch, C., and Chanson, H. (2009). "Turbulence Measurements in Positive Surges and Bores." *Journal of Hydraulic Research*, IAHR, Vol. 47, No. 1, pp. 29–40 (DOI: 10.3826/jhr.2009.2954).

[16] Le Méhauté, B., Divoky, D., and Lin, A. (1968). "Shallow Water Waves: a Comparison of Theories and Experiments." *Proc. 11th Intl Conf. on Coastal Eng.*, London, UK, ASCE Publ., Vol. I, pp. 86–107.

[17] Lewis, A.W. (1972). "Field Studies of a Tidal Bore in the River Dee." *M.Sc. thesis*, Marine Science Laboratories, University College of North Wales, Bangor, UK.

[18] Liggett, J.A. (1994). "Fluid Mechanics." *McGraw-Hill*, New York, USA.

[19] Montes, J.S. (1998). "*Hydraulics of Open Channel Flow*." ASCE Press, New-York, USA, 697 pages.

[20] Murphy, D. (1983). "Pororoca!." *Calypso Log*, Cousteau Society, Vol. 10, No. 2, June, pp. 8–11.

[21] Open University Course Team (1999). "Waves, Tides and Shallow-Water Processes." *Butterworth-Heinemann*, Oxford, UK, 2nd edition, 227 pages.

[22] Peregrine, D.H. (1966). "Calculations of the Development of an Undular Bore." *Jl. Fluid Mech.*, Vol 25, pp. 321–330.

[23] Ponsy, J., and Carbonnell, M. (1966). "Etude Photogrammétrique d'Intumescences dans le Canal de l'Usine d'Oraison (Basses-Alpes)." ('Photogrammetric Study of Positive Surges in the Oraison Powerplant Canal.') *Jl Soc. Française de Photogram.*, Vol. 22, pp. 18–28.

[24] Rayleigh, Lord (1908). "Note on Tidal Bores." *Proc. Royal Soc. of London, Series A containing Papers of a Mathematical and Physical Character*, Vol. 81, No. 541, pp. 448–449.

[25] Wiegel, R.L. (1960). "A Presentation of Cnoidal Wave Theory for Practical Application." *Jl of Fluid Mech.*, Vol. 7, No. 2, pp. 273–286.

*Environmental Hydraulics – López-Jiménez et al (eds)*
*© 2010 Taylor & Francis Group, London, ISBN 978-0-415-56697-1*

# Flow-organism interactions in running waters: Interplay between flow mechanics, biomechanics, and ecology

Vladimir I. Nikora
*School of Engineering, Fraser Noble Building, Kings College, University of Aberdeen, UK*

ABSTRACT: The paper promotes a research area of flow-organism interactions that has recently emerged at the interfaces between environmental fluid mechanics, biomechanics, and aquatic ecology. This new area, *Hydrodynamics of Aquatic Ecosystems*, bridges these disciplines together and is defined as a study of flow-organism interactions at multiple scales with particular focus on relevant transport processes and mutual physical impacts. Being an important part of its mother disciplines, *Hydrodynamics of Aquatic Ecosystems* deals with two key interconnected issues: (i) physical interactions between flow and organisms (e.g., due to an interplay between flow-induced forces and reaction forces generated by organisms); and (ii) ecologically relevant mass-transfer-uptake processes (e.g., due to molecular and turbulent diffusion). The paper outlines some key concepts and hypotheses of *Hydrodynamics of Aquatic Ecosystems* that may be useful in studying flow-biota interactions at multiple scales.

*Keywords*: Aquatic Organisms, Turbulence, Transport Processes, Boundary Layers, Mixing Layers.

## 1 BACKGROUND

There is a great variety of aquatic environments on our planet ranging from deep-ocean hydrothermal vents to cold Antarctic lakes. The running surface waters are probably the most critical among them as without streams and rivers human civilisation would almost certainly fail. Indeed, these 'lotic' waters have offered human settlements vital services many of which have come from lotic ecosystems. The key feature that differentiates lotic systems (e.g., streams and rivers) from other aquatic habitats, such as deep ocean or lakes, is strong interaction between shallow unidirectional water flow and sedimentary or rocky beds. The flow-bed interactions occur over a wide range of spatial and temporal scales and involve a variety of scale-dependent physical mechanisms such as turbulence, sediment transport, and channel morphodynamics. This habitat complexity and heterogeneity have been evolutionarily imprinted into the striking diversity of lotic ecosystems that has fascinated generations of aquatic biologists. In spite of their great efforts, however, there are still many knowledge gaps on structure and function of lotic ecosystems. One of most significant questions to be answered is how exactly does flow affect lotic ecosystems at multiple scales and vice versa? This lack of knowledge has to be urgently addressed if we want to advance conservation and sustainable use of streams and rivers in challenging times of growing human activities and climate change.

There is mounting evidence showing that flow effects account for far more than 50% of variability in the ecological responses of lotic ecosystems, which may strongly depend on the scale of consideration[1]. Indeed, flow (velocity) fluctuations in lotic systems cover wide ranges of temporal and spatial scales, from milliseconds to many years and from sub-millimetres to tens of kilometres. The amplitude of velocity fluctuations typically increases with period and wavelength (i.e., with the scale). This dependence can be conveniently summarised using velocity spectra showing how the energy of fluctuations is distributed across the scales[2] (Fig. 1). The low frequency (large periods) range in the frequency spectrum is formed by intra-annual and inter-annual hydrological variability while the high-frequency (small periods) range is formed by flow turbulence (Fig. 1a). The low wave-number (large spatial scale) range in the wave-number spectrum is formed by morphological variability along the flow such as bars and/or meanders (Fig. 1b). At small spatial scales (comparable to and less than the flow width) velocity fluctuations are due to turbulence.

Depending on the scale of consideration, the described flow variability affects ecosystem structure and function differently. The survey of publications shows that among the scale ranges in Fig. 1, research on the effects of hydrological and geomorphologic variability on lotic ecosystems is a lot more extensive than studies of the turbulence range effects, although they are much more relevant to the organisms. There are at least three reasons for such unevenness in the current knowledge. First, flow and organism measurements at small scales still represent major challenges and data related to this scale range remain very scarce. Second, the biomechanical properties of lotic organisms are still a missing dimension in studies of flow-organism interactions making data interpretation and conceptualisations vague. Third (and probably most important), the subject of small-scale flow-organism interactions lies on the borders between fluid mechanics, ecology, and biomechanics, i.e., at the discipline interfaces which are typically avoided by researchers. As a result, the progress in studies of small-scale flow-biota interactions is slow and a solid unifying interdisciplinary platform is urgently required to accelerate it and to supplement mainstream ecological concepts such as the habitat templet theory. Fifteen years ago a prominent lotic ecologist B. Statzner, a pioneer of hydraulics implementation in lotic ecology, stressed that "*a broader incorporation of aspects of fluid dynamics into studies of various ecosystems will advance general ecological theory faster than past or current research routes, which largely ignore(d) the physical principles of moving air or water*"[1]. Today's situation is not much different[3], highlighting the urgency of a truly interdisciplinary approach which can be defined as *Hydrodynamics of Aquatic Ecosystems*. This emerged research area can be formally defined as a *study of flow-organism interactions with particular focus on relevant transport processes and mutual physical impacts occurring in a range of scales from the sub-organism scale to the organism patch mosaic scale (comparable to flow width)*. The appearance of word "*Hydrodynamics*" is due to the fact that flowing water is the environment where ecological, hydrodynamic, and biomechanical processes occur and are interlinked. This paper highlights some key concepts and hypotheses of *Hydrodynamics of Aquatic Ecosystems* that may be useful in studying flow-biota interactions at multiple scales.

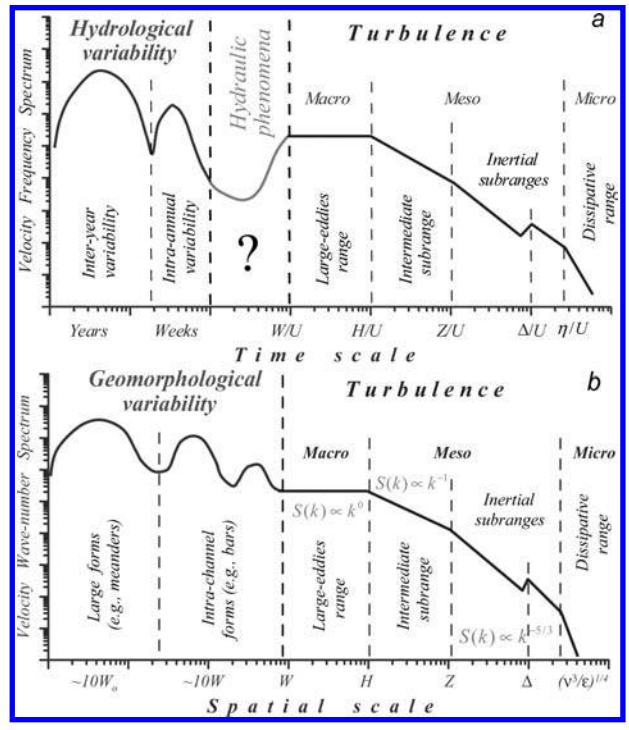


Figure 1. Schematised velocity spectra in rivers: (a) frequency spectrum; and (b) wave-number spectrum ($W_o$ and $W$ = river valley and river channel widths, $H$ = depth, $Z$ = distance from the bed, $\Delta$ = roughness height, $U$ = flow velocity, $\eta$ = turbulence micro-scale.

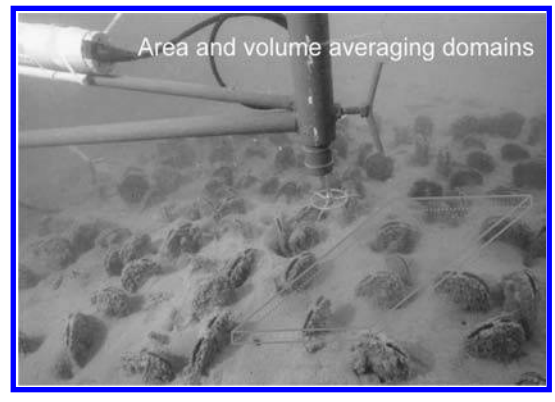


Figure 2. An example of the spatial averaging volume that includes mussels.

## 2 CONCEPTS AND HYPOTHESES OF HYDRODYNAMICS OF AQUATIC ECOSYSTEMS

### 2.1 *Unifying framework*

Physical interactions and ecologically relevant mass-transfer processes occur in a wide range of scales and depend on how physical scales match biological scales such as organism dimensions, patch/community dimensions, life cycles, and others. This multi-scale property together with the physical and biological complexity of boundary conditions in aquatic ecosystems highlight a need for an appropriate unifying framework that would serve for flow-biota coupling and integration (i.e., up-scaling) of physical interactions and mass-transfer processes. It is feasible that the unifying framework should be (1) quantitative by nature; (2) capable of coupling fluid mechanical, ecological, and biomechanical processes in a reasonably rigorous way; (3) a convenient and rigorous tool for upscaling small-scale flow-organism interactions to a larger scale (e.g., from the organism scale to patch or patch mosaic scale); (4) suitable as a basis for mathematical modelling and computer simulations; and (5) appropriate for guiding field and laboratory studies and data interpretation and generalisation. A promising approach for such a framework can be based on spatially averaged (but instantaneous in time domain) hydrodynamic, transport, and biomechanical equations, which couple flow and organisms together through a rigorous spatial averaging operation (over local volume or area in the plane parallel to the mean bed surface, Fig. 2). Such spatially averaged equations can be formulated for both fluid (considering organisms as embedded media) and organisms (considering fluid as embedded media), which are coupled through interface terms covering physical interactions and/or exchange of substances (e.g., the same term describing transport of nutrients through organisms' surface will be included in both 'flow' and 'organism' equations, but with opposite signs). The spatially-averaged instantaneous equations can be additionally time-averaged to produce the double-averaged (in time and space) equations, often defined as the 'double-averaging' methodology (DAM)[4,5]. The spatial averaging methodology allows scale decomposition (or separation of scales) and can be viewed as a scaling-up procedure that changes the scale of consideration from one level in time-space-probability domain to another level. In other words, this methodology provides a

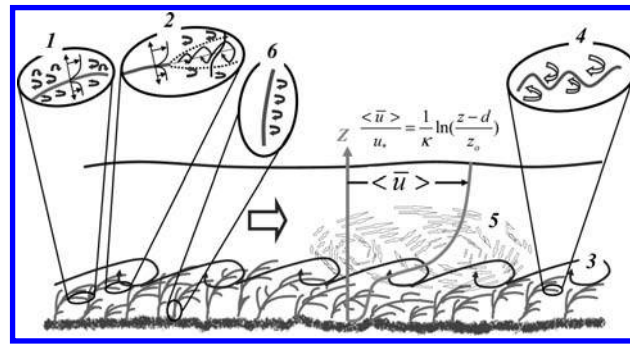


Figure 3. Hypothesised flow patterns for the case of vascular plants as an example (with a boundary layer above the canopy where the log velocity distribution may occur as shown on the sketch; overbar defines time averaging while angular brackets define spatial averaging; $u_*$ is shear velocity, $d$ is displacement height, and $z_o$ is roughness length)[6].

natural way for up-scaling, i.e., integrating small-scale biophysical processes into large-scale behaviour, and thus may serve as a unifying framework in flow-biota studies.

### 2.2 *Hypotheses*

Based on recent studies, *the primary hypothesis* of flow-organism interactions can be formulated as: *organism functioning, morphology, and role in lotic ecosystems are largely driven by the interplay of two key groups of environmental processes: (i) physical interactions between flow and organisms (e.g., due to flow-induced forces and reaction forces generated by organisms); and (ii) ecologically relevant mass-transfer-uptake processes, (e.g., due to molecular/turbulent diffusion), including photosynthesis aspects when relevant.* It is very likely that lotic organisms have evolutionarily adjusted to flow in such a way that these two groups of processes have become closely interrelated and optimised to enhance the overall organism performance/fitness. Of course, there is a number of other important external factors affecting organism life such as water temperature and chemistry, concentration of nutrients, suspended sediments, interactions with other aquatic organisms, and many others. They often can be considered as background conditions which in general, however, may alter the character of the hydrodynamic effects in flow-organism interactions. This *primary hypothesis* leads to a number of secondary hypotheses three of which are outlined below as examples.

*Secondary hypothesis #1: Within a wide range of scales* (*from the sub-organism scale to the patch mosaic scale comparable to the lateral flow size*) *there are distinct characteristic scales where flow-organism interactions and transport processes are scale-specific and interconnected. There are at least four such characteristic scales: sub-organism scale, organism scale, patch scale, and patch mosaic scale.* The data suggest that the strength of interaction between the scales diminishes with increase in scale separation, although there may be certain long-range correlations between the scales.

*Secondary hypothesis #2: To enhance adaptation to lotic environment, the organisms effectively control and optimise hydrodynamic drag forces at multiple scales by adjusting shape, flexibility, and flow itself.* In lotic systems, benthic organisms encounter substantial drag forces, which can be largely considered as the superposition of two components: skin friction at the water-organism interfaces and form (pressure) drag with associated flow separation. To survive, the organisms can minimise the total drag by utilising at least two approaches: (1) minimising and smoothing the organism surface area (to minimise skin drag); and/or (2) making organisms streamlined and/or flexible to prevent or reduce flow separation by organism reconfiguration (to minimise form drag). *This hypothesis* can be illustrated using aquatic plants as an example. The plants ability to use the first approach is limited by the necessity of having a larger plant surface area to satisfy the requirements for nutrient uptake and photosynthesis. The second approach is much less limited in this respect and thus the total drag acting on plants can be effectively reduced by minimising the form drag. This latter task can be achieved by an appropriate combination of organism geometry and flexibility in such a way that the form drag is suppressed, at least at a scale(s) where it is most significant. The relative magnitudes of the skin drag and form drag may vary across the scales and should also depend on the relative position of the organism within a patch (e.g., a mussel at the patch edge may experience significantly higher drag force compared to a mussel in the middle of the patch).

*Secondary hypothesis #3: To enhance adaptation to lotic environment, the organisms effectively control and optimise transport processes at multiple scales by creating new turbulence-generation mechanisms and modifying existing flow patterns*. Indeed, the turbulence structure within and around the lotic organisms must have some special features and mechanisms reflecting the biophysical interactions at multiple scales. These features may include (Fig. 3): (1) generation of small-scale turbulence within local boundary layers attached to organism surfaces; (2) generation of small-scale turbulence behind thin organism parts (e.g., plant leaves or mussel shells) serving as small 'splitter plates' that generate local leeward mixing layers, with subsequent turbulence production through the Kelvin-Helmholtz instability (most likely occurring when the organism surface roughness differs between sides); (3) patch-height-scale turbulence resulting from the Kelvin-Helmholtz instability at the upper boundary of the organism patch (known as mixing-layer analogy[4,7]); (4) turbulence generation due to organism waviness at a range of scales (if biomechanical properties allow it: e.g., in the case of periphyton, moss, or vascular plants); (5) 'conventional' depth-scale shear-generated turbulence which may be significantly altered by the organisms (e.g., by mussel filtering activity); and (6) generation of small-scale 3D to large-scale 2D turbulence associated with flow separation at organism characteristic scales, including organisms aggregations such as mussel patches and patch mosaics. The importance of particular turbulence-generation mechanism(s) and associated turbulent energy and turbulence scales, as well as the inter-mechanism interactions, should depend on a variety of factors. These include bed topography and substrate, organism shape and biomechanical properties, relative submergence, and many others. Thus, *this hypothesis*, in combination with *previous hypotheses*, suggests that the turbulence structure within, around, and above the organisms and their assemblages may be altered by the organisms in such a way that their performance is enhanced through optimising mass-transfer, drag forces, and, when relevant, light penetration and photosynthesis.

### 2.3 *Concepts*

The combined consideration and tests of the above hypotheses lead to a number of testable concepts which are currently under development in the author's group. For example, the hypotheses outlined in the previous section suggest that the most persistent organism patches (e.g., mussel patches) should maintain intermediate (not too low – not too high) densities, which balance the effects of drag forces and mass-transfer-uptake processes (and photosynthesis when relevant). Indeed, with increase in organism patch density from low to high values, the mean total drag acting on individual organisms will reduce from undesirable large values at low density to favourable small values at high density. This positive trend, however, occurs simultaneously with a negative trend in mass-transfer (and light penetration when relevant), which changes from favourable large values at low density to adverse small values at high density. The interplay between these two contradicting trends should lead to *a self-regulation mechanism that controls organism density (number) within a patch*. Using Fig. 3 as an illustration, we highlight mixing layer eddies (3) as one of such self-regulation mechanisms that may control mass-transfer and drag forces in the organism 'canopies'. Responding to changing flow conditions, organism aggregations can regulate the depth of penetration of large mixing layer eddies into 'canopies' by controlling interrelationships between organism density, geometry (morphology), and 'canopy' height. The organisms may either maximise this penetration to secure full access to nutrients and oxygen or, in some circumstances, the depth of penetration may also be reduced to decrease sediment re-suspension within canopies and/or reduce drag forces. Thus, it is quite likely that the organisms 'canopies' not only create mixing layers at their tops (Fig. 3) but also control them through a self-regulation mechanism involving organism density, geometry and height. The described concept can be defined as *the intermediate patch density concept*. Similar concepts may also be considered and tested for a patch mosaic scale[6].

## 3 CONCLUSIONS

The establishment of a new research area *Hydrodynamics of Aquatic Ecosystems* should eliminate multiple knowledge gaps at the borders between fluid mechanics, ecology and biomechanics, i.e., areas where probability of new discoveries is the highest. The *Hydrodynamics of Aquatic Ecosystems* will provide a missing research platform that will 'synchronise' and enhance flow-biota studies in aquatic ecology. It will also provide a solid biophysical basis for eco-hydraulics which has been formed as an applied research area based on largely empirical or semi-empirical approaches. *Hydrodynamics of Aquatic Ecosystems* promises not only step changes in current understanding of our aquatic environments but also responds to the growing demands for advanced knowledge in numerous applications, including civil and environmental engineering, resource management, aquaculture, and bio-security.

## ACKNOWLEDGEMENT

The author is grateful for collaboration and stimulating discussions of flow-biota interactions to I. Albayrak, J. Aberle, B. Biggs, S. Coleman, A. Dittrich, J. Finnigan, D. Goring, D. Hart, C. Howard-Williams, I. Jowett, N. Lamouroux, S. Larned, A. Marion, S. McLean, O. Miler, N. Nikora, M. O'Hare, G. Parker, S. Rice, T. Riis, M. Righetti, P. Rowinski, P. Sagnes, B. Statzner, A. Sukhodolov, A. Suren, and S. Thrush. The work was partly supported by the Leverhulme Trust, Grant F/00 152/Z "Biophysics of flow-plants interactions in aquatic systems".

## REFERENCES

[1] Statzner, B., Borchardt, D. (1994), "Longitudinal patterns and processes along streams: modelling ecological responses to physical gradients." In: Aquatic Ecology: Scale, Pattern, and Process. Eds. P.S. Giller, A.G. Hildrew, D.G. Raffaelli. Blackwell Scientific Publications, Oxford, pp. 113–140.

[2] Nikora, V. (2008), "Hydrodynamics of gravel-bed rivers: scale issues." In: Developments in Earth Surface Processes, v. 11, Gravel-Bed Rivers – VI, H. Habersack, H. Piegay, M. Rinaldi, eds., Springer, pp. 61–81.

[3] Statzner, B. (2008), "How views about flow adaptations of benthic stream invertebrates changed over the last century." Intern. Rev. Hydrobiol., Vol. 93, pp. 593–605.

[4] Finnigan, J. J. (2000), "Turbulence in plant canopies." Annu. Rev. Fluid. Mech., Vol. 32, pp. 519–571.

[5] Nikora, V., McEwan, I., McLean, S., Coleman, S., Pokrajac, D., Walters, R. (2007), "Double averaging concept for rough-bed open-channel and overland flows: Theoretical background." J. Hydraul. Eng., ASCE, Vol. 133(8), pp. 873–883.

[6] Nikora, V. 2009. Hydrodynamics of aquatic ecosystems: an interface between ecology, biomechanics and environmental fluid mechanics. River Research and Applications (accepted).

[7] Nepf, H,M, Ghisalberti, M. (2008), "Flow and transport in channels with submerged vegetation." Acta Geophysica, Vol. 56(3), pp. 753–777.

*Mathematical and numerical modeling of environmental fluid mechanics problems*

*Environmental Hydraulics – López-Jiménez et al (eds)*
*© 2010 Taylor & Francis Group, London, ISBN 978-0-415-56697-1*

# Development of a simplified model to solve 2D surface flow in basins

D. López-Barrera, P. García-Navarro, J. Burguete & P. Brufau
*Fluid Mechanics, University of Zaragoza C.P.S., Zaragoza, Spain*

ABSTRACT: A distributed numerical model of hydraulic processes based on a kinematic-wave approximation of the shallow water equations is presented in this work. The development of suitable connected hydrological-hydraulic models can be a tool to achieve a plan of integral management of basins from the point of view of water resources.

The kinematic-wave model application range has been extended to real cases via the local addition of diffusion. The numerical model is designed to be quick, robust and to depend on few parameters with physical meaning.

The model has been discretized explicitly for quadrilateral meshes by means of a first order upwind scheme with entropy correction. The stability limits of the numerical scheme have been analyzed to achieve a variable time step of the hydraulic model.

Finally the model has been validated in different test cases.

*Keywords*: Kinematic wave model, Diffusive wave model, finite volumes, upwind schemes.

## 1 INTRODUCTION

The two dimensional kinematic wave (KW) and the two dimensional diffusive wave (DW) approximations have been used extensively to calculate the surface component of the water flow in hydrological problems due to the advantages they offer in terms of computational time with respect to the complete Saint-Venant model[1,2,3,4,5].

The KW model presents a set of advantages when compared with the DW model but also restrictions in the applicability to real problems. In zero or adverse bed slopes the KW is unable to simulate correctly the problem. The range of application of the KW model can be extended by a local switching to the DW model. That extended range KW model will be denoted as Extended Kinematic Wave model (EKW).

In this work, the EKW model has been discretized using a finite volume explicit upwind scheme developed for quadrilateral meshes with entropy correction. The numerical scheme stability condition has been analyzed and the time step is chosen to guarantee the model stability.

The use of this kind of tools in complex situations may lead to different numerical problems. For this reason it is essential to study the behaviour of the numerical method in the situations in which exact solutions exist, even though they are far from real cases. A set of test cases with exact solution is presented to validate the model used.

## 2 THE EXTENDED KINEMATIC-WAVE MODEL (EKW)

Both the KW and DW models can be represented by equation:

$$\frac{\partial h}{\partial t} + \nabla q = \frac{\partial h}{\partial t} + \nabla \frac{h^{5/3}}{n\sqrt{|S|}} S = 0 \tag{1}$$

being $h$ the water depth, $n$ the Manning roughness coefficient, $\mathbf{q}$ the discharge and $S = (S_x, S_y)$ the slope defined as:

$$S_x = \frac{\partial (z_b + mh)}{\partial x} \qquad S_y = \frac{\partial (z_b + mh)}{\partial y} \tag{2}$$

with $z_b$ the magnitude that describes the terrain topography elevation and $m$ a parameter ($0 \le m \le 1$). When $m = 0$ the KW model is recovered, when $m = 1$ equation (2) represents the DW model[6].

## 3 DISCRETIZATION OF THE EQUATIONS

A finite volume scheme has been chosen to discretize the equation. It is a first order in space and time upwind scheme applied to a squared finite volume $\Omega_{i,j}$. Then, denoting cell edges as $(i+1/2,\ j)$, $(i-1/2,\ j)$, $(i,\ j+1/2)$ and $(i,\ j-1/2)$:

$$h_{i,j}^{n+1} = h_{i,j}^{n} - \frac{\Delta t}{\Delta x \Delta y} \left(\delta q_x^n\right)^+_{i\ 1/2,j} \Delta x + \left(\delta q_x^n\right)_{i+1/2,j} \Delta x + \left(\delta q_y^n\right)^+_{i,j\ 1/2} \Delta y + \left(\delta q_y^n\right)_{i,j+1/2} \Delta y \tag{3}$$

with $\Delta x$, $\Delta y$ the length of the edges and

$$\left(\delta q_x^n\right)_{i+1/2,j}^{+} = \frac{1+\mathrm{sign}\left(\left(\lambda_x^n\right)_{i+1/2,j}\right)}{2}\left[\left(q_x^l\right)_{i+1,j}^n \quad \left(q_x^l\right)_{i,j}^n\right] \qquad \left(\delta q_x^n\right)_{i+1/2,j} = \frac{1 \quad \mathrm{sign}\left(\left(\lambda_x^n\right)_{i+1/2,j}\right)}{2}\left[\left(q_x^r\right)_{i+1,j}^n \quad \left(q_x^r\right)_{i,j}^n\right]$$

$$\left(\delta q_y^n\right)_{i,j+1/2}^{+} = \frac{1+\mathrm{sign}\ \left(\lambda_y^n\right)_{i,j+1/2}}{2}\ \left(q_y^t\right)_{i,j+1}^n \quad \left(q_y^t\right)_{i,j}^n \qquad \left(\delta q_y^n\right)_{i,j+1/2} = \frac{1\ \ \mathrm{sign}\ \left(\lambda_y^n\right)_{i,j+1/2}}{2}\ \left(q_y^b\right)_{i,j+1}^n \quad \left(q_y^b\right)_{i,j}^n \tag{4}$$

where:

$$\left(q_x^l\right)_{i,j} = \frac{h_{i,j}^{5/3}\left(S_x\right)_{i\ 1/2,j}}{n_{i,j}\sqrt{|S|}_{j\ 1/2,j}} \qquad \left(q_x^r\right)_{i,j} = \frac{h_{i,j}^{5/3}\left(S_x\right)_{i+1/2,j}}{n_{i,j}\sqrt{|S|}_{j+1/2,j}}$$

$$\left(q_y^b\right)_{i,j} = \frac{h_{i,j}^{5/3}\left(S_y\right)_{i,j\ 1/2}}{n_{i,j}\sqrt{|S|}_{i,j\ 1/2}} \qquad \left(q_y^t\right)_{i,j} = \frac{h_{i,j}^{5/3}\left(S_y\right)_{i,j+1/2}}{n_{i,j}\sqrt{|S|}_{i,j+1/2}} \tag{5}$$

The superindex $n$ and $n+1$ represent the value of the variables at times $t$ and $t+\Delta t$ respectively being $\Delta t$ the discrete time step. $\lambda$ is the advection velocity defined as:

$$\lambda = \left(\lambda_x, \lambda_y\right) = \frac{\partial q_x}{\partial h}, \quad (6) \approx \frac{5h^{2/3}S_x}{3n\sqrt{|S|}}, \frac{5h^{2/3}S_y}{3n\sqrt{|S|}} \tag{6}$$

where the value $h$ and $n$ are evaluated at the edge and calculated as the mean value of $h$ and $n$ across the edge. In the case of the KW model equation (6) is exact.

As will be shown in section 4 to guarantee the stability of this method applied to the DW model it is not enough to satisfy the Courant-Friedrich-Lewy condition[7] $\Delta t_i = \mathrm{CFL}\frac{\Delta x}{2\max|\lambda_{x_{i+1/2,j}}|,|\lambda_{y_{i,j+1/2}}|}$ with $CFL \le 1$. For this reason condition (7) is proposed:

$$\Delta t_i = \mathrm{CFL}\ \frac{\Delta x}{2\max\left|\left(\lambda^*_{x\,i+1/2,j}\right)^{+}\right|,\left|\left(\lambda^*_{x\,i+1/2,j}\right)\right|,\left|\ \lambda^*_{y_{i,j+1/2}}\ ^{+}\right|,\left|\ \lambda^*_{y_{i,j+1/2}}\right|} \tag{7}$$

with $CFL \le 1$ where

$$\lambda^*_{y_{i,j+1/2}}\ ^{+} = \frac{1+\mathrm{sign}\ \left(\lambda_y^n\right)_{i,j+1/2}}{2}\frac{\left(q_y^t\right)_{i,j+1}^n \quad \left(q_y^t\right)_{i,j}^n}{h_{i,j+1} \quad h_{i,j}} \qquad \text{if} \quad (h_{i,j+1} \quad h_{i,j}) \neq 0$$

$$\lambda^*_{y_{i,j+1/2}} = \frac{1 \quad \mathrm{sign}\ \left(\lambda_y^n\right)_{i,j+1/2}}{2}\frac{\left(q_y^b\right)_{i,j+1}^n \quad \left(q_y^b\right)_{i,j}^n}{h_{i,j+1} \quad h_{i,j}} \tag{8}$$

$$\lambda^*_{y_{i,j+1/2}}\ ^{\pm} = \left|\frac{5h^{2/3}S_y}{3n\sqrt{|S|}}\ \ 1+\frac{3}{20}\frac{m\pi h|S|^2}{\Delta x S_y}\right|^2 + (2\ \ \sqrt{2})\frac{3}{20}\frac{m\pi h|S|^2}{\Delta x S_y}\Bigg|_{i,j+1/2} \qquad \text{if} \quad (h_{i,j+1} \quad h_{i,j}) = 0$$

To extend the application range of the KW model to more problems a local change on the value of $m$ evaluated at the edge $k$ is proposed:

$$m = 1 \quad \text{if} \quad \left(\delta(z_b + h)\right)_k = 0 \quad \text{or} \quad \frac{\delta z_b}{\delta(z_b+h)}_k \le 0$$

$$m = 0 \quad \text{if} \quad \frac{\delta z_b}{\delta(z_b+h)}_k > 0 \tag{9}$$

### 3.1 *Entropy correction*

Lax[8] introduced the concept of entropy correction as a condition that the numerical schemes must satisfy for the solution to be physically acceptable near sonic points in the context of gas dynamics. In the case of the upwind scheme applied to EKW model there is no entering information in points with a local maximum in the bed level where the slope changes from negative to positive. Then, when the entropy correction is introduced the final scheme is:

$$h_{i,j}^{n+1} = h_{i,j}^n \quad \frac{\Delta t}{\Delta x \Delta y}\ \left(\delta q_x^n\right)_{i\ 1/2,j}^{+}\Delta x + \left(\delta q_x^n\right)_{i+1/2,j}\Delta x + \left(\delta q_y^n\right)_{i,j\ 1/2}^{+}\Delta y + \left(\delta q_y^n\right)_{i,j+1/2}\Delta y$$

$$\frac{\Delta t}{\Delta x \Delta y}\left(\mu_x\left(|q^r| + |q^l|\right)\Delta x + \mu_y\left(|q^t| + |q^b|\right)\Delta y\right)_{i,j}^n \tag{10}$$

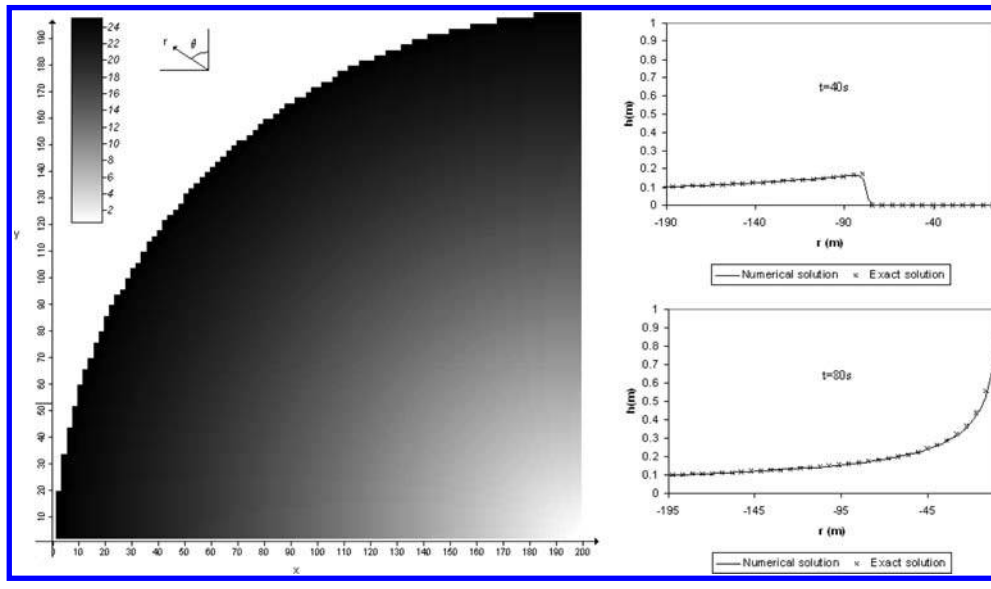


Figure 1. Left: Basin topography. Right: Numerical and exact radial profiles at t = 10s and t = 30s.

where:

$$\mu_{x_{i,j}} = \begin{cases} 1 & \text{if } \operatorname{sign}\left(S_{x_{i\ 1/2,j}}\right) \neq \operatorname{sign}\left(S_{x_{i+1/2,j}}\right) \text{ and } S_{x_{i+1/2,j}} > 0 \\ 0 & \text{if } \operatorname{sign}\left(S_{x_{i\ 1/2,j}}\right) = \operatorname{sign}\left(S_{x_{i+1/2,j}}\right) \text{ or } S_{x_{i+1/2,j}} < 0 \end{cases}$$

$$\mu_{y_{i,j}} = \begin{cases} 1 & \text{if } \operatorname{sign} S_{y_{i,j\ 1/2}} \neq \operatorname{sign} S_{y_{i,j+1/2}} \text{ and } S_{y_{i,j+1/2}} > 0 \\ 0 & \text{if } \operatorname{sign} S_{y_{i,j\ 1/2}} = \operatorname{sign} S_{y_{i,j+1/2}} \text{ or } S_{y_{i,j+1/2}} < 0 \end{cases} \tag{11}$$

## 4 MODEL STABILITY

The explicit EKW stability can be studied via a classical Fourier analysis. For simplicity a pure 1D phenomenon in a uniform mesh is studied. A small sinusoidal perturbation is introduced over a non-perturbed state in a uniform steep plane with slope $S_{0x} = \delta z_b / \Delta x$ in the way $h = h_0 + h_1 e^{ikx}$. Thus the result is that, to guarantee the model stability it must be satisfied the condition:

$$\Delta t \leq \frac{\Delta x}{\dfrac{5h_0^{2/3}\sqrt{S_0}}{3n}\left(1+\dfrac{3}{20}\dfrac{m\pi h_0}{\Delta x S_{0x}}\right)^2 + \left(2\sqrt{2}\right)\dfrac{3}{20}\dfrac{m\pi h_0}{\Delta x S_{0x}}} \tag{12}$$

The solution of equation (7) coincides with (12). Equation (12) shows that, for the same problem, $\Delta t_{max}$ is greater in the case of using the KW ($m = 0$) than in the case of the DW ($m = 1$).

## 5 MODEL VALIDATION

A set of test cases with exact solution has been proposed to check the EKW model discretization. As an example, the case of the wetting front advance over an initially dry impervious circular quadrant shaped basin and the final steady state are presented. The inlet boundary condition is a constant hydrograph $h(t) = 0.1$m and the Manning roughness coefficient is 0.03 s/m$^{1/3}$. Figure 1 left shows the basin topography. figure 1 right shows in the upper side the numerical and exact profiles in radial direction at $t = 40$s and in the lower side the numerical and exact stationary radial profiles.

## ACKNOWLEDGEMENTS

This research has been funded by the D.G.A. (Aragon General Deputation) under research projects no PM088/2006, PI032/08 and budget application 17030 G/5423/480072/91001.

## REFERENCES

[1] Mahmood K. and Yevjevich V. (1975), *Unsteady flow in open channels*, Water Resources Publications, Fort Collins, Colorado.
[2] Yu, D. and Lane, S.N. (2007), "Coupling of a 2d diffusion-based flood inundation model to a 1d river flow for urban flood inundation modelling", *Proceedings of the Congress- IAHR, Conf 32; Vol 1, p. 30.*
[3] Hunter N.M., Horrit M.S., Bates P.D., Wilson M.D. and Werner M.G.F. (2005), "An adaptative time step solution for raster-based storage cell modelling of floodplain inundation", Advances in Water Resources, Vol 28, p. 975–991.

[4] Horrit M.S., and Bates P.D. (2001), “Predicting floodplain inundation: Raster-based modelling versus the finite element approach”, Hydrological Processes 15, p. 825–842.
[5] Luo Q. (2007), “A distributed surface flow model for watersheds with large water bodies and channel loops”, Journal of Hydrology, 337, p. 172–186.
[6] Cunge J.A., Holly Jr F.M. and Verwey A. (1980), *Practical aspects of Computational River Hydraulics*, Pittman Publishing.
[7] Murillo J., García-Navarro P., Burguete J. and Brufau P. (2006) “A conservative 2d model of inundation flow with solute transport over dry bed”, Int. Journal for Numerical Methods in Fluids, vol. 52, issue 10, pp. 1059–1092.
[8] Lax P.D. (1973), *Hyperbolic systems of conservation laws and the mathematical theory of shock waves*. SIAM publications, Philadelphia.

*Environmental Hydraulics – López-Jiménez et al (eds)*
*© 2010 Taylor & Francis Group, London, ISBN 978-0-415-56697-1*

# Optimizing design in open channel

Juan A. Pina, Martin Hidalgo & Dante Bragoni
*Facultad de Ingeniería, Universidad Nacional de Cuyo Centro Universitario, Ciudad de Mendoza, Argentina*

ABSTRACT: The paper develops a review of several mathematic simulations of the original geometry of a partition structure. The partitions structures are one of the most important devices of water management. The project also includes developing the proper hydraulic design that improves the actual working conditions of the partition section. Due to the particular landscape of the region under consideration, supercritical flow conditions take place in the channel as a consequence of high velocities. This problem has a direct influence on the partition structures design to work under subcritical flow conditions. As a result, the channel water level fluctuates and the flow distribution no longer remains proportional to the cross section. Mathematic simulations with a CFD (Computational Fluid Dynamics) program were very important in order to find answers to the hydraulic behavior of the structures under analysis. These simulations were carried out to study the actual structure and the possible solutions.

*Keywords*: Hydraulic Design, Mathematic Simulations, Supercritical Flow.

## 1 INTRODUCTION

The province of Mendoza is located at 33 degrees south and 69 degrees west next to the Andes mountains. Being a desert region with an average 220 ml of rainfall a year, water is a fundamental and precious resource. Therefore, efficient use of water is a major issue.

In order to optimize the water management and improve the operation of the channels, CFD modeling was carried out to analyze and study its hydraulic behavior.

Hydraulic and Structural Engineering of water conductions are the lines of research to which the project is related.

The methodology includes the study and analysis with mathematical simulation modern tools, and develops experimental physical model in the Laboratory of Hydraulics.

## 2 GENERAL CHARACTERISTICS

### 2.1 Geometry

- section upstream the partition: chute section
- section downstream the partition: chute section
- hydraulic regime: supercritical
- channel slope upstream the partition: $>1\%$
- channel slope downstream the partition: $>1\%$
- transition length of chute section to rectangular section: $12.40\,\text{m} + 7.50\,\text{m}$ of rectangular section to the bottom step
- length of rectangular section of the partition: 30,23 m

### 2.2 *Damage in partitions structure*

Because of:

- shear stresses present in the channel walls and floor
- pressure fluctuations in the bottom of the channel

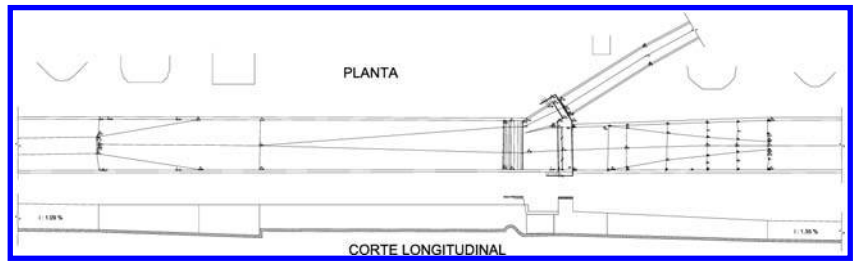


Figure 1. Geometry of the channel.

Figure 2. Upstream view from the partition structure.

Figure 3. View of the partition structure from upstream.

Figure 4. Detail of the turbulence due to the bottom step.

Figure 5. Lateral scour.

Figure 6. Hole aside the bottom step.

Figure 7. Detail of the hole.

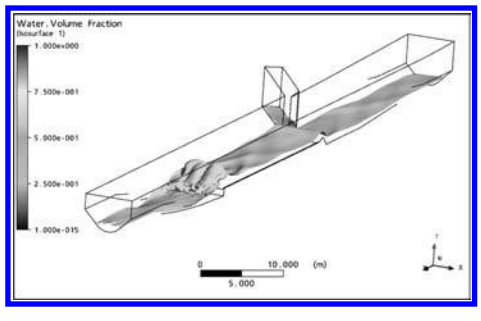


Figure 8. Model 3: Tailwater level.

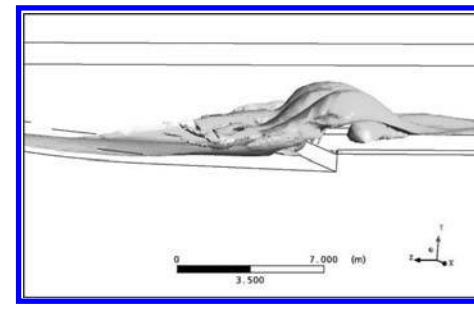


Figure 9. Model 3: Detail of the bottom step.

## 3 MATHEMATICAL SIMULATION

### 3.1 *Analyze models*

To carry out the mathematic simulation, the following cases were studied:

- Model 1: discharge = 11,25 $m^3/s$
- Model 2: discharge = 22,5 $m^3/s$
- Model 3: discharge = 26 $m^3/s$
- Model 4: discharge = 45 $m^3/s$

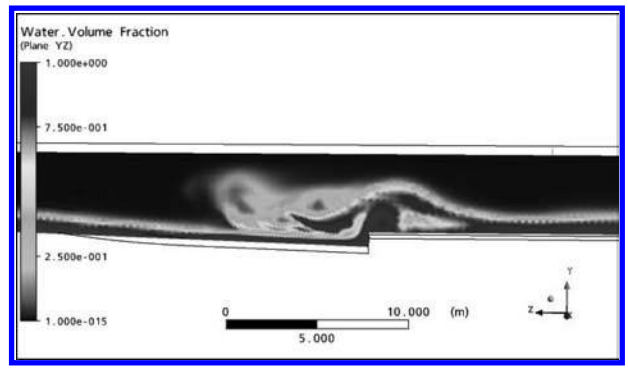


Figure 10. Model 3: Detail of the bottom step.

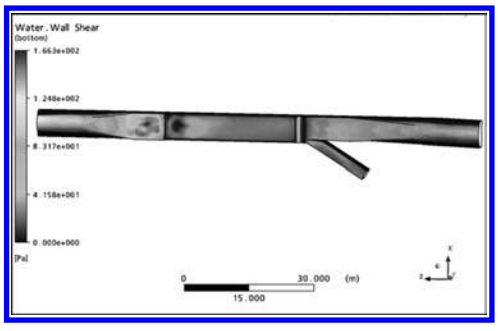


Figure 11. Model 3: Shear stresses.

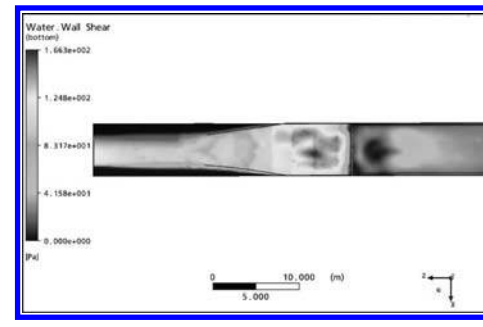


Figure 12. Model 3: Detail of the bottom step.

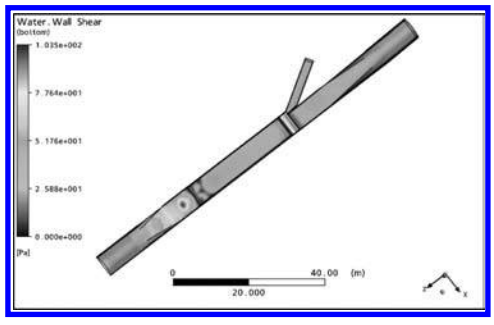


Figure 13. Model 4: Shear stresses.

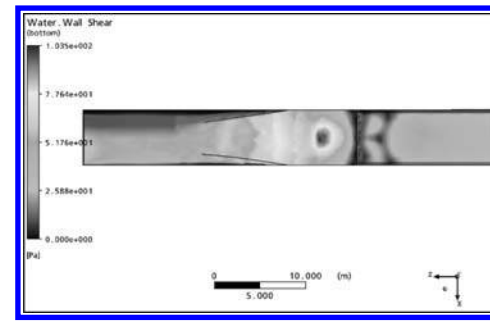


Figure 14. Model 3: Detail of the bottom step.

### 3.2 *Obtained results*

- Tailwater level
- Shear stresses at the bottom of the channel

## 4 CONCLUSIONS

- CFD allowed modeling the water behavior in the channel and the partition in a very precise way, accurately representing the physical problems present in the real structure.
- CFD allowed an improvement in the design process carried out to solve the problems that come to light during the analysis phase of the project. all in all, the whole process was more agile enabling to try different solution proposals in considerably short periods of time.

## REFERENCES

[1] Ansys Corporation (2007), *Theory Reference*, Ansys User Manual, USA
[2] Ansys Corporation (2007), Documentation *for ANSYS Workbench*, Ansys User Manual, USA
[3] Ansys Corporation (2007), *Documentation for ANSYS ICEM CFD*, Ansys User Manual, USA
[4] Ansys Corporation (2007), *Documentation for ANSYS CFX*, Ansys User Manual, USA
[5] Blevins, R., (1984), *Applied Fluid Dynamics Handbook*. Ed. Van Nostrand Reinhold Co. New York
[6] Escribá Bonafe, D., (1988), *Hidráulica para Ingenieros*, Librería Editorial Bellisco. Madrid
[7] Rouse, H., (1950), *Engineering Hydraulics*, Ed. John Wiley & Sons. New York
[8] Rouse, H., (1960), *Hidráulica – Mecánica Elemental de Fluidos*, Ed. Dossat. Madrid
[9] Sturm, T., (1981), *Open Channels Hydraulics*, Ed Mac Graw Hill. New York
[10] Chow, V.T., (1983), *Hidráulica de los Canales Abiertos*, Editorial Diana. Mexico

*Environmental Hydraulics – López-Jiménez et al (eds)*
*© 2010 Taylor & Francis Group, London, ISBN 978-0-415-56697-1*

# Numerical simulation of flow in the bifurcation of the Mezcalapa River

J.A. Sánchez-Muñoz, W. Vicente-Rodríguez, M. Salinas-Vázquez,
J. Osnaya-Romero, J. Gracia-Sánchez & E. Carrizosa-Elizondo
*Instituto de Ingeniería, Universidad Nacional Autónoma de México, México D.F., México*

ABSTRACT: Computational model is used in this work in order to review and predict the behavior of the flow in bifurcation of Mezcalapa River. This bifurcation is formed by Carrizal River and Samaria River. This approximation can help to calculate the flow distribution. The geometry, represented by the bathymetry, is simulated with a Cartesian grid through a cut cell method.

The numerical simulation is carried out with an alternative of Reynolds averaged Navier-Stokes equations. The transport equations that govern the movement of the flow are solved by means of a finite volume method. The turbulence is represented by the standard k-e. model. Predictions of flow at outlet are compared with experimental data.

*Keywords*: Computational Fluids Dynamic, Bifurcation, flow, river.

## 1 INTRODUCTION

Tabasco, a Mexican state, is located in the Southeast of the country and contains several important hydrographic regions. Therefore, it discharges to Gulf of Mexico about 125 millions cubic meters of water, which represents 35% of the total discharge of the country.

One of these hydrographic regions is the Grijalva-Usumacinta zone, which contains to Mezcalapa River and it is divided in two branches called Carrizal River and Samaria River.

In the last few years the distribution of the flow in Mezcalapa River has been changing, so that the flow captured by the Carrizal has changed too. This has caused that Villahermosa, the main city of Tabasco, suffer floods.

In order to give a solution to this problem the Institute of Engineering from UNAM has proposed to build a physical model, Osnaya et al. (2007)[1], and a numerical model with the intention to know the behavior of river flow in this region.

This numerical simulation use the Cut cell method, which consists in overlapping a Cartesian grid with a complex geometry created by specialized software, in this way the computational domain has three kinds of cells, solid cells which obstruct the flow of the fluid, cells of fluid, and cut-cells which obstruct partially the flow.

For this simulation the transport equations are solved using the finite volume method and the turbulence convection term is closed via k-e standard model.

## 2 CONFIGURATION OF THE SIMULATION

The computational domain includes 1800 m upstream of the bifurcation, this region represents Mezcalapa River and 4200 m downstream of the bifurcation that represents Carrizal River and Samaria, figure 1.

At the inlet, the flow has a speed of 0.9496 [m/s] and a water depth of 6.0 [m]. This condition produces a flow rate of 3300 [$m^3$/s] at the Mezcalapa River. Figure 2 shows a configuration of domain to study.

## 3 NUMERICAL MODEL

The hydrodynamics is modeled after solving the averaged transport equations of continuity and momentum by the finite volume method. The system is closed via model of turbulence. This work uses standard k-$\varepsilon$ model, (Launder (1974) y Jones (1972)[2].

In order to solve the coupling between pressure and velocity is used SIMPLE algorithm[3].

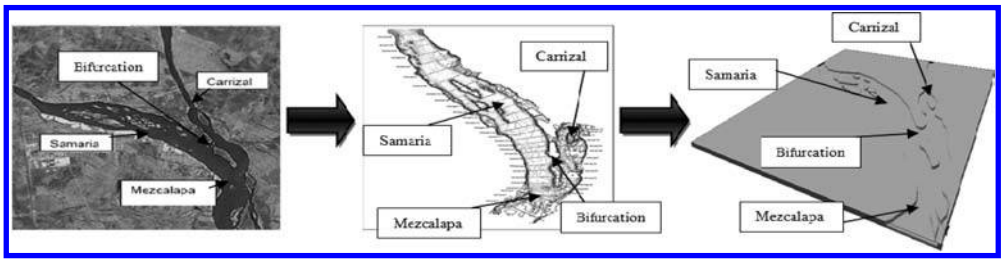


Figure 1. The left figure shows a picture of the bifurcation, the middle figure shows the digitization of the bathymetry in *Autocad* ® and the figure on the right shows the three-dimensional model created by *SolidEdge* ®.

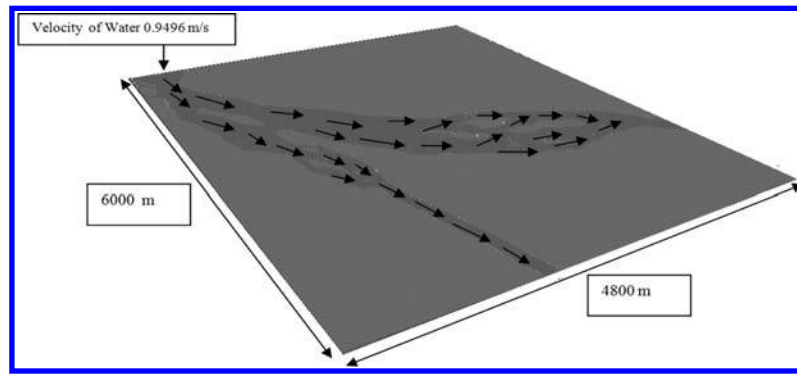


Figure 2. Configuration of the simulation.

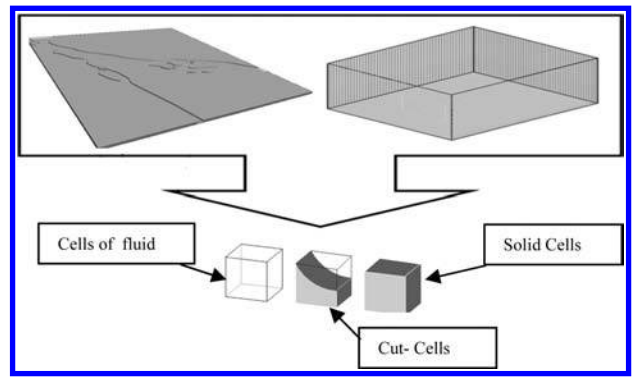


Figure 3. Method ASAP. The overlap between Cartesian grids with a complex geometry creates three kinds of cells, fluid cells, solid cells and Cut-cells.

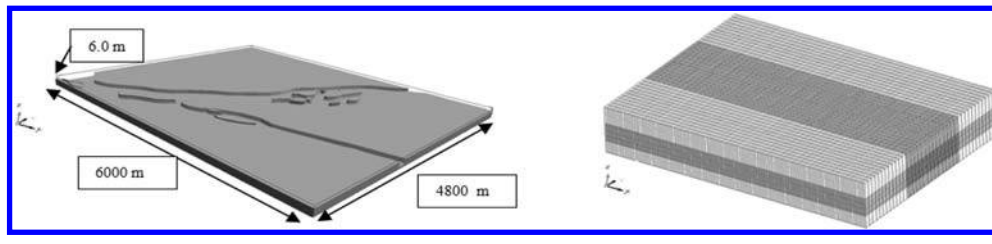


Figure 4. Dimensions of the complex geometry created by SolidEdge ®and the discretization used.

The ASAP method (Arbitrary Source Allocation Procedure)[4], a cut-cell method, uses a Cartesian grid with an internal border, which is generally a solid body with a complex geometry. Cells inside the complex geometry obstruct the flow through them. All the advantages of using a Cartesian grid are conserved for cells outside of the body, where the fluid flows. Cells partly free, with one part inside the body need special treatment. In the case of the finite volume method, the intersections are determined between the mesh and the body, in this way the free volumes are obtained. For these cells the transport equations are modified by source terms that are related to different kinds of interpolations, figure 3.

In this work bodies with complex geometry, like a bathymetry, are made by AutoCAD ® and SolidEdge ®. In Figure 4 shows the body obtained by SolidEdge ® and the mesh where the hydrodynamics was solved numerically.

## 4 NUMERICAL DETAILS

The computational domain has in the direction of x axis a length of 6000 [m], in the direction of the y axis a length of 4800 [m] and the direction of the z axis a length of 6.0 [m]. This method uses a discretization of $300 \times 300 \times 6$ that is showed in the figure 4. A larger number of cells were used to verify the mesh independence.

## 5 RESULTS

This section presents the results for the numerical simulation of the behavior of the flow in the bifurcation of the Mezcalapa River. The magnitudes of velocity increased in zones where the cross sectional area decreases, figure 5.

The Figure 6 shows the distribution of the flow for the Carrizal River that represents 27% of the flow of the Mezcalapa River. This means, with an outflow of 3300 m3/s on the Mezcalapa River, 891 m3/s are received for the Carrizal River. This information is important because in this way is possible to design appropriate hydraulic structures, capable to control the flow that cross Villahermosa.

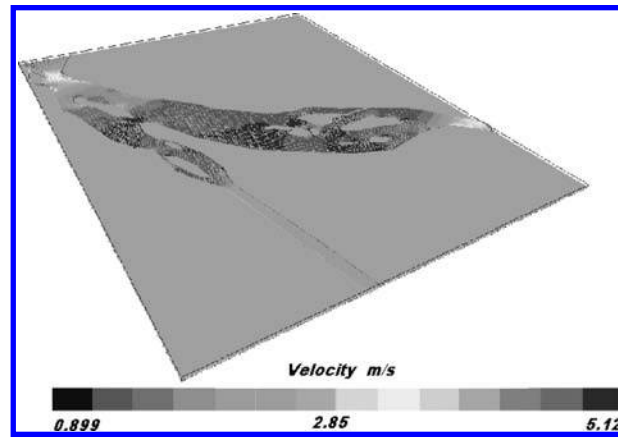


Figure 5. Velocity fields.

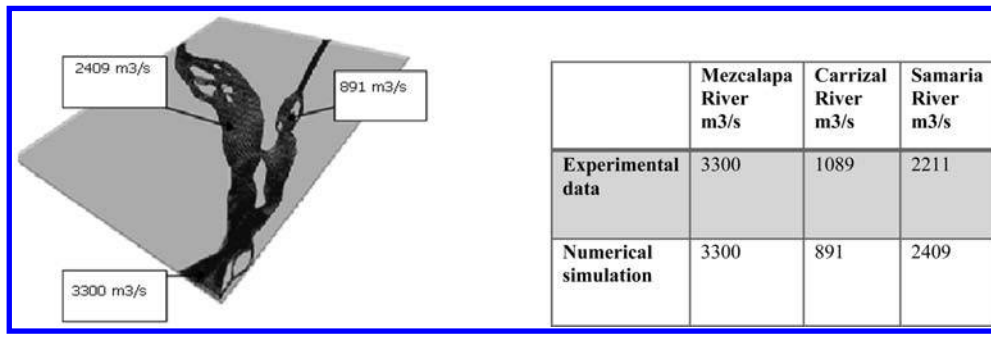


| | Mezcalapa River m3/s | Carrizal River m3/s | Samaria River m3/s |
|---|---|---|---|
| **Experimental data** | 3300 | 1089 | 2211 |
| **Numerical simulation** | 3300 | 891 | 2409 |

Figure 6. Flow distribution in the bifurcation for the numerical simulation and a comparative table with measurements taken in 1999 on Mezcalapa River.

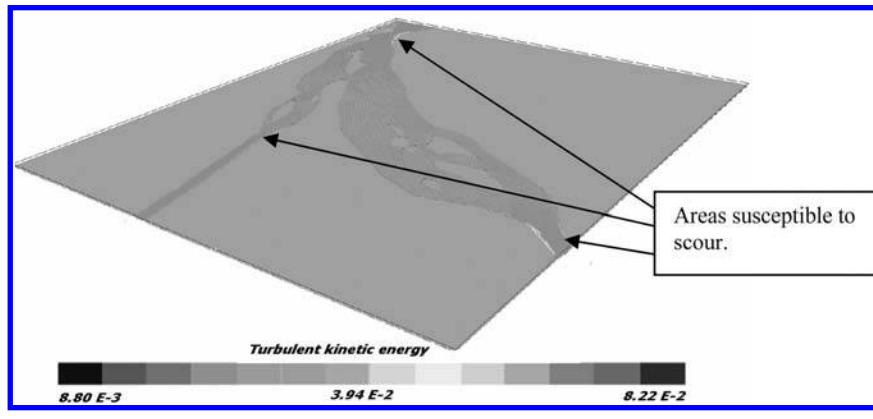


Figure 7. Turbulent kinetic energy.

Also the Figure 6 shows measurements taken in 1999 on Mezcalapa River[5], where flow is similar. The percentage received in the Carrizal River from Mezcalapa River is 33%. The results obtained in the numerical simulation show that just 27% of the total flow of Mezcalapa River is received for the Carrizal River. That means a good approximation.

Another important magnitude in drag and sediment transport is the turbulent kinetic energy, figure 7. This energy is generated by changing the flow velocity. This behavior occurs mainly where the flow undergoes abrupt changes of direction. It is important to know these areas because they are susceptible to scour.

## 6 CONCLUSIONS

The numerical model can allow a detailed study of the flow in order to evaluate the distribution in the bifurcation of the Mezcalapa River, in this way is possible to help to design appropriate hydraulic structures that can control the flow that cross Villahermosa. It is important to do more numerical simulations by changing the flow on the river Mezcalapa, in order to have more information about the behavior of the flow at the bifurcation.

This model can help to know the areas with important changes in turbulent kinetic energy, this with the intention to know areas susceptible to scour.

The advantage of this model lies in its versatility to use complex geometries applied in Cartesian mesh, which will impact on computation time and ease of convergence of the numerical method.

REFERENCES

[1] Osnaya R J (2007), “Revisión en modelo físico, del cierre de la estructura de control sobre el río Carrizal, Tabasco”, Informe del Instituto de Ingeniería para la CNA, 25pp, noviembre 2007.
[2] Launder B.E. and Spalding D.B. (1974), “The Numerical Computation of Turbulent Flows” *Comp. Meth. Appl. Mech. Eng*., 3:269:289
[3] Patankar, S.V. and Spalding, D.B. (1972). A Calculation Procedure for Heat, Mass and Momentum Transfer in Three Dimensional Parabolic Flows. Intern. J. of Heat and Mass Transf., 15:1787.
[4] Ji H. et al. (2006), “An Efficient Second-Order Accurate Cut-Cell Method for Solving the Variable Coefficient Poisson Equation with Jump Condition on Irregular Domains. *International Journal for Numerical Methods in Fluids*, 52, pp. 723–748
[5] Gracia J. (2007), “Estudio de la bifurcación de un rio con modelación numérica”. Series del Instituto de Ingeniería para la CNA, 47 pp, Marzo. 2007

*Environmental Hydraulics – López-Jiménez et al (eds)*
*© 2010 Taylor & Francis Group, London, ISBN 978-0-415-56697-1*

# Numerical analysis of hydraulic structures on the Carrizal River with computational fluid dynamics

J. Cubos-Ramírez, W. Vicente-Rodríguez, M. Salinas-Vázquez, J. Gracia-Sánchez,
J. Osnaya-Romero & E. Carrizosa-Elizondo
*Instituto de Ingeniería, Universidad Nacional Autónoma de México, México*

ABSTRACT: A Computational Fluid Dynamic (CFD) model is used to simulate the flow in a short reach of the Carrizal River influenced by a hydraulic structure that includes a channel with discharge controlled by three radial gates on the left bank of the river and a spillway channel on the right, built in order to control the outflow in this river. Strong spatial variability of the velocity and turbulent kinetic energy fields demonstrated the necessity of three-dimensional model approach under such fluvial conditions. So the hydrodynamic is modeled after solving transport equations for mass conservation and momentum conservation averaged over time (Reynolds averaged) by the finite volume method. The system is closed with a k-$\varepsilon$ turbulent model. The numerical predictions were compared with experimental data in order to validate the turbulence model in term of velocities and outflow discharged at each channel.

*Keywords*: CFD, hydraulic structure, outflow, turbulence, river.

## 1 INTRODUCTION

In recent years a river work have been built in order to make possible the water control in areas close to populations such as Villahermosa city of the southeastern of Mexico (Figure 1). In 2004, a study was exhibited a first scale model of the hydraulic structure over the "Carrizal" [4]. However, after largest flood in Tabasco history occurred in 2007 the need for a more complex hydraulic design in the area is crucial. While the study in scale models of hydraulic structures is essential, the use of numerical models is a necessary practice in the modern hydraulic technology; in addition, this kind of models is an inexpensive way that offers the ability to assess the response of hydraulic systems against a variety of practical situations. The scale models of hydraulic structures allow more flow info, shorter study times and easy handling of results. For these reasons, this work presents an alternative design of hydraulic structures, based on computational fluid dynamics (CFD).

## 2 THEORY

Usually hydraulic structures design is made with one-dimensional and two-dimensional mathematical models, based on theoretical assumptions and empirical factors widely recommended in the bibliography literature [5] with good approximations. However, because of the water flow in these structures is three-dimensional; it is always recommended that any design of a hydraulic project of this magnitude should be revised with a scale model.

In laboratory conditions free surface flows are in general investigated on hydraulic scale models based on the Froude-law, which takes inertia and gravity forces into account. However, this approach cannot take into account the effects of viscous, also flow features related to turbulence play a significant role for example in sediment transport processes, such models cannot describe correctly these phenomena. On the other hand, numerical flow models supplied with high level turbulence closure modules do not need to be scaled, what means that these models can handle domains in their original extensions, as one of the clear advantages of such CFD models.

The CFD solver used in this study is the CFD code called PHOENICS[7]. It solves the Reynolds-averaged Navier-Stokes equations[2] with the two equation $k$-$\varepsilon$ turbulence closure[1] in three space dimensions to compute the water flow using the finite volume approach as discretization method and the alternative "cut-cell" in order to generate the mesh. The governing equations are solved in a finite volume context by pressure using the SIMPLE algorithm[3] on a three-dimensional, structured grid.

## 3 CASE STUDY

### 3.1 *Experimental configuration*

The simulated experimental configuration includes a section of the Carrizal River (Figure 1). This section is located at the starting point of the rivers Carrizal and Samaria, on the border between Chiapas and Tabasco.

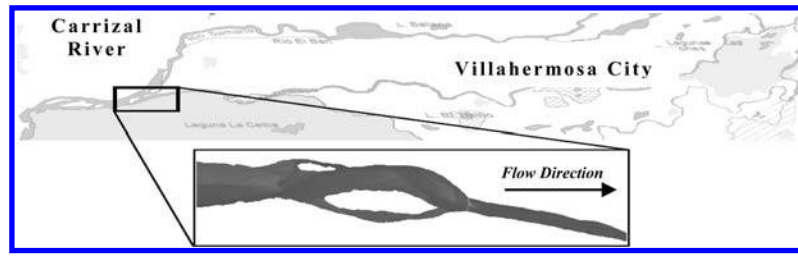


Figure 1. Study river reach of Carrizal.

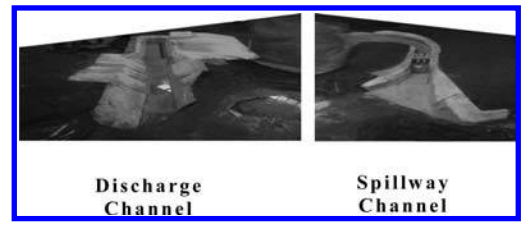


Figure 2. Scale model.

Table 1. Domain discretization.

| Direction | Regions | Cells | Length [m] |
|---|---|---|---|
| X | 3 | 225 | 12 |
| Y | 3 | 275 | 10 |
| Z | 3 | 11 | 1 |

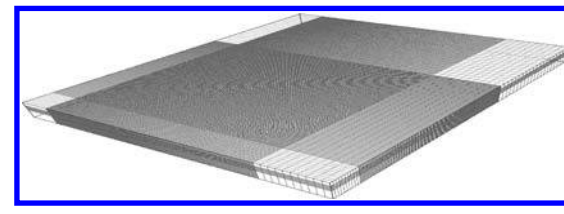

Figure 3. Computational domain.

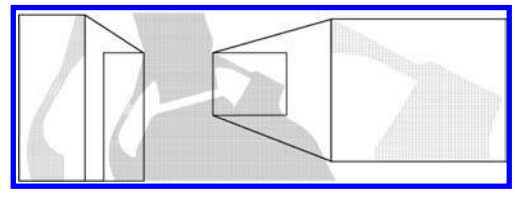

Figure 4. Horizontal layout of the structured grid of the simulated river reaches.

*Specifications*

This structure is characterized by including a discharge channel with discharge controlled by three radial gates on the left bank of the river (with one stilling basin and three sills) and a spillway channel on the right. The scale model (Figure 2) was built with a 1:60 scale in the Fluvial Hydraulics Laboratory of the Institute of Engineering[4].

## 4 NUMERICAL DETAILS

### 4.1 *Boundary and initial conditions*

Hydraulic properties in rivers are usually irregular and it is reasonable to do assumptions consistent with empirical observations and experiences[5]. In this way the conditions of natural flow in these channels become manageable through the analytical treatment of the theoretical hydraulic. The velocity distribution in open channels is generally three-dimensional. The flow velocity is zero on the lateral surfaces and on the channel bed due to the non-slip condition. The normal component of velocity relative to the solid surface is zero along one side of which is set in the boundary condition[5]. Boundary conditions in the upper and lower sides of this simple domain are specified as a non-slip. The shear stress is zero along the free surface of a river. With this simplification the fluid to slide along the surface, the viscous shear caused by the air that is above the fluid is small and despised in this case. The depth water is fixed in the computational domain equal to 5.5$[m]$, with a constant velocity of 07$[m/s]$.

### 4.2 *Computational domain*

The simulation of the flow is three-dimensional and due to the complex geometry we used the alternative “Cut-Cell” where the background is cut to shape the geometry of interest and a special treatment is applied to cells which are cut by solid bodies, thus retaining a boundary conforming grid. This method provides a flexible and efficient alternative to traditional boundary fitted grid methods. The computational domain (Figure 3) is discretized as follows:

## 5 RESULTS

Relevant results of numerical modeling are displayed here. Further analysis has been done in the structures area (Figure 4); also this place has a fine mesh. The main feature of this work is to control the outflow of 850 $[m^2/s]$ in this section of the Carrizal River.

### 5.1 *Velocity*

In a study without hydraulic structure on the river (Figure 5) the velocities increase where the river cross section is reduced. This behavior produces scour on the lateral surfaces. The highest velocities are concentrated on the free surface of water due to the width and the depth of water.

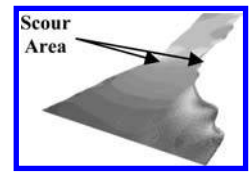


Figure 5. Velocity profile.

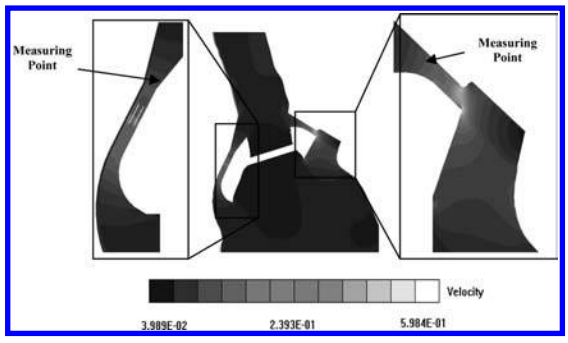


Figure 6. Velocity contours.

Table 2. Highest velocities at each channel.

| | Velocity m/s | |
|---|---|---|
| | Numerical model | Scale model |
| Discharge Channel | 1.55 | 1.42 |
| Spillway Channel | 2.45 | 2.55 |

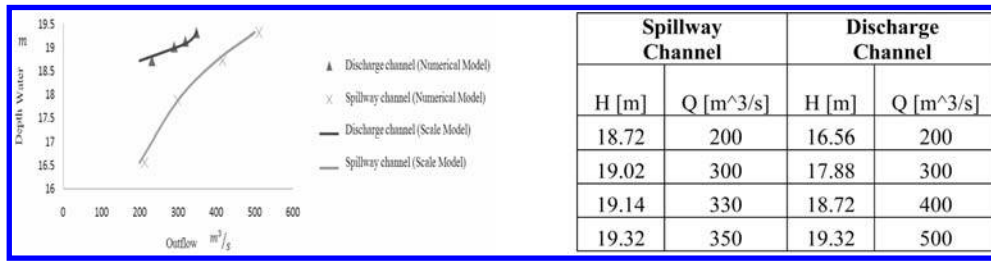


| Spillway Channel | | Discharge Channel | |
|---|---|---|---|
| H [m] | Q [m^3/s] | H [m] | Q [m^3/s] |
| 18.72 | 200 | 16.56 | 200 |
| 19.02 | 300 | 17.88 | 300 |
| 19.14 | 330 | 18.72 | 400 |
| 19.32 | 350 | 19.32 | 500 |

Figure 7. Calibration curves.

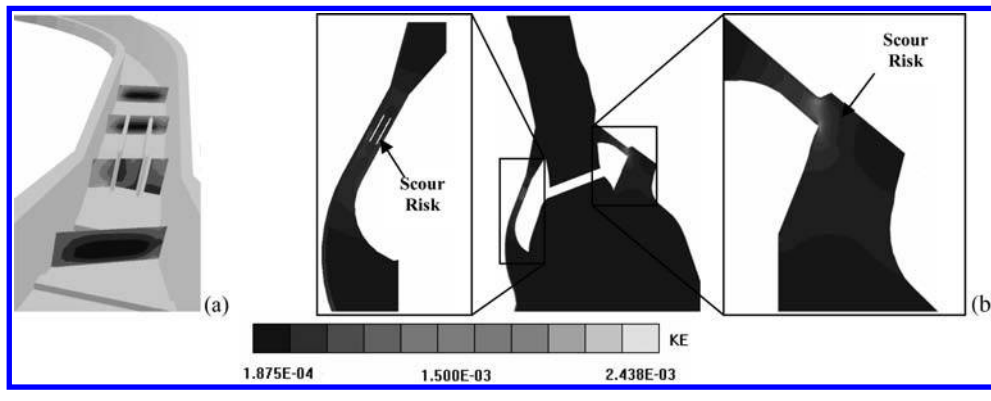


Figure 8. Turbulent kinetic energy.

In the structure area the highest velocities are in the collector channel inlet where the cross section is reduced. However, downstream of these structures we have a backwater area and a homogenous flow. In addition the flow is directed toward the center of the river, without causing scour in the area (Figure 6).

There is a very good approximation between the values of velocity scale model and numerical model (table 2). This is especially true for higher speeds of flow; velocities were measured in each section and in the same areas (Figure 6).

The left channel discharge 60 percent of the total outflow of 850 $[m^2/s]$ while the spillway channel discharge the remaining 40 percent for a depth of water of 5.5$[m]$. The calibration curves of the structures for different elevations of the free surface are shown in the figure 7.

*Turbulent kinetic energy*

Terms of turbulence can be well characterized by the distributions of turbulent kinetic energy, which represents the physical transport properties by turbulent motion. It is an indicator of the spatial and temporal changes in the properties flow. This energy is generated by changing the flow velocity. This behavior occurs mainly when the flow enters in the stilling basin, where the flow undergoes abrupt changes of direction (Figure 8b). The highest values develop in the line of highest velocities close to the lateral surfaces and on the channel bed surface (Figure 8a).

Locally high values of turbulent kinetic energy represent the capacity to carry sediment. Therefore one aspect that deserves attention in hydraulic structures design is kinetic energy dissipation of gained by increasing the flow velocity.

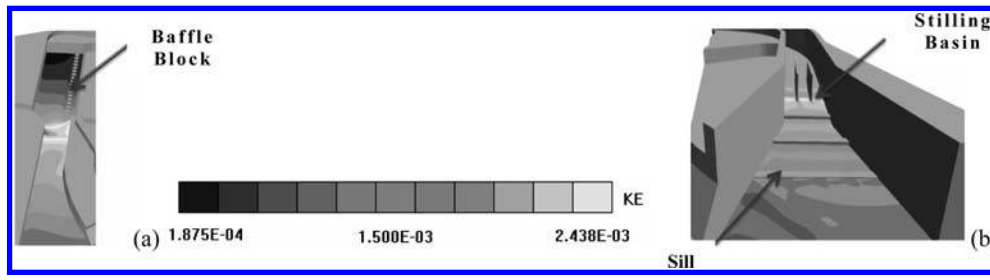


Figure 9. Designs implementations.

This design is characterized by including a stilling basin in both channels. It also placed a row of baffles on the collector channel (Figure 9a) built right in the chute, on the other hand three sills were added downstream of the radial gates on the left channel (Figure 9b)[6]. These mechanisms act as barriers to water flow, i.e., they function as sink of excess energy in this way to prevent the undermining of the downstream structures. These structures rapidly reduce the velocity of flow on a floor protected until a point where the flow loses its ability to undermine the natural bed or even damage the structures. This material is deposited in areas where it can obstruct the flow and divert the river cause.

## 6 CONCLUSION

The chosen numerical turbulence model was successfully adapted to the Carrizal River study and it can be used to allow a detailed study of the flow in order to evaluate hydraulic structures in a simple way in a river with complex bed geometry.

This design allows low levels of velocity fluctuation and eddy current (turbulence). Besides it homogenizes the velocity profile in both channels. The implementations of design dispelled adequately the turbulent kinetic energy; this will be reflected in the transport of material from one section to other sections of the river, due to erosion and scour. This material could be also deposited in areas where it can obstruct the flow and divert the river cause.

There is a very good approximation between the values of velocity scale model and numerical model; comparisons showed that errors were less than 10 percent. Finally the hydraulic structure has the capacity to discharge the volume rate flow of design with an error less than 10 percent compared with the scale model prediction.

## REFERENCES

[1] Launder, B. E., Spalding, D. B., (1972), *Lectures in Mathematical Models of Turbulence*, Academic Press, London.
[2] Ferzinger, H. H., Peric, M., (1996), *Computational Methods for Fluid Dynamics*, Springer-Verlag, Berlin Heidelberg.
[3] Patankar, S. V., (1980) *Numerical Heat Transfer and Fluid Flow*, McGraw-Hill Book Company, New York.
[4] Jiménez, A. A., Osnaya, J., Gracia, J. y Franco, V., (2004) "Estudio en un modelo físico de las estructuras de control sobre el río Carrizal, en el Estado de Tabasco", Informe final elaborado para CNA, Instituto de Ingeniería, UNAM.
[5] Chow V. T., (1997), *Hidráulica de Canales Abiertos*, McGRAW-HILL Interamericana.
[6] Moffatt, F., Novak, P., Nalluri, C., Narayanan, R., (2001) *Hydraulic Structures, Third Edition*, Taylor and Francis Group, London and New York.
[7] Spalding, D. B., (2006), *PHOENICS Overview*, CHAM, London.

*Environmental Hydraulics – López-Jiménez et al (eds)*
*© 2010 Taylor & Francis Group, London, ISBN 978-0-415-56697-1*

# Modeling 2D laminar steady-state flow over a rectangular cavity

C. Gualtieri
*Hydraulic, Geotechnical and Environmental Engineering Department (DIGA), University of Napoli "Federico II", Napoli, Italy*

ABSTRACT: Cavity flows are a significant topic in environmental hydraulics because they could be applied as idealized model for the flow over rivers and lakes cavities, the wind-driven flows in closed body of water, etc. In these cases the main concern is the mass exchange process between the cavity and the overlying flow and the mixing of contaminants downstream the cavity. The objective of the paper is to present the results of a numerical study undertaken to investigate the flow patterns inside a rectangular cavity located on the floor of a duct. Therefore, 2D steady-state numerical simulations were performed with Multiphysics 3.5a™ in a duct-cavity geometry with a cavity bottom. The duct flow had parabolic inlet velocity profile and laminar flow was considered for a Reynolds number based on the cavity depth $Re_D$ equal to 3000. Cavity aspect ratio was 1.0. Numerical results for the flow field were successfully compared with the experimental data collected by Bogatyrev et al. in the same geometry for the same operative conditions.

*Keywords*: Environmental hydraulics; cavity flow; mass-transfer; numerical simulations; Multiphysics 3.5a™.

## 1 INTRODUCTION

Cavity flows are relevant in many areas of engineering and science, such as aerospace engineering, mechanical engineering and environmental engineering. Therefore, they have been intensively studied since some decades to highlight their fluid mechanics characteristics. The lid-driven cavity flow has become a common benchmark case for experiments, theoretical analysis and computational fluid dynamics (CFD) codes [1–3]. This is due to its simple geometry and to the possibility to use the lid-driven cavity flow as idealized model for many engineering applications. The flow over a rectangular cavity situated on the floor of a duct or a channel is a particular case of cavity flow which has received a minor amount of attention[4–9]. In the environmental sciences and engineering field, such as environmental fluid mechanics, the flow over a cavity represents a model for the flow in a river or lakes bottom cavities, the flow in closed bodies of water driven by wind or the flow in urban canyons, etc. In these cases, the main concern is the mass exchange process between the cavity and the overlying flow and the mixing and dispersion of chemicals and contaminants downstream the cavity. However, few studies on this problem are available [10–11].

The objective of the paper is to present the results of a numerical study undertaken to investigate the flow patterns inside a rectangular cavity located on the floor of a duct. Therefore, 2D steady-state numerical simulations were performed with Multiphysics 3.5a™ in a duct geometry with a cavity bottom. The duct flow had parabolic inlet velocity profile and laminar flow was considered for a Reynolds number based on the cavity depth $Re_D$ equal to *3000*. Cavity aspect ratio was *1.0*. Numerical results for the flow field were compared with the experimental data collected by Bogatyrev et al.[12] in the same geometry for the same operative conditions.

## 2 PHYSICAL MODEL AND NUMERICAL SIMULATIONS

The flow inside a cavity situated on the bottom of a duct represents a case of separation flow due to the presence of a backward-step and forward-step. Thus, that flow exhibits different patterns depending on characteristics of the flow and on the shape and the geometry of the duct and the cavity. Also, possible difference in density between the fluid inside the cavity and in the duct should be considered[11]. Particularly, for a rectangular cavity, if the fluid density in the cavity is the same as that for the duct fluid and a parabolic inlet velocity profile exists, we could consider three parameters as governing the flow patterns:

- the cavity Reynolds number $Re_D$, which is defined as:

$$Re_D = \frac{U_{max}\, D}{\nu} \tag{1}$$

where $U_{max}$ is the maximum channel velocity, $D$ is the cavity depth and $\nu$ is the fluid kinematic viscosity;

- the aspect ratio of the cavity $AR$, which is the ratio of the cavity lenght $W$ to its depth $D$;
- the ratio between cavity depth $D$ and duct height $H$.

These parameters control the evolution of the flow patterns inside the cavity. In fact, in shallow cavities and at low flow velocities, the flow is mainly controlled by the backward step, resulting in the flow patterns of a backward facing step flow, with a separation region near the step, which is characterized by recirculating vortices and flow reversal [13–14]. Downstream the reattachment point, a boundary layer immediately develops. This is termed reattaching type flow (RF) (Fig. 1a). As the cavity depth and the flow velocity increase, the recirculation region take up the entire cavity volume and the flow pattern change from the reattaching flow to the so-called cavity flow (CF) (Figure 1b).

The release flux of dissolved substances, such as environmental contaminants, from the cavity bottom to the flowing water varies depending on the flow patterns inside and over the cavity and on the characteristics of these substances. For a fixed substance, in the reattaching flow, the diffusional mass-transfer is due to the development of a diffusive boundary layer

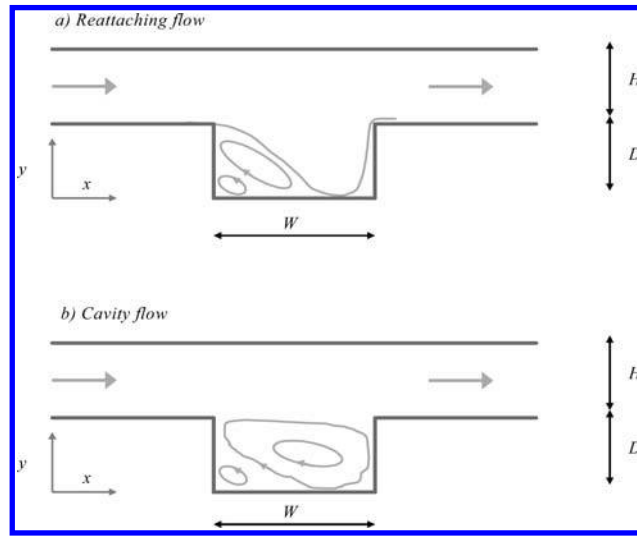


Figure 1. Sketch of the flow patterns in flow over a cavity.

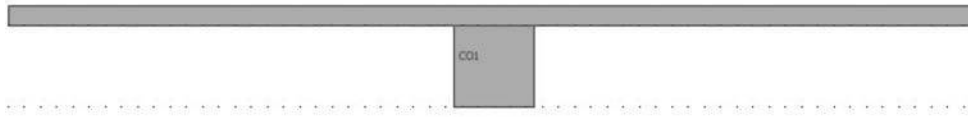


Figure 2. Cavity geometry investigated in this study.

downstream the recirculation region, whereas in the cavity flow the release flux is dominated by the exchange of water between the cavity zone and the overlying layer[10].

Therefore, in order to clarify the interaction between flow structures inside the cavity and mass-transfer from its bottom, numerical simulations of a laminar 2D steady-state flow were first performed. The flow over a cavity located on the bottom of a duct is governed by the mass conservation equation and the Navier-Stokes equations of motion. For a planar, incompressible and steady-state flow conditions these equations are, respectively:

$$\frac{\partial u}{\partial x}+\frac{\partial v}{\partial y}=0 \tag{2}$$

$$\begin{aligned}\rho\left(u\frac{\partial u}{\partial x}+v\frac{\partial u}{\partial y}\right)&=-\frac{\partial p}{\partial x}+\mu\nabla^2 u\\ \rho\left(u\frac{\partial v}{\partial x}+v\frac{\partial v}{\partial y}\right)&=-\frac{\partial p}{\partial y}+\mu\nabla^2 v\end{aligned} \tag{3}$$

where $\rho$ and $\mu$ are the density and the viscosity of the fluid and $u$, $v$ are velocity components in the $x$ and $y$ directions, respectively. These equations were solved using Multiphysics 3.5a™, which is a commercial multiphysics modeling environment[15]. Multiphysics 3.5a™ was applied to the 2D cavity geometry presented in Fig. 2. This is the side view of the channel used by Bogatyrev et al.[12]. They conducted their experiments in a duct with a rectangular section of $0.1 \times 0.01$ m, where a rectangular cavity was arranged at a distance of $1.5$ m from the start of the duct. The experimental cavity, with dimensions of its cross section of $0.04 \times 0.04$ m, was located at the lower wall of the duct. The width of the cavity was equal to the width of the duct section ($0.1$ m). Therefore, the investigated cavity geometry had an aspect ratio $AR = 1.0$ (square cavity) and a ratio $D/H = 4.00$. The velocity of the motion of the liquid was measured using a laser Doppler velocimeter. The authors carried out consecutive measurements of the transverse and longitudinal components of the mean velocity of the flow. The minimal distance from the walls at which the velocity was measured was about $0.001$ m. The averaging time with the measurement of one value of the velocity was established within the limits 3–5 sec. The presented values of the velocity were the average values of 3–4 measurements. After measurements of the longitudinal component of the vector of the velocity, the optical scheme of the laser Doppler velocimeter was changed over for measurement of the transverse component of the velocity. The velocity was measured at 2–3 cross sections of the channel ahead of the cavity, along the whole section of the cavity with a spacing of 1–2 mm (both with respect to the longitudinal and the transverse coordinates), and in 1–2 cross sections in the duct beyond the cavity. Experiments were carried out both in laminar and turbulent flow conditions. The experiments in laminar flow were carried out for a $Re_D = 3000$, which corresponds to the value of $1500$ applied by the authors[12].

In the performed numerical simulations several *boundary conditions* were required. For the Navier-Stokes equations, boundary conditions were assigned at the inlet, the outlet, and at the walls:

- at the duct inlet, an *inflow* type boundary condition was applied, with a parabolic velocity profile. To obtain the parabolic velocity profile, the boundary condition at the inlet was $u = (6 \cdot U_{mean} \cdot s \cdot (1-s)$, where $s$ is a boundary parameterization variable that runs from 0 to 1 along the boundary. The value of $U_{mean}$ was selected to obtain the $U_{max}$ value corresponding to $Re_D = 3000$;
- at the duct outlet, a constant static pressure $p = 0$ was assumed;

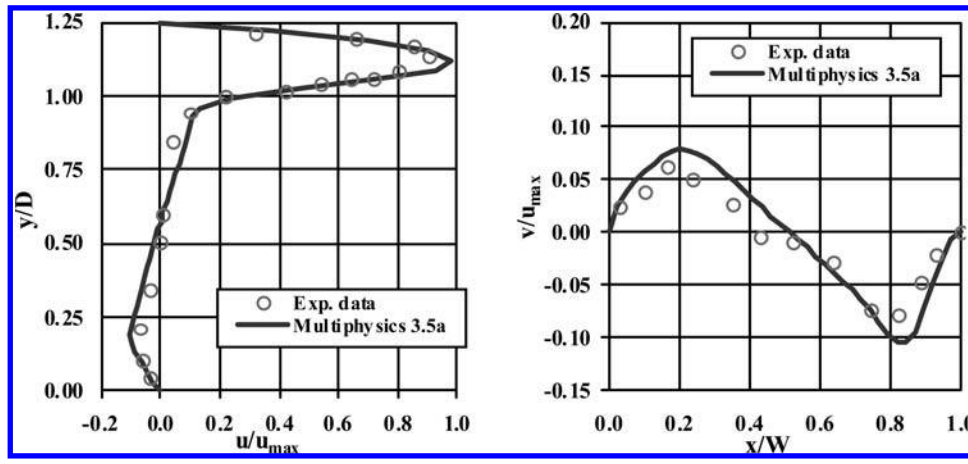


Figure 3. Comparison between numerical results and experimental data. $u$ at $x/W = 0.55$ (left) and $v$ at $y/D = 0.35$ (right).

- no-slip boundary conditions were applied at the upper and lower walls of the duct and at both the steps and the bottom of the cavity.

For the simulation water with density $\rho = 997$ Kg/m$^3$ and molecular viscosity $\mu = 8.90 \cdot 10^{-4}$ Kg/m $\times$ s, was selected as fluid. The mesh generation process was made assuming, among the others, as global maximum element size $5.0 \cdot 10^{-4}$, $2.5 \cdot 10^{-4}$ and $2.0 \cdot 10^{-5}$ in the duct, in the cavity and at their interface, respectively. Thus, the used mesh had *12561* elements, *1173* boundary elements, with a minimum element quality of *0.6728*. The number of degrees of freedom was *161265*. About the solver settings, stationary segregated solver with non-linear system solver was used, where the relative tolerance and the maximum number of segregated iterations were set to $1.0 \cdot 10^{-3}$ and *100*, respectively.

## 3 NUMERICAL RESULTS COMPARISON WITH THE EXPERIMENTAL DATA DISCUSSION

Numerical simulations provided as outputs velocity field and pressure values throughout the flow domain. It was observed that a fully developed circulating motion raised in the square cavity. The region adjacent to the upper section of the cavity can be regarded as the zone of the mixing of the jet (mixing layer), forming after the breakaway of the duct flow with the flow in the cavity. After the impact of the jet against the rear wall of the cavity, a jet is formed near the wall, propagating along all the walls of the cavity and producing a central, main eddy inside the cavity. Also two smaller corner eddies were located at the cavity bottom. This flow field is a good agreement with that observed in the experiments.

Comparison between numerical results and experimental data showed that in the mixing layer for the $x$-component $u$ their difference was in average about 10% . A good agreement was found for the $u$ also over the whole transverse profile (Fig. 3a), while a lower level of agreement was found for the $y$-component $v$ (Fig. 3b). From the analysis of the profile of the transverse velocity $v$ at the interface between the duct and the bottom cavity it was found that the dimensionless exchange rate was about *0.0137*. This value is not far from experimental values collected in square cavity for turbulent flows[15].

## 4 CONCLUSIONS

Cavity flow is a significant topic in environmental hydraulics because they could be applied as idealized model for the flow over rivers and lakes cavities, the wind-driven flows in closed body of water, etc. This extended abstract presented some results of a numerical study of the laminar flow in a duct geometry with a cavity bottom. Comparison between literature experimental data and numerical outputs resulted in an acceptable agreement. Further research will be addressed to investigate in this geometry the interaction between flow hydrodynamics and fluxes of solutes coming from the bottom of the cavity.

## REFERENCES

[1] Ghia U., Ghia K.N., and Shin C.T. (1982). High Resolutions for incompressible flow using Navier-Stokes equations and a multi-grid method. *Journal of Computational Physics*, Vol.48, 387–411

[2] Ramanan N., and Homsy G.M. (1994). Linear stability of lid-driven cavity flow. *Physics of Fluids A*, Vol64, n.8, August 1994, 2690–2701

[3] Yang Y., Stratman A.G., Martinuzzi R.J., and Yanful E.K. (2002). A study of laminar flow in low aspect ratio lid-driven cavities. *Can. J. Civ. Eng.*, Vol 29, 436–447

[4] Chilikuri R., and Middleman S. (1983). Circulation, diffusion and reaction within a liquid trapped in a cavity. *Chem. Eng. Commun.*, Vol.22, 127–138

[5] Shen C., and Floryan J.M. (1985). Low Reynolds number flow over cavities. *Physics of Fluids A*, Vol.28, n.11, November 1985, 3191–3202

[6] Chang H.N., Ruy H.W., Park D.H., and Park Y.S. (1987). Effect of external laminar channel flow on mass transfer in a cavity. *Int. J. Heat and Mass Transfer*, Vol.30, 2137–21

[7] Fang L.C., Nicolaou D., and Cleaver J.W. (1999). Transient removal of a contaminated fluid from a cavity. *Int. J. Heat and Fluid Flow*, Vol.20, 605–613

[8] Fang L.C., Nicolaou D., and Cleaver J.W. (2003). Numerical simulations of time-dependent hydrodynamic removal of a contaminated fluid. *Int. J. Numer. Meth. Fluids*, Vol.42, 1087–1103

[9] Ashcroft G., and Zhang X. (2005). Vortical structures over rectangular cavities at low speed. *Physics of Fluids*, Vol.17, n.1, pp. 015104-1–015104-8.
[10] Higashino M., and Kanda T. (2001). Diffusional mass-transfer across the sediment-water interface for turbulent flow in a rectangular trench. *Journal of Hydroscience and Hydraulic Eng.*, Vol.19, n.2, November 2001, 129–137
[11] Chang K., Costantinescu G., and Park S. (2005). Flow and mass exchange processes between a channel and a cavity filled with either a neutrally buoyant or a dense miscible contaminant. *XXXI IAHR Congress*, Seoul (Korea), September 11/16, 2005, 2221–2232
[12] Bogatyrev V.Y., Dubnishehev Y.N., Mukhin V.A., Nakoryakov V.E., Sobolev V.S., Utkin E.N. Utkin, and Shmoilov N.F. (1976). Experimental investigation of flow in a trench. Zhurnal Prikladnoi Mekhaniki i Tekhnicheskoi Fiziki, No. 2, pp. 76-86, March–April, 1976
[13] Tihon J., Legrand J., and Legentilhomme P. (2001). Near-wall investigation of backward-facing step flows. *Experiments in Fluids*, 31, 484–493
[14] Gualtieri C. (2005). Numerical simulations of laminar backward-facing step flow with FemLab 3.1. *ASME Fluids Engineering Summer Conference (FEDSM2005)*, Houston (USA), June 19/23, 2005
[15] Multiphysics 3.5 (2008). *User's Guide*, ComSol AB. Sweden.
[16] Muto, Y., Imamoto, H., and Ishigaki, T. (2000). Velocity measurements in a straight open channel with a rectangular embayment, *Proceedings of the 12 APD-IAHR, Bangkok, Thailand*.

*Environmental Hydraulics – López-Jiménez et al (eds)*
*© 2010 Taylor & Francis Group, London, ISBN 978-0-415-56697-1*

# Simulation of the filling and emptying processes between a river and its storage areas

Dieter Meire, Liesbet De Doncker, Peter Troch & Ronny Verhoeven
*Hydraulics Laboratory, Ghent University, Ghent, Belgium*

ABSTRACT: One of the traditional and effective flood protection measures is the use of storage areas. By their controlled filling and emptying, inundation risks for downstream areas with higher vulnerability can be reduced. They not only have an influence on the flood level, but also on the residence time of the water in the river ecosystem, which is an important biological parameter. A good prediction of storage flow is therefore necessary in an integrated ecosystem model. In such model, which is being developed by the universities of Ghent and Antwerp, and where biological, biogeochemical and hydraulic processes are coupled.

In this paper, a one-dimensional hydrodynamic module of the integrated STRIVE (STReam RIVer Ecosystem) model, which is based on the Saint-Venant equations and solved by the Preissmann scheme, is adapted to be able to include flow exchange with storage cells. By this the one-dimensional model is upgraded to a quasi two-dimensional model. Flow between the storage cells and the river is controlled by weirs (flooded river banks). Connection between storage cells is also made possible. Special attention will be paid to the propagation of the flood wave through the river system.

*Keywords*: storage cell, Saint-Venant equations, Preissmann scheme, flooding

## 1 INTRODUCTION

For a long time massive dikes with high crest levels were considered as the most efficient flood protection measure. However, nowadays a combination with storage areas becomes more popular because of its effectiveness. Although storage is most efficient when controlled, by the proper management of control gates[1], storage can also be achieved in an uncontrolled way. Here, the flow between river and storage cells is over the (lowered) dikes and so, the dikes are acting as weirs between the river main channel and the storage cells[2].

Models of different complexities may be applied for the hydrodynamic simulation of storage[1]. An appropriate modelling approach should in the first place be chosen depending on the objective of the study. When the propagation of the inundation flow in the storage area has to be known, e.g. for erosion and sedimentation processes, a two-dimensional hydrodynamic model of the storage area is essential. However, as we are only interested in the studying of the exchange of water between storage cells and river and the residence time of the water in the storage area, a one-dimensional model for the river which is coupled with a storage cell may be sufficient.

Because a combination is made between 1D flood routing (main channel) and 0D storage cells, special attention will be paid to the propagation of the peak discharge in the river system.

## 2 STRIVE MODEL

STRIVE, or "STReam RIVer Ecosystem" model, is an integrated ecosystem modelling package, developed by the universities of Antwerp and Ghent. STRIVE is written within a Fortran environment, called FEMME[3]. The flood routing in the model is described by the Saint-Venant equations. The differential equations are discretised by the Preissmann-scheme and solved by a double sweep algorithm.

Water flow between the storage cell and the river is modelled by the Poleni formula (1) or the formula for a submerged weir (2) depending on the situation (see respectively Figure 1 and Figure 2). In this formulas, $C_d$ is a coefficient of discharge, b the width of the weir, $h_{over}$ and $h_{sover}$ are the water heights above the dike crest levels in respectively the river and storage cell[4]. The velocity $V_0$ in the storage cell is assumed zero and therefore the second term in equation 2 can be neglected.

$$Q = \frac{2}{3} C_d \, b \sqrt{2g} \, h_{over}^{3/2} \tag{1}$$

$$Q = \frac{2}{3} C_d \, b \, h_{over} \sqrt{2g \left(h_{sover} + \frac{V_0^2}{2g}\right)} \tag{2}$$

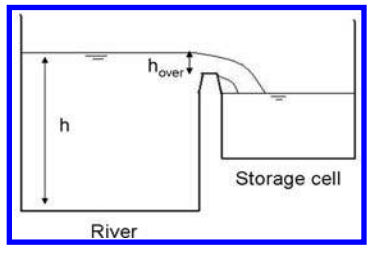


Figure 1. Flow between river and storage cell in the situation of a free overfall sharp-crested weir.

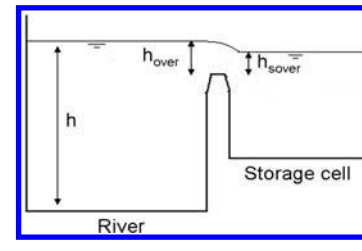


Figure 2. Flow between river and storage cell in the situation of a submerged weir.

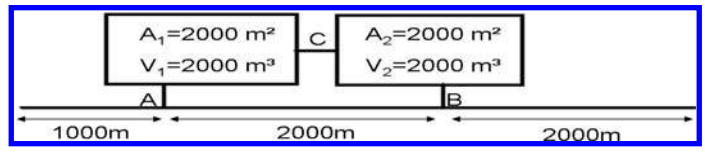


Figure 3. Layout of the river system under study. A, B are the weirs connecting the storage cells to the river and C is the weir connecting both storage cells.

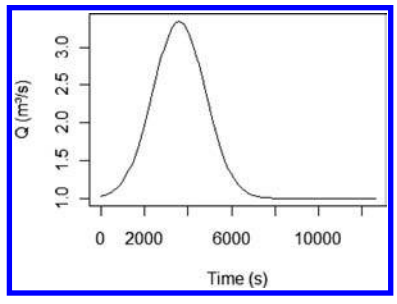


Figure 4. Upstream boundary hydrogram.

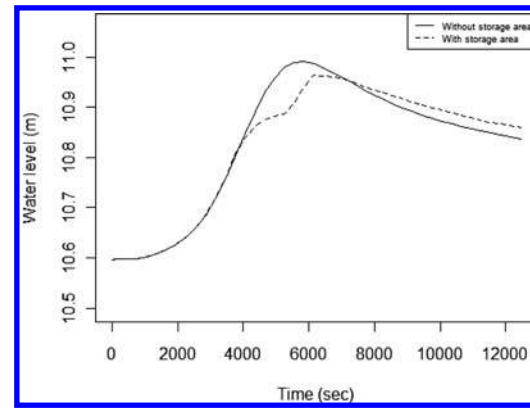


Figure 5. Simulated water level in a cross section 50 m downstream from the storage area.

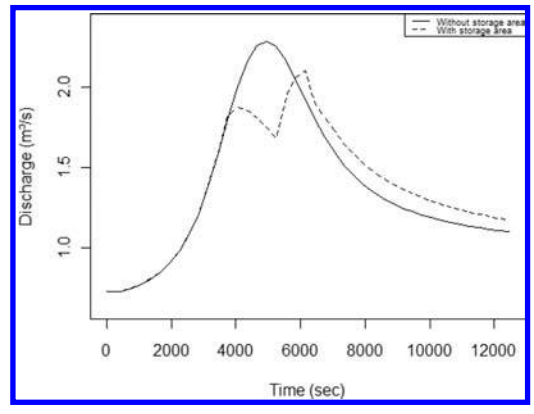


Figure 6. Simulated discharge in a cross section 50 m downstream from the storage area.

In the nodes where the river is connected with the storage cells, the original disctretised continuity equation resulting from the Preissmann discretisation, have to be adapted[5].

## 3 DESCRIPTION OF THE STUDY LAYOUT AND HYDROLOGIC INPUT

The situation under study is sketched in Figure 3. With this layout, several situations can be simulated because weirs A, B and C can be alternatively set in use.

For the model simulations a river width of 10 metres, a bottom slope of 0.0002 $mm^{-1}$ and a Manning coefficient of 0.1 is used. As an upstream boundary condition a designed hydrograph is used (Figure 3). The setting of the parameters and the design of the inflow hydrogram is based on measurements made on the Aa river (Belgium)[6]. The downstream boundary condition is implemented as a known height-discharge relation. The dike crest levels at storage cell 1 and 2 are respectively set at 10.8 m and 10.5 m above datum.

## 4 RESULTS

*Test Case 1: River – Storage cell connection*

After a normal flood routing, is performed (results are not shown), a connection between storage cell and main river is established. This is done for the first and second storage cell, but because of the analogy, only the results of the first storage cell are presented.

In Figure 5 and 6 it can clearly be seen that, when the water level exceeds the dike level, water is stored in the cells. Later, when the water level of the storage cell is higher than the main channel, water will flow back and discharge and water level are higher compared with the situation without storage area.

*Test Case 2: River – Storage cell 1 – Storage cell 2 connections*

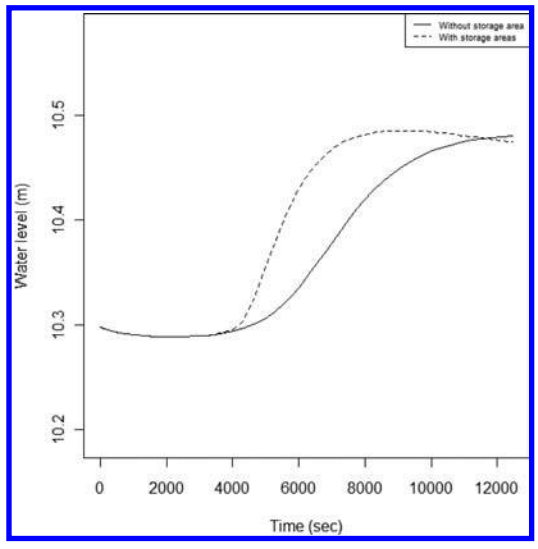


Figure 7. Simulated water level in a cross section 50 m downstream from the last storage area in the case of two connected storage cells.

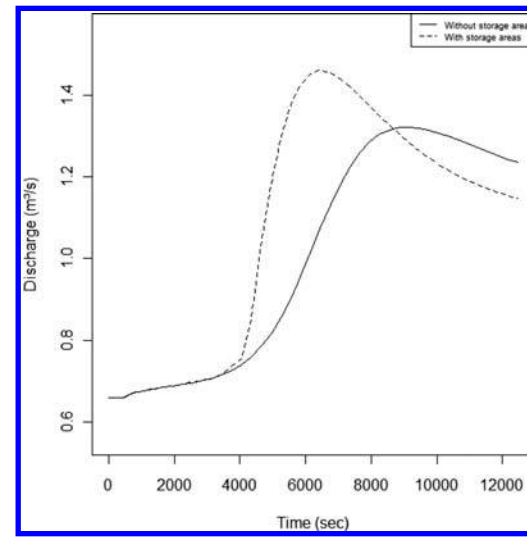


Figure 8. Simulated discharge in a cross section 50 m downstream from the storage area in the case of two connected storage cells.

In this test case, all possible connections in the proposed layout (see Figure 3) are made. The initial waterlevel in the storage cells is set at the same height as the levee, to assure a quick reaction of the system. The results of the STRIVE model, in a section 50 meters after the last storage cell, are presented in Figure 7 and 8. In both figures, it can clearly be seen that the peak discharge and maximum water level are occurring earlier in the situation where all storage cells are implemented compared with the situation without storage areas. It can also be remarked that the peak values are higher.

This phenomenon can be explained by the way the storage cells are implemented in the model. As these cells are represented as points, water can move from one side of the storage cell to the other one in one time step of the model. In the main channel however, the flow is computed with de Saint-Venant equations.

This can also explain the higher value of the peaks in both figure 7 and 8 and increased steepness of the curves. After all, if no flow is supposed, no dissipation effects due to friction, etc. and therefore flattening of the curves will occur.

## 5 CONCLUSIONS

In an ecosystem model, not only the longitudinal connection (river) need to be modelled, but also the lateral connections have to be taken into account. A first attempt to extend the current 1D approach is made here by implementing storage cells.

The results of the first test case clearly show that the STRIVE model can simulate a situation with storage cells without problems. Both inflow as outflow from the storage cells can be computed by the model. However, if storage cells are connected with each other and the main channel, which is simulated in test case 2, unrealistic flood routing behaviour can be observed in the STRIVE model. To obtain a more realistic flood routing with the coupled STRIVE model, and therefore a good prediction of the residence time of the water in the river system, an appropriate method has to be implemented to slow down the flow between the storage cells. The results will be compared with model of the same system obtained by the Hec-Ras model.

## REFERENCES

[1] Förster, S. Chatterjee, C., Bronstert, A. (2008) “Hydrodynamic simulation of the operational management of a proposed flood emergency storage area at the middle Elbe river”, River Research and Applications, Vol. 124, pp. 900–913.

[2] Sanders, B.F., Jaffe, D. A. (2001), “Engineered levee breaches for flood mitigation”, J. of Hydraulic Engineering, Vol. 127, No. 6, pp. 471–479.

[3] Soetaert, K., deClippele, V., Herman, P., (2002) “FEMME, a flexible environment for mathematically modelling the environment”, Ecological Modelling, Vol. 71, Iss. 2–3, pp. 177–193.

[4] Chaudry, M. H. (1993), “Open-channel flow”, Prentice-Hall, New Jersey.

[5] Declercq, F., (2007). “Overstromingsgebieden: experimentele opzet en numerieke modellering in “Femme”. Master Thesis, Ghent University.

[6] De Doncker, L., Troch, P., Verhoeven, R., Bal, K., Meire, P. (2006) “Influence of aquatic plants on the flow resistance and the hydraulic capacity of vegetated rivers”, River Flow Proceedings, pp. 593–602.

*Environmental Hydraulics – López-Jiménez et al (eds)*
*© 2010 Taylor & Francis Group, London, ISBN 978-0-415-56697-1*

# Circulation and numerical modeling of the Manzanillo harbor, Colima, Mexico

Ariosto Aguilar-Chavez, Rubén Morales-Pérez & Jorge A. Laurel-Castillo
*Mexican Institute for Water Technology, Jiutepec, Mexico*

Héctor Vélez-Muñoz
*Universidad Autonoma Metropolitana, Unidad Iztapalapa, Mexico City, Mexico*

ABSTRACT: In this paper, a two-dimensional hydrodynamic depth average model is implemented to investigate the dynamics of the circulation in the Manzanillo harbor. The model is mainly forced by tidal elevations. In order to validate the model a circulation field experiment was made with ADCP (Acoustic Doppler Current Profile) deployed at the harbor entrance and on a moving boat. The field data showed a baroclinic circulation pattern. However, the mean flow circulation was simulated satisfactorily. Finally, the model results are used to generate an environmental management tool for the API-Manzanillo (Harbor administration office)[4].

*Keywords*: numerical models, shallow water equations

## 1 INTRODUCTION

The Manzanillo harbor is located in the southern part of Mexico (Colima state). The entrance channel to the harbor is about 230 m width. The harbor size is about 2.5 km in length, 0.6 km width and a depth average of 15 m. The dynamic of the harbor is driven by tidal forcing which is mainly semidiurnal. Due to the harbor enlargement there is a strong interest to understand the actual conditions of harbor dynamics. Therefore, field measurements and numerical modeling were made to investigate the circulation of the harbor.

Field ADCP measurements were carried out, during April 2009, on a moving boat and a deployment. The experiment was set to measure the currents and level during a spring tidal period. Also the vertical structure of the water column was measured in the bay and inside the harbor. For the assessment of the circulation, a two-dimensional depth average hydrodynamic model was implemented[6].

The numerical model was used to generate scenarios for actual and enlargement conditions. Finally, numerical simulations will be used to plan different changes in the harbor morphology for an optimum enlargement[4].

## 2 DATABASE INFORMATION

### 2.1 *Tides*

The boundary condition for the flow generation in the numerical model was the tide. The tide data in the Manzanillo harbor is form factor $f = 0.96$[5]. There is a type mixed predominantly semidiurnal tide. In the local tide records the high tide is 1.14 m and the entry for the minimum low tide is −0.42 m. This data is compared to the low bottom half. The maximum tidal range is 1.56 m. For the hydrodynamic simulation seven harmonic constituents of the tide were considered (Table 1). The amplitude values and each component phase along the calculation domain boundary were obtained from the tide database[5].

### 2.2 *Bathymetry*

To generate the numerical grid three bathymetric databases were used. The first one, GEBCO [2], covers the entire globe with a resolution of one degree in latitude and longitude; in this application a domain of approximately 370 × 450 km was extracted (Figure 1). The second database was the nautical chart number 21342A of the Navy Ministry[1]. The third database is the bathymetry measured by API Manzanillo.

Table 1. Tidal constituents used in the simulation.

| Constituents | | T (h) | C (m) | a |
|---|---|---|---|---|
| K1 | Luni-solar | 23.934470 | 0.141565 | 0.736 |
| O1 | Principal lunar | 25.819342 | 0.100514 | 0.695 |
| Q1 | Elliptical lunar | 26.868357 | 0.019256 | 0.695 |
| M2 | Principal lunar | 12.420601 | 0.242334 | 0.693 |
| S2 | Principal solar | 12.000000 | 0.112841 | 0.693 |
| N2 | Elliptical lunar | 12.658348 | 0.046398 | 0.693 |
| K2 | Luni-lunar | 11.967235 | 0.030704 | 0.693 |

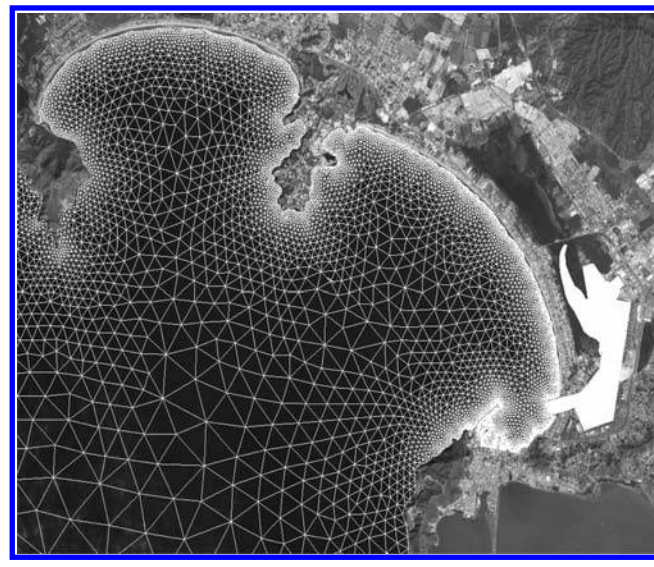

Figure 1. Bays mesh detail.

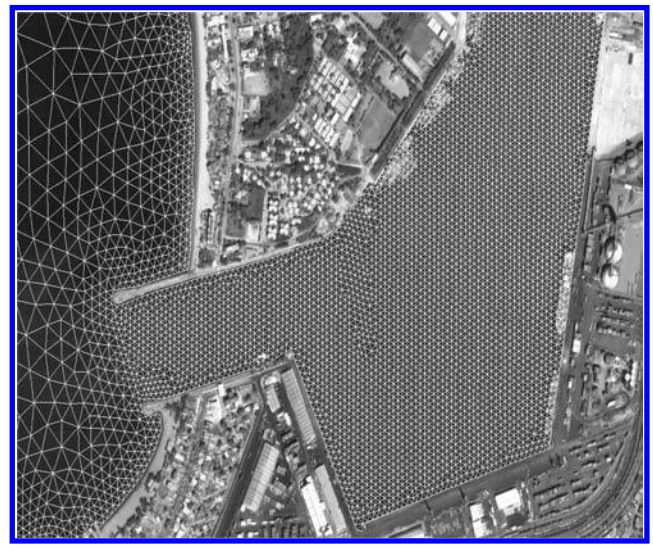

Figure 2. Manzanillo harbor mesh detail.

## 3 NUMERICAL MODEL

For modeling the hydrodynamics of the Manzanillo harbor actual conditions, as well as the enlargement scenarios, the numerical model ADCIRC[6] was used.

The ADCIRC is a circulation depth-integrated hydrodynamic model, in which the shallow water equations are solved through the finite element method. The ADCIRC uses the Generalized Wave Continuity Equation (GWCE) formulation. In the GWCE formulation, the continuity equation is substituted by a linear combination of mass conservation and the momentum equations, which is cast in wavelength form[6].

The hydrodynamic simulation domain of the general circulation model ADCIRC is a semicircle with a radius of 135 km with the center at the Manzanillo and Santiago bays inlet. This domain was discretized with an unstructured-triangular mesh (Figures 1 and 2).

The resulting mesh was of 39,420 elements and 20,841 nodes, with an element size within the port of 15 m. The overall view of the mesh can be seen in Figures 1 and 2. These figures show the mesh detail in the Manzanillo and Santiago bays, and the port navigation channel, respectively.

The numerical simulation covers a period of 35 days, with the start time on April 3, 2009 at 00:00 hr. The results are shown after the fifth day of simulation (Figure 3) and illustrate the tidal sign obtained in the harbor estuary during the period of printing results.

For purposes of model validating, comparisons were made between the results of numerical simulation and the ones obtained from an acoustic profiler ADCP (1.2 MHz) which was anchored near to the buoy 8 in the port navigation channel[4].

It can be observed that the simulated levels correspond with the measured levels in phase, magnitude and time (Figure 3). The magnitude of the velocity integrated in the vertical has some variations, but the values are acceptable (Figure 4). It is important to say that the modeling considers a barotropic condition, and according to field measurements, the flow is baroclinic, so be careful when interpreting the speeds dropped by modeling this or any other two-dimensional or three dimensional in which density gradients are not considered.

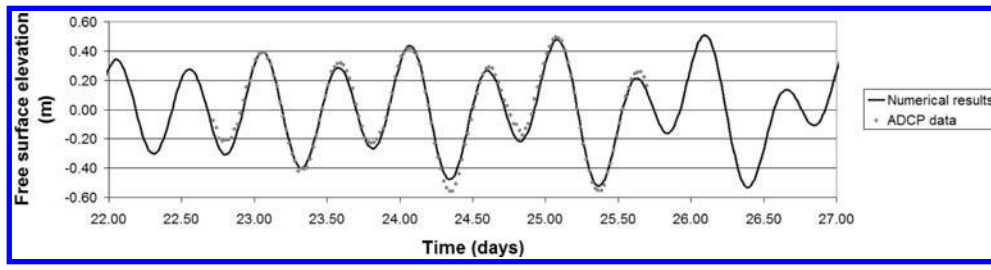


Figure 3. Comparison of the measured and simulated levels of the free surface.

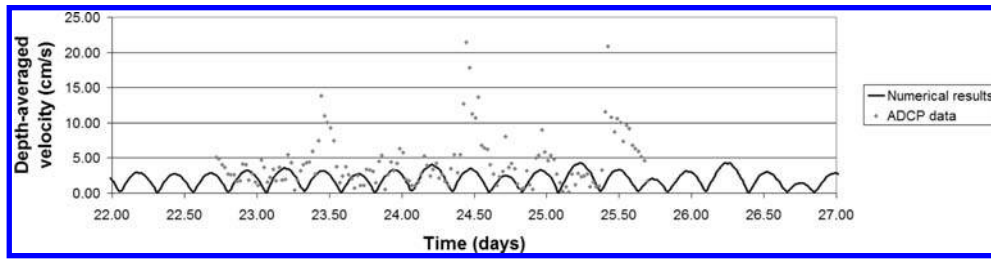


Figure 4. Comparison of the depth-integrated velocity, measured and simulated.

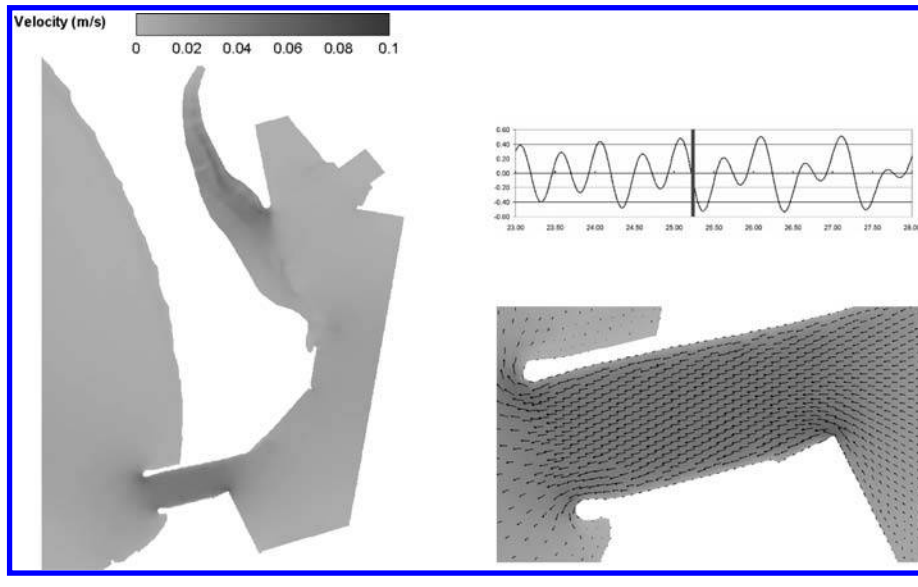


Figure 5. Velocity field. April 25, 2009. 05:30 a.m.

## 4 MODELING RESULTS

In the spring tide period, maximum and minimum levels of the sea free surface had values of 0.45 and −0.5 m (MSL), respectively. As the Figure 5 shows, the harbor access channel and the northern part are the more dynamic areas. In the access channel, the depth-integrated velocities reached 3 cm/s in flow conditions and 5 cm/s under reflux conditions. In the northern harbor part, velocities reached values of around 3.5 cm/s for the flow conditions and 4.5 cm/s in reflux conditions. Under current conditions, it was observed that the tidal wave does not present a significant buffer in the harbor inside[4].

## 5 CONCLUSIONS

The modeling of the general circulation using the ADCIRC model was according to the mean field measured circulation induced by tides (Figures 3 and 4). Comparison of modeled and measured levels is in agreement for the phase and amplitude relation during the period from April 21 to 25, 2009, as well as for the average velocities. Finally, the modeling results will be used as an environmental management tool for the enlargement of Manzanillo harbor, and to evaluate its impacts on the Las Garzas lagoon ecosystem[4].

## REFERENCES

[1] Carta batimétrica. Num. 21342A. *Secretaría de Marina-Armada de México*.
[2] General bathymetric chart of the oceans. GEBCO. http://*www.gebco.net/data_and_products/gridded_ bathymetry_data/*

[3] Le Provost C., Genco M. L., Lyard F., Vincent P. and Canceil P. (1994) “Spectroscopy of the world ocean tides from finite element hydroynamic model”. Journal of Geophysical Research. 99(C129 24,777–24,797).
[4] Morales-Perez R., Aguilar-Chávez A, Laurel-Castillo A. Velez-Muñoz H. and Hernández-Meza D. (2009) “Estudio con el análisis de escenarios de modelación de la Unión de la Laguna de las Garzas con la Dársena de San Pedrito en Manzanillo”, *Colima*, Contract API-MAN-CON-10-09/HC-0920.3, Instituto Mexicano de Tecnología del Agua, Jiutepec, Morelos, México.
[5] Secretaría de Marina (2005) Dirección general adjunta de oceanografía hidrografía y meteorología, “Tablas numéricas de predicción de mareas 2005, Océano pacífico”.
[6] Westerink, J.J., Blain, C. A., Luettich, R. A. and W, Scheffner. N. (1994) “ADCIRC: An advanced three-dimensional circulation model for shelves coasts, and estuaries. Report 2”, User’s manual for ADCIRC-2DDI, Department of the Army, U.S. Army corps of engineers. Washington, DC.

*Environmental Hydraulics – López-Jiménez et al (eds)*
*© 2010 Taylor & Francis Group, London, ISBN 978-0-415-56697-1*

# Dynamic ultrafiltration modelling for a submerged membrane bioreactor based on neural networks

Y.M. Carreño-Martínez, J.A. Mendoza-Roca, E. Lobo-Colominas, A. Bes-Pia & F.J. Martínez-Francisco
*Instituto de Seguridad Ambiental, Radiofísica y Medio Ambiente (ISIRYM), Universidad Politécnica de Valencia, Valencia, España*

L. Pastor-Alcañiz
*Depuración de Aguas del Mediterráneo (DAM), Paterna, España*

ABSTRACT: A neural network (NN) model to predict the membrane performance in a scale pilot submerged membrane bioreactor (SMBR) has been developed. This SMBR has been used for the aerobic treatment of municipal wastewater. The aim of this work was to predict the dynamic behavior of the transmembrane pressure (TMP) as a function of three operating parameters, i.e., permeate flux, the mixed liquor suspended solids and the hydraulic cleaning cycles. The applied NN was a multilayer perceptron network (MLPN) and the Levenberg–Marquardt (LM) optimization algorithm was employed for its training.

*Keywords*: membrane bioreactor, ultrafiltration, neural networks.

## 1 INTRODUCTION

Membrane bioreactor (MBR) is a variation of the conventional activated sludge treatment where the secondary settler is replaced by a membrane process (ultrafiltration or microfiltration) for the separation of the treated effluent from the sludge. The main advantages in comparison with the conventional process are a smaller footprint and the better quality of the final effluent[1]. The first one allows a higher mixture liquor suspended solids (MLSS) concentration can be maintained in the reactor. Thus, in regions with water scarcity, the MBR process has a promising future since wastewater reuse is a necessity and the quality of its effluent is higher than that obtained by a conventional activated sludge system.

Nevertheless, the MBR operating costs are higher due to the aeration energy needed to cover both the biological oxygen demand (to oxidize the organic matter) and to promote turbulence (to avoid the deposition of the sludge flocks onto the membrane surface). Membrane fouling has to be minimized in order to reduce the operating costs[2], e.g. chemicals used for cleaning, membrane replacement, etc.

On the other hand, ultrafiltration (UF) is a membrane process whose driving force is the pressure difference between both sides of the membrane (feed and permeate sides). This pressure difference is called transmembrane pressure (denoted by $\Delta P$). UF in submerged MBRs is usually operated by applying a vacuum pressure in the permeate side. The permeate flow rate will depend on the established $\Delta P$ according to Darcy's equation:

$$J = \frac{\Delta P}{R\mu} \tag{1}$$

where $J$ is the flux given in $m^3m^{-2}s^{-1}$, i.e., the permeate flow rate divided by the membrane surface. Note that $\Delta P$ is given by Pa, $R$ is the resistance of the membrane given in $m^{-1}$ and $\mu$ is the permeate viscosity given in Pa·s.

Membrane fouling phenomena will entail an increase of $\Delta P$, which can not be higher than a predefined limit (approximately 0.3 bar). Thus, some techniques have to be implemented in order to avoid the $\Delta P$ increases, such as membrane relaxing (aeration on, permeate pump off), periodic membrane cleaning with backpulses (with stored permeate) and membrane cleaning with chemicals. Thus, optimizing the operating cycles of the MBR, the MLSS, and the permeate flow rate will conduct to a minimization of $\Delta P$, and subsequently the membrane fouling and the operating costs will decrease.

On the other hand, neural networks (NN) are mathematical models designed to mimic certain aspects of neurological functioning of the brain. A NN is a parallel structure consisting of nonlinear processing elements (neurons) grouped into layers and interconnected by fixed or variable weights. During the last two decades, NNs have become in a powerful tool to solve many problems due to the ability of modelling and control of complex systems with highly non-linear relationships by learning from data[3][4][5].

In the current literature, some works applying NNs to a MBR, or to the ultrafiltration, can be found[6][7]. Thus, Çinar et al. applied an artificial NN to a MBR for predicting the effluent quality. Da Silva and Flauzino used NNs to estimate the behavior of the cross-flow filtration processes like UF process. In the Silva and Flauzino's work, the input variables were the initial concentration of the fluid, the filtration time, the transmembrane pressure, and the density of the particles to be filtered.

As a new useful extension of previous works, in this paper the prediction of the ultrafiltration transmembrane pressure in a MBR is carried out by means of the application of a MLPN.

## 2 METHODOLOGY

### 2.1 *Membrane bioreactor*

The experimental MBR plant consist of an aerobic reactor divided into two compartments, and a submerged ultrafiltration module BIO-CEL ®provided by ECOLOGÍA TÉCNICA S.A. (ECOTEC), with 10 $m^2$ of active membrane surface. The total

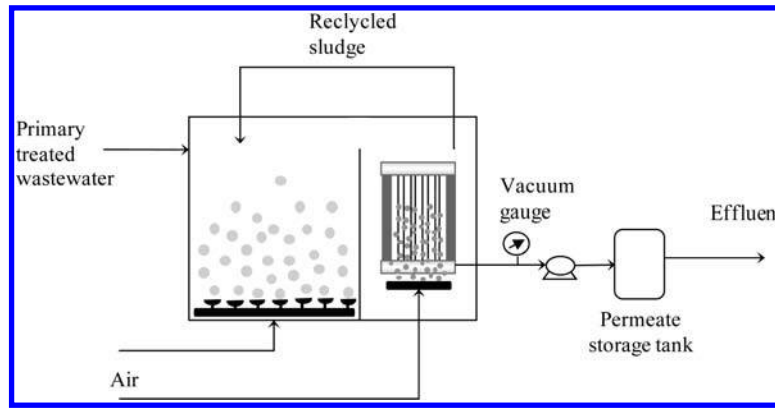


Figure 1. Schematic diagram of the SMBR pilot plant.

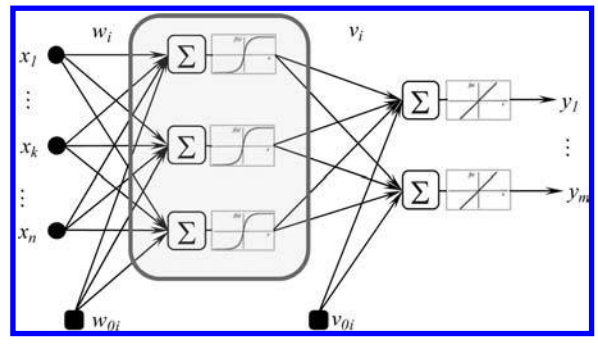


Figure 2. Structure of a neural network with three layers.

volume of the bioreactor is 1.05 $m^3$. The pilot plant was fed with primary effluent from a municipal sewage treatment plant. Cycles with eight minutes of filtration and two minutes of relaxation, and backpulses with stored permeate for the membrane cleaning were carried out. During the operation time no chemical cleaning of the membrane was performed.

A scheme of the plant is shown in Figure 1.

The MLSS in the sludge and the chemical oxygen demand (COD) in the permeate were analyzed each day during operation time. The network variable inputs were permeate fluxes, the mixed liquor suspended solids, the hydraulic cleaning cycles, and the operation time. The output was the TMP.

## 2.2 *Neural modeling*

A MLPN with a hidden layer and linear nodes in the output layer is introduced to approximate the nonlinear function. The structure for a NN with three layers with multiple inputs ($x_n$) and multiple outputs ($y_m$) is shown in the Figure 2. The first layer receives weights ($w_i$) from the input. Each subsequent layer receives weights from the input and all previous layers. The bias on a typical hidden unit is denoted $w_{0i}$; the bias on a typical output unit $y_k$ is denoted by $v_{0i}$.

The net input to a hidden node *zj* is denoted as follows:

$$zj = w_{0j} + \sum_i x_i v_{ij} \tag{2}$$

The last layer is the network output. Only the direction of information flow for the feed-fordward phase of operation is shown. A hyperbolic tangent sigmoidal function is used as the activation function in hidden layers while a linear one is used in the output layer. The hyperbolic tangent sigmoidal function is defined as follows:

$$\tanh(x) = \frac{e^x - e^{-x}}{e^x + e^{-x}} \tag{3}$$

During the backpropagation phase of learning, signals are sent in the reverse direction[3].

Currently, the most widely employed algorithm for training NNs is the backpropagation approach[5],[8]. The mathematical basis for the backpropagation algorithm to adjust the network weights, minimizing the root-mean-square error (RMSE) between the actual values and the predicted values, is the traditional optimization technique known as gradient descendent. However, the backpropagation techniques are known to converge slowly[9]. In this paper, the fast LM optimization technique[10] is used for training the network.

The best network artificial NN architecture was determined using a trial and error approach (multiple runs). All simulations were performed with the NN toolbox from MATLAB (The MathWorks Inc., USA). In this study a multilayer feed-forward network was adopted to model the submerged membrane bioreactor receiving municipal wastewater. The operational data over 45 days were used in the artificial NN modeling.

Table 1. Operating conditions of the SMBR experimental runs

| Input variables | Min | Max |
|---|---|---|
| MLSS ($mgl^{-1}$) | 2425 | 10000 |
| Permeate fluxes ($lh^{-1}m^{-2}$) | 8 | 20 |
| Frequency of backflushing (cycle number)* | 1 | 10 |

*1 cycle = 8 minutes of filtration and 2 minutes of relaxation.

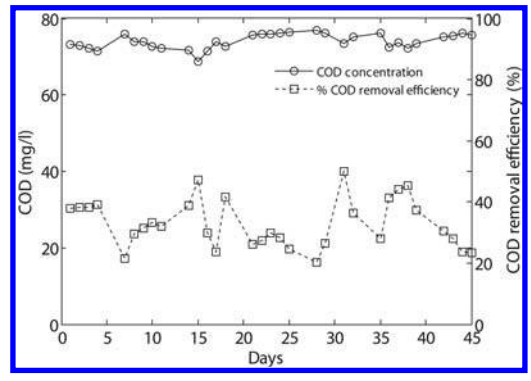


Figure 3. COD: effluent concentration and removal efficiency.

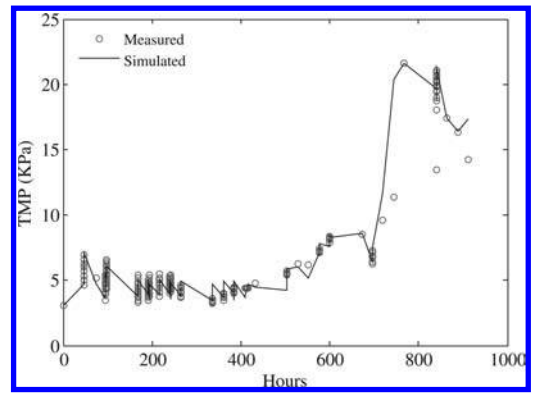


Figure 4. Evolution of TMP with operation time

## 3 RESULTS

The ranges of the operating conditions of the experiments performed at the SMBR are shown in Table 1.

The performance during operation days of the SMBR pilot plant was studied to assess the ability and stability of the system to provide the required COD removal efficiency. The measured data of COD in the effluent and the COD removal efficiency are shown in Figure 3. The COD removal efficiency was higher than 95% for concentrations of MLSS typical for industrial scale MBRs (higher than 6000 $mg \cdot l^{-1}$).

The best neural architecture obtained from exhaustive simulations was composed of one hidden layer and seven neurons in the hidden layer. The adaptation of the neural network in relation to the experimental points can be verified through Figure 4, where the evolutions of the measured and simulated TMP versus the operation time are shown. The value of the correlation coefficient was $R^2 = 0.964$. However, the high data dispersion observed in some zones suggests that the predictive capability of the network could be affected by both the amount and the level noise within the collected operational data.

## 4 CONCLUSIONS

A feed-forward neural network has been built to model the dynamic behavior of the TMP of a SMBR used for the aerobic treatment of municipal wastewater. For this study, the SMBR was subjected to series of different operating conditions. The network inputs were the permeate fluxes, the mixed liquor suspended solids, the hydraulic cleaning cycles, and the operation time. It has been verified that using the Levenberg–Marquardt optimization technique a faster training of the network is feasible. Simulations of the trained network yielded TMP, which are very close to the experimental values. The results of this study have shown that the artificial neural network is a robust tool suitable for predicting the performance of SMBRs.

## ACKNOWLEDGEMENTS

Authors thank ECOLOGÍA TÉCNICA S.A. (ECOTEC) for providing the MBR pilot plant and for the technical support.

REFERENCES


[1] Stephenson, T., Judd, S., Jefferson, B., Brindle, K., (2000), *Membrane bioreactors for wastewater treatment*, IWA-publishing, London.

[2] Le-Clech, P., Chen, V., Fane, T.A.G., (2006), "Fouling in membrane bioreactors used in wastewater treatment", J. of Membrane Science, Vol. 284, pp. 17–53.

[3] Tang, H., Chen Tan, K., Yi, Z., (2007), *Neural Networks: Computational Models and Applications*, Springer-Verlag, Berlin.

[4] Bloch, G., Denoeuxb, T., (2003), "Neural networks for process control and optimization: Two industrial applications", ISA Transactions, Vol 42, pp. 39–51.

[5] Abbas, A., Al-Bastaki, N., (2005), "Modeling of an RO water desalination unit using neural networks", Chemical Engineering Journal, Vol 114, pp. 139–143.

[6] Çinar, Ö., Hasar, H., Kinaci, C., (2006), "Modeling of submerged membrane bioreactor treating cheese whey wastewater by artificial neural networks", J. of Biotechnology, Vol 123, pp. 204–209.

[7] Da Silva, I.N., Flauzino, R.A., (2008), "An approach based on neural networks for estimation and generalization of crossflow filtration processes", Applied Soft Computing, Vol 8, pp. 590–598.

[8] Goh, A.T.C. (1995). "Back-propagation neural networks for modeling complex systems", Artificial Intelligence in Engineering, Vol 9, pp.143–151.

[9] Samani, N., Gohari-Moghadam, M., Safavi, A.A, (2007), "A simple neural network model for the determination of aquifer parameters", Journal of Hydrology, Vol 340, pp 1–11.

[10] Adeloye, A.J., De Munari, A., (2006), "Artificial neural network based generalized storage-yield-reliability models using the Levenberg-Marquardt algorithm", Journal of Hydrology, Vol 362, pp. 215–230.

*Environmental Hydraulics – López-Jiménez et al (eds)*
*© 2010 Taylor & Francis Group, London, ISBN 978-0-415-56697-1*

# Energy production in water supply systems: Computational analysis for new design solutions

Helena M. Ramos
*DECivil – CEHIDRO, Instituto Superior Técnico – IST, Technical University of Lisbon, Portugal*

Alexandre Borga
*Instituto Superior de Engenharia de Lisboa – ISEL, Portugal*

Mariana Simão
*Instituto Superior de Engenharia de Lisboa – ISEL, Portugal*

ABSTRACT: This study is a result of a running research work under HYLOW – EU project from the 7FP about "Energy converters for very low heads" and aims at optimization analyses of new cost-effective turbines for possible implementation in water supply systems. Detailed investigation for alternative typical energy converters are under development on the basis of mathematical and physical fundamentals. A search for a rotating volumetric converter and rotor-dynamic turbines are being considered as a decentralized energy solution either for urban or rural systems.

*Keywords*: Energy production, Water supply systems, New energy converters, Micro-hydro.

## 1 INTRODUCTION

The challenge of this research work is to provide engineering designs and implementation methods that can effectively be customized for a wide range of situations. The turbine technology for low heads application in the micro hydro range has been vastly neglected despite places available in scattered regions of small river flows, in water supply systems, wastewater and irrigation schemes or associated to water treatment plants, where the available heads or discharges are small. Micro-hydro power technologies have an important role to play in the future energy supply, particularly with decentralized, efficient and low cost solutions. It is an attractive alternative to diesel technologies. The potential sites for small scale power devices can be both in urban and rural zones which permit power to the end users at low transmission costs.

It is well known for small heads axial flow hydro turbines[1][3] have become as the best solution reaching higher operating efficiencies. The design and development of micro turbines cannot be based on the methodology of simple scaling down from large turbines due to both economic and manufacturing constraints, which gives a scope for a creative design work under challenging boundary conditions.

## 2 HYDRAULIC MACHINES SIMILARITY

The transfer of the mechanical energy from a flow to a shaft in rotation can be done by (i) volumetric machines of alternative or rotational movement, such as the positive displacement (PD) machines, or by (ii) roto-dynamics machines. Taking as base-study the operating principles applicable to positive displacement (PD) pumps and centrifugal pumps, respectively for volumetric and roto-dynamic turbomachines, there is a significant difference in the pump's response to a system's head/flow curve. Properly applied, positive displacement (PD) pumps offer significant opportunities to improve processes, efficiencies, and to reduce costs. PD pumps create flow and centrifugal pumps create pressure. In volumetric machinery the flow is confined to one or more compartments of variable size. The change in volume can be achieved through a movement of alternative translation or rotation and the compartments can occupy a fixed position or moving up along the machine. In roto-dynamic machines the transfer of power is done through a runner with blades and the flow through the blades. Figure 1 shows the typical classification of pumps. Positive displacement (PD) pumps are divided into two broad classifications, reciprocating and rotary.

In a comparison analysis between PD rotary and centrifugal pumps the mains factors can be enhanced: (i) PD rotary is most adequate for higher viscous fluids; (ii) rotary pumps accept maximum discharges of 208 l/s while centrifugal pumps present a

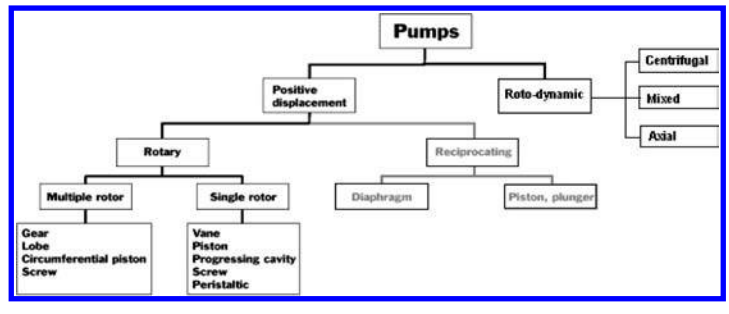


Figure 1. Typical classifcication of pumps.

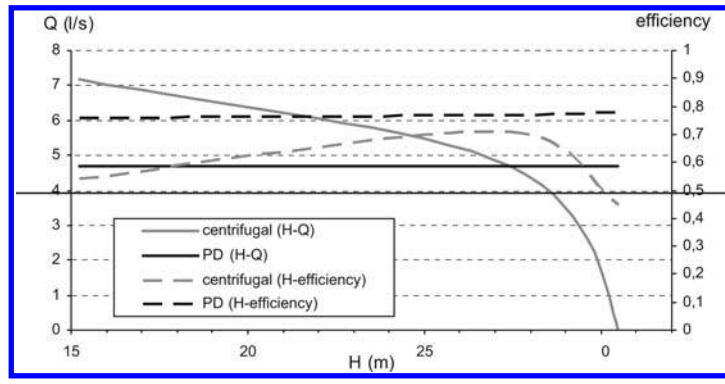


Figure 2. Typical characteristic curves for centrifugal and PD pumps: flow rate and efficiency versus pressure.

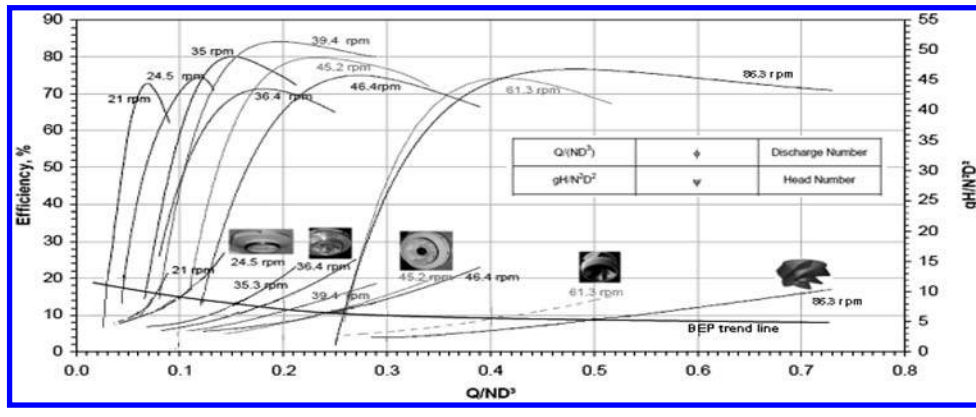


Figure 3. Performance curves of radial and mixed flow PATs (adapted from[1][4][5]).

pump maximum capacity of 7600 l/s; (iii) pump efficiency and energy costs are in general much better for PD rotary machines; (iv) PD rotary machines present a better flow control; (v) both machine types have equivalent good life-cycle costs. However the choice of a centrifugal or a Positive Displacement pump is not always clear. To make a good choice between these pump types it is important to understand the pumps behave very differently [1] (Figure 2).

In the recent years, small and micro hydro has become a possible new application area for pumps as turbines (PAT)[2]. A pump operating as a turbine is very sensitive towards changing boundary parameters, namely head and discharge. Hence a wrong pump selection will result is shift of the operating point, delivering the non-desired output and ultimately may even cause the failure of the project. In Figure 3 there is a large representation of head number ($\psi$) and discharge number ($\phi$) curves, from lower to higher specific speeds values.

## 3 CFD ANALYSIS

### 3.1 Fundamentals

The use of CFD analysis provides much more information than could be explored using experimental tools associated to the real set-up limitations. Researchers and manufacturers use these advanced models for the design of new products and for specific analyses of the flow behavior.

The flow within any energy converter, in particular in a rotary PD turbine, propeller or in a PAT is known to be very complex. The turbulence model commonly used is k-(epsilon), one of the most prominent models which is implemented in most general purpose CFD codes and is used for simulations. The set of equations that describe the process of momentum and mass transfer are known as the Navier-Stokes equations. Within computational fluid dynamics, CFDs are important tools to validate all the experimental results. These tools give a better comprehensible on the hydraulic behaviour of different turbine runners and flow conditions.

### 3.2 Computational simulations

This study deals with innovative solutions as feasible answer to solve the energy in a pressurized integrated-solution for still small available powers.

A new rotary PD-epicycloid energy converter, a mixed flow PAT and a simpler propeller are devices which can operate as new turbines using whether a volumetric or flow changing, imposing a rotation in an impeller and suggesting a high potential of these possible future power converters in the present energy scenario which must be improved.

The numerical simulations help to investigate different types of configurations and parameters that are not easily adopted or measured experimentally. A mesh size has been appropriately chosen as presented in Figure 4. The flow patterns are shown in Figure 5.

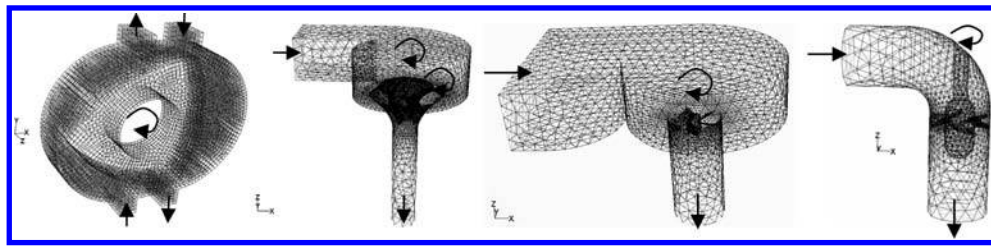

Figure 4. Computational mesh for a) new rotary PD-epicycloid turbine; b) mixed flow PAT; c) volute rotation propeller; d) pipe curve axial flow propeller.

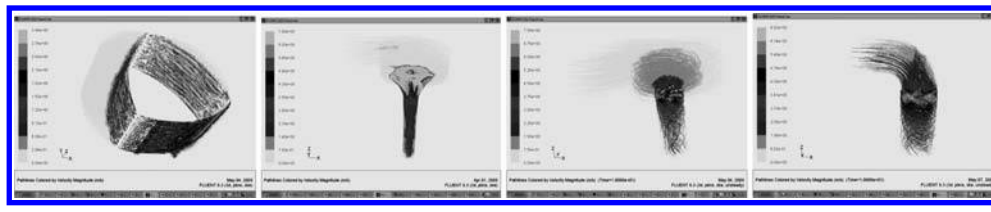

Figure 5. Pathlines by velocity magnitude (m/s): a) new rotary PD-epicycloid turbine; b) mixed flow PAT; c) volute rotation-axial flow propeller; d) pipe curve axial-rotation flow propeller.

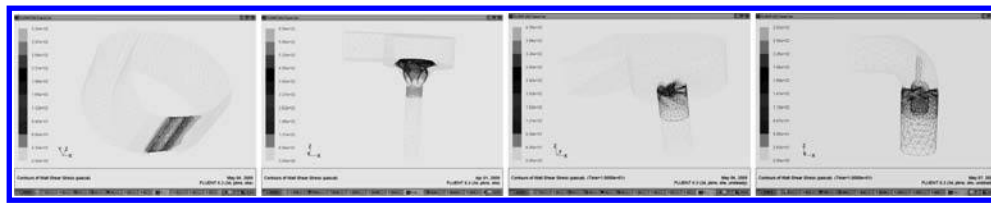

Figure 6. Contours of wall shear-stress variation (in Pascal): a) new rotary PD-epicycloid turbine; b) mixed flow PAT; c) volute rotation-axial flow propeller; d) pipe curve axial-rotation flow propeller.

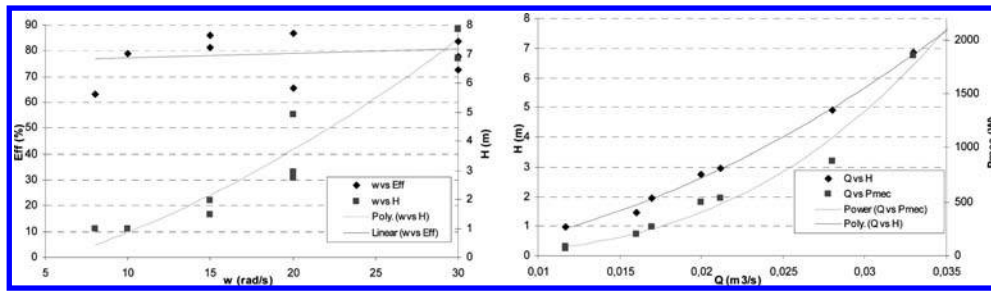


Figure 7. Performance curves estimated for the new rotary PD-epicycloid turbine.

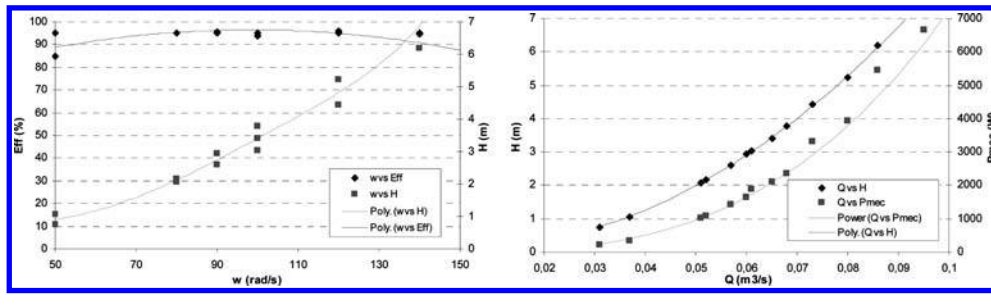


Figure 8. Performance curves estimated for the volute rotation-axial flow propeller.

### 3.3 Performance curves estimation

After detailed analyses of several characteristic parameters for the all types of turbines proposed in this research study, promising values for efficiency are obtained, as well as for the net head, rotational runner speed, shaft power and turbine discharge. It was tested different situations in terms of available head and discharge.

In this document only for the new PD-epicycloid turbine and propellers with a volute or in a pipe section. For a PAT there are already several studies on this subject and for this reason it was not chosen to present here.

It was very significant the influence of the blades inlet and outlet slopes and the thickness of blades in the efficiency value. Thinner blades presented better efficiency values (Table 1).

Table 1. Characteristic parameters estimated for the pipe axial-rotation flow propeller.

| v (m/s) | Qef (m3/s) | M (N.m) | w (rad/s) | Pmec (w) | Y (N/m3) | h (m) | Ph (w) | η (%) |
|---|---|---|---|---|---|---|---|---|
| 2,55 | 0,0195 | -6,1 | -140 | 854 | 9800 | 8,276378 | 1581,616 | 54 |
| 1,5 | 0,0114 | -2,1 | -140 | 294 | 9800 | 2,901837 | 324,1932 | 91 |

| v (m/s) | Qef (m3/s) | M (N.m) | w (rad/s) | Pmec (w) | Y (N/m3) | h (m) | Ph (w) | η (%) |
|---|---|---|---|---|---|---|---|---|
| 2,55 | 0,021 | -6,56 | -140 | 918,4 | 9800 | 6,113469 | 1258,152 | 73 |
| 2 | 0,016 | -4,03 | -140 | 564,2 | 9800 | 3,806959 | 596,9312 | 95 |
| 2,29 | 0,0186 | -5,31 | -100 | 531 | 9800 | 4,930071 | 898,6534 | 59 |
| 1,58 | 0,0124 | -2,37 | -100 | 237 | 9800 | 2,247985 | 273,1751 | 87 |
| 1,40 | 0,011 | -1,81 | -100 | 181 | 9800 | 1,737041 | 187,253 | 97 |
| 1,53 | 0,012 | -2,18 | -100 | 218 | 9800 | 2,080306 | 244,644 | 89 |

## 4 FINAL REMARKS

The exhaustive search and analyses developed for the optimization of new possible energy converters with small power outputs have demonstrated possible future success for new energy converters. The optimized energy converters based velocity triangles at the inlet and outlet of the runner blades can deliver between 100 and 6000 W of hydraulic power at small heads and discharges (between 0,5–6 m and 10–90 l/s) with quality performance curves (hydraulic efficiencies $>60\%$ for the PAT and $>80\%$ for the remaining turbines analyzed, depending on the significance of the scale effects).

The most interesting conclusions of this study are the internal optimization of these new energy converters. The computational analysis with theoretical methodologies helped in understanding the internal hydraulic phenomenon from the inlet, through the impeller until the outlet subjected to different geometric modifications, which comprised the study of the behavior of the shaft power, discharge and impeller hydraulic losses for different values of gross head and turbine speeds.

## ACKOWLEDGEMENTS

The research leading to these results has received funding from the European Community's Seventh Framework Program [FP7/2007-2013] under grant agreement n° 212423, as well as FCT through the project PTDC/ECM/65731/2006.

## REFERENCES

[1] Ramos, H.M., Borga, A., Simão, M. (2009). "Cost-effective energy production in water pipe systems: theoretical analysis for new design solutions", *IAHR2009*, Vancouvre.

[2] Singh, P. (2005). "Optimization of the Internal Hydraulic and of System Design in Pumps as Turbines with Field Implementation and Evaluation", Ph.D Thesis, University of Karlsruhe, Germany, 2005.

[3] Singh, P., Nestmann, F. (2009). "Experimental Optimization of a Free Vortex Propeller Runner for Micro Hydro Application", Experimental Thermal and Fluid Science, 2009.

[4] Ramos, H., Borga, A. (2000). "Pumps as Turbines: Unconventional Solution to Energy Production." Urban Water International Journal, Elsevier Science Ltd., Exeter, Volume 1, N° 3, PP. 261-265, Reino Unido, ISSN 1462–0758.

[5] Ramos, H.; Borga, A. (2000). "Pumps Yielding Power." Dam Engineering, Water Power & Dam Construction, Volume x, Issue 4, PP. 197–217, Reino Unido, ISSN 0-617-00563-X, 2000B.

*Environmental Hydraulics – López-Jiménez et al (eds)*
*© 2010 Taylor & Francis Group, London, ISBN 978-0-415-56697-1*

# CFD simulation of the filling cycles in a potable water storage tank

Diego F. Muriel, Fabio H. Garzon & Carolina Mosquera
*Grupo de Investigación en Gestión Avanzada del Agua Urbana, GIGAAU,*
*Departamento de Ingeniería Civil, Pontificia Universidad Javeriana Cali, Cali, Colombia*

ABSTRACT: All 42 potable water storage tanks of the Water Distribution System in Cali, Colombia, show a reduction in disinfectant residual levels up to 50% after passing through these facilities. One of the tanks showed 20–50% decrease in disinfectant levels as well as aged water entering the distribution system. Therefore, in order to rewrite the operations directive for this facility and preserve water quality, a hydrodynamic study was conducted to describe flow patterns and to locate recirculation zones created during filling cycles. The methodology involved Computational Fluid Dynamic simulations based on HydroTank® supported by a one year long term operational data series. The computational model provided velocity fields required to describe the filling cycles of the study case, in which three specific zones (transfer of energy, presence of vortices and wall influenced behavior) and seven major vortexes were identified during the worst case scenario. The CFD application provided a low cost methodology that determines prior implementation of any decision, the operative scheme that preserves better the water quality within storage tanks.

*Keywords*: CFD, Water Storage Tanks, Hydrodynamic Analysis.

## 1 INTRODUCTION

In order to prevent considerable reduction of disinfectant residual levels, a potable water storage tank (PWST) should present a complete mixed flow regimen during its filling cycle. In addition, unlikely clear well chambers and contact basins, PWST should not be designed or operated in plug flow regimens[2]. Therefore, whether the tank operates with simultaneous inflow and outflow or fill and draw scheme, storage tanks designed for plug flow will lose more disinfectant than those designed for a mixed flow.

Frequently, the only source of mixing in PWST is the energy of the incoming water which is provided through the formation of a turbulent jet. The absence of enough inflow energy or an undeveloped inflow jet will lead to dead parcels and recirculation zones, creating a number of biological, physical and chemical waterborne problems[4]due to the aged water remaining in these regions. Grayman et al. (2004)[3] stated that avoiding the stagnation zones should be one of the implicit objectives in the design and operation of PWST, as a consequence, it is critical to determine where and under which conditions the recirculation and dead zones will appear during the filling cycle, as well as to describe the inflow jet characteristics.

A 15 Ml PWST located in a tropical environment in the city of Cali (Colombia) showed a 20–50% reduction in disinfectant residual levels[6]. The hypothesis of this behavior was the existence of recirculation and dead zones, causing aged water to enter into the distribution system in draw cycles. This problem required a methodology that would allow a complete description of inflow jets and exact locations of recirculation zones of the PWST under study.

Several works have discussed the capability to describe hydrodynamic behaviors of a broad selection of methodologies applied to different study cases. Grayman et al. (1996)[1] applied and discussed the advantages and disadvantages of physical scale models, Computational Fluid Dynamics (CFD) and system models to determine how different configurations affect water quality in PWST. Grayman et al. (2004)[3] gave a broader description of tools to assist in the design, retrofit or operation of PWST, making a clear differentiation between monitoring (water quality, hydrodynamic and temperature) and modeling (physical scale models, system models and CFD). Mahmood et al. (2005)[5] applied and demonstrated that CFD, water temperature measurements and chlorine residual measurements are useful tools in predicting mixing characteristics in PWST.

Based on these studies, Computational Fluid Dynamic is a cost and time effective solution to detect and accurately locate recirculation zones of aged water. CFD is the best methodology to represent the hydraulic behavior of a PWST under different operative schemes and configurations. But, despite the advantages and existence of several studies of CFD in PWST, applications of CFD based on analysis of operational data have yet to be reported.

As consequence, a CFD analysis of filling cycles established from operational data is presented in this paper. The characteristic filling cycles drawn of a one year long term data series, and the CFD transient and isothermal simulation of this facility provided answers for: Are there any recirculation and dead zones present in filling cycles? And if these zones exist, where are they located?

## 2 METHODOLOGY

Nápoles PWST is a cylindrical tank located in the City of Cali (Colombia) at 1000 a.m.s.l. It has a maximum water level of 9,5 m and a diameter (D) of 45 m for a 15Ml of maximum storage. It operates in successive fill and draw cycles and has only one 24 in (d) pipe centered in the bottom of the tank and facing upward. The analysis performed on one year long data series provided the characteristic filling cycles (Table 1) based on statistical procedures not reported herein.

A CFD simulation using Hydrotank® (CFD commercial code[2]) followed the operational characterization. The computational methodology solved equations of conservation of mass, momentum and energy to provide velocity values in time and space for four filling cycle cases. This CFD code, developed under a Water Research Foundation (formerly AWWA Research Foundation) research project, reduces first, the complexity associated with the selection of the mathematical model that represents the fluid processes, second, the numerical representation of the mathematical model, and third, the method for solving the numerical representation. In other words, Hydrotank® is a one purpose focused program enhanced by a graphical user

Table 1. Filling cycle cases simulated with Hydrotank®.

| Case | Flow rate | | Water level | |
|---|---|---|---|---|
| 1 | Maximum | 1,55 $m^3/s$ | Highest | 5,0 m |
| 2 | Maximum | 1,55 $m^3/s$ | Lowest | 1,0 m |
| 3 | Minimum | 0,04 $m^3/s$ | Highest | 5,0 m |
| 4 | Minimum | 0,04 $m^3/s$ | Lowest | 1,0 m |

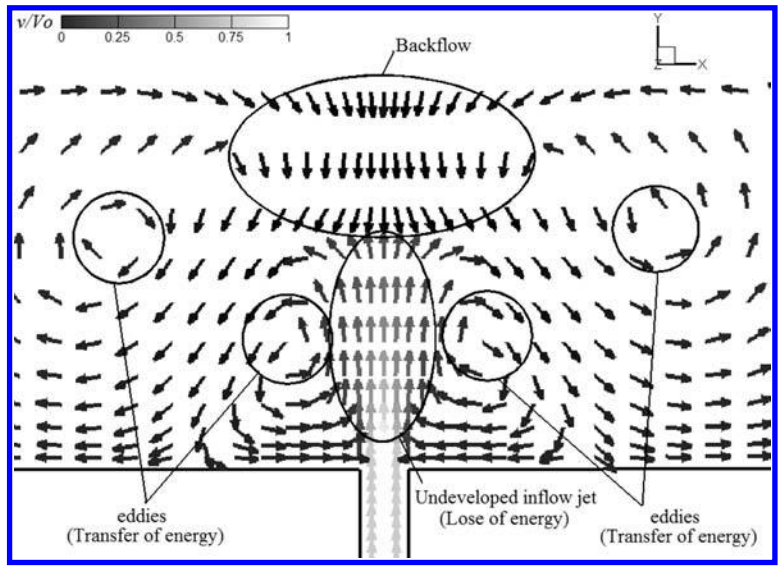


Figure 1. The inflow jet and the presence of backflow and eddies.

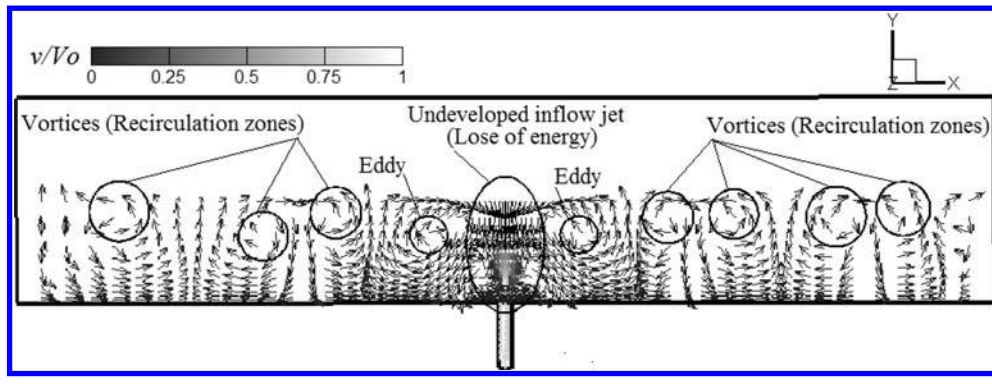


Figure 2. Presence of recirculation zones and eddy formations for the minimum flow rate and highest water level.

interface (GUI) that applied the CFD methodology to PWST, requiring few input information, and no manipulation of the source code or mesh configuration.

The model input data were: maximum and minimum inflow rate; highest and lowest water level drawn of a one year long time series; diameter of the cylindrical tank (D = 45 m); inlet/outlet diameter (d = 24 in); height (h = 9,5 m); and inlet/outlet orientation and location (centered in the bottom and facing upward).

The initial conditions established were as follow: fill and draw operation scheme; isothermal analysis; constant inflow rate during the analysis; transient analysis; coarse mesh size; and 10 minutes real time analysis (representing 25% of the expected filling cycle duration). Additionally, the boundary conditions were preset by the CFD program.

## 3 RESULTS

As expected, the most critical condition considering stratifications was experienced by the combination of *minimum inflow rate* and *highest water level*. This represents the less energy available, mixing the highest water mass stored for this tank. Among the four situations analyzed, this one showed the most problematic mixing process.

Due to the low inflow energy, the inflow jet was not completely developed (Figure 1) reducing the amount of energy available for transferring from the jet to the surroundings. The undeveloped jet created a backflow which reduces in a higher degree the inflow energy. Nevertheless, the transfer of energy from the inflow to the surrounding fluid was done by four eddies clearly identifiable in Figure 1.

The combination of an undeveloped mixing mechanism and a low inflow energy rate created 7 identifiable zones of recirculation (Figure 2). These stagnated zones produce aged water with a lower quality and a highly reduced level of disinfectant residual. Then in the draw cycle, these parcels will enter the distribution system and will be consumed with a considerable decreased water quality compared with that of the parcel which left the water treatment plant.

The asymmetry of the velocity field in this case is attributed to the grid resolution. A finer grid will produce better results but would compromise the CFD program execution time and precision: it is important to consider that finer grid sizes will

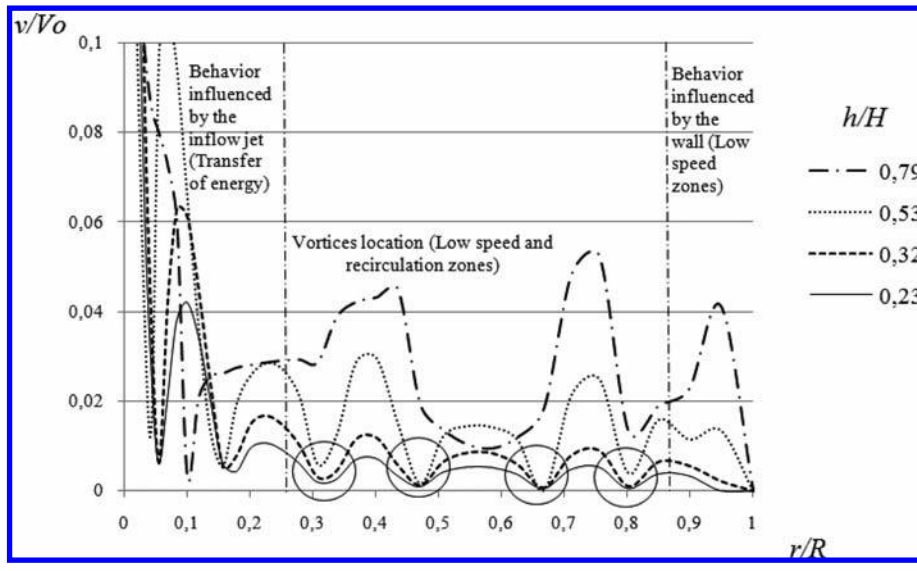


Figure 3. Location of vortices at the plane Z = 0.

introduce stability and convergence problems to the CFD code used in this study, representing not accurate flow fields[2]. So, for this practical engineer focused problem the results are considered acceptable.

Then, after solving precision and convergence, and identifying recirculation zones and inflow jet, the result of the simulation showed three general areas (Figure 3, where ***Vo*** and ***H*** is the maximum velocity and height respectively, and ***R*** is the radius). Due to scale problems, the nominal velocity is presented from 0 to 0,1 in order to allow a better description of the behavior in the low velocity zones.

Based on Figure 3, the first zone, influenced by the inflow jet, presents the energy transfer mechanism and its four eddies. This zone shows the highest nominal velocities and therefore the best mixing process. The middle zone is the most stagnated region: it shows the main vortices of aged water. In this zone each vortex is precisely located by the confluence of the nominal height series. The third zone presents low and cero velocity data due to wall influence, which is a slip or semi-slip boundary condition preset by the CFD program.

## 4 DISCUSSION

The CFD simulation of the characteristic filling cycles allowed the location of recirculation zones for the case under study: it presented 7 vortices on the most critical condition of mixing. These vortices are producing aged water that enters the distribution system with low disinfectant residual levels in the draw cycles of the actual scheme of operation.

In addition, the simulation also provided information about the energy transfer mechanism: the critical case showed an undeveloped inflow jet with a back flow toward it. It also presented 4 eddies that transfer the energy provided by the incoming water to the surrounding fluid.

Three general areas were also identified based on post-processed data of the critical case: a zone of transfer of energy in the middle of the tank influenced by the inflow jet, a low speed zone located near the wall representing the preset slip boundary condition, and a third zone of low speed between the first two areas that presented the 7 vortices.

In general, the municipal facility operators could take a step toward the physical, biological and chemical problems caused by the presence of aged water in the distribution system. Operative schemes of this storage tank could be drawn in further studies of the extensive data provided by the CFD simulation.

On top of all, as described by Grayman et al. (2004)[3], the only mixing mechanism and source of energy in this type of facility is the inflow jet, and an undeveloped jet caused poor eddies and low transfer of energy in this study case. As a result, several recirculation and dead zones appeared, and as consequence, aged water is constantly introduced into the distribution system unless new operative schemes are implemented.

## REFERENCES


[1] Grayman, W. M., Deininger, R. A., Green, A., Boulos, P. F., Bowcock, R. W. and Godwin, C. C.(1996). “Water quality and mixing models for tanks and reservoirs”, J. of American Water Works Association, Vol. 88, Num. 7, pp.70–83.

[2] Grayman, W. M., Rossman, L. A., Arnold, C., Deininger, R. A., Smith, CH., Smith, J. F., Schnipke, R. (2000), *Water quality modeling of distribution system storage facilities*, American Water Works Association Research Foundation, Denver.

[3] Grayman, W. M., Rossman, L. A., Deininger, R. A., Smith, C. D., Arnold. C. N. and Smith, J. F. (2004). “Mixing and aging of water in distribution system storage facilities”, J. of American Water Works Association, Vol. 96, Num. 9, PP. 77–87.

[4] Kirmeyer, G. J., Kirby, L., Murphy, B. M., Noran, P. F., Martel, K. D., Lund, T. W., Anderson, J. R., Medhurst, R. (1999), *Maintaining water quality in finished water storage facilities*, American Water Works Association Research Foundation, Denver.

[5] Mahmood, F., Pimblett, J. G., Grace, N. O. and Grayman, W. M. (2005), “Evaluation of water mixing characteristics in distribution system storage tanks”, J. of American Water Works Association, Vol. 97, Num. 3, pp. 74–88.

[6] Muriel, D. F. (2008), *empleo de modelos matemáticos basados en parámetros geométricos e hidráulicos para evaluar la posibilidad del deterioro de la calidad del agua potable en tanques de almacenamiento o compensación de la ciudad de cali*, Pontificia Universidad Javeriana Cali: Undergraduate Thesis, Cali.

*Environmental Hydraulics – López-Jiménez et al (eds)*
*© 2010 Taylor & Francis Group, London, ISBN 978-0-415-56697-1*

# Effects of the pipe-wall rheological behaviour on hydraulic transient pressures

Alexandre K. Soares
*Department of Environmental and Sanitary Engineering, Federal University of Mato Grosso, Cuiabá, Brazil*

Dídia I.C. Covas
*Instituto Superior Técnico, Technical University of Lisbon, Lisbon, Portugal*

Luisa F.R. Reis
*São Carlos School of Engineering, University of São Paulo, São Carlos, Brazil*

Helena M. Ramos
*Instituto Superior Técnico, Technical University of Lisbon, Lisbon, Portugal*

*Keywords*: Hydraulic transients, Field tests, Experimental data, Metal pipes, Plastic pipes.

## 1 INTRODUCTION

The current research work focuses on the analysis of hydraulic transients in three pipe systems composed of different pipe material. Transient data collection tests have been carried out in real life system – a cast iron water pipeline – and in two pipe rigs, being one composed of polyvinyl chloride (PVC) pipes and the other one composed of high density polyethylene (HDPE) pipes. Numerical results incorporating different unconventional dynamic effects in the hydraulic simulator (i.e., unsteady friction and viscoelasticity) are compared with collected data. Comments are drawn on hydraulic transient analyses in metal and in plastic pipes for design and operation of water pipe systems.

## 2 HYDRAULIC MODELS

Equations that describe the one-dimensional transient-state flows in closed conduits are the momentum and continuity equations (Eq. 1 and 2, respectively). Since the flow rate and piezometric head (dependent variables) in transient flows are functions of time and space (independent variables), these equations are a set of two hyperbolic partial differential equations[1,2,3]:

$$\frac{\partial H}{\partial x}+\frac{1}{gA}\frac{\partial Q}{\partial t}+h_f=0 \tag{1}$$

$$\frac{\partial H}{\partial t}+\frac{a_0^2}{gA}\frac{\partial Q}{\partial x}=0 \tag{2}$$

where $x$ = coordinate along the pipe axis; $t$ = time; $H$ = piezometric head; $Q$ = flow rate; $a_0$ = celerity or elastic wave speed (dependent on the fluid compressibility, and on the physical properties and external constraints of the pipe); $g$ = gravity acceleration; $A$ = pipe cross-sectional area; and $h_f$ = head loss per unit length ($h_f = fQ|Q|/2DA^2$ in turbulent conditions, in which $f$ = Darcy-Weisbach friction factor and $D$ = pipe inner diameter). The unsteady-state friction component has been calculated by using Vítkovský *et al.*'s[4] formulation, in which the unsteady head loss component is function of both local and convective accelerations. This approach is relatively accurate to describe hydraulic transients in metal pipes, which exhibit linear elastic behaviour of the pipe walls; however, it is considerably imprecise for plastic pipes (e.g. polyethylene and polyvinyl chloride), which have an immediate-elastic response and a retarded-viscous response. In this way, strain can be decomposed into an instantaneous-elastic strain, $\varepsilon_e$, and a retarded strain, $\varepsilon_r$:

$$\varepsilon(t)=\varepsilon_e+\varepsilon_r(t) \tag{3}$$

In order to take into account the viscoelastic behaviour of the pipe-wall, the continuity equation (Eq. 2) has to be derived again from the Reynolds transport theorem. Whilst the third term represents the retarded effect of pipe-wall, the elastic strain is. The two components of strain have to be taken into account: (i) the elastic strain, which is included in the piezometric head time derivative and in the elastic wave speed, and (ii) the retarded strain, which is represented by the third term in continuity equation:

$$\frac{dH}{dt}+\frac{a^2}{gA}\frac{\partial Q}{\partial x}+\frac{2a^2}{g}\frac{d\varepsilon_r}{dt}=0 \tag{4}$$

In this paper, the set of differential Eqs. (1) and (4) together with the strain-stress equation has been solved by the Method of Characteristics (MOC).

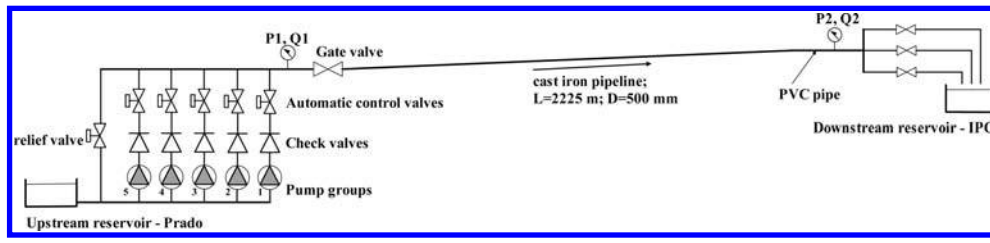


Figure 1. Simplified scheme of Guarda water pipeline system.

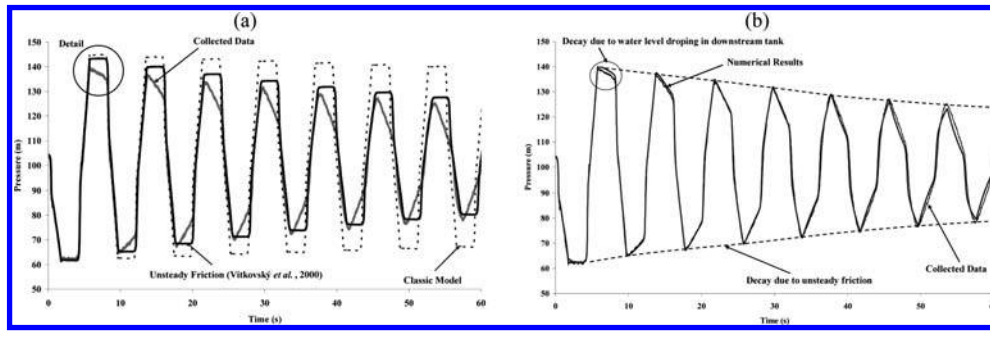


Figure 2. Observed pressure heads at Location p1 versus numerical results: (a) classic elastic model and elastic model taking into account unsteady friction (constant-level reservoir as downstream end boundary condition); (b) elastic model taking into account unsteady friction and variable level tank as downstream end boundary condition (Q0 = 72 L/s).

## 3 RESULTS

### 3.1 *Hydraulic transients in metal pipes*

The pumping system, which connects storage tanks of Prado to IPG, managed by Zêzere and Côa Water in the city of Guarda, Portugal, has been analyzed in this work during the occurrence of simulated transient flows caused by one pump trip-off. Prado pumping station is composed of five groups, being three of them of submergible type and the other two of centrifugal type. These groups are linked to a cast iron pipe with diameter of 300 mm (discharge line), having in each connection an automatic control valve and a gate valve. As a protection device, a pressure relief valve with diameter of 200 mm and with a gate valve is installed at the upstream of the discharge line. The discharge line with 300 mm diameter extends to the inspection chamber located outside the pumping station, where there is the transition to the cast iron rising main with 500 mm diameter. Such pipeline extends from the inspection chamber to the entrance of IPG tank, being its length of 2,225 m. The total length of the pipeline system, from the Prado pumping station to the IPG reservoir, is approximately 2,240 m. Figure 1 presents the simplified scheme of Guarda water pipeline system.

The celerity was estimated in 1,132 m/s and two different scenarios have been considered: (i) constant-level reservoir as the downstream boundary condition and calculating the head losses with and without the unsteady friction component; and (ii) a variable level tank as the downstream boundary condition and considering unsteady friction effects. All the field tests were carried out with the relief valve out of service (i.e., by closing the gate valve immediately at downstream). In this way, such protection device did not influence the system behaviour, which reduced the uncertainties related to the different effects in pressure variations, such as the attenuation and dispersion due to unsteady friction and the pressure relief due to the variable level tank. Figure 2a presents pressure heads observed at Location P1 (immediately downstream the check valve) and the numerical results obtained from the classic elastic model (with a steady-state friction model) and the numerical results obtained from the elastic model taking into account unsteady friction losses. In this scenario, a constant-level reservoir has been considered as downstream end boundary condition. The numerical results obtained for the second scenario (elastic model taking into account unsteady friction losses and variable level tank as downstream end boundary condition) and the pressure heads observed at Location P1 are presented at Figure 2b.

Numerical results fitted extremely well with collected pressure data and the model can describe transient pressure wave attenuation, dispersion and shape. It can be noted the description of pressure relief in the first maximum pressure peak by the model when the downstream end boundary condition is defined as a variable level tank. Whilst such assumption is on the safest side for design purposes as it predicts higher overpressures, it is not accurate for water pumping system operation and calibration purposes, once outlet pipes are typically separated from the receiving tank. Numerical results of the elastic model were fitted to the observed data in terms of damping and phase shift of pressure waves, when unsteady friction effects were taken into account and the downstream end boundary condition was properly defined as a small storage tank with a variable level and a free discharge into the downstream end reservoir.

### 3.2 *Hydraulic transients in PVC pipes*

Transient data were collected from tests carried out in an Experimental Hydraulic Circuit (EHC) at the Department of Hydraulics and Sanitary Engineering, São Carlos School of Engineering, Brazil (Figures 3a). The EHC is composed of PVC pipes with a nominal pressure of 750 kPa and a total length of 203.20 m. The supply system includes two parallel centrifugal pumps with powers of 0.7355 kW and 3.68 kW, with a swing check-valve located immediately downstream. There is a ball valve with 1½ inches diameter at the downstream end to generate water hammer.

According to the manufacturer, the modulus of elasticity of PVC varies between 2.40 and 2.75 GPa, which corresponds to wave speeds of 411 and 438 m/s, respectively. According to pressure data collected, wave speed was estimated as approximately

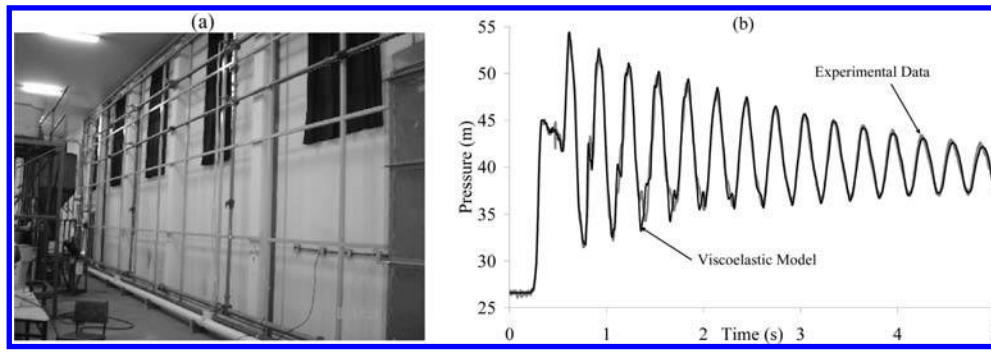


Figure 3. (a) PVC pipe rig; (b) numerical results of the viscoelastic transient solver versus transient pressure data at downstream end of the pipeline.

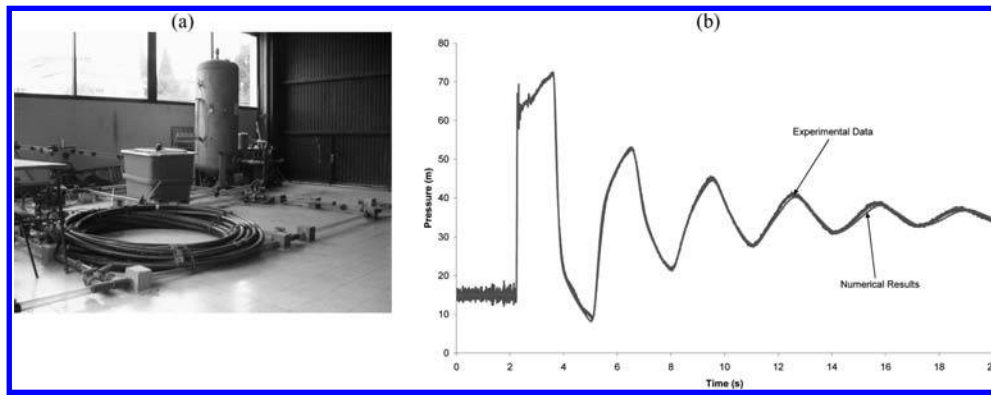


Figure 4. (a) Experimental set-up composed of HDPE pipes; (b) numerical results of the viscoelastic transient solver versus transient pressure data at downstream end of the pipeline.

440 m/s, the corresponding modulus of elasticity being equal to 2.78 GPa. When comparing observed data with the results of numerical simulations using wave speeds between 411 and 440 m/s and a classic transient solver, large discrepancies were observed: calculated transient pressures were delayed in time and lower in amplitude than observed pressures. Actually, wave speed in plastic pipes is a time-dependent function rather than a constant parameter as it relates to linear elastic materials due to both fluid inertial and frictional effects (unsteady friction) and pipe-wall viscoelasticity. Transient pressures calculated with $a_0 = 460$ m/s have shown good results in terms of maximum observed pressures, though pressure wave attenuation and dispersion were not well described.

Afterwards, two main approaches were followed to calibrate the developed transient solver. First, the model was calibrated considering only steady and unsteady friction effects. Second, a viscoelastic transient solver was used and a creep function was determined by inverse calibration, neglecting unsteady friction effects. Discrepancies between numerical results and observed data showed that elastic transient solvers even when considering unsteady friction effects cannot describe transient pressure attenuation and dispersion in PVC pipes. A second attempt to describe the transient event in the PVC pipe system was carried out by using the viscoelastic transient solver developed in this study neglecting unsteady friction. Numerical results obtained by using the linear viscoelastic transient solver are presented in Figure 3b at downstream end of the pipeline. Numerical results fitted extremely well observed pressure data. This shows that the calibrated transient solver can accurately describe transient pressure wave attenuation, dispersion and shape. With regard to the modulus of elasticity, there is an error up to 28% whether the manufacturer's value is selected in the simulations. For design purposes, the modulus of elasticity has to be raised when the classic water hammer theory is adopted.

### 3.3 *Hydraulic transients in HDPE pipes*

A pipe rig assembled at the Department of Civil Engineering, Instituto Superior Técnico, Portugal, has been used for the analyses of hydraulic transients in high density polyethylene (HDPE) pipes. The experimental set-up has a Reservoir-Pipe-Valve configuration with nominal diameter 50 mm and total length 203 m (Figure 4a).

Transient pressure data have been collected in order to calibrate the developed viscoelastic transient solver. The unsteady-state friction losses have been calculated by using Vítkovský *et al.*'s[4] formulation. The decision variables (viscoelastic parameters) have been determined by an inverse model based on both pressure data and the Levenberg-Marquardt method. The elastic wave speed was estimated in 350 m/s, which is equivalent to the modulus of elasticity 1.8 GPa, being 1.8 to 2.5 times bigger than the modulus of elasticity of HDPE according to the manufacturers (0.7 to 1.0 GPa). Numerical results obtained by using the linear viscoelastic transient solver are presented in Figure 4b for the downstream end of the pipeline. Numerical results fitted extremely well observed pressure data. With regard to the modulus of elasticity, there is an error up to 150% whether the manufacturer's value is selected in the simulations. For design purposes, the modulus of elasticity has to be raised when the classic water hammer theory is adopted.

## 4 CONCLUSIONS

The current paper presents three case studies with pipe systems composed of different pipe materials (i.e., cast iron, PVC and HDPE). The cast iron pipeline was analyzed and the numerical results obtained have shown that the classical water hammer theory is very imprecise for the description of the hydraulic system behaviour, as well as the assumption of a constant-level reservoir at the downstream end. Results obtained from the tests in the two experimental setups composed of plastic pipes (PVC and HDPE) have shown that the viscoelastic rheological behaviour of the pipe wall has to be considered in the mathematical model. For design purposes, classic models can accurately predict extreme transient pressures in plastic pipes as long as the modulus of elasticity used is 1.5 times higher than the value suggested by manufacturers for PVC pipes and 2.0 higher for HDPE pipes.

## REFERENCES


[1] Almeida, A.B., Koelle, E. (1992), *Fluid Transients in Pipe Networks*, Computational Mechanics Publications, Glasgow.

[2] Chaudhry, M.H. (1987), *Applied Hydraulic Transients*, Van Nostrand Reinhold Company, 2nd Ed., New York.

[3] Wylie, E.B.; Streeter, V.L. (1993), *Fluid transients in Systems*, Prentice-Hall, New Jersey.

[4] Vítkovský, J.P.; Lambert, M.F.; Simpson, A.R. (2000), "Advances in unsteady friction modelling in transient pipe flow". *Proceedings of 8th International Conference on Pressure Surges – Safe Design and Operation of Industrial Pipe Systems*, Ed. Anderson, A., Pub. BHR Group Ltd., Publication No. 39, Suffolk, UK, 471–498.

*Environmental Hydraulics – López-Jiménez et al (eds)*
*© 2010 Taylor & Francis Group, London, ISBN 978-0-415-56697-1*

# Mathematical modeling of pressurized system behaviour with entrapped air

Sandra C. Martins
*ISEL – Instituto Superior de Engenharia de Lisboa, Portugal*

Helena M. Ramos & António B. Almeida
*IST – Instituto Superior Técnico, Lisboa, Portugal*

ABSTRACT: The presence of entrapped air in pressurized hydraulic systems is considered a critical condition for the infrastructure security, due to the transient pressure enhancement related with its dynamic behaviour, similar to non-linear spring action. A mathematical model for the assessment of hydraulic transients resulting from rapid pressurizations, under referred condition is presented. Water movement was modeled through the elastic column theory considering a moving liquid boundary and the entrapped air pocket as lumped gas mass, where the acoustic effects are negligible. The method of characteristics was used to obtain the numerical solution of the liquid flow. The resulting model is applied to an experimental set-up having entrapped air in the top of a vertical pipe section and the numerical results are analyzed.

*Keywords*: entrapped air, pressurization, elastic model.

## 1 INTRODUCTION

Entrapped air pockets are particularly harmful during pressurization and further start-up of hydraulic systems. By establishing a physical discontinuity in the liquid medium its dynamic behaviour is frequently responsible for the decrease in safety and reliability levels of the hydraulic infrastructures. Some previous case studies clearly elucidate this problematic and the dimension of entrapped air potential damaging effects[1][2].

One of the first studies evaluating the effect of entrapped air in hydraulic systems [4] assumed that the elastic effects from the liquid as well as the variation on the liquid column length could be disregarded. The analysis of these simplification procedures was deeply examined later [3][4]. The rigid theory was also applied to modeling the filling of pipes with irregular profile, in the presence of $n$ entrapped air [5]. The authors pointed out that the maximum pressure reached at the first air pocket does not change with other blocking columns, with the case having just one air pocket ($n = 1$), representing the most interesting one in the analytical point of view. Almeida and Koelle [2] stated about the existence of critical volumes associated to maximum pressure values. In the study implemented by Lee [6], the influence of acoustic effects on air pockets is quite limited or even negligible when compared to those effects obtained in the liquid phase.

A mathematical model for the assessment of hydraulic transients in pipeline systems with entrapped air, based on the elastic column theory, with a moving liquid boundary, is presented. This model was applied to an experimental set-up having entrapped air in the top of a vertical pipe section.

## 2 HYDRAULIC SYSTEM AND INITIAL ASSUMPTIONS

The simple case represented in Figure 1 was considered. The pipe connected to the hydro pneumatic reservoir (source of pressurization) has a transparent vertical section at its downstream edge in which top the air pocket is entrapped. The ball valve is controlled by a pneumatic actuator. For modeling the transient regime caused by the valve opening, the following basic assumptions were considered:

- air mass unchanged with its compression and expansion following the polytropic equation of the perfect gases: $p^* \forall^n = C$, where $p^*$ = absolute air pressure, $\forall$ = entrapped air volume, $n$ = polytropic exponent and $C$ = constant determined by the initial conditions;
- acoustic propagation of disturbances in the air pocket negligible;
- air-water interface flat and normal to the pipe axis;
- the quasi-stationary hypothesis concerning the liquid flow is assumed, with the head losses being calculated by the friction factor of Dairy-Weisbach ($f$);
  – isothermal deformation of the liquid characterized by its bulk modulus compressibility.

## 3 MATHEMATICAL MODELING

### 3.1 *Liquid column*

The well known equations for the elastic model – a first order quasi-linear hyperbolic system of partial differential equations – describing the one-dimensional transmission of disturbances for quasi-incompressible fluids in uniform pipes, were transformed by the method of characteristics, into a pair of simpler ordinary differential equations,

$$dH \pm \frac{a}{g} dV \pm \frac{f}{2gD} V|V| dx = 0 \quad (1)$$

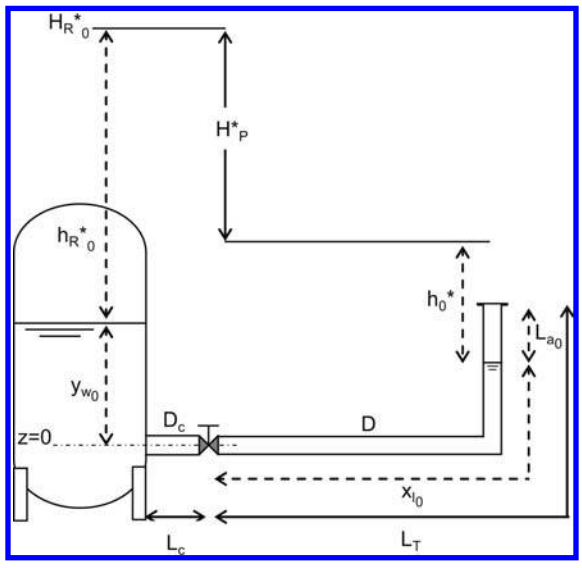


Figure 1. Scheme of the experimental facility.

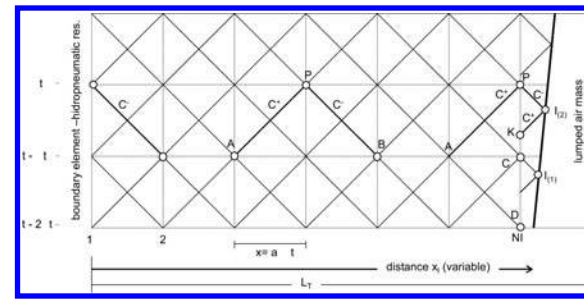


Figure 2. Computational grid on plane.

where H = hydraulic head, V = fluid velocity, a = wave speed propagation, f = friction factor, g = gravitational acceleration, D = inside pipe diameter, valid along the characteristic lines $C^+$ and $C^-$ on the $(x;t)$ plane, defined by $dx = \pm\, a\,dt$. Its numerical integration was done through an explicit and specified time interval technique, in a direct computational grid on plane $(x;t)$ with a constant $\Delta t$ and $\Delta x = a\Delta t$ (Fig. 2). A first order scheme for the integration of the friction terms was used, being the number of computational section variable according to the length of the liquid column.

### 3.2 *Downstream mobile boundary: air interface*

To obtain the solution in air-liquid interface, the formulation developed by Lee [6] was adopted. The liquid front position $(x_{I(2)}; t_{I(2)})$, within the interval $t$ e $t - \Delta t$, verifies the kinematic equation having its origin in $(x_{I(1)}; t_{I(1)})$,

$$x_{I_{(2)}} = x_{I_{(1)}} + \frac{1}{2}\left(V_{I_{(1)}} + V_{I_{(2)}}\right)\left(t_{I_{(2)}} \quad t_{I_{(1)}}\right) \tag{2}$$

and the characteristic equation $C^+$ with its origin in $K$ (Fig. 2),

$$H_{I_{(2)}} = H_K + \frac{a}{g} V_K \quad \frac{f\left(x_{I_{(2)}} \quad x_P\right)}{2gD} V_K |V_K| \quad \frac{a}{g} V_{I_{(2)}} \tag{3}$$

being $H_K$ and $V_K$ determined through linear interpolations between points $C$ and $D$ or $P$ and $C$. Assuming the polytropic relation to model entrapped air behaviour, the hydraulic head at the interface $H^*_{I_{(2)}}$ (absolute units) is then defined,

$$H^*_{I_{(2)}} = z_{I_{(2)}} + \frac{p^*_0}{\gamma} \quad \frac{L_T \quad x_{I_{(0)}}}{L_T \quad x_{I_{(2)}}} \psi \quad ^n + \frac{V^2_{I_{(2)}}}{2g} \tag{4}$$

where the coefficient $\psi$ expresses the local effect of the radial and circumferential pipe deformations To get the iterative solution $x_{I(2)}$, the Newton-Raphson method was applied to find the root of the combined equation. The superscript * denote pressure values referred to the absolute vaccum.

### 3.3 *Upstream boundary condition: hidropneumatic reservoir*

The fluid compressibility and material elasticity of the components are not taken into account (rigid theory). The association of concentrated parameters of resistance, inertia and fluid capacitance of its individual components, namely the reservoir (a non linear capacitant component), the connecting pipe section (having resistance and inertial descriptors) and the valve control (resistance descriptor) lead to the next overall equation:

$$H_R \quad H_1 = I_G \frac{dV_E}{dt} + R_G |V_E| V_E \tag{5}$$

where $H_R =$ hydraulic head in reservoir, $H_1 =$ hydraulic head in the computational section 1 (reservoir connection), $I_G$ and $R_G$ = inertia and global resistance descriptors of the element and $V_E$ = instantaneous velocity in the connecting pipe section of the boundary element. Using a 1st order approach for the descriptors $I_G$ and $R_G$ the following constitutive equation is obtained, from the numerical integration of (5), within time interval between $t - \Delta t$ and $t$,

$$H^*_{R(t)} \quad H^*_{1(t)} = H^*_{1(t \ \Delta t)} \quad H^*_{R(t \ \Delta t)} \quad \frac{2I_G}{\Delta t} V_{E(t \ \Delta t)} + \left(\frac{2I_G}{\Delta t} + 2R_G |V_{E(t \ \Delta t)}|\right) V_{E(t)} \tag{6}$$

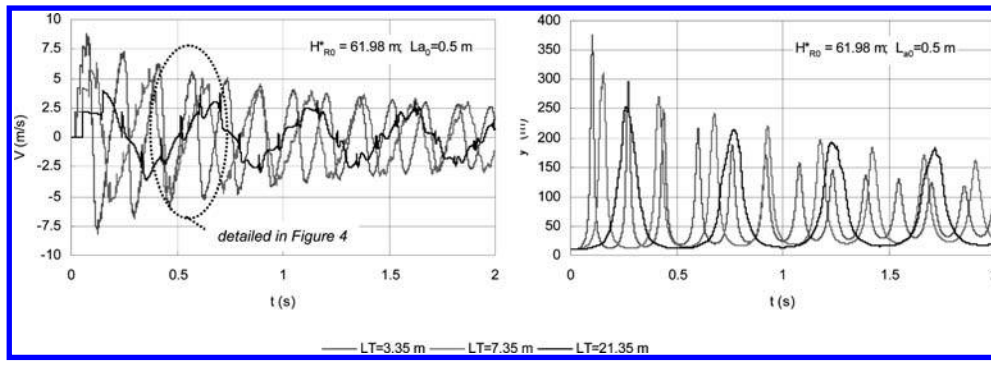


Figure 3. Effect of the experimental pipe length in the hydraulic transient response.

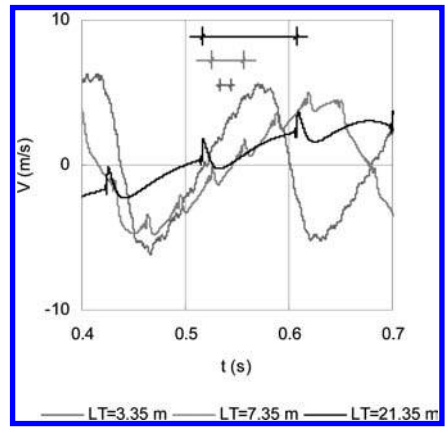


Figure 4. Velocity diagram detail.

Taking into account the continuity and the polytropic equations of the perfect gases to model the air pressure variation inside the reservoir, $H^*_{R(t)}$ is modelled by the following equation:

$$H^*_{R(t)} = z_R + y_{w(t\ \Delta t)} \quad \Delta t \left(\frac{D_c}{D_R}\right)^2 \frac{V_{E(t\ \Delta t)} + V_{E(t)}}{2} + \frac{p^*_{R_0} \forall^n_{R_0}}{\forall_{R(t\ \Delta t)} + \Delta t \frac{\pi D_c^2}{4} \frac{V_{E(t\ \Delta t)} + V_{E(t)}}{2}}^n + \frac{1}{2g}\left(\frac{D_c}{D_R}\right)^4 V^2_{E(t)} \tag{7}$$

At last, the $C^-$ characteristic equation from the node 2, allows to define the relationship between $H^*_{1(t)}$ and $V_{E(t)}$. The method of Newton-Raphson was applied to get the solution $V_{E(t)}$.

## 4 COMPUTATIONAL RESULTS AND DISCUSSON

In order to get additional information to support the further experimental research, this computational model was used to accomplish an analytical study concerning the different parameters which can affect the peak pressure. For this purpose it was considered the instantaneous opening of the ball valve, connecting the pressurization source and the pipe. It has also been admitted: theoretical value $\psi = 1$, a polytropic expansion and compression of the air in the reservoir with $n = 1.2$, an adiabatic expansion and compression of the entrapped air at the downstream section of the pipe ($n = 1.4$) and a celerity value $a = 460$ m/s.

In the scope of this analysis it was verified that the initial pressure of the entrapped air considerably affects the extreme transient values, as well as the variation occurred in $h^*_{max}$ due to $L_{a_0}$, which is deeply reduced for $p^*_0 > 1bar$. Under similar air pocket sizes ($La_0$) and hydraulic head in the hydro pneumatic reservoir ($H^*_{R_0}$), to the higher initial pressure values in the air pocket ($p^*_0$) correspond the lower $h^*_{max}$ achieved and the higher surge periods. The greatest relative surges occurred when $p^*_0 = 1$ bar, with exception of those obtained under a reduced pressurization head, since relative surges incrised with the initial pressure, for any initial air pocket size assayed.

In addition, the effect of the experimental pipe length in the hydraulic transient response is shown in Figure 3. Three different lengths for the horizontal pipe section were considered (2 m, 7 m e 20 m), all of them being connected to the same vertical downstream pipe section (1.35 m), which allowed the comparative analysis under the same pressurization head ($H^*_P = 50,8$ m). The transient response obtained from shorter liquid columns ($L_T = 3.35$ m) is faster, presenting higher pressure and velocity extreme values, with the hydraulic damping being more pronounced as well (Figure 3).

From the velocity diagram, two overlapping types of oscillation can be identified (Figure 4). One, having a large surge period, is related with elastic and mass oscillations of the liquid column while the other, with considerably shorter amplitude and period, is associated with the entrapped air pocket oscillation.

The extreme pressures achieved under different hydraulic head conditions in the hydro pneumatic reservoir ($H^*_{R_0}$) and initial air volumes, here represented by the axial dimension of the air column ($L_{a_0}$), were also evaluated for the three distinct pipe configurations (Figure 5).

To the greater $H^*_{R_0}$ value and shorter liquid columns corresponded the highest air pressure peaks and the lowest characteristic periods of the hydraulic transient, with the liquid front reaching higher maximum velocity. Under lower heads, the variation in

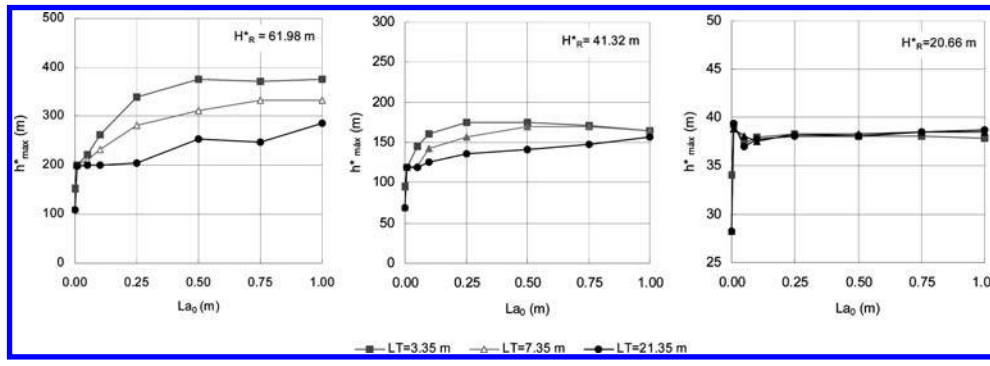


Figure 5. Numerical maximum head $h^*_{\max}$ obtained under different $H^*_{R_0}$ and $L_{a0}$ conditions ($p^*_0 = 1$bar).

the maximum pressure with the initial size of the air pocket is extremely reduced, with the results obtained under the distinct pipe configuration being almost coincident. The variation increases with the $H^*_{R_0}$ value, being particularly noticeable in the presence of small air volumes.

## ACKNOWLEDGEMENTS

The authors wish to acknowledge the financial support of this research work to the Portuguese Foundation for Science and Technology (FCT) for grants reference PTDC/ECM/68694/2006 and SFRH/BD/39502/2007 as well as CEHIDRO, the Hydrosystems' Research Centre from the Department of Civil Engineering, at Instituto Superior Técnico (Lisbon, Portugal).

## REFERENCES

[1] Almeida, A. B. (1991), "Accidents and Incidents", *Proceedings of the 9th Round Table on Hydraulic Transients with Water Column Separation, IAHR, Valencia, Spain, pp. 379–400*.

[2] Almeida, A. B. d. and E. Koelle (1992), *Fluid Transients in Pipe Networks*, Computational Mechanics Publications and Elsevier Applied Science. UK.

[3] Abreu, J., E. Cabrera, et al. (1991). "Boundary between elastic and inelastic models in hydraulic transients analysis with entrapped air pockets", *Proceedings of the 9th Round Table on Hydraulic Transients with Water Column Separation, IAHR, Valencia, Spain, pp. 159–179.*

[4] Cabrera, E., J. Abreu, et al. (1992), "Influence of liquid length variation in hydraulic transients", Journal of Hydraulic Engineering 118: 1639–1650.

[5] Izquierdo, J., V. S. Fuertes, et al. (1999). "Pipeline start-up with entrapped air." Journal of Hydraulic Research 37(5): 579–590.

[6] Lee, N. H. (2005), *Effect of Pressurization and Expulsion of Entrapped Air in Pipelines*, School of Civil and Environmental Engineering, Georgia, Georgia Institute of Technology, PhD Thesis.

*Environmental Hydraulics – López-Jiménez et al (eds)*
*© 2010 Taylor & Francis Group, London, ISBN 978-0-415-56697-1*

# CFD model of flow intrusion through a failure inside a pipe caused by negative pressure

Jesús Mora-Rodríguez, P. Amparo López-Jiménez, Francisco García-Mares & Xitlali Delgado-Galván
*Centro Multidisciplinar de Modelación de Fluidos, Universidad Politécnica de Valencia, Valencia, España*

ABSTRACT: This study describes two ways of measuring the flow that could enter in a drinking water network due to pathogen intrusion. The simulation was made by both experimental and numerical modelling. The representation of the hydraulic event was analyzed using steady state simulation. Pathogen intrusion contaminates drinking water and it is caused by the entrance of fluids with different physical, chemical, and biological characteristics than safe water. In this case, the analysis represents intrusion through an orifice in pipes and normally represents leakages. The event was simulated considering negative pressure conditions inside the pipe. This situation occurs in some cases of poor design or accidents during the operation of the system. The modelling process is based on physical and computational flow dynamics (cfd) solutions. In this case, leakage through corrosion failure is the simulated event. As a result, the simulation shows the analogy of the intrusion model combining both theories: Torricelli and favad (fixed and variable area discharged).

*Keywords*: Pathogen Intrusion, water supply, leakage pipe, experimental model.

## 1 INTRODUCTION

Water distribution systems conduct drinking water to supply the population. Water quality is controlled by the water treatment plant. However, the networks are not completely physically safe. Some operations by network staff can cause entry of external fluids. This phenomenon is termed pathogen intrusion and can cause a pollution problem for the network[1]. Polluted drinking water can generate waterborne disease outbreaks (wbdo). Several countries maintain historical registers of these events. Some studies have classified the different routes of intrusion.

The objective of this paper is to make a steady state approach to the rate of flow intrusion occurring through an orifice representing the failure made by corrosion in a pipe. The theories of Torricelli and Favad are used to model water leakages and the performance of the distribution network.

## 2 THE PATHOGEN INTRUSION PHENOMENON

The report *Pathogen Intrusion Into the Distribution System* made by the American Water Works Association Research Foundation (AWWARF) and published in 2001 refers cross connections as the direct entry pathways. These ways include: storage facilities, water main installation and repairs sites, and transitory contamination through water main leakage points[2]. This research is related to the last pathway, contamination through water main leakage points.

### 2.1 *Causes and problems of pathogen intrusion*

During the last years the proportion of drinking water outbreaks reports varies on the origin place[2]. Outbreaks associated with community water systems deficiencies have increased since 1991; i.e. 13% (91–92), 29% (93–94), and 60% (95–96). For this same period, the proportion that was attributed to water treatment plant deficiencies has steadily declined i.e. 63% (91–92), 36% (93–94), and 30% (95–96).

In 2006 a scheme was presented differentiating wbdo related with the water system deficiency. Sources were classified on five categories[3]: Deficiency in water treatment, distribution system deficiency, untreated ground water, miscellaneous or unknown deficiency and untreated surface water. The analysis was made during the period since 1971 to 2002 in the United States. The causes of this analysis are related with the evolution of the distribution system deficiency (Figure 1). Water distribution system deficiencies have increased due to wbdo. These deficiencies have the following characteristics: tend to be small, as contamination usually affects only a portion of the distribution system, limiting the potential exposure. Although a chemical etiology is often found (35% of the wbdo), distribution system wbdo are also caused by bacterial (17%), protozoan (14%), viral (4%), or undetermined (30%) pathogens.

### 2.2 *Corrosion failure pipes*

Leakage related to corrosion are failures usually producing hole shape. Those failures are caused by electrochemical interaction resulted from the soil, water and degradation of the pipe material along the years. Metal Pipes are an important element on the water distribution networks, most of the half mains installed during the twenty century were metallic[4].

Considering the kind of failure or the damage size, the corrosion could be classified on hole corrosion, or high grade or severity corrosion (Figure 2); and depending of that the flow through this failures vary of different way. Analyzing some studies, when considering same pressure, the leakage flow vary with the pressure on exponential form, if the failure is a simple hole the flow is related with an exponent of 0,5 with the pressure value, but if the failure is an extremely corrosion the relation between

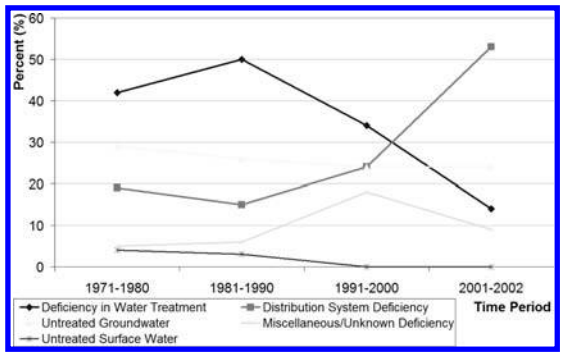


Figure 1. Sources of wbdo.

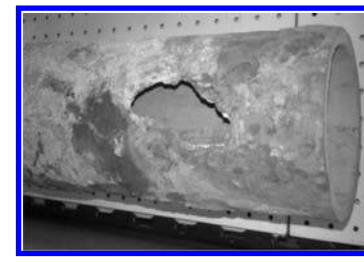

Figure 2. Severity corrosion.

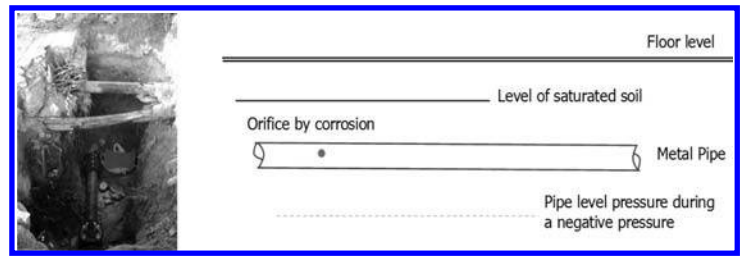


Figure 3. Prototype of the pathogen intrusion through an orifice.

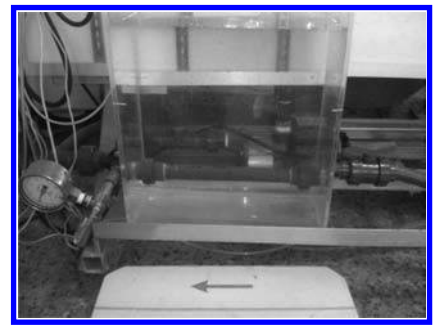

Figure 4. Physical model.

the operational pressure and the flow through the failure the exponent can arise up to 2,0 approximately[4]. Those results are considerer in the case of leakage and the data was obtained from different references studies.

## 3 INTRUSION MODEL

### 3.1 *Prototype of the pathogen intrusion by a corrosion failure*

This failure is a defect that occurred on metallic mains due corrosion. The failure of the pipe was represented by a circular orifice; this geometry was selected in order to control the data on the simulations model. The pathogen intrusion is established by a negative pressure on the pipe. Contaminated water is represented by a source of constant level of water over the pipe. These conditions represent a typical leakage that is situated on a saturated environment with a hydraulic level of water (Figure 3).

The size of the orifice is determined according to the theory of small orifices discharging. There are two different type of small discharge according to the relation between the size and thickness of the orifice. The discharge could be of thin or gross wall. In this case, it was simulated a thin wall, the characteristics of the orifice are: 5 mm diameter and 2 mm thickness.

### 3.2 *Experimental model*

The prototype was built in laboratory representing the leakage of the pipe with an orifice. The first component to be considered is a suitable assembly developed in the laboratory (Figure 4). It is oriented to obtain the hydrodynamic parameters, both velocity and pressure around the orifice in order to get the physical data occurring during intrusion.

The negative pressure has been simulated with a pumping system in collaboration with a partial close of valve. The experiment has been designed to measure pressure and velocity in certain points. A suitable interface has been designed by means of *labview*. The intrusion flow was taken in a volumetric way; in each one of the simulations a specific time was establish in order to obtain this intrusion flow.

In this physical model each scenario was simulated five times for every one of the five different opening of the main valve. Considering the theory of flow through orifices during the simulations was obtained the following results (table 1).

Table 1. Orifice parameters of the model.

| Parameter | Prototype | Rank | Theory consideration |
|---|---|---|---|
| Diameter (d) | 5 mm | – | – |
| Thickness (t) | 2 mm | – | – |
| Kind of wall (w = t/d) | 0,4 | Less than 0,5 | Thin wall |
| The operation | – | – | Submerged |
| Differential head ($\Delta h$) | 0,4 to 7,2 mca | – | – |
| Relative dimension (d/$\Delta h$) | $1{,}7 \times 10^{-2}$ to $7 \times 10^{-4}$ | Less than 1/3 | Small orifice |
| Velocity (v) | 2,4 to 8,3 m/s | – | – |
| Reynolds number | $1{,}2 \times 10^{-4}$to $4{,}1 \times 10^{-4}$ | – | – |
| Discharge Coefficient | 0,63 to 0,61 | From figure 5 | – |

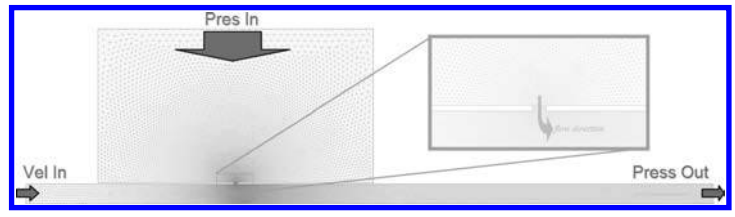


Figure 5. Numerical Model.

Table 2. Boundary parameters on cfd model.

| Case | $V_{in}$ (m/s) | $P_{out}$ (pa) | $P_{sla}$ (pa) | Re | It (%) | Dh (m) |
|---|---|---|---|---|---|---|
| 1 | 1,9 E−02 | −6,7 E+04 | 3,5E+03 | 2,4E+04 | 4,5 | 2,8E−02 |
| 2 | 2,1 E−02 | −5,5 E+04 | | 2,7E+04 | 4,5 | |
| 3 | 2,3 E−02 | −3,7 E+04 | | 3,0E+04 | 4,4 | |
| 4 | 2,5 E−02 | −2,1 E+04 | | 3,2E+04 | 4,4 | |
| 5 | 2,8 E−02 | −0,7 E+04 | | 3,5E+04 | 4,3 | |

### 3.3 *Computational fluid dynamics model (CFD)*

Numerical model simulates the prototype in two dimensions (Figure 5), using a program based on cfd, which displays the fields of physical components. In order to simulate numerically the five scenarios, the software © FluentInc has been used. Focus on the conditions model, the *RNG k-ε* turbulent model is used. Equations consider some terms that improve the accuracy for flows that are filtered rapidly, solve accurately the phenomenon of vortices in the flow, and also manage with differential effective viscosity to consider effects of small Reynolds numbers[5].

In order to improve the accuracy of the solution, second-order discretization was used for numerical method. The gradient option was modified from cell-based to node-based in order to optimize energy conservation; this option is more suitable for tri-elements meshes[5]. Finally, the computation made requested minimum 2.000 iterations on the cases that obtain the residuals on $1 \times 10^{-6}$ or 4.000 on the scenarios where it does not get it.

## 4 RESULTS

By both, mathematical and physical models, it is proposed to have a better knowledge of quantities that can not be measured during a flow intrusion through an orifice. By cfd models it could study aspects of turbulence, pressure fields, concentrations, etc. existing in mixing processes related to external intrusion.

### 4.1 *Model validation*

Three sections were chosen for validation. On the inlet section pressure results obtained from the cfd model are compared with experiments. On the orifice section the velocity and the pressure will be compared. Finally on the outlet section velocity mean value will be validated. Nash-Sutcliffe efficiency ($E$) was used[6]. It is defined as one minus the sum of the absolute squared differences between the predicted and observed values normalized by the variance of the observed values during the period under investigation. It is calculated as shown in equation (1).

$$E = 1 - \frac{\sum_{i=1}^{n} \left(Exp_i - Num_i\right)^2}{\sum_{i=1}^{n} \left(Exp_i - \overline{Exp_i}\right)^2} \tag{1}$$

*Exp* refers to the results obtained on the physical model, while *Num* refers to the cfd model results in every one of the five simulations made during the models. The range of $E$ lies between 1,0 (perfect fit) and $-\infty$. An efficiency of lower than zero

Table 3. Results of Nash-Sutcliffe Efficiency.

| Section | Parameter | Nash-Sutcliffe (E) | Validation |
|---|---|---|---|
| Inlet | Pressure (pa) | 0,996 | Fine numerical predictor |
| Intrusion | Velocity (m/s) | 0,987 | Fine numerical predictor |
| Intrusion | Pressure (pa) | 0,965 | Fine numerical predictor |
| Outlet | Velocity (m/s) | lower than zero | Without numerical predictor |

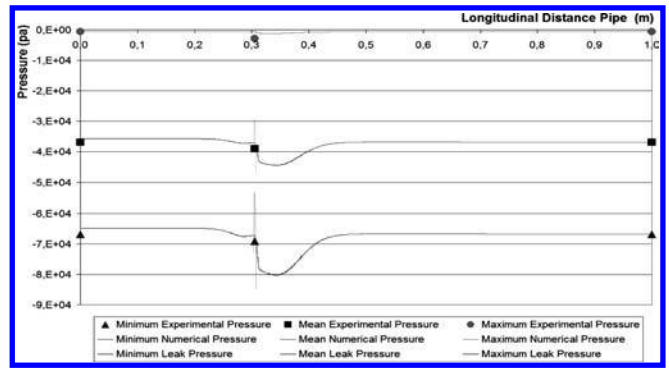


Figure 6. Mean pressure of both models.

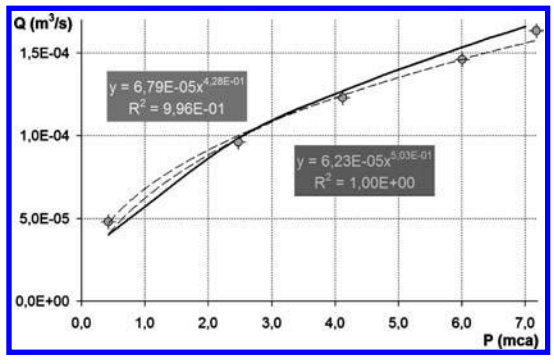


Figure 7. Results from the orifice.

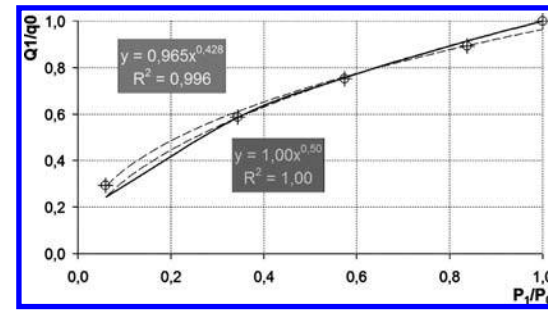


Figure 8. Favad solution to intrusion model.

indicates that the mean value of the experimental would have been a better predictor than the numerical model. In this case, as show in table 3, we assess the velocity and pressure of both models in every section indicated previously.

The cfd model results represent the effect of the intrusion motivating by the negative pressure, this fitting could be obtained of visual manner too, as shown in figure 6. This figure shows the pressure for maximum, intermediate and minimum flow simulated on the mean pressure along the pipe, in contrast with the mean pressure at the mean section of the orifice resulted from the numerical an the experimental models.

### 4.2 *Validation of the theory trough orifices*

The intrusion model was similar to the Torricelli's Theorem. In general, the drop of pressure and flow in orifices present a relation between both magnitudes. The relation for leakage was established in 1994 by May. He proposed the *Favad* theory: the flow depends directly on the pressure with a variable exponent, eq. (2). The exponent varies from 0,5 to 2,5; according to the expansion of the orifice or failure. For some individual leakage path, also the failure section depends of pressure. The analogy of intrusion flow with both theories, Torricelli and Favad is explained with the following results (Figures 7 and 8).

$$Q = P^N \qquad 0{,}5<N<2{,}5 \tag{2}$$

From the experimental model, the adjust on intrusion flow is 0,996 considering a coefficient $k$ of $6{,}79 \times 10^{-5}$ with an exponent $N = 0,43$. On the case of the numerical model, the adjust is 1,0; the coefficient $k$is equal to $6{,}23 \times 10^{-5}$ and the exponent $N = 0{,}50$. In consequence, those data could verify with the discharge coefficient and the intrusion area. The coefficient $k$could be obtained of theoretical way; $k = C_d(2g)^N A$ (table 4).

If the result is considered analogous to favad theory on the solution $k$ has to be a unit and graphically with this model it obtained the following figure 8.

Table 4. Calculated Coefficient $k$.

| Model | Intrusion Area ($m^2$) | N | $C_d$ mean (table 1) | $k$ calculated |
|---|---|---|---|---|
| Teo. | 1,96E−05 | 0,5 | 0.62 | 5.38E−05 |
| Exp. | 1,96E−05 | 0,428 | 0,62 | 4,34E−05 |
| Num. | 1,96E−05 | 0,503 | 0,62 | 5,44E−05 |

## 5 CONCLUSIONS

The representation of the theories used in order to considering the relation of leakage fluid, will consider the both works efficient to simulate the inverse case, the intrusion of the flow through an orifice.

The numerical adjust between the experimental and numerical models presents a good fit on the intrusion section, which is the main objective of the simulations.

Considering the Torricelli's theorem the exponent obtained from the models is practically 0,5; the difference is observed graphically on figure 7. With respect the coefficient $k$ when the pressure is equal to 1mca, the value of the flow is different between the models and the calculated values.

## ACKNOWLEDGMENTS

This article has been made possible through actions of the CMMF researchers, involved in the following projects: *DANAIDES: Desarrollo de herramientas de simulación para la caracterización hidráulica de redes de abastecimiento a través de indicadores de calidad del agua. REF. DPI2007-63424. Ministerio de Educación y Ciencia de España.*

## REFERENCES

[1] López, A., Martínez, J., López, G., Fuertes, V., "Análisis de la Problemática de Calidad de los Abastecimientos: Desde la Planta de Tratamiento hasta el Grifo", V Congreso Ibérico sobre Gestión y Planificación del Agua, Faro, Portugal, Dec, 4th 2006.

[2] Kirmeyer G. J., Friedman M., Martel K., Howie D., LeChevalier, M., Abbaszadegan M., Karim M., Funk J., Harbour J., (2001), *Pathogen Intrusion Into Distribution Systems*, AWWARF and USEPA, USA.

[3] Craun, F. M., Craun, F. G., Calderon, L. R., Beach, J. M., (2006), "Waterborne outbreaks reported in the United Status", J. Water and Health, 04. Supl. 2, pp. 9–30.

[4] Mora, J., López, A., Delgado X., Alonso, C., "Estudio sobre la Modelación de Defectos en Tuberías", *VIII Seminario Iberoamericano, Alterações climáticas e gestão da Água e Energia em Sistemas de Abastecimento e drenagem, SEREA, 2008, Lisboa, Portugal, July 2008.*

[5] Fluent, (2005), *User's Guide, Fluent 6.2*, © Fluent Inc.

[6] Krause, P., Boyle, D. P., Bäse, F., (2005). "Comparison of Different Efficiency Criteria for Hydrological Model Assessment", Advances in Geosciences, 5, pp. 89–97.

*Environmental Hydraulics – López-Jiménez et al (eds)*
*© 2010 Taylor & Francis Group, London, ISBN 978-0-415-56697-1*

# Modelling of the stirring of a sludge tank using Computational Fluid Dynamics

P. Martínez, R. Granell, S. Martínez & R. Suay
*Instituto Valenciano de Investigaciones Agrarias (IVIA), Moncada, España*

ABSTRACT: The objective of this study is to model a sludge tank using Computational Fluid Dynamics (CFD) in order to improve the management of the tank in terms of stirring and handling.

Difficulties have arisen when handling the sludge due to its highly variable density and other physical characteristics such as viscosity or solids content. These features make pumping operations to be difficult and irregular. In order to deal with this situation, a model of the tank is proposed to analyse different options of stirring the sludge and thus reach a homogeneous density that will ease handling operations.

First of all, experimental data will be gathered from the tank for validation purposes as well as fluid characterization. Secondly, a finite volume mesh will be generated using GAMBIT 2.4. Finally, the model will be calculated using a CFD commercial code (FLUENT 6.3) under a Reynolds Averaged Navier-Stokes (RANS) approach. A k-$\varepsilon$ model will be used to implement the turbulence.

After validation, this model will be used in further research to analyse different stirring configurations and define the best option in terms of mixing and homogenization of the sludge.

*Keywords*: Sludge tank, Stirrer, CFD, Turbulence model, Fluent.

## 1 INTRODUCTION

A sludge tank located in a pig farm near Segorbe (Valencia, Spain) is used to manage the slurry originated in the farm. This management allows re-using the slurry for agriculture and thus reducing any potential damage to the environment in an economic way[1].

The sludge has a highly variable density due to its composition which makes it difficult to handle. A stirrer is currently installed in the tank to mix the sludge, but there is uncertainty about what is the most effective configuration to obtain a homogeneous fluid.

The aim of this study is to develop a validated model of the tank. This model will be then applied in further research to optimize the stirring of the tank and thus improve the sludge management.

## 2 MATERIALS AND METHODS

### 2.1 *Materials*

The tank has the shape of a decahedral prism of 3 m height and 7.66 m width as figure 1 shows. The total volume of the tank is 144 $m^3$. A stirrer is installed in the tank side (as shown in figure 2) to mix the sludge. The stirrer is an *Eisele Tauchmotor*

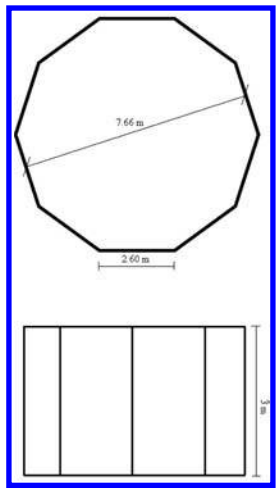


Figure 1. Plan and elevation of the tank.

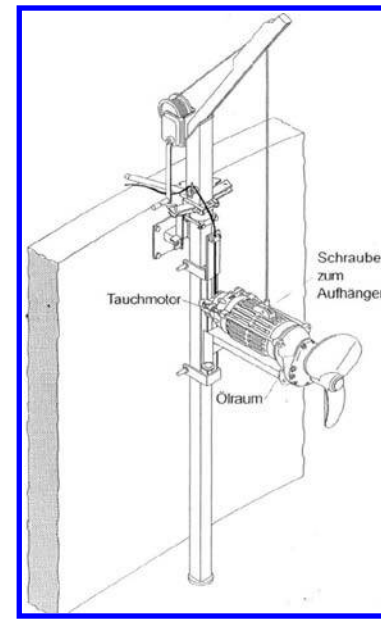


Figure 2. Stirrer in the side of the tank.

Figure 3. Camera placed on top of the tank for velocity measurements.

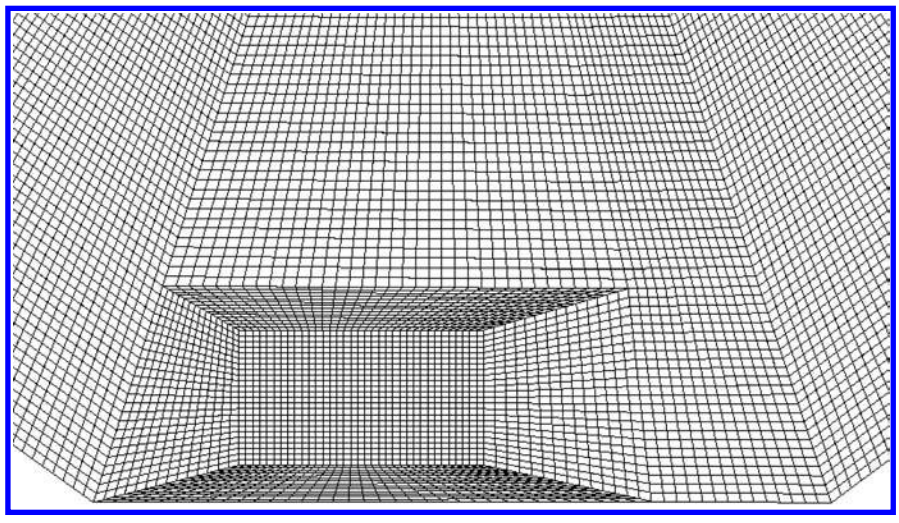

Figure 4. Detail of the mesh (plan of the stirrer and one side of the tank).

model GTWS 740 (Franz Eisele u. Söhne GmbH u.Co.KG, Sigmaringen, Germany) capable of 5.5 kW of power. Depth of the stirrer within the tank and horizontal angle can be modified to optimize stirring.

### 2.2 *Methods*

First of all, experimental data will be gathered from the tank for model validation. In order to do this, the stirrer will be turned on to homogenize the sludge. Then, samples will be taken to measure physical properties such as density and viscosity. It is assumed that the fluid becomes homogeneous enough when stirred to be characterized with only one density value. In the case of viscosity, as common viscosimeters are not suitable due to the sludge high content of solids, an Atwood Machine will be used.

Surface velocity will be also measured using tracers and recording their movement with a camera (see figure 3) under different configurations of the stirrer. The recordings will be then processed to obtain velocity vectors in certain parts of the surface for validation purposes.

Secondly, a finite volume mesh will be generated using GAMBIT 2.4 (Ansys Inc., Canonsburg, Pennsylvania, USA). Due to time and software constraints, a Reynolds Averaged Navier-Stokes (RANS) approach has been chosen and thus mesh density will be set accordingly. A k-$\varepsilon$ turbulence model will be used to deal with turbulent flow as it is a well established model and it has been used by some authors[2],[3] in similar cases with good results. An example of the kind of mesh generated can be seen in figure 4.

Finally a CFD commercial code (FLUENT 6.3, Ansys Inc., Canonsburg, Pennsylvania, USA) will be used to run the model. The stirrer will be implemented using the Fan function available in FLUENT by means of fixing a constant pressure drop. This value of pressure will be calibrated through simulations using part of the data gathered from the tank.

Simulations will be done for three meshes of different densities (from one to four millions of elements) in order to evaluate the sensibility of the model to the mesh size. As a convergence criterion, continuity residuals will be expected to fall under 1E-6 and reach stability. Once the model is converged, it will be validated with the experimental data previously obtained.

## 3 RESULTS

Average results obtained from sludge samples are detailed in figure 5. Experimental viscosity was found to be very high compared to values found in literature[4] and thus it was decided to calibrate this parameter during the simulations.

This decision was then confirmed as the simulations done with the experimental value gave results which were not in good agreement with experimental velocities. A calibrated value of viscosity (0.09 Pa.s) gave velocity profiles more similar to those

| Density (kg/m$^3$) | Viscosity (Pa.s) | Solids content (g/kg) |
|---|---|---|
| 1210 | 9.58 | 42 |

Figure 5. Experimental sludge properties.

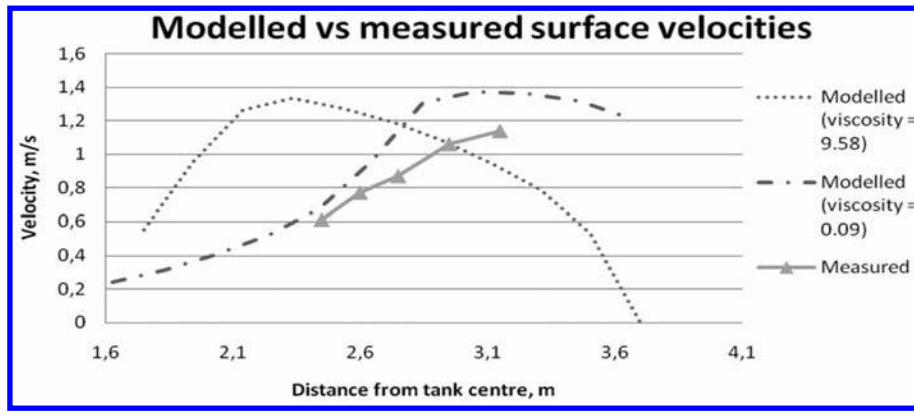


Figure 6. Comparison of results between simulations with different viscosity values.

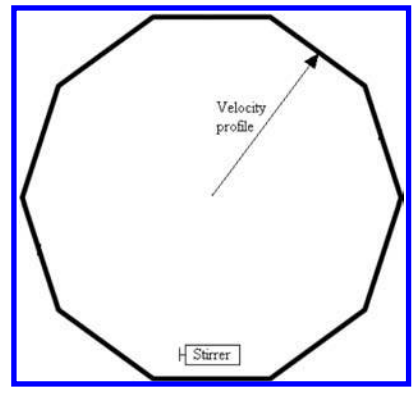


Figure 7. Tank radius where surface velocities were measured for validation.

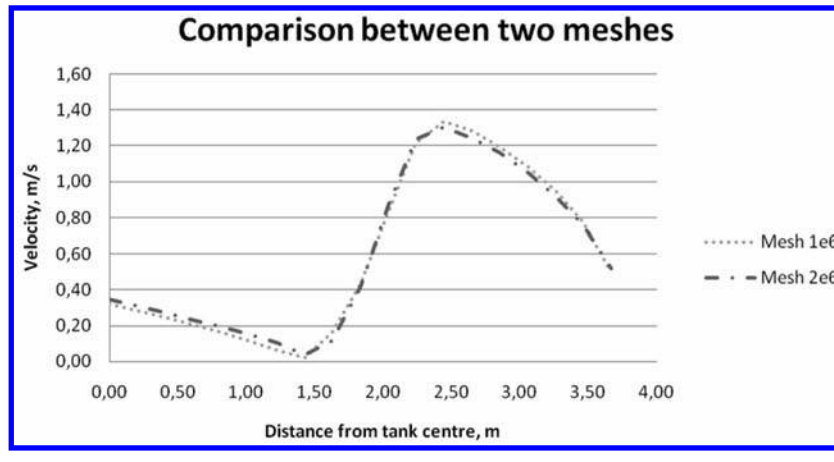


Figure 8. Comparison of results obtained from meshes of different size.

measured in the tank as seen in figure 6 (Comparison is done along radius shown in figure 7). This is because higher values of viscosity increase the influence of the borders and thus highest velocities tend to appear at more distance from the tank walls.

The analysis of sensibility proved that for a mesh of one million elements or more the model provides the same results and thus it is not affected by the mesh size. Figure 8 shows the surface velocity modelled along the radius shown in figure 7 with two meshes of different size and equal parameters.

Finally, the model has been validated with the experimental data available and is expected to predict flow patterns in the tank under different stirring configurations with enough accuracy to be used in further investigations. An example of the results provided by this model is shown in figure 9.

As a conclusion, this model could be used to analyze the best stirring option to homogenize the sludge and improve its management. Despite this, some improvements may be suggested for further development of the model. For example, refined numerical approaches (Second order resolution schemes) may provide more accurate results. Extended recordings in the tank, with advanced image treatment, are also recommended, as this will surely give better experimental data for calibration and validation.

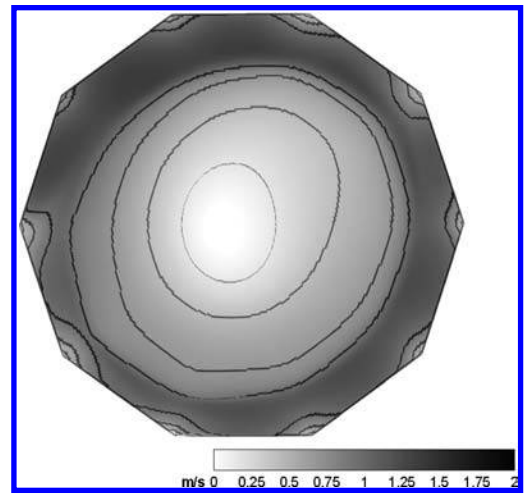


Figure 9. Velocity contours in the tank surface.

## REFERENCES

[1] UK Department for Environment, Food and Rural Affairs (2009), Protecting our water, soil and air: A code of Good Agricultural Practice for farmers, growers and land managers, available at: http://www.environment-agency.gov. uk/netregs/businesses/agriculture/61889.aspx (accessed 29/05/09).

[2] Kohnen, C. and Bohnet, M. (2001), "Measurement and simulation of fluid flow in agitated solid/liquid suspensions", Chemical Engineering and Technology, Vol. 24, Issue 6, pp. 639–640.

[3] Wu, B. and Chen, S. (2007), "CFD simulation of non-Newtonian fluid flow in anaerobic digesters", Biotechnology and Bioengineering, Vol. 99, Issue 3, pp. 700–711.

[4] El-Mashad, H. M., van Loon, W., Zeeman, G. and Bot, G. (2004): "Rheological properties of dairy cattle manure", Bioresource Technology, Vol. 96, Issue 5, pp. 531–535.

*Environmental Hydraulics – López-Jiménez et al (eds)*
*© 2010 Taylor & Francis Group, London, ISBN 978-0-415-56697-1*

# Two dimensional hydrodynamic modelling for floods assessment in San Luis Potosí Industrial Zone (Mexico)

Teresa de J. Soriano Pérez & Arturo Dufour Candelaria
*Facultad de Ingeniería, Universidad Autónoma de San Luis Potosí, San Luis Potosí, México*

ABSTRACT: There are evidences of San Luis Potosí Industrial Zone (Mexico) floods due to streams runoff[1]. For that, study aim was to elaborate cartography characterization in order to evaluating the possible inundation impact by rainfall and streams runoffs, through two dimensional modelling using the SOBEK model (WL|Delft Hydraulic[3]) in a total surface area of 9233 hectares. Firstly, the digital terrain model ($5 \times 5$ m) is presented as the base cartography. Next, hydrology data and boundary conditions that define the general model topology are described. Lather, maximum depths maps are calculated for return periods T = 50, 100 y 500 years and presented as numerical simulation results. Finally, it is concluded that San Luis Potosí Industrial Zone floods are due to rainfall runoff. Three bridges of 57 Highway (México-Querétaro) built in 2008 are the consequence of area flooding, their embankments work as dikes blocking the flow, the most affected area is it north part. Actually, San Luis Potosí Industrial Zone has an inappropriate drainage system.

*Keywords*: two hydrodynamic modelling, urban flooding.

## 1 INTRODUCTION AND OBJECTIVE

San Luis Potosi city is located on the central part of Mexico at an altitude of 1850 m. The climate is semi-desert, characterized by low rainfall concentrated in high-intensity storms that occur during the wet season, usually June through October. Since 1965, San Luis Potosí city has an area specially designated for the location of businesses, known as Industrial Zone, in 1980 it doubles the surface area extending to the south. Nowadays, made up of over 300 companies and 50% are foreign direct investments from Europe, United States, Canada and Japan.

San Luis Potosí Industrial Zone is bounded on the north by "Libramiento Oriente" road, east by the Mexico-Queretaro 57 highway, west by the Mexico-Laredo via train (see figure 1). Runoff coming from eastern watersheds produces significant flooding problems in the Industrial Zone [1]. Moreover, flooding problem becomes worse during wet season due to the lack of a proper drainage system.

Because of the evidence of floods in San Luis Potosí city, study aim was to elaborate a characterization in cartography terms of the flooding risk level in the Industrial Zone (figure 1) by applying 2D dimensional mathematical model (SOBEK, Delft Hydraulics[3]).

## 2 MATHEMATICAL MODEL CHARACTERISTICS

### 2.1 *SOBEK, 2D mathematical model*

The SOBEK model, developed by WL|Delft Hydraulics[3], was used for the hydrodynamic simulations because of the 2D dimensional flow characteristics at the study area. This model computes velocities and water depths in each node grid of the computational domain. A two dimensional transitory flow is solved by the Delft Flooding System module, in subcritical and supercritical flow, as well as the terrain flooding or drying. SOBEK model solves the Saint-Venant equations in each grid cells [2], it uses a digital terrain model (DTM), which allows making an interactive modelling and it is very useful tool for identifying flooding areas and to understand the 2D flow dynamics [4].


Figure 1. Localization and view of Industrial Zone in San Luis Potosí (Mexico).

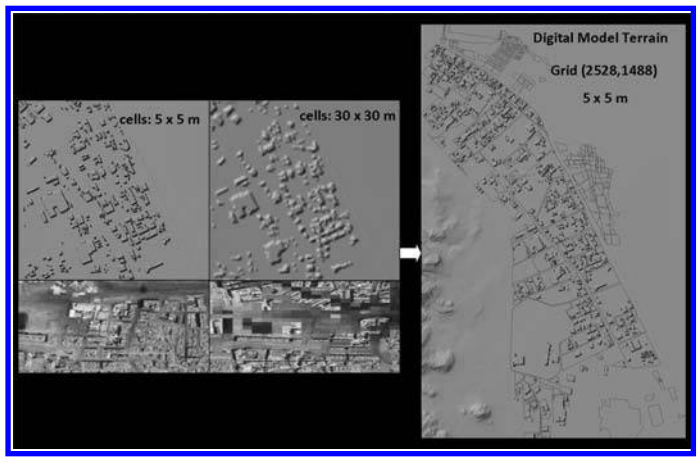


Figure 2. Industrial Zone (San Luis Potosí, Mexico) model topology used for 2D hydrodynamic modelling.

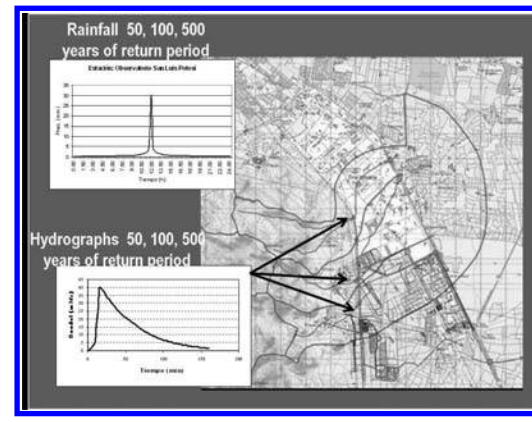


Figure 3. Hydrologic data applied to two hydrodynamic modelling with SOBEK.

### 2.2 *Model topology*

The base cartography for the 2D hydrodynamics modelling was obtained from the topographic charts of INEGI[5] (Instituto Nacional de Estadística Geografía e Informática), through vector processing level curves to generate a digital terrain models (DTM) of several grid spatial resolutions (30 × 30, 20 × 20, 10 × 10 and 5 × 5 m) including the edifications of the urban area of Industrial Zone San Luis Potosí.

A sensitivity analysis of grid cell size of the DTMs at the urban area allowed to determinate the final model topology to be used for the hydrodynamic simulations with SOBEK model. DTM used for this purpose has a grid (2528, 1488), surface area of 9233 hectares, cell size of 5 × 5 m (see figure 2).

## 3 TWO HYDRODYMANIC SIMULATIONS

In the eastern part of San Luis Potosi city are located “La Cantera”, “Atarjeas”, “San Antonio” and “Palillos” streams (figure 3), runoff coming from these produces flooding problems in the Industrial Zone [1].

### 3.1 *Hydrological data*

Rainfall data was obtained from the “Observatorio San Luis Potosí” and “Zaragoza” climatology stations, both located in a region with similar climatic and hydrological characteristics. These stations have a record of annual maximum rainfall of 52 years ranging from 1949 to 2004, where a rainfall of 50, 100 and 500 years were computed and applied to 2D hydrodynamic model.

Meanwhile, hydrographs data were obtained from previous study carried out by Universidad Autónoma de San Luis Potosí (Mexico) [1]. for return periods of 50, 100 and 500 years, where watersheds were identified using INEGI[5] data.

### 3.2 *Results*

Runoff coming from streams and rainfall gives as result a two dimensional flow through the San Luis Potosi Industrial Zone, flow direction depends on urbanization distribution.

Once geometry (topography, terrain roughness), flow (hydrographs, rainfall on the area) and boundary conditions are introduced, hydrodynamic simulations were carried out using SOBEK model for return periods of 50, 100 and 500 years.

From numerical simulation results had been obtained several maximum water depths maps, which’s allows to delimitate the most critical zones due to water level. In order to identify the risky flooding areas a carefully analysis was carried out of maps (maximum water depths), in dry season (runoff coming from the streams) and wet season in San Luis Potosí city, some of results are presented at figure 4.

These 2D hydrodynamic simulations allowed to determinate the present conditions and the future actuations of flood control in San Luis Potosí Industrial Zone.

## 4 CONCLUSIONS

Flooding in San Luis Potosí Industrial Zone (México) is mainly due the runoff during wet season, it’s amazing flood extension and its implication of risk level to the population and enterprises, mainly because does not have a proper drainage system.

57 Highway (México-Querétaro) close to Industrial Zone has 3 bridges (built in 2008), highway and bridges are the reason of flooding area, nevertheless bridges in great proportion. Highway embankment works as dikes blocking the flow coming from west part, after water is retained and stored along the lateral via, in this place is computed at least 1.0 m of water depth.

It is evident that flooding at San Luis Potosí Industrial Zone produces it‘s own development decrease, reason why nearly cities are preferred to establish new industrial enterprises.

A solution of flooding problem is government investment for implementation of a new drainage system throughout the San Luis Potosí Industrial Zone, this is a new pluvial collector designed for 50 years of return period.

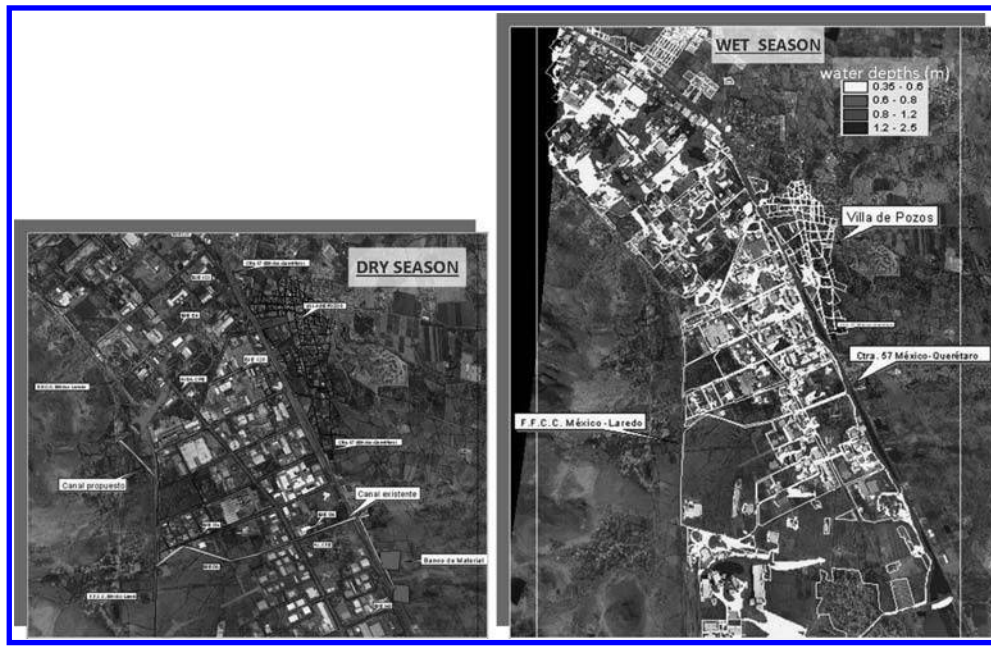


Figure 4. Risky flooding areas in Industrial Zone (San Luis Potosí, Mexico), dry and wet season.

Figure 5. Highway and bridges in San Luis Potosí Industrial Zone (Mexico).

## REFERENCES

[1] Dufour Candelaria, A. (2008), "Modelación de áreas de inundación y análisis hidráulico e hidrológico para la rectificación y encauzamiento del arroyo San Antonio por el eje 132 para protección contra inundaciones en la parte oriente de la zona industrial de San Luís Potosí, S.L.P.", CIEP, Facultad de Ingeniería, UASLP, Mexico.

[2] Soriano Pérez, T de J. (2002), "Modelado matemático de la evolución de contaminantes en sistemas fluviales.", PhD, Departamento Ciencias y Técnicas del Agua y del Medio Ambiente, Universidad de Cantabria, Santander, Spain.

[3] WL|Delft Hydraulics (2009). SOBEK-Rural Manual, version 2.11.002, Netherlands.

[4] Verwey, A. (2001), "Latest Developments in Floodplain Modelling – 1D/2D Integration", *Proceedings of 6th Conference on Hydraulics in Civil Engineering, The Institution of Engineers Australia, Hobart*.

[5] INEGI, Instituto Nacional de Estadística Geografía e Informática (2009), *Institución Gubernamental de México.*

*Environmental Hydraulics – López-Jiménez et al (eds)*
*© 2010 Taylor & Francis Group, London, ISBN 978-0-415-56697-1*

# Environmental hydraulics master program in Andalusia: An integrated approach to a professional and scientific profile oriented to multidisciplinary work groups

María José Polo
*Universidad de Córdoba, Campus de Rabanales, Córdoba, España*

Asunción Baquerizo & Luis Cruz
*Universidad de Granada, CEAMA, Granada, España*

Ramón Fernández-Feria
*Universidad de Málaga, Málaga, España*

Miguel Á. Losada
*Universidad de Granada, Granada, España*

ABSTRACT: The Water Framework Directive has established the need for rigorous multidisciplinary professionals capable of analyzing water systems and their evolution for an integral management goal. In Andalusia, agriculture and tourism compete in water demand with the environment and return great amounts of nutrients, suspended sediments and other elements to water bodies. This document resumes the development and structure of the Master Program on Environmental Hydraulics, conducted by the Universities of Granada, Cordoba and Malaga. The MP derived from a previous doctorate program with Quality Certification by the Ministry of Education. Along its 3-year editions, the Master students have found a professional post in both research institutions and technical consultings related to their specialty degree. This fac, together with the renewal of the Quality Certification are the main indicator of the high excellence formation provided by the Master Program.

*Keywords*: education, environmental hydraulics, multidisciplinary teams.

## 1 INTRODUCTION

The European Union, conscious of the important role of both seawater and freshwater ecosystems, promulgated in 2000 the Water Framework Directive[1], for the protection of continental surface water, transition water, coastal water and groundwater. Its main objective was to guarantee a good ecological state of water bodies along the EU territory, and its member states must regulate actions to achieve such goals, by means of a sustainable water use and integrated management which assures a long term protection on water resources.

But water bodies are not isolated systems in nature. Continental processes do influence littoral processes, and these, reversely, constitute a contour condition to water flow and element dispersion in fluvial systems. Soil uses constitute one of the major pollutant sources to groundwater, and transition waters are usually affected by the intense human activities that concentrate around them. Moreover, the ecological state of waters depends not only on the biological activity in aquatic systems, but also on water, nutrient, pollutant and energy flows and their evolution.

Nowadays, both experimental and measurement techniques have evolved from traditional methods to automated high resolution ones, and what is more, numerical and statistical techniques together with technology provide the society with powerful simulating tools capable of reproducing complex environments and their interactions. To understand such conditions, adequately simulate them, and explore the effects of different actions on aquatic systems requires skilled professionals who are able not only to approach such problems, but also to have a multidisciplinary background to join integrated work groups to address such issues. Particularly, for an integral management of water resources, such professionals must have any or some of the following competences,

- Identify and understand the major processes in the dynamics of surface water, groundwater and coastal water.
- Quantify the exchanges between water bodies and their contour systems
- Include both quality and quantity criteria in water resource planning.
- Include socioeconomic and environmental costs criteria in water use, water management and territorial management.
- Make diagnosis and prognosis studies, with uncertainty sources assessment.

This work presents the structure of a Master Programme in Andalusia devoted to Environmental Hydraulics with both orientations: technical and scientific, especially focused in an integral formation capable to join multidisciplinary teams. Previous steps in its development are resumed, and some examples of work done during the three year experience so far are included at the end. Finally, a brief resume of the current position of the postgraduate students is presented as conclusions.

## 2 ENVIRONMENTAL HYDRAULICS MASTER PROGRAM IN ANDALUSIA

### 2.1 *Objectives*

The EHMP aims to provide the students with a rigorous advanced formation specialized on Environmental Hydraulics focused on an integral management of water resources and an introduction to research multidisciplinary work. To achieve such goal,

such formation includes the general capacity of students to,

- Describe, characterize and model natural processes related to water, substances and organisms flow, and their interaction with the structures involved in water management.
- Optimize marine and terrestrial water resource management, and their associated fluxes, taking into account the social, environmental and economic effects of water planning, after de Water Framework Directive.
- Describe and evaluate the uncertainty inherent to natural processes, their diagnosis and forecasting.
- Develop analysis based on the scientific ground and with critical attitude.

Together with those, the following skills are pursued,

- Use of tools and methods for prediction oriented to actions in water bodies.
- Use of tools for territory representation and description
- Use of numerical and statistical tools for data processing and analysis.
- Use of programming languages.
- Oral and presentation skills, and fluent use of English specific terms in Environmental Hydraulics.

### 2.2 *Antecedents and administrative structure*

This EHMP is the transformation of an existing Doctorate Programme between the Universities of Granada, Cordoba and Málaga, coordinated by the first one, which achieved the Quality Certification of the National Ministry of Education every edition since it was first launched. The adaptation to Bolonia goals and European directives for postgraduate studies was achieved after a previous analysis and modification proposal which was selected by the Andalusia Regional Government for funding. First edited along the academic year 2006/07, the current structure has inherited the main core of those studies: one year consisting of a common group of subjects for all students in the first quarter, which aims to provide with fundamental processes knowledge and experimental and mathematical tools applied to Environmental Hydraulics, followed by a specific group of subjects depending on the specialization profile the student selects among the four areas offered during the second quarter. Courses in the first quarter are all given at the University of Granada with a view to providing students with the theoretical foundations and basic knowledge of Environmental Hydraulics. Courses in the second quarter are given at each of the participating universities, depending on the specialization chosen by each student. Each specialization focuses on offering students an in-depth knowledge of the area selected and developing their personal skills in the field, and is coordinated locally by one of the professors. These areas and their coordinator are:

1. Integrated management of Ports and Coastal Zones, University of Granada: To examine and study the marine environment and shoreline processes as well as their use and management, with special emphasis on the integrated management of ports and coastal zones as well as their mutual interaction.
2. Integrated basin management, University of Cordoba: To examine and study hydrological processes in the soil and fluvial environment, and the use and conservation of water and soil resources for the integrated management of basins.
3. Vehicle aero-hydrodynamics, University of Malaga: To analyze and control the aerodynamics of land and air vehicles as well as the hydrodynamics of submarine vehicles. This knowledge will be used for the design and improvement of the automatic and crewed navigation of such vehicles for environmental control.
4. Management of Aquatic Ecosystems, University of Granada: To quantitatively and qualitatively analyze and evaluate the state and ecological potential of natural and artificial ecosystems (lakes, rivers, wetlands, reservoirs, estuaries, coastal lagoons, marine environments, etc.) with a view to establishing and applying models as well as management and restoration programs.

The four coordinators together with the chief coordinator of the Master Program constitute the Academic Committee, in charge of decision making such as students admission criteria, academic organization, selection of tutors, etc. Figure 1 shows the general structure of EHMP and the final possible academic degrees for the student,

### 2.3 *EWMP course modules*

The master courses are grouped in modules (CM) which comprise several subjects units (U):

First Quarter. Obligatory Courses, 30 ECTS credits (CEAMA-UGR)

CMI. Foundations and Methods of Environmental Hydraulics, 14 ECTS credits
- UI.1 Mathematical methods
- UI.2 Numerical methods
- UI.3 Experimental methods
- UI.4 Statistical methods

CMII. Dynamics of Biogeochemical Fluids, 16 ECTS credits
- UII.1 Fluid mechanics
- UII.2 Aquatic ecology

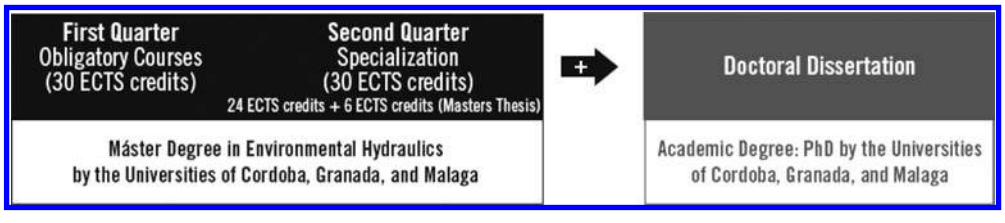


Figure 1. General structure of EHMP and academic degrees.

UII.3 Transport and mixing processes
UII.4 Atmospheric dynamics

Second Quarter. Specializations

*Integrated Management of Ports and Coastal Zones*, 30 ECTS credits (University of Granada)
CM III. Dynamics of Geophysical Fluids, 7 ECTS credits
CM IV. Littoral Processes and Coastal Evolution, 6 ECTS credits
CM V. Planning and Management, 5 ECTS credits
CM.VI. Integrated Management of Coastal Zones and Port Areas, 6 ECTS credits
Masters Thesis, 6 ECTS credits

*Integrated Basin Management*, 30 ECTS (University of Córdoba)
CM VII. Hydrological Processes, 6 ECTS credits
CM VIII. Erosion Processes and Geomorphology, 5 ECTS credits
CM IX. Planning and Management of Water Resources, 8.5 ECTS credits
CM X. Integrated Basin Management, 4.5 ECTS credits
Masters Thesis, 6 ECTS credits

*Vehicle Aerodynamics*, 30 ECTS (University of Malaga)
CM XI. Hydraulic Systems and their Control, 6 ECTS credits
CM XII. Non newtonian and compresible fluids, 6 ECTS credits
CM XIII. Experimental and Numerical Techniques in the flow around Vehicles, 6 ECTS credits
CM XIV. Control and Optimization, 6 ECTS credits
Masters Thesis, 6 ECTS credits

*Management of Aquatic Ecosystems*, 30 ECTS credits (University of Granada)
CM XV. Management of Aquatic Epicontinental Systems, 8 ECTS credits
CM XVI. Tools and Techniques for the Study of Pelagic Ecosystems, 8 ECTS credits
CM XVII. Management of Coastal Ecosystems and Transition, 6 ECTS credits
Masters Thesis, 6 ECTS credits

### 2.4 *Learning methodology*

During the common first quarter, the students attend lessons and practical experiences from the different modules as an unique group. Techniques and mathematical methods required for the resolution of examples and practical cases in Course Module II are explained and exercised in parallel in Course Module I, so that coordination between the professorate in the first quarter is one of the key points of the efficiency of the modules. Along the first month of the program, each student is assigned a topic for the final Master Thesis work and a tutor. Related to that topic, a practical integrated work intended for the evaluation of the first quarter is presented to the student, with different questions and problems from every unit of each module. The student must work through the practical work proposed, formulate solutions and quantify certain aspects. Some of the questions are very similar in approach and structure but address to different environments, and during this period working in group is greatly enhanced between the students.

At the end of the quarter, the students present their results to a commission formed up by the proffessors in a special oral session attended by all the students, where they must answer the questions addressed and argue possible criticism to the decisions made during work. This first final work has an important weight in the evaluation of the first quarter, and constitutes a first experience for the students on the topic of final master thesis, and also makes it possible for them to get partially involved in topics from all the specialty areas.

During the specialty second quarter the students group is divided into the different universities participating in the Master Program. Individual work, tutorial assistance and lessons are distributed along the week so that the students can work on their Master Thesis, with increasing dedication as the end of the quarter gets closer. Master Thesis works are presented in public session to an external commission, and those with a quality standard published in the Master Program website (www.hidraulicaambiental.com).

As a final remark, a scientific and technical seminar program is run along the academic year. Experts from Spain and other countries, together with young researchers in the groups who support the Master Program, are invited to give a lecture on any topic related to Environmental Hydraulics in a general sense. The seminar program is very successful and provides a forum for knowledge and analysis exchange, and an excellent experience for both students who begin their research career and those oriented to the professional market.

The EHMP website is also a tool for communication between professors and students in a whole sense. The open sections contain all the information about the program; a restricted area is used to check the students assistance, news, teaching material, evaluation results, and so on.

## 3 3-YEAR OF RESULTS

### 3.1 *Some working lines developed by the students*

Maritime structures
Littoral morphodynamics: beaches
Meteorological and climatic forcing in semiconfined seas
Risk-based integral management of water resources
Regional analysis of precipitation
Soil loss and soil management in olive orchards
Field monitoring techniques oriented to hydrological and erosive processes
Erosive processes characterization

Superficial aquifers influence on the hydrological response of basins.
Geomorphologic control of hydrological response of basins.
Hydrological data assimilation by remote sensing techniques.
Water dynamics in marsh areas
Scale effects in hydrological modeling
Runoff generation by snowmelt in the Southern face of Sierra Nevada (Granada)
Atmospheric and terrestrial forcing of Mar Menor lagoon (Murcia)
Solote transfer from soil to runoff
Nonpoint pollution modeling in watershed modeling
Distributed modeling of interception at watershed scale
Irrigation water management
Water stress monitoring in plants
Mobile robotics
Hydrodynamic stability and control in vehicles aerohydrodynamics
Numeric simulation of fluid flow aroung vehicles.
Spectral plancton size applied to marine ecosystems dynamics.
Wetlands as global change sensors

### 3.2 *Current position of EHMP previous students*

Most of EHMP students are currently in positions related to Environmental Hydraulics in research or technical consulting activities in representative professional sectors. The website includes such information and is updated as the best indicator of EHMP results and demand, and the excellence formation provided the academic and research team. The renewal to the Quality Certification in every edition is a guarantee of the quality of the people that make it possible every year.

## 4 CONCLUSIONS

In a region as Andalusia, with a high length of coastline, highly variable climatic and meteorological conditions from the East to the West with a marked Mediterranean character, an economic system based mainly on both agriculture and tourism…water resource management is one of the main concerns and the need for skilled professional poses a challenge for the current university system. The Environmental Hydraulics Master Program by the Universities of Granada, Cordoba and Malaga has proven an efficient tool to provide with multidisciplinary professionals for both research and consulting sectors.

## REFERENCES

[1] European Council (2000), *Directive 2000/60/CE of the European Parlament and the Council which establishes a community framework for actuations in water policy*. Brussels.

*Environmental Hydraulics – López-Jiménez et al (eds)*
*© 2010 Taylor & Francis Group, London, ISBN 978-0-415-56697-1*

# Computational aspects on hybrid ANN-FE-groundwater flow calculations

Lars Weber & K.-Peter Holz
*Lehrstuhl Bauinformatik, Cottbus, Germany*

ABSTRACT: The paper illustrates a hybrid approach to represent substructures of Finite-Element discrete systems for groundwater flow simulations by neural networks. Information exchange between the discrete FE-represented part of the grid and the neural represented substructures within this kind of hybrid model is established by dynamic interaction at connecting grid. The paper covers the computational aspects for the design, training, simulation and interaction of neural represented substructures in the hybrid neural-numerical ANN-FE environment.

*Keywords*: Groundwater Flow, Hybrid Modeling, Finite Element Method, Neural Networks

## 1 INTRODUCTION

Modern engineering applications, planning and construction processes require studies of variations of systems. These time consuming investigations often demand for complex changes in element geometries, changes in time and space of the numerical and physical parameters or boundary conditions. They need many iterative calculations, within which the whole computational domain has to be recalculated. The aim of this approach is the support numerical calculations by using neural network representation of subsystems to increase calculation speed for variational studies. The advantage of neural network technology, fast response time for pre-trained patterns representing subsystems, will be used in a hybrid model in combination with numerical FE-calculations.

## 2 BASIC PRINCIPLES

This paper focuses on groundwater flow calculations. The equations describing groundwater flow are the second order Laplace or Poisson differential equations. These equations are frequently solved by approximation methods such as Finite Element Method (FEM). In this approach the computational domain is subdivided into triangles. The physical values (pressure heads or element flow velocities) are represented by form functions on the element level. For given boundary conditions the FE-method calculates the pressure head or flow velocity distribution. For large-scale systems with complex physical behaviour, iterative or time dependent calculations can lead to very large computation time during the design phase.

Artificial Neural Networks (ANN) try to emulate the behaviour of the human brain in a very basic form. They have the ability to "learn" (represent) a resulting behaviour from a given input data set. After a neural network was trained the calculation time to simulate the output for a given input is very small. If sufficient input data within a range of different input patterns are given the neural network can "predict" output data for "unknown" (not trained) input data combinations. This feature is a large motivation to integrate neural networks in a hybrid system in combination with numerical schemes.

A hybrid – Neural Network/Finite Element – system is a model that incorporates artificial neural network nodes into a numerical scheme of discrete nodes. Information is interchanged, in real time, between the numerical and ANN components in a manner that the results from one will directly affect the other[1]. In this approach the ANN may represent subsystems which are defined as polygonal surrounded areas within the FE- Mesh (see Figure 2: $NN_2$).

The substructure information is represented at the interaction nodes ($K$) on the polygons between the neural represented substructure and the overall FE-system.

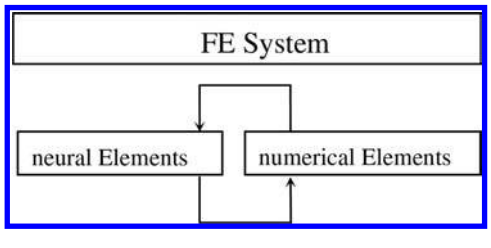


Figure 1. Hybrid model approach.

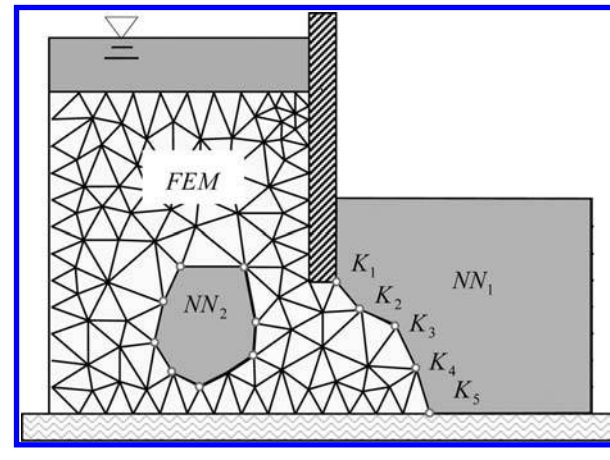


Figure 2. FEM: numerical represented substructure, ANN: neural represented substructures.

The hybrid system calculation works in two steps. The FE-structure is treated and calculated as a FE-system. The areas contained in the polygons are substructures which respond as ANNs. The input data for training the ANNs are generated within preconditioning calculations within which the full system is represented as discrete FE-system. Once trained the ANN-subsystems are integrated into the final FE-calculation thus saving expensive numerical recalculation of these subsystem areas.

## 3 COMPUTATIONAL ASPECTS

The paper describes the computational aspects for the training and simulation of pressure heads at interaction nodes between one FE- numerical and one ANN-embedded neural substructure. All information from the neural represented substructure $S2_{NN}$ is available at the nodes $K$ interacting with the numerical FE-system. In this example the mesh is a triangular finite element grid representing an excavation pit with a slotted wall. The mesh contains 3110 triangles in total for training. For the hybrid representation the FE-mesh is reduced to 2532 triangles while the neural subsystem represents a mesh of 578 nodes. For the generation of training data the full system is calculated by FEM for different load case scenarios. Inside the neural represented substructure pumps or sinks could be contained.

Two different ANN-approaches were investigated for matching the FE- and the ANN-areas using the pressure heads at the interaction nodes for different load case scenarios. In the first approach the pressure heads were trained individually within one neural network for each matching node. In the second approach training and simulation of all pressure head values at all interaction nodes was done within one (global) neural network. The full paper will also discuss calculation and access time analysis.

## 4 EXAMPLES

### 4.1 *Training of the pressure head value at one interaction node at a time*

Example 4.1 describes the first approach for the training and testing of pressure head values at one interaction node at a time only. Exemplarily the investigations were done for node $K1$ in Figure 3. The input data is the pressure head information from every neighbour node of interaction node $K1$, within the FE-represented subsystem $S1_{FEM}$ plus predefined pressure head boundary conditions at the inner nodes $I1, I2, I3$. The pressure head information from pumps or wells within the ANN-represented substructure $S2_{NN}$ is used as additional external input data. The output values are the pressure head information at the interaction nodes $K1$, $K2$ and $K3$. The neural training was developed for different load case scenarios.

After training the hybrid model is able to predict pressure heads at the interaction node for unknown load cases.

The neural network architecture is a three layer feedforward network without recurrence. The network uses five input, three hidden and three output neurons with sigmoid activation functions between input and hidden layer and linear activation functions between hidden and output layer.

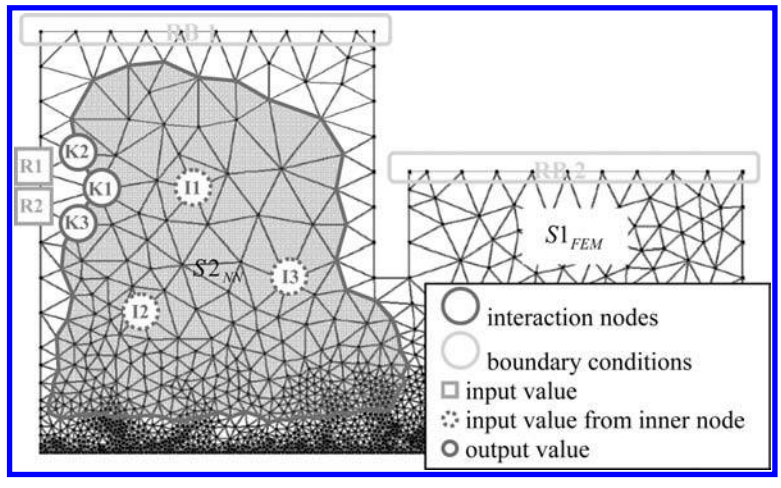


Figure 3. Training and testing environment for interaction node K1.

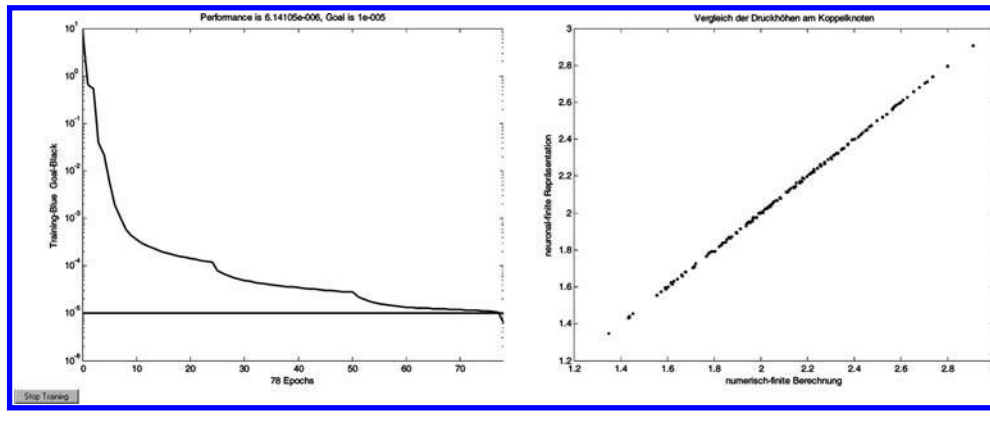


Figure 4. Left: training MSE 0.00001, right: comparison FE-calculation and ANN representation.

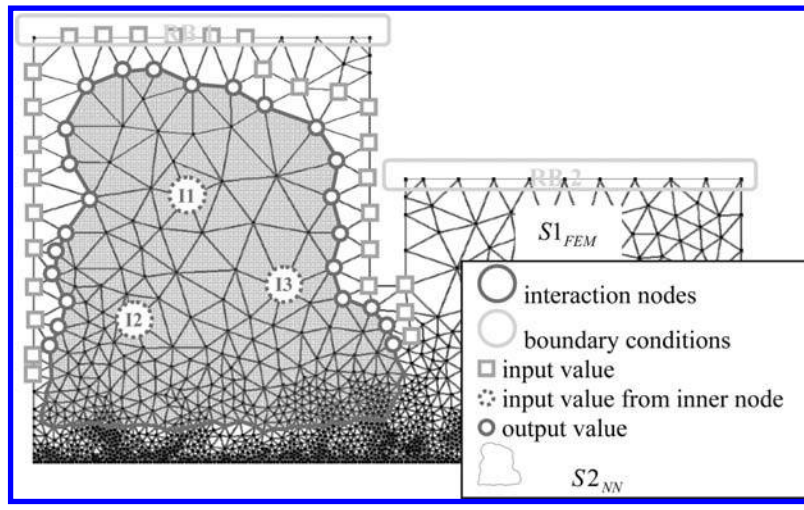


Figure 5. Training and testing environment for all connection nodes (not all are shown).

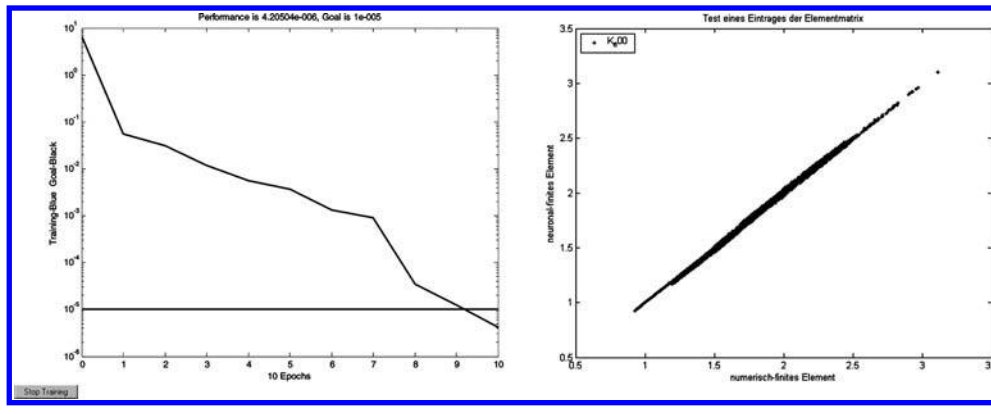


Figure 6. Left: training MSE $< 0.00001$, right: comparism FE-calculation and ANN representation.

The training pattern set contains 135 load case scenarios for the boundaries $RB$ 2, and the inner nodes $I1$, $I2$ and $I3$. For training the Levenberg-Marquardt-algorithm was used. The training stopped at a MSE of $10^{-5}$ or after 500 training epochs. After training the results of the neural representation were compared with results from complete numerical FE-calculations for unknown load case scenarios. Figure 4 illustrates the training and testing results.

### 4.2 *Training of the pressure head value at all interaction nodes within one step*

In example 4.2 the pressure heads at all interaction nodes between the numerical and neural substructures were trained and represented within one neural network. Again the neural network architecture is a three layer feedforward network without recurrence. The network uses 101 input, 15 hidden and 82 output neurons with sigmoid activation functions between input and hidden layer and linear activation functions between hidden and output layer. The training patterns include the same 135 load case scenarios for the boundaries $RB$ 2, and the inner nodes $I1$, $I2$and $I3$.

The neural network is trained again with Levenberg-Marquardt-algorithm up to a MSE of $10^{-5}$ or until 500 training epochs are reached. The results were compared with numerical FE-calculations with unknown load cases.

## 5 RESULTS AND CONCLUSIONS

The results from the presented investigations show the feasibility of a hybrid model for groundwater flow calculations. For loading conditions which had not been used for training purposes, the neural networks did a simulation for the pressure heads at the boundary nodes of the ANN substructure. These values interact directly at the connection nodes with the numerical solution which is calculated for the remaining discrete FE-system. For the training, testing and simulation of the hybrid model a software system was developed. More information is available in[2].

Especially for time dependent iterative processes this approach might help to save computational time during the modelling process. The integration of this approach into other, more complex numerical schemes with more complex differential equations is an area of future research.

## REFERENCES

[1] L. H. C. Chua, K.-P. Holz (2005) “Hybrid Neural Network – Finite Elemen Triver Flow Model”, *ASCE Journal of Hydraulic Engineering, 313, NO. 1, PP. 52–59*, ISSN 0733-9429/2005/1-52-59

[2] Weber L., HOLZ K. P.: “ANN-FEM Mixed Simulation in Groundwater Flow”, *The 8TH International Conference on Hydroinformatics, January 12–16, 2009, Concepción, Chile*, ISBN 978-981-08-2099-2

*Turbulence modeling, dispersion and transport*

*Environmental Hydraulics – López-Jiménez et al (eds)*
*© 2010 Taylor & Francis Group, London, ISBN 978-0-415-56697-1*

# Impact of water depth confinement on turbulent open-channel flows over rough walls

E. Florens, O. Eiff & F.Y. Moulin
*Université de Toulouse; INPT, UPS; IMFT (Institut de Mécanique des Fluides de Toulouse), Toulouse, France*
*CNRS; IMFT Toulouse, France*

ABSTRACT: Turbulent open-channel flows over macro-roughnesses were investigated experimentally using a high spatial resolution particle image velocimetry (PIV) technique. In particular, the effect of increased confinement, i.e. the roughness height h to the water-depth D ratio, on the logarithmic law was studied. The double averaging concept was used with the spatially-resolved mean and turbulent velocity fields to estimate the roughness parameters, i.e. the friction velocity $u^*$, the roughness length $z_0$ and the zero-plane displacement d. The effect of h/D for 2 bed roughnesses and Froude numbers on the parameters is analyzed and discussed.

*Keywords*: fully-rough turbulent boundary layer, macro-roughness, open-channel flows, logarithmic law, double averaging.

## 1 INTRODUCTION

In his recent review, Jimenez[7] points out that in order to attain the universal structure described by the logarithmic law, the boundary layer height $\delta$ should significantly exceed the roughness element height $h$ ($\delta/h > 40$ or more). Combined with the requirement that the equivalent roughness height, $k_s^+ = k_s u^*/\nu$, be larger than 80, this yields a Reynolds number $Re_\delta = u^*\delta/\nu > 4000$, where $u^*$ is the friction velocity. The mean velocity profile, in the inertial or overlap layer can then be expressed in different but equivalent forms, such as:

$$\frac{\bar{u}}{u^*} = \frac{1}{\kappa}\ln\frac{z-d}{z_0} \qquad \text{or} \qquad \frac{\bar{u}}{u^*} = \frac{1}{\kappa}\ln\frac{z-d}{k_s} + B \tag{1}$$

where $B = 8.5$, $z_0 = k_s/33$, is the roughness length and $d$ the zero-plane displacement.

Jimenez[7] notes that $k_s$ (and equivalent $z_0$) is a "hydrodynamic concept that needs to be related to the surface geometry". In the case of atmospheric boundary layers, Bottema[1], for example, found $z_0$ and $d$ to depend only on the roughness geometry. However, whereas in atmospheric boundary layers the blockage factor requirement is usually met, it is more rarely so in open channels, or rivers. Nevertheless, the logarithmic and the derived friction laws are still commonly used in this context, even if the blockage ratio is significantly less than 40. Castro[2] investigated the mean flow universality of developing boundary layers in wind tunnels for small blockage ratios. He concluded that the mean flow at least, is universal down to $\delta/h \sim 5$, i.e. for much lower blockage ratios. Here we propose to investigate the boundary layer structure in open-channel for low blockage ratios, i.e. for strong confinement by the free surface, given by $\alpha = h/D \leq 1$, where $D$ is the water depth. Particular attention is paid to use high spatial-resolution PIV measurements for the benefit of correctly accounting for spatial dispersion effects near the canopy via the double averaging method (see Raupach et al.[9] in the atmospheric context and Nikora et al.[8] in the hydraulic one).

## 2 EXPERIMENTAL SETUP

In order to attain fully rough and developed conditions, experiments were conducted in a specifically designed 20 m long × 1.1 m wide × 0.5 m deep glass-walled open-channel. The relatively wide channel permits secondary circulations effects to be reduced while allowing a large number of large roughness-obstacles to be used. The water discharges $Q$ ranged from 10 to 150 L.s$^{-1}$, with a controlled sluice gate controlling the water depth $D$. The homogeneous rough bed was placed between 2 m and 15.2 m after the end of the tranquilization section, and measurements were made at 10.7 m downstream of the rough bed beginning, when the boundary layer is fully developed.

The rough beds were made with 20 mm plastic cubes arranged in two configurations (see Figure 1) with frontal densities (frontal area to plan area) of $\lambda_f = 0.19$ and 0.39, respectively referred to here as the S1 and S2 surfaces, expected to yield different roughness lengths.

To investigate the influence of the confinement as well as the Froude numbers, (defined respectively as $\alpha = h/D$ and $Fr = U/(gD)^{1/2}$, with $h$ the height of the cube and $U$ the bulk velocity, measurements were performed for three flow regimes with Froude numbers (∼0.22, 0.54) and confinement numbers (0.15, 0.33). The experimental parameters for the four experiments are given in Table 1. Here, the Reynolds number $Re_D$, sometimes referred to as the Kármán number, is defined as $u^*D/\nu$.

The PIV measurements were performed with a high-resolution 2048 × 2048 pixel 14-bit CCD camera and a pulsed Nd-Yag 30mJ laser. For both roughness configurations (see Figure 1), the measurements were performed in three different vertical planes aligned with the flow. Their transverse positions were $y = 0$, 2.25 and 3.25 cm for S1, and $y = 0$, 0.5 and 1.125 cm for S2, in order to obtain good estimations of the double-averaged quantities.

For each vertical plane, 1000 independent instantaneous velocity fields, yielding the longitudinal and vertical components $u$ and $w$, were calculated using spatial correlation techniques with peak-locking reduction algorithms developed by Fincham & Spedding[6], and Fincham & Delerce[5]. The smallest scale resolved was around 2 mm, i.e. about 10–30$\eta$, where $\eta$ is the Kolmogorov scale based on the friction velocity. Each vertical plane yields 80 vertical profiles along one periodic roughness pattern in the streamwise direction.

Table 1. Experimental parameters.

| | $\lambda_f$ | $D$ (cm) | $U$ (cm/s) | $Re_D$ | $Fr$ | $\alpha$ |
|---|---|---|---|---|---|---|
| S1A | 0.19 | 13.5 | 70 | 7700 | 0.54 | 0.15 |
| S1B | 0.19 | 13.5 | 30 | 3300 | 0.23 | 0.15 |
| S1C | 0.19 | 6 | 22 | 1100 | 0.21 | 0.33 |
| S2C | 0.39 | 6 | 23 | 1300 | 0.21 | 0.33 |

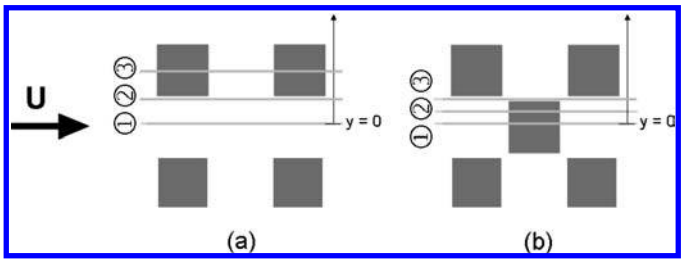


Figure 1. Top view of the position of the PIV measurement vertical planes in (a) S1 and (b) S2 configurations.

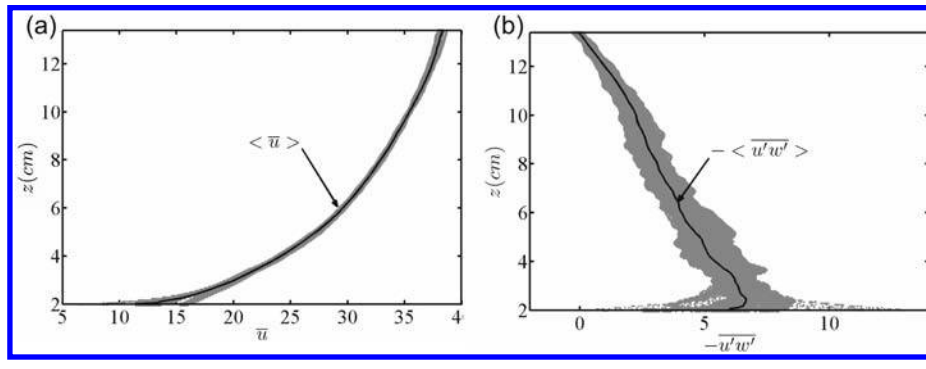


Figure 2. Time averaged profiles in the three vertical planes (gray points) and double averaged profiles (solid lines) for (a) the streamwise velocity and (b) the Reynolds stress. Regime S1B.

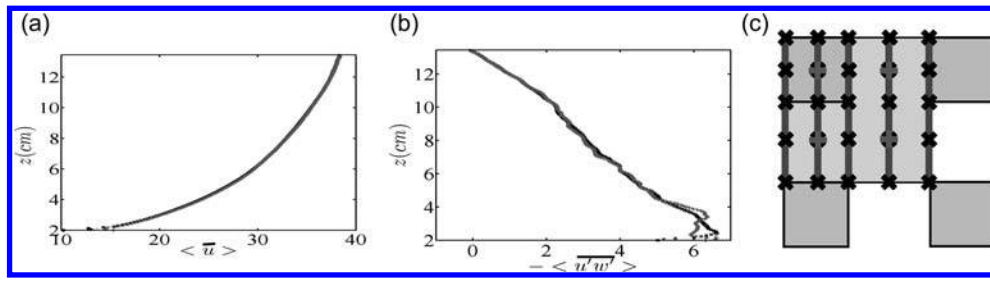


Figure 3. Double-averaged profiles of (a) streamwise velocity and (b) Reynolds stress, estimated from 4 profiles (green +), 25 profiles (blue ×) and 400 profiles (red°) in the S1B regime. (c) Top view of the reduced vertical profiles positions.

## 3 RESULTS

### 3.1 Double-averaged profiles

Following Nikora et al.[8] and Cheng & Castro[3], double averaged quantities, i.e. time ($-$) and horizontally averaged ($<>$) quantities, were computed. Each measurement node in the horizontal plane was given a weight factor proportional to its influence aera in the periodic pattern.

In Figures 2 (a) and (b), time-averaged velocity and Reynolds stress vertical profiles, respectively, are plotted for regime S1 B. In the upper part of the flow, above the roughness sublayer, very little scattering around the double averaged profiles is expected. Still, some scattering of the Reynolds stress profiles appears, likely because the data is not completely converged yet. Nevertheless, the transition at the top of the roughness sublayer is clearly demarcated near $z = 3$cm (i.e. $z = 1.5\,h$).

In previous studies (e.g. Cheng & Castro[3]), LDV measurements were used that provided less numerous vertical profiles than the PIV measurements performed here. In order to investigate how many vertical profiles are required to get a good estimation of the double-averaged quantities, sampling numbers of 4, 25, and 400 were used (see Figure 3 (c)). It can be in Figure 3 (b) that most significant impact of the sampling number is a modification of the lower part of the Reynolds stress profiles, which behaves quasi-linearly only with the full data set (400 profiles). Linearity above the roughness top is indeed expected from the double-averaged streamwise momentum equation, the small deviation based on 400 profiles being most likely due to secondary circulations. In the following, the full data set will be used, assuring better estimations of the friction velocity based on the Reynolds stress profiles.

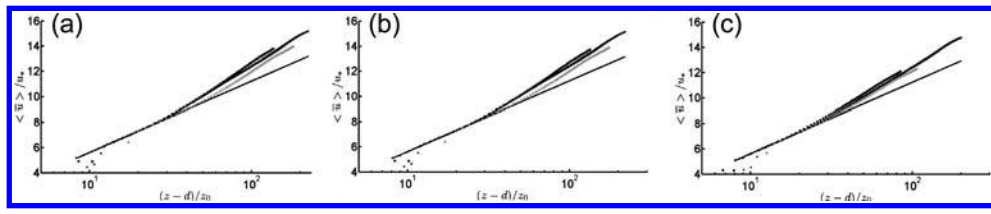


Figure 4. Double-averaged velocity profiles for regimes S1 A (red ×), S1 B (blue •), S1 C (green +) and S2 C (purple *), and logarithmic law (solid line), using the (a) "mean", (b) "maximum" and (c) "extrapolation" methods.

Table 2. Location and parameters of the logarithmic law obtained with three different methods.

| | $Z_{MIN}/H$ | | | $Z_{MAX}/D$ | | | $U^*/U_{MAX} \times 100$ | | | $D/H$ | | | $Z_0$ (MM) | | |
|---|---|---|---|---|---|---|---|---|---|---|---|---|---|---|---|
| | Max | Mean | Extra | Max | Mean | Extra | Max | Mean | Extra | Max | Mean | Extra | Max | Mean | Extra |
| S1A | 1.2 | 1.2 | 1.2 | 0.2 | 0.2 | 0.2 | 6.59 | 6.57 | 6.57 | 0.77 | 0.77 | 0.77 | 0.54 | 0.53 | 0.54 |
| S1B | 1.3 | 1.3 | 1.3 | 0.2 | 0.2 | 0.2 | 6.74 | 6.64 | 6.54 | 0.79 | 0.79 | 0.80 | 0.59 | 0.56 | 0.53 |
| S1C | 1.1 | 1.1 | 1.1 | 0.4 | 0.4 | 0.4 | 7.21 | 7.16 | 8.17 | 0.82 | 0.82 | 0.75 | 0.24 | 0.23 | 0.41 |
| S2C | 1.1 | 1.1 | 1.1 | 0.4 | 0.4 | 0.4 | 7.21 | 7.17 | 8.68 | 0.89 | 0.89 | 0.83 | 0.31 | 0.31 | 0.62 |

Table 3. Non-dimensional values of the roughness length.

| | S1A | S1B | S1C | S2C |
|---|---|---|---|---|
| $z_0/D$ | 0.0040 | 0.0044 | 0.0040 | 0.0052 |
| $z_0/h$ | 0.027 | 0.030 | 0.012 | 0.016 |

### 3.2 Friction velocities and logarithmic law

Linear regression of the logarithmic law, here with three parameters (assuming $\kappa = 0.41$) only yields two parameters without additional constraints (e.g. Macdonald 2000). The first parameter, $u^*$, was thus obtained via the Reynolds stress profiles $< \overline{u'w'} >$ using three methods: (i) the maximal value of $(< \overline{u'w'} >)^{½}$ , (ii) the mean value of $(< \overline{u'w'} >)^{½}$ in the fitting interval for the logarithmic law (Cheng & Castro[3]), (iii) via a linear extrapolation of the Reynolds stress profile at z = d (Castro [2]). With the $u^*$'s obtained via the three different methods, the logarithmic law can now be used to find $z_0$ and $d$ via linear regression of mean velocity profile. However, given the effect of strong confinement and the expected reduced range of the logarithmic law, care was taken to optimize the range of the fit. This was achieved by performing linear regression of wide range of $z$-values and chosing the final result as the one corresponding to the lowest regression error. Thus, in addition to the ($u^*$, $z_0$, $d$) triplets associated with each of the three methods to determine $u^*$, the range of logarithmic law velocity [$z_{min}$, $z_{max}$] was also obtained (see Table 2). The fitted curves are shown in Figure 4.

The three $u^*$-determining methods yield approximately the same results for $u^*$ itself, $z_{min}$ and $z_{max}$, $z_0$ and $d$. The largest differences appears for the most confined regime C with the "extrapolation" method because, due to the slope of the Reynolds stress profile that is naturally far greater in this regime, the value of $u^*$ at $z = d$ is found larger than with the two other methods.

Whereas Bottema[1] propose $z_{min} \approx 2h$, in line with most usual estimations of unconfined boundary layer, here $z_{min}/h$ is about 1.1–1.3. This is consistent with Cheng & Castro[3]'s results who claim that the logarithmic law can extend into the roughness sublayer defined here by dispersion. In addition, for the most confined regime S1C, $z_{max}/\delta$ (with $\delta = D$ here) is about 0.4, far larger than the usual limit of 0.1-0.2. Therefore, a logarithmic region seems to persist even for strongly confined regimes but tends to move downwards while keeping the same extend. For identical confinement and Froude numbers with two different roughnesses, a change in the location and extension of the logarithmic region is not observed.

Among the three parameters $u^*$, $z_0$ and $d$, only $z_0$ appears to depend on the flow regime in particular confinement whereas $u^*$ and $d$ are quite insensitive to the confinement. This latter result supports the often-used assumption that the zero-plane displacement $d$ only depends on the bottom geometry. To investigate whether in the presence of confinement $z_0$ depend on the flow regime, $z_0$ as obtained by the "maximum" method was normalized by $D$ and $h$. The results are given in Table 3.

Again no dependence with the Froude number is observed. On the other hand, at constant Froude number, increased values of the confinement number $\alpha$ (S1C and S2C) yield a significant change of $z_0/h$. Combined with the fact that $z_0/D$ does not exhibit any dependence for the given roughness bed S1, this result confirms that $z_0$ is not simply dependent on roughness geometry for confined lows, but also on flow parameters.

## 4 CONCLUSION

PIV measurements were performed in order to study the water-depth confinement effect on the existence and the parameters of the logarithmic profile. This is shown that correct estimations of the double-averaged quantities require a relatively high sampling number of vertical profiles, in particular for second-order moment components such as the Reynolds stress $\overline{u'w'}$. Using minimization of the regression error of experimental data with a logarithmic law for three different estimation methods for the friction velocity $u^*$, we show that a logarithmic region is seen to persist even at high confinement, moving downwards to the canopy while the roughness length $z_0$ decreases. By contrast, the zero-plane displacement $d$ does not seem appear to be much affected by the confinement, supporting the usual assumption that is depends on roughness geometry. Measurements

with the roughness S2 for regimes A and B have also been performed and are currently being processed. They will complete the data presented here and enrich the discussion on the confinement effects.

## REFERENCES


[1] Bottema, M. (1996), “Roughness parameters over regular rough surfaces: Experimental requirements and model validation”, J. Wind Eng., Vol. 64, pp. 249–265.

[2] Castro, I.P. (2007), “Rough-wall boundary layers: mean flow universality”, J. Fluid Mech., Vol. 585, pp. 469–485.

[3] Cheng, H., Castro, I.P. (2002), “Near wall flow over urban-like roughness”, Bound.-Layer Meteor., Vol. 104, pp. 229–259.

[4] Fincham, A.M., Delerce, G. (2000), “Advanced optimization of correlation imaging velocimetry algorithms”, Exp. in Fluids, Vol. 39, pp. S13–S22, suppl.

[5] Fincham, A.M., Spedding, G.R. (1997), “Low cost, high resolution DPIV measurements of turbulent fluid flow”, Exp. in Fluids, Vol. 23, pp. 449–462.

[6] Jimènez, J. (2004), “Turbulent flows over rough walls”, Annu. Rev. Fluid Mech., Vol. 36, pp. 173–196.

[7] Macdonald, R.W. , (2000), “Modelling the mean velocity profile in the urban canopy layer”, Bound.-Layer Meteor., Vol. 97, pp. 25–45.

[8] Nikora, V., Goring, D., McEwan, I., Griffiths, G., (2001), “Spatially averaged open-channel flows over rough bed”, J. Hydraul. Eng., Vol. 127, n°2, pp. 123–133.

[9] Raupach, M.R., Antonia, R.A., Rajagopalan, S. (1991), “Rough wall turbulent boundary layers”, Appl. Mech. Rev., Vol. 44, n°1, pp. 1–25.

*Environmental Hydraulics – López-Jiménez et al (eds)*
*© 2010 Taylor & Francis Group, London, ISBN 978-0-415-56697-1*

# Lateral mixing in a meandering open channel flow

F. Folke
*Institute for Water and River Basin Management, University of Karlsruhe, Karlsruhe, Germany*

I. Moncho-Esteve
*Rural Engineering Department, Hydraulic Division. Valencia, Spain*

M. García-Villalba & C. Braun
*Institute for Hydromechanics, University of Karlsruhe, Karlsruhe, Germany*

G. Palau-Salvador
*Rural Engineering Department, Hydraulic Division, Valencia, Spain*

ABSTRACT: A large eddy simulation of flow in a periodic meandering open channel with a rectangular cross-section is presented. The Reynolds number based on the channel height is 40.000 and the aspect ratio of the cross-section is 4.48. Furthermore, the transport and mixing of a passive scalar is analysed using three different positions of release, e.g. on the inner bank, on the outer bank and on the center of the cross section. The obtained depth-average concentration profiles show good agreement with available experimental data. The role of the secondary motions in the mixing processes is the main focus of the discussion.

*Keywords*: Large Eddy Simulation, Scalar Transport, River Flow, Turbulence.

## 1 INTRODUCTION

The environment is strongly influenced by rivers which form our landscape continuously and are important for the transport of freights as well as waste water. A natural river follows a watercourse characterized by curves, the so called meanders. Meanders have an inner and an outer-bank and can be seen to a first approximation as being periodic. They are formed through erosion processes on the outer-banks and sedimentation processes at the inner banks. As a result sediments are transported from the outer to the inner-bank through which the shape of a river is changed continuously. This transport of sediment is induced by secondary motions. The secondary motions have also a strong influence on the transport and mixing properties of contaminants. These secondary motions are characterized by the classical and relatively well known center-region cell and an additional second cell near the outer-bank. The complex mechanisms associated with the secondary motions are still a challenge to scientists and engineers. They have a major impact on the control and regulations of rivers, e.g. on river restoration, navigability, water quality and the production of energy. It is therefore of great interest to understand the various governing mechanisms.

Fischer[1] was among the first who discussed the influence of meandering channel and its secondary motions on the mixing processes. Based on the experimental secondary profiles by Rozovskii[2] and the shear-flow analysis of Taylor[3] and Elder[4]he proposed a very strong influence of the secondary motions in meandering rivers on heat and mass transfer, and therefore on the distribution of pollutants. According to his analysis, the lateral spreading of pollutants is increase by the secondary motions due to the higher turbulence intensities. However, Boxall and Guymer[5] argued that the longitudinal spreading is decreased by the same effects. In contrast to Fischer[1], Demuren and Rodi[6] argued that in meandering channels convective transport of heat or mass has a stronger effect on the mixing than the turbulence itself. Despite the differences, the authors agree that the mixing process and consequently the effective mixing in meandering channels is very different to that in straight channels.

In this paper, a large eddy simulation (LES) is performed employing the same geometry as in the experimental study by Chang[7]. The three-dimensional mechanisms which govern the mixing processes are analyzed using three different positions of release, i.e. inner bank, outer bank and center of the cross section. The case was studied previously by Demuren and Rodi[6]in the context of a RANS simulation.

## 2 EXPERIMENTAL SETUP

The experiments of Chang [7] were carried out in a small flume with rectangular cross-section through seven consecutive meanders, one is shown in Figure 1. The cross-section was 0,254 cm wide and the water level was at 0,057 cm. The total length of the channel measured along the centerline was 25.91 m. The seven meanders consist of 13 identical 90°-bends (curvature radius of 0.914 m) in alternate directions linked with straight sections of 0.476 m length and a bottom slope of 0.0012. The velocity measurements were performed with a 1.588 mm standard Prandtl-type pitot tube. The dispersant used for this study was neutrally buoyant solution obtained by mixing salt water and methanol. It was injected by a right-angle 3.175 mm brass tube, connected by a tygon tube to a funnel hanging beneath the orifice as a continuous point source. The discharge was located in the eighth bend at Section 8C (see Figure 1) at three different positions in mid-depth: right bank (RB), left bank (LB) and center line (CL) and whereby the RB and LB was 0,0254 m away of the respective channel wall. The three scalars are named as S1, S2 and S3, respectively.

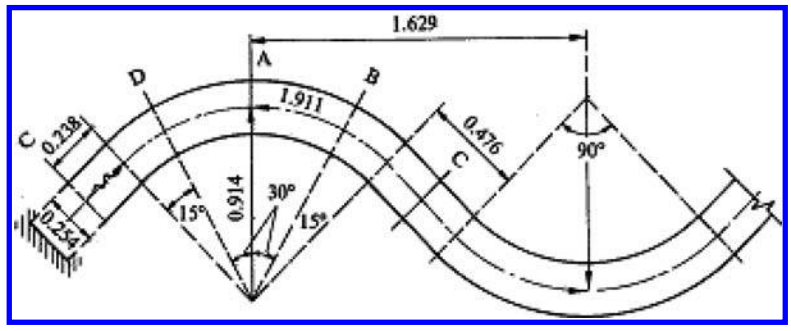


Figure 1. Sketch of one of the meanders used in the experiments (adapted from chang [7]).

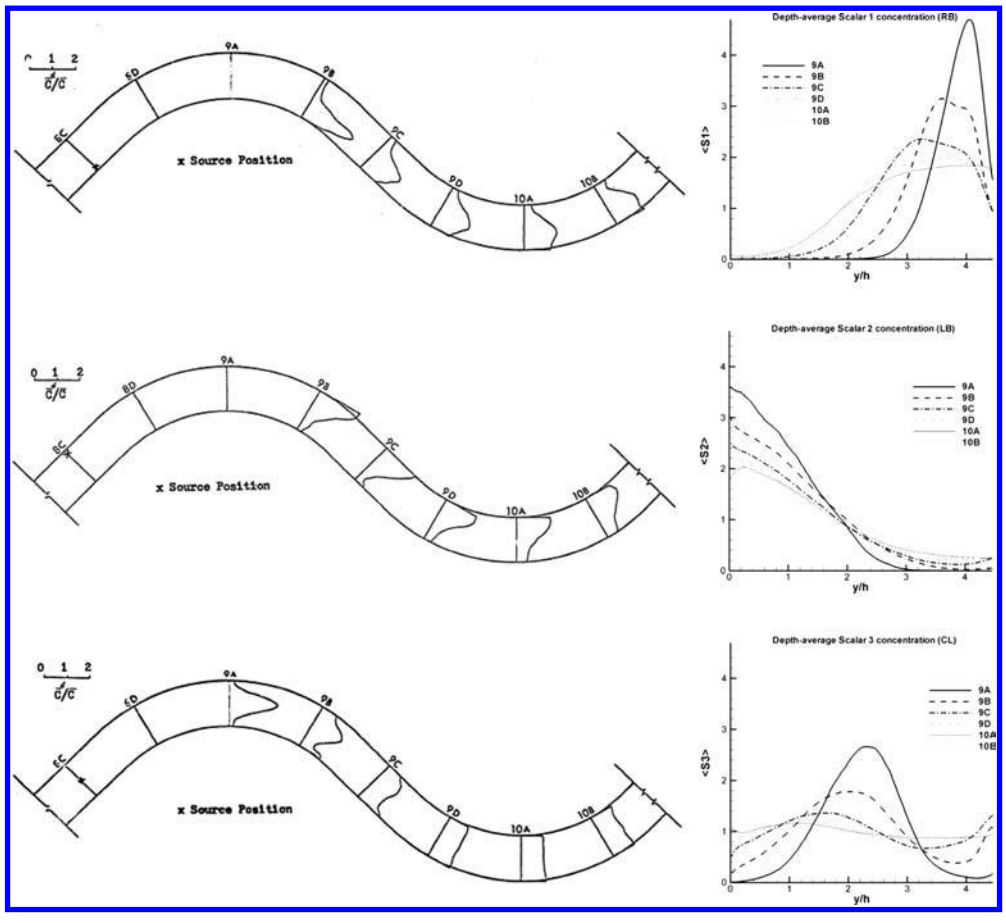


Figure 2. Depth-average concentration profiles for the three different release locations. Left: experimental results by Chang [7]; right: LES results.

## 3 NUMERICAL METHOD

The LES was performed with the in-house code LESOCC2 (Large Eddy Simulation On Curvilinear Coordinates). It is a successor of the code LESOCC developed by Breuer and Rodi [8]. The code solves the Navier-Stokes equations on body-fitted, curvilinear grids using a cell-centered finite volume method with collocated storage arrangement. Second-order central differences are employed for the convection as well as for the diffusive terms. The time integration is performed with a predictor-corrector scheme, where the explicit predictor step for the momentum equations is a low-storage three-step Runge-Kutta method. The corrector step covers the implicit solution of the Poisson equation for the pressure correction. The subgrid-scale (SGS) stresses, resulting from the unresolved motions, are modelled using the approach of Smagorinsky [9] with a model parameter of Cs=0.1.

In addition to the flow field, concentration fields due to tracer discharge from point sources have been simulated. Herefore, an additional transport equation is solved for each of the passive scalars using the bounded HLPA scheme for the convection term in this equation. An eddy diffusivity model was employed to account for the subgrid-scale contribution with a turbulent Schmidt number of 0.6. For the molecular Schmidt number a value of 1 was used.

For the numerical calculation a global coordinate system was used, while for the data analysis the quantities were transformed on a body-fitted coordinate system. The x-axis is hereby along the centerline of the channel bed, the y-axis along the spanwise and the z-axis along the vertical direction. The Reynolds number based on the bulk-velocity and the water depth is 40.000. The cross-sectional aspect ratio of channel width to water depth is 4.48. The computational grid consists of $448 \times 169 \times 58 = 4.4 \cdot 10^6$ grid points in x-, y- and z-direction.

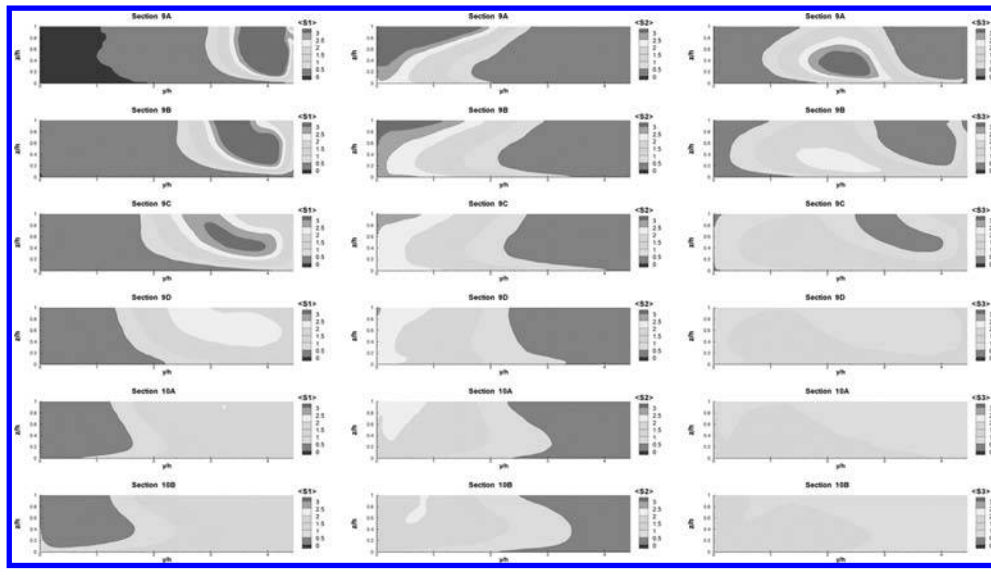

Figure 3. Concentration fields in 6 different planes along the meander. Left, S1; middle, S2; and right, S3.

The computational grid is uniform along the centerline in x-direction and stretched in y- and z-direction to achieve a better resolution of the near wall motions. The stretching ratio is kept to a fix value around 1.03. The grid sizes near the wall in terms of wall units are $\Delta y^+ = \Delta z^+ \approx 17$ and $\Delta x^+ \approx 430$. The simulation was carried out using one meander and periodic boundary conditions in streamwise direction. The Werner-Wengle model was employed at the bottom boundary and lateral walls jointly with a rigid-lid assumption for the free surface.

## 4 RESULTS AND DISCUSION

The comparison of the LES flow field statistics and the prediction of the secondary motions with the experimental data by Chang [7] can be found in Folke et al.[10], which shows in general a fairly good agreement. In this paper, our focus is given on the transport and lateral mixing of a passive scalar released close to the inner bank (scalar 1) and the outer bank (scalar 2), as well as in the center of the cross-section (scalar 3). The positions of release are according to the once used by Chang[7] described above.

The depth-averaged normalized concentrations for the three different positions of release, additionally averaged in time, are shown in Figure 2. The concentrations are normalized with the local mean concentration defined as $\bar{C}\frac{h}{Q}\sum_{j=1}^{n}\bar{C}_j^d\bar{u}_j^d\Delta y$, with, h, the water depth, Q, the flow discharge, $\overline{C}_j^d$, the depth-average concentration, $\overline{u}_j^d$, the depth-averaged streamwise velocity. Hereby, the sum over all the positions j in spanwise direction and $\Delta y$ the corresponding spanwise grid size are computed. As it can be seen in Figure 2, the predicted depth-average concentration profiles show fairly good agreement with the measurements for the three release locations. The strongest mixing is achieved by the position of release is at the center line (CL) (bottom of Figure 2). Due to the presence of the center region cell [10] the scalar is almost immediately mixed throughout the cross section and a nearly uniform depth-average concentration profile is obtained at section 10B. When the position of release is near the bank sides, the mixing is weaker and a clear concentration of scalar close to the wall can be observed in both cases. However, slightly better mixing is obtained for the release on the outer bank. One possible reason could be the presence of the outer bank cell.

The arguments above are confirmed in Figure 3, where the concentration field is shown at 6 different planes along the meander. On the left and the middle columns, the evolution of the scalar released at the inner and outer bank is shown. The effect of the secondary motions on the mixing process and on the evolution of the center-region cell is clearly visible. Additionally, the maximum value observed in the scalar 1 concentration correlates with the shift of the maximum streamwise velocity from the inner to the outer bank. On the other side, the right side of the figure shows the evolution of the concentration when the release is located at the center line. Clearly, the mixed process is higher due to the effect of the center-region cell and after less than two bends (section 10B) is almost uniform in the whole section which agrees well with the experimental results from Chang [7].

## 5 CONCLUSIONS

In this paper the results of a large eddy simulation of the mixing process in a periodic meandering channel were presented. The comparison with experimental data of the depth-averaged concentration profiles was very satisfying. Three different positions of release for a passive scalar have been compared. From the results one can conclude that secondary motion influences considerably the lateral mixing of pollutants. Moreover, the spreading of the passive scalar is strongly dominated by the center-region cell. As a result, the mixing of the scalar released on the center of the cross-section is stronger than the mixing of the scalar released on the sides, due to the effect of the center-region cell.

## REFERENCES

[1] Fischer, H.B. (1969), “The effects of bends on dispersion in streams”, Water Resour. Res., Vol. 5 (2), pp. 496–506.

[2] Rozovskii, I.L. (1957), “Flow of Water in Bends of Open Channels”, *Ac. Sc. Ukr. SSR, Isr. Progr. Sc. Transl., Jerusalem.*
[3] Elder, J.W. (1959), “The dispersion of marked fluid in turbulent shear flow”, J. Fluid Mech., Vol. 5, pp. 544–560.
[4] Taylor, G.I. (1954), “The dispersion of matter in turbulent flow through a pipe”, Proc. R. Soc. London, Ser. A, Vol. 233, pp. 446–468.
[5] Boxall, J.B. and Guymer, I. (2003), “On the analysis and prediction of transverse mixing coefficients in natural channels”, J. Hydraul. Eng., ASCE, Vol. 129 (2), pp. 129–139.
[6] Demuren, A.O. and Rodi, W. (1984), “Calculation of turbulence-driven secondary motion in non-circular ducts”, J. Fluid Mech., Vol. 140, pp. 189–222.
[7] Chang, Y.C. (1971), “Lateral mixing in meandering channels”, Ph.D. thesis, University of Iowa, USA.
[8] Breuer, M. and Rodi, W. (1996), *Large eddy simulation of turbulent flow through a straight square duct and a 180° bed. Fluid Mechanics and its Applications*, Kluver Academic, pp. 273–285.
[9] Smagorinsky J. S. (1963), “General circulation experiments with the primitive equations. Part I: The basic experiment”, Monthly Weather Review, Vol. 91, pp. 99–152.
[10] Folke F., Moncho-Esteve I., García-Villalba M., Braun C., and Palau-Salvador G., (2009), “Large eddy simulation of flow in meandering open channels” 33rd International Association of Hydraulic Engineering & Research (IAHR) Biennial Congress, Vancouver, 9-14 August.

*Environmental Hydraulics – López-Jiménez et al (eds)*
*© 2010 Taylor & Francis Group, London, ISBN 978-0-415-56697-1*

# Momentum dispersion and wall friction in free surface flows above non-uniform bottom roughness

A. Soualmia
*Laboratoire Science et Technique de l'eau de l'INAT, INAT, Tunis, Tunisie*

L. Masbernat
*Institut de Mécanique des Fluides de Toulouse, Toulouse, France*

S. Zaouali & A. Kaffel
*Laboratoire de Modélisation en Hydraulique et Environnement de l'ENIT, ENIT, Tunis, Tunisie*

ABSTRACT: The effects of secondary flows on the momentum dispersion were analyzed in this study, for the case of free surface flows above non-uniform bottom roughness. In a first step, 3D-simulations were achieved using an anisotropic Reynolds stress model to determine the wall friction and the dispersion terms present in the depth averaged momentum equation. In a second step closure assumption of these terms were tested to define a 2D-Saint Venant model which is solved to calculate the transverse profile of the depth-averaged velocity. This approach was applied, to experiments achieved in a free surface flows above non-homogeneous rough bottom in a rectangular channel (realized at the 'Institut de Mécanique des Fluides de Toulouse –IMFT-'), and also to experimental results available in literature, and witch are achieved in open channels with periodic transverse variation of the bottom roughness.

*Keywords*: Wall friction, Saint Venant equations, Secondary flows, dispersion, roughness, turbulence.

## 1 INTRODUCTION

We have to note that works on the modeling of wall friction and dispersion in closed or open channels were devoted to parallel or quasi-parallel flows like in the first works of Taylor[1], Elder[2], and Fisher[3], and after Ayyoubzadeh and al[4]. On the other hand, the effects of secondary motions notably on the momentum dispersion are not ever considered in the 2D-Saint Venant models. To progress in this way, in the present work, the closure problems of the 2D Saint-Venant model were analyzed using the results of 3D-simulations with an anisotropic algebraic Reynolds stress model.

## 2 POSITION OF THE PROBLEM AND RESULTS

In this study were analyzed the effects of secondary flows on the momentum dispersion, particularly on the transverse distribution of the depth average velocity in free surface flows above non-uniform bottom roughness. In a first step, 3D-simulations were achieved using an anisotropic Reynolds stress model[5],*and*[6] to determine the wall friction and the dispersion terms present in the depth averaged momentum equation. In a second step closure assumptions of these terms were tested to define a 2D-Saint Venant model which is solved to calculate the transverse profile of the depth-averaged velocity. This approach was applied to opened channels with transverse variation of the bottom roughness with reference to experimental results available in[7],[8],[9] and[10].

The two dimensional Saint Venant model (2D) rises from the vertical integration of the Reynolds equations, by adopting various fundamental assumptions of which the hydrostatic pressure. The momentum equation, resulting from this integration, is expressed for a fully developed flow by[11]:

$$-\frac{d}{dy}(h\Phi_{SF} + h\Phi_T) + \rho h g \sin\alpha - \tau_b = 0 \tag{1}$$

Where:

$$\Phi_T = \rho < \overline{uv} >,\ \Phi_{SF} = \rho < u'' v'' > \tag{2}$$

In this case the depth-averaged quantities are only dependent on the lateral coordinate y. To predict the transverse evolution of $< U >$, equation (1) requires closure models for the local shear stress velocity $u^*$ (appearing in the bottom friction $\tau_b = \rho u^{*2}$), or the local friction coefficient $c_f = 2u^{*2}/ < U >^2$ and the dispersion fluxes $\Phi_T$ and $\Phi_{SF}$.

For these three terms the same approach was followed: first they were determined from the 3D-simulations with the anisotropic model, then it was attempted to define algebraic relations to express them as functions of $< U >$.

To propose a wall friction law applicable to rough, smooth and intermediate regimes, it was used the logarithmic formulation developed by Labiod[9] from his experiments in a rectangular open channel with a sharp variation of the bottom roughness.

The 3D-simulations shown that it's possible to propose the following expression for $\Phi_T$:

$$\Phi_T = \rho < \overline{uv} > = -D_T \rho u^* h \frac{d}{dy} < U > \quad \text{where} \quad D_T = Cte \tag{3}$$

In non-dimensional form we can write: $\Phi_T^+ = \rho < \overline{uv} > / \rho g h \sin\alpha$

Without any physical argument except the opposite sign observed between $\Phi_T$ and $\Phi_{SF}$, it was considered that $d < U > /dy$ was a driven force for the flux $\Phi_{SF}$ and it was written:

$$\Phi_{SF} = \rho < u'' v'' >= \lambda_{SF} \rho u^* h \frac{d}{dy} < U > \quad \text{and} \quad \lambda_{SF} = Cte \tag{4}$$

And the non-dimensional form is: $\Phi_{SF}^+ = \rho < u'' v'' > / \rho g h \sin\alpha$

In Fig.1, are presented the secondary flow patterns obtained from the simulations of Labiod[9] and Zaouali[10] experiments, realized at the 'Institut de Mécanique des Fluides de Toulouse -IMFT-', and Muller[8], and Wang[9] experiments, achieved with the anisotropic algebraic Reynolds stress model [5]and[6]. For the case of Labiod and Zaouali experiments (figure 1), the gap of roughness at y = 0.9 cm, produces an important cell oriented from the central rough zone towards the lateral wall (that is in agreement with the measurements). Wile for the cases of Muller and Wang (figure 2) secondary flows are organized in two counter-rotating cells, oriented, near the wall, from the rough strip towards the smooth strip. In these two cases, because the effect of the lateral walls was neglected (the simulations were limited to a symmetrical cell), the corner effects due to anisotropy were not present. We note here that the main characteristics of this observed secondary flow are near to the experimental results, in fact the maximum magnitude of the secondary velocity vectors is about 0.025 $U_m$ for the case of Muller and 0.02 $U_m$ for the case of Wang, where $U_m$is the average primary velocity.

On Fig. 4, were plotted profiles of the non-dimensional bottom friction $\tau_b^+ = \tau_b / \rho g h \sin\alpha$ versus the non-dimensional transverse coordinate $\zeta = y/\lambda$. In all the figures, the results of the anisotropic model (3D model) are referred by the abbreviation NPF, (for Non Parallel Flow). On the same figures are also presented results obtained by assuming the flow is parallel (V=W=0): this case is referred by the abbreviation PF. In this Figure it is observed the effect of the sharp roughness change on the distribution of $\tau_b$, and a correct agreement with Labiod, Zaouali, and Muller experiments. The differences between NPF and PF simulations underline the effects of secondary flows.

On Figures 5 and 6, were plotted the curves of $\Phi_T^+$ and $\Phi_{SF}^+$ given by Equations (3) and (4) with $D_T = 0.05$ and $\lambda_{SF} = 0.23$ for the cases of Muller and Wang; wile $D_T = 0.08$ and $\lambda_{SF} = 0.1$ for the IMFT experiments (in this last case these are slight different due to the difference of the secondary flow intensity). Note that, for Muller and Wang experiments, the calculations are achieved by smoothing the term $u^* d < U > /dy$ to remove its discontinuities, due to sharp variations of the bottom roughness. In this way, a correct prediction of $\Phi_T^+$ and $\Phi_{SF}^+$ was obtained.

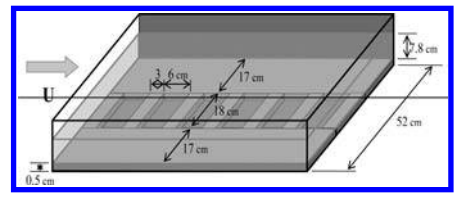


Figure 1. The open channel with the transverse variation of bottom roughness (According to[9],[12],[13] and [14]).

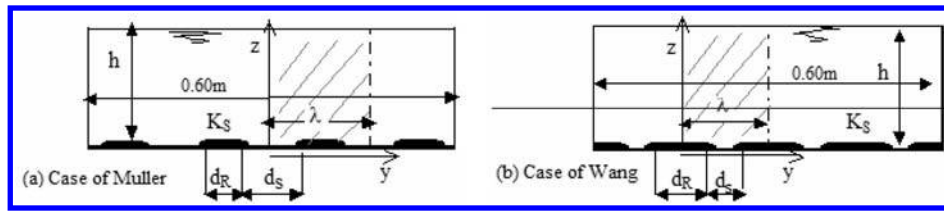


Figure 2. Shapes of the bed forms in Muller (a), and Wang (b) experiments.

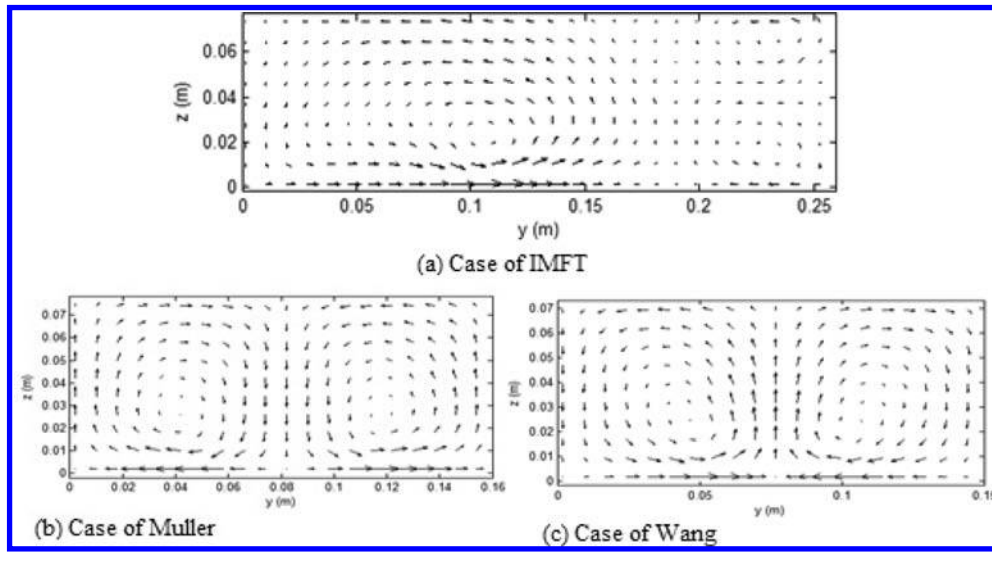


Figure 3. Secondary flow patterns.

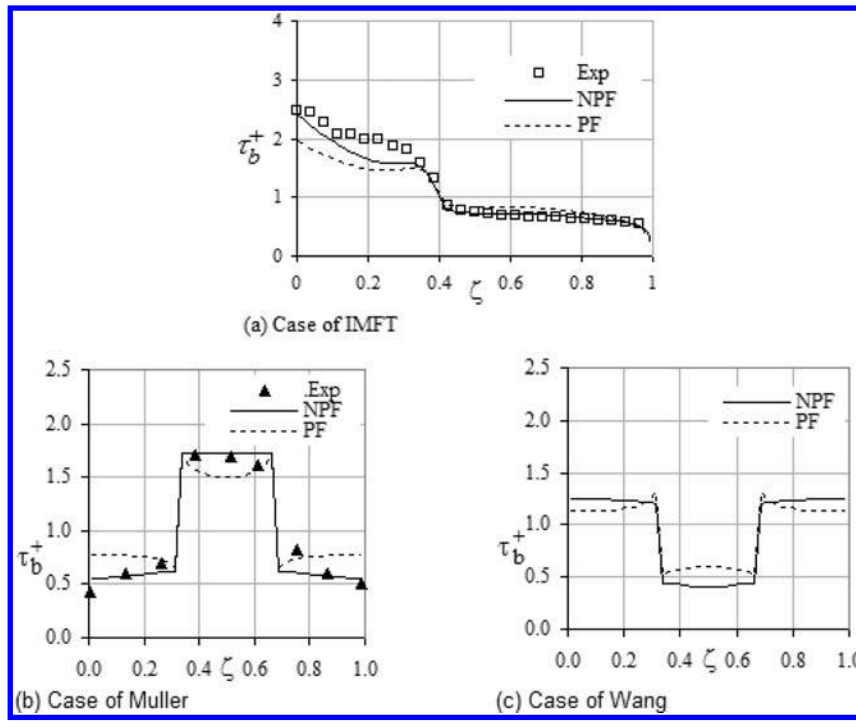


Figure 4. Transverse distribution of bottom friction.

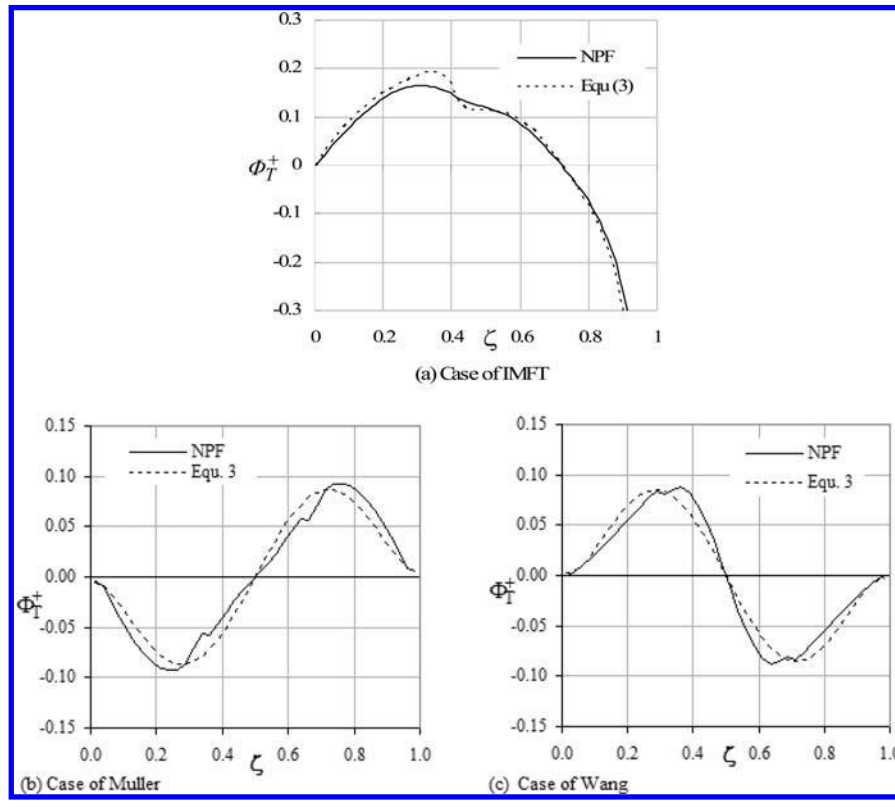


Figure 5. Transverse distribution of turbulent flux: (a) IMFT; (b) Muller; (c) Wang.

For the case of Muller, in figure 7, were plotted the numerical solutions $< U^+ > (\zeta)$ of the differential equation (1) using the closure laws (3), (4), and the logarithmic law[9] for the wall friction. These curves are denoted by the abbreviations 2D and 2D-I. The curves 2D, obtained with $D_T = 0.05$ and $\lambda_{SF} = 0.23$ are near the curves NPF obtained with the anisotropic 3D-model. On the other hand, the curves 2D-I, calculated with $D_T = 0.05$ and $\lambda_{SF} = 0$, are near the parallel flow solutions.

## 3 CONCLUSION

In this study, were analyzed the closure problems of 2D-Saint Venant equations from simulations with a 3D-model including an anisotropic algebraic Reynolds stress model. This approach was applied to experiments achieved in a free surface flows above non-homogeneous rough bottom in a rectangular channel realised at the 'Institut de Mécanique des Fluides de Toulouse', and

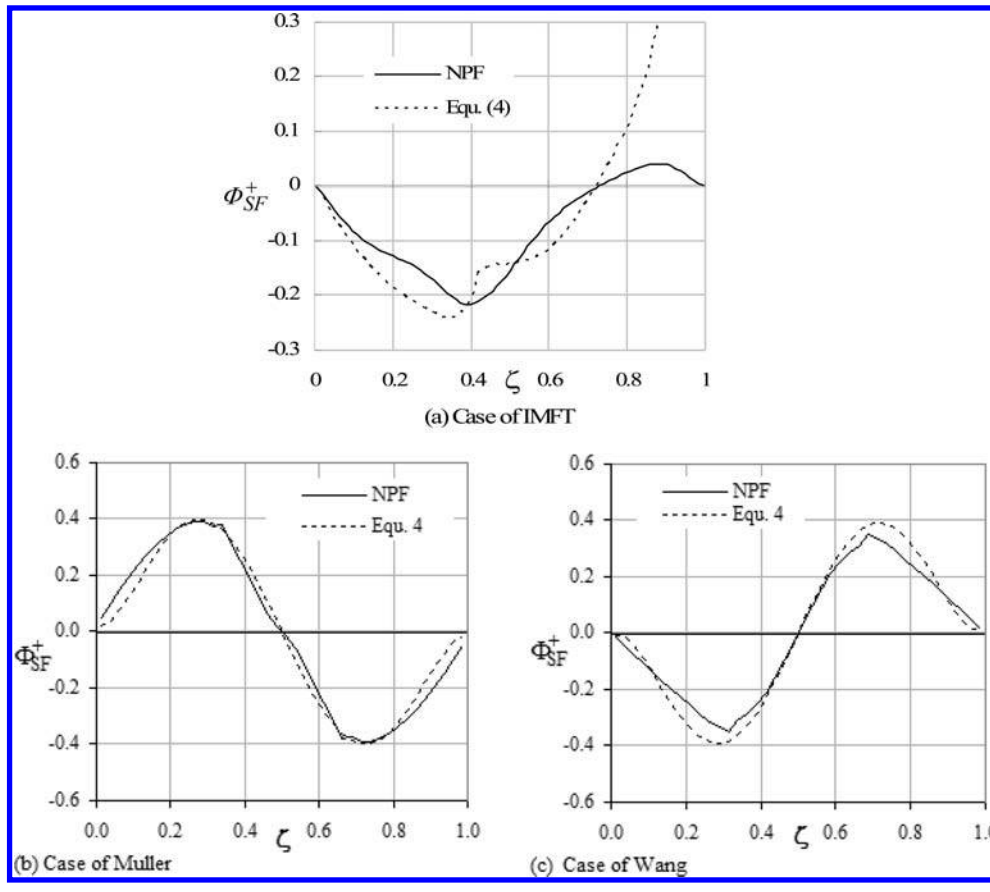


Figure 6. Transverse distribution of secondary motion transport flux: (a) IMFT; (b) Muller; (c) Wang.

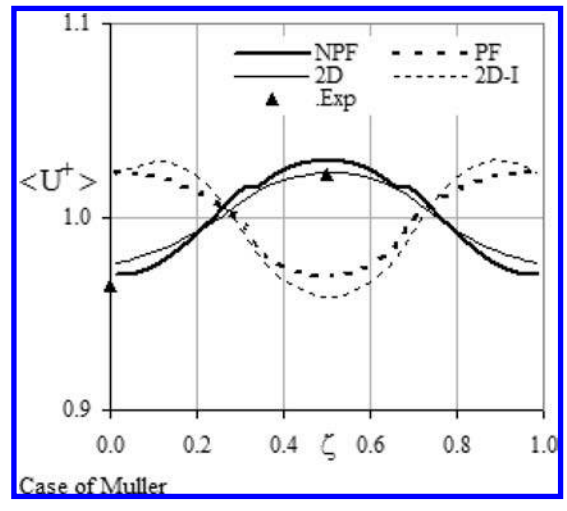


Figure 7. Transverse distribution of non-dimensional depth averaged velocity.

also to experimental results available in literature, that are achieved in open channels with periodic transverse variation of the bottom roughness. Calculating the wall friction and the momentum fluxes transported by the turbulence and the secondary motions, it was possible to test closure laws for these terms and solve this Saint Venant model. The preliminary results obtained, emphasize the interest of the change scale analyse of the hydraulic models, in complex configuration from the 3D field models. In perspective, in the case of this studied roughness, particularly in periodic roughness, the realisation of the Large Eddy Simulations will be certainly fruitful, and we project to put it in work.

## REFERENCES

[1] Taylor, G.I. (1954), "The Dispersion of Matter in Turbulent Flow through a Pipe", *Proceeding of the Royal Society of London Series a-Mathematical and Physical Sciences, 223(1155) 446–468.*

[2] Elder, J.W. (1959), "The dispersion of a marked fluid in turbulent shear flow", Journal of Fluid Mech, 5(4) 544–560.

[3] Fischer, B.H. (1975), "Discussion on simple method for predicting dispersion in streams. by R.S. Mc Quiveyand T.N Keefer", J Environ Eng Div ASCE, Vol 101, 453–5.

[4] Ayyoubzadeh, S.A, Faramarz, M. and Mohammadi, K. (2004), "Estimating longitudinal dispersion coefficient in rivers", *Proceedings of the 6th International Conference on Hydroinformatics, Singapore, June 21–24.*

[5] Gibson, M.M. and Rodi, W. (1989), “Simulation of free surface effects on turbulence with a Reynolds stress model. Journal of Hydraulic Research. Vol. 27. PP 233–245.
[6] Zaouali, S., Soualmia, A. and Masbernat, L. (2007), “Numerical simulation of an open channel flow with cross stream variation of the bottom roughness”, *Proceedings of the Fifth International Symposium on Environmental Hydraulics, December 4–7, Arizona State University.*
[7] Muller, A. and Studerus, X. (1979), “Secondary Flow in open Channel”, *Proceedings of Congress of the International Associations for Hydraulic Research, Italy. PP 19–24.*
[8] Wang, Z.Q., and Cheng, N.S. (2006), “Time-mean structure of secondary flows in open channel with longitudinal bed forms”, Adv water Resources. 1–16.
[9] Labiod, C. (2005), “Etude des écoulements à surface libre sur fond rugueux”, PHD Thesis, INPT.IMFT, France. No.2242
[10] Zaouali, S. (2008), “Structure et modélisation d’écoulements à surface libre dans des canaux de rugosité inhomogène”, PHD Thesis, I.N.P.Toulouse/E.N.I.Tunis, pp. 163.
[11] Soualmia, A., Masbernat, L., and Kaffel, A. (2010), “Wall friction and momentum dispersion in free surface flows with non uniform wall roughness”. Journal of PCN, Vol.51.
[12] Labiod, C., Soualmia, A. and Masbernat, L. (2007), “Turbulence in open channel flow with a cross-stream variation of the bottom roughness”, *Proceedings of the Fifth International Symposium on Environmental Hydraulics, December 4–7, Arizona State University.*
[13] Soualmia, A. (2008), “Structure et modélisation de systèmes de fluides industriels et environnementaux”, Habilitation Universitaire En Génie Hydraulique.
[14] Zaouali, S., Soualmia, A., Masbernat, L., and Labiod, C. (2008), “Experiments on Turbulence in open channel flow on rough bottom wall”, *Proceedings of the 2nd International Symposium on Shallow Flows, December 10–12, The Hong Kong University of Science and Technology (HKUST).*

*Environmental Hydraulics – López-Jiménez et al (eds)*
*© 2010 Taylor & Francis Group, London, ISBN 978-0-415-56697-1*

# Evaluation of viscous models for simulation of flow over round-shaped weirs

Miroslav Spano & Vlastimil Stara
*Water structures institute, Brno University of Technology, Faculty of Civil Engineering, Brno, Czech Republic*

ABSTRACT: In connection with the process of dam safety enhancement, emergency spillways of dams are being widely upgraded in Czech Republic. The aim is to enhance their capacity to satisfy the requirement for safety management of 10 000-year flood passage. Round-shaped weirs are often used for this purpose. They are easy to build, which is their main advantage. Round-shaped weirs were used for example in the reconstruction and capacity enhancement of the emergency spillway on the Bystřička dam or the Šance dam. The most important parameters of each spillway are its capacity and discharge coefficient. Hydraulic models are usually used to assess the capacity and discharge coefficient of given weir shape. However, numerical simulations are taking place here too. A 2D numerical simulation of flow over round-shaped weir was performed in combination with nine viscous models. The aim of work is to find which viscous model is most suitable for simulating of flow over round-shaped weirs. All computations were made on the same grid and with the same initial and boundary conditions. Simulations were performed using commercial software ANSYS-Fluent which uses finite volume method. Results from simulation were compared with results from hydraulic research.

*Keywords*: Round shape weirs, viscous models, CFD.

## 1 INTRODUCTION

The behaviour of water discharging over weirs and its capacity belongs to the main questions of water engineering. The spillway capacity is mainly defined by the weir shape which is covered in the discharge coefficient. Most discharge coefficients are determined in hydraulic research for the given weir shapes. Recently, numerical models have been carried out in this field. This paper is dealing with question of which viscous model is most suitable for this case. Simulations of flow for nine viscous models were performed for a given 0.4 m height and 0.1 m thick weir. The problem was solved with commercial CFD software ANSYS-Fluent, which uses a finite volume method (FVM). All achieved results were further compared with results from hydraulic research. Simulations were made for a flow rate of $0.029\,m^3.s^{-1}$ because the water head (above the weir crest) of 0.1 m was measured at this flow rate. Compared were water and energy heads above the weir crest measured 0.5 m upstream of the weir, pressures along the weir crest, and shapes of water along the weir crest. Shape and dimensions of the weir are shown in Figure 1.

## 2 EXPERIMENTAL SETUP

Hydraulic research was performed in a 0.4 m wide channel. A model of the weir was made from plexiglass. Water levels upstream of the weir were measured with a point gauge. Pressures along the weir surface were measured using piezometric holes. The precision of water level measurement was determined up to 5%, while the precision of pressure measurements was estimated up to ±200 Pa (0.020 m of water column). Pressure deviation was higher at higher discharges and also along the section with negative gauge pressure.

Various sets of measurements were performed. In this case a flow of the water head $h = 0.100$ m above the weir crest (corresponding to flow rate $0.029\,m^3.^{-1}$) was simulated. A detailed description of the hydraulic research is summarized in[1].

## 3 VISCOUS MODELS AND BASIC DOMAIN

Nine 2D viscous models of incompressible open channel flow were used for simulation of flow over the weir. Short overview of used modes is summarized in Table 1. Detailed description of each model can be found in user guide[2]. Water levels were reconstructed with the volume of fluid (VOF) method. Water was considered viscous (except of inviscid flow) with a constant density of $\rho_w = 998.2\,kg.m^{-3}$ and viscosity $\mu_w = 1.003.10^{-3}$ Pa.s. The density and viscosity of air were also considered as constant.

The boundary conditions (BC) were set as a wall at the bottom, pressure outlet with zero gauge pressure at the outflow and at the top boundary. Velocity inlet BC was set up at the inflow as known velocity profile. In this case a uniform velocity of $0.184\,m.s^{-1}$ was used at lower 0.4 m of the boundary and $0.0\,m.s^{-1}$ at the rest part of the boundary. A detailed description of the boundary types and its application can be found in user guide[2]. The initial condition was set up such that a volume of fluid with a head $h = 0.100$ m was located at the crest of the weir. Figure 1 shows a general layout of the problem.

Triangle cells were used for discretisation of the domain. The grid size varied from 2 mm near the weir (at rounded section and downstream face) to 10 mm near the top boundary and in the basin upstream of the weir. The grid consist from 79 459 cells with 40 165 nodes.

A proper time step which provides converged results is a function of grid size. Time step value of $\Delta t = 1.10^{-4}$ s was chosen. According to the results in [3*or*4], the value of the Courant number $C = 0.9$ or 0.7 respectively should ensure a stable solution.

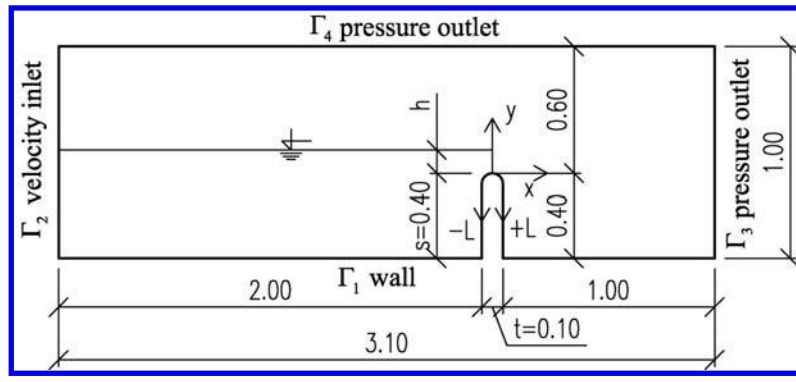


Figure 1. A general layout of the problem and boundary conditions.

Table 1. Overview of viscous models used for simulation.

| No | Mark | Description |
|---|---|---|
| 1 | inv | Inviscid flow |
| 2 | lam | Laminar flow |
| 3 | sa | Spalart-Allmaras model |
| 4 | ske | Standard k-$\varepsilon$ model |
| 5 | rngke | RNG k-$\varepsilon$ model |
| 6 | rke | Realizable k-$\varepsilon$ model |
| 7 | skw | Standard k-$\omega$ model |
| 8 | lowrersm | Raynolds stress model with low Re stress-$\omega$ model |
| 9 | quadrsm | Raynolds stress model with quadratic pressure-strain model |

Table 2. Summary of measured and computed energy heads.

| Variable | | Measured | inv | lam | Sa | ske | rngke | rke | skw | lowrersm | quadrsm |
|---|---|---|---|---|---|---|---|---|---|---|---|
| h | m | 0.100 | 0.099 | 0.098 | 0.098 | 0.095 | 0.096 | 0.098 | 0.097 | 0.096 | 0.109 |
| $h_0$ | m | 0.101 | 0.100 | 0.100 | 0.099 | 0.096 | 0.097 | 0.099 | 0.098 | 0.097 | 0.110 |
| $v_{mean}$ | $m.s^{-1}$ | 0.147 | 0.148 | 0.146 | 0.146 | 0.149 | 0.148 | 0.146 | 0.147 | 0.146 | 0.139 |
| Re | – | 8.4E + 04 | 8.4E + 04 | 8.3E + 04 | 8.3E + 04 | 8.4E + 04 | 8.4E + 04 | 8.3E + 04 | 8.3E + 04 | 8.3E + 04 | 7.9E + 04 |
| $\alpha$ | – | 1.05* | 1.01 | 1.05 | 1.05 | 1.06 | 1.05 | 1.05 | 1.08 | 1.05 | 1.04 |

* estimated value

The maximum Courant number across the domain here reached up to $C = 0.4$. A pressure based solver with the parameter setup recommended for this purpose was used, see[2].

## 4 RESULTS AND DISCUSSION

### 4.1 *Energy head*

The energy head was computed from equation (1):

$$h_0 = h + \frac{\alpha}{2g}\left(\frac{Q}{B\,(h+s)}\right)^2 \text{ [m]} \tag{1}$$

where $Q$ is discharge $Q = 0.029\ m^3.s^{-1}$, $g$ – gravity acceleration $g = 9.81\ m.s^{-2}$, $h$ and $h_0$ – energy and water head respectively above the weir crest [m], $\alpha$ – energy coefficient [-], $B$ – channel width upstream of the weir $B = 0.40$ m, $s$ – height of the weir $s = 0.40$ m.

The energy coefficient depends on the velocity profile and therefore slightly differs for each model. An analysis has shown that the value of energy coefficient is up to $\alpha = 1.08$ (1.05 for most models). A comparison of measured and computed energy heads is summarized in Table 2.

The results have shown a quite good agreement between the measurements and simulations. Most of viscous models compute lower energy head in order of millimetres in comparison with measurements. This is probably due to the assumption of a perfectly smooth wall (see [5]). In reality (on a physical model), some additional energy losses can occur. Also, the effect of the turbulent boundary layer and the wall function should be further investigated.

### 4.2 *Pressure along weir surface*

A comparison of pressures along the spillway surface is shown in Figure 2. The pressures computed fit well with the data measured. However, some models (skw, ske, quadrsm) tend to underestimate the peak value of negative gauge pressure. Also, some deviation can be seen in the pressure values on the downstream face of the weir regardless the model used.

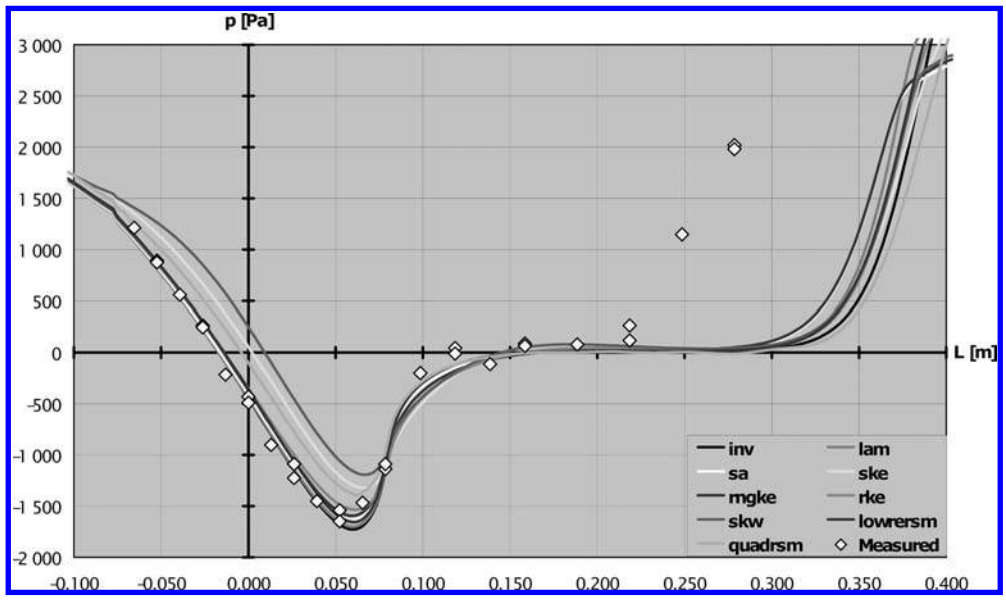


Figure 2. A comparison of pressure distribution along the spillway surface; $L$ – distance along weir surface [m], $p$ – pressure (relative to atmospheric pressure) [Pa]; $L = 0$ at the weir crest.

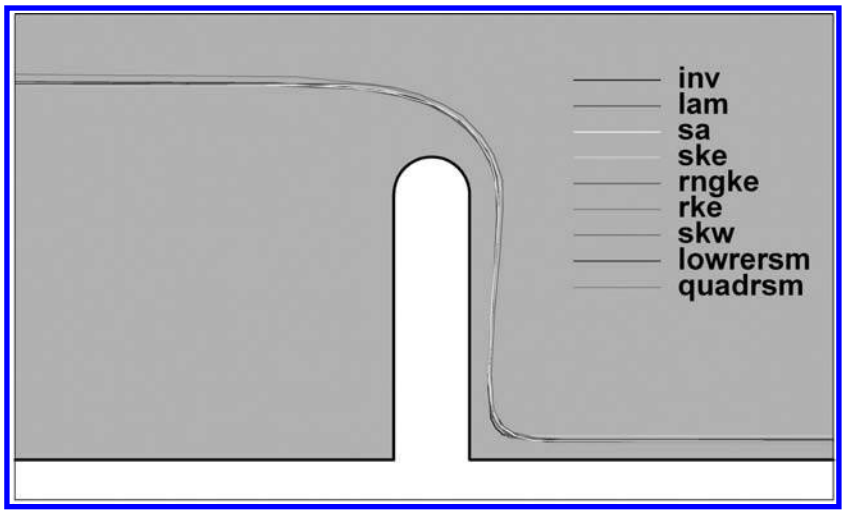


Figure 3. A comparison of the nappe profiles.

### 4.3 *Water levels along the weir crest*

A comparison of the nappe profiles is shown in Figure 3. All models provide very similar nappe profiles.

## 5 CONCLUSION

From the above-mentioned results it can be concluded that most of the viscous models used are suitable for prediction of the spillway capacity (and the discharge coefficient) of round-shaped weirs. However, the simulations tend to compute lower water heads than are those provided by measurements. Further investigation of this effect is needed to find both the reasons and the solution for this problem. The results of simulations are significantly influenced by the proper grid. Improper meshing leads to singularities in results (e.g. improbable steps in pressure or velocity profiles).

The pressure values fit well with the experiment only in the upper section of the weir. The location of a section with negative gauge pressure was always computed very accurately. The absolute values of gauge pressure computed by some models are quite underestimated. Also, some differences were observed between the measured and the computed pressure profiles. The nappe profiles computed are very similar regardless the model used.

Generally, it can be concluded that the most suitable viscous models for this case are Spalart-Allmaras model, Laminar flow, Inviscid flow, RNG k-$\varepsilon$ model, and Realizable k-$\varepsilon$ model.

## ACKNOWLEDGEMENT

This work has been carried out with a financial support of the Ministry of Education, Youth, and Sports of the Czech Republic, Project No. 1M0579, and the Czech Science Foundation, Project No. GA103/08/P538.

REFERENCES


[1] Koutková, H., Stara, V., "Součinitel přepadu přelivu s kruhově zaoblenou korunou z fyzikálních experimentů" [Coefficients of discharge for round-shaped weirs obtained from physical experiments] in *3. Vodohospodářská konference 2003 s mezinárodní účastí 2003*, Conference Proceedings, Brno University of Technology, Brno, 2003, pp. 379–387.

[2] Fluent Inc., *FLUENT 6.3 User guide*, Fluent Inc., Centerra Resource Park, 10 Cavendish Court, Lebanon, NH 03766, 2006.

[3] Abdolmaleki, K., Thiagarajan, K. P., and Morris-Thomas, M. T., "Simulation of the dam break problem and impact flows using a Navier-Stokes solver" in *15th Australian Fluid Mechanics Conference-2004*, Conference Proceedings, The University of Sydney, Sydney, Australia, 2004.

[4] Bhajantri, M. R., Eldho, T. I., and Deolalikar, P. B., "Hydrodynamic modelling of flow over a spillway using a two-dimensional finite volume-based numerical model", *Sadhana-Academy Proceedings in Engineering Sciences,* Vol. 31, Part 6, pp. 743–754, 2006.

[5] Ho, D., Boyes, K., Donohoo, S., and Cooper, B., "Numerical flow analysis for spillways" in *43rd ANCOLD Conference 2003*, Conference Proceedings, ANCOLD, Hobart, Tasmania, 2003.

*Environmental Hydraulics – López-Jiménez et al (eds)*
*© 2010 Taylor & Francis Group, London, ISBN 978-0-415-56697-1*

# Swirl strength analysis of a turbulent round jet

Vesselina Roussinova & Ram Balachandar
*Department of Civil and Environmental Engineering of University of Windsor, Windsor, Canada*

ABSTRACT: Particle image velocimetry (PIV) measurements were conducted in the vertical (x-y) central plane of a round jet. From the instantaneous velocity fields, in-plane two-dimensional swirling strength evaluations are carried out and used to identify turbulent structures. Here, swirling strength is defined as the imaginary portion of the complex eigenvalue of the local velocity gradient tensor and it is unambiguous measure of rotation. From the swirling strength analysis, statistics of the vortex cores and their rotational sense is extracted. A vortex identification algorithm was employed to identify the size and distribution of the vortices.

*Keywords*: Turbulent jet, Particle image velocimetry (PIV), vorticity, swirling strength.

## 1 INTRODUCTION

Mixing and dilution capabilities of a submerged round jet are important in hydraulic engineering applications involving discharge of jet effluent into an ambient fluid. Extensive measurements of mean velocity and statistical turbulence properties have been reported in literature (e.g., Rajaratnam, 1976; Fischer et al., 1979; Wood et al., 1993; for review). The decay rate of mean jet centerline velocity and the growth rate of jet width are usually analyzed to indicate the efficiency of jet spreading and mixing. Inlet jet condition and the jet Reynolds number have been found to influence the jet development zone (Xu and Antonia, 2002). One of the remarkable properties of turbulence is its capacity to mix either a vector or a scalar extremely rapidly. In the near field of the jet, effluent dilution occurs due to the momentum driven turbulent entrainment into the effluent stream, which is proportional to a characteristic velocity of the jet. Whereas in the far field of the jet, dilution occurs due to turbulent diffusion at a rate dependent on the level of turbulence in the receiving fluid. When effluents are released as turbulent flows into a receiving fluid they possess a range of turbulence scales/structures. Common features of the turbulent structures include rotation about their axis, and induction of the velocity in the surrounding fluid. For a turbulent jet, large–scale structures have been found to reside near the boundary of the jet where the flow is intermittently turbulent. Smaller vortical structures exist across the entire body of the jet. Very few studies discussed the effect of the vortical structures present in the jet, and their effect on the jet mixing and spreading. The aim of the present experimental study is to investigate the statistics of the vortices along the vertical plane of the jet by examining the probability density functions (PDF). Results include PDF of vortex populations according to swirling strength, rotational sense and vortex size as a functions of radial position.

## 2 EXPERIMENTS

Experiments were performed in a tank 2 m long, 1 m wide and 0.7 m deep. A turbulent jet was generated by using a nozzle and a flow conditioning system. The flow conditioner consisted of a settling chamber with a straight section 100 mm long and 50 mm in diameter packed with drinking straws (length/diameter = 30) which act as flow straighteners. The nozzle itself was made of two arcs each of radius 10 mm and the nozzle opening was a circular opening of diameter 10 mm. The exit of the nozzle was fixed flush with the inside wall of the tank and the nozzle axis was perpendicular to the wall. The nozzle exit velocities were 1 m/s, 3 m/s, and 5.5 m/s which correspond to Reynolds number of 10,000, 30,000, and 55,000, respectively. The origin of the co-ordinate system is located at the nozzle exit. The flow was pumped to an overhead reservoir which provided a constant supply head of 2 m. The flow from the reservoir was controlled by valves and monitored using a calibrated flowmeter. Water was discharged from the overhead reservoir through the nozzle halfway between the floor of the tank and the free surface, as shown in Figure 1.1. The constant head tank and flow conditioner delivered a steady supply of water to the nozzle. A downstream sharp-crested weir ensured that the depth of water in the tank was maintained at 0.6 m at all times.

Three overlapping fields-of-view (FOV), each measuring a length of approximately 4D, was chosen to obtain the PIV measurements, starting from the nozzle exit and covering a total distance of 12 nozzle diameters. The size of each FOV is 44 mm × 44 mm, yielding a spatial resolution of 0.4 mm. PIV measurements were made along the centerline of the jet in the vertical plane and in the horizontal plane. The PIV system uses a 50 mJ, dual pulse Nd:YAG laser. The laser sheet was oriented through the axis of the jet with the camera perpendicular to it. After filtering the water through a 1$\mu$m filter, it was seeded with 12$\mu$m hollow glass spheres with a specific gravity of 1.13, yielding a Stokes settling velocity of 0.01 mm/s. The ratio of particle response time to the turbulence time scale of a free jet (Longmire and Eaton, 1992) ranges between $3.3 \times 10^{-4}$ for a Reynolds number of 10,000, and $2 \times 10^{-3}$ for a Reynolds number of 55,000, so the particles were expected to follow the flow faithfully.

Images were captured using a TSI Powerview Plus 4MP CCD camera with a resolution of 2048 × 2048 pixels, synchronised with the laser using a TSI laser pulse synchroniser. The camera was fitted with a 70 to 300 mm Nikon lens and adjusted to provide the desired field-of-view. Two thousand images were captured in each field-of-view at a frequency of 1.0 Hz and analysed using Insight 3G developed by TSI. Image analysis was performed in two steps. The images were first analyzed with interrogation areas of 32 × 32 pixels, using the Hart correlator between pairs of images. The displacement information from the first step was used to determine the interrogation area offset, and the image was re-analyzed using smaller interrogation areas of 16 × 16 pixels. The offsetting was performed to improve the signal-to-noise ratio by reducing the number of random pairing of

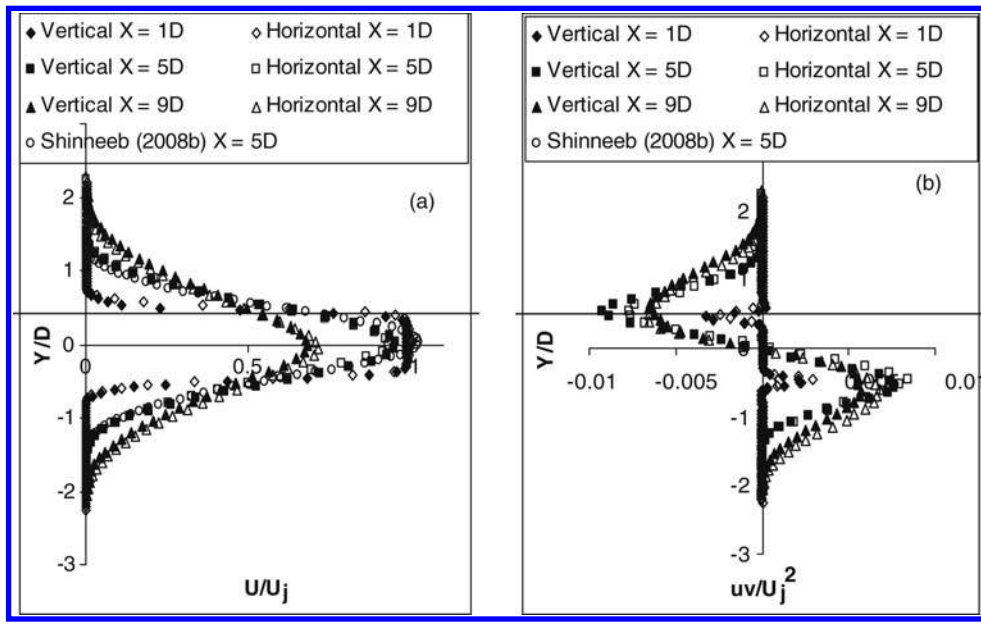


Figure 1. Mean velocity and Reynolds shear stress profiles in the jet vertical and horizontal plane.

images from different particles. The correlation peak was located to sub-pixel accuracy using a Gaussian curve fitting method. No peak locking effects were noticed in the PIV measurements. After the correlation analysis was complete, velocity outliers were rejected using the cellular neural network method with a variable threshold as proposed by Shinneeb et al. (2004). The percentage of rejected vectors was about 3% and they were replaced using a Gaussian-weighted mean interpolation of their neighbours.

Figures 1a and 1b show the mean axial velocity ($U/U_j$) and mean Reynolds shear stress ($-\overline{uv}/U_j^2$) profiles at various distances from the jet exit, respectively. The profiles have been time averaged from each field-of-view at Re = 30,000. Both figures validate the present PIV measurements with the previous data in the literature. The present data compares well with that obtained by Shinneeb (2006) at X = 5D. The mean velocity has a top-hat shape close to the nozzle exit and slowly evolves to a Gaussian type profile. The shear stress profiles show sharp peaks at the edges of the jet and reduce to zero at the jet center line. The profiles in the vertical and horizontal plane are very similar and the jet exhibits an axisymmetric behavior.

## 3 SWIRL STRENGTH

One of the established techniques for vortex detection is based on the calculation of the swirling strength (Christensen and Adrian, 2001). Swirling strength is closely related to vorticity but it can discriminate between vorticity due to shear and vorticity resulting from rotation. The advantage of the swirling strength ($\lambda$) is that it is frame independent since it uses the velocity gradient to identify the local swirling motion. It is defined as the imaginary part of the complex eigenvalue of the local velocity gradient tensor (Zhou et al., 1999). The two-dimensional swirl calculated form the instantaneous in-plane velocity components is defined by

$$\begin{vmatrix} \frac{\partial u'}{\partial x} - \lambda_{ci} & \frac{\partial u'}{\partial y} \\ \frac{\partial v'}{\partial x} & \frac{\partial v'}{\partial y} - \lambda_{ci} \end{vmatrix} = 0 \qquad (1)$$

In Equation (1), the unsigned swirling strength $\lambda_{ci}$ is always $\geq 0$, but a sign can be prescribed based of the value of the local vorticity to show the eddy sense of rotation. Thus, $\lambda = \lambda_{ci}\omega_z/|\omega_z|$ is computed to discriminate counter-clockwise (CCW) rotating vortices ($\lambda > 0$) from the clockwise (CW) ones ($\lambda < 0$). In Figure 2, signed swirling strength (or modified swirling strength) is used in the $(x-y)$ -plane to provide information for the vortices, their location and strength.

## 4 RESULTS

Figure 2 reveals that the jet contains a substantial number of CW or CCW rotating eddies with different swirls. Eddies are concentrated at the plane of the jet and they are equally probable to occur in either side of the jet centerline. Further, we calculate the probability of occurrence of an eddy with a given rotation (CW or CCW) by counting separately the number of CW and CCW eddies, and simultaneously calculating the average swirl from the 2000 PIV images.

In Figure 3, contours of average swirl ($\overline{\lambda}$) are presented at Re = 55,000. Due to the symmetric geometry, average swirling strength distribution is also symmetric. In the upper half-plane of the jet $\lambda > 0$, while $\lambda < 0$ below the jet centerline. The maximum average swirling strength is observed at the locations of the high Reynolds shear stress. As the jet progresses, the average swirling strength is reduced. In the core region of the jet, the average swirling strength is zero. This is not unusual since on average, equal numbers of CCW and CW vortices occur in this region. The strongest average swirl is concentrated at the edges of the jet and decays further at larger $|Y/D| > 0.5$. The probability of occurrence of vortices with $\lambda < 0$ and $\lambda > 0$ is presented in Figure 4, corresponding to Re = 55,000 and X/D = 10.4. The distributions of the CCW and CW rotating vortices is symmetrical with a maximum at locations Y = ±0.6 D. These are the locations where maximum shear stress is observed as shown in Figure 1b. In the jet core region, due to high intermittency, eddies will spend only a fraction of their time, therefore

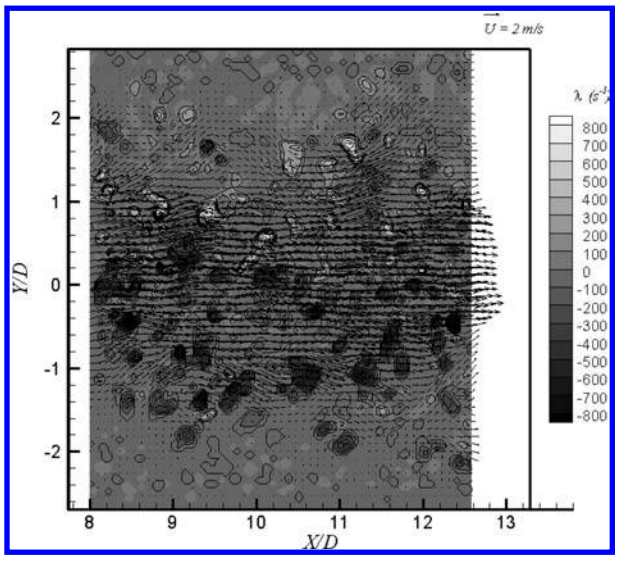


Figure 2. Contours of the instantaneous swirling strength at Re, = 55,000.

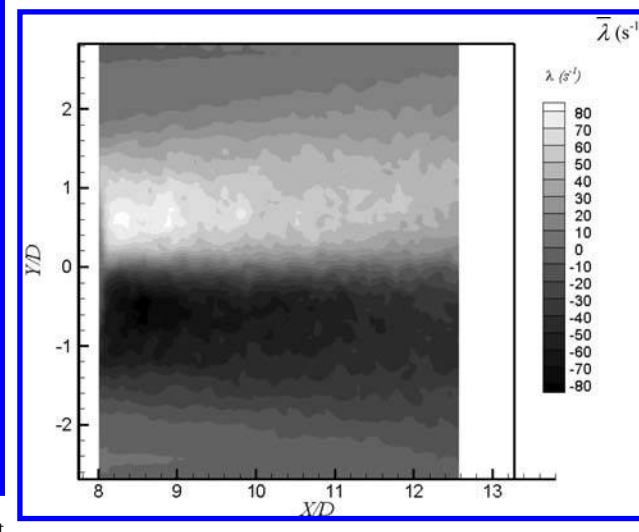


Figure 3. Contours of the average swirling strength at Re = 55,000.

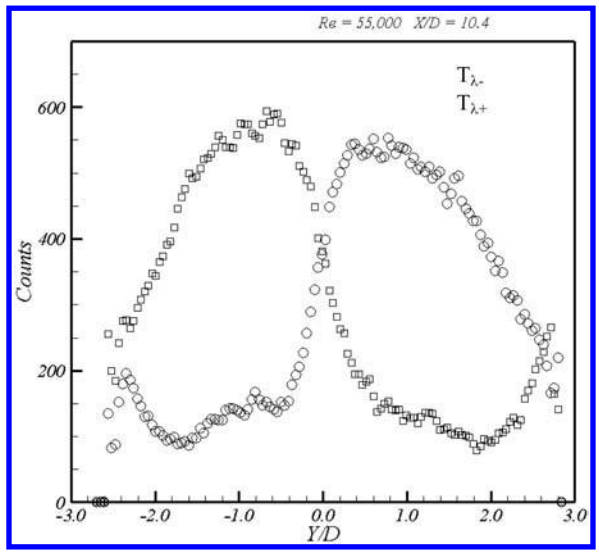


Figure 4. Frequency of occurrence of CCW ($T_\lambda+$) and CW ($T_\lambda-$) eddies in the jet (Re = 55,000, X/D = 10.4).

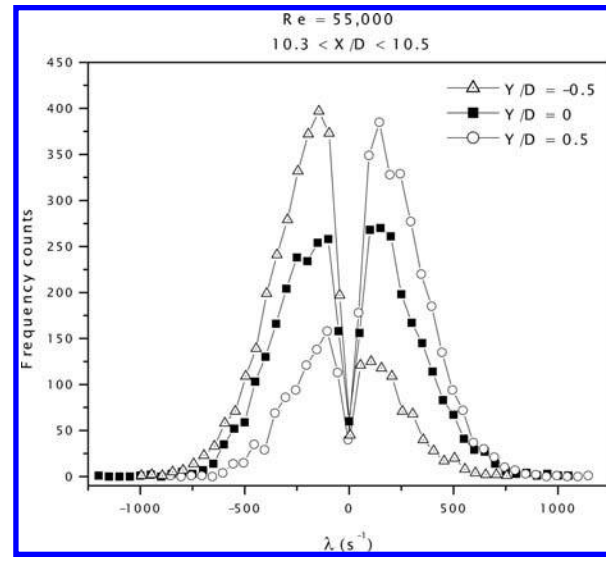


Figure 5. PDF of swirling strength at the center of the jet and at the points of maximum Reynolds shear stress (Re = 55,000).

the number (and probability) of finding eddies becomes low. The number of eddies also reduces in the radial position away from the jet at $|Y/D| > 1$. At $|Y/D| \approx 2.5$ equal probability finding CW and CCW eddies are noted. This corresponds to the border between the turbulent and non-turbulent motions.

The distributions of the swirling strength at three radial locations (Y/D = −0.5, 0 and 0.5) are shown in Figure 5. In order to avoid cluttering, all points with $\lambda = 0$ are excluded from the PDF's. At the jet centerline, the distribution of the swirling strength is symmetrical with two peaks corresponding to CCW and CW rotating eddies. These peaks have equal amplitude and therefore the net average swirling strength will be low as shown from the contours in Figure 3. At X/D = −0.5, the PDF has two peaks with different amplitudes. The highest swirling strength correlates with the relatively larger population of the CW rotating vortices ($\lambda < 0$). Conversely at X/D = 0.5, the highest peak of the swirling strength distribution is noted for the CCW rotating vortices ($\lambda > 0$).

## 5 CONCLUSIONS

In this paper, probability density distributions of number of eddies, rotational sense and swirl, are presented as functions of radial locations for the case of the far-field of the axisymetric turbulent jet. Vortices were identified by calculating the swirling strength for every individual PIV snapshot. A substantial number of positive and negative rotating vortices populate the entire plane of the jet. It was observed that the average swirling strength is zero in the core of the jet and also outward of the jet at $|Y/D| > 1$. The PDF's of the number of CCW and CW rotating vortices reviled that the maximum number of vortices are found at the edges of the jet, where maximum of the shear stress is observed. The distributions of the swirling strength show that vortices with the strongest swirl are located at the edges of the jet.

REFERENCES


[1] Rajaratnam N (1976) *Turbulent Jets*. Elsevier Scientific Publishing Co.
[2] Fischer, H. B., List, E. J., Koh, R. C. Y., Imberger, J., Brooks, N. H. (1979). *Mixing In Inland and Coastal Waters*. New York: Academic.
[3] Wood IR (1993) "Asymptotic Solutions and Behaviour of Outfall Flumes". J Hydr. Eng. Asce, Vol. 119, PP. 555–580.
[4] Xu, G, Antonia, R. A. (2002) "Effect of Different Initial Conditions on a Turbulent Round Free Jet", Exp Fluids Vol 33, PP. 677–683
[5] Longmire, E.K. and Eaton, J.K., (1992), "Structure of a Particle-Laden Round Jet", *J. FLUID MECH.*, VOL. 236, PP. 217–257.
[6] Shinneeb, A. M., Bugg, J.D. and Balachandar, R. (2004), "Variable Threshold Outlier Identification in PIV Data", Meas. Sci Tech., Vol. 15, PP. 1722–1732.
[7] Shinneeb, A.-M., (2006), "Confinement Effects in Shallow Water Jets," Ph.d. Thesis, University of Saskatchewan, Canada.
[8] Christensen, K. T, Adrian, R. J. (2001) "Statistical Evidence of Hairpin Vortex Packets in Wall Turbulence." J. Fluid Mech., Vol. 431, PP. 433–443.
[9] Zhou, J., Adrian, R. J., Balachandar, S. and Kendall, T. M. (1999) "Mechanisms for Generating Coherent Packets of Hairpin Vortices in Channel Flow." J. Fluid Mech., Vol. 387, PP. 353–396.

*Environmental Hydraulics – López-Jiménez et al (eds)*
*© 2010 Taylor & Francis Group, London, ISBN 978-0-415-56697-1*

# A numerical study of flow in emerged and submerged groyne fields

Manuel García-Villalba & Wernher Brevis
*Institute for Hydromechanics, University of Karlsruhe, Karlsruhe, Germany*

ABSTRACT: Large eddy simulations of flow in emerged and submerged groyne fields are presented. It is shown that the submergence of the groynes change significantly the flow structure leading to completely different mass-exchange processes with the main stream. The shear-stress at the bottom wall is also observed to increase in the submerged case.

*Keywords*: groyne field, dead zone, mass exchange, wall-shear stress, large eddy simulation

## 1 INTRODUCTION

Groyne fields constitute an application area of considerable importance in river engineering practice. From a hydrodynamic point of view, the main effect of the groynes is to generate large-scale recirculating volumes of water that are stagnant compared with the faster flow occurring in the main stream, so called dead zones. There are many processes affected by the presence of dead zones. They are mainly associated to the sediment and dissolved mass transport, and with the improvement of the aquatic environment. It has been shown that they create favorable flow conditions for the fluvial flora and fauna, and as a consequence are currently being created for environmental applications as, for example, river restoration[1,2]. These improvements of the environmental conditions are associated to the existence of low velocity zones, which increase the retention time of substances, an important factor, for example, to increase the production of riverine phytoplankton and to create nursery zones for young fishes [3]. The flow structure (see Fig. 1) is typically composed by one or more gyre structures [4,5]. These structures are driven by shear instabilities generated at the interface between the dead zone and the main stream. Important differences in the flow structure have been observed for the submerged case, which occurs when the water surface is located above the maximum height of the groynes (see Figure 1-right), as compared to the more quiet emerged case (see Figure 1-left). The submerged case occurs, for example, in a flood event or can be the design condition in many cases. In this study, we complement the experiments of Brevis[6], by performing large eddy simulations of flow in a groyne field under both emerged and submerged conditions.

## 2 COMPUTATIONAL DETAILS

The calculations were performed with the in-house code LESOCC2 (Large Eddy Simulation On Curvilinear Coordinates), which is a successor of the code LESOCC developed by Breuer and Rodi [7]. The code solves the Navier-Stokes equations on body-fitted, curvilinear grids using a cell-centered finite volume method with collocated storage arrangement. Second order central differences are employed for the convection as well as for the diffusive terms. The time integration is performed with a predictor-corrector scheme, where the explicit predictor step for the momentum equations is a low-storage three-step Runge-Kutta method. The corrector step covers the implicit solution of the Poisson equation for the pressure correction. The subgrid-scale (SGS) stresses, resulting from the unresolved motions, are modeled using the approach of Smagorinsky[8] with a model parameter $Cs = 0.1$.

The simulations were designed so as to retain the most important features of the experiments of Brevis[6]. For example, the geometric relations were the same as in the experiments, $L/W = 2$ or $d/W = 0.2$ (see Fig. 2), where L is the distance between two groynes, W is the groyne length and d the groyne thickness. However, for simplicity, the shape of the groynes was selected to be rectangular in the simulations. In the emerged case, the groynes are as high as the water depth $H/W = 0.28$, where H is the water depth, while in the submerged case the height of the groynes is $h/W = 0.2$, i.e. $h/H = 0.71$. The Reynolds number based on W and the velocity in the main stream is $Re = 15000$, somewhat higher than in the experiments. Another difference concerns the number of groynes. In the experiments, a series of about 20 groynes was placed in a flume and the surface flow was investigated using Particle Tracking Velocimetry. In the simulations, two groyne fields were computed with the corresponding calculation domain shown in Fig. 2. In previous investigations[9] only one groyne field was computed for the emerged case and good agreement with corresponding experiments was obtained. For the present case, preliminary calculations of the submerged case with only one groyne field were unsatisfactory, indicating that some physical processes involve the interaction between two or more groyne fields. The numerical mesh contains $400 \times 250 \times 70$ cells in streamwise, spanwise and wall-normal directions, respectively. The boundary conditions in the horizontal plane are shown in Fig. 2. At the bottom wall a no-slip condition is used while the free-surface is modeled using a rigid-lid assumption, i.e. a free-slip condition is used at the top boundary. The Froude number during the experiments was $Fr = U/\sqrt{gH} = 0.13$, for this flow condition the water surface fluctuations were measured, and the rigid lid assumption validated after no detection of important fluctuations. In order to visualize the mass-exchange processes in the groyne fields, an additional passive scalar equation has been computed. The tracer has been continuously released at the edge of the first groyne.

## 3 RESULTS

A fairly good agreement has been observed between the results of the simulations and the experimental data (not shown here due to lack of space). We concentrate here on the main differences between the emerged and submerged cases. For the submerged

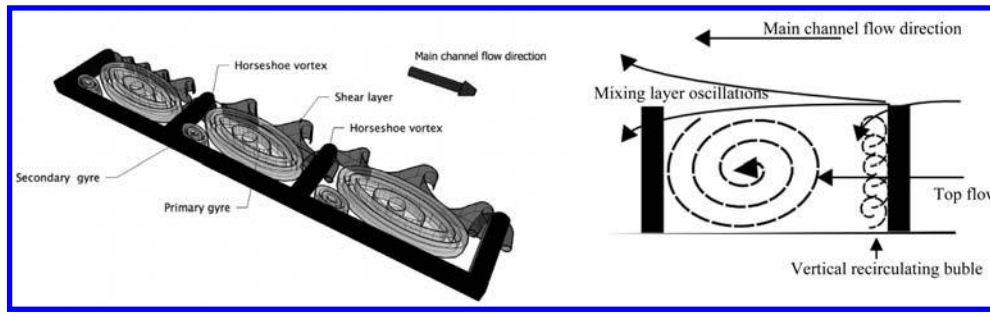


Figure 1. *Left* : Sketch of the flow structure in a emerged shallow dead-zone sequence. *Right*: Schematic flow patterns observed during experiments for submerged condition (submerged flow structures are shown in dashed lines).

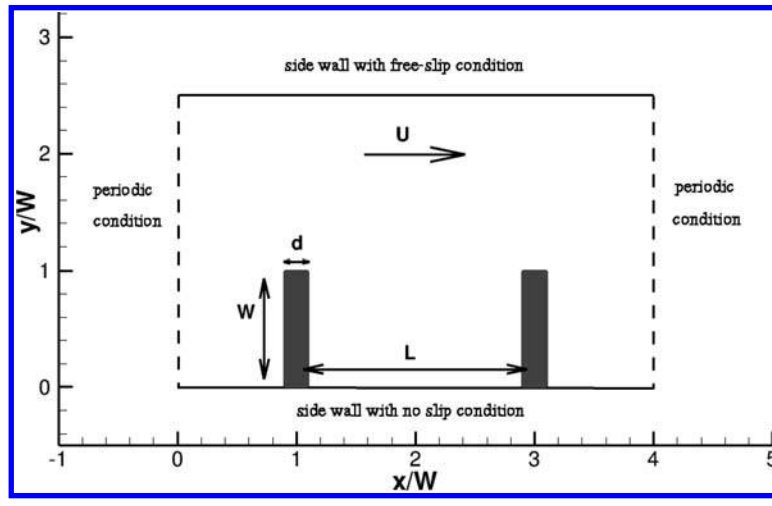


Figure 2. Top view of the computational domain and boundary conditions.

case, two main regions have been observed, an upstream one governed by the top mixing layer developed by the flow passing over the groynes, and a downstream region dominated by the dynamic of the lateral mixing layer. Moreover, it was observed that the flow patterns are modified periodically, due to an oscillation of the lateral mixing layer. This oscillation mechanism generates ejection-like events that seem to enhance the mass exchange between dead zone and main channel. This can be clearly observed in Fig. 3 that shows two snapshots of the scalar concentration on a horizontal plane located roughly in the middle of the computational domain, for both cases. In the submerged case, the snapshots displayed present the two extreme positions of the lateral shear layer, outwards (top) and inwards (bottom). In the emerged case, on the other hand, the motion of the lateral mixing layer was not present, and the tracer does accumulate in the dead zone due to the continuous impingement of the interfacial coherent structures against the downstream groyne, a situation that, as mentioned before, is favorable to reduce the flow velocities, dealing with the improvement of the aquatic environmental conditions.

There are some important quantities that could not be measured in the experiments and are available in the simulations. One of them is the bottom shear-stress. This quantity is also relevant for environmental conditions, e.g. high stresses could lead to the wash-out of fish eggs deposited at the bottom of the dead zone or to remobilize sedimented material such as nutrients. Fig. 4 displays the probability density function (p.d.f.) of the bottom shear-stress for both cases. The p.d.f. has a similar distribution with a peak at low values. It is clear, however, that higher stresses are more common in the submerged case. This could be due to the oscillation of the shear layer that generates higher outwards velocities, but also to the impingement at the bottom of the flow that goes over the groyne.

## 4 CONCLUSIONS

In this extended abstract, the results of large eddy simulations of the flow in submerged and emerged groyne fields have been briefly discussed. The results of the simulations complement the experimental data measured by Brevis[6], allowing more accurate observations of the flow dynamics due to the better spatial resolution of the simulated flow field compared with the measured one. Moreover, the simulations provide additional information of flow quantities that were not measured during the experiments.

An important change of the flow patterns in most of the groyne region was observed for the submerged case respect to the emerged one. In addition, the numerical approach used here, was able to capture a strong oscillation of the lateral mixing layer induced by the submergence, and also observed during the experiments. The visualization of the passive scalar concentration has shown that the mixing-layer lateral oscillation plays an important role on the mass-exchange dynamics for that condition. In addition, the probability density function of the bottom-shear stresses was calculated, showing the higher levels induced by the submerged condition over the channel when compared with the emerged one.

The authors believe that the present results provide a direct quantification of the flow changes induced by the submergence in a groyne field, for similar flow and geometrical conditions, and especially of the changes induced by the flow over the

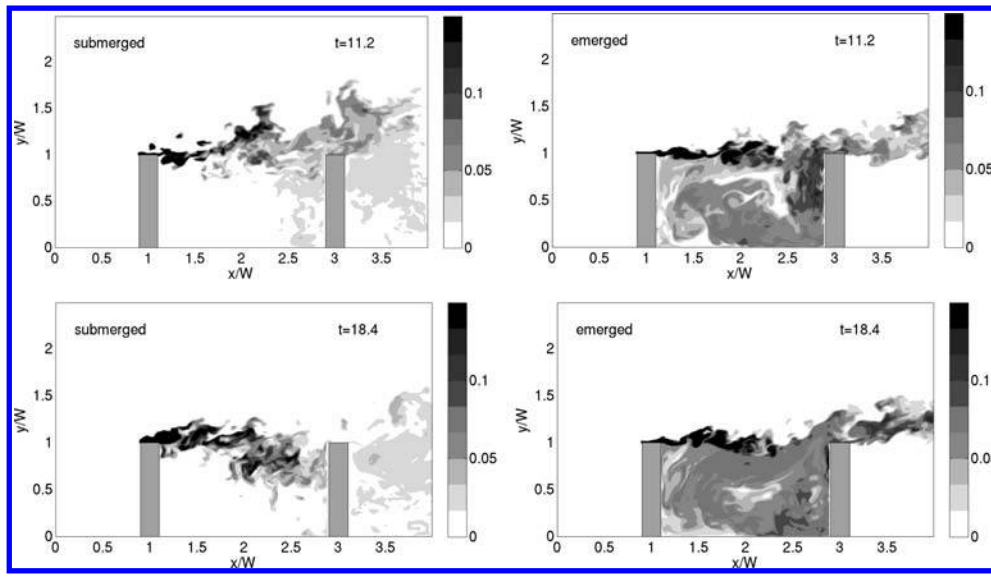


Figure 3. Instantaneous snapshots of scalar concentration in a horizontal plane at middle height. Left, submerged case. Right, emerged case.

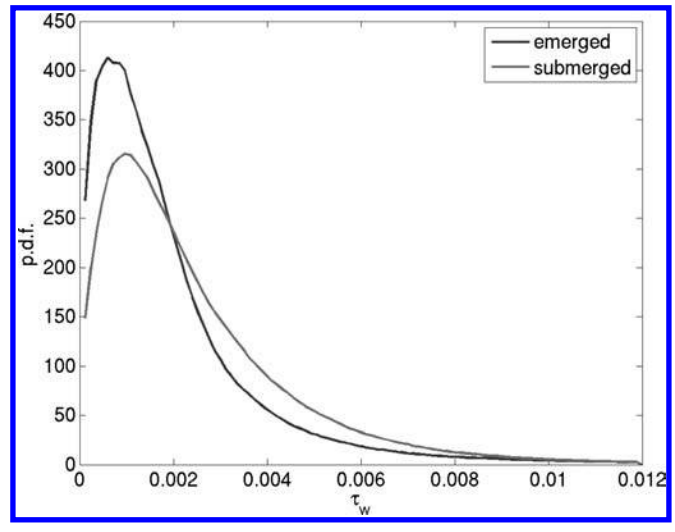


Figure 4. Probability density function of the bottom-shear stress in the dead zone region.

bottom shear-stresses, a key parameter for the understanding of several ecological process ranging from sediment transport until habitat restoration.

## REFERENCES


[1] Reynolds, C. & Carling, P. (1991). “Flow in river channels: new insights into hydraulic retention." Archiv für Hydrobiologie. Vol 121(2), pp 171–179.

[2] Shields Jr, F., Cooper, C. & Knight, S. (1995). “Experiment in stream restoration.” J. Hydr. Eng. . Vol. 121(6), 494–502.

[3] Schiemer, F., Keckeis, H., Reckendorfer, W. & Winkler, G. (2001). “The ’inshore retention concept’ and its significance for large rivers.” Arch. Hydrobiol.(Suppl.)(Large Rivers) , 135 (2), pp 509–516.

[4] Uijttewaal, W., Lehmann, D. & Mazijk, A. (2001). “Exchange processes between a river and its groyne fields: model experiments”. J. of Hydr. Eng. Vol. 127(11), pp 928–936.

[5] Weitbrecht, V., Socolofsky, S. & Jirka, G. H. (2008). “Experiments on Mass Exchange between Groin Fields and Main Stream in Rivers.” J. Hydr. Eng. , Vol. 134, pp 173.

[6] Brevis, W. (2009). “Experimental investigation of the flow hydrodynamics in open-channel dead zones” Ph.D. thesis. Universidad de Chile. Santiago de Chile, Chile.

[7] Breuer, M. and Rodi, W. (1996). “Large eddy simulation of turbulent flow through a straight square duct and a 180° bed.” *Fluid Mechanics and its Applications*, Kluver Academic, 273–285.

[8] Smagorinsky J. S (1963). “General circulation experiments with the primitive equations. Part I: The basic experiment.” Monthly Weather Review, Vol. 91, 99–152.

[9] Hinterberger, C., Fröhlich, J. & Rodi, W. (2007). “Three-Dimensional and Depth-Averaged Large-Eddy Simulations of Some Shallow Water Flows.” J. Hydr. Eng. Vol. 133(8), pp 857–872.

*Environmental Hydraulics – López-Jiménez et al (eds)*
*© 2010 Taylor & Francis Group, London, ISBN 978-0-415-56697-1*

# An efficient and conservative model for solute transport in unsteady shallow water flow

B. Latorre, P. García-Navarro, J. Murillo & J. Burguete
*Fluid Mechanics, CPS, University of Zaragoza, Zaragoza, Spain*

ABSTRACT: A new numerical method to model the transport of a solute in shallow water flow is presented. The method solves the solute transport in a coupled form and can be applied to any numerical scheme that is suitable for the shallow water system. The proposed conservative formulation is based on a numerical model of mass mixing ensuring a monotone behaviour in the numerical solution of the solute concentration. Examples of one-dimensional flow including bed slope source terms and flow discontinuities are presented in order to focus on the main properties of the technique: preservation of a constant concentration value and monotone time evolution of concentration values.

*Keywords*: solute transport, shallow water flow, mass mixing model, conservative solution.

## 1 MOTIVATION

The development of numerical models to predict the time evolution of concentration of solutes in surface water is required by the interest of water resources scientists[1]. As a simplification, the mixing problem can be modelled in some circumstances by means of a depth averaged solute mass conservation law in the form of a convection-dispersion or transport equation. The resulting equations must be solved making use of suitable numerical techniques seeking the best compromise between accuracy and efficiency. In this work, a new numerical method to model the transport of a solute in shallow water flow is reported. The formulation is based on a numerical model of mass mixing; this technique ensures a physical behaviour in the numerical solution of the solute concentration. Test cases have been oriented to study the main properties of the method: preservation of a constant concentration value and monotone time evolution of concentration distribution.

## 2 DESCRIPTION OF THE METHOD

The 1D shallow water model can be formulated as:

$$\partial_t \vec{u}(x,t) + \partial_x \vec{f}(x,t) = \vec{s}(x) \tag{1}$$

where $\vec{u}$ is the vector of conserved variables, $\vec{f}$ is the vector of physical fluxes and $\vec{s}$ is the vector of source terms. They are written in terms of the water depth $h$, the unit discharge $q = vh$, with $v$ the depth averaged velocity and the bed elevation $z$ as follows:

$$\vec{u} = \begin{pmatrix} h \\ q \end{pmatrix}, \qquad \vec{f} = \begin{pmatrix} q \\ \dfrac{q^2}{h} + \dfrac{gh^2}{2} \end{pmatrix}, \qquad \vec{s} = \begin{pmatrix} 0 \\ -gh\partial_x z \end{pmatrix} \tag{2}$$

We are interested in solving system (1) in a one-dimensional domain using a uniform grid spacing $\Delta x$. In our notation $\vec{u}_i^t$ is the value of the conserved variables in cell $i$ at time $t$. From a given state of the system at time $t$, the solution provides the evolution to time $t + \Delta t$ by means of a conservative numerical scheme that follows:

$$\vec{u}_i^{t+\Delta t} = \vec{u}_i^t - \frac{\Delta t}{\Delta x}\left(\vec{f}_{i+\frac{1}{2}} - \vec{f}_{i-\frac{1}{2}} + \vec{s}_i\right) \tag{3}$$

where $\vec{f}_{i+1/2}$ denotes the numerical flux at the interface between cells $i$ and $i+1$ and is a numerical approximation of the mass and momentum exchanges through that edge. The discrete representation of the source term introduces a non-conservative contribution to the momentum equation, which will be called numerical source term $\vec{s}_i$ and associated to the cell. It also introduces a conservative contribution to the mass equation that will be associated to the interface and is assumed included in the vector $\vec{f}_{i+1/2}$. The components of these vectors are:

$$\vec{f}_{i+\frac{1}{2}} = \begin{pmatrix} f^h \\ f^q \end{pmatrix}_{i+\frac{1}{2}}, \qquad \vec{s}_i = \begin{pmatrix} 0 \\ s^q \end{pmatrix}_i \tag{4}$$

Many numerical schemes can be used for the numerical solution of system (1), provided that the vectors in (4) are defined. The next goal is the numerical solution of a passive solute transport in that flow. The process can be formulated with the

following additional conservation law:

$$\partial_t m + \partial_x\left(\frac{qm}{h}\right) = 0 \tag{5}$$

being m = m(x, t) the solute mass.

This work is concerned with the formulation of an algorithm that preserves the original form of the numerical scheme used for the shallow water equations (3), but enlarges the vectors of conserved variables $\vec{u}_i^t$, numerical flux $\vec{f}_{i+1/2}$ and numerical source term $\vec{s}_i$ as follows:

$$\vec{u}_i = \begin{pmatrix} h \\ q \\ m \end{pmatrix}_i, \quad \vec{f}_{i+\frac{1}{2}} = \begin{pmatrix} f^h \\ f^q \\ f^m \end{pmatrix}_{i+\frac{1}{2}}, \quad \vec{s}_i = \begin{pmatrix} 0 \\ s^q \\ 0 \end{pmatrix}_i \tag{6}$$

All the discrete approximations in (6) are already defined except the solute mass numerical flux $f^m_{i+1/2}$. To define it, a numerical model of mass mixing will be developed. The numerical flux $f^h_{i+1/2}$ produces water mass variations in cells *i* and i + 1 that are interpreted as a water mass exchange through the interface. Assuming that the exchanged water retains the solute concentration of the original cell, the following can be written:

$$f^m_{i+\frac{1}{2}} = \begin{cases} f^h_{i+\frac{1}{2}}\left(\frac{m}{h}\right)_i & \text{if} \quad f^h_{i+\frac{1}{2}} > 0 \\ f^h_{i+\frac{1}{2}}\left(\frac{m}{h}\right)_{i+1} & \text{if} \quad f^h_{i+\frac{1}{2}} < 0 \end{cases} \tag{7}$$

This method is a simple way to solve the solute transport in a coupled form to any numerical scheme that is suitable for the shallow water system. It guarantees a conservative and monotone behavior in the numerical solution of the solute concentration.

In the present work, the proposed technique will be compared with an uncoupled formulation of the shallow water and solute transport processes. The uncoupled formulation is based on the solute transport considering only the advection provided by the velocity field. The numerical flux is expressed as:

$$f^m_{i+\frac{1}{2}} = \begin{cases} \left(\frac{qm}{h}\right)_i & \text{if} \quad v_{i+\frac{1}{2}} > 0 \\ \left(\frac{qm}{h}\right)_{i+1} & \text{if} \quad v_{i+\frac{1}{2}} < 0 \end{cases} \tag{8}$$

where $v_{i+1/2}$ represents the average value at the interface. This scheme is not able to capture the water and solute transfers due to water depth differences between cells so that, in presence of source terms, can lead to unphysical numerical results.

## 3 NUMERICAL RESULTS

### 3.1 *Test 1*

As a first test case, a dam-break problem defined by an initial discontinuity in the water depth, a frictionless flat bed with a step in the bottom and a uniform solute concentration is considered. The initial values are:

$$\vec{u}(x, 0) = \begin{cases} h = 1.0,\ q = 0.0,\ m = 1.0,\ z = 0.0 & \text{if} \quad 0 < x < 2.5 \\ h = 0.25,\ q = 0.0,\ m = 0.25,\ z = 0.1 & \text{if} \quad 2.5 < x < 5.0 \end{cases} \tag{9}$$

The flow evolution is solved using the numerical scheme described in [2]. For the solute transport, the numerical results from the coupled scheme defined by (7) and the uncoupled scheme defined by (8) are compared. The spatial domain $x \in [0, 5]$ is discretized using $\Delta x = 0.1$ and the time step $\Delta t$ corresponding to CFL = 0.9.

Figure 1 represents the profile of concentration as computed with (7) and (8) at t = 0.25 s and t = 0.50 s. The former is able to preserve exactly the uniform distribution of concentration in presence of discontinuities and source terms. The second displays oscillatory behaviour and non-physical concentration values.

### 3.2 *Test 2*

As a second test case, the initial conditions of water depth and bed level of the previous test case are used again together with an initial discontinuity in the solute concentration. The values used are:

$$\vec{u}(x, 0) = \begin{cases} h = 1.0,\ q = 0.0,\ m = 1.0,\ z = 0.0 & \text{if} \quad 0 < x < 2.5 \\ h = 0.25,\ q = 0.0,\ m = 0.0,\ z = 0.1 & \text{if} \quad 2.5 < x < 5.0 \end{cases} \tag{10}$$

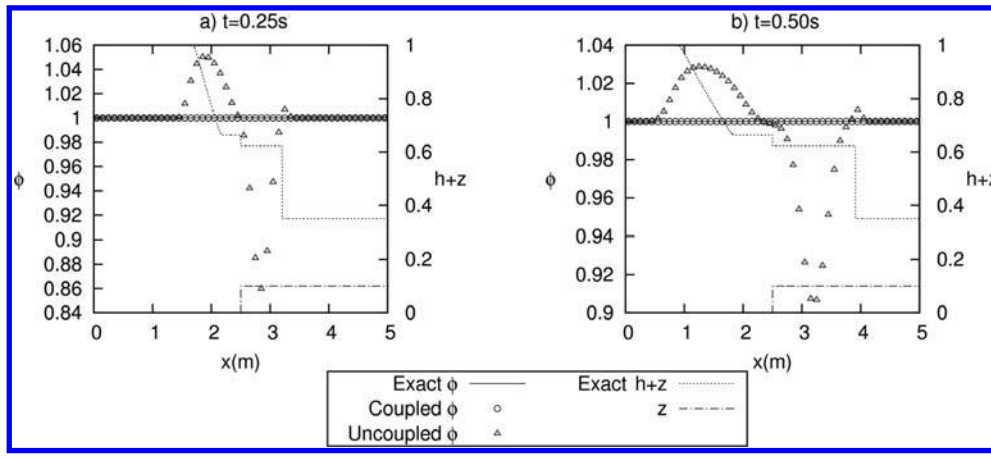


Figure 1. Concentration profiles at t = 0.25 s and t = 0.5 s in test 1.

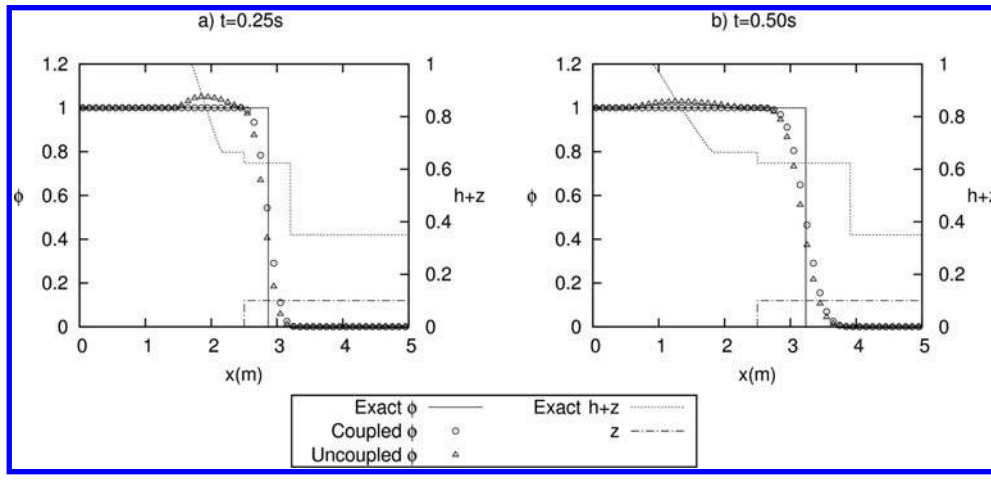


Figure 2. Concentration profiles at t = 0.25 s and t = 0.5 s in test 2.

The domain has been discretized using $\Delta x = 0.1$ and the time step according to the condition given by CFL = 0.9. Again, the shallow water flow is solved using the finite volume scheme described in[2] and the schemes (7) and (8) are applied to the solute transport.

Figure 2 shows the longitudinal profiles of solute concentration at times t = 0.25 s and t = 0.50 s. It can be observed that the coupled scheme is able to transport the discontinuity with a monotone behaviour in the numerical solution of the solute concentration contrary to the uncoupled scheme.

## 4 CONCLUSIONS

A new numerical method to model the transport of a solute in shallow water flow has been presented. The proposed conservative formulation can be applied to any numerical scheme suitable for the shallow water system. The method is based on a numerical model of mass mixing. This technique ensures a physical behaviour in the numerical solution of the solute concentration. Examples of solute transport in one-dimensional flow including bed slope source terms and flow discontinuities have been presented. Test cases have been oriented to study the main properties of the technique: preservation of a constant concentration value and monotone time evolution of concentration distribution.

## ACKNOWLEDGEMENTS

This research work has been partially funded by the Spanish Ministry of Science and Education under research project CGL2005-07059-C02-02.

## REFERENCES

[1] J.C. Rutherford. (1994), River Mixing, Wiley, New York.
[2] M.E. Vázquez-Cendón, PhD thesis, Universidad de Santiago de Compostela (1994), “Estudio de Esquemas Descentrados para su Aplicación alas leyes de Conservación Hiperbólicas con Términos Fuente”.

*Environmental Hydraulics – López-Jiménez et al (eds)*
*© 2010 Taylor & Francis Group, London, ISBN 978-0-415-56697-1*

# Dispersion measurement in transient open channel flows by PLIF

J.A. García
*Fluid Mechanics Department, LITEC(CSIC)-University of Zaragoza, C.P.S., Zaragoza, Spain*

B. Latorre
*Fluid Mechanics Department, University of Zaragoza, Spain*

S. Ambroj
*Suelo y Agua., Estación Experimental de Aula Dei., CSIC., Zaragoza, Spain*

López-Barrera D.
*Fluid Mechanics Department, University of Zaragoza, Spain*

ABSTRACT: The Planar Laser Induced Fluorescence (PLIF) technique is used in this work for the characterization of the mixing process of a passive solute in some transient open channel flows. Following an eulerian approximation, the time evolution of the concentration distribution at a complete transversal section in a rectangular channel is obtained. The studied cases correspond to mixing in transient flow. The laboratory setup, the measurement procedure, the image data post-processing and the results are described in detail.

*Keywords*: concentration measurements, PLIF, open channel flow, transient flow, scalar mixing, image processing.

## 1 INTRODUCTION

The knowledge of the mixing process in free surface water flows is important mainly in the environmental field. In water quality modelling, the understanding of the effects of water movement in mixing and transport is needed.

In the search for a complete experimental characterization of the mixing process, it is interesting to get flow data as well as concentration data. Among the various techniques available, for transient phenomena whole field laboratory techniques are advantageous in comparison with local techniques, mainly because the use of local techniques requires multiple repetitions of the experiment for a complete characterization. Most of the experimental works in open channel flow are made using local techniques.

The aim of this work is to essay and analyse the suitability of Planar Laser Induced Fluorescence (PLIF) technique for concentration measurements in transient flows. Nichols 1972[7], Dewey 1976[4], Liu 1977[6] and Dimotakis 1983[5] can be cited as pioneers in the use of PLIF technique. Intense fluorescence is the principal property that makes some dyes suitable for use in water tracer studies. As a recent work we can cite, over an open channel flow, Agelinchaab 2006[1].

The analysis of the time evolution of concentration data distributed over a well controlled region can improve the understanding of the involved mechanics. On the other hand, these data can be used to calibrate predictive numerical simulation models. In this work, concentration evolution measurements in transient open channel flow using PLIF are reported. This non intrusive technique has been selected since it offers some advantages, mainly high spatial and temporal resolutions.

## 2 EXPERIMENTAL SETUP

Figure 1 shows a sketch of the laboratory facility. The channel used in this study, made in methacrylate, has a constant rectangular cross section, is 6 m long, 0.24 m wide and 0.16 m deep. The water is supplied by a centrifugal pump to an upstream reservoir. An electromagnetic flow meter was installed in the water supply pipe to continuously measure the flow discharge to the channel. The flow rate is adjusted by a regulation valve.

A small lateral reservoir was built. Initially, it is separated from the channel by a gate and containing the dye solution, (see Fig. 1). The gate was provided with a pneumatic cylinder that enabled the instantaneous opening and dye release. The activation of the pneumatic cylinder was electronically controlled, allowing the simultaneous start of the image capturing process.

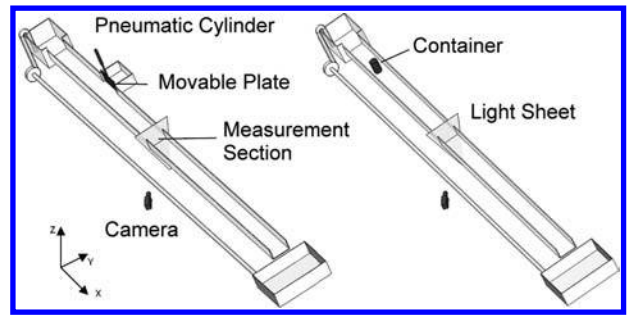


Figure 1. Schema of the experimental setup.

The time evolution of the solute concentration was measured at a complete channel cross section located at 1275 mm from the end of the lateral reservoir. The measurement section was illuminated using a continuous Ar+ laser (Innova 70C-5), with two main emission lines: 488 nm and 514.5 nm. The laser beam is expanded in order to generate a light sheet using an optical system that includes a spherical lens and a cylindrical divergent lens of 20 mm focal distance. A PIV CAM 10/30 is used to acquire the images (1000 × 1016 pixels, 256 levels) and, as sketched in Figure 1, is positioned forming an angle with the normal direction to the illuminated plane. A Nikon 50/2.8 objective was mounted, with a low pass coloured filter. In all cases, the laser was operated to 3 W, and the numerical aperture of 2.8 was used for the objective. For most of the cases the image acquisition rate was 15 images/s with an aperture time for each image of 33 ms.

### 2.1 *Experimental conditions*

The first set of experiments (Experiment 1) was oriented to the study of the solute mixing due to a lateral spill into the main channel flow. The main channel is prismatic of rectangular cross section and is based on the basic channel configuration as displayed in Figure 1. Different initial water levels in the reservoir, with reference to the channel water level near the gate, were tested.

The second experiment was designed to measure the mixing from a solute source located in the center of the channel cross section. The solute is contained in a cylindrical reservoir that is manually open by two lateral apertures. The initial condition, before the solution spill, corresponding again to a constant discharge, was not steady in the channel. Instead, the flow pattern was oscillatory following a Von Karman vortex street pattern, which governs the mixing process in this case (Experiment 2).

## 3 MEASUREMENT PROCEDURE

PLIF technical details can be found in Van Cruyningen 1990[8] and Crimaldi 2008[3] and will not be given here.

Disodic fluorescein was chosen for the location of its absorption and emission peaks, at 490 nm and 515 nm respectively (Coppeta 1998[2]). It is also interesting that this dye has relatively low sensitivity to temperature changes and shows no effects upon either the genotoxicity or the ecotoxicity.

It must be emphasized that the illumination at the measurement section is inhomogeneous. This is due mainly to the gaussian profile of the laser beam, the lack of collimation and reflections on the internal surfaces of the channel. Therefore, it is necessary to find a relation, preferably linear, between intensity and concentration for each pixel of the CCD (Charge Coupled Device).

On the other hand, the local intensity is typically unknown, is not independently measured and varies spatially according to the Beer-Lambert law. Following Crimaldi 2008[3] if the next expression is verified the attenuation effect is negligible and the system can be called 'optically thin'

$$\varepsilon \int_{l_0}^{l_1} C\,(l)\,dl << 1 \qquad (1)$$

The absorption coefficient, $\varepsilon$, depends on the water temperature and pH, so instead of using documented values of this coefficient a test was made to ensure a linear relation between intensity and concentration, as test result we found that concentration in the range 0.01–0.14 mg/l were suitable for a laser power of 3 W. Thus, the concentration at the section is adjusted in order to avoid errors due to the light attenuation and, at the same time, to ensure a linear relation between intensity and concentration.

The electronic noise and the shot noise are another source of error. These errors were noise was quantified by means of the analysis of images of clean water, leading to an error of about 1% (approximately 2 pixel levels) of the maximum concentration.

A calibration pre-process, with two solutions of known concentration, was performed, previous to each measurement, in order to determine a linear relation for each pixel. The calibration for each pixel is necessary due to the inhomogeneous illumination.

As stated before, the concentration measurements were performed over a complete channel cross section lightened with the help of a laser beam and whose images were captured with a camera located next to the channel. The images obtained with this configuration contain a perspective aberration as objects become more distant they appear smaller, because their visual angle decreases. It is also important to note that, during the measurements in the channel water the light crosses air and water. A method to correct the perspective distortion has been developed. The method requires the taking of an image of a calibration mesh previous the measurement.

## 4 RESULTS

The experimental procedure followed is outlined in what follows. For every experiment, a series of photographs of the measurement section were taken during a time interval. The perspective of these images was corrected and the concentration was calibrated following the methods described in section 3, thus leading to complete measurements of the time evolution of the concentration at the control section for the case considered. The concentrations obtained were divided by the initial value of concentration at the reservoir in order to generate dimensionless quantities. All the measurements were repeated to verify the consistency of the results.

### 4.1 *Experiment 1: Lateral reservoir*

From a common steady flow in the channel (giving a level of 1.75 cm at the reservoir position), three different water levels, summarized in table 1, in the reservoir were used. The tracer concentration in the water reservoir of every case was adjusted in order to ensure optimum concentration values at the measurement section, within the linear range. The experimental conditions are summarized in Table 1, where $H_r$ means the reservoir/container initial level and $C_r$ means the initial fluorescein concentration.

Table 1. Summary of experimental conditions for the experiment 1.

| Experiment | Case | Discharge ($m^3$/h) | Hr (cm) | Cr (mg/l) |
|---|---|---|---|---|
| 1 | A | 2.4 | 0.85 | 0.25 |
| 1 | B | 2.4 | 1.75 | 0.14 |
| 1 | C | 2.4 | 3.50 | 0.14 |

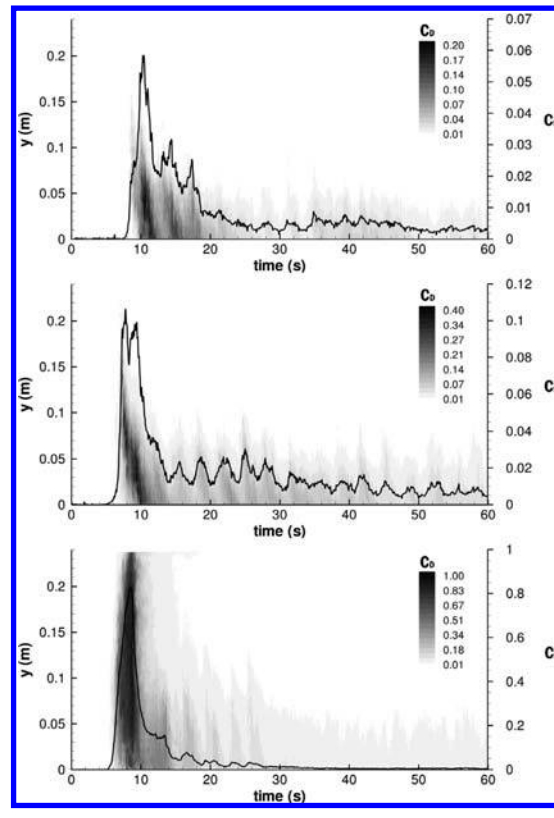


Figure 2. Black line: mean concentration evolution for the case A, B, C; Color: depth concentration average evolution.

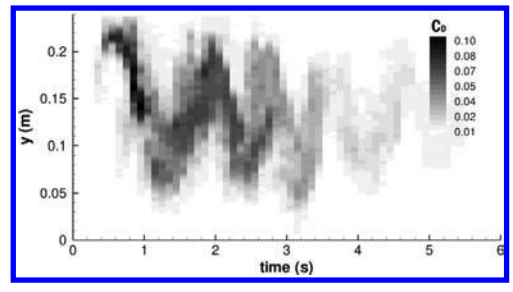


Figure 3. Evolution of the depth concentration average for the Experiment 2.

A first analysis can be made from the time evolution of the cross sectional average of the concentration at the measurement section in this case, as displayed in continuous black line in Figures 2A, 2B, 2C. The arrival time of the tracer to the control section, dominated by the advective effect of the steady channel flow, is similar in the three cases. It can be observed that the most important concentration values appear at the beginning. This is due to the advective flushing of the reservoir, leading to an exponential decay concentration distribution. The second effect is mainly relevant in the third case, where the initial reservoir water level is twice the water level in the channel. Additionally, an oscillatory behavior can be observed in the three cases measured in this experiment due to the recirculating flow pattern generated within the reservoir after the gate opening.

In the three cases considered the maximum values of concentration appear in the region of the cross section closer to the side where the reservoir is located. As the initial water level in the reservoir increases, and thus the amplitude of the surface wave generated by the gate opening, the tracer concentration is displaced towards the opposite direction in the first moments.

### 4.2 *Experiment 2: Flow past a cylinder*

The interest of this experiment is the study of the mixing from a solute source located in the centre of the channel cross section. In this case, the flow before the solution spill corresponded to a constant inlet discharge but was not steady. Instead, the flow pattern was oscillatory following a Von Karman vortex street pattern.

Figure 3 shows the time evolution of the depth averaged concentrations in the control section. It can be observed that the vortex generated behind the cylinder deflect the tracer giving rise to an also oscillatory concentration pattern.

A mass conservation test was performed over the measurements in this case, comparing the detected fluorescein mass with the actual spilled mass. The mass crossing the control section is compared with the initial tracer mass in the cylinder, leading to relative error less than 5%.

## 5 CONCLUSIONS

The PLIF technique has been used to get time series of concentration data at a cross section in an open channel flow during unsteady flow. The main advantages of this technique are high spatial and temporal resolution and lack of flow perturbation. The use of the technique requires being careful with the laser power and the concentration range. A suitable laser power should be selected and a previous test of linearity between CCD levels and concentration should be performed to avoid non linearity problems due to attenuation. The captured images must be postprocessed in order to obtain concentration values. Due to this configuration an additional perspective correction has been required. Computational codes have been developed to correct the perspective effect and to obtain the concentrations and averages from the calibration and measure images.

The first experiment, concerned with the mixing of a tracer from a lateral spill into the channel flow, was useful to study the influence of both the channel characteristics and the ratio of water levels between the channel and reservoir. In all the cases the concentration distribution at the control section shows that the influence of the initial water level ratio is limited to the first moments when the maximum peak appears and is followed by an oscillatory decreasing curve. The oscillations seem to be related to recirculating flow established in the reservoir and the momentum transfer to/from the channel flow.

## ACKNOWLEDGEMENTS

This research work has been partially funded by the Spanish Ministry of Science and Education under research project CGL2005-07059-C02-02. 17030. López-Barrera D. has been supported by the Aragon local government (DGA) G/5423/480072/91001. Ambroj S. has been supported by a Spanish Ministry of Science and Education scholarship, JAEPre053.

## REFERENCES

[1] Agelinchaab M. and Tachie M.F. (2006). “Open channel turbulent flow over hemispheral ribs”. International Journal of Heat and Fluid Flow, 27(6), 1010–1027.

[2] Coppeta J., Rogers C. (1998). “Dual emission laser induced fluorescence for direct planar scalar behaviour measurement”, Experiments in fluids, 25 (1), 1–15.

[3] Crimaldi J.P. (2008). “Planar laser induced fluorescence in aqueous flows”. Experiments in Fluids, 44, 851–863.

[4] Dewey C. (1976). “Qualitative and quantitative flows field visualization utilizing laser-induced fluorescence”. *Proceedings of the AGARD conference of non-intrusive instrumentation in fluid flow research*, 17, 1–7.

[5] Dimotakis P. E., Miake-Lye R. C., Papantoniou D. A. (1983). Structure and dynamics of round turbulent jets. Physics of Fluids, 26(11), 3185–3192.

[6] Liu H.-T., Lin J.-T., Delisi D. P., Robben E A. (1977). Feasibility study of a dye-fluorescence technique for measuring concentrations in fluids. NBS Special Publication no. 484, *Proceedings of the symposium on flow in open channels and closed conduits held at NBS*, Gaithersburg, MD, Feb 23–25.

[7] Nichols D.S., Brown C.H., Dewey C.F. (1972). Laser-induced fluorescence as a method for measuring mass-transfer rates and for flow visualization. Bulletin of the American Physical Society, 17(11), 1091–1091.

[8] Van Cruyningen I., Lozano A. and Hanson R. K. (1990). “Quantitative imaging of concentration by planar laser-induced fluorescence”. Experiments in Fluids, 10, 41–49.

*Environmental Hydraulics – López-Jiménez et al (eds)*
*© 2010 Taylor & Francis Group, London, ISBN 978-0-415-56697-1*

# A 1D approximation to solute transport in shallow water flows over porous media

María Nofuentes & María José Polo
*Grupo de Hidrología e Hidráulica Agrícola, Universidad de Córdoba, Córdoba, España*

ABSTRACT: Solute transport in surface flows over porous media is greatly influenced by the infiltration dynamics which determines not only the partition between surface and subsurface mass balance, but also the transient conditions of surface water flow for a given input. 1D transport modeling in shallow water flows thus requires a proper selection of the infiltration function and the effective value for the longitudinal dispersion coefficient that assumes all those effects. This work presents the combination of both effects on surface transport, infiltration and predominant transient conditions, in a 1D approach which includes a characteristic function for E modeling to provide simulations with an a priori value for operational purposes.

*Keywords*: solute transport, longitudinal dispersion, shallow water.

## 1 INTRODUCTION

Shallow water flow over porous media is greatly influenced by the control that soil characteristics exert, mainly due to its infiltration capacity besides its surface roughness. The infiltration term can be neglected in surface water flow modeling when high water flow values are involved, as in the case of big, permanent rivers. But in arid and semiarid environments, many situations require the inclusion of this infiltration term to adequately describe the evolution of surface flows, such as reaches downstream dams, ephemeral rivers, gullies, snowmelt flows, derivation channels over porous bed, or irrigation furrows. The approach selected for modeling the infiltration flow, that is, the equation for the local evolution of infiltration velocity during the process, further determines the best-fit results in the coupling of surface and soil water flows. Solute transport simulation in water is strongly affected by the accuracy in water flow modeling, and the partition between infiltration and runoff influences the mass balance associated to the superficial and soil fluxes. Particularly, besides the flow equations agreement with the real conditions, all the diffusion effects, whatever the scale, are included in the longitudinal dispersion coefficient, $E$, whose effective value is related to water velocity field, turbulence regime, geometry, and transient conditions, and also takes into account the numerical effects of 1D modeling and equation solving[1].

Classical approaches for E estimation to be used in transport problems modeling use a constant value for this parameter for a given set of flow conditions, related to permanent regime[2][3][4][5]. Alternatively, some expressions for variable E depending of the cross section average velocity have been included in the advection-dispersion equation, as the Rutherford equation, to estimate a value of $E$ changing in time and in space[6]. However, a constant dispersivity parameter must be calibrated in turn.

This work presents a 1D model for solute transport over porous media, which combines the selection of the infiltration flow equation with a characteristic function for E values that, despite constant for a given study case, allows a different estimation for this parameter depending on the predominance of the transient water flow conditions along the solute transport process.

## 2 MODEL DESCRIPTION

### 2.1 *Water flow on porous bed*

Instantaneous water flow rate values and section-averaged velocity were calculated along the channel from a 1D numerical model following the McCormack method[7][8]. This method was applied to the cross-integrated Saint-Venant equations for mass and momentum conservation in surface flow,

$$\frac{\partial A}{\partial t}+\frac{\partial Q}{\partial x}+\frac{\partial Z}{\partial t}=0 \tag{1}$$

$$\frac{\partial Q}{\partial t}+\frac{\partial}{\partial x}\left(\frac{Q^2}{A}+\frac{1}{2}gAh\right)=gA\left(S_0-S_f\right) \tag{2}$$

where, at a time t and a distance x from the water source, $A$ is the cross-sectional area; $Q$ is the instantaneous volumetric water flow rate; $Z$ is the accumulated infiltration volume per unit length; $S_0$ and $S_f$ are the bed and friction slopes, respectively; $h$ is the water depth, and $g$ the acceleration of gravity. The Manning equation was used to calculate the friction slope needed to solve equation (2).

### 2.2 *Water infiltration*

The infiltration of water through soil can be generally described by Darcy equation. From this, different approaches can be found depending on the context. In furrow irrigation, the temporal evolution of Z is usually estimated from the Kostiakov–Lewis equation[9],

$$Z=k\cdot t_{opp}^{a}+f_0\cdot t_{opp} \tag{3}$$

where $t_{opp}$ is the opportunity time, ($t_{opp}=t-t_{ad}$), $t$ is the current time, $t_{ad}$ (advancing time) is the time when the water front arrives at a point located at a distance $x$ from the water source; $k$ and $a$ are empirical fitting parameters; and $f_0$ stands for

the steady-state value that the unit length infiltration rate tends to reach, provided sufficient time has elapsed. To improve the infiltrated volume and the advancing water time estimations, a numerical modification[10] was used in the results of this work. In hydrological applications, the Green-Ampt equation[11] is commonly used, which is based on Darcy equation and derives from a simplification of the vertical wetness profile in soil,

$$i \simeq k_s \left( \frac{(\psi_{mf} + h)\Delta\theta}{I} + 1 \right) \tag{4}$$

where $I$ is the accumulated infiltration volume per unit area; $I$, the infiltration rate; $k_s$, the saturated hydraulic conductivity; $\psi_{mf}$, the matrix potential at the water front in soil; and $\Delta\theta$, the maximum water content increment during the process.

### 2.3 *Solute transport*

Non-reactive substance transport in longitudinal systems, such as streams or channels, can be described by the cross-section integrated 1D form of the advection-dispersion equation[1], which can be written as equation (5) for non-uniform flows[2],

$$\frac{\partial(AC)}{\partial t} + \frac{\partial(QC)}{\partial x} + PiC = \frac{\partial}{\partial x}\left( AE\frac{\partial C}{\partial x} \right) \tag{5}$$

where $C$ is the average values of solute concentration at a cross-section, for the time $t$; $P$ the wetted perimeter of the cross section; and $E$ is the longitudinal dispersion coefficient. Since this coefficient is assumed to be constant, this accounts for vertical and cross-velocity gradient contributions to the dispersion term. Equation (4) is solved numerically in three steps, the advective (coupled to equations (1) y (2)), dispersive and infiltration terms[2].

## 3 INFILTRATION FUNCTION EFFECTS ON SURFACE SOLUTE TRANSPORT

To test the effects of the infiltration function selected on the evolution of solute transport in the surface flow, some experimental field results from furrow fertigation[8] were used. Table 1 resumes the experimental design, where $Q_0$ and $C_0$ are the water constant inflow rate in the furrow and the concentration of the tracer application in the furrow head, respectively; $t_{advance}$, the time when water flow reaches the end of the furrow, and $t_{application}$, the time when the each of three applications of a tracer 7 min-pulse begins to be applied. Tables 2 and 3 show the calibrated values for parameters in equation (3) and (4), and the resulting $E$ values, respectively.

In general, the Kostiakov-Lewis equation fitted better to the temporal evolution of the surface water advance whereas the Green-Ampt equation was in better agreement with the concentration values measured in the water flow. Figures 1 and 2 show, respectively, the measured and simulated concentrations evolution in five monitoring stations along the furrow.

Table 1. Characteristics of the fertigation furrow experiment used in this work.

| $Q_0$ (L/s) | $C_0$ (g/L) | $t_{advance}$ (min) | $t_{aplication}$ (min) | | |
|---|---|---|---|---|---|
| 0.66 | 19.4 | 39.5 | 34.5 | 58.4 | 87.4 |

Table 2. Calibrated water flow parameter values.

| Kostiakov-Lewis | | | | Green y Ampt | | | | RMSE (K-L/G-A) | |
|---|---|---|---|---|---|---|---|---|---|
| n (S.I.) | k ($m\,s^{-a}$) | a | f0 ($m\,s^{-1}$) | $k_s$($m\,s^{-1}$) | $\psi$ m (m) | $\theta$ | n (S.I.) | $t_{advance}$ | runoff |
| 0.018 | 0.005 | 0.20 | 3.80 10–7 | 8.1 10–7 | −0.98 | 0.34 | 0.018 | 3.40/5.05 | 0.20/0.31 |

Table 3. Calibrated values of $E$ for each tracer application.

| | $E$ ($m^2\,s^{-1}$) | | |
|---|---|---|---|
| Infiltration eq. | Ap. 1 | Ap. 2 | Ap. 3 |
| *Kostiakov-Lewis* | 0.028 | 0.078 | 0.098 |
| *Green y Ampt* | 0.019 | 0.052 | 0.079 |

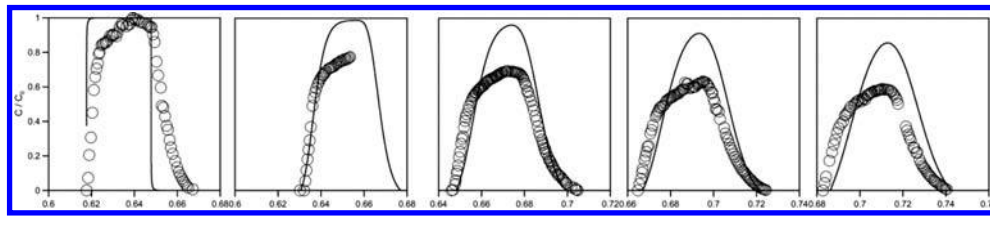

Figure 1. Measured and simulated concentration values in five monitoring points along the furrow (Kostiakov-Lewis).

## 4 EFFECTIVE VALUES FOR THE LONGITUDINAL DISPERSION COEFFICIENT

A characteristic curve for the a priori selection of an effective value of the longitudinal dispersion coefficient in equation (5) is proposed from the whole set of experimental field results from furrow fertigation[8] used in the previous section. The effective value of $E$ depends on the flow characteristics during the period that the solute is present in the flow; to select an adequate value depending of the interval of solute residence in transient flows, different expressions were tested and finally the following non-dimensional terms were selected (equation (6)), whose relationship is shown in figure 3 and equation (7). Such terms include, directly or indirectly, most factors that determine the transient character of the flow conditions during solute transport.

$$E^* = \frac{E \cdot t_{advancing} \cdot f_0}{Q_0} \quad ; \quad T^* = \frac{t_{application}}{t_{steady}} \tag{6}$$

$$E^* = \frac{a_1}{a_2 + e^{(-a_3 \cdot T^*)}} \tag{7}$$

The proposed function was validated from additional experimental results[12] in the same furrow sets, and figure 4 show the experimental and simulated curves for tracer concentration evolution in the monitoring stations under the resulting $E$value from equation (7). The results show satisfactory agreem

ent and validate the usefulness of characteristic curves for $E$ selection.

## 5 CONCLUSIONS

Despite the implicit simplifications in 1D transport model in free surface water flow, such approach is of interest in many applications. The model allows the selection of the infiltration equation depending on the situation under study, and the methodology proposed to derive characteristic functions for a priori values of $E$, has proved adequate to the transport process simulation; what is more, its use provides with better results than a constant value for a given water flow configuration independently. Further work is currently being carried out to identify the characteristic terms for other situations such as herbicide tran

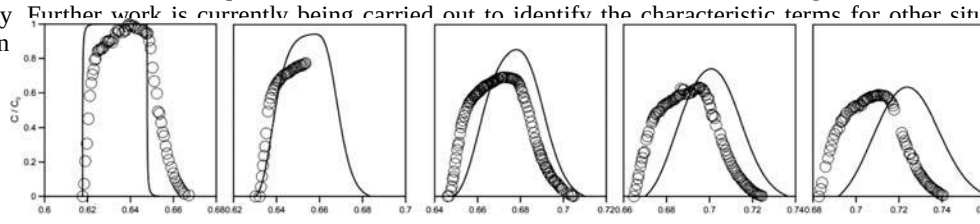

Figure 2. Measured and simulated concentration values in five monitoring points along the furrow (Green-Ampt).

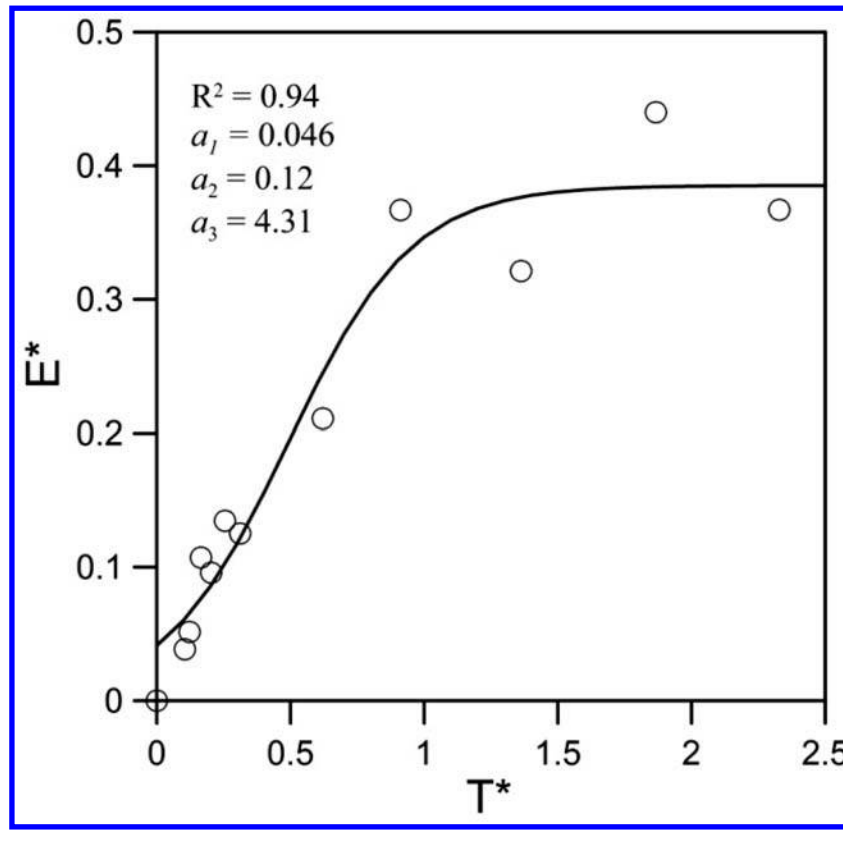


Figure 3. Non-dimensional parametric function for effective values of $E$ in transient flows.

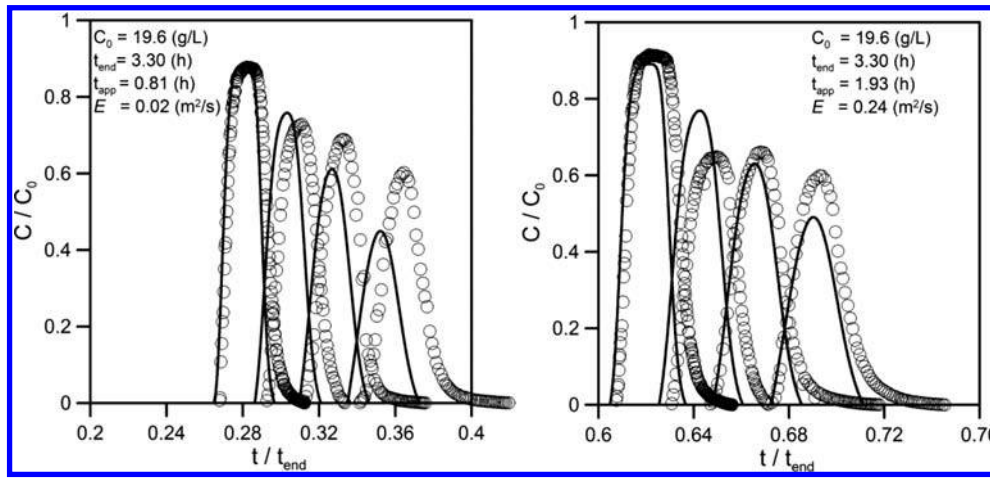


Figure 4. Measured and simulated concentration values for a validation test of equation (7).

## REFERENCES


[1] Rutherford, J.C. (1994), *River Mixing*, Wiley, Chichester.

[2] García-Navarro, P., Playán, E. and Zapata, N. (2000). "Solute transport modeling in overland flow applied to fertigation", J. Irrig Drain. Eng., Vol. 126, pp. 33–40.

[3] Abbassi, F., Feyen, J., Roth, R. L., Sheedy, M. and van Genuchten, M. Th. (2003). "Water flow and solute transport in furrow-irrigated fields", Irrig. Sci., Vol. 22, pp. 57–65.

[4] Zerihun, D., Furman, A., Warrick, A. W. and Sánchez, C. A. (2005). "Coupled surface subsurface solute transport model for irrigation borders and basins. I. Model development". J. Irrig Drain. Engng., Vol. 131, pp. 396–406.

[5] Zerihun, D., Furman, A., Warrick, A. W. and Sánchez, C. A. (2005). "Coupled surface subsurface solute transport model for irrigation borders and basins. II. Model evaluation". J. Irrig Drain. Engng., Vol. 131, pp. 407–419.

[6] Zapata, N., Burguete, J., Santos, E. P., Playán, E. and García-Navarro, P. (2007). "Furrow fertigation simulation model, calibration, validation and application". *International Workshop on Numerical modelling of hydrodinamics for water resources, Zaragoza, 18–21 June*, pp. 339–343.

[7] Burguete, J. and García-Navarro, P. (2004). "Improving simple explicit methods for unsteady open channel and river flow", Int. J. Num. Meth. In Fluid., Vol. 45, pp. 125–156.

[8] Nofuentes, M. (2007). *Solute transport in water flow in furrow irrigation*. Ph.D. Thesis. (In Spanish). University of Cordoba.

[9] Playán, E. and Faci, J. M. (1997). "Border fertigation: field experiments and simple model". Irrig. Sci., Vol. 17, pp. 163–171.

[10] Maikaka, M. 2004. *Numerical 1D models in surface irrigation*. Ph. D. Thesis. (In Spanish), University of Zaragoza.

[11] Chow, V. T. 1959. *Open Channel Flow*. McGraw-Hill. New York

[12] Domínguez, E. M., Jiménez, R. C., Polo, M. J., Giráldez, J. V. and Mateos, L. 2003. Búsqueda de buenas prácticas de fertirriego por surcos: resultados preliminares. *Actas XXI Congreso Nacional de Riegos, Mérida (Badajoz), B5*.

*Environmental Hydraulics – López-Jiménez et al (eds)*
*© 2010 Taylor & Francis Group, London, ISBN 978-0-415-56697-1*

# Analytical methods for velocity distribution and dip-phenomenon in narrow open-channel flows

Rafik Absi
*EBI, Inst. Polytech. St-Louis, Cergy-Pontoise, France*

ABSTRACT: In this study, we present analytical tools for velocity distribution in steady uniform open-channel flows. Simple dip-modified laws are presented. An ordinary differential equation based on an analysis of the Reynolds-averaged Navier-Stokes (RANS) equations is proposed. Comparisons of predicted velocity profiles with experimental data show good agreement. It is well known that dip-phenomenon depends on aspect ratio Ar (ratio of the channel width b to the water depth h). Results show that it should depend also on channel slope and friction velocity.

*Keywords*: Open-channel flows, free surface, velocity distribution, dip phenomenon, aspect ratio, channel slope.

## 1 INTRODUCTION

In open-channel flows, the vertical velocity profile is well described by the classical log law in the inner region ($\xi < 0.2$, where $\xi$ is the ratio of the distance from the bed $y$ to the water depth $h$). However, in the outer region ($\xi > 0.2$) this law deviates from experimental data. This deviation is accounted for by adding the Coles' wake function. In 2D open-channel flows, the log-wake law appears to be the most reasonable extension of the log law [5]. However, in narrow open-channels (i.e. aspect ratio $Ar$ smaller than 5, where $Ar$ is the ratio of the channel width b to the water depth h) the maximum velocity appears below the free surface (i.e. the velocity dip phenomenon) involving deviation from the log-wake law. This phenomenon is related to secondary currents which appear in 3D open-channel flows. Coles' wake function is unable to represent this behavior since it predicts a velocity which increases with distance from the bed.

In order to predict the velocity dip phenomenon, empirical relations were proposed. However, these empirical laws need a certain number of parameters such as dip position. Based on an analysis of the Reynolds-averaged Navier-Stokes (RANS) equations, Yang et al.[6] proposed a dip-modified log law which consists of two logarithmic distances, one from the bed (i.e. the log law), and the other from the free surface. This law presents the advantage that it contains only one parameter of dip-correction $\alpha$. The dip-modified log law reverts the classical log law for $\alpha = 0$.

In our study, we will point out that even if the dip-modified log law [6] predicts dip-phenomenon, it presents important difference with experimental data. In most cases, it is not possible to improve velocity profiles by adjusting the parameter $\alpha$. The aim of this study is to improve the prediction of velocity distribution with dip phenomenon in open channel flows.

The shortcoming of the dip-modified log law will be analyzed and a simple dip-modified log-wake law, which allows improving predicted velocity profiles, will be presented. An ordinary differential equation, based on an analysis of the Reynolds-averaged Navier-Stokes (RANS) equations, will be proposed. Predicted profiles will be compared with experimental data of measured velocities in open-channels.

## 2 MODEL EQUATIONS

For steady uniform open-channel flows, using the continuity equation, the Reynolds-averaged Navier-Stokes (RANS) momentum equation becomes in the streamwise direction $x$

$$\frac{\partial U V}{\partial y} + \frac{\partial U W}{\partial z} = \nu \frac{\partial^2 U}{\partial y^2} + \nu \frac{\partial^2 U}{\partial z^2} + \frac{\partial - \overline{u v}}{\partial y} + \frac{\partial - \overline{u w}}{\partial z} + g \sin\theta \tag{1}$$

where $x, y$ and $z$ are respectively the streamwise, vertical and lateral directions and $U, V$ and $W$ the three corresponding mean velocities ($u, v$ and $w$ are the turbulent fluctuations), $\nu$ the fluid kinematic viscosity, $g$ the gravitational acceleration, and $\theta$ is the angle of the channel bed to the horizontal axis [1][2].

## 3 DIP-MODIFIED LAWS

### 3.1 *Dip-modified log law*

From an analysis of the Reynolds-averaged Navier-Stokes (RANS) equations and by assuming a parabolic profile for the eddy viscosity, Yang et al.[6] proposed the following law:

$$\frac{U}{u_*} = \frac{1}{\kappa} \left[ ln\left(\frac{y}{y_0}\right) + \alpha\, ln\left(1 - \frac{y}{h}\right) \right] \tag{2}$$

where $u_*$ is the friction velocity, $h$ the water depth, $\kappa$ the von Karman constant ($\approx$0.41) and $y_0$ the distance at which the velocity is hypothetically equal to zero. This law is referred as the dip-modified log law. It presents the advantage that it contains only one parameter $\alpha$ and it reverts the classical log law for $\alpha = 0$.

Figure (1) presents comparisons of predicted velocity profiles obtained by dip-modified log law (Eq. 2) for different values of coefficient $\alpha$ with experimental data [4]. This figure shows that Eq. (2) with $\alpha$ given by empirical formula $\alpha = 1.3 \exp(-\mathrm{Ar}/2)$ proposed by Yang et al. (solid lines) is able to predict a small deviation from log law profile (dip phenomenon). We notice that,

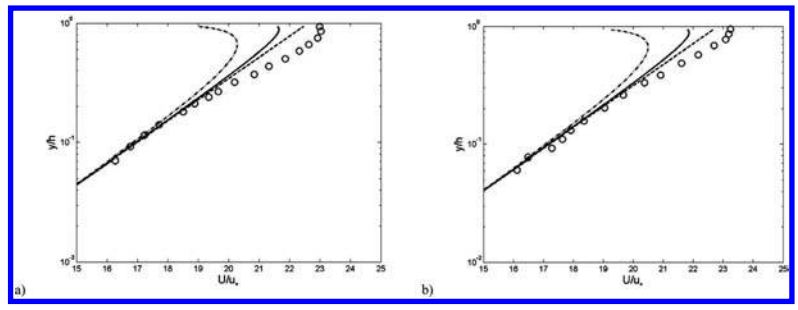

Figure 1. Comparison of dip-modified log law profiles (Eq. 2) [6] for different values of coefficient $\alpha$ with experimental data; dashed lines: $\alpha = 0$ log law profile, solid lines: $\alpha = 1.3 \exp(-Ar/2)$ proposed by Yang et al.[6], dash-dotted lines: $\alpha = 0.5$; Symbols: measurements [4] for (a) C4, $Ar = 4.68$ and $S = 0.00401$, (b) C3, $Ar = 4.68$ and $S = 0.00296$.

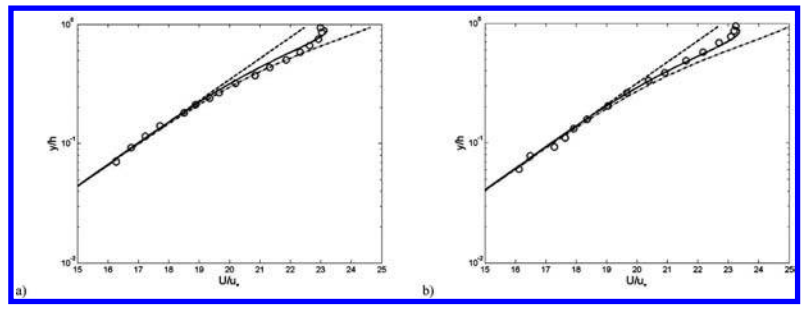

Figure 2. Comparison of our simple dip-modified log-wake law profiles (Eq. 4, solid lines) with experimental data; Symbols: measurements [4], dashed lines: log law profile ($\alpha = 0$ and $\Pi = 0$), dash-dotted lines: log-wake law profiles ($\alpha = 0$ and $\Pi = 0.2$), solid lines: simple dip-modified log-wake law (Eq. 4) with (a) $\alpha = 0.22$ and $\Pi = 0.2$ (C4 for $Ar = 4.68$ and $S = 0.00401$), (b) $\alpha = 0.27$ and $\Pi = 0.2$ (C3 for $Ar = 4.68$ and $S = 0.00296$).

it is not possible to improve predicted velocity profiles by adjusting the parameter $\alpha$; since by increasing $\alpha$, the deviation from experimental data increases (dash-dotted lines, with $\alpha = 0{:}5$) and by decreasing the value of $\alpha$ predicted profiles approach log law profiles (dashed lines).

### 3.2 *A simple dip-modified log-wake law*

Figure 1 shows that log law profiles (dashed lines) are valid only in the inner region ($\xi = y/h < 0.2$). In the outer region ($\xi > 0.2$) log law deviates from experimental data. In 2D open-channel flows, this deviation is accounted for by adding the Coles wake function as

$$\frac{U}{u_*} = \frac{1}{\kappa}\left[ln\left(\frac{y}{y_0}\right) + 2\,\Pi\, sin^2\left(\frac{\pi\, y}{2\, h}\right)\right] \tag{3}$$

where $\Pi$ is the Coles parameter expressing the strength of the wake function. It was found experimentally that $\Pi$ increases with the Reynolds number Re in zero-pressure-gradient boundary layers, attaining an asymptotic value of $\Pi = 0.55$ at high Re. Examination of the log-wake law in the outer layer of 2D open-channel flows [5], shows that $\Pi$ increases from zero with the friction Reynolds number $Re_*$ and becomes nearly constant $\Pi \approx 0.2$, for $Re_* > 2000$. In 2D open-channel flows, the log-wake law appears to be the most reasonable extension of the log law.

However, in 3D open-channel flows with secondary currents, the log-wake law is unable to predict velocity dip-phenomenon (Figure 2). A suitable simple law is possible by adding to log law both Coles' wake function and the term linearly proportional to the logarithmic distance from the free surface as

$$\frac{U}{u_*} = \frac{1}{\kappa}\left[ln\left(\frac{y}{y_0}\right) + 2\,\Pi\, sin^2\left(\frac{\pi\, y}{2\, h}\right) + \alpha\, ln\left(1 - \frac{y}{h}\right)\right] \tag{4}$$

Figure 2 presents comparisons of predicted velocity profiles obtained by our simple dip-modified log-wake law (Eq. 4) with experimental data of Lyn [4] for an aspect ration $Ar$ equal to 4.68 but for different channel slope $S = 0.00296$ for C3 (Figure 2.a) and $S = 0.00401$ for C4 (Figure 2.b). Our profiles (solid lines) are also compared to log law profiles (dashed lines, $\alpha = 0$ and $\Pi = 0$) and log-wake law profiles (dash-dotted lines, $\alpha = 0$ and $\Pi = 0.2$). Comparison with experimental data shows reasonable agreement. Velocity profiles (solid lines) are obtained by dip-modified log-wake law with $\Pi = 0.2$ but with different coefficients $\alpha$. This indicates that coefficient $\alpha$ is not dependent only on aspect ration $Ar$, as proposed by Yang et al. [6], but should depend also on channel slope S.

### 3.3 *Modified log-wake law*

Guo and Julien [3] proposed a modified log-wake law as

$$\frac{U}{u_*} = \left[\frac{1}{\kappa}\, ln\left(\frac{y\, u_*}{\nu}\right) + B\right] + \frac{2\,\Pi}{\kappa}\, sin^2\left(\frac{\pi\, y}{2\,\delta}\right) - \frac{1}{3\,\kappa}\left(\frac{y}{\delta}\right)^3 \tag{5}$$

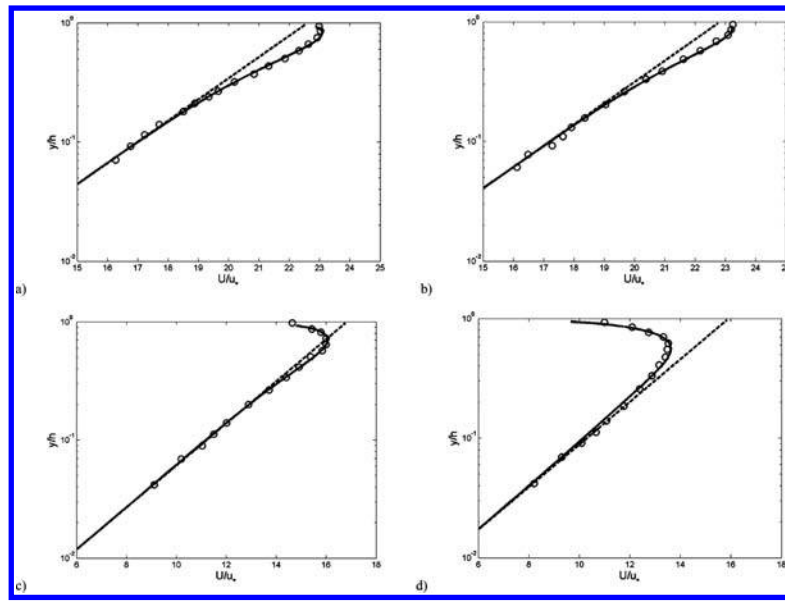

Figure 3. Comparison of velocity profiles obtained from ODE (Eq. 6) with experimental data [4] [7]: Symbols; dashed lines: log law profiles ($\alpha = 0$ and $\Pi = 0$); solid lines: solution of ODE (Eq. 6) with: (a) $\alpha = 0.21$ and $\Pi = 0.55$ (C4 for $Ar = 4.68$ and S = 0.00401 [4]), (b) $\alpha = 0.15$ and $\Pi = 0.4$ (C3 for $Ar = 4.68$ and S = 0.00296 [4]), (c) $\alpha = 0.42$ and $\Pi = 0.55$ (C4 for $Ar = 4.98$ and $u_* = 0.1688$ m/s[7]), (d) $\alpha = 0.78$ and $\Pi = 0.45$ (C3 for $Ar = 4.98$ and $u_* = 0.1244$ m/s[7]).

where $\delta$ is the dip distance from the bed. Eq. (5) fits better experimental data. However, it needs a certain number of parameters such as $\delta$ the dip position. This seems to exclude the possibility of its adoption in predictive and practical applications.

## 4 AN ORDINARY DIFFERENTIAL EQUATION

From the analysis of the Reynolds-averaged Navier-Stokes (RANS) equations and by using a more appropriate approximation for the eddy viscosity in accordance to log-wake law, we obtain the following ordinary differential equation (ODE)[2].

$$\frac{d\,U_a}{d\,\xi} = \frac{1}{\kappa}\left(1 - \alpha\,\frac{\xi}{1-\xi}\right)\left[\frac{1}{\xi} + \pi\,\Pi\,sin\,(\pi\,\xi)\right] \tag{6}$$

where $\xi = y/h$, $U_a = U/u_*$. Eq. (6) shows the interest that for $\alpha = 0$ and $\Pi = 0$ it gives the log law and for $\alpha = 0$ it gives the log-wake law.

Figure (3) presents comparisons of predicted velocity profiles obtained from the proposed ODE (Eq. 6, solid lines) with experimental data of Lyn (1986) [4] (Fig. 3.a, 3.b) for an aspect ration $Ar = 4.68$ and Sarma et al.[7] (fig. 3.c, 3.d) for an aspect ration $Ar = 4.98$. In these figures, $\alpha$ and $\Pi$ are chosen to give the best fit. Predicted profiles show good agreement. This figure confirms that the parameter $\alpha$ is not only a function of aspect ratio but should include effect of channel slope and friction velocity.

## 5 CONCLUSION

In this study, we proposed an ordinary differential equation based on an analysis of the Reynolds-averaged Navier-Stokes (RANS) equations. Comparisons of predicted velocity profiles with experimental data show good agreement. Our results show that coefficient $\alpha$ is not dependent only on aspect ration $Ar$, but should depend also on channel slope S and friction velocity.

## ACKNOWLEDGEMENTS

The author would like to thank J. Guo for providing the experimental data files.

## REFERENCES

[1] Absi, R. (2008), "Comments on 'Turbulent velocity profile in fully-developed open channel flows"'. Environmental Fluid Mechanics, Vol. 8, pp. 389–394.
[2] Absi, R. (2009), "An ordinary differential equation for velocity distribution and dip phenomenon in open channel flows", *EBI, Inst. Polytech. St-Louis, Site du Port, Cergy-Pontoise, France*, Res-Rep. 05-09.
[3] Guo, J. and Julien, P. Y. (2008) "Application of the modified log-wake law in open-channels", J. Applied Fluid Mechanics, Vol. 1(2), pp. 17–23.
[4] Lyn, D.A. (1986), "Turbulence and Turbulent Transport in Sediment-Laden Open-Channel Flows", *W. M. Keck Laboratory of Hydraulics and Water Resources, California Institute of Technology, Pasadena, CA*, Rep KH-R-49.
[5] Nezu, I and Nakagawa, H. (1993), *Turbulence in open-channel flows*, A.A. Balkema (ed), The Netherlands.
[6] Yang, S.Q., Tan, S.K. and Lim, S.Y. (2004), "Velocity distribution and dip-phenomenon in smooth uniform open channel flows", J. Hydraulic Engineering, Vol. 130(12), PP. 1179–1186.
[7] Sarma, K.V.N., Prasad, B.V.R. and Sarma, A.K. (2000), "Detailed study of binary law for open channels", J. Hydraulic Engineering, Vol. 126(3), pp. 210–214.

*Environmental Hydraulics – López-Jiménez et al (eds)*
*© 2010 Taylor & Francis Group, London, ISBN 978-0-415-56697-1*

# Effect of sedimentation on 3D turbidity currents

M. La Rocca, P. Mele & G. Sciortino
*Dipartimento di Scienze dell'Ingegneria Civile, Università degli Studi RomaTRE, Rome, Italy*

M.A. Boniforti
*Dipartimento di Idraulica, Trasporti e Strade, Università di Roma "La Sapienza," Rome, Italy*

ABSTRACT: In this paper a mathematical model for 3D turbidity currents has been presented. The model consists in a system of partial differential equations in conservative form, formulated in the framework of the shallow water equations and it accounts for the main features of the turbidity currents: entrainment of environment fluid, settling and resuspension of particles, variation of density. A numerical investigation has been performed to assess the influence of the settling of particles on the turbidity current. To this aim different turbidity currents have been simulated, with the same excess density and initial volume, but realized with silicon carbide particles with increasing diameter. Numerical results are compared with experimental results by La Rocca et al.[8]. The agreement is fairly good and shows the ability of the proposed model in reproducing the main features of the physical phenomenon.

*Keywords*: Turbidity currents; gravity currents; sedimentation; hyperbolic partial differential equations

## 1 INTRODUCTION

A large amount of scientific work has recently regarded turbidity currents, that is dense currents consisting of a suspension of heavy particles in an environment fluid. The scientific interest arise from the fact that, by means of sedimentation and erosion processes, these currents interact with the external environment, so that experimental and numerical investigation on turbidity currents is important from a geological, oceanographical and environmental point of view[1]. A lot of different aspects of the phenomenon have been investigated[2]. In particular, the 2D turbidity currents dynamics have been largely studied by using shallow water models which are able to give a reliable description of the phenomenon in terms of macroscopic quantities like the thickness of the current, the depth-averaged velocities, concentration of particles etc.[3],[4],[5],[1]. On the contrary, 3D turbidity currents have not been investigated to the same extent. So this paper is aimed to formulate a shallow water model for 3D turbidity currents. The model is developed starting from the work of Bradford et al.[6], based on the layer-averaged approach of Parker et al.[7]. By considering a 3D turbidity current consisting of a mixture of water and sediments with $n_{sed}$ different median diameters flowing under an infinitely deep layer of environment fluid, a partial differential system of $3 + n_{sed}$ equations can be obtained: the mixture mass balance equation, the $x$ and $y$ components of the mixture momentum balance equation and a single equation for the concentration of each uniform class of sediment. Assuming then that the mixture is made with an uniform sediment, characterised by one median diameter, whose depth averaged concentration is $C$, an hyperbolic partial differential system of four equations is obtained which can be put in conservative form. Then a finite volume numerical solver, based on the Godunov formulation together with a Roe's approximate Riemann solver, is applied.[8]. A first validation for the this model was given in La Rocca et al.[15], where a gravity current is considered and numerical results are compared with the experimental ones by La Rocca et al.[8]. In this paper moreover, the influence of the sediment velocity is highlighted by suitable numerical simulations. As the fundamental process of sedimentation and resuspension of particle is absent, these results cannot be considered representative for a turbidity current. Indeed, unlike gravity currents, turbidity currents are non-conservative currents since sediments may be settled out of or be re entrained into the flow, so that the excess density is not conserved over the whole mass of the current[2]. Nevertheless the comparison is interesting and the variable turbidity current density is an innovation element with respect to the gravity current model proposed in La Rocca et al.[8].

## 2 THE MATHEMATICAL MODEL AND THE CLOSURE RELATIONS

Consider a layer of liquid, height $h$, density $\rho$, evolving under a layer of a quiescent, lighter liquid, height $H$, density $\rho_e$ ($\rho > \rho_e$) (Fig. 1). The ratio $h/H$ is such that: $h/H << 1$. The density $\rho$ of the heavier liquid can be expressed as:

$$\rho = \rho_e + (\rho_s \quad \rho_e)c \tag{1}$$

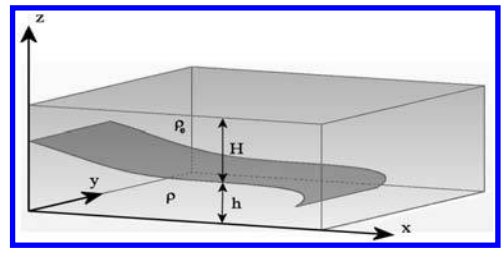


Figure 1. The\frame of reference and the turbidity current.

being $\rho_s$ the density of a fine uniform sediment, diluted in the heavier liquid layer, and $c$ its dimensionless concentration measured in $m^3$ of sediments per $m^3$ of water. Here, the layer-averaged approach[6],[7] is used in order to obtain the equations governing a turbidity current. The equations are then:

$$\begin{cases} \dfrac{\partial h}{\partial t}+\dfrac{\partial Uh}{\partial x}+\dfrac{\partial Vh}{\partial y}=\alpha U_e \\ \dfrac{\partial Uh}{\partial t}+\dfrac{\partial U^2h}{\partial x}+\dfrac{\partial UVh}{\partial y}=\alpha UU_e \quad \dfrac{(\rho_s \quad \rho_e)g}{\rho_e}\dfrac{\partial}{\partial x}\left(C\dfrac{h^2}{2}\right)+\dfrac{1}{\rho_e}T_{xz}\Big|_{z=0} \\ \dfrac{\partial Vh}{\partial t}+\dfrac{\partial UVh}{\partial x}+\dfrac{\partial V^2h}{\partial y}=\alpha VU_e \quad \dfrac{(\rho_s \quad \rho_e)g}{\rho_e}\dfrac{\partial}{\partial y}\left(C\dfrac{h^2}{2}\right)+\dfrac{1}{\rho_e}T_{yz}\Big|_{z=0} \\ \dfrac{\partial Ch}{\partial t}+\dfrac{\partial CUh}{\partial x}+\dfrac{\partial CVh}{\partial y}=\alpha CU_e+u_s(e_s \quad c_b) \end{cases} \tag{2}$$

being $U$, $V$ the depth averaged velocity components along $x$ and $y$ directions, $C$ the depth averaged concentration, $\alpha$ the entrainment coefficient, $e_s$ the resuspension coefficient and $c_b$ a near-bed value of the local concentration. These two latter terms account for resuspension and sedimentation of sediments. $u_s$ is the fall velocity of the suspended sediment and $U_e$ is the entrainment velocity. Finally, terms $T_{xz}|_{z=0}$, $T_{yz}|_{z=0}$ account for friction forces exerted on the current due to the contact with the bottom. These latter can be calculated by means of the following expression, where $\lambda$ is the friction factor:

$$\begin{cases} \dfrac{1}{\rho_e}T_{xz}\Big|_{z=0}=\dfrac{\lambda}{8}U\sqrt{U^2+V^2} \\ \dfrac{1}{\rho_e}T_{yz}\Big|_{z=0}=\dfrac{\lambda}{8}V\sqrt{U^2+V^2} \end{cases} \tag{3}$$

The mathematical model is valid in the limit of the Boussinesq's approximation:

$$\frac{\rho \quad \rho_e}{\rho_e}=C\frac{\rho_s \quad \rho_e}{\rho_e}<<1 \tag{4}$$

This condition is verified in turbidity currents. Indeed, assuming the values of 2650 $kgm^{-3}$ for the density of the sediment, 1000 $kgm^{-3}$ for the density of the water and $10^{-2}$ for the concentration, the parameter at RHS of (4) is equal to 0.0165.

The mathematical model (4) must be completed with suitable closure relations, by means of which $\alpha$, $e_s$, $c_b$, $u_s$, $U_e$ and $\lambda$ are expressed as function of the resolved variables: the depth averaged velocity components $U$, $V$, the concentration $C$, and the turbidity current thickness $h$.

The entrainment coefficient $\alpha$ can be put as[1] : $\alpha = \frac{0.00153}{0.0204+\mathrm{Ri}}$, where $Ri=\frac{gCh}{U^2+V^2}\left(\frac{\rho_s-\rho_e}{\rho_e}\right)$is the Richardson number. The resuspension coefficient $e_s$ is assumed to be negligible with respect to the quantity $c_b$[9][10],[11],[12][13]. Instead this latter can be assumed proportional to the concentration $C$ by means of the dimensionless coefficient $r_0 \geq 1 : c_b = r_0 C$. If $C \leq 10^{-2}$ the fall velocity of the suspended sediment can be expressed by[3]:

$$u_s=\frac{1}{\sqrt{C_R}}\sqrt{\frac{4}{3}\left(\frac{\rho_s \quad \rho}{\rho}\right)gd_s} \tag{5}$$

being $C_R$ the drag coefficient of the sphere and $d_s$ the diameter of the sediment particle. $U_e$ can be estimated as the velocity modulus. Finally, for fully developed turbulent open channel flows, the friction coefficient may be estimated by:

$$\lambda = 0.25 \Big/ \left[ Log\left(\frac{\varepsilon}{3.71\,Hf}\right)\right]^2$$

where $f$ is a shape factor which, in the present case, can be considered as a calibration parameter and the flow can be safely assumed turbulent. Assuming the kinematic viscosity of water $\nu = 10^{-6}\ m^2s^{-1}$ and the concentration $C = 10^{-2}$, the Reynolds number $Re=\sqrt{\frac{gCh^3}{\nu^2}\left(\frac{\rho_s-\rho_e}{\rho_e}\right)}$ has an order of magnitude greater than $10^5$ for gravity currents heights larger than 0.1 m.

## 3 RESULTS AND CONCLUSIONS

The partial differential system (2) is hyperbolic[6] and it can be put in conservative form. Thanks to these properties a numerical solver[8], based on the Godunov formulation of the finite volume method, together with the adoption of the Roe's approximate Riemann solver, has been applied. Such a method, aimed to the simulation of 3D gravity currents, had been already used and validated in La Rocca et al.[8],[14] where results obtained from the partial differential system (2) with constant concentration are compared with experimental results concerning with 2D, axysimmetric and 3D gravity currents.

In this paper the numerical method is applied to the case of variable concentration and the numerical results will be compared to the 3D lock exchange experiments performed in La Rocca et al.[8]. Such experiments have been realised in a rectangular tank (Fig. 2), divided into two square section reservoirs (height $H$) by a rigid wall, filled with transparent tap water (density $\rho_e$) and

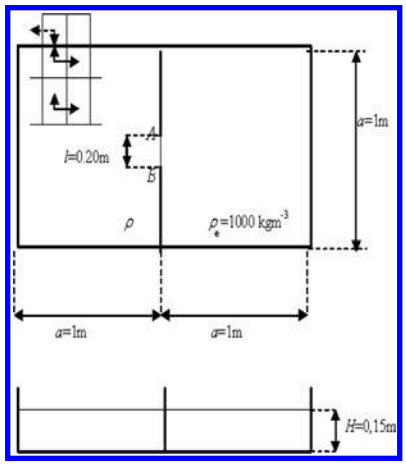


Figure 2. Definition sketch of the tank used to perform the experiments.

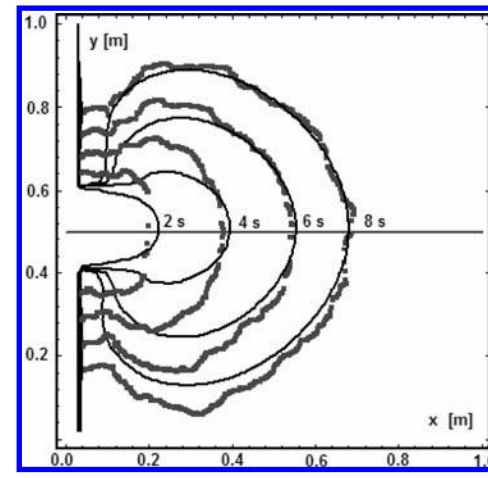


Figure 3. Experimental and numerical shape of the gravity current's top view ($\rho = 1015\,\mathrm{kgm^{-3}}$)

coloured salt water (density $\rho$, $\rho > \rho_e$). When a sliding gate AB positioned on the centre of the wall is removed, a gravity current originates. The bottom surface of the tank is made rough by gluing onto it uniform sediment material, with a diameter $r$. Two initial density conditions: $\rho = 1015\,\mathrm{kgm^{-3}}$, $\rho = 1025\,\mathrm{kgm^{-3}}$, and five roughness conditions have been considered: $r = 0.0$ mm, $r = 0.7$ mm, $r = 1.0$ mm, $r = 1.6$ mm, $r = 3.0$ mm.

The implementation of the numerical approach described in La Rocca et al.[8],[14] is straightforward. In order to ensure stability to the numerical calculations, the CFL stability condition is set[14]. All of the numerical simulations have been performed on a grid of 5000 elements, most of them square with side $\Delta = 0.02$ m, the others rectangular. The number of elements was deduced by preliminary numerical tests as a reasonable compromise between the convergence of results and the computational time needed for the simulation. The order of magnitude of the time step, determined by imposing the CFL condition, was $10^{-3}$–$10^{-4}$ s. Numerical results have been obtained setting to zero the fall velocity of the suspended sediment (5), as the gravity current under observation was realised with a mixture of water and NaCl without using sediments.

A numerical comparison between the behaviour of a gravity current and a turbidity current with the same initial density difference has been realised. In this case, the fall velocity of the suspended sediment has been calculated, according to (5), assuming particles of silicon carbide ($\rho_s = 3217\,\mathrm{kgm^{-3}}$) with diameter $d_s$: $9\,\mu\mathrm{m} \leq d_s \leq 53\,\mu\mathrm{m}$. The evolution of the current is characterized by a mushroom shape[8] expanding from the gate toward the right wall of the tank. The numerical top view obtained from the contour plot of the gravity current numerical surface are compared with the experimental top view of the gravity current. Experimental and numerical shape of the gravity current's top view are shown in Fig. 3, relative to the case $\rho = 1015\,\mathrm{kgm^{-3}}$ with smooth bottom. The agreement is quite good, practically the same obtained with the constant density model[8] and it improves with the time.

In the present model settling and resuspension of sediments are accounted for by the second term at RHS of the concentration equation. In particular, the resuspension is assumed to be negligible and only the settling is calculated, whose effect is of increasing the dilution of the current, thus reducing the excess density of the current and the driving buoyancy force[5]. Consequently the turbidity current travel more slowly than a gravity current with the same initial excess density. Following Bonnecaze et al.[15], the ability of the proposed model to reproduce such a behaviour was tested by comparing numerical results relative to the gravity current with $\rho = 1015\,\mathrm{kgm^{-3}}$ and numerical results relative to turbidity currents, with the same initial density, consisting of a suspension of water and silicon carbide particles with diameter $9\,\mu\mathrm{m} \leq d_s \leq 53\,\mu\mathrm{m}$. Due to the high density of the silicon carbide the order of magnitude of the initial value of the concentration $C$ is smaller than that of the gravity current ($O(C) \approx 10^{-3}$), so the assumption on the fall velocity (5) is valid. Results are shown in Fig. 4, where the numerical time histories of the current's front position are plotted. The front position is made dimensionless dividing all the front position's values by the front position attained by the gravity current at the last instant of time (10 s after the start of the run). So the values reported on the vertical axis represent the percentage of the distance travelled at any instant of time by the turbidity current's front with respect to that travelled by the gravity current's front. The behavior is in qualitative agreement with that shown in Bonnecaze et al.[16]: the front position increases more slowly increasing the particles diameter, as the larger particles settle out more quickly, thus reducing the density difference between the current and the environment fluid and then the driving buoyancy force. However, during a very initial phase ($t < 1.5$ s) few particles settle out of the currents, so the front position is the same for all the currents.

The influence of the particles settling on the profile of the current's thickness is shown in Fig. 5, where the thickness profiles obtained at $t = 8$ s and relative to the currents considered in Fig. 4 are shown. Such profiles are dimensionless, with respect to the initial height ($H = 0.15$ m). Also the distance from the origin is dimensionless, with respect to the maximum extension attained by the gravity current's profile. The particles settling reduces the turbidity current's density, while causing a negligible variation of its volume, due the small value of the particles concentration. This appear quite evident from Fig. 5. Indeed the profiles relative to the different currents are distorted, because of their different front velocity. Moreover, the distortion increases with the diameter of the particle. Nevertheless the area of the profile seems to remain quite constant. Integration of the thickness of the current over the whole area of the experimental setup reveals that the maximum relative variation of volume occurs for the turbidity current with particles of diameter $d = 53\,\mu$ and is equal to: $100 \times \left| \frac{V_0 - V_{53}}{V_0} \right| = 1.35\%$

The results obtained with the proposed model are in good agreement with experimental and numerical results published in La Rocca et al.[8]. The results confirm, also for 3D turbidity currents, that the settling of particles causes the dilution of the current and then the decrease of the buoyancy driving force and the front velocity: consequently the current slows down, while preserving practically the initial volume.

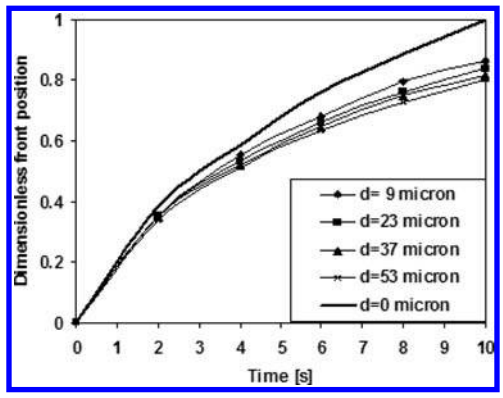


Figure 4. Comparison between the numerical gravity current and the turbidity currents obtained with particles of increasing diameters. The initial density is the same: $\rho = 1015\,\mathrm{kgm}^{-3}$.

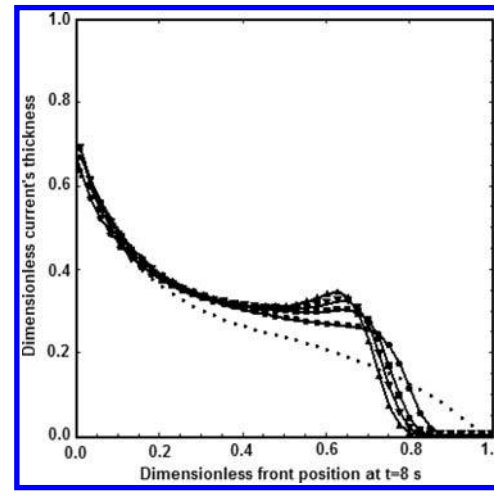


Figure 5. Dimensionless current's thickness versus dimensionless front position. Dotted line: gravity current, circles: $d = 9\,\mu$, squares: $d = 23\,\mu$, overturned triangles: $d = 37$, upright triangles: $d = 53\,\mu$.

REFERENCES


[1] Kostic, S, Parker, G (2007). "Conditions under which a supercritical turbidity current traverses an abrupt transition to vanishing bed slope without a hydraulic jump," J Fluid Mech, Vol 586, pp 119–145.

[2] Cantero, MI, Balachandar, S, Garcia, MH (2008). "An Eulerian-Eulerian model for gravity currentsb driven by inertial particles," Int J Multiphase Flow, Vol 34, pp 484–501.

[3] Bonnecaze, RT, Huppert, HU, Lister, J (1993). "Particle driven gravity currents," J Fluid Mech, Vol 250, pp 339–369.

[4] Choi, SU, Garcia, MH (1995). "Modeling of one-dimensional turbidity currents with a dissipative-Galerkin finite element method," J Hydraul Res, Vol 33, pp 623–647.

[5] Hogg, JA, Ungarish, M, Huppert, HE (2000). "Particle-driven graviyu currents: asymptotic and box model solutions," Eur J Mech B – Fluids, Vol 19, pp 139–165.

[6] Bradford, F, Katopodes, ND, Parker, G (1997). "Characteristic analysis of turbid underflows," J Hydraul Eng, Vol 123, pp 420–431.

[7] Parker, G, Fukushima, Y, Pantin, HM (1986). "Self-accelerating turbidity currents," J Fluid Mech, Vol. 171, pp 145–181.

[8] La Rocca, M, Adduce, C, Sciortino G, Bateman Pinzon, A (2008). "Experimental and numerical simulation of three-dimensional gravity currents on smooth and rough bottom," Phys of Fluids, Vol 20 (10), pp 106603-1-15.

[9] Hallworth, MA, Hogg, AJ, Huppert, HE (1998). "Effects of external flow on compositional and particle gravity currents," J Fluid Mech, Vol 359, pp 109–142.

[10] Maxworthy, T (1999). "The dynamics of sedimenting surface gravity currents," J. Fluid Mech, Vol. 392, pp 27–44.

[11] Gladstone, C, Woods, A (2000). "On the application of box models to particle-driven gravity currents," J Fluid Mech, Vol 416, pp 187–195.

[12] Kostic, S, Parker, G (2003a). "Progradational sand–mud deltas in lakes and reservoirs: Part 1. Theory and numerical modelling," J Hydraul Res, Vol 41 (2), pp 127–140.

[13] Kostic, S, Parker, G (2003b). "Progradational sand–mud deltas in lakes and reservoirs: Part 2. Experiment and numerical simulation," J Hydraul Res, Vol 41 (2), pp 141–152.

[14] Chippada, S, Dawson, CN, Martinez, ML, Wheeler, MF (1998). "A Godunov-type finite volume method for the system of shallow water equations," Comput. Methods Appl. Mech. Eng, Vol 151, pp 105–129.

[15] La Rocca M., Adduce C., Mele P., Sciortino G., (2009). "Numerical simulation of 3D submarine turbidity currents," ISOPE Proceedings 2009.

[16] Bonnecaze, RT, Lister, J (1999). "Particle driven gravity currents down planar slopes," J. Fluid Mech, Vol. 390, pp75–91.

*Environmental Hydraulics – López-Jiménez et al (eds)*
*© 2010 Taylor & Francis Group, London, ISBN 978-0-415-56697-1*

# Numerical modelling of nearshore waves, currents, and sediment transport: Validation with laboratory data

Pham Thanh Nam
*Department of Water Resources Engineering, Lund University, Lund, Sweden*
*Center for Marine Environment, Research and Consultation, Institute of Mechanics, Hanoi, Vietnam*

Magnus Larson & Hans Hanson
*Department of Water Resources Engineering, Lund University, Lund, Sweden*

Le Xuan Hoan
*Department of Water Resources Engineering, Lund University, Lund, Sweden*
*Center for Marine Environment, Research and Consultation, Institute of Mechanics, Hanoi, Vietnam*

ABSTRACT: A numerical model of nearshore waves, currents and sediment transport was developed. The wave conditions were calculated by the Modified-EBED model and the surface roller was modeled following the approach of Dally and Brown (1995) with an enhancement of the energy flux term in the alongshore direction. Nearshore currents and wave setup were determined by the depth-averaged momentum equations together with the continuity equation. Sediment transport rates in the offshore and surf zone were modeled based on the formulas of Camenen and Larson (2005) and the advection diffusion equation, whereas the swash zone transport rates were obtained by the formulas of Larson and Wamsley (2007) .The model was validated based on the high-quality data from the Large Scale Sediment Transport Facility (LSTF) at the Coastal and Hydraulics Laboratory, in Vicksburg, U.S. Good agreement between the computations and measurements was obtained regarding the significant wave height, longshore current, and sediment transport. The present model will form the basis for predicting the bathymetric evolution in the nearshore due to waves and currents.

*Keywords*: mathematical modeling, random waves, surface roller, nearshore currents, swash zone, sediment transport.

## 1 INTRODUCTION

A quantitative understanding of nearshore waves, currents, and sediment transport is necessary in coastal engineering projects. Sediment is mobilized and transported under the actions of waves and currents. The gradients in sediment transport cause erosion and deposition, affecting the local bathymetry. Therefore, a reliable and robust model of nearshore waves, currents, and sediment transport is required to effectively predict the beach morphological evolution for the purpose of engineering analysis and design.

There are a number of studies on numerical modeling of nearshore waves, currents, and sediment transport. However, the hydrodynamics and sediment transport processes are highly complex in the nearshore and swash zone. Moreover, the lack of high-quality and synchronized experiment data makes model validation difficult. Therefore, presently there is no general model that can produce reliable predictions to be used in engineering projects for a wide range of conditions.

The objective of the present study was to develop a robust and reliable numerical model of nearshore waves, currents, and sediment transport which can be used in the engineering projects. In order to do this, a multi-frequency-angular random wave transformation model, which was originally developed by Mase (2001), was modified to improve the prediction of wave conditions in the nearshore. The surface roller associated with wave breaking was modeled after Dally and Brown (1995) and Larson and Kraus (2002), which improved the wave forcing due to wave breaking and roller. The nearshore current model was formulated based on the depth-averaged momentum equations and continuity equation. In the present study, we only focus on the wave-induced currents, although the model can be applied to nearshore currents generated by breaking waves, wind, and tides. The swash zone sediment transport was formulated by Larson and Wamsley (2007), and the sediment rates in the nearshore and offshore were calculated by Camenen and Larson (2005) together with the advection-diffusion equation. The model was validated based on the several high-quality data sets from the Large Scale Sediment Transport Facility (LSTF) at the Coastal and Hydraulics Laboratory, in Vicksburg, U.S.

## 2 MODEL DESCRIPTION

### 2.1 *Modified-EBED model*

Mase (2001) developed a random wave transformation model called EBED in which the diffraction term was included in the energy balance equation. The EBED model is stable and can be applied coastal areas containing structures, such as detached breakwaters and groins. However, it typically produces an overestimation of the wave conditions in the surf zone. The main cause of the overestimation is related to the algorithm for calculating the energy dissipation due to wave breaking.

In the present study, a new approach to calculate the energy dissipation was employed after the Dally *et al.* (1985) model. This approach improved the calculation of the energy dissipation due to wave breaking, and the model can produce better description of the wave conditions in the surf zone. The model is referred to as the Modified-EBED model here after.

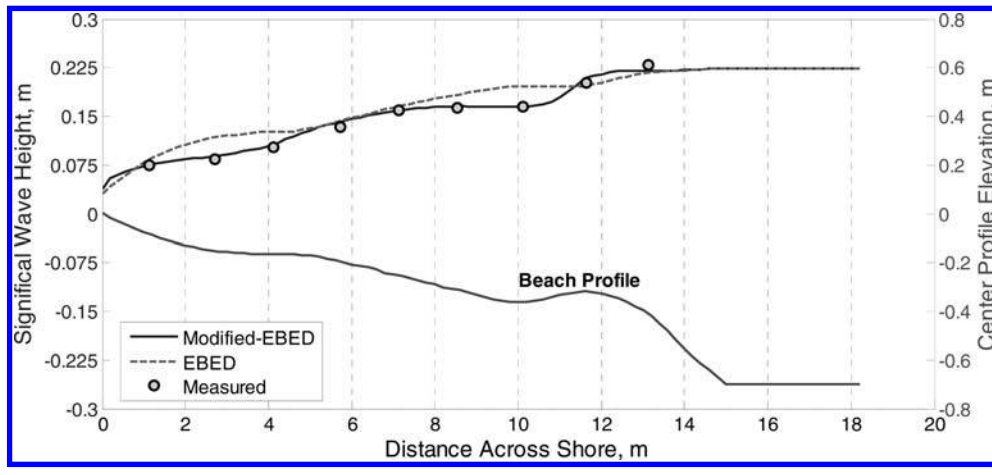


Figure 1. Comparison of calculated significant wave height with measurements, LSTF Base Case 1.

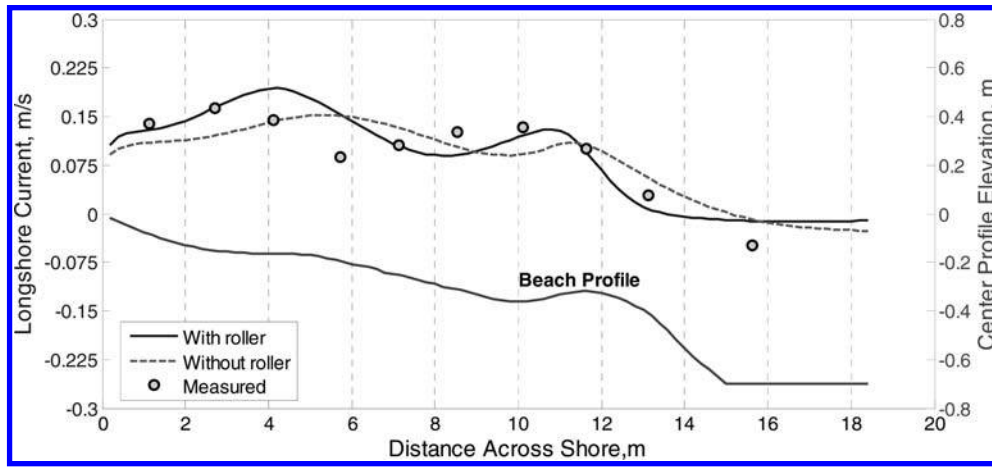


Figure 2. Comparison of calculated longshore current with measurements, LSTF Base Case 1.

### 2.2 *Surface roller model*

Research has demonstrated that the surface roller plays a key role in the generation of nearshore current. However, the surface roller energy is often only considered in the cross-shore direction. In this study, the approaches by Dally and Brown (1995) and Larson and Kraus (2002) were followed, and the energy flux term in the alongshore direction was included in the energy balance equation for the roller.

### 2.3 *Nearshore current model*

In order to extend the model capacity to a variety of conditions, including complex alongshore bathymetry, a general depth-averaged two-dimensional model of nearshore currents generated by breaking waves, wind, and tides was developed. However, the present study only focuses on the wave-induced currents. The wave stresses were derived from the Modified-EBED model, and the surface roller model. With the modification of random wave transformation and the surface roller models, the calculation of the wave stresses was improved, producing more reasonable results on wave-induced currents in the nearshore.

### 2.4 *Sediment transport model*

The sediment transport rate in the swash zone was calculated from Larson and Wamsley (2007). The bed load was determined based on the formula of Camenen and Larson (2005). The suspended load was obtained by solving the advection diffusion equation in which the pick-up and deposition rates were modified, and the boundary condition at the still-water shoreline was given by the calculation of transport rate in the swash zone. The total load, based on the bed load and suspended load by the above method, is referred to as the AD-Lund-CIRP formula here after. The computational results for the sediment transport in the swash and nearshore zones were in good agreement with the measurements for the investigated data sets from LSTF.

## 3 SELECTED RESULTS

Model validation was based on several unique, high-quality laboratory data sets from experiments in the LSTF basin of the Coastal and Hydraulics Laboratory (CHL) in Vicksburg, U.S. (Gravens *et al.*, 2006; and Gravens and Wang, 2007). These data encompassed measured cross-shore variation in significant wave height, longshore current, mean water level, and total flux of sediment in alongshore direction for different wave input and beach conditions. Fig. 1 shows that the significant wave height obtained from Modified-EBED model was in better agreement with measurements than the original EBED model. The computations of longshore current and wave setup with roller agreed well with measurement (Fig. 2 and Fig. 3). The computed longshore sediment flux obtained from AD-Lund-CIRP formula was also in quite good agreement with measurements (Fig. 4).

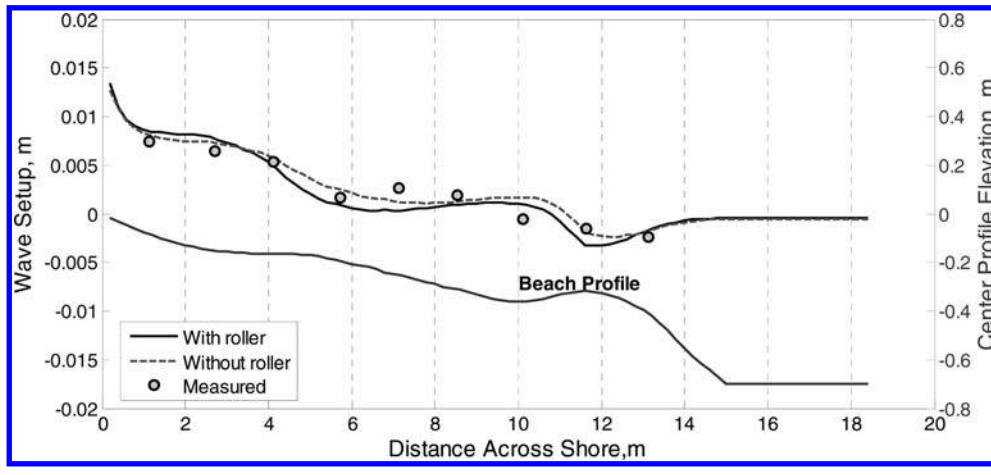


Figure 3. Comparison of calculated wave setup with measurements, LSTF Base Case 1.

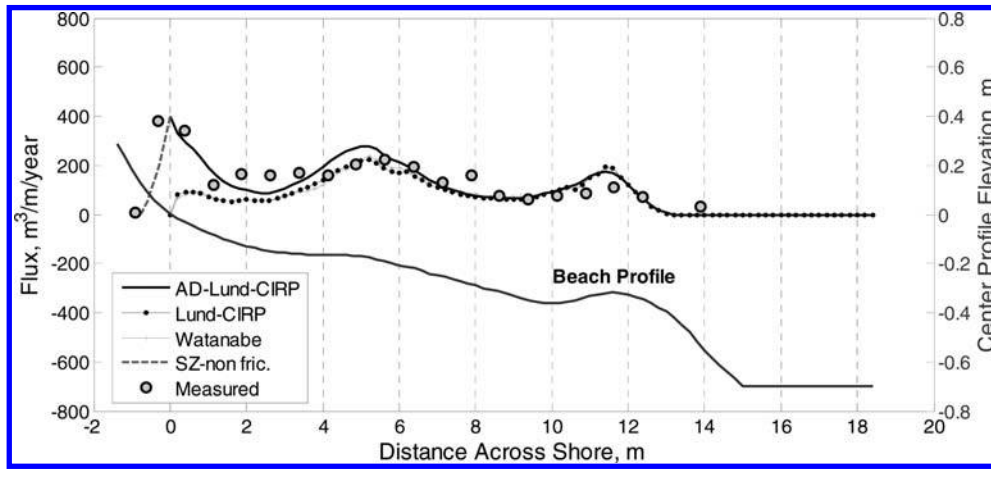


Figure 4. Comparison of calculated longshore sediment flux with measurements, LSTF Base Case 1.

In general, the model can produce satisfactory predictions of the conditions studies. The validation is continuing against other data sets in order to improve the predictive capability of the model.

## REFERENCES


[1] Camenen, B., Larson, M. (2005), "A general formula for non-cohesive bed load sediment transport", Estuarine, Coastal and Shelf Science Vol. 63, pp. 249–260.

[2] Dally, W. R., Dean, R. G., and Dalrymple, R. A. (1985), "Wave height variation across beaches of arbitrary profile", J. Geophys. Res., Vol. 90(C6), PP. 11917–11927.

[3] Dally, W. R., and Brown, C. A. (1995), "A Modeling investigation of the breaking wave roller with application to cross-shore currents", J. Geophys. Res., Vol. 100(C12), PP. 24873–24883.

[4] Gravens, M.B., and Wang, P. (2007), "Data report: Laboratory testing of longshore sand transport by waves and currents; morphology change behind headland structures", *Technical Report*, ERDC/CHL TR-07-8, Coastal and Hydraulics Laboratory, US Army Engineer Research and Development Center, Vicksburg, MS.

[5] Gravens, M.B., Wang, P., Kraus, N.C., and Hanson, H. (2006), "Physical model investigation of morphology development at headland structures" *Proc., 30th Int. Conf. on Coastal Eng. World Scientific Press, San Diego*, pp. 3617–3629.

[6] Larson, M., and Kraus, N.C. (2002), "NMLONG: Numerical model for simulating longshore current; Report 2: Wave-current interaction, roller modeling, and validation of model enhancements", *Technical Report ERDC/CHL TR-02-22*, US Army Engineer Research and Development Center, Vicksburg, MS.

[7] Larson, M., Wamsley, T.V. (2007), "A formula for longshore sediment transport in the swash", *Proceedings Coastal Sediments '07, ASCE, New Orleans*, pp. 1924–1937.

[8] Mase, H. (2001), "Multi-directional random wave transformation model based on energy balance equation", Coastal Engineering Journal, Vol. 43(4), pp. 317–337.

*Environmental Hydraulics – López-Jiménez et al (eds)*
*© 2010 Taylor & Francis Group, London, ISBN 978-0-415-56697-1*

# Application of an integrated sediment transport model at a large gravel bed river – Bridging the gap between measurements and calculations

Bernhard Schober, Michael Tritthart, Marcel Liedermann & Helmut Habersack
*BOKU – University of Natural Resources and Applied Life Sciences / Department of Water, Atmosphere and Environment, Institute of Water Management, Hydrology and Hydraulic Engineering, Vienna, Austria*

ABSTRACT: This paper presents the investigation of bedload transport modeling with an integrated sediment transport model at a four kilometer reach of the Austrian Danube. Various measurements using bedload basket samplers and tracer stones were carried out for the purpose of providing data for direct calibration of the model. For the computation of sediment transport a notation of the Meyer-Peter/Müller equation was used, which included a hiding-exposure correction in order to account for nonuniform sediment transport. A sensitivity analysis of two of the parameters in this formula showed that the hiding-exposure coefficient $\alpha$ strongly influences bedload transport capacities whereas the mobility parameter $\theta_c$ causes mostly shifts in the transported grain sizes. Furthermore, due to its nonuniform formulation the model predicts bedload transport even for low discharges, which is entirely in agreement with measurements. This provides valuable information for further investigations, e.g. for a projected granulometric bed stabilization.

*Keywords*: Sediment transport model, bedload, hiding-exposure coefficient, mobility parameter.

## 1 INTRODUCTION

Today's river engineers are faced with a broad spectrum of challenges occurring in the context of river training and/or river restoration. An integrated view at problems associated with river degradation, geomorphology, habitat structures and draughts demands the consideration of numerous processes like flow pattern, sediment transport, lateral erosion, connectivity between channel and floodplain, etc[1].

For this task, the modeling of flow and sediment transport in rivers has become a powerful and popular tool in estimating the environmental impact of anthropogenic influences[2]. Thus, various numerical models characterized by different dimensionality and degree of sophistication have been developed over time. There are numerous one- and two-dimensional models which were successfully used to predict important river engineering aspects including sediment transport[3].

Although there is a large number of sediment transport models available by now, many uncertainties in the choice of correct parameters still exist. Furthermore, calibration is most often a difficult task due to the lack and/or the great variability of measured values.

Hence, this paper presents how an integrated sediment transport model using direct measurements of bedload as calibration input was successfully applied to estimate sediment transport at the Danube River, a large gravel bed river in Europe, and which of the calibration parameters turned out to be of great sensitivity.

## 2 STUDY REACH

This study focuses on a 48 km long reach of the Danube between Vienna and Bratislava, which is one of the last free flowing sections of the Austrian Danube (see fig. 1). This reach is not impounded and therefore navigation is often limited by shallow water depths during low flow conditions. On the other hand, the Danube River is integral part of the Donau-Auen National Park with its floodplains and side arm systems.

One of the most severe problems arising in this reach of the Danube is the ongoing bed incision of 2 to 3.5 cm/year with increasing tendency. To deal with this problem a bundle of measures has been planned ranging from the adaption of groins to addition of bedload or to the restoration of river banks to a more natural state. The core of the package of measures is a granulometric bed stabilization, which intends to add coarser bed material ($d = 40$–$70$ mm) to the natural bed material ($d_m = 26$ mm). The grain sizes of the added material are still within the natural range but are expected to reduce bedload transport to 10–15% of the current rate[4]. For planning and monitoring of these measures accurate computations of sediment transport are indispensable. Hence, the new integrated sediment transport model iSed[5] was applied to a 4 km section of this reach.

## 3 METHODS

To allow for investigations in sediment transport and morphodynamics the study reach was subjected to numerous measurements, which were regularly carried out from 2006 to 2009. Having this dense set of data, calibration of the numerical sediment transport model was done directly using the measurements.

### 3.1 *Direct measurements*

The river bed topography was surveyed by multi beam scans; banks and floodplains by laser scan data. Sediment grain size distributions of the river bed were obtained from 50 different freeze cores and evaluated for every 10 cm of depth. Suspended

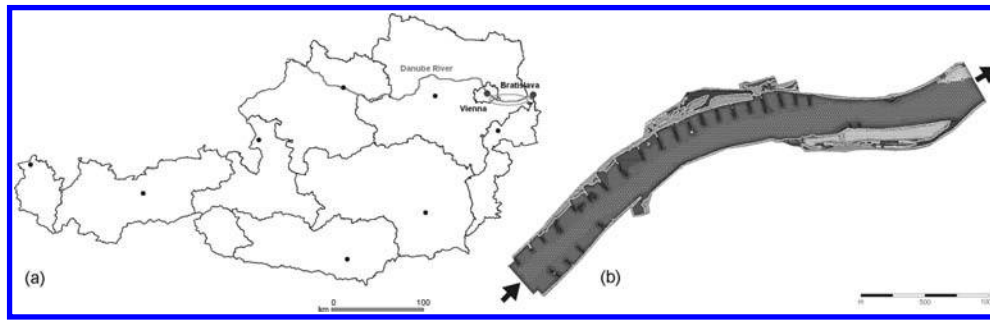


Figure 1. (a) Location of the project reach east of Vienna (Austria); (b) Computation mesh of the test reach.

sediment transport was measured with a US P-61-A point integrating suspended sediment sampler at various cross-sections during several different runoffs. Bedload data was obtained through basket samplers at various discharges. However, as bedload transport is generally subject to a high spatio-temporal variability it was found that bedload transport in this section of the Danube exhibits differences in the measured values of about one order of magnitude for the same discharge. Furthermore, tracer stones of different sizes containing radio transmitters were inserted giving information about incipient motion and transport paths[6].

### 3.2 *Integrated sediment transport model*

For the calculation of sediment transport the new numerical model iSed[5] was applied to the study reach. Basis for the simulation of sediment transport processes is the availability of the flow field, water depths and bed shear stress patterns in the entire computational domain. The iSed sediment transport model does not compute these properties by itself but obtains them from an external 2-D hydrodynamic model which is automatically executed for every time step.

The total sediment transport is split into suspended sediment and bedload. All computations are performed for an unlimited number of sediment size fractions. At the end of every time step, the change in bed levels for every node is obtained from calculating the sediment balance by means of the Exner equation, accounting for multiple sediment layers in the river bed. As erosion and deposition are known for every size fraction, a sorting equation can be evaluated to yield the new grain size distribution for every computation node.

This work focuses on the computation of bedload transport, which can be calculated in iSed with four different empirical bedload transport formulae. For the application at the Danube River the Meyer-Peter/Müller equation was used, including a hiding-exposure correction in order to account for nonuniform sediment transport[2].

$$q_{si} = p_i c_{MP} \sqrt{\frac{\rho_s - \rho}{\rho} g d_i^3} \left[ \left( \frac{d_i}{d_{ref}} \right)^{\alpha} \frac{u^{*2}}{\frac{\rho_s - \rho}{\rho} g d_i} - \theta_c \right]^{\frac{3}{2}} \tag{1}$$

In Eq. 1, $q_{si}$ denotes the bedload transport capacity of the fraction i, $p_i$ the portion of the sediment fraction within the granular structure, $\rho_s$ the sediment density, $\rho$ the density of water, $g$ the gravitational acceleration, $d_i$ the size of the sediment fraction and $d_{ref}$ a reference diameter, selected as $d_{ref} = d_{50}$. The parameter $\theta_c$ denotes the critical mobility, $u^*$ the shear velocity and $\alpha$ is the hiding-exposure coefficient, which must be calibrated. The factor $c_{MP}$ was set equal to 5 instead of 8.

The mobility parameter $\theta_c$ is most often set constant with the commonly known Shields value of 0.047 but it can be calculated for different sediment size fractions from a parameterization of the Shields curve as well. In this context, Shields (1936) derived by means of experimental studies on the basis of a non-dimensional grain diameter $D^*$ (which is determined by the grain diameter $d$, the sediment density $\rho_s$, the density of water $\rho$, the kinematic viscosity of water $\nu$ and the gravitational acceleration $g$) various values of $\theta_c$ for different ranges of $D^*$[2].

## 4 RESULTS

A sensitivity analysis for the hiding-exposure coefficient $\alpha$ and the mobility parameter $\theta_c$ of the Meyer-Peter/Müller formula (1) exhibited a great influence of $\alpha$ on the bedload transport capacity whereas different approaches of estimating $\theta_c$ resulted in a shift in the transported grain sizes.

Transport capacities were calculated for various values of $\alpha$ in the range of 0.2 to 0.5 (see Fig. 2a) and compared to the mean values of several basket-sampler measurements, due to the high spatio-temporal variability of bedload transport in nature. Figure 2a also shows that the results of the computations are highly sensitive to the hiding-exposure coefficient employed. Figure 2b depicts a comparison between the mean values of the measurements of bedload transport capacity and the computed scenarios with different values of $\alpha$. While the general shape of the bedload profiles is reproduced by the numerical model, the exact values are not. However, as bedload transport is generally subject to a high spatio-temporal variability and was found to exhibit a high variation for the same discharge at this section of the Danube River, an exact match could not be expected.

Computations with either a constant mobility parameter $\theta_c$ of 0.047 or a parameterization of the Shields curve for different sediment size fractions did not result in any large changes in bedload transport capacity but indicated a shift in the transported grain sizes (see fig. 3). In the case of the Danube bedload it was found that a constant $\theta_c$ shifted the transported grain sizes to coarser fractions.

Different combinations of the tested parameters showed in comparison with the measurements that the best match was obtained using $\alpha = 0.25$ and a constant $\theta_c = 0.047$. Next, sediment transport was computed for various discharges. In figure 4

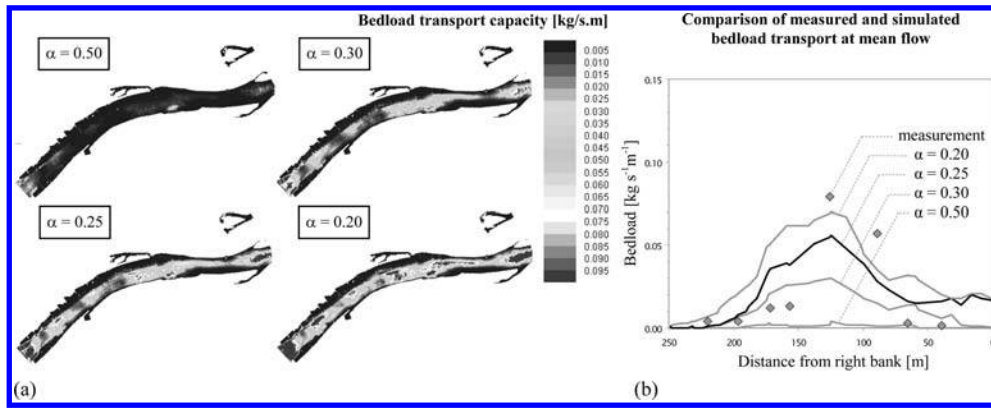


Figure 2. (a) Simulated bedload transport capacities for mean flow (1930 $m^3 s^{-1}$) using different values of the hiding-exposure coefficient $\alpha$, (b) Comparison of measured and simulated sediment transport profiles at mean flow for different values of $\alpha$.

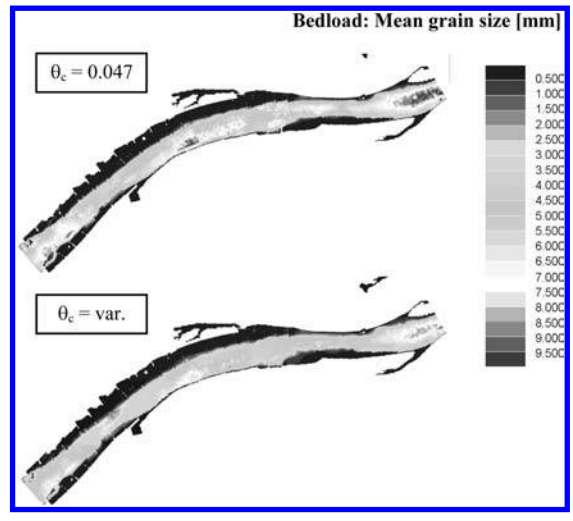


Figure 3. Simulated mean grain size diameters of bedload for mean flow (1930 $m^3 s^{-1}$) using either a constant or a parameterized mobility parameter $\theta_c$ (for $\alpha = 0.25$).

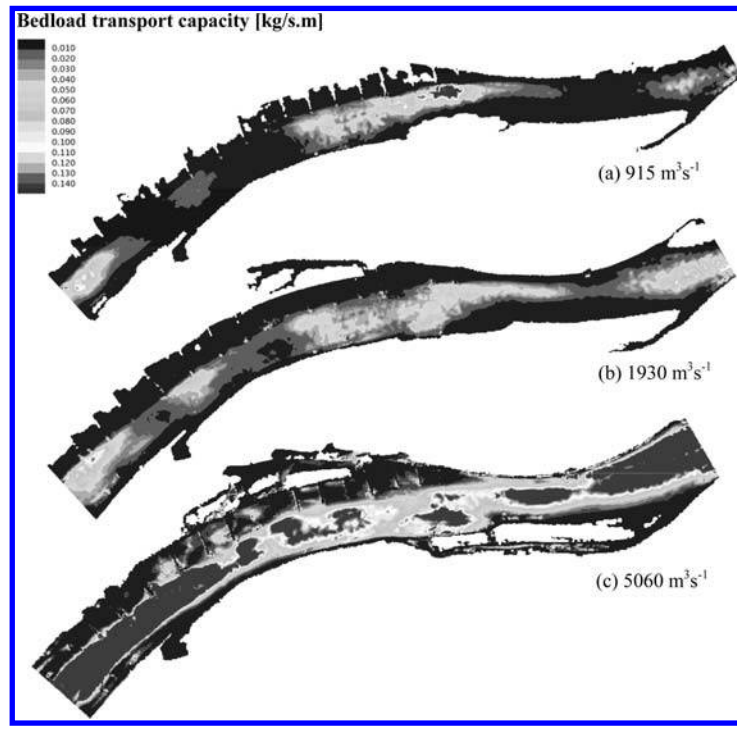


Figure 4. Modeled bedload transport capacity for three discharges; (a) low flow (915 $m^3 s^{-1}$); (b) mean flow (1930 $m^3 s^{-1}$); (c) highest navigable flow (5060 $m^3 s^{-1}$).

the simulated bedload transport capacities for three runoffs ranging from low flow up to highest navigable flow are depicted. Due to the nonuniform formulation of sediment transport, the model predicts bedload transport even for low discharges, which is entirely in agreement with measurements. However, the commonly applied sediment transport relations based on a mean diameter predict incipient motion to take place at discharges higher than mean flow[6],[7], thus consequently underestimating sediment transport at low flow rates.

## 5 CONCLUSIONS

A sensitivity analysis was carried out for the hiding-exposure coefficient $\alpha$ and the mobility parameter $\theta_c$ of the Meyer-Peter/Müller formula (1), whereas $\alpha$ was highly influencing bedload transport capacities and $\theta_c$ was shifting the range of transported grain sizes. The applied nonuniform formulation of sediment transport exhibits bedload transport even for low discharges, which is entirely in agreement with measurements. As a consequence, bedload transport calculations over longer periods (e.g. using hydrographs with a wide range of discharges) must not neglect low and mean flow periods, thus underestimating total bedload transport. This also provides valuable information for further investigations, e.g. for a projected granulometric bed stabilization.

## ACKNOWLEDGEMENTS

This research was carried out in the monitoring task of the Integrated River Engineering Project on the Danube East of Vienna, financed by the European Union, the Austrian Ministry of Transport, Innovation and Technology, and via donau. The authors thank Margit Gerstl and Philipp Gmeiner for participating in the bedload measurements and analysis.

## REFERENCES

[1] Fischer-Antze, T. (2005), *Assessing river bed changes by morphological and numerical analysis*, Doctoral thesis, Vienna University of Technology.
[2] ATV-DVWK (2003), *Feststofftransportmodelle für Fließgewässer*, Report, German Association for Water, Wastewater and Waste, Hennef, Germany.
[3] Zeng, J., Constantinescu, G. and Weber, L. (2008), "A 3D non-hydrostatic model to predict flow and sediment transport in loose-bed channel bend", Journal of Hydraulic Research, Vol. 46, pp. 356–372.
[4] Zottl & Erber (2006), *Flussbauliches Gesamtprojekt östlich von Wien – Generelles Projekt*, Project Report, via donau, Vienna, Austria.
[5] Tritthart, M., Schober, B., Liedermann, M. and Habersack, H. (2009), "Development of an Integrated Sediment Transport Model and its Application to the Danube River", Proceeding for the 33rd *IAHR Congress, Vancouver, 9–14 August*, [in print].
[6] ARGE University of Vienna and BOKU Vienna (2008), *Endbericht Premonitoring 2007 zum Naturversuch Bad Deutsch Altenburg*, Project Report, via donau, Vienna, Austria.
[7] Habersack, H., Nachtnebel, H. and Laronne, J. (2001), "The continuous measurement of bedload discharge in a large alpine gravel bed river", Journal of Hydraulic Research, Vol. 39, pp. 125–133.

*Environmental Hydraulics – López-Jiménez et al (eds)*
*© 2010 Taylor & Francis Group, London, ISBN 978-0-415-56697-1*

# Application of computational fluid dynamics to an investigation of sediment accumulation in the Bondi STP bypass channel

Karen M. Riddette, Edrick K. Lo & Ken J. Wright
*WorleyParsons Services Pty Ltd, North Sydney, Australia*

Jason R. Smith
*Sydney Water Corporation, Australia*

ABSTRACT: This paper examines the application of sediment transport theory to a complex real-world problem, through the use of Computational Fluid Dynamics (CFD) modelling. The Bondi Sewage Treatment Plant (STP) effluent bypass channel is used only for emergency discharge, however the channel has a tendency to accumulate significant volumes of sand and other sediments, compromising the discharge capacity of the channel. The CFD analysis was carried out to gain a greater understanding of the wave processes occurring in the channel, to identify mechanisms for the accumulation of sediments in the bypass channel, and establish a methodology for the assessment of proposed remedial actions. This paper describes the analysis method used to model wave effects in the bypass channel, validation of the model against field data and the criteria developed to examine the effectiveness of potential mitigation options.

*Keywords*: sediment transport, CFD, waves, validation, accretion, erosion.

## 1 INTRODUCTION

### 1.1 *Bondi Sewage Treatment Plant*

The Bondi STP is located to the north of Sydney's iconic Bondi Beach. Most of the plant is located underground, in the high cliff faces typical of Sydney's coastline. From the time when the STP was constructed in the 1950s, treated effluent was discharged through a tunnel which exited at the cliff face below the low tide level. In 1991 the Bondi deep ocean outfall was completed, transporting treated effluent further offshore, and the cliff-face tunnel was modified for use as a bypass channel in the event of an emergency shutdown of the deep ocean outfall.

The bypass channel is a gently sloping unlined rock-excavated tunnel, with a low-level outlet at the cliff face below low tide level (Figure 1). A triangular channel weir is located just downstream of the emergency overflow weir. Larger sediments (rubble debris) have tended to accumulate throughout the tunnel downstream of the triangular weir, while sands have tended to wash beyond the triangular weir and formed a beach-like profile, as seen in the photo at Figure 2. Initial CFD modeling of the channel capacity revealed that the present level of sand accumulation potentially reduced the discharge capacity of the bypass channel by 50%. This was of concern to the operator (Sydney Water Corporation) and required remedial actions to be investigated.

### 1.2 *Rate of sand accumulation*

A series of inspections were carried out between February 2007 (when the previous sand build-up was completely removed) and April 2008. Over this period it was estimated that approximately 100 $m^3$ of sand had accumulated in the area upstream of the channel weir. The earlier inspections showed a greater rate of accumulation than the later ones, indicating a rapid build-up of a 'beach' profile, followed by slower gradual accretion of that profile. The later inspections suggested an accretion rate of approximately 80kg of sand per tide cycle.

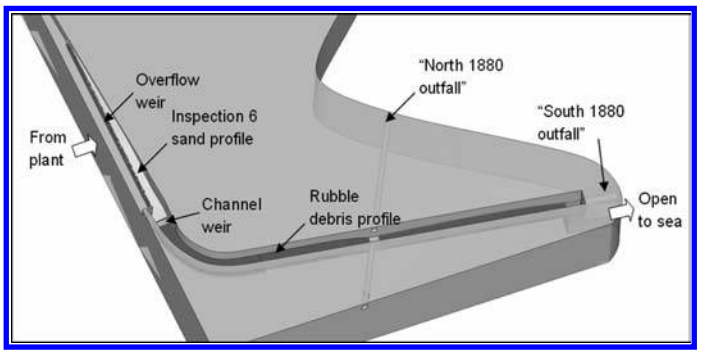


Figure 1. Bypass channel geometry and terminology.

Figure 2. Sand accumulation upstream of the channel weir. The overflow weir can be seen on the left.

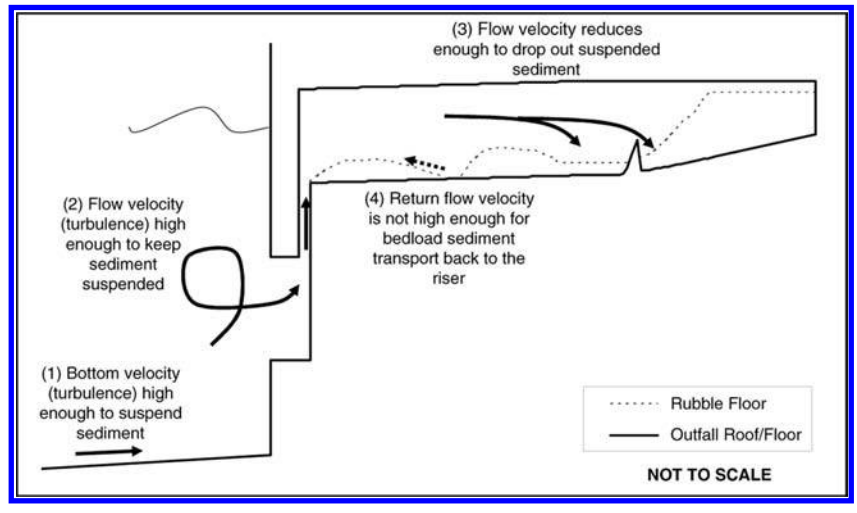


Figure 3. Schematic diagram showing sediment transport processes required to accumulate sediment in the bypass channel (not to scale).

### 1.3 *Sediment types*

During a site visit to the tunnel, several sediment samples were collected. Of particular interest were samples showing the 'beach' comprises angular shell (calcareous) sand particles, rather than the fine rounded silica sands found at the nearby Bondi Beach. Also of interest were large quantities of golf balls, and even larger sediments including construction rubble, steel reinforcement bars and large sandstone blocks over 100mm in diameter.

A journal paper by Field and Roy[1] examined sand transport in the Bondi region. Seismic scanning of the sea-bed showed two significant sand bodies, located in the area immediately adjacent to the outfall. Sediment samples indicated similar properties to the sand found inside the bypass channel.

Since the sand build-up is the key problem associated with the loss of discharge capacity, this sediment type has been examined in the present paper, however the methodology described could be equally applied to the other sediments.

## 2 SEDIMENT TRANSPORT PROCESSES

Sediment transport theory has traditionally been subdivided into bedload (along the floor) and suspended (above the floor) transport. Numerous studies have been carried out to better explain the relationship between the sediment properties, flow conditions and observed data. Readers are referred to Chanson[2] for an excellent summary of the then state of understanding of sediment transport processes.

At the present time, all sediment transport theories remain semi-empirical, with significant variations between the formulations of different researchers.

Figure 3 highlights the key processes required for the bypass channel to accumulate sediments.

### 2.1 *General accretion/Erosion potential*

Research studies of beach sediment transport have shown that the tendency for sediment to undergo accretion or erosion is highly sensitive to the flow conditions. Miles et al[3] found that the concentration of suspended sediment in a wave was an order of magnitude greater than the amount of sediment actually accreted or eroded.

For beaches, researchers have shown that accretion typically occurs under small wave conditions, while erosion is prevalent under large (storm) waves. Ahren and Hands[4] suggested that under a wide range of conditions, the prevalence of accretion or erosion was more sensitive to the outgoing velocity than the incoming velocity. Higher outgoing velocities were more likely to lead to erosive conditions.

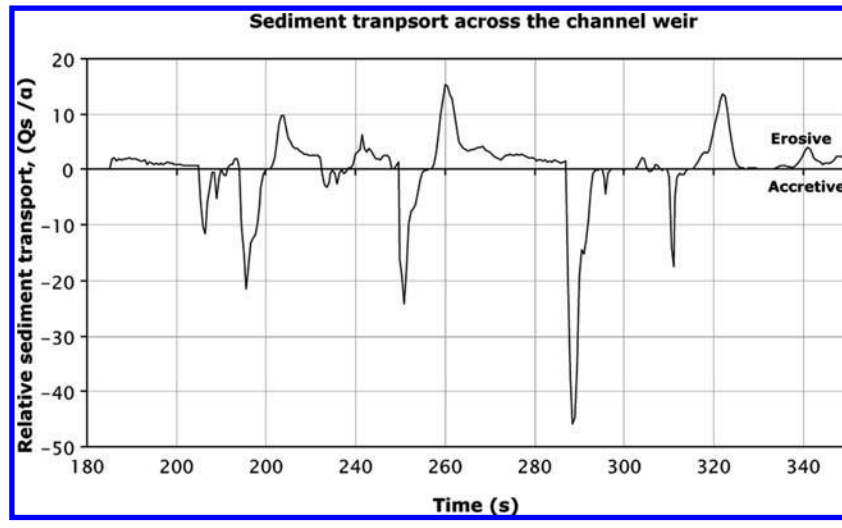


Figure 4. Relative sediment transport rate, $Q_s/\alpha$

The conditions inside the bypass channel may not act like a beach, however it could be expected that conditions that result in higher inflow velocities and lower outflow velocities would be more accretive than those with low inflow and high outflow velocities.

### 2.2 *Quantity of sediment transport*

Empirical correlations for estimating the bedload sediment transport rate have been proposed by a number of researchers. The formulation proposed by Nielsen[5] was used to estimate the rate of sand transport as a function of velocity. It was found that the transport rate is highly dependent on the bottom roughness of the floor, in addition to the sediment properties, but in general the transport rate can be simplified to Equation 1:

$$Q_s = \alpha.V^3 \tag{1}$$

where: $Q_s$ = volume flow rate of sediment
$\alpha$ = scaling factor to allow for sediment properties, channel width and bottom roughness
V = flow velocity near the floor

Due to uncertainties in the value of $\alpha$, only the general trend for the transport to be accretive or erosive was assessed. At a particular location in the channel, the variation of the floor velocity over time can be determined from the CFD analysis. The relative instantaneous sediment transport rate ($Q_s/\alpha$) is then be calculated (shown in Figure 4 for a typical result). The net transport for the total wave train is determined by summing the area under the curve. For the case shown, a positive sum indicates that net erosion is likely, while a negative value implies accretive conditions.

## 3 CFD MODEL SETUP

The CFD model was carried out using FLOW-3D commercial software developed by Flow Science in New Mexico, USA. This software is particularly recognised for its ability to model the free surface using a volume of fluid (VOF) formulation. The geometry was modeled using Rhinoceros, and post-processing carried out using both FLOW-3D and Tecplot. The model geometry is shown in Figure 1 and included the current sand and rubble profiles along the channel.

### 3.1 *Meshing and fluid properties*

The CFD model was subdivided into several mesh blocks of differing sizes to provide a suitable mesh density without causing excessive analysis runtime. A single-fluid model was used, with suitable density and viscosity applied to represent the sea-water, while the air was modeled as a void, with no computation in this region. This formulation is reasonable due to the high ratio of densities between the air and water, although it would not capture any potential air pressure surges which may occur due to wave action.

### 3.2 *Wave boundary*

A wave boundary model was used at the ocean-side boundary to generate the complex wave profiles required to carry out the study. The software allows the addition of up to one hundred linear sinusoidal waves with independent frequency, amplitude and phase angle to be superimposed at a boundary to create a complex profile. The wave profile was generated from the selected characteristic wave trains using a Discrete Fourier Transform algorithm to extract the hundred most dominant frequencies. The software then applies the appropriate boundary velocity, pressure and water surface level values to the mesh boundary cells at each time step. These values are generated using Airy linear wave theory. The wave train was repeated once to allow time for any initial conditions to dissipate, and results were extracted from the second wave train period (Figure 5 shows a sample 3D result).

One limitation of this wave boundary technique is its inability to equalize against excess water in the model. As a result, it was not possible to include the effects of surging flows entering the bypass channel through a secondary opening which allowed flows to enter, but not to escape. When this additional pipe was modeled, the water level in the bypass channel increased

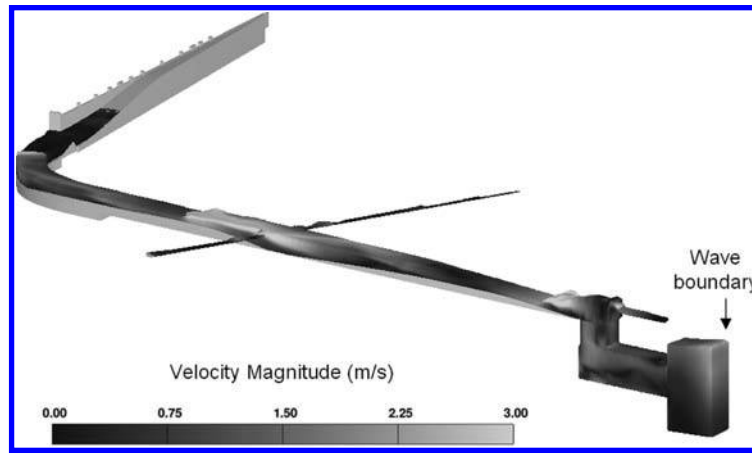


Figure 5. Typical output from CFD model, showing waves moving along the channel.

Table 1. CFD analysis cases

| Case | Wave height | Tide level |
|---|---|---|
| A | Small | Mean Sea Level (MSL) |
| B | Small | Mean High Water (MHW) |
| C | Large | Mean Sea Level (MSL) |

unnaturally and the analysis had to be terminated. For the sediment transport study, the secondary pipe was found to add only a small proportion of the total flow, and was not included in the model.

### 3.3 *Sediment transport model*

Due to the uncertainties associated with the transport of sediment, it was unrealistic to try to directly model sediment transport in the CFD analysis. This type of scour/transport/deposition analysis would be highly computationally intensive (due to the quantity of particles) and would require a prohibitive number of runs to satisfactorily calibrate the model. Instead, the CFD model was used to generate the likely flow conditions inside the channel, and the velocity data was then assessed for its sediment transport potential.

## 4 MODEL VALIDATION

Due to the complexity of the model, it was essential to carry out validation against real-world data to ensure that the CFD model was accurately predicting the flow conditions inside the bypass channel.

### 4.1 *Measured data*

In conjunction with the modeling project, Sydney Water Corporation undertook monitoring of the water level at a location inside the bypass channel over a two-month period. This data could then be compared against the sea level state, available from two offshore Waverider buoys maintained by the NSW Government. The data from both sources was analysed to identify two key wave train profiles representative of small (common) and large (storm) wave conditions. The CFD model was analysed for the three cases shown in Table 1.

### 4.2 *Validation*

Figure 6 compares the measured significant wave height level inside the channel (average hourly data for a month) with those occurring out in the ocean. The ocean waves were assumed to undergo minimal transformation between offshore and the cliff-face. The offshore wave heights were typically 6–10 times greater than those measured inside the bypass channel. This data is overlaid with the three CFD cases, comparing the computed wave heights at the boundary and at a location inside the bypass channel close to the actual monitoring equipment. The data points are differentiated by tide level range.

The results indicate that the CFD model gives a reasonable representation of the actual bypass channel, with a similar order-of-magnitude change in wave height under both small and large wave conditions and good correlation with the measured data.

## 5 ANALYSIS RESULTS

Centreline results were extracted at seven locations throughout the model and included the fluid surface height and near-floor velocity. A series of animations of the wave passage along the channel were also generated. From these results, plots were generated showing the average wave height, average peak velocity under the crest and under the trough (ie, incoming and outgoing velocity – see Figure 7) and the relative net bedload transport for the wave train.

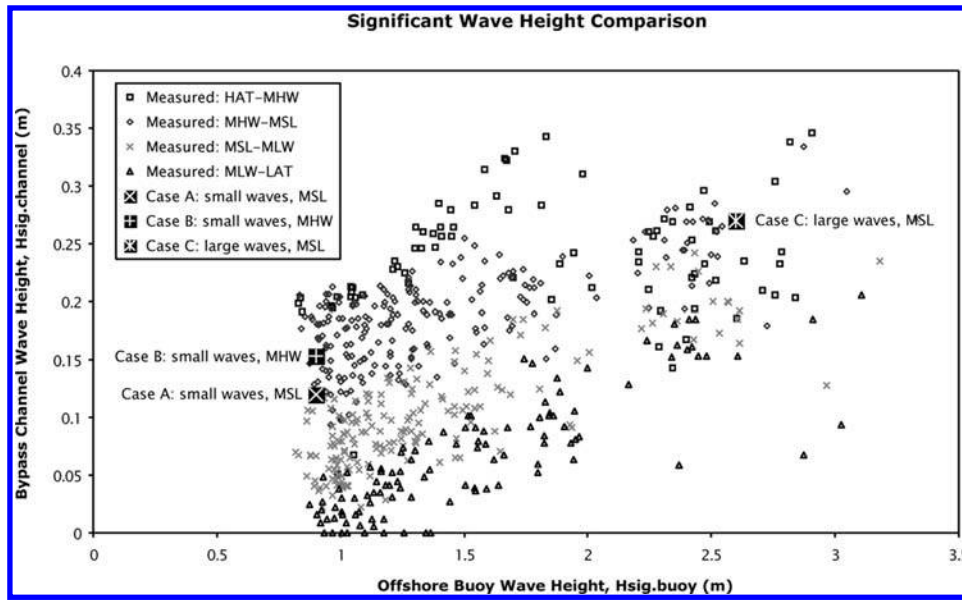


Figure 6. Model validation using wave height comparison.

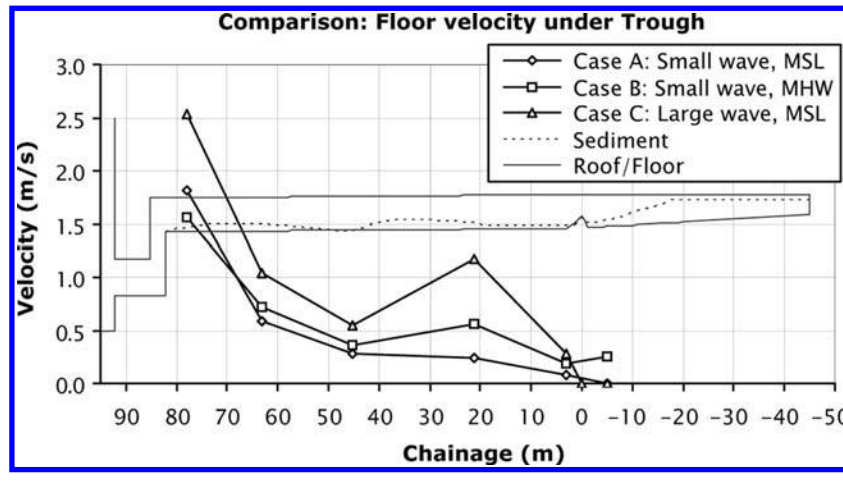


Figure 7. Variation of average peak velocity under the wave trough (outgoing velocity).

The analysis identified the high points of the rubble mounds and the triangular channel weir as key contributors to the sand accumulation problem. These locations trap pools of water behind them, which act to dissipate the energy of waves travelling into the channel, subsequently dropping out any suspended sediments and reducing the strength of the return flows which might have carried the sediments away through bedload transport.

## 6 CONCLUSION

The use of a CFD model to examine the behaviour of the bypass channel allowed Sydney Water Corporation to gain a good understanding of the flow processes involved in the accumulation of sand behind the triangular channel weir. The complex geometry of the riser and weir, together with the presence of rubble debris made the configuration difficult to assess using theoretical models.

The model was found to reasonably reproduce measured results, improving the level of confidence in the model. By assessing the modeled velocity results for potential bedload transport, an understanding of the general accretion / erosion trends throughout the channel was achieved. This method was used for assessing the effectiveness of proposed solutions to the sand accumulation problem.

## REFERENCES

[1] Field, M.E., Roy, P.S. (1984), "Offshore Transport and Sand-Body Formation: Evidence from a Steep, High-energy Shoreface, Southeastern Australia", Journal of Sedimentary Petrology, Vol 54, No 4, pp1292–1302.

[2] Chanson, H (1999), *The Hydraulics of Open Channel Flow an Introduction*, Arnold Publishers, London.

[3] Miles, J., Butt, T., Russell, P. (2006), "Swash Zone Sediment Dynamics: A Comparison of a Dissipative and an Intermediate Beach", International Journal of Marine Geology, Geochemistry and Geophysics, Vol 231, pp181–200.

[4] Ahrens, J.P., Hands, E.B. (1998), "Velocity Parameters for Predicting Cross-Shore Sediment Movement", Journal of Waterway, Port, Coastal, and Ocean Engineering, Vol 124, No 1, pp16–20.

[5] Nielsen, P. (1992), "Coastal bottom boundary layers and sediment transport", *Advanced Series on Ocean Engineering, Vol 4*, World Scientific, Singapore.

*Experimental experiences related to hydraulic models of environmental problems. Models validation*

*Environmental Hydraulics – López-Jiménez et al (eds)*
*© 2010 Taylor & Francis Group, London, ISBN 978-0-415-56697-1*

# Experimental study of a river biofilm growth on artificial cobbles in contrasted flow conditions

F.Y. Moulin, Y. Peltier & C. Pen
*Université de Toulouse, INPT, UPS, IMFT (Institut de Mécanique des Fluides de Toulouse) Toulouse, France*
*CNRS, Toulouse, France*

F. Garabétian
*UMR 5805 EPOC-OASU, Station marine d'Arcachon, Université Bordeaux, Archachon, France*

J. Sanchez-Pérez, S. Sauvage & D. Baqué
*Laboratoire d'Ecologie Fonctionnelle (ECOLAB), UMR 5245 CNRS-UPS-INPT, Castanet-Tolosan, France*

O. Eiff
*Université de Toulouse, INPT, UPS, IMFT (Institut de Mécanique des Fluides de Toulouse) France*
*CNRS, France*

ABSTRACT: Experiments of river biofilm growth in controlled hydrodynamic conditions are performed for a bed of large roughness elements (4 cm diameter artificial cobbles) representative of in situ conditions. Local hydrodynamical conditions are measured by Particle Image Velocimetry (PIV) and interactions between the turbulent boundary layer and the biofilm evolution are investigated. Different biofilm structures are successfully grown for different flow conditions but their impact on local flow parameters are clarified only for very long filaments exceeding the size of the macrorugosities. Sloughing tests were performed for 40 days old biofilms and yield results which support the idea that river biofilms do not resist an increase of friction velocity beyond what they experienced during their growth.

*Keywords*: River biofilm, epilithon, sloughing, flow-biofilm interaction, benthic turbulent boundary layer, biogenic roughness.

## 1 INTRODUCTION

In fluvial ecosystems dominated by fixed biomass at the bottom, the epilithic biofilm, a microbial community mainly composed of algae that grow attached to substrata, must be included in numerical modelling of biogeochemical fluxes. Although it is a phototrophic community that requires light, the flow and the nutrient concentrations are in general the two major factors that control its accrual (see Saravia et al.[1]). The flow forcing generally appears under a parametrized form in an erosion term that limits the biomass accumulation.

In this context, recent studies focusing on the flow near the bed showed how local descriptors were more relevant than vertically integrated flow descriptors such as the discharge Q to describe the impact on biofilm growth (see e.g. Labiod et al.[3]). For fully turbulent river flows near the biofilm, it is appropriate to describe the local flow conditions by the classical log law profile reading

$$\frac{\underline{u}}{u*} = \frac{1}{\kappa}\log\left(\frac{z-d}{z_o}\right) \tag{1}$$

where $\kappa$ is the Karman constant ($\kappa = 0.41$), u* the friction velocity, $z_0$ the roughness length and d the displacement height. The underline symbol indicate time-averaged quantities.

The log-law is satisfied in the so called "inertial sublayer", a region confined to the lower part of the boundary layer, generally defined as $z < 0.1\delta$ in most studies, with $\delta$ the boundary layer thickness (equal to the water depth D for free surface flows in equilibrium). Alternatively, the equivalent roughness height established by Nikuradse, noted $k_s$, can be used instead of $z_0$ (they are related by $k_s \approx 30\ z_0$).

The friction velocity u* measures the drag exerted by the bottom on the flow, and retroactively, is then related to the drag exerted on the biofilm by the flow (at least when the bed is completely and homogeneously covered with a mat of biofilm). During its growth, the biofilm modifies the bottom boundary condition for the turbulent flow and different values of the roughness length $z_0$ are found at different stages (see Labiod et al.[3]). Contradictory evolutions of $z_0$ were found by previous authors for biofilms growing on gravels or small size artificial substrates, enlightening the importance of the displacement height d to obtain accurate measurements of $z_0$. These studies also underlined the complexity of biofilm-flow interactions, with biofilm structures (length of filaments, porosity) adapting to local flow conditions.

In previous studies mostly growth of biofilm on small substrates was considered, and only a few works focused on experiments with larger substrates representative of river beds covered with cobbles (see e.g. Nikora et al. [4]). Therefore, we decided to investigate the growth of epilithic biofilm on large roughness elements and adopted the recent methodology discussed e.g. in Nikora et al.[5] to calculate double-averaged quantities, that have been shown to be more appropriate to describe turbulent canopy-like flows with strong three-dimensional patterns (see e.g. Castro et al.[6]). In the present work, different flow conditions were generated simultaneously in a specially designed indoor hydraulic flume covered with large artificial cobbles (hemispheres) and monitored by PIV measurements.

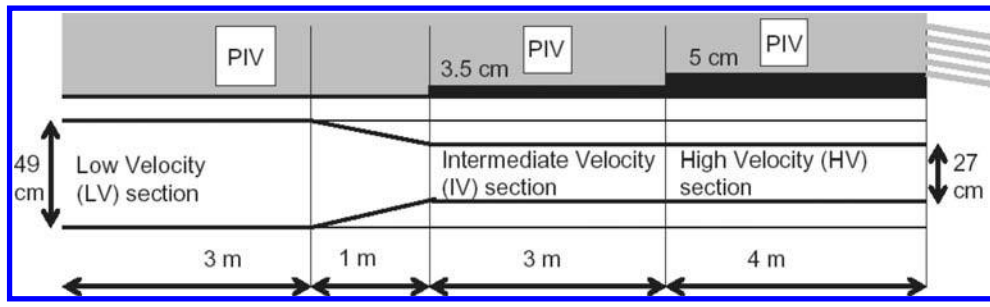


Figure 1. Sketch of the laboratory flume, with locations of the PIV measurement access windows.

## 2 EXPERIMENTAL SET-UP

Experiments of epilithic biofilm – turbulent flow interactions were performed in an 11-m long by 50-cm wide by 20-cm deep laboratory flume, situated on the right bank of the River Garonne at Toulouse, France. The same experimental flume as in Labiod et al.[3] was adapted for the present study to be run using a partially re-circulating system opened in the River Garonne in order to benefit from natural water with no limiting nutrients and natural physico-chemical changes while controlling the hydrodynamical conditions. The flume was supplied with filtered water from the Garonne River with a flow discharge allowing a complete turnover of water in the system every 4 h. Illumination was supplied by six 1.5 m long racks of 5 neon tubes connected to a timer that ensure a photoperiod of 16 hours of day and 8 hours of night. The bottom of the flume was completely covered by artificial cobbles, consisting in 37 mm-diameter and 20 mm in height sand-ballasted polyurethane resin hemispheres. They were regularly and periodically placed on the bottom without any fixation in order to be sampled. Three different flow conditions in the flume were created by modifying the width and the depth of the flume (see Figure 2), in order to obtain bulk velocities of 10, 25 and 45 cm $s^{-1}$ (respectively, in sections noted LV for low velocity, IV for intermediate velocity and HV for high velocity). The Garonne River water was filtered at 1 µm in order to control the water entering the system.

At the beginning of experiments, biofilms taken from a natural river and grown on artificial substrates in a laboratory were used to seed the flume. The dry mass (DM) and the ash-free dry mass (AFDM) biomasses were measured by collecting biofilm covered artificial cobbles. Biological parameters were monitored by regular samplings of the biofilm. Particle Image Velocimetry (PIV) measurements were performed in two vertical planes in the middle of the tank (one longitudinally aligned plane just over the top of the hemispheres, and another one 1 cm apart) in the three different sections. The laser sheet was created by a pulsed Nd:YAG laser system (532 nm, 2 × 30 mJ/pulse), and the images were captured by a Sensicam camera (1280 × 1024 pixels, 12 bits) with resolutions from 75 to 150 pixels/cm. PIV particles were injected upstream the measurement region to improve the quality of images.

After 40 days of growth in the three different flow regions in the second campaign, the resistance to sloughing of the three different cultivated biofilms was investigated by exposing samples to increasing flow velocities in a separate flume: a 20-m long by 21-cm wide by 40-cm deep laboratory flume whose last 12 meters were covered with artificial cobbles. A 10 cm space was left free to place the substrates covered with the 40 days old biofilm, 6 m downstream the beginning of the section covered with artificial cobbles. The friction velocity for different flow discharges was calibrated by PIV measurements. During sloughing tests, samples were exposed to increased discharges from 5 to 30 $Ls^{-1}$ by 5 $Ls^{-1}$ increments every 2 minutes and monitored by a DV camera. Biomasses (DM and AFDM) were measured before (2 samples) and after (2 samples) this sloughing test for biofilms grown in the three sections.

## 3 RESULTS AND DISCUSSION

### 3.1 *Evolution of the log law parameters during biofilm growth*

As shown by Nikora et al.[5], double-averaged quantities, i.e. quantities averaged in the two horizontal directions (noted with brackets $<>_{xy}$ with subscripts indicating the spatial coordinate(s) along which the averaging is performed) must be used to describe intrinsically three-dimensional flows just over the canopy (in the so-called "roughness sublayer"). According to Castro et al.[6] and as confirmed in Florens et al.[7], such double-averaged quantities extend the validity range of the log-law equation (1) towards the top of the roughness, deep inside the roughness sublayer, leading to more robust estimations of the boundary layer parameters u*, $z_0$ and d.

To fit the data with the log-law equation (1), we followed Castro et al.[6] to determine the friction velocity u* from vertical profiles of the turbulent shear stress $<u'w'>_x$: we took the square root of the averaged value of the turbulent shear stress in both the roughness and inertial sublayers. For nude cobbles before the *inoculum*, it corresponded to the region between the top of the hemispheres at z = H and the top of the inertial sublayer, taken as z = 0.1(D-H) where D is the water depth. For biofilm-covered cobbles, algal filaments moved in the camera field, so that the top for the roughness could not be clearly identified like for nude cobbles. Therefore, we used the maximal height reached by the filaments, noted $z_{top}$, as the lower limit of the fitting range of the log-law equation (1). Naturally, with biofilm accrual, this lower limit gradually raised up from 2 cm for the nude cobbles to 3.5 cm for the 28 days old biofilm in the low velocity section. The upper limit of the fitting range was chosen equal to the top of the inertial sublayer at $z = z_{top} + 0.1(D\text{-}z_{top})$. Values of the turbulent boundary layer parameters are given in Table 1, along with the biomass (DM). Corresponding top view images of the biofilm structure in the LV and HV regions are drawn in Figure 2.

The turbulent boundary layer parameters obtained for the artificial cobbles without biofilm are in relatively good agreement with previous works on artificial canopy flows: values of d are close to 0.75H that is widely used to estimate d for log-law profiles over canopies ; values of $k_s$ are all around 1 cm for large aspect ratio flows (i.e. with D = 12 cm), while larger values of $k_s$ and smaller values of d are measured as the confinement increases (D/H = 4 and 3 in the IV and HV regions) like in Bayazit[8].

Table 1. Biomass and flow parameters evolution during biofilm growth in the three different regions.

| Section | Age (days) | DM ($gm^{-2}$) | D (cm) | $z_{top}$ (cm) | u* ($cms^{-1}$) | $z_0$ (cm) | $k_s$ (cm) | D (cm) |
|---|---|---|---|---|---|---|---|---|
| LV | nude | – | 12.8 | 2.0 | 0.85 | 0.0396 | 1.19 | 1.61 |
| | 14 | 35 | 12.2 | 2.5 | 1.13 | 0.0349 | 1.05 | 2.19 |
| | 21 | 66 | 12.8 | 3.0 | 1.23 | 0.0349 | 1.05 | 2.41 |
| | 28 | 96 | 12.8 | 3.5 | 1.01 | 0.0121 | 0.36 | 2.86 |
| IV | nude | – | 8.35 | 2.0 | 2.61 | 0.0491 | 1.47 | 1.52 |
| | 14 | 30 | 8.4 | 2.5 | 2.29 | 0.0196 | 0.589 | 2.02 |
| | 21 | 63 | 8.8 | 2.6 | 2.40 | 0.0245 | 0.735 | 2.05 |
| HV | nude | – | 5.5 | 2.0 | 4.49 | 0.0614 | 1.84 | 1.41 |
| | 14 | 19 | 5.5 | 2.1 | 3.32 | 0.0115 | 0.344 | 1.72 |
| | 28 | 56 | 6.0 | 2.5 | 3.63 | 0.0106 | 0.318 | 1.84 |

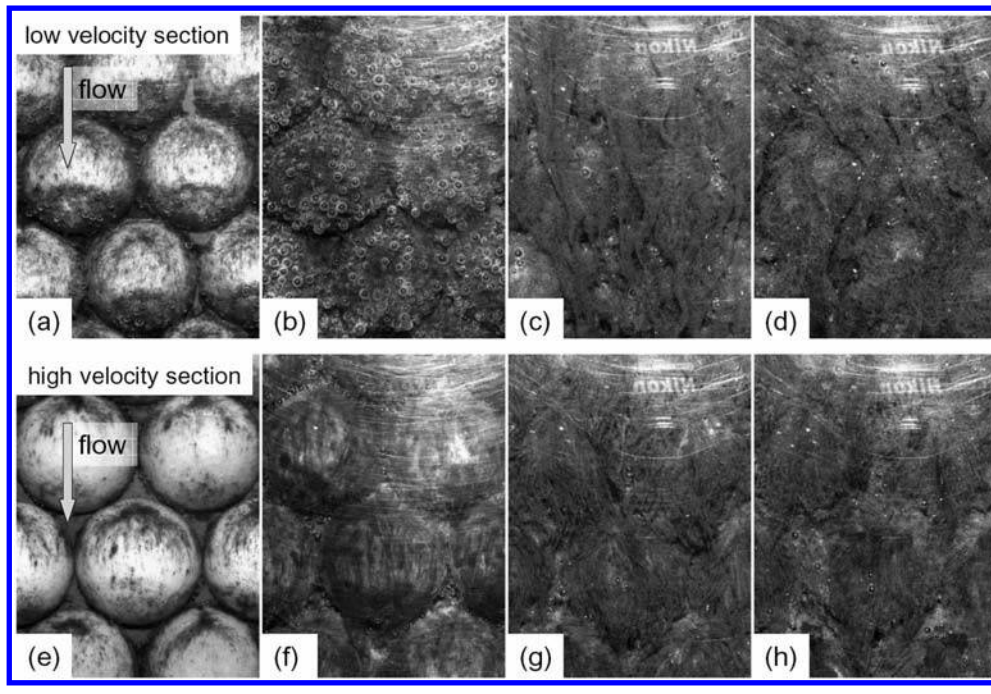


Figure 2. Top view of the epilithic biofilm evolution in the LV and HV sections at (a,e) 8, (b,f) 14, (c,g) 21 and (d,h) 28 days after *innoculum* (flow from top).

For biofilm growing on these artificial cobbles in relatively deep water conditions ($D \approx 12$ cm), no significant modification of the roughness length was observed in the first phase of growth in the LV section, with $k_s$ values remaining initially close to the value found for artificial cobbles without biofilm, i.e. 1 cm. Then, a very clear drop in $k_s$ was measured as soon as long and thick filaments became dominant. In particular, low friction velocity conditions allowed the growth of a porous mat of long filaments that exceeded the initial spatial wavelength prescribed by the artificial cobbles (see Figure 2(d)). By contrast, for biofilm growing in shallow water conditions, a very quick drop in $k_s$ is quickly observed. One difficult point here is the dependence of this parameter with the chosen fitting range for the log-law: the available interval scales as $0.1(D\text{-}z_{top})$ and is then equal to 0.65 and 0.4 cm for IV and HV sections, the lower position being not easily defined. Indeed, the structure of the boundary layer for very confined flows is actually questioned (see Florens et al.[7]) and the large drop in $k_s$ measured in IV and HV sections could be also amplified by a drop of the confinement effect in addition to the smoothening by the biofilm growth.

In the present work, biofilms with different structures were successfully triggered by solely different flow conditions. By contrast with previous studies where the biofilm was grown on small substrates that were quickly covered (see Labiod and al.[2]), fully rough turbulent flows were generated here, and the biofilm was not necessarily covering completely the artificial substrates. As a consequence, competitive contributions from the wake and skin frictions behind cobbles and along algal filaments may explain the complex evolution of the roughness length $z_0$, a quantity that is known to integrate all the processes occurring in the canopy (see e.g. Nikora et al.[5]).

### 3.2 *Sloughing tests*

After 40 days, four large samples (12 artificial cobbles fixed on a PVC plate) were collected in each section, two of them being exposed to increasing flow conditions in the sloughing test flume (u* up to 6.36 $cms^{-1}$). Biomass measurements for samples without and with sloughing test are given in table 2. Sloughing occurs almost as soon as the friction velocity value exceeds the time-averaged value in the considered growth section. A part of the biofilm strongly attached to the artificial cobbles always remains on it while a part composed of filaments is taken away by the flow.

Table 2. Biomass loss during sloughing test after exposure to a 6.36 $cms^{-1}$ friction velocity turbulent layer flow.

| Flume section | u* ($cms^{-1}$) during growth | DM ($gm^{-2}$) without sloughing | DM ($gm^{-2}$) after sloughing | Detached proportion |
|---|---|---|---|---|
| LV | 1.0 | 121.4 | 57.9 | 52% |
| IV | 2.5 | 100 | 70.7 | 29% |
| HV | 4.0 | 104.5 | 93.5 | 11% |

## 4 CONCLUSION

In this experimental work, we confirm that the biofilm growth on large substrates lead to a complex evolution of the hydrodynamic parameters of the turbulent boundary layer. Moreover, we put in evidence how different growth flow conditions yield different river biofilm structure and mechanical resistance, and how these characteristics are poorly correlated with the biomass indicator used here (DM or AFDM): almost similar biomass amounts at the end of the growth experiment behave very differently when they undergo a strong increase of the local flow drag (yielding from 10% to 50% of biomass loss). This latter result gives a new light on the role of the catastrophic detachment term associated with floods in the predictive equation of Uehlinger[2] for biofilm evolution and raises questions about the relevancy of single descriptor modelling of the biofilm growth in rivers and streams.

## REFERENCES


[1] Saravia L. A., Momo F. and Boffi Lissin L. D. (1998), "Modelling periphyton dynamics in running water". Ecological Modelling, Vol. 114, 35–47.

[2] Uehlinger, U., H. Bürher and P. Reichert (1996). "Periphyton dynamics in a floodprone préalpine river: evaluation of significant processes by modelling". Freshwater Biology 36: 249–263.

[3] Labiod C., Godillot R. and Caussade B. (2007), "The relationship between stream periphyton dynamics and near-bed turbulence in rough open-channel flow". Ecological Modelling, Vol. 209, pp. 78–96.

[4] Nikora V.I., Goring D.G. and Biggs B. J. F. (2002), "Some observations of the effects of micro-organisms growing on the bed of an open channel on the turbulence properties". Journal of Fluid Mechanics, Vol. 450, pp. 317–341.

[5] Nikora V., McEwan I., McLean S., Coleman S., Pokrajac D. and Walters R. (2007), "Double-averaging Concept for rough-Bed Open-Channel and overland flows: theorical background". Journal of Hydraulic Engineering, Vol. 133(8), pp. 873–883.

[6] Castro I. P., Cheng H. and Reynolds R. (2006), "Turbulence over urban-type roughness: deductions from wind-tunnel measurements". Boundary-Layer Meteorology, Vol. 118(1), pp. 109–131.

[7] Florens E., Eiff O., Moulin F.Y. (2009), "Impact of water depth confinement on turbulent channel flows over rough wall". Submitted to the international Workshop on Environmental Hydraulics, IWEH 2009.

[8] Bayazit M. (1976), "Free surface flow in a channel of large relative roughness". Journal of Hydraulic Research, Vol. 14, pp. 115–126.

*Environmental Hydraulics – López-Jiménez et al (eds)*
*© 2010 Taylor & Francis Group, London, ISBN 978-0-415-56697-1*

# Experimental study of the benthic boundary layer above a bed of shells

F.Y. Moulin, K. Mülleners & C. Bourg
*Université de Toulouse; INPT, UPS; IMFT (Institut de Mécanique des Fluides de Toulouse), Toulouse, France*
*CNRS: IMFT, Toulouse, France*

ABSTRACT: Turbulent boundary layers over shell molds, representative of some biogenic roughness elements, are investigated experimentally in an open channel flow using Particle Image Velocimetry (PIV) technique. Three different roughness distributions of Crepidula Fornicata shells are studied with frontal densities $\lambda_f = 0.05$, 0.12 and 0.24 representative of in situ configurations. Parameters of the log-law profile are extracted from double-averaged profiles of the Reynolds stress and the streamline velocity and compare well with predictions for urban-like canopies. Measurements inside the canopy are used to estimate an exchange velocity that controls the exchanges between the canopy and the free flow above.

*Keywords*: Benthic turbulent boundary layer, biogenic roughness, transport, exchange.

## 1 INTRODUCTION

The near-bottom boundary layer over rough surfaces has been already studied in a very wide range of contexts (see e.g. Jiménez [1] for a recent review). In the lower part of the boundary layer, an inertial sublayer (IS) exists where the classical log-law profile is found for the mean streamwise velocity $\underline{u}$ (time-averaged quantities are noted here with an underline). This IS begins at the top of the so-called roughness sublayer (RS), a region of the flow where time-averaged quantities are still dependant of the roughness distribution on the bed. This roughness sublayer includes the canopy itself, defined as the region below the top of the roughness elements. The log-law profile in the IS reads

$$\frac{u}{u*} = \frac{1}{\kappa} \log \frac{z - d}{z_o} \tag{1}$$

where $\kappa$ is the Karman constant ($\kappa = 0.41$), d is the displacement height, $z_0$ the roughness length and u* the friction velocity related to the drag exerted on the flow by the bottom ($\tau = \rho u*^2$ with $\rho$ the fluid density).

In the roughness sublayer, double-averaged quantities have been introduced by previous authors (see e.g. Nikora et al.[2] for river flows), noted $<>_{xy}$ and obtained by performing an horizontal spatial averaging of mean quantities. With these new quantities, log-law profiles were found to extend beyond the lower boundary of the classical IS, deep inside the upper part of the RS (above the canopy where drag occurs, see Cheng and Castro[3])

Attempts have been also made to infer the transport of matter (dissolved or in suspension) between the canopy and the flow above from purely hydrodynamical descriptions of the canopy flow and the log-law above (see Bentham and Britter[4]). This latter issue is of great importance for organisms living at the bottom of seas and rivers, since their growth is directly related to the flow ability to provide them with nutrients and/or oxygen, among other substances. In this context, the modelling of biological activity in aquatic ecosystems requires simple parametrization of the transport properties that could take the form of this exchange velocity $U_E$.

## 2 EXPERIMENTAL SET-UP

### 2.1 *Hydraulic flumes and bed roughness*

Three experiments were performed in a 20 m long, 21 cm wide hydraulic flume (called small flume). An aluminium grid was placed at the upstream end to tranquilize the flow entering the flume. The water depth was controlled by an end-valve, and the measurements were performed 10 m downstream of the channel entrance. Another experiment was performed in a 18 m long, 110 cm wide hydraulic flume (called large flume). Eight representative chains of *Crepidula Fornicata* of average height H = 3.2 cm were collected, dried and used to produce plastic molds (see Moulin et al.[5] for dimensions and Figure 1(a) for a picture of a typical mold) attached at the bottom of the small flume in three different regular configurations with frontal densities $\lambda_f$ (as defined by McDonald[6]) equal to 0.05 (experiment A), 0.12 (experiment B) and 0.24 (experiment C) (see Figure 1(b) for a sketch of the three configurations). In the experiment in the large flume (experiment B'), the eight different chains were used and yield frontal density $\lambda_f$ equal to 0.12. In the small flume, identical external flow conditions were chosen for the experiments presented here, with a water depth D = 30 cm in the measurement section and a discharge $Q = 20\,Ls^{-1}$. The experiment in the large flume was performed with a water depth D = 29 cm and a discharge $Q = 80\,Ls^{-1}$.

### 2.2 *PIV measurements*

Velocity measurements were carried out using a Particle Image Velocimetry (PIV) technique in different vertical planes across the width of the channel, every 2.5 cm in the transverse direction y, in order to perform double-averaging and extract vertical profiles of the streamwise velocity $<\underline{u}>_{xy}$ and Reynolds tensor $<\underline{u'w'}>_{xy}$. Hollow glass spheres with a diameter of 12 µm (DANTEC dynamics) were used as PIV tracers and illuminated by a Quantel Twin Ultra double pulsed Nd:YAG laser system (532 nm, 2 × 30 mJ). A set of optics was minutely adjusted in order to generate a laser sheet and have it cross vertically the free

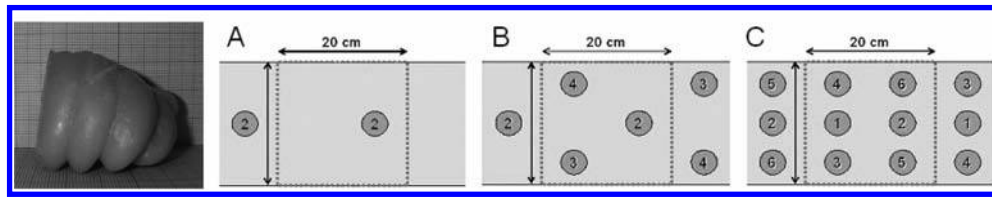


Figure 1. Typical crepidula fornicata mold and the three different mold distributions A, B and C.

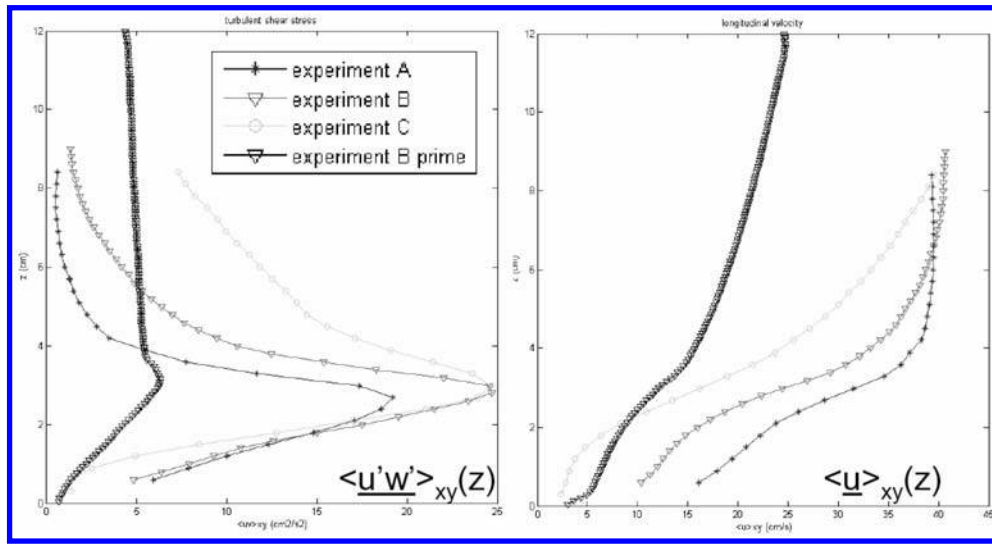


Figure 2. Profiles of the double-averaged turbulent stress $\langle u'w' \rangle_{xy}$ (left) and streamwise velocity $\langle u \rangle_{xy}$ (right).

surface of the flow through a thin boat-like glass window. PIV image pairs were captured by a PCO 2000 camera (2048 × 2048 CCD camera with a 14 bites dynamical range).

The PIV calculations were performed using the algorithms of Fincham and Spedding[7] and Fincham and Delerce[8], with image pre-processing and PIV algorithm parameters allowing spatial resolutions up to 0.2 cm with low peak locking and high correlations. Sequences of around 1000 image pairs were treated and time-averaged to extract reliable estimations of the mean streamwise $\underline{u}$ and Reynolds stress $\underline{u'w'}$.

## 3 RESULTS AND DISCUSSION

### 3.1 *Parameters of the log-law for increasing shell densities*

In figure 2 are plotted vertical profiles of the non-dimensional streamwise velocity $\langle \underline{u} \rangle_{xy}$ and turbulent stress $\langle \underline{u'w'} \rangle_{xy}$. Indeed, below the top of the shells, the double-averaging procedure is done with available experimental data that do not include parts of the flow hidden by the first shell in the camera field. Nevertheless, such profiles are complete to describe the flow in the roughness sublayer above the canopy, and provide still valuable information on the flow in the canopy. As expected, an increase in shell frontal density $\lambda_f$ leads to a strong deceleration of the flow in the canopy for identical external flow conditions, as shown by the profiles of $\langle \underline{u} \rangle_{xy}$ for experiments A,B and C in Figure 2.

Above the shells, competition between the bottom and side-wall boundary layers in the small flume leads to very limited linear portions of the turbulent stress tensor $\langle \underline{u'w'} \rangle_{xy}$ (see figure 2), especially for experiment A. The situation is far better in experiment B' in the wide flume: the bottom boundary layer is well developed and not constrained by the side walls. This vertical confinement of the bottom boundary layer in experiments A, B and C leads to relatively large uncertainties in the determination of u* from $\langle \underline{u'w'} \rangle_{xy}$ profiles. Following Cheng and Castro[3], we determined the top of the roughness sublayer and defined the inertial sublayer as a region where $\langle \underline{u'w'} \rangle_{xy}$ do not decrease below 95% of its value at the top of the roughness sublayer.

Values of the roughness length $z_0$ and the displacement height d were extracted by fitting the streamwise velocity profiles $\langle \underline{u} \rangle_{xy}$ with the log law equation (1) on both the roughness and inertial sublayers. Different methods are available to estimate the friction velocity u* from the turbulent stress profiles $\langle \underline{u'w'} \rangle_{xy}$ (see Florens et al.[9]), but due to the secondary circulations, the most consistent results were obtained using the maximal value of $\langle \underline{u'w'} \rangle_{xy}^{½}$ as an estimate for u*. Values of the parameters describing the boundary layer in the four experiments obtained with this definition of u* are given in Table 1.

The values for the boundary layer parameters we found in these experiments with shells are in relatively good agreement with those found by McDonald[6] for equivalent urban canopies. However, we obtain values of d/H larger than him, probably because of different values of the planar density $\lambda_p$ in our experiments and smoother shapes of the obstacles that yield a porosity function (see Nikora et al.[2]) increasing with z in the canopy region. The most striking fact is the absence of the local maximal value for $z_0$ found by McDonald[6] for $\lambda_f$ around 0.12 for cubes: the progressive disappearance of sweeping and ejection events for $\lambda_f$ above this critical value invoked by previous authors to explain the bell curve of $z_0$ with $\lambda_f$ is probably threshold towards larger values or even suppressed for shell-like roughness (for which complete obstruction is not possible as for cubes).

Table 1. Turbulent boundary layer parameters deduced from PIV measurements of <u> and <u'w'>.

| Exp | $\lambda_f$ | H (cm) | $z_{IS}$ (cm) | u* | $z_0/H$ | d/H | $u_H/u^*$ | $\alpha$ | $u_C/u^*$ | $u_E/u^*$ |
|---|---|---|---|---|---|---|---|---|---|---|
| A | 0.047 | 3.20 | 4 | 4.38 | 0.0272 | 0.38 | 7.90 | 1.0 | 5.4 | 0.26 |
| B | 0.122 | 3.23 | 4.2 | 4.84 | 0.0429 | 0.59 | 5.56 | 1.45 | 3.5 | 0.21 |
| B' | 0.120 | 3.16 | 8.0 | 2.27 | 0.0455 | 0.51 | 5.74 | 1.08 | | |
| C | 0.24 | 3.33 | 5.4 | 4.96 | 0.075 | 0.63 | 3.81 | 2.37 | 1.9 | 0.17 |

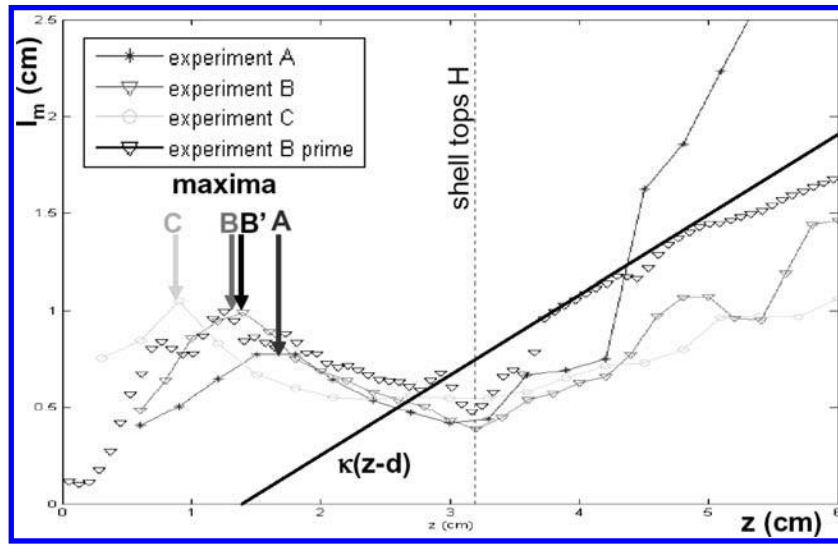


Figure 3. Vertical profiles of the mixing length $l_m$ inferred from double-averaged quantities.

### 3.2 *Flow characteristics in the canopy*

In the canopy region, profiles exhibit an exponential behaviour already observed by McDonald[6] for urban canopies. The velocity profiles can then be fitted by an exponential law with a non-dimensional exponential factor $\alpha$ that depends on the frontal density and describes the decay of the streamwise velocity inside the canopy region. Values of $\alpha$ and $u_H/u^*$, the non-dimensional streamwise velocity at the top of the canopy, are given in Table 1. As expected, a slight increase of $\alpha$ is observed for increasing values of $\lambda_f$ and our values are in good agreement with those found by McDonald[6] for equivalent urban canopies.

With double-averaged quantities, the classical definition of the mixing length $l_m$ can be extended to the whole roughness sublayer. The knowledge of the mixing length $l_m$ inside the canopy, when combined with a parametrization of the drag vertical distribution (using for instance a wake drag coefficient $C_d$), leads to a complete 1D vertical description of the turbulent boundary layer. For the shells used in the present study, the vertical profiles of $l_m$ plotted in Figure 3 clearly take a bell shape with a local maximum of $l_m$ found at midway from the top. This behaviour is relatively different from the constant $l_m$ models developed by some authors to predict the values of $z_0$ in urban canopies. In our experiments, we also observe a slight translation and increase of this $l_m$ maximum towards smaller values of z as $\lambda_f$ increases.

### 3.3 *Exchange velocity between the canopy and the free stream*

In the conceptual model of Bentham and Britter[4], the canopy is considered as a region of strong mixing for passive tracers, filled with a relatively homogenous concentration $C_C$. Then, the vertical flux of tracers $\Phi_{tracer}$ from the canopy region to the flow above is written as $\Phi_{tracer} = U_E(C_{ref}\text{-}C_C)$, where $C_{ref}$ is a reference concentration in the flow above and $U_E$ is the so-called exchange velocity. For flows with turbulent Schmidt number equal to unity, this exchange velocity $U_E$ is controlled by turbulent eddies and appears also explicitly in the vertical flux of horizontal momentum $\Phi_U$ between the canopy and the flow above, that reads $\Phi_U = U_E(U_{ref}\text{-}U_C)$ where $U_{ref}$ and $U_C$ are now respectively a reference velocity in the flow above and a mean velocity in the canopy. $U_C$ is defined as the square root of the mean value of $U^2$ in the canopy since the momentum exchange is related to the drag. In Bentham and Britter[4], $z = 2.5H$ is adopted as a reference level to calculate $U_{ref}$ and $C_{ref}$.

Measurements of the turbulent Schmidt number for our beds of shells (see Moulin et al.[10]) have shown that values are close to unity in the roughness sublayer and above, supporting the exchange velocity concept. Values of $U_E$ were estimated by their method in our experiments with shells and are given in Table 1. They compare reasonably well with those obtained by Bentham and Britter[4] and Hamlyn and Britter[11], and decreases slowly as the frontal density $\lambda_f$ increases.

## 4 CONCLUSION AND PERSPECTIVES

Turbulent boundary layers over shells, here *Crepidula Fornicata* shells, clearly exhibit characteristics very similar to those of urban-like canopies. An exponential decay of the velocity field below the top of the shells is confirmed. However, the evolution of the roughness length $z_0$ and the displacement height d is qualitatively different (see e.g. McDonald[6]): no local maximum of $z_0$ was observed, raising questions about the existence of this feature of urban canopies. For the transport of nutrients and oxygen between the canopy and the free flow that is an important issue in the description of benthic ecosystems, a useful and relatively simple parametrization is proposed, based upon the exchange velocity concept developed by Bentham and Britter[4].

REFERENCES


[1] Jiménez J. (2004), “Turbulent flows over rough walls”, Annu. Rev. Fluid Mech, Vol. 36, pp. 173–96.

[2] Nikora V., McEwan I., McLean S., Coleman S., Pokrajac D. and Walters R. (2007), “Double-averaging Concept for rough-Bed Open-Channel and overland flows: theorical background”. Journal of Hydraulic Engineering, Vol. 133(8), pp. 873–883.

[3] Cheng H. and Castro I.P. (2002), “Near wall flow over urban-like roughness”. Bound. Layer Meteorol., Vol. 104, pp. 229–259.

[4] Bentham T., Britter R. (2003), “Spatially averaged flow within obstacle arrays”, Atmos. Environ., Vol. 37, pp. 115–125.

[5] Moulin F.Y., Guizien K., Thouzeau G., Chapalain G., Mülleners K. and Bourg C. (2007), “Impact of an invasive species, Crepidula fornicata, on the hydrodynamics and transport properties of the benthic boundary layer”. Aquatic Living Resources, 20: 15–31.

[6] McDonald R.W. (2000), “Modelling the mean velocity profile in the urban canopy layer”. Bound. Layer Meteorol., Vol. 97, pp. 25–45.

[7] Fincham A.M. and Spedding G.R. (1997), “Low cost, high resolution DPIV for measurement of turbulent flow”. Experiments in Fluids, Vol. 23, pp. 449–462.

[8] Fincham A. and Delerce G. (2000), “Advanced optimization of correlation imagin velocimetry algorithms”, Experiments in Fluids, Vol. 29, S013–S022.

[9] Florens E., Eiff O., Moulin F.Y. (2009), “Impact of water depth confinement on turbulent channel flows over rough wall”. Submitted to the international Workshop on Environmental Hydraulics, IWEH 2009.

[10] Moulin, F.Y., Mülleners K., Bourg C., Cazin S. (2008), “Experimental study of the impact of biogenic macrorugosities on the benthic boundary layer”, *Advances in Hydro-Science and Engineering (Proceedings of the 8th International Conferenceon Hydro-Science and Engineering, Nagoya University, Japan, September 9–12 2008)*, Vol. VIII, pp.736–746.

[11] Hamlyn D. and Britter R. (2005), “A numerical study of the flow field and exchange processes within a canopy of urban-type roughness”. Atmos. Environ., Vol. 39, pp. 3243–3254.

*Environmental Hydraulics – López-Jiménez et al (eds)*
*© 2010 Taylor & Francis Group, London, ISBN 978-0-415-56697-1*

# Environment friendly structures named Bandalling for river bank erosion protection

Md. Lutfor Rahman
*Department of Civil Engineering (Ph.D. Student), Dhaka University of Engineering and Technology, Gazipur, Bangladesh*

B.C. Basak & Md. Showkat Osman
*Department of Civil Engineering, Dhaka University of Engineering and Technology, Gazipur, Bangladesh*

ABSTRACT: An experimental investigation was conducted in the mobile bed river at the laboratory of River Research Institute, Faridpur, Bangladesh. A series of test runs were completed for the different scenarios using Bandalling for the river bank erosion protection. The low cost Bandalling structures are placed at the laboratory river bank at an angle 40 degree with flowing water direction for its spacing 2 times the length. It was observed that water flow diverted towards the main river due to Bandals resulting maximum velocity accumulated at the centre of the river whereas comparatively less velocity appeared near the river bank where Bandals are placed resulting sediment deposition. The sedimentation near the river bank as well as river bed erosion at the main channel of the river gives an indication that the Bandalling structures can be used successfully for the river bank erosion protection.

*Keywords*: Bandalling, Velocity, Erosion, Laboratory

## 1 INTRODUCTION

### 1.1 *Brief description of bandalling structure*

Bandals are one of the local low cost structures and there is an opening below bandal while obstruct flow near the water surface and allow it to pass near the riverbed. Bandals are positioned at an angle with the direction of flowing water. Naturally available materials such as bamboo and timber are used for bandals. The surface current is being forced from upstream side of the bandals and pushed it down near the bed towards bank at the down streamside. More sediment flow than water flowing towards the bank from the river side so that excess sediment deposited near the riverbank. There is a considerable pressure difference between the upstream and downstream side of the bandal. Much sediment is supplied towards the countryside and relatively much water is transported to the riverside. More water flows with little sediment moves towards the main channel that develop deeper navigational channels there. So the effect of bandals is to shift the sediment transport partially to countryside as because the flow partially diverted to the riverside. The bottom flow is directed perpendicular to bandal. The reduced flows passing through the opening of bandals are not sufficient to transport all the sediment resulting sedimentation over there (bank side) & river bank erosion is protected.The working principles of bandals are showed in Figure 1.The bandals are made of bamboo & placed with the angles of flow direction.

### 1.2 *Literature review*

Efficient and potentially affordable solutions to the problem of bank erosion have been developed and tested in the FAP (Flood Action Plan) 21/22 “Bank Protection and River Training/Active Flood Plain Management (AFMP) Pilot Project”. The FAP 21 component dealt with structures to stabilize banks, where as FAP 22 component dealt more generally with measures and strategies to train the river channels and, at the same time , to increase or to maintain the hydraulic efficiency of the river in transporting water and sediments in combination with an optimum use of the flood plains. The performances of the bank protection structures and the recurrent measures, as well as the response of the river, have been monitored for several years,

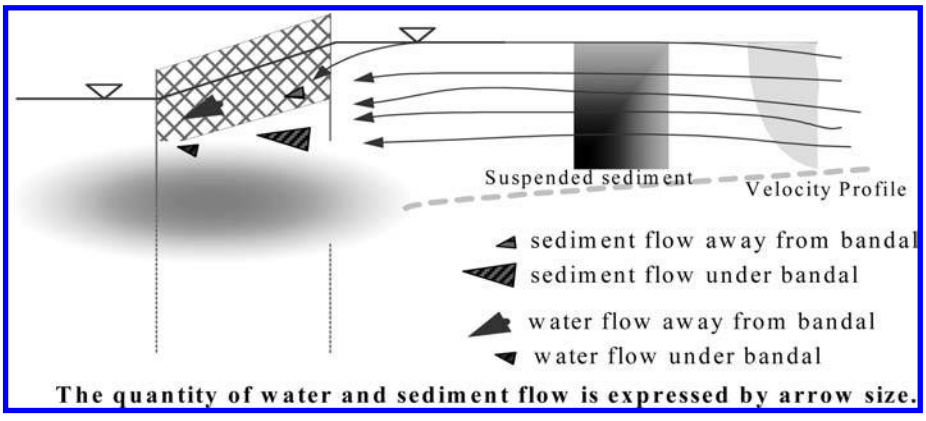


Figure 1. Working principles of bandals.

Table 1. Comparison among implementation cost of different bank protection structures.

| Type of structure | River | Agency | cost US$/m | Effectiveness |
|---|---|---|---|---|
| Guide Bank | Jamuna Bridge | Foreign | 33,000 | Effective |
| Hard point | Sirajganj (Jamuna) | Foreign | 21,000 | Effective |
| Solid spur | Kalitola (Jamuna) | Foreign | 12,500 | Effective |
| Revetment (Geobags) | Jamuna | Foreign | 2000–3000 | On going |
| Revetment | Jamuna | BWDB | 3800–4000 | 70–80% |
| RCC spur | Jamuna/ Ganges | BWDB | 950 | 60–70% |
| RCC spur | Teesta | BWDB | 350 | 100% |
| Bandalling structures | Sirajganj (Jamuna) | RRI | 50 | On going |

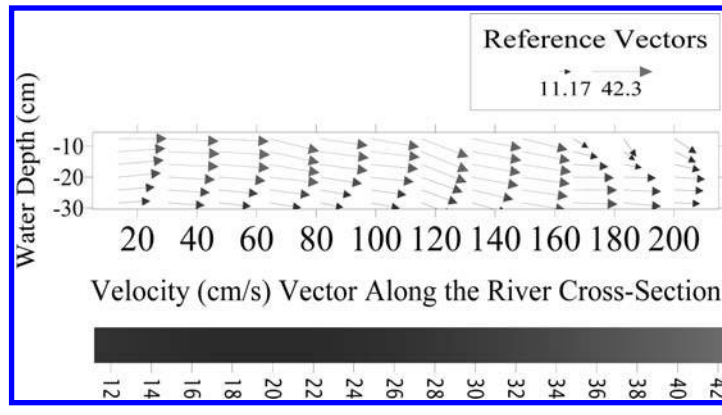


Figure 2. Velocity vector at the downstream of the bandalling.

developing and applying new techniques of measuring. FAP 21 produced some progress in process based modeling of two mechanisms by which the mere presence of bank protection structures increases the loads on these structures : (i) the deeper bend scour due to stopping of bank migration[1]; and (ii) the attraction of channels and associated flow attack towards scour holes[2]. The stopping of bank erosion is assumed to produce deeper bend scour through: (i) prevention of bank sediment supply, (ii) channel narrowing due to retarded point bar growth, (iii) bend deformation due to local prevention of channel migration and (iv) vortices generated by flow impingement. A method was developed based on empirical laws derived from a large set of satellite images. Brahmaputra-Jamuna.Spur & revetment are constructed for river bank erosion protection. Sand bars are developed between the spurs & again the river bank erosion expedited & result the failure of spur. After the failure of these spurs erosion is being continued. Cost comparison of different structures shown in table 1. There was given a idea so that the there is needed to optimize the bandals spacing for better result & to conduct experiment in larger scale[3].

## 2 METHODOLOGY

### 2.1 *Experimental setup*

There is an experimental set-up to conduct the experiment at the laboratory of River Research Institute (RRI), Faridpur, Bangladesh. The experimental set-up with water supply system in the laboratory of RRI in which the test run were conducted for the different test scenarios. It is mention here that the river channel is 20 meter long & 2.2 meter wide. During test run it is allowed to pass water discharge 200 liter per second. After the experimental test run with an angle of 40 degree with the flow direction, the river water depth is measured by the sounding method. The initial bed levels as well as final level are measured to find out the change in bed level.

### 2.2 *Data collection*

To analysis the velocity distribution, velocity data were measured in the laboratory river channel at the River Research Institute (RRI), Faridpur during flowing water in the channel by using the Electromagnetic Velocity Meter (EMV). The depth of the river channel were also measured by sounding method before the test run as well as after the test run in the river channel. The velocity component was measured at 10 cm interval. The velocity data were colleted from the entire river channel along the river cross-section in the laboratory. The point velocity is also measured at the upstream, downstream as well as at the location of the bandalling. Initial bed level reading is taken before starting the experiment with the bandals. Final bed level data is also taken to find the erosion & deposition in the river bed.

## 3 DATA ANALYSIS

For the analysis of water depth, the cross-sectional data over the entire bandalling area is taken at 10 cm interval before & after the test runs. In the figure 1 shows the working principle of bandals where as figure 2 to figure 3 shows the effect of bandalling on the river flow and morphology due to bandals construction in the river. Figure 3 shows that maximum velocity at the upstream of the bandals where as low or minimum velocity at the downstream of the bandals where huge amount of

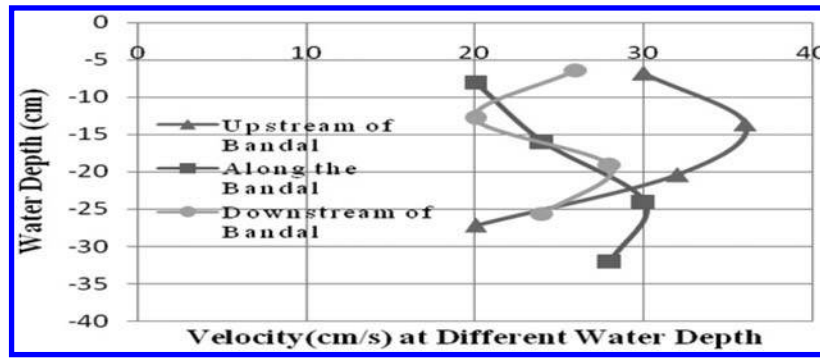


Figure 3. Comparison of velocity distribution due to effect bandalling.

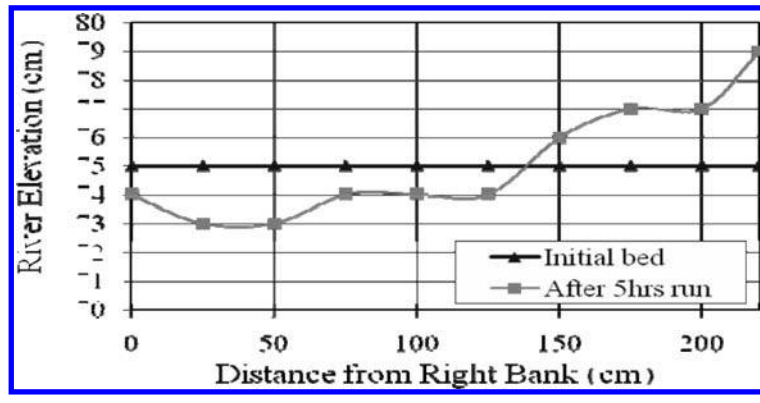


Figure 4. Accretion near the river bank and that of scour/erosion away from the river bank.

sediments are deposited near the river bank. This is the indication of the river bank erosion protection with bandalling. It is also agreed as in the figure 4 that there is siltation/deposition near the left bank of the river channel where as erosion experienced in the main stream of the river that increase the navigability of the river.

## 4 RESULT AND DISCUSSIONS

The velocity magnitude is relatively higher at the upstream channel section as in figure 2 where as comparatively less velocity at the location of the bandals as well as at the downstream of the bandals as in figure 3. Also as in the figure 3 it is found from the point velocity plot that the velocity is maximum at the upstream of the bandals where as it is less at the downstream of the bandals. It is appeared that always maximum velocity at the middle of the section. It is also found from data analysis as in figure 3 that the bandalling upstream velocity is amplified by 1.1 to 1.5 times than that of the downstream velocity. The main river channel is eroded & that the thalweg is created indicating the navigational improvement of the river channel. It is also found from figure 4 that the maximum sedimentation in between the bandalling near the bank that indicates the river bank erosion protection.

## 5 CONCLUSION

In conclusion, it can be stated that sedimentation occurs near the river bank in between the bandalling. This sedimentation indicates the river bank erosion protection. The near bank velocity in between bandalling is very less than that of the velocity at the middle channel as well as the velocity in the upstream of the bandalling is maximum.

## ACKNOWLEDGEMENT

The authors express their gratitude to River Research Institute, Faridpur, Bangladesh for providing all support for this study. The authors would like to thank all other persons for their help during laboratory data collection.

## REFERENCES

[1] Mosselman, E., Shishikura, T. and Klaassen, G.J.(2000). Effect of bank stablization on bend scour in anabranches of braided rivers.Phys. Chem. Earth, Part B, 26(7–8), 699–704.

[2] Mosselman, E. and Sloff, C.J. (2002). Effect of local scour holes on macroscale river morphology. In: River Flow 2002: Proceeding of the International Conference on Fluvial Hydraulics, Vol. 2, Louvain la Neuve, Belgium, 4-6 September (Eds D.Bousmar and Y.Zech), pp. 767–772. Balkema, Lisse.

[3] Uday DAS, Shamima NASRIN,and Munsur RAHMAN(2007), “Effect of Bandal Spacing on Formation of Navigation Channels: Experiments.” Pre-Conference Paper Volume of International Conference on Water and Flood Management, Institute of Water & Flood Management (IWFM), Bangladesh University of Engineering & Technology (BUET), Dhaka, Bangladesh, 12–14 March, 2007. Vol 1 pp.**117**, 117–123.

*Environmental Hydraulics – López-Jiménez et al (eds)*
*© 2010 Taylor & Francis Group, London, ISBN 978-0-415-56697-1*

# Dynamics of the Chacahua tidal inlet: Measurements and modelling

Rubén A. Morales
*Instituto Mexicano de Tecnología del Agua, Jiutepec, México*

Héctor S. Vélez
*Universidad Autonoma Metropolitana – Iztapalapa, México DF, México*

Guillermo Gutiérrez
*CICESE, La Paz, La Paz, BCS, México*

Jorge A. Laure
*Instituto Mexicano de Tecnología del Agua, Jiutepec, México*

ABSTRACT: The Chacahua lagoon is located in southern México on the Pacific coast. The Chacahua lagoon is connected to the ocean by a 2 km channel with an approximately width of 150 m and a mean depth of 3 m. During the end of the rainy season (November 2008) and the dry season (March 2009), currents (ADP), tides and CTD measurements were carried out in the Chacahua channel. The channel has particular features since the first one km is mostly uniform but suddenly there is a hollow of 7 to 8 m which decreases gradually until the end of the channel. These topographic features play an important role in the circulation and seem, during this period, to induce a stationary front at the vicinity of the hollow induced by the sudden increase in depth. The current vertical structure was measured with an ADP along and across the channel and the effect of the hollow on the frontal intrusion is quite evident. Finally, the modeling (ELCOM) of the circulation of the channel tidal intrusion allows to gain an insight into the effect of the hollow on the movement of the frontal intrusion.

*Keywords*: tidal fronts, coastal lagoon, currents and modeling.

## 1 INTRODUCTION

The Chacahua lagoon is located in southern México on the Pacific coast. It is part of the Chacahua-Pastoria lagoon system (Fig. 1). Both lagoons were connected to the ocean, however, actually just the Chacahua lagoon is connected to the ocean by a 2 km channel with an approximately width of 150 m and a mean depth of 3 m. During flooding and ebb tides the tidal front moves back and forth along the channel and it can be easily observed by the formation of the foam line along the front. At the entrance of the channel with the ocean, the front behaves as a typical front observed in estuarine systems. However, field measurements of the bathymetry of the channel shows a steep change in depth from 2 to a 14 m. The hollow is present at the interior part of the channel and seems to play an important role in the tidal front dynamics of the channel. In order to understand the role played by this bathymetric feature a series of current (ADP) and CTD measurements were made during November 2008 and March 2009. Also, efforts are made to model the role played by the hollow in the circulation of the channel.

## 2 FIELD MEASUREMENTES

As part of an environmental impact project the coastal area and the Chacahua-Pastoria lagoons were studied. Environmental data was measured in the lagoon and consisted of meteorological, sea level, CTD and current (ADCP and drifters) data. Three field experiments were carried out during September and November 2008 and March 2009. The first two corresponds to the rainy season and the last to the dry season. All the freshwater present in the lagoons drains from the watershed due to the lack of a proper perennial river. Initially, the first experiment was focus on the establishment of the general circulation in the channel and the lagoon area (Chacahua-Pastoria). For the measurements an Acoustic Doppler Current Profiler (ADP) Sontek de 1.5 MHz was used mounted on a catamaran. During the second experiment evidences of the channel depression were observed and consequently their induced circulation was measured. However, during this experiment a 3 MHz ADP was used to measure the currents and consequently its short range (6 m) did not allow to sample the currents at the deeper part of the hollow. But the CTD and ADP data showed strong evidences of the plunging of the mixed seawater into the deepest part of the hollow and forming a frontal stationary foam line which indicate the separation of the freshwater from the lagoon and the seawater (Figure 2).

During March 2009, the 1.5 MHz ADP was used to measure the currents along the channel so a complete depiction of the bathymetric feature is described along with the currents entering the lagoon. It is evident that these topographic features play an important role in the circulation and seem to control temporally the movement of the frontal system.

## 3 NUMERICAL MODELING

Finally, efforts are made to model the hydrodynamics of the channel. The ELCOM model was implemented to model the circulation and to gain an insight into the effect of the hollow on the movement of the frontal intrusion. Preliminary simulations of the channel are qualitatively according to the field observations. However, further systematic measurements are under way

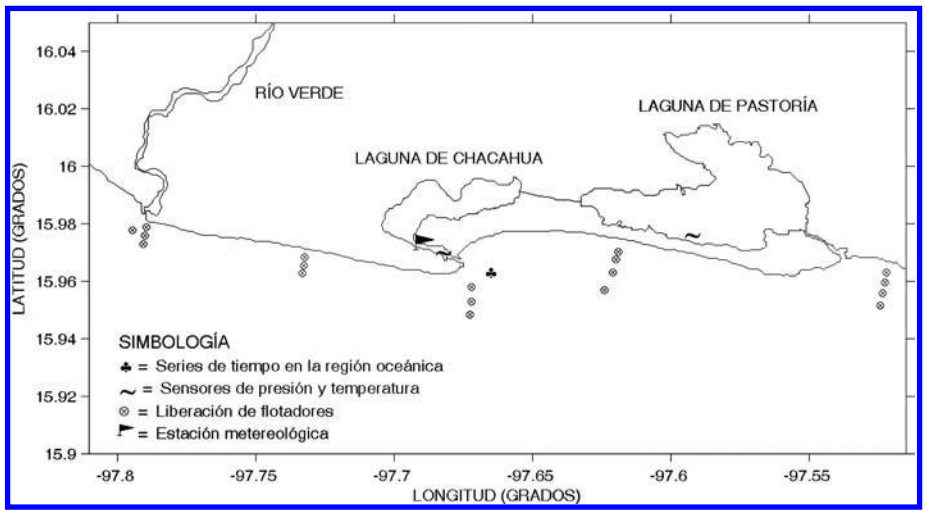


Figure 1. The Chacahua and Pastoría lagoon system located in southern México on the pacific coast.

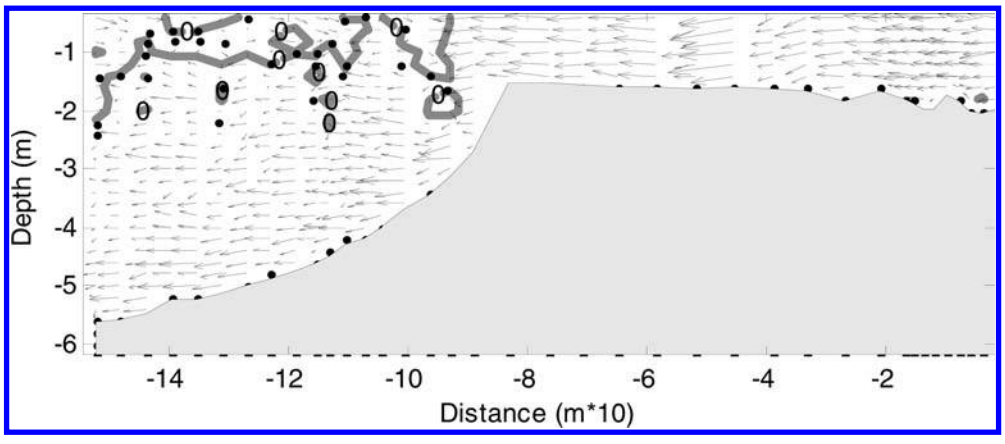


Figure 2. Longitudinal section of the current The Chacahua channel during September 2008 (left = west; right = east). The current is entering to the lagoon. Since the water is denser it plunges moving close to the bottom.

to finally understand the dynamics of the frontal system. In addition the numerical simulations will be used to synthesize the field observations and to gain an insight into the dynamics of the tidal front.

## 4 CONCLUSIONS

ADP and CTD measurements were carried out in the coastal lagoon of Chacahua and Pastoria. The channel which communicate the Chacahua lagoon showed a bathymetric depression which seems to control temporally the behavior of the tidal frontal system. The topographic features seem to play an important role not just in the dynamics of the frontal system. Also there are evidences of a significant increase of the biological activities around the topographic depression.

## REFERENCES

[1] Simpson, J.E, 1997. *Gravity Currents*. Cambridge University Press. Cambridge, pp. 88–104.

*Environmental Hydraulics – López-Jiménez et al (eds)*
*© 2010 Taylor & Francis Group, London, ISBN 978-0-415-56697-1*

# Calibration of friction coefficients for a 3D hydrodynamic model

Mauricio Escalante-Estrada, Rubén Morales-Pérez, & Patricia Echeverría Vaquero
*Mexican Institute of Water Technology, Jiutepec, México*

ABSTRACT: A 3D hydrodynamic model calibration by means of friction coefficients adjusting is presented. The YAXUM3/D was originally developed in the Mexican Institute of Water Technology to study shallow lake hydrodynamics and applied to Pátzcuaro Lake, Mexico.

Different simulations tests were made in order to evaluate the 3D hydrodynamic model. Numerical simulations were made taking in account all, steady and cyclic winds, as well as initial wind of excitation for 24 h with posterior calm. The results showed that the hydrodynamics conditions repeat after 3 cycles, this means those three days of simulation are required to overcome the initial condition of calm.

Wind forcing and bottom friction are the main mechanisms of the hydrodynamic and circulation patterns. Coefficients Cd, bottom friction (Chezy) as well as vertical eddy viscosity were estimated to describe the most realistic simulations describing the best adjustment between measurements and simulations in lake circulation were determined.

*Keywords*: Hydrodynamic model, calibration, lakes.

## 1 INTRODUCTION

The Mexican Institute of Water Technology together with other institutions has made many studies for the assessment of the water quality and actions for recovery for the Pátzcuaro Lake.

It used the YAXUM/3D model to assess the impact of the discharges in the lake, both in terms of its area of influence as the transportation within the same lake, identifying areas of accumulation, such implementation requires be calibrated with measurements in field of velocity of currents and wind, since the latter is the principal agent that moves the waters. The model is built in from equations general of the hydrodynamics and he coupled the equation of transport of scalar. In this article we turn to the factors which for the model of hydrodynamics.

## 2 MEASUREMENTS OF FIELD

There were 2 measuring campaigns of hydrographic parameters in Pátzcuaro Lake, the first day 3 to 13 June and the second from 15 to 22 October 2003. The field work was carried out with the participation of staff of the Metropolitan Autonomous University Unit (UAM-I).

The campaigns were designed with the aim of analyzing hydrographic data to infer the hydrodynamics of lake, and generate a database to permit the application and calibration of numerical models of movement. The measurement system consisted of several monitoring teams of parameters hydrographic (current, level of surface water, wind, salinity and temperature). These instruments were mounted in permanent stations to register at the time its variability. Details of the campaigns and equipment used are described below.

There were 4 regions, defined according to the morphology and bathymetry of lake and the distribution of islands. The stations (one for each region) were located toward the central part of each region, looking at a time, the deeper areas (figure 1).

The current measurement was my through an RDI −600 KHz acoustic profiler, in time series of 48 hours, with intervals of sampling of 30 minutes, the direction and magnitude of the flow to each meter deep (this, only for the regions 2 to 4, in the region was not possible due to the shallow). It was also obtained vertical profiles of temperature, oxygen and water salinity through a probe multi-parametric water quality-6600 YSI. An satellite positional GARMIN GPS 45 XLS-. It used further laptop computers, for set up, operate and obtain information from each instrument of measurement. The registration of information was done every hour, during a period of 24 hours in all regions.

The table 1 shows the main features taken into account in each region. It is necessary to comment that in the region 1 of lake, was not possible to make the current measurements, under which is the most shallow lake and was not possible to locate any area with appropriate depths (require at least 3.5 meters) in order to operate on a continuous the streams.

For the registration of flows, the ADCP was placed in a specially designed metal base and constructed (using a not magnetic material, to avoid disruptions to compass). Once placed on the bottom, the head was located at an altitude of 70 cm. According to this, the depths to which was possible to obtain information were valid, for the region 4, 2, 3, 4, 5, 6 and 7 m on the head of the instrument, i.e, to 6.5, 5.5, 4.5, 3.5, 2.5 and 1.5 m deep.

For the region 3 the corresponding to 2, 3, 4, 5 and 6 m on the head of the instrument, i.e, to 5.6, 4.6, 3.6, 2.6 and 1.6 m in depth. In the region 2 in this case, the only depth to which was possible to obtain valid data was the corresponding to the 2 m on the head of the team, i.e, 1 m from the surface.

## 3 HYDRODYNAMIC SIMULATION

The YAXUM/3D is a three-dimensional model that was developed to study the hydrodynamics shallow lakes. The model includes contributions hydrological; a module for the study of flows horizontal and vertical recirculation, and its influence in

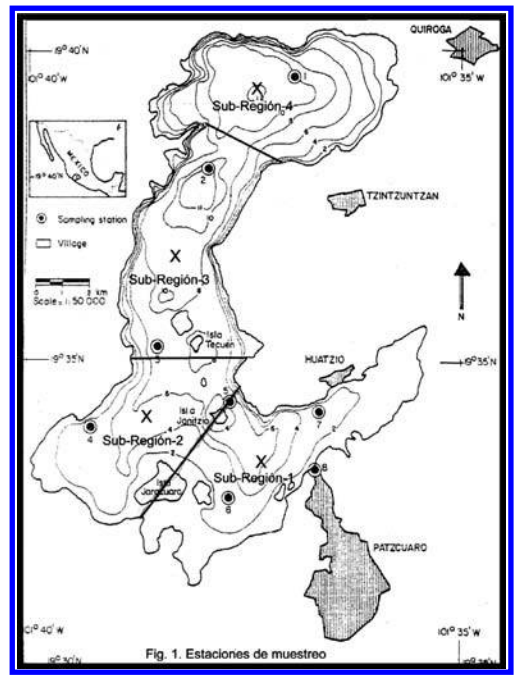


Figure 1. Location of the sampling stations.

Table 1. Sampling points.

| Region | Location | Depth | Climatological station |
|---|---|---|---|
| North (region 4) | 19.656°N, 101.591°W | 9.20 m | Chupícuaro |
| Central channel (region 3) | 19.636°N, 101.629°W | 8.30 m | Pacanda |
| Southwest (region 2) | 19.5924°N, 101.6784°W | 3.70 m | Arocutin |
| Southeast (region 1) | 19.5582°N, 101.6475°W | 2.92 m | |

the mixed processes. The three dimensional formulation resolves a mesh nets on a horizontal plane and integration by layers in the vertical. It takes into account balances thermodynamic also in a module specific and another for the study of the water quality in where you solve variations temporal and spatial biochemical components, BOD, DO and primary production, among others. Applications individuals have been carried out in the Coyuca lagoon in Guerrero, in the Chapala Lake, and in the Valle de Bravo reservoir. The reader interested in developing the model can refer to[1] and on its application to the Pátzcuaro Lake[2].

The YAXUM/3D model applied to the Pátzcuaro Lake, using a calculation mesh of square cells of 100 m length, with a domain of 150 per 156 elements in the horizontal level. In the vertical were of 1.0 m, proving a domain of 12 cells.

## 4 TESTS OF OPERATION

### 4.1 *Simulation with constant wind*

The conditions of simulation of 120 hours, are under a constant wind, with value in the X direction of 0.34 m/s and in the Y direction of 1.15 m/s. The coefficients of friction used are Chezy = 25 and coefficient of drag by wind Cd = 0065. In the figures 2 displays the result of the simulation for 48 hours.

### 4.2 *Periodic wind simulation*

The scenario proposed is a medium wind averaged the components of the month during 24 hours, which is repeated until 5 times. It varied the friction coefficients and drag by wind Cd, to verify the performance. In the tests are varied also the $\nu z$ value of 0.005, 0.01 and 0.02, these values are within the ranks according to Wang et al (2001).

### 4.3 *Simulation of wind by 24 h and subsequent wind void*

There was a test with an initial excitement a wind average hours over 24 hours and wind void the rest of the time simulation. The results show that under these conditions the speeds in the lake tend to zero, situation that was expected because the wind is the main force that produces the movement in the lake. The speeds tend to zero without reaching precisely in this value because the strength of is still present.

The results of velocities in both directions X, Y, and the behavior of the hydrodynamics are shown in Figures 3. The lines of flow behave in this way because the speeds are very small throughout the domain.

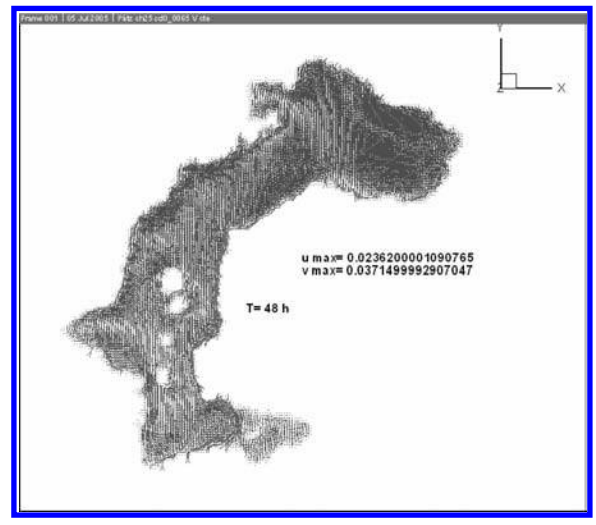


Figure 2. Vectors and streamtraces, constant wind, 48 hrs.

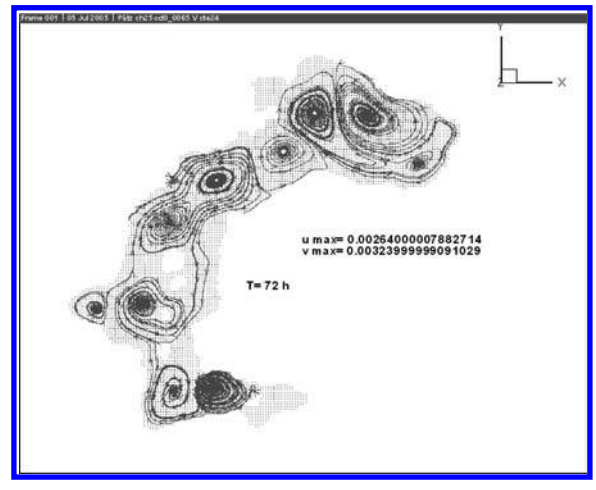


Figure 3. Vectors and streamtraces with 24 h wind and subsequent calm.

## 5 ADJUSTMENT OF FRICTION COEFFICIENT

For a representation as faithfully as possible the conditions of hydrodynamics that exist in the lake according to what obtained in campaigns of measurement, had to make an adjustment in the coefficients of friction (and coefficient of drag by wind) involved in the equations that govern the 3D phenomenon.

This calibration was conducted by making several simulations with different coefficients to compare with the measurements in two points in the lake, different depths. The wind is submitted from 5 to 11 June 2003, in the meteorological station, date during which was conducted the campaign of measurements basins in the Patzcuaro Lake.

There were only two points (Region 3 and 4) due to the depths in regions 1 and 2 did not obtain a velocity profile for comparison with the simulations.

The velocities obtained with the various tests that were conducted still in a very similar to the behavior of the wind. It came to the selection of coefficients of friction that produced the behavior in the speeds, considering that the points of monitoring are distributed throughout the lake through regions representative, not necessarily the region of influence of the weather station.

The tests resulted that the best coefficients are Chezy $=18$, $Cd = 0.016$ ($\nu z = 0.005$) with which was achieved the best adjustment in the two points compared (region 3 and 4). Figures 10 and 11 presents the values obtained compared with measurements, in region 3 and 4 monitoring, respectively. About the Y axis shows the vectors, with their respective direction, the speeds in the lake in the different layers of its depth, distributed. The upper vectors shown the wind (divided by 20) to be the same size as the other vectors. In red are the results of the simulation, and in blue the results recorded by the measurement.

The simulations were made for 120 hours, and monitoring took place during 60 hours. The adjustment in terms of size is quite acceptable, according to US Army Corps of Engineers, (1993), a good calibration occurs when the results of simulation are close to the majority of the measured data, not necessarily that data and results coincide exactly. It is believed that the imbalances or errors are presented to try set both points considering a wind for the entire lake. The simulation are shown in Figures 4 and 5.

## 6 CONCLUSIONS

The comparison of the numerical and measurements is necessary to note that the coefficients that best reproduced the dynamics of Lake according to the results of the campaign of measurement are Chezy $= 18$, vertical viscosity 0,005 and coefficient of drag by wind Cd of 0.016.

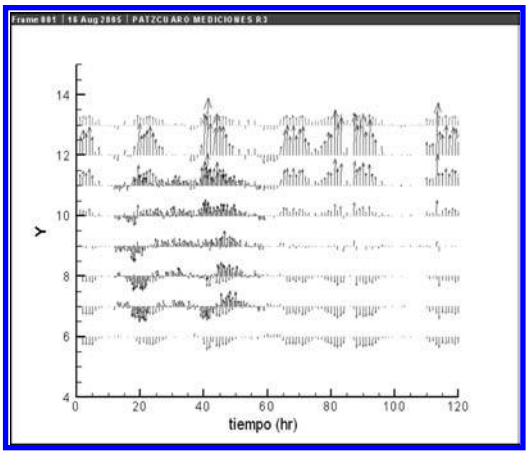


Figure 4. Simulation and measurement region 3.

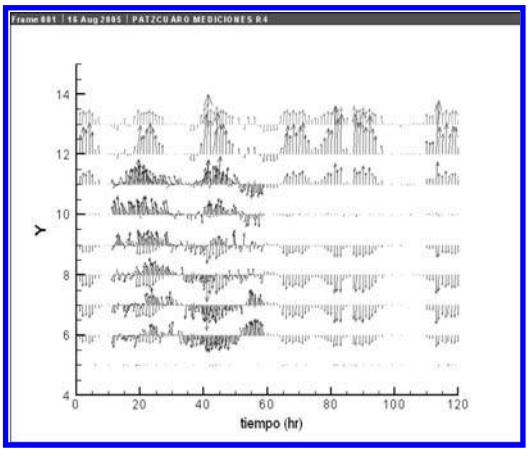


Figure 5. Simulation and measurement region 4.

With regard to the results of the simulations, in the first case that is use the wind with magnitude and direction constant, conditions hydrodynamic (surface level free and speeds) stabilized at 36 hours, whose result represents a steady state with such conditions.

As to the proof of a wind average schedule that was repeated during five days, were observed the maps of speeds and lines of flow, and one can say that since the fourth day patterns were repeated, namely that these conditions the first three days served to “warmed up” and subtract the influence simulate from the rest. A test was done on the reverse, once the system excited by the wind, this was amended to wind void, and the response was to 3 days after the lake came to rest. In conclusion, for each outcome is necessary “warmed up” the system simulating 3 days, where the effects inertial is couple to new conditions.

Finally were modified the coefficients of drag by wind, resistance to flow by fund (), and of viscosity turbulent vertical, and were compared with the conditions measures (wind and speeds of flows) finalized the coefficients that best adjusted to reproduce such measurements.

## REFERENCES

[1] Escalante, E. M.; Ramírez L. H, Morales P. R.(2001); YAXUM/3D, a Three-dimensional circulation and water quality model for coastal lagoons. *3rd. International Symposium on Environmental Hydraulics.* Tempe Arizona EUA.

[2] Escalante E. M., González V. J. A., Salcedo S. E., Morales P., R., Rodríguez C. C., (2004) *Simulación del impacto de diversas acciones de recuperación sobre el lago de Pátzcuaro* INFORME TECNICO IMTA.

*Environmental Hydraulics – López-Jiménez et al (eds)*
*© 2010 Taylor & Francis Group, London, ISBN 978-0-415-56697-1*

# Calibration of friction coefficients for a 3D hydrodynamic model

Mauricio Escalante-Estrada, Rubén Morales-Pérez, & Patricia Echeverría Vaquero
*Mexican Institute of Water Technology, Jiutepec, México*

ABSTRACT: A 3D hydrodynamic model calibration by means of friction coefficients adjusting is presented. The YAXUM3/D was originally developed in the Mexican Institute of Water Technology to study shallow lake hydrodynamics and applied to Pátzcuaro Lake, Mexico.

Different simulations tests were made in order to evaluate the 3D hydrodynamic model. Numerical simulations were made taking in account all, steady and cyclic winds, as well as initial wind of excitation for 24 h with posterior calm. The results showed that the hydrodynamics conditions repeat after 3 cycles, this means those three days of simulation are required to overcome the initial condition of calm.

Wind forcing and bottom friction are the main mechanisms of the hydrodynamic and circulation patterns. Coefficients Cd, bottom friction (Chezy) as well as vertical eddy viscosity were estimated to describe the most realistic simulations describing the best adjustment between measurements and simulations in lake circulation were determined.

*Keywords*: Hydrodynamic model, calibration, lakes.

## 1 INTRODUCTION

The Mexican Institute of Water Technology together with other institutions has made many studies for the assessment of the water quality and actions for recovery for the Pátzcuaro Lake.

It used the YAXUM/3D model to assess the impact of the discharges in the lake, both in terms of its area of influence as the transportation within the same lake, identifying areas of accumulation, such implementation requires be calibrated with measurements in field of velocity of currents and wind, since the latter is the principal agent that moves the waters. The model is built in from equations general of the hydrodynamics and he coupled the equation of transport of scalar. In this article we turn to the factors which for the model of hydrodynamics.

## 2 MEASUREMENTS OF FIELD

There were 2 measuring campaigns of hydrographic parameters in Pátzcuaro Lake, the first day 3 to 13 June and the second from 15 to 22 October 2003. The field work was carried out with the participation of staff of the Metropolitan Autonomous University Unit (UAM-I).

The campaigns were designed with the aim of analyzing hydrographic data to infer the hydrodynamics of lake, and generate a database to permit the application and calibration of numerical models of movement. The measurement system consisted of several monitoring teams of parameters hydrographic (current, level of surface water, wind, salinity and temperature). These instruments were mounted in permanent stations to register at the time its variability. Details of the campaigns and equipment used are described below.

There were 4 regions, defined according to the morphology and bathymetry of lake and the distribution of islands. The stations (one for each region) were located toward the central part of each region, looking at a time, the deeper areas (figure 1).

The current measurement was my through an RDI −600 KHz acoustic profiler, in time series of 48 hours, with intervals of sampling of 30 minutes, the direction and magnitude of the flow to each meter deep (this, only for the regions 2 to 4, in the region was not possible due to the shallow). It was also obtained vertical profiles of temperature, oxygen and water salinity through a probe multi-parametric water quality-6600 YSI. An satellite positional GARMIN GPS 45 XLS-. It used further laptop computers, for set up, operate and obtain information from each instrument of measurement. The registration of information was done every hour, during a period of 24 hours in all regions.

The table 1 shows the main features taken into account in each region. It is necessary to comment that in the region 1 of lake, was not possible to make the current measurements, under which is the most shallow lake and was not possible to locate any area with appropriate depths (require at least 3.5 meters) in order to operate on a continuous the streams.

For the registration of flows, the ADCP was placed in a specially designed metal base and constructed (using a not magnetic material, to avoid disruptions to compass). Once placed on the bottom, the head was located at an altitude of 70 cm. According to this, the depths to which was possible to obtain information were valid, for the region 4, 2, 3, 4, 5, 6 and 7 m on the head of the instrument, i.e, to 6.5, 5.5, 4.5, 3.5, 2.5 and 1.5 m deep.

For the region 3 the corresponding to 2, 3, 4, 5 and 6 m on the head of the instrument, i.e, to 5.6, 4.6, 3.6, 2.6 and 1.6 m in depth. In the region 2 in this case, the only depth to which was possible to obtain valid data was the corresponding to the 2 m on the head of the team, i.e, 1 m from the surface.

## 3 HYDRODYNAMIC SIMULATION

The YAXUM/3D is a three-dimensional model that was developed to study the hydrodynamics shallow lakes. The model includes contributions hydrological; a module for the study of flows horizontal and vertical recirculation, and its influence in

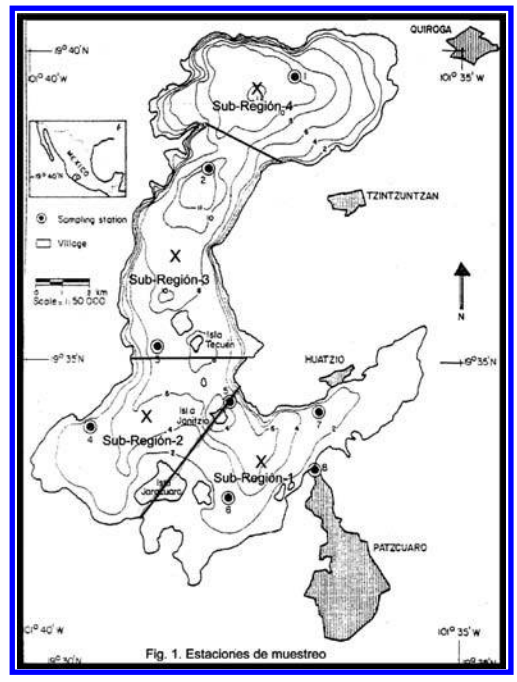


Figure 1. Location of the sampling stations.

Table 1. Sampling points.

| Region | Location | Depth | Climatological station |
|---|---|---|---|
| North (region 4) | 19.656°N, 101.591°W | 9.20 m | Chupícuaro |
| Central channel (region 3) | 19.636°N, 101.629°W | 8.30 m | Pacanda |
| Southwest (region 2) | 19.5924°N, 101.6784°W | 3.70 m | Arocutin |
| Southeast (region 1) | 19.5582°N, 101.6475°W | 2.92 m | |

the mixed processes. The three dimensional formulation resolves a mesh nets on a horizontal plane and integration by layers in the vertical. It takes into account balances thermodynamic also in a module specific and another for the study of the water quality in where you solve variations temporal and spatial biochemical components, BOD, DO and primary production, among others. Applications individuals have been carried out in the Coyuca lagoon in Guerrero, in the Chapala Lake, and in the Valle de Bravo reservoir. The reader interested in developing the model can refer to[1] and on its application to the Pátzcuaro Lake[2].

The YAXUM/3D model applied to the Pátzcuaro Lake, using a calculation mesh of square cells of 100 m length, with a domain of 150 per 156 elements in the horizontal level. In the vertical were of 1.0 m, proving a domain of 12 cells.

## 4 TESTS OF OPERATION

### 4.1 *Simulation with constant wind*

The conditions of simulation of 120 hours, are under a constant wind, with value in the X direction of 0.34 m/s and in the Y direction of 1.15 m/s. The coefficients of friction used are Chezy = 25 and coefficient of drag by wind Cd = 0065. In the figures 2 displays the result of the simulation for 48 hours.

### 4.2 *Periodic wind simulation*

The scenario proposed is a medium wind averaged the components of the month during 24 hours, which is repeated until 5 times. It varied the friction coefficients and drag by wind Cd, to verify the performance. In the tests are varied also the $\nu z$ value of 0.005, 0.01 and 0.02, these values are within the ranks according to Wang et al (2001).

### 4.3 *Simulation of wind by 24 h and subsequent wind void*

There was a test with an initial excitement a wind average hours over 24 hours and wind void the rest of the time simulation. The results show that under these conditions the speeds in the lake tend to zero, situation that was expected because the wind is the main force that produces the movement in the lake. The speeds tend to zero without reaching precisely in this value because the strength of is still present.

The results of velocities in both directions X, Y, and the behavior of the hydrodynamics are shown in Figures 3. The lines of flow behave in this way because the speeds are very small throughout the domain.

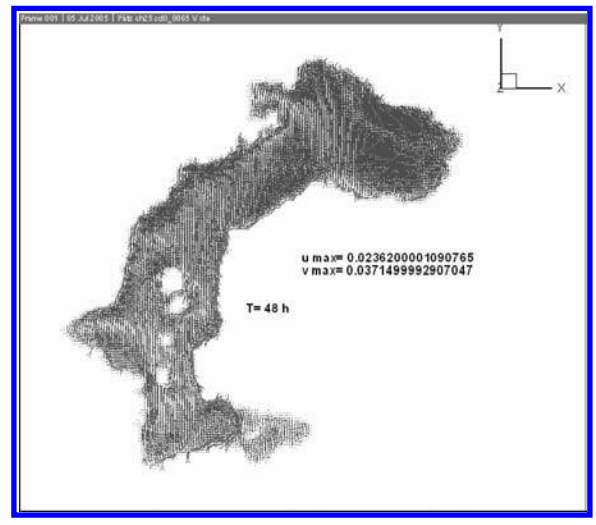


Figure 2. Vectors and streamtraces, constant wind, 48 hrs.

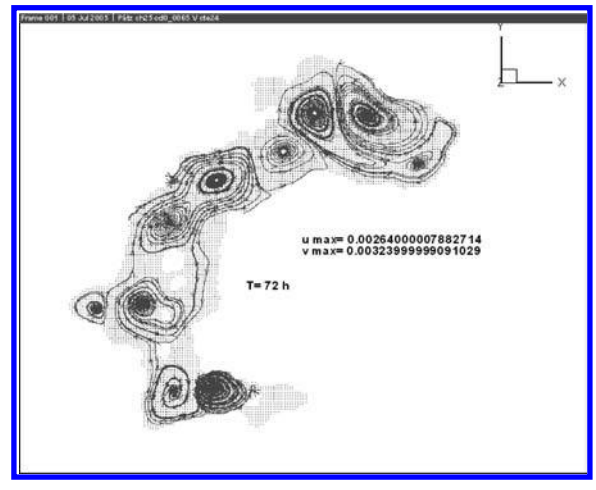


Figure 3. Vectors and streamtraces with 24 h wind and subsequent calm.

## 5 ADJUSTMENT OF FRICTION COEFFICIENT

For a representation as faithfully as possible the conditions of hydrodynamics that exist in the lake according to what obtained in campaigns of measurement, had to make an adjustment in the coefficients of friction (and coefficient of drag by wind) involved in the equations that govern the 3D phenomenon.

This calibration was conducted by making several simulations with different coefficients to compare with the measurements in two points in the lake, different depths. The wind is submitted from 5 to 11 June 2003, in the meteorological station, date during which was conducted the campaign of measurements basins in the Patzcuaro Lake.

There were only two points (Region 3 and 4) due to the depths in regions 1 and 2 did not obtain a velocity profile for comparison with the simulations.

The velocities obtained with the various tests that were conducted still in a very similar to the behavior of the wind. It came to the selection of coefficients of friction that produced the behavior in the speeds, considering that the points of monitoring are distributed throughout the lake through regions representative, not necessarily the region of influence of the weather station.

The tests resulted that the best coefficients are Chezy $=18$, $Cd = 0.016$ ($\nu z = 0.005$) with which was achieved the best adjustment in the two points compared (region 3 and 4). Figures 10 and 11 presents the values obtained compared with measurements, in region 3 and 4 monitoring, respectively. About the Y axis shows the vectors, with their respective direction, the speeds in the lake in the different layers of its depth, distributed. The upper vectors shown the wind (divided by 20) to be the same size as the other vectors. In red are the results of the simulation, and in blue the results recorded by the measurement.

The simulations were made for 120 hours, and monitoring took place during 60 hours. The adjustment in terms of size is quite acceptable, according to US Army Corps of Engineers, (1993), a good calibration occurs when the results of simulation are close to the majority of the measured data, not necessarily that data and results coincide exactly. It is believed that the imbalances or errors are presented to try set both points considering a wind for the entire lake. The simulation are shown in Figures 4 and 5.

## 6 CONCLUSIONS

The comparison of the numerical and measurements is necessary to note that the coefficients that best reproduced the dynamics of Lake according to the results of the campaign of measurement are Chezy $= 18$, vertical viscosity 0,005 and coefficient of drag by wind Cd of 0.016.

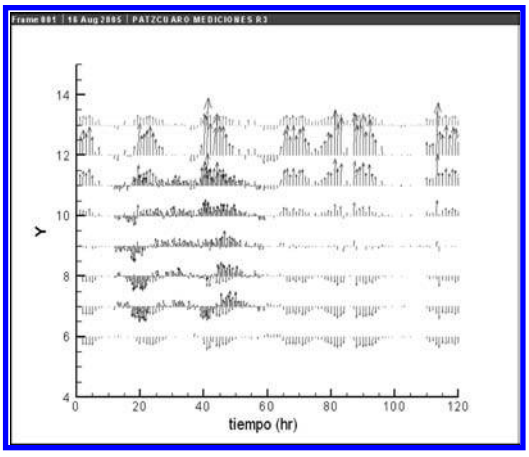


Figure 4. Simulation and measurement region 3.

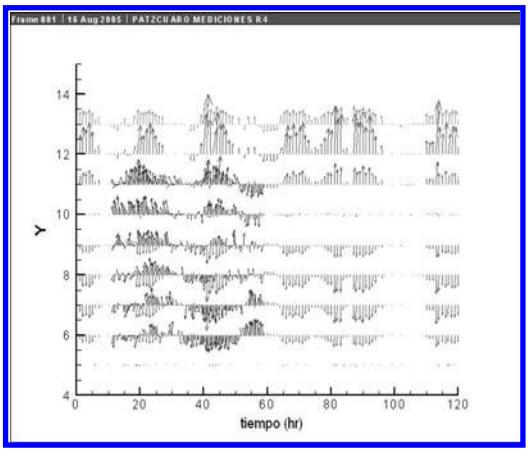


Figure 5. Simulation and measurement region 4.

With regard to the results of the simulations, in the first case that is use the wind with magnitude and direction constant, conditions hydrodynamic (surface level free and speeds) stabilized at 36 hours, whose result represents a steady state with such conditions.

As to the proof of a wind average schedule that was repeated during five days, were observed the maps of speeds and lines of flow, and one can say that since the fourth day patterns were repeated, namely that these conditions the first three days served to “warmed up” and subtract the influence simulate from the rest. A test was done on the reverse, once the system excited by the wind, this was amended to wind void, and the response was to 3 days after the lake came to rest. In conclusion, for each outcome is necessary “warmed up” the system simulating 3 days, where the effects inertial is couple to new conditions.

Finally were modified the coefficients of drag by wind, resistance to flow by fund (), and of viscosity turbulent vertical, and were compared with the conditions measures (wind and speeds of flows) finalized the coefficients that best adjusted to reproduce such measurements.

## REFERENCES

[1] Escalante, E. M.; Ramírez L. H, Morales P. R.(2001); YAXUM/3D, a Three-dimensional circulation and water quality model for coastal lagoons. *3rd. International Symposium on Environmental Hydraulics.* Tempe Arizona EUA.

[2] Escalante E. M., González V. J. A., Salcedo S. E., Morales P., R., Rodríguez C. C., (2004) *Simulación del impacto de diversas acciones de recuperación sobre el lago de Pátzcuaro* INFORME TECNICO IMTA.

*Environmental Hydraulics – López-Jiménez et al (eds)*
*© 2010 Taylor & Francis Group, London, ISBN 978-0-415-56697-1*

# Experimental investigation of flow and deposit patterns in rectangular shallow reservoirs: Preliminary analysis

Matthieu Dufresne
*Université de Liège (ULg), Secteur MS²F, Département ArGEnCo, Unité Hydrologie, hydrodynamique appliquée et constructions hydrauliques (HACH), Liège, Belgium*

Benjamin J. Dewals
*Université de Liège (ULg), Secteur MS²F, Département ArGEnCo, Unité Hydrologie, hydrodynamique appliquée et constructions hydrauliques (HACH), Liège, Belgium*
*Belgian fund for scientific research (F.R.S.-FNRS), Belgium*

Sébastien Erpicum, Pierre Archambeau & Michel Pirotton
*Université de Liège (ULg), Secteur MS²F, Département ArGEnCo, Unité Hydrologie, hydrodynamique appliquée et constructions hydrauliques (HACH), Liège, Belgium*

ABSTRACT: This document is a preliminary analysis (dimensional analysis, bibliographic review) for an experimental study about flow and deposit patterns in rectangular shallow reservoirs. The experimental device and first results are also presented.

*Keywords*: deposit, experiments, flow, shallow reservoir.

## 1 INTRODUCTION

Tanks, basins, ponds, lagoons (called reservoirs below) are commonly used in environmental hydraulics. Because of generally quiescent conditions, these works are conducive to the settling of particles. Therefore reservoirs must be carefully designed according to the role they will play. For example, sedimentation must be maximized in settling basins (stormwater treatment, protection of irrigation or hydro-electric power structures, *etc*.) whereas it must be minimized in storage facilities (irrigation, electric power generation, flood control, *etc*.).

The prediction of deposits as a function of the geometry of the reservoir, the hydraulic conditions and the sediment characteristics is still a great challenge. While empirical and semi-empirical methods[1] have been developed for the last sixty years to determine the amount of deposits, they cannot determine their location, which is required to well define the sediment removal strategy. To get this information, the knowledge of the flow pattern is a prerequisite (possible various size recirculations).

This study focuses on rectangular shallow reservoirs, as illustrated in figure 1. Here, $L$ is the length of the reservoir; $B$, its breadth; $b$, the breadth of the inlet and outlet channels; $\Delta B$, the lateral expansion; and $h$, the water depth.

The aim of this study is firstly to describe all the flow patterns in rectangular shallow reservoirs (typology of flow). Secondly, to determine prediction criteria of the flow. Finally, to define a typology of short-term deposits. This paper presents a dimensional analysis, a brief bibliographic review, the experimental device and first results.

## 2 DIMENSIONAL ANALYSIS

We assume that the flow in rectangular shallow reservoirs is governed by nine parameters: the length of the reservoir ($L$), its lateral expansion ($\Delta B$), the breadth of the inlet and outlet channels ($b$), the water depth ($h$), the mean depth-averaged velocity ($U$), the bed shear stress ($\tau$), the water density ($\rho$), the water viscosity ($\mu$) and the gravitational acceleration ($g$). Using dimensional analysis principles[2], the relationship between these nine variables may be reduced to a relationship between six dimensionless parameters, which are for example a lateral expansion ratio, a longitudinal confinement, a vertical confinement, a Reynolds number, a Froude number, and a bed friction coefficient (see equation 1). Any dimensionless parameter of this equation may be replaced by a product of powers of itself and others.

$$f\left(\frac{\Delta B}{b}, \frac{\Delta B}{L}, \frac{\Delta B}{h}, \frac{4\rho U h}{\mu}, \frac{U}{\sqrt{gh}}, \frac{2\tau}{\rho U^2}\right) = 0 \qquad (1)$$

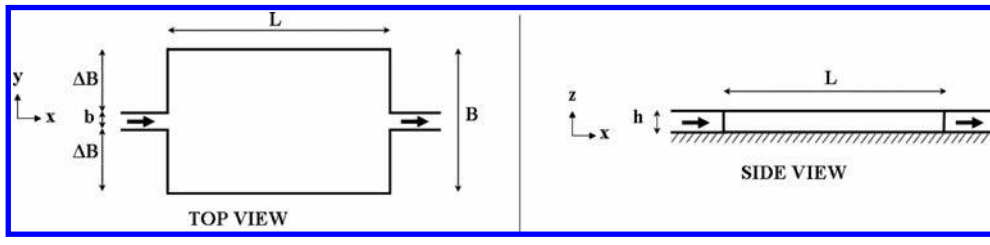


Figure 1. Schemes of a rectangular shallow reservoir.

## 3 BRIEF BIBLIOGRAPHIC REVIEW

The objective of this bibliographic review is to show the influence of these dimensionless parameters (or combinations of any of them) in similar conditions.

Abbott & Kline[3] intensively studied the stall of turbulent free surface flows over double lateral expansions using dye visualization. They showed that the recirculation zones in each side of the expansion were equal in length for expansion ratio (as defined in equation 1) less than ∼0.25. For expansion ratio greater than ∼0.25, the reattachment lengths were different.

Abbott & Kline claimed that the flow pattern was not sensitive to the Reynolds number, provided the flow is fully turbulent before the expansion. Casarsa & Giannattasio[4] carried out PIV measurements in order to check this behavior and showed that the influence of this dimensionless parameter on the shorter recirculation length was not completely negligible (a few percents).

Vertical confinement leads to modify the turbulence mechanisms[5] so that the flow properties (velocity field, concentration profile in case of dye transport) are in scale with the water depth[6,7]. For example, Giger et al.[6] showed that a characteristic feature of shallow jets was the formation of meandering structures at distances from the orifice larger than ten times the water depth.

Experimental studies about the shallow recirculating flow over single lateral expansions[8,9,10] highlighted two asymptotic behaviors, depending on the bed friction number (defined as the product of a vertical confinement coefficient and a bed friction coefficient). For small values of this number, the length of the recirculation zone is only dependent on the lateral expansion. For large values, the length of the recirculation zone is only dependent on the friction length scale (defined as the ratio of the water depth to the bed friction coefficient). Chen & Jirka[11] showed that for Reynolds numbers greater than 6000 (as defined in equation 1), the shallow wake generated by a two-dimensional body was uniquely dependent on a similar number (the shallow wake parameter).

Kantoush[12] experimentally studied the flow field in rectangular shallow reservoirs (as illustrated in figure 1), varying the length of the reservoir, its breadth, the water depth and the inflow velocity. His benchmark case was a 0.2 m high water flow entering a 6 m long and 4 m wide reservoir by a 0.25 m wide channel at a velocity of 0.14 m/s. In this situation, the main flow was deflected on the right wall, leading to the formation of a large counter clockwise recirculation in the whole structure and a small clockwise recirculation zone in the right inlet corner (the sense may be reverse, depending on the experiment). Similar patterns have been observed with decreasing the breadth of the reservoir (3 m, 2 m, 1 m and 0.5 m for which a plug flow takes place in the downstream zone of the reservoir). Asymmetry disappeared with decreasing the length of the reservoir (5 m, 4 m, 3 m). For these geometries, the main flow was not deflected at issuance in the reservoir, leading to the formation of two large symmetrical recirculation zones.

With decreasing the water depth to 0.15, 0.1 and 0.075 m (but increasing the Froude number in the same time), Kantoush showed that the flow started to meander (in a similar way to the observations of Giger et al.[6] and those of Chen & Jirka[11]).

## 4 EXPERIMENTAL DEVICE

We decided to focus on the lateral expansion, the longitudinal confinement, the vertical confinement and the Froude number, provided that the Reynolds and the bed friction number are respectively high and low so that they do not significantly influence the flow pattern.

The experimental device consists of a ∼10 m long and ∼1 m wide glass channel in which blocks (to change $\Delta B$) and walls (to change $B$) can be arranged to build different reservoir geometries (see pictures below). The sizes of these blocks and walls have been chosen, based on an assumption about the influence of the geometry of the shallow reservoir on the flow pattern.

This assumption is based on the combination of the experimental data of Abbott & Kline[3] and Kantoush[12], numerical simulations of Dufresne[13], and preliminary analysis of Dufresne[13] and Dewals et al.[14]; it is illustrated in figure 2. In region $\delta$, the flow field is dominated by two large symmetric recirculation zones (see Kantoush[12]). In region $\gamma$, a large asymmetric recirculation zone (clockwise or counter clockwise) takes place in the whole reservoir (see Kantoush[12]). In region $\beta$, the flow field is still asymmetric but fully reattached in the downstream zone of the reservoir (see Abbott & Kline[3] and Kantoush[12]). In region $\alpha$, the flow is still fully reattached in the downstream zone of the reservoir but, contrarily to region $\beta$, the two upstream recirculation zones are equal in length (see Abbott & Kline[3]).

The vertical axis of Figure 2 is the lateral expansion ratio, as defined in equation 1; therefore regions $\alpha$ and $\beta$ are separated by a horizontal line (see Abbott & Kline[3]). Based on preliminary analysis of Dufresne[13] and Dewals et al.[14], the horizontal axis is a combination of the longitudinal confinement and the lateral expansion ratio, so that the border between regions $\gamma$ and $\delta$ is a vertical line. The expression of this dimensionless number is not final yet; this study will allow us to define it precisely.

In Figure 2, the zone that will be experimentally investigated corresponds to the four horizontal grey lines (two sets of blocks times two breadths).

## 5 FIRST RESULTS

First results are illustrated in figure 3. Here, the reservoir is ∼7 m long and ∼1 m wide; the lateral expansion is equal to 0.35 m.

Using several dye and sawdust injections, we observed that a first reattachment was clearly identifiable on the right wall (but not completely stable). A second one was sometimes present on the left wall (in the downstream zone of the reservoir), showing that the flow is highly unsteady. This flow pattern is so located around the border between region $\beta$ and region $\gamma$ in figure 2. Given these results, we developed a protocol to measure not only the mean reattachment lengths but also their temporal variations (using dye injections at different locations).

Concerning the deposits, we can see in the right side of Figure 3 that they are massively located in the core of the recirculation zone.

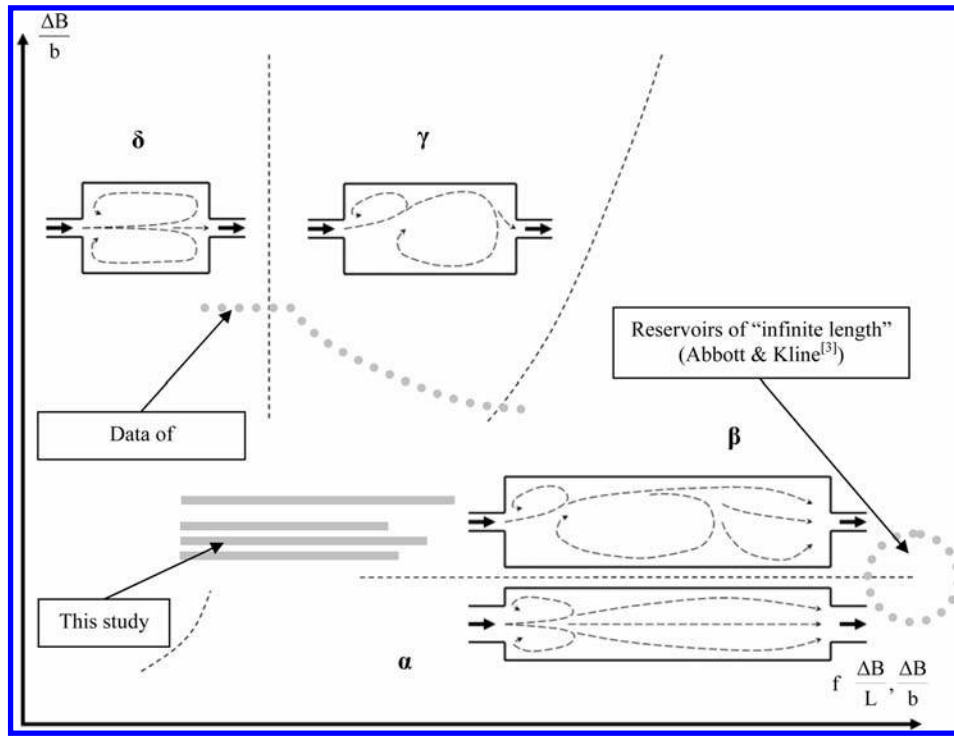


Figure 2. Assumption about the influence of the reservoir geometry on the flow pattern (dimensions of the reservoirs are not to scale).

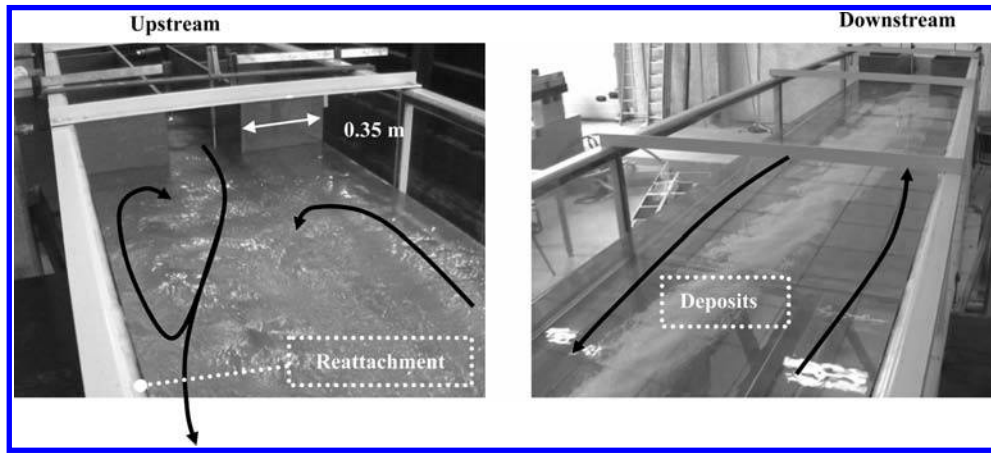


Figure 3. Illustration of flow pattern and deposits.

## 6 CONCLUSIONS AND PERSPECTIVES

Based on dimensional analysis and bibliographic review, an experimental device has been built in order to study the flow and deposit patterns in rectangular shallow reservoirs.

Next weeks will be dedicated to the measurement of reattachment lengths (mean position and temporal variation), varying four dimensionless parameters (the lateral expansion ratio, the longitudinal confinement, the vertical confinement and the Froude number). Deposits will be mapped for each flow pattern.

Based on the work of Dewals et al.[14], numerical simulations will also be carried out. After validation against experimental data, they will be used to explore unknown zones in figure 2.

## ACKNOWLEDGMENTS

We would like to acknowledge Alain Dewart, Didier Lallemand, Maurice Salme and Denis Stouvenacker who participated in the building of the experimental device. We would like to also acknowledge the University of Liège for the allocation of a postdoctoral fellowship to the first author.

## REFERENCES

[1] Garde, R.J., Ranga Raju, K.G. and Sujudi, A.W.R. (1990), "Design of settling basins", Journal of Hydraulic Research, Vol. 28(1), pp. 81–91.

[2] Langhaar, H.L. (1951), *Dimensional analysis and theory of models*, John Wiley & Sons, New York.
[3] Abbott, D.E. and Kline, S.J. (1962), "Experimental investigation of subsonic turbulent flow over single and double backward facing steps", Journal of Basic Engineering, Vol. 84, pp. 317–325.
[4] Casarsa, L. and Giannattasio, P. (2008), "Three-dimensional features of the turbulent flow through a planar sudden expansion", Physics of Fluids, Vol. 20, pp. 5103:1–15.
[5] Jirka, G.H. and Uijttewaal, W.S.J. (2004), "Shallow flows: a definition", *Shallow flows*, Taylor & Francis, London, pp. 3–11.
[6] Giger, M., Dracos, T. and Jirka, G.H. (1991), "Entrainment and mixing in plane turbulent jets in shallow water", Journal of Hydraulic Research, Vol. 29(5), pp. 615–642.
[7] Chen, D. and Jirka, G.H. (1999), "LIF study of plane jet bounded in shallow water layer", Journal of Hydraulic Engineering, Vol. 125(8), pp. 817–826.
[8] Babarutsi, S. and Chu, V.H. (1991), "Dye-concentration distribution in shallow recirculating flows", Journal of Hydraulic Engineering, Vol. 117(5), pp. 643–659.
[9] Babarutsi, S., Ganoulis, J. and Chu, V.H. (1989), "Experimental investigation of shallow recirculating flows", Journal of Hydraulic Engineering, Vol. 115(7), pp. 906–924.
[10] Chu, V.H., Liu, F. and Altai, W. (2004), "Friction and confinement effects on a shallow recirculating flow", Journal of Environmental Engineering and Science, Vol. 3, pp. 463–475.
[11] Chen, D. and Jirka, G.H. (1995), "Experimental study of plane turbulent wakes in a shallow water layer", Fluid Dynamics Research, Vol. 16(1), pp. 11–41.
[12] Kantoush, S.A. (2008), Experimental study on the influence of the geometry of shallow reservoirs on flow patterns and sedimentation by suspended sediments, PhD thesis, Ecole Polytechnique Fédérale de Lausanne.
[13] Dufresne, M. (2008), Modélisation numérique 3D du transport solide dans les bassins en assainissement: du pilote expérimental à l'ouvrage réel, PhD thesis, Université Louis Pasteur (Strasbourg 1), in French.
[14] Dewals, B., Kantoush, S., Erpicum, S., Pirotton, M. and Schleiss, A. (2008), "Experimental and numerical analysis of flow instabilities in rectangular shallow basins", Environmental Fluid Mechanics, Vol. 8, pp. 31–54.

*Environmental Hydraulics – López-Jiménez et al (eds)*
*© 2010 Taylor & Francis Group, London, ISBN 978-0-415-56697-1*

# Dynamics of SS in the Guadalquivir estuary: Monitoring network and database management

Simona Bramato
*Grupo de Dinámica de Flujos Ambientales, Universidad de Granada, CEAMA, Granada, España*

Eva Contreras & María José Polo
*Grupo de Hidrología e Hidráulica Agrícola, Universidad de Córdoba, Córdoba, España*

Asunción Baquerizo
*Grupo de Dinámica de Flujos Ambientales, Universidad de Granada, CEAMA, Granada, España*

Gabriel Navarro
*Instituto de Ciencias Marinas de Andalucía, CSIC, Puerto Real, España*

Manuel Díez-Minguito & Miguel Á. Losada
*Grupo de Dinámica de Flujos Ambientales, Universidad de Granada, CEAMA, Granada, España*

ABSTRACT: The description of the climatic agents that control and definen the Guadalquivir River estuary dynamics is made from a dataset made up of experimental measurements from the study site together with external sources. The complete database comprises wave, wind, atmospheric pressure, meteorological and astronomic tide, water inflow, turbidity, salinity, and other relevant parameters in water quality. Such information has been derived from data monitoring in (1) maritime stations in front of the river mouth at different water depth, (2) fluvial stations along the main channel of the river and different tributaries to the estuary, and finally (3) different stations located along the contributing area to the estuary. Data sources are varied (ICMAN, Puertos del Estado, Junta de Andalucía, etc.) anda t least monthly updating is made, with many variables weekly updated to monitore sudden increases in suspended sediment concentrations. The final result is a continuous quasi-real time monitoring of forcing agents in the estuary together with the state variables relevant for different processes. Global management of the database is made through PROGE, a Matlab program with a visual interface, where the information from each monitoring point is gathered in a structure, providing not only a quick and easy access and visualization of the data, but also a precise and complete information of the monitoring process, and post-processing análisis.

*Keywords*: database management, estuary monitoring, Guadalquivir estuary.

## 1 INTRODUCTION

Estuaries form and area is constantly altered by the erosion and deposition of sediment along their extent, and strongly affected by the variations in the sea level at different time scales. Their wide range of forms is the result of the complex interaction between riverine and marine processes. Estuaries are continually evolving, changing their shape, adapting to changes in river flow and weather pattern, changing the phase and amplitude of the input signals, with effects on salinity, temperature, suspended sediments (SS) and nutrients distribution in water in time and space[1]. In estuaries, sediment dynamics is a complex process where tidal cycles, density currents, freshwater inflows and mixing atmospheric agents, among others, interact determining deposition and erosion patterns and suspended sediment concentration distribution and evolution. Suspended sediments in seawater tend to flocculate, diverting from their behaviour in the fluvial reaches upstream.

Suspended sediment concentration in water may greatly influence other state variables such as dissolved oxygen, turbidity, temperature, density … and thus poses a big threat for the ecological state of waters. Most of the estuaries along the developed countries coastline are strongly modified by dam regulation upstream and socioeconomical uses of the estuary area, such as agriculture and acuiculture, and tourism. An integrated management not only of water resource but also of soil use in their contributing area is a necessary approach to restore and preserve the diversity of life and nutrient fluxes in our estuaries. The Guadalquivir River Estuary in Southern Spain is a good example of such demanding situation, with a great reduction of freshwater input due to the great regulation system upstream along the river, periodic dredge labors to maintain navigation upstream to Seville Port, and acuiculture systems and big rice crop areas downstream which require low suspended sediment concentration and moderate levels of salinity in water, respectively.

But to model rigorously SS dynamics in such an estuary requires to couple riverine and marine hydrodynamics together with a proper biogeochemical analysis to evaluate its current state and trend, and to simulate future states under different management strategies and/or subject to sea level rise and climate variability trends. A big amount of data from the system must be processed to include all relevant processes in the analysis and to feed and calibrate the final models[2].

This work presents a data management tool, PROGES, under Matlab programming language, developed for the monitoring system of the Guadalquivir Estuary in the framework of the Project *Method Proposal for the Diagnosis and Prognosis of Human Actions Consequences on the Guadalquivir Estuary*, financed by the Port Authority of Seville and coordinated by the ICMAN, Institute of Marine Science of Andalusia (Cádiz).

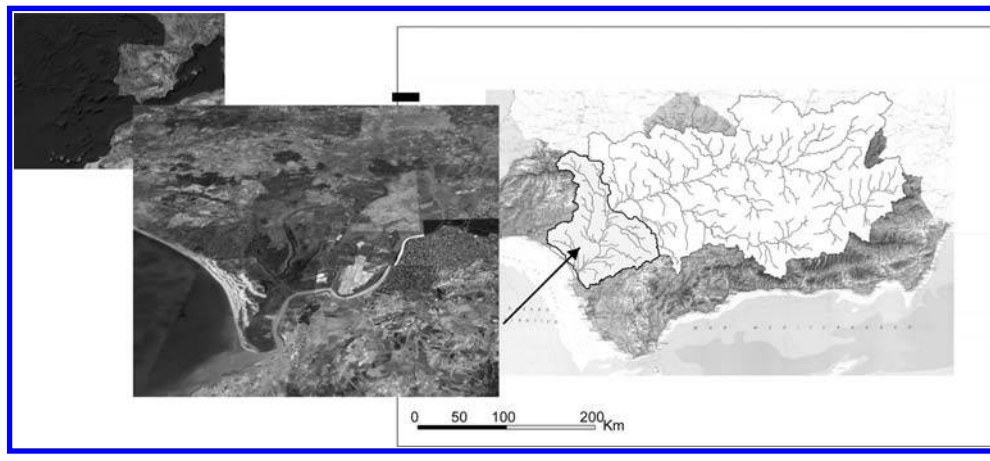


Figure 1. The Guadalquivir estuary location and contributing basin.

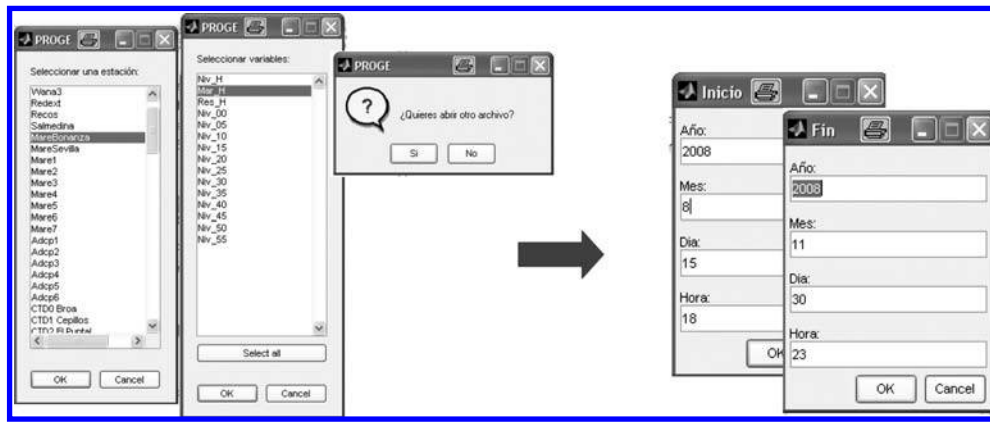


Figure 2. PROGE displays for data source and variable selection and period of visualization.

## 2 STUDY SITE AND MONITORING SYSTEM DESCRIPTION

The Guadalquivir River estuary receives inflows from a 57400 km$^2$ basin which spreads along Cádiz, Huelva, Sevilla, Córdoba and Jaén. The low reach of the river travels across a wide alluvial plain, from Palma del Río (Córdoba) to the mouth; freshwater discharges to the estuary mainly come from the Alcalá del Río dam, upstream Sevilla, which can be thus considered as the estuary head, and tidal influence is significant up to 15 km upstream Sevilla. Downstream, Doñana National Park constitutes one of the greatest coastal wetland in Europe. Figure 1 shows the Guadalquivir Estuary location together with its contributing basin.

The monitoring network and data necessary for the estuary analysis and modeling comprises several sources and databases[3][4].:

- Meteorological data from the automatic station network of the Junta de Andalucia.
- Tidal gauges network from different sources.
- WANA data in the outer platform, from the AEMET
- Water quality data from the Water Policy periodic campaigns along the estuary
- Water quality data from the Guadalquivir Water Administration (ICA network)
- Water discharges from the Alcala del Rio dam, and other contributing rivers to the estuary
- CTD monitoring network along the main channel in the estuary, implemented by the ICMAN, with continuus register of temperature, salinity, turbidity, velocity, among other variables, including also meteorological variables at the monitoring point.
- AWAC and ACDP monitoring points in the outer platform implemented by the Dynamic of Environmental Fluxes Group.
- Specific field campaigns during the Project.

Due to the characteristics of every dataset: frequency, time series extent, datasource, format, a huge amount of work deals with data validation, filtering, preprocessing, and format conversion. After one year of data collecting and analysis, the need for a management tool was patent, together with the need of up-to-date continuous actualization of the whole database from every responsible team in the research group, to trace sudden episodes of suspended sediment increases that periodically create alarm among the estuary economic users, such as rice farmers and acuiculture enterprises.

## 3 PROGE, THE DATA MANAGEMENT TOOL FOR THE GUADALQUIVIR ESTUARY

A Matlab program for data analysis and visualization was developed on the basis of the structured complete database created in the Project. The database is weekly updated, which involves a first screening of each new data set, filtering and filling of time series, and sometimes, changes in format for analysis requirements. In PROGE, each dataset is filed as a structure, which contains numeric and text information comprising information about the location and identification of the data source

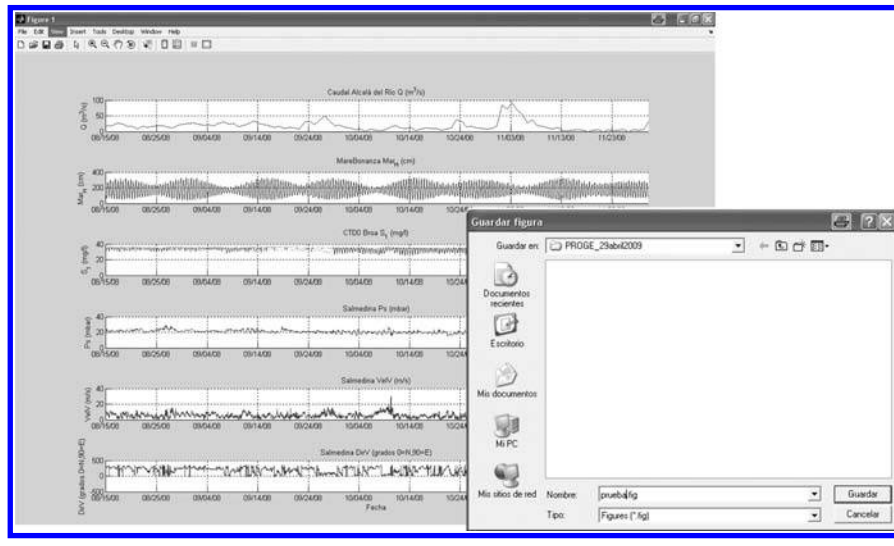


Figure 3. An example of PROGE figures and *Save* menu.

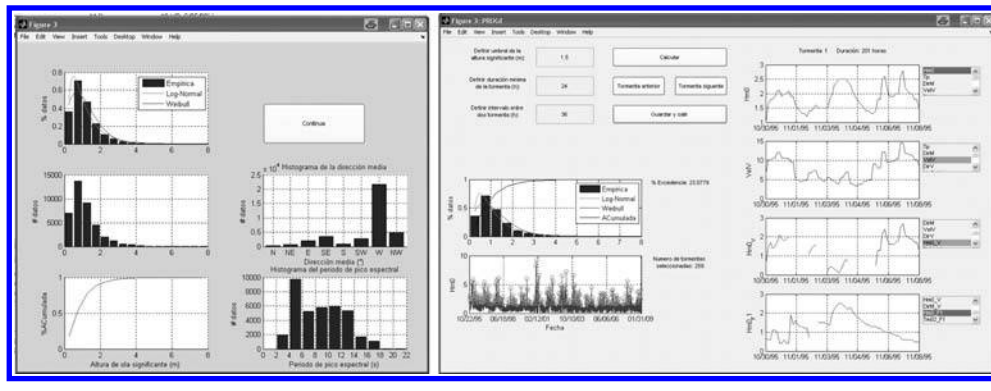

Figure 4. Wave data extreme values analysis and extreme event identification in PROGE.

point, information about the instrumentation involved in the register, information about the original data and the preprocessing analysis, and the time series. PROGE is currently run under a Spanish version.

The main core of PROGE allows a simultaneous visualization of several variables data from different periods or some analysis made from a given data set. The program includes an interface for users, which guides in an easy manner through the selection process and later analysis. The following figures show some examples of PROGE displays.

The final figures provided by PROGE can be filed in different format in order to be later imported by document processing additional tools.

Usual analysis made up from certain groups of datasets are being included in PROGE utilities, such as the identification of extreme values periods for different event definition. Figure 3 shows an example, consisting of extreme values analysis of wave data (significant wave height, peak values period and average direction), together with the extreme events identification and visualization from the previous analysis.

## 4 CONCLUSIONS

The complex and multiscale processes that interact in an estuary requires integrated monitoring of a wide variety of environmental variables from different sources. The Guadalquivir River estuary is currently being modeled and the huge amount of datasets arising from the Project work together with external sources has been efficiently structured in a database and the management data tool, PROGE, developed on Matlab, provides the whole research group with a validated data information and a strong, easy-to-handle, tool to visualize and further process such data. The database and management tool will be accessible from internet sources with different access users in the future, for further studies on the area, under the maintenance of the research group.

## REFERENCES

[1] Dyer, K.R. (2000), *Estuaries: A Physical Introduction*, Wiley, Chichester.

[2] Hardisty, J. (2007), *Estuaries. Monitoring and Modeling the Physical System*, Blackwell, Singapore.

[3] Navarro, G., Gutiérrez, F.J., Roque, D., García, R., Fernández, J.L., Losada, M.A. and Ruiz, J. (2009). "Red de monitorización en tiempo real de las propiedades hidráulicas y de calidad ambiental de las aguas portuarias de Sevilla", *X Jornadas de Costas y Puertos, 28–29 Junio, Santander (Spain).* In Press.

[4] Díez-minguito, M., García-Contreras, D., Bramato, S., Ruiz, J. and Losada, M.A. (2009), "Modelo de circulación mareal y submareal en el estuario del Guadalquivir", *X Jornadas de Costas y Puertos, 28–29 Mayo, Santander (Spain).* In Press.

*Environmental Hydraulics – López-Jiménez et al (eds)*
*© 2010 Taylor & Francis Group, London, ISBN 978-0-415-56697-1*

# Monitoring and decision support systems for impacts minimization of desalination plant outfall in marine ecosystems

Jose M. Hernandez Torres
*Tecnoma S. A. C/ Antiga senda de Senent, Valencia, Spain*

Aina Hernandez Mascarell
*Typsa, Madrid, Spain*

Marta Navarro Hernandez & Miguel Martin Monerris
*Department of Hydraulic and Environmental Engineering, Polytechnic University of Valencia, Valencia, Spain*

Rafael Molina
*Typsa., Madrid, Spain*

Jose M. Cortes
*SIDMAR Bernhard Pack S.L. Avda. Benissa, Spain*

ABSTRACT: ASDECO is a R&D project whose main objective is to design a system that allows the implementation of an Adaptive Management for brine discharges from desalination plants into the sea. The project has two phases: to design and to adapt the instrumental system to the characteristics of the brine plume, achieving the required reliability and precision. An information and forecast system has also been constructed to compile and validate the data, as well as to activate the alarm protocols required for the Environmental Impact Declarations. The application of forecast systems will provide the outfall management with the necessary flexibility to adapt to the favourable conditions of the marine environment, maximizing dilution and minimizing brine impact. The system is currently being implemented and tested in the Alicante Channel desalination plant (Alicante – Spain).

*Keywords*: ASDECO, brine discharge, brine plumes, Ocean-meteorological Data Acquisition System, Brine Dispersion Forecast System, Support tool for decision making, Adaptive

## 1 INTRODUCTION

The development of Seawater Desalination Plants (SWDP) for urban supply and agricultural purposes in different areas of Spain has increase greatly in recent years as a way of lessening the water scarcity. There are currently 900 desalination plants in Spain, which have an installed capacity that is greater than 1.5 $Hm^3$/day[2]. This capacity will be exceeded through the upcoming implementation of more than 34 desalination plants that are currently in different phases of development and that will add around 700 $Hm^3$/year to the existing desalination production (140 $Hm^3$/year – 2004).

From an environmental point of view, the waste discharge management where brine is the main component is the most important problem [6]. When the raw water is taken from the sea, the effluent salinity can increase between 10% and 70%, depending on the technology used [2]. In the case of effluent discharge into the sea, and especially in the presence of communities of particular biological interest (as marine phanerogam grasslands that have a poor tolerance to increases in salinity[1]), outfall management should be carried out based on the principles of caution and sustainability. In order to achieve appropriate discharge management, we must increase our knowledge and provide the authorities and the entities that are developing and managing the installations. Using the appropriate tools, the discharge efficiency can be improved by the increase the effectiveness of brine dilution into the sea.

The implementation of many of the abovementioned desalination projects requires the authorities to meet the requirements of the Environmental Impact Declaration (EID), which involve strict monitoring programmes that activate protocols for the periodic stoppage of the plant mainly by the activation of alarms when the salinity values are exceeded in the protection perimeters of the most vulnerable biological elements.

TECNOMA, in collaboration with SIDMAR, is developing the ASDECO Project (Automated System for Desalination Dilution Control. www.proyectoasdeco.com). This research is subsidized within the National Programme of Environmental Science and Technology of the National R&D Plant 2004-2007 and is coordinated by the Ministry of the Environment and Rural and Marine Affairs.

This applied research project aims to create a prototype that adapts and improves the control of desalination plant discharges in the marine environment. The goal is to combine the capacity of Decision Support Systems (DSS) and the latest instrument innovations. As a pilot case for the development of the system, we are currently implementing the prototype at the Alicante Channel Desalination Plant, thanks to the collaboration of the "Canales del Taibilla" Association.

## 2 OBJECTIVES

The high variability of marine conditions during the year means that sustainable and efficient management of the outfall must be available for these conditions. At present, there are few options that offer control and adaptation tools in the ordinary

management of brine discharge into the marine environment. Therefore, the main objective of ASDECO is to develop a prototype that provides this capacity in the following ways:

- Improve operation control: Supervise the correct operation of the plant and the brine discharge and corroborate compliance with the Environmental Impact Declarations and outfall authorization. Have a real-time time monitoring system that enables awareness of the behaviour of the discharge.
- Adaptation: Avoid rigid discharge management by adapting to the climate and marine conditions. A sustainable management strategy would be based on maximizing the dilution of the waste in the most unfavourable conditions and minimizing if those conditions allow lesser impact on the environment (maximum turbulence conditions).

The main purpose of ASDECO is to offer this adaptation in the ordinary management of the desalination plant outfall. In order to do this, a tool has been designed to provide information in real time about the conditions of the marine environment. It uses this information to predict the behaviour of the hypersaline plume, which will allow Adaptive Management to be implemented in the desalination plant. The prototype developed can also be used as a powerful alarm and information tool for development authorities, the developing authorities, the companies operating the installation and the pertinent environmental authorities.

The ASDECO System uses real-time analysis of ocean-meteorological data from the marine environment and the effluent in order to optimize the marine environment mixing capacity to maximize the efficiency of the outfall system, without harming the marine ecosystems. In the case of ocean-meteorological conditions that favour dilution, the system could help to optimize the operational cost by acting on the pumping capacity of the dilution water or reducing the pressure in the discharge outlet diffusers.

## 3 ASDECO PHASES

ASDECO has been developed in the following fases:

a. Design and integration of the instrumentation.
b. Development of an Alarm and Information System.
c. Development of a Decision Support System (DSS).
d. Integration of the system into the Ordinary Management of a pilot installation.

a. Design and integration of the instrumentation. In this first phase, a prototype of the ocean-meteorological data acquisition station was designed. The station was optimized for plume control, both in near field and far field. The aim of this optimization was to adapt its components and provide them with the necessary precision and reliability requirements. The basic objective was to design a compact and reliable solution that allows the integration of a large number of sensors: CTD, current, wind, and wave height profilers and water quality (dissolved oxygen, temperature, turbidity, redox, chlorophyll a, green algae, etc).

The prototype design allows for the integration of additional functions such as the following selection of buoys that house all of the components; the optimization of a mooring system; the energy system; the incorporation of a positioning system in case of loss to help determine the drift; the incorporation of multiple communication systems (GSM, radio, WIMAX, Satellite). A sensors selection included in prototype have been included in figure 1.

b. Development of an Alarm and Information System. The information system allows the information that is acquired in real time by multiple systems to be recompiled and validated. This is done by incorporating an error identification protocol, testing the state of the instrumentation, and making easier its analysis. The Information System uses a corporate database that

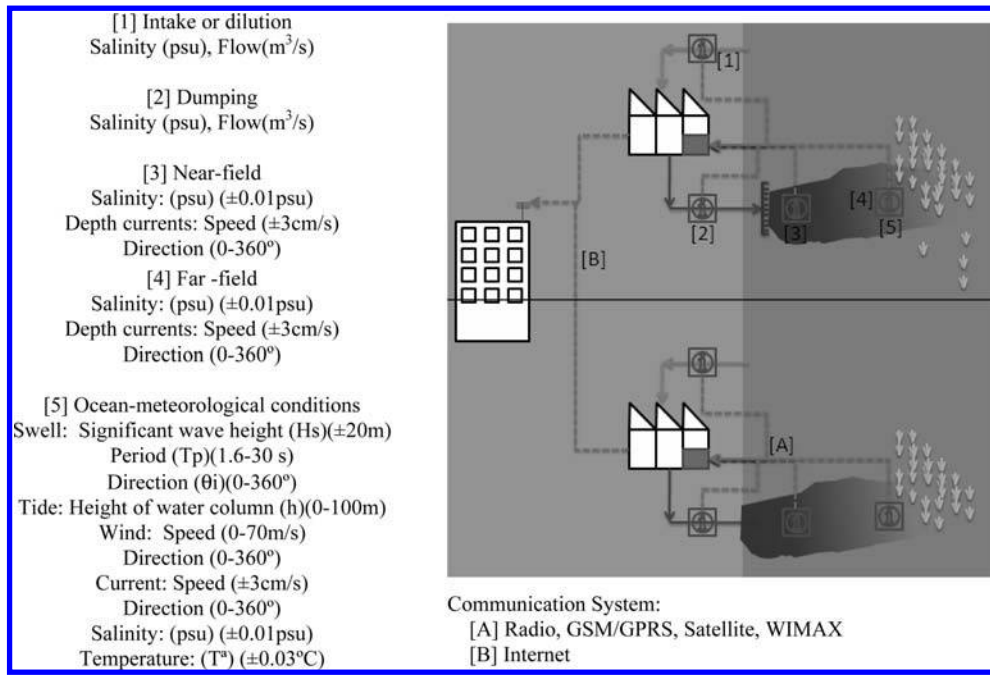


Figure 1. Outline of the implementation of sensors and communications.

is based on SQL and is integrated with a GIS viewer that displays cartographic, vectorial and raster information associated to each desalination plant. This information system generates automated reports in an easy-to-use web environment, providing development authorities the necessary tools for early control and vigilance of the desalination plants. This tool can be shared with environmental agencies or be made available to the public.

This management and supervision tool is designed to centrally recompile and monitor brine discharge in several plants. The alarm generation is especially useful when certain salinity threshold values are exceeded over certain periods of time (exceeded percentile) (Figure 2). These thresholds can define several action levels (alarm level, emergency level, etc.) in accordance with the criteria defined in the EID or in the discharge authorization. The system has a communication module that informs of the alarm activation via email or SMS.

c. Development of a Decision Support System (DSS). This phase is mainly dedicated to the production of a decision tool that analyzes the instant and seasonal operation of the brine discharge. This tool provides management measures to maximize the brine dilution and thus reduce its impact on the receiving medium. The core of the tool is based on a forecast module that uses a combination of fuzzy logic and neural networks to forecast the distribution of the plume and predict salinity levels in the protection perimeters. The use of neural networks associated to oceanographic forecasts has been extensively used[4][5]; however, their combination with fuzzy logic techniques are very recent, for example those associated with predicting the ecological state of continental surface water bodies[8] or the analysis of reservoir water quality[7].

This forecast system makes use of the instrumental network implemented to train and validate the neural network in such a way that, at a monitoring point, the salinity will depend on the ocean-meteorological conditions of the marine environment and the flow and salinity of the desalination plant discharge (see Figure 3). The forecast system will also be connected to the operation networks of the National Sea Port System to correlate their climatic forecasts with the brine discharge environment (6, 12, 24, 48 and 72 hours). This facilitates Adaptative Management by providing feed back data to the predictive system. The system will create predictive alarms similar to the ones provided by the real time control that allow the desalination plant managers to advance the management to the brine impact.

The system focuses on two fundamental management scenarios:

1. The system is pointed to the detection of salinity values in the near field that could be potentially transported to the protection perimeter (Figure 4). The forecast tool continuously evaluates the salinity values, the outfall, the bottom salinity conditions in near-field, and the conditions at the edge of the marine environment. When necessary alternative management of the outfall is proposed to avoid possible disruption (e.g. increase the planned dilution, increase the number of outlets, or increase the outflow speed) (Figure 4).

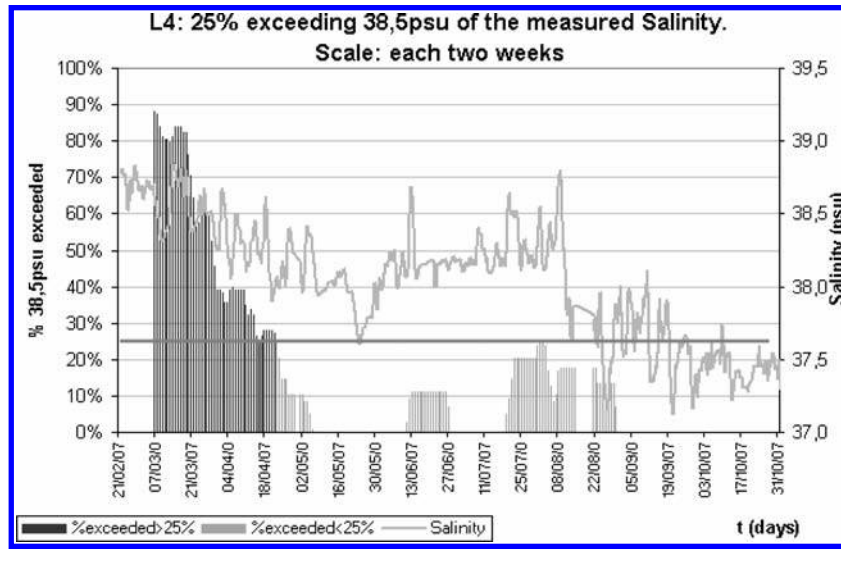


Figure 2. Evolution of observed salinity (psu) (Green line) every hour at a depth of 20 cm in a monitoring CTD of a brine dump. Alarm levels represented as mobile exceeded percentile (%) on time (2 weeks).

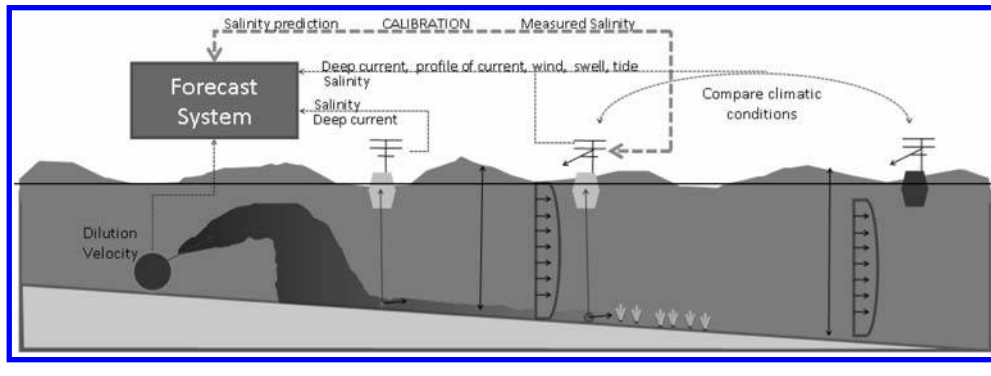


Figure 3. Outline of the interaction of the sensors and the forecast system during training, calibration and validation.

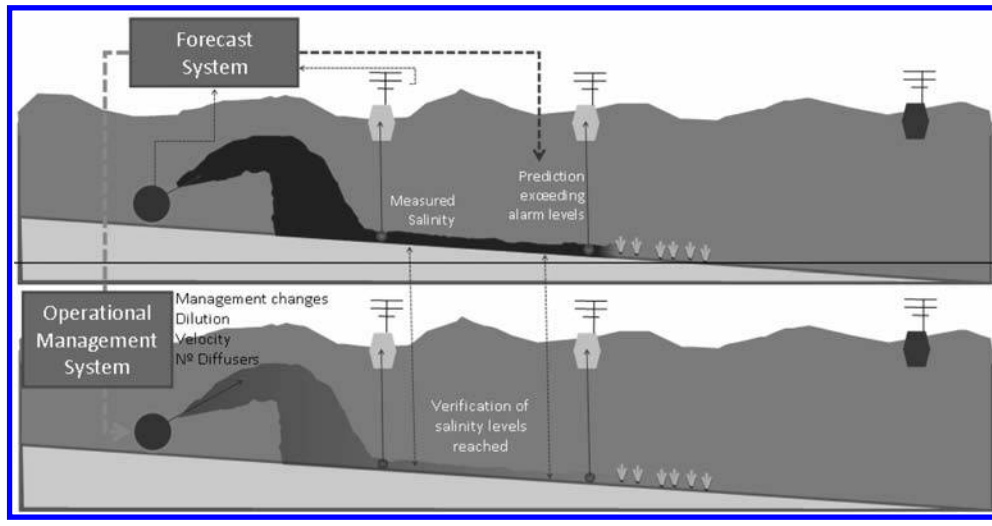


Figure 4. Conceptual outline of the Adaptive Management operation in forecasting disruptions.

2. Other use is pointed to detect changes in the energy state of the sea and, therefore, in the dilution efficiency of the plume in both near-field and far-field. A very useful management protocol might be to link the outfall management and progress over time. This would not only prevent possible disruptions caused by low energy, but it would also make use of greater turbulence scenarios, which allows plume dilution.

d. Integration of the pilot system into ordinary management. The pilot system has been integrated into the Alicante Channel desalination plant. The desalination plant has a treatment capacity of 130.000 $m^3$/day. It is currently in operation to provide drinking water to the metropolitan area of Alicante City. This area on the coast of Spain has a large tourist sector and is characterized by a water deficit. Desalination is one of the greatest structural solutions developed to alleviate the region's deficit, even though the sustainability, of the area requires preserving the great wealth of the marine environment (e.g. *Posidonia Oceanica* grasslands as a prime example).

The Alicante Channel desalination plant carries out its dumping on the surface of the coastline which generally has a dilution on a range of 1:2/1:4. The discharge generates 7 $m^3$/s average flows with a salinity of 50 psu. This discharge is currently the object of an intensive monitoring programme due to the existence of *Posidonia Oceanica* grasslands that are located approximately 1.6 km in front of the discharge point.

The integration of this pilot system consists of the installation of an Acquisition System for Oceanographic Data in near-field and far-field, including this characterization of the specific conditions of the brine discharge. The buoys and data acquisition instrumentation are complemented with a CTD field due to the characteristics of the seabed. There are multiple preference channels, which allow for the diffusion of the plume in more than one main direction depending on the marine conditions. With this information a spatial campaign was carried out to characterize the plume distribution. These data will not only provide knowledge about the plume behaviour, but it also provides a large number of records for the training and validation of the forecast system. The pilot installation and integration of the system has been underway since November 2008, and the implementation of the first system validation, has been completed (previous data was acquired by the EID monitoring plan). These first results indicate the great influence of the maximum wave height in the dispersion of the brine plume. With regard to the calibration of the forecast system, some favourable adjustments have been obtained with $R^2$ greater than 0.80 (Figure 5).

The pilot application has been also useful to validate the ability to anticipate alarms for the forecast system. Figure 6 shows the system capacity to predict exceeded periods of salinity thresholds. Thereby it allows adapting the management of the outfall. Nowadays the forecast system is being improved through the incorporation of new variables, especially those that are related with daily fluctuation in salinity and with the cumulative effect of marine energy states.

## 4 CONCLUSIONS

The ASDECO R&D project is close to achieving the complete development of a system that allows the implementation of Adaptive Management in brine discharges from desalination plants into the sea. Great effort has been made to adapt the most recent and innovative sensors to the system monitoring capacities. The integration of this real-time acquisition system with a Brine Dispersion Forecast Tool represents a great technical advance in creating a complete Decision Support Tool that achieves adaptative brine outfall management.

The pilot implementation shows that the use of neural diffuse types such as ANFIS can be a very useful option for the follow-up and control of waste brine into the sea. At least, until the deterministic models finally adjust correctly to the turbulent dispersion processes in the problem of transport and brine dispersion and computational requirements are adjusted for real-time applications.

The experience shows that the most important variables increasing trend in salinity is due to the increase in salt load and the decrease in maximum wave height. It is worth mentioning that the maximum wave height does not explain the average dispersion condition of the plume in the sea or the occasional decrease peaks of salinity: for extended periods of calm, the

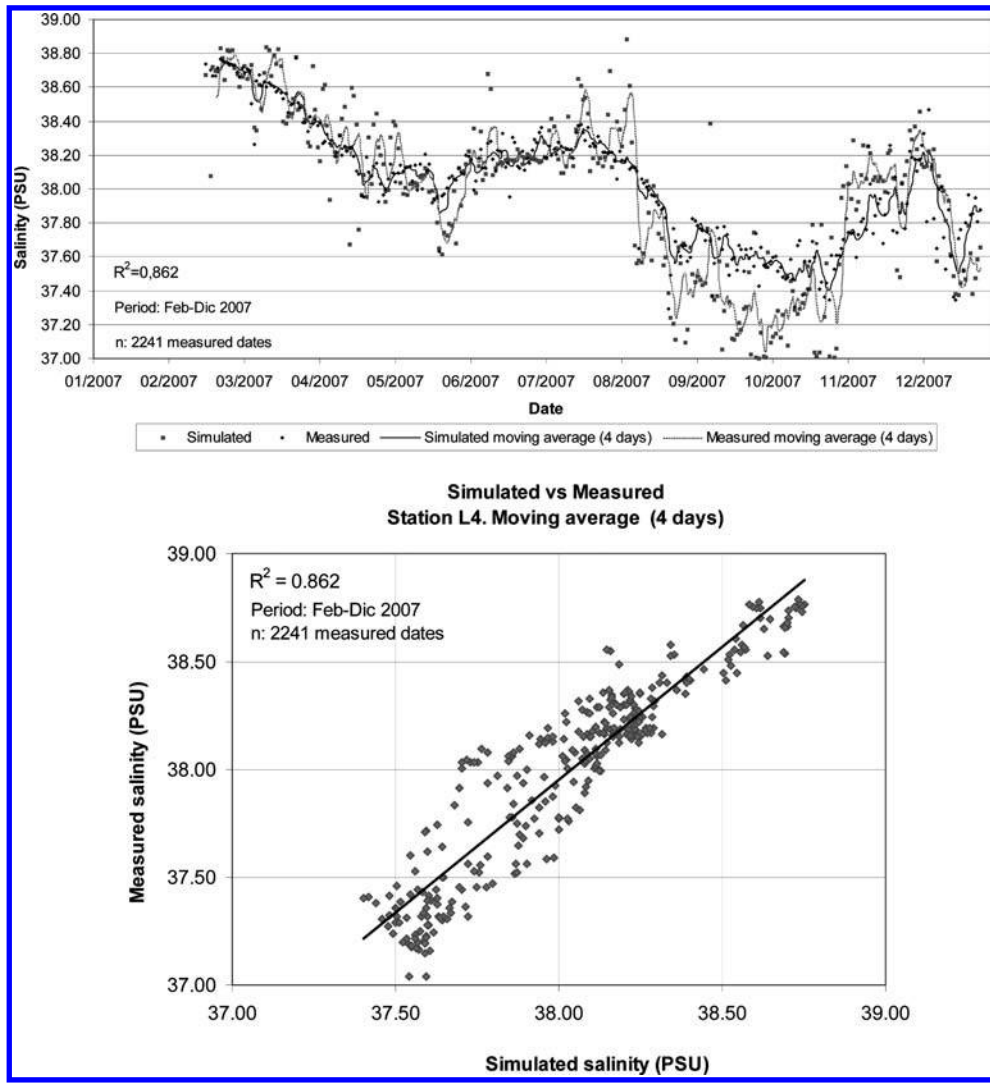


Figure 5. Time series comparison and measured and predicted value analysis for a control station in *Posidonia Oceanica* edge.

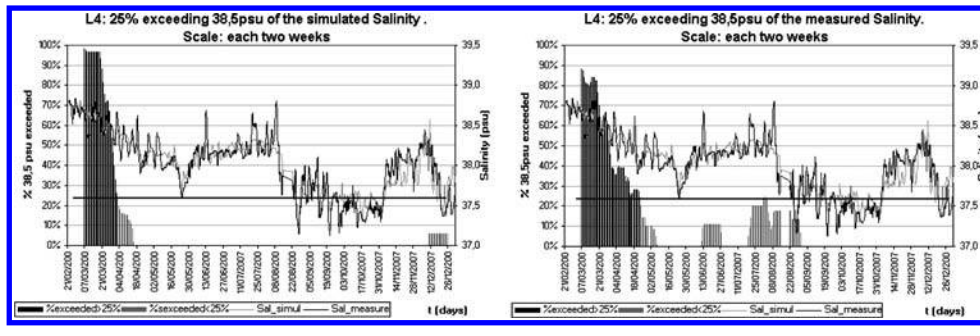


Figure 6. Predicted [a] and measured [b] alarm comparison based on time exceedance percentil.

salinity increase with respect to the salinity base values is high, while for relevant wave height, the plume undergoes more dispersion.

## REFERENCES


[1] Fernández-Torquemada, Y.; Sánchez-Lizaso, J.L.; González-Correa, J.M. 2005. Preliminary results of the monitoring of the brine discharge produced by the SWRO desalination plant of Alicante (Spain). *Desalination*. 182 (2005), 395–402.

[2] Ruiz-Mateo, A. 2007. Los vertidos al mar de las plantas desaladoras. Centro de Estudios de Puertos y Costas. Ministerio de Fomento. Ministerio de Medio Ambiente. *Ambienta, Revista del Ministerio de Medio Ambiente*, 62, 51–57.

[3] Sánchez-Lizaso, J.L.; Romero, J.; Ruiz,J.; Garcia, E.; Buceta, J.L.; Invers, O.; Fernández-Torquemada, Y.; Mas, J.; Ruiz-Mateo, A.; Manzanera, M. 2007. Salinity tolerance of the Mediterranean seagrass *Posidonia oceanica*: recommendations to minimize the impact of brine discharges from desalination plants. *Desalination* 221 (2008), 602–607.

[4] Medina, J.R., 2004, "Improving wave predictions with artificial neural networks, by O. Makarynskyy", Ocean Engineering, vol. 32, no. 1, pp. 101–103.

[5] Mandal, et al. 2008. Application of Neural Networks in Coastal Engineering – an overview. The 12th International Conference of International Association for Computer Methods and Advances in Geomechanics (IACMAG).
[6] Meerganz von Medeazza, G.L. 2005. Direct and socially-induced environmental impacts of desalination. Desalination. 185 (2005), 57–70.
[7] Marce, R. et al. A neuro-fuzzy modeling tool to estimate fluvial nutrient loads in watersheds under time-varying human impact. Limnology and Oceanography: Methods 2, 2004, 342–355.
[8] Ocampo-Duque, W et al. 2007. A neural-fuzzy approach to classify the ecological status in surface waters. Environmental Pollution 148, 2007, 634–641.

*Environmental Hydraulics – López-Jiménez et al (eds)*
*© 2010 Taylor & Francis Group, London, ISBN 978-0-415-56697-1*

# Lab-cultured biofilm stabilization of non-cohesive sediments: Quantifying the elastic constant, k

E. Vignaga, H. Haynes & W.T. Sloan
*Department of Civil Engineering, University of Glasgow, Glasgow, UK*

A. Fernandes & M. Jarvis
*Department of Chemistry, University of Glasgow, Glasgow, UK*

T.K. Beattie
*Department of Civil Engineering, University of Strathclyde, Glasgow, UK*

V.R. Phoenix
*Department of Geographical and Earth Science, University of Glasgow, Glasgow, UK*

ABSTRACT: A monoculture of cyanobacterium (Phormidium sp.) was grown for up to 10 weeks on spherical glass beads ($d_{50} = 1.09$ mm) under constant unidirectional flow conditions. Using a 0.3 m × 15 m flume facility, the strength of biofilm-sediments adhesion was tested at the threshold of entrainment. High speed videographic analysis focussed on biofilm entrainment at two different scales (small = 4.5 cm × 3.4 cm; large = 20 cm × 20 cm) and image post processing employed the software ImageJ. Results indicated a 23–77% increase in the threshold of entrainment of biostabilized sediment, compared with that of abiotic sediment. The biofilm was sufficiently strong that tensile testing could be employed to elucidate its material properties and those of the composite of biofilm and sediment. Both exhibited elastic behaviour which could be characterized by Hooke's Law. Describing the strength of biofilm in this manner will allow modification of traditional abiotic models of sediment transport to incorporate the binding effects of an elastic biofilm.

*Keywords*: Biofilm, Biostabilization, Flume, Non-Cohesive Sediment, Entrainment, Tensile Test.

## 1 INTRODUCTION

Biological populations (such as bacteria, algae, diatoms) colonize almost all surfaces in both fresh-water and marine environments. Their growth and structural development alters the morphology of the boundary and the associated local hydrodynamics. In many cases this has undesirable outcomes for science and engineering research. For example, 'biofouling' increases the frictional resistance of the hulls of marine vehicles, resulting in increased fuel costs to the operator of up to 8–18% [1],[2]. Similarly, biofouled canals and pipelines increase drag and reduce the capacity of hydroelectric power schemes [3]. In river systems, pathogens such as *E. coli* and *Salmonella* have been found to be more highly concentrated in river sediments coated by biofilm [4]. However, one research avenue that has received more notable attention is the 'biostabilization' effect that microbial colonisation has on sediment boundaries, reducing scour and particle transport [5],[6],[7],[8],[9]. This research is critical to understanding, *inter alia*, morphological change, navigation, structural foundation stability and habitat suitability in riverine and marine environments. Gaining this understanding requires advances in: (i) quantifying the effect of biofilm on sediments coarser than fine sand; (ii) quantifying the biostabilization of fresh water and river sediments [10],[11], rather than well-studied marine environments; (iii) characterizing the behaviour of individual environmental conditions on biofilm development[12],[13]; and (iv) developing theoretical models for the entrainment of biostabilized substrates.

A key difficulty in developing theoretical models of entrainment for biotic sediments is the quantification of biofilm forces. Many researchers have proved that biofilms have elastic [14],[15] and visco-elastic [16],[17],[18] properties due to their polymeric nature. This has led to some researchers modelling biofilm strength as a spring, characterized by an elastic constant [19]. However, our understanding of the mechanical structure and macroscopic material properties of biofilms is hazy. This is exacerbated by the many different non comparable experimental techniques that are used to measure cohesive strength [20]. If theoretical models are therefore to be developed, robust analysis of the mechanical strength of biofilm is essential.

This paper presents experimental data from preliminary investigations designed to address some of the unsolved problems in biofilm research. Specifically, experiments on a biofilm cultured over a coarse substrate in a controlled laboratory flume facility were used to analyse three factors: (i) the effect of biofilm growth duration on biofilm adhesion to the substratum; (ii) the change in biomass with growth duration; (iii) mechanical analysis of biofilm adhesion and cohesion.

## 2 METHODOLOGY

### 2.1 *Laboratory growth and adhesion test at entrainment threshold*

A monoculture of cyanobactrium (*Phormidium* sp.) was cultured for up to 10 weeks in a small recirculating flume (5 m long × 0.6 m wide; slope ∼1/200). The growth substratum was transparent spherical glass beads ($d_{50} = 1.09$ mm; sphericity = 90%; density $\rho_s = 2.65$ g/cm$^3$) contained within nine removable Perspex boxes (20 cm long × 20 cm wide × 2 cm deep) arranged in three rows 1m apart. To permit colonization, 200 ml of bacteria and nutrient medium was added to the freshwater reservoir of the flume at the start of the experiment. All other significant variables for bacterial growth were

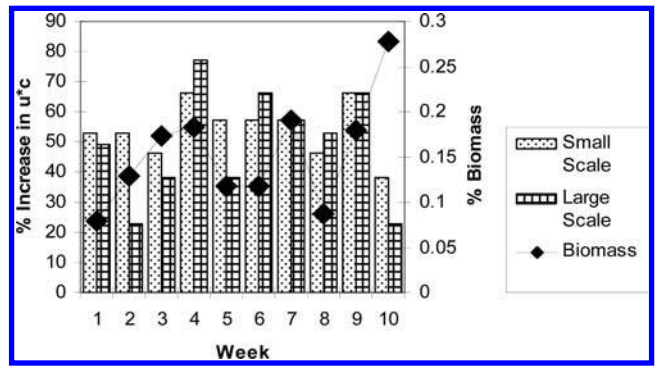


Figure 1. Temporal growth relationships (1–10 weeks) with biomass (% by weight of core sample) and entrainment threshold (% increase in critical shear velocity for small scale samples and % increase in critical shear velocity for maximum eroded area in between two flow steps for the large scale).

controlled: (i) constant temperature, 28°C; (ii) constant lighting; (iii) full strength BG11 + Nitrate nutrient medium [21]; (iv) constant flow and shear velocity of 0.88 l/s and 2.06 cm/s respectively. Biofilms were grown for between 1–10 weeks. Growth was monitored weekly by taking cores (2.6 cm in diameter) of the full depth of the bed and analyzing their biomass content using the standard HIMOM laboratory analysis procedure [22]. At the end of each week, one box was transferred to a larger flume facility (15m long x 0.3m wide; slope ~1/200) to test the strength of the biofilm under a range of applied flows. Flow was increased in incremental steps and, due to use of quasi-uniform flow in shallow flow depths, the applied shear stresses were calculated using two methods: (i) the depth-slope product for uniform flow; and (ii) the Mayer-Peter & Müller equation for non-uniform flow. High speed videography (*Sony* HDR-SR5E) of the bed surface was recorded at a small scale (4.5 cm × 3.4 cm, resolution 33pixels/mm) for 10 minutes during each flow step, using the software ImageJ [23]. This permitted investigation of particle vibration and the bed's entrainment threshold (based on the Yalin criterion [24]). Still images at the large scale (20 cm × 20 cm) aided analysis of biofilm–bead adhesion through evaluation of the entrainment threshold and the spatial extent of biofilm erosion at each flow step. Small and large scale recordings offered respectively information on single grain entrainment and macro scale erosion trend; using ImageJ the number of grains moving at every step was counted at the small scale whereas the area of biofilm removed at every step was thresholded and measured at the large scale.

### 2.2 *Mechanical properties of the biofilm*

Eight tensile tests were carried out on: (i) biofilm only (B), having various thicknesses presented in Table 1 (Experiments B1-B6); and (ii) composite film samples (C) (biofilm and glass bead) grown for 9 weeks (Experiments C1 and C2). B samples were all taken from the same biofilm cultured into an incubator chamber over a growth timeframe approximately comparable to that of the composite material. Each sample was cut into a rectangular strip approximately 2–3 cm long and 1cm wide. The ends of the biofilm were glued to paper strips and clamped vertically into a 5N *Tinius Olsen* H1KS tensile machine with controlled extension velocity set at 0.5 mm/min. All samples were tested when moist. The dimensions (length, width and thickness) of the sample were measured using a metric ruler, callipers (Experiments B1-B6) or high resolution camera (Experiments C1 and C2). Given that the samples tended to extend before tearing and failing, dimensional data permitted analysis of the relationship between load (N) over the extension (m); this is identified as the constant of elasticity, k (N/m), typical of a spring behaving as the Hooke's Law.

## 3 RESULTS

### 3.1 *Laboratory growth and adhesion test at entrainment threshold*

Data indicate that biomass increases by 247% from 1 to 10 weeks of biofilm growth (Figure 1). The increase is approximately linear between 1 and 4 weeks (127% increase), yet more variable biomass data is recorded between weeks 5-9; observations suggest this variability is related to the temporal structural development of the biofilm. Figure 1 also indicates that the critical shear velocity ($u_c^*$) required to entrain the biostabilized bed increases by 23–77% compared to that calculated for a clean, abiotic sand of equivalent grain diameter [25]. Using both the small and large scale videography of entrainment threshold, it is evident that the strongest beds are formed after 4 and 9 weeks of growth (Figure 1). Furthermore, it is these two samples (weeks 4 & 9) where the detachments of grains is observed as flocs of 4–7 grains: this is distinct from weaker beds where entrainment is as single particles and suggests that increased bed strength is related to stronger, denser binding of particles by the biofilm.

### 3.2 *Mechanical properties of the biofilm*

Table 1 presents the overall results for biofilm only and composite material tensile tests.

In tests B1, B2, B5, C1 and C2 the samples failed gradually with the material ripping somewhere near the centre. Tests B3, B4 and B6 catastrophic failure occurred close to one of the clumps early in the test procedure (elongation < 12%). The high elastic constants (k) of B4 and B6 suggest that the failure may have been due to the biofilm drying out and, therefore, these tests have been removed from all subsequent analysis. The behaviour of the biofilm and biofilm/bead composites showed some similarities in that the range of elongation experienced by both materials in between 25 and 52%. More data will allow the statistical distribution of elongation values for each material to be calculated and more rigorous comparison of their properties.

It is clear however, from the results presented in Figure 2 that there is a distinct difference in the overall strength of the two materials. Data clearly shows that the peak of the elastic trend in experiment B5 (Figure 2a) is 0.19 N yet only 0.04N in

Table 1. Tensile tests results for biofilm only specimens (B1-B6) and for composite material (C1-C2).

| Test | Width (mm) | Length (mm) | Thickness (mm) | Elongation (mm) | Elongation (%) | Constant k (N/m) | k (N/m) at failure |
|---|---|---|---|---|---|---|---|
| B1 | 3 | 17 | 0.23 | 5.46 | 32 | 17 | 30.0 |
| B2 | 14 | 29 | 0.51 | 10.50 | 36 | 15 | 1.1 |
| B3 | 7 | 28 | 1.02 | 2.03 | 7 | 13 | – |
| B4 | 12 | 17 | 0.60 | 2.00 | 12 | 257 | – |
| B5 | 7 | 22 | 1.02 | 11.1 | 50 | 45 | 2.2 |
| B6 | 8 | 13 | 0.80 | 1.17 | 9 | 717 | – |
| C1 | 18 | 24 | 2.14 | 5.96 | 25 | 11.5 | 5.2 |
| C2 | 9 | 13 | 1.12 | 6.73 | 52 | 5.3 | 6.5 |

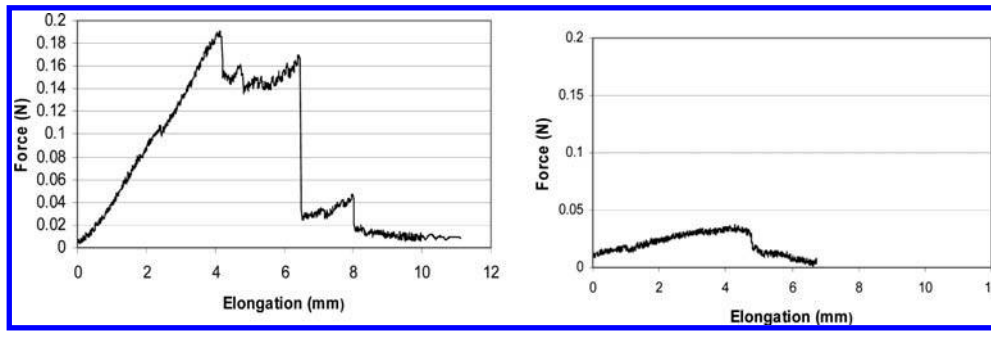


Figure 2. *Tinius Olsen* H1KS tensile test of the: **(a)** biofilm only sample, B5; and **(b)** composite material sample, C2.

C2 (Figure 2b), this unequivocally illustrates that composite material is nearly 5 times weaker than the biofilm only sample, most likely due to lower overall densities of biofilm and resultant binding strength. Validation for use of an elastic constant (k) comes from Figures 2a and 2b. These clearly show a linear relationship between force and elongation for the first part of both the biofilm only and composite material; this trend is common to elastic materials. Fluctuations in Figure 2a suggest localized tearing prior to failure and highlight spatial variability in biofilm strength; this is not apparent in the composite sample.

## 4 CONCLUSIONS

Data prove that: (i) biofilm has a notable stabilizing effect on sediments larger than fine sand; (ii) tensile testing is suitable for analysis of biotic and composite materials; and (iii) biofilm strength can be modelled as an elastic force with constant of proportionality k. This early data set is therefore being extended using a wider range of grain sizes and Particle Imaging Velocimetry technology for flow turbulence analysis with the intention of developing a robust, experimentally-validated data set for k such that a suitable sediment entrainment model with integrated biofilm force considered as an elastic spring can be adequately developed.

## REFERENCES


[1] Schultz, M.P. and Swain, G.W. (1999), "The Effect of Biofilms on Turbulent Boundary Layers", ASME J. Fluids Eng., N. 121, pp. 44–51.
[2] Bohlander, G.S. (1991), "Biofilm Effects on Drag: Measurements on Ships", Polymers in a Mar. Env., N. 23–24, pp. 135–138.
[3] Andrewartha, J.M., Sargison, J.E. and Perkins, K.J. (2008) "The Influence of Freshwater Biofilms on Drag in Hydroelectric Power Schemes", WSEAS Trans. on Fl. Mech., N. 3, pp. 201–206.
[4] Droppo, I.G., Liss, S.N., Williams, D., Nelson, T., Jaskot, C. and Trapp, B. (2009), "Dyanamic Existence of Waterborne Pathogens within River Sediment Compartments. Implications for Water Quality Regulatory Affairs", Environ. Sci. Technol., N. 43, pp. 1737–1743.
[5] Grant, J. and Gust, G. (1987), "Prediction of coastal sediment stability from photopigment content of mats of purple sulphur bacteria", Nature, N. 330, pp. 244–246.
[6] Lelieveld, S.D., Pilditch, C.A. and Green, M.O. (2003), "Varition in sediment stability and relation to indicators of microbial abundance in the Okura Estuary, New Zealand", Est., Coast. & Shelf Sci., N. 57, pp. 123–136.
[7] Black, K.S., Tolhurst, T.J., Paterson, D.M. and Hagerthey, S.E. (2002), "Working with natural cohesive sediments", J. Hyd. Eng, N. 128, pp. 1–8.
[8] Paterson, D.M. and Daborn, G.R. (1991), *Developments In Coastal Engineering*. Peregrine, D.H. and Loveless, J.H., University of Bristol Press.
[9] Droppo, I.G., Lau, Y.L. and Mitchell, C. (2001), "The effect of depositional history on contaminated bed sediment stability", Sci. Tot. Env., N. 266, pp. 7–13.
[10] Righetti, M. and Lucarelli, C. (2007), "May the shields theory be extended to cohesive and adhesive benthic sediments?", J. Geophys. Res., N. 112, pp. C05039.
[11] Speras, B.M., Saunders, J.E., Davidson, I. and Paterson, D.M. (2008), "Microalgal sediment biostabilisation along a salinity gradient in the Eden Estuary, Scotland: unravelling a paradox", Mar. & Freshwat. Res., N. 59, pp. 313–321.
[12] Dade, W.B., Davis, J.D., Nichols, P.D., Nowell, A.R.M., Thistle, D., Trexler, M.B., White, D.C. (1990), "Effects of bacterial exopolymer adhesion on the entrainment of sand", Geomicrob. J., N. 8, pp. 1–16.

[13] Tolhurst, T.J., Consalvey, M. and Paterson, D.M. (2008), “Changes in cohesive sediment properties associated with the growth of a diatom biofilm”, Hydrob., N. 596, pp. 225–239.
[14] Ohashi, A., Koyama, T., Syutsubo, K. and Harada, H. (1999), “A novel method for evaluation of biofilm tensile strength resisting erosion”, Water. Sci. Technol, N. 39, pp. 261–268.
[15] Stoodley, P., Lewandowski, Z., Boyle, J.D. and Lappin-Scott, H.M. (1999), “Structural deformation of bacterial biofilms caused by short-term fluctuations in fluid shear: an in situ investigation of biofilm rhehology”, Biotechnol. and Bioeng., N. 65, pp. 83–91.
[16] Klapper, I., Rupp, C.J., Cargo, R., Purvedorj, B., Stoodley, P. (2002), “Viscoelastic fluid description of bacterial biofilm material properties”, Biotechnol. Bioeng., N. 80, pp. 289–296.
[17] Shaw, T., Winston, M. Rupp, C.J., Klapper, I. and Stoodley, P. (2004), “Commonality of elastic relaxation times”, Phys. Rev. Lett., N. 93, pp. 98102-1-98102-4.
[18] Vinogradov, A.M., Winston, M., Rupp, C.J. and Stoodley, P. (2004), “Rehology of biofilms formed from the dental plaque pathogen Streptococcus mutans”, Biofilms, N. 1, pp. 49–56.
[19] Alpkvist, E. and Klapper, I. (2007), “Description of Mechanical Response including detachment using a novel particle model of biofilm/flow interaction”, Wat. Sci. & Technol., N. 55, pp. 265–273.
[20] Ahimour, F., Semmens, M.J., Novak, P.J. and Haugstad, G. (2007), “Biofilm cohesiveness measurement using a novel atomic force microscopy methodology”, Appl. and Environ. Microbio., N. 73, pp. 2897–2904.
[21] Ripkka, R., Deruelles, J., Waterbury, J.B., Herdman, M. and Stanier, R.Y. (1979). “Genetic assignments, strain histories, and properties of pure cultures of cyanobacteria”, J. Gen. Microbiol., N. 111, pp.1–61.
[22] HIMOM (2005), Hierarchical Monitoring Methods. European Commission Fifth Framework Programme. Contract: EVK3-CT-2001-00052. (Brokman Consult, Geesthacht).
[23] Abramoff, M.D., Magelhaes, P.J., Ram, S.J. (2004), “Image Processing with ImageJ”, Biophotonics Int., N. 11, pp. 36–42.
[24] Yalin, M.S. (1972), *Mechanics of sediment transport*, Oxford, Pergamon: pp. 290.
[25] Chepil, W.S. (1959), “Equilibrium of soil grains at the threshold of movement by wind”, Soil. Sci. Soc. Am. Proc., N. 23, pp. 422–428.

*Environmental Hydraulics – López-Jiménez et al (eds)*
*© 2010 Taylor & Francis Group, London, ISBN 978-0-415-56697-1*

# Air-water flow structure in a vertical pipe: Experimental results and CFD modelling

S. Chiva
*Department of Mechanical Engineering and Construction, Universitat Jaume I, Castellón de la Plana, Spain*

S. Mendez & J.L. Muñoz-Cobo
*Department of Chemistry and Nuclear Engineering, Universidad Politécnica de Valencia, Valencia, Spain*

E. Julia & L. Hernandez
*Department of Mechanical Engineering and Construction, Universitat Jaume I, Castellón de la Plana, Spain*

F. Pellacani
*Fakultät für Maschinenwesen, Lehrstuhl für Nukleartechnik, Technische Universität München, Garching, Deutschland*

ABSTRACT: An upward isothermal co-current air-water flow in a vertical pipe (52 mm inner diameter) has been experimental investigated. Local measurements of void fraction, interfacial area concentration (IAC), interfacial velocity and Sauter mean diameter were measured using a four sensor conductivity probe. Liquid velocity and turbulence intensity were measured using Laser Doppler Anemometry (LDA). Different air-water flow configurations was investigated for a liquid flow rate ranged from 0.491 m/s to 3 m/s and a void fraction up to 25%. For each two-phase flow configuration twenty five radial position and three axial locations were measured by the conductivity probe methodology, and several radial profiles was measured with LDA at different axial positions. Some of these experiments were modeled using a computational fluid dynamic code, ANSYS-CFD where some models for the force applied to the gas phase were introduced.

*Keywords*: sensor conductivity probe, LDA, Interfacial Area Concentration, two-phase flow structure, CFD.

## 1 INTRODUCTION

One of the most important key in the two-phase flow is the existence of multidimensional interfaces between both phases. The correct behaviour prediction of this interfaces, and its quantification is one of the frontiers in the theoretical and experimental studies of this kind of flow, and up to now, there is not an effective technique and methodology for the multidimensional interface characterization in two-phase flow measurement[1]. Then, experimental works play a very important role in the development of new theoretical models and it is essential for design, analysis and behaviour analysis of existing and futures scenarios. In this work a detailed experiments are performed in order to have a good data base about the main parameters in two-phase flow characterization in upward co-flow in vertical pipes.

The basic structure of a two-phase flow can be characterized by three fundamental parameters. These are the void fraction, Sauter mean diameter (for bubbly flow mainly) and interfacial area concentration (IAC)[2]. The void fraction expresses the phase distribution and it is a required parameter for hydrodynamic and thermal design in various industrial processes. On the other hand, the interfacial area describes available area for the interfacial transfer of mass, momentum and energy, and it is a required parameter for a two-fluid model formulation. Various transfer mechanisms between phases depend on the two-phase interfacial structures. Therefore, an accurate knowledge of these parameters is necessary for any two-phase flow analyses.

The void fraction measurement is not so complicated using intrusive methods like conductivity probes with only two sensors. But IAC, defined by the quantity of interface between both phases, measured in area units per each unit of mixture volume, is quite complex itself, and with a large difficulties to be measured. [3] defined the local time-averaged IAC at a fixed position in space derived on the basis of velocities measurements according to the expression:

$$\overline{a}^{t} = \frac{1}{W}\sum_{j} \frac{1}{\left|\vec{V}_{j} \times \hat{n}_{j}\right|} \tag{1}$$

That definition opens the door to measure the interfacial area using the velocity of the interphase, if it is measured with enough detail together its vector components. The theoretical fundaments for this technique was originally proposed by Kataoka[4], and during the last fifteen years numerous researcher have used and improved that technique using intrusive probes of two, four and five sensors.

In this work we have used four-sensor probes in order to characterize the two-phase flow parameters. The IAC and interface velocity can be calculated using the distance between the probe tips, but a calibration factor, based in a Mote-Carlo methodology, is proposed to relate the real magnitude to that measured from the experimental signal. It is necessary to introduce a calibration factor, based on statistical methods, to be able to take on account the possible deviation from the vertical direction and the presence of missing bubbles, bubbles that produces bad signals or bubble that only produce a signal in only one of the tips. Interfacial velocity, void fraction, Sauter mean diameter and IAC were measured using four-sensor probe. Also in this work, we include a detailed liquid velocity and turbulence intensity measurements using LDA. Accurate magnitude information about liquid is basic for a good results interpretation.

ANSYS-CFX code is used to model the experiments. The two-phase flow was modeled by applying the Euler/Euler approach. We consider the liquid phase as a continuous media and the gas phase as dispersed media. One of the key in order to obtain

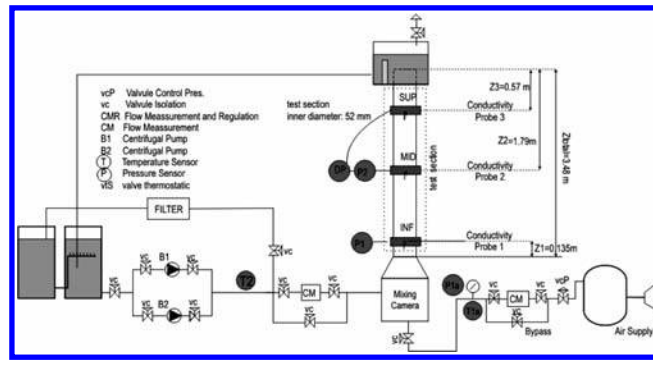


Figure 1. PUMA facility scheme.

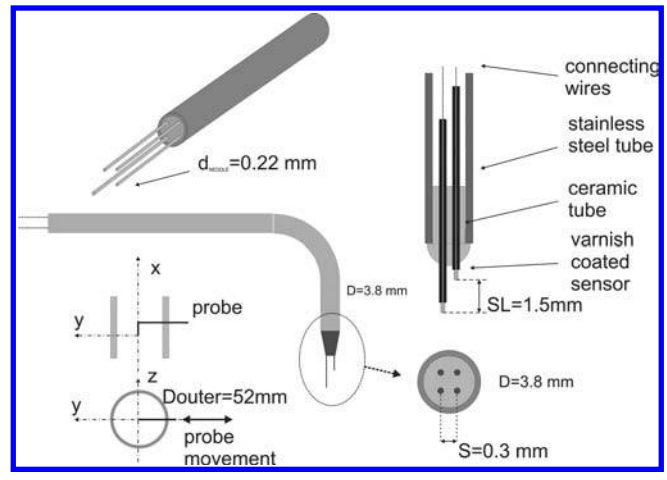


Figure 2. Schematic diagram of four sensor conductivity probe.

accurate solution is to considerer the momentum exchange between the phases with enough detail. Apart from the drag acting in flow direction, the non-drag forces must be considered. Those forces non-drag have their actuation vector mainly perpendicular to the flow direction. The non-drag forces are mainly the lift force, the turbulent dispersion force and the wall lubrication force. The lift force acts in the direction of decreasing liquid velocity in the case of co-current upward flow, with a change in its direction as a function of the bubble diameter. The turbulent dispersion force considers the turbulent mixing of the bubbles and consequently acts to smooth the spatial gas fraction distribution. The wall lubrication force reflects the need for a repelling effect of the wall on bubbles. Detailed models for the non-drag forces were introduced in the CFD model in order to modeling the experiments performed.

## 2 EXPERIMENTAL FACILITY AND INSTRUMENTATION

### 2.1 *Experimental facility*

The experimental work was performed using a thermo-hydraulic loop placed at the Energy Engineering Institute in Polytechnic University of Valencia (Spain). The loop is schematically illustrated in Figure 1. It consists of a test section, a round transparent tube made by Plexiglas with constant section, an upper plenum and a lower plenum where air and water are mixed. The test section has a 52 mm inner diameter and a length of 3340 mm. The water was circulated by two centrifugal pumps controlled by a frequency controller. The air was supply by a compressor, and it was introduced to the test section through a porous sinter element with an average pore size of 10 mm installed below the mix chamber. The LDA equipment consists of a 0.5W $Ar^+$ Ominichrome laser, Dantec Fiberflow beam separator, Dantec FVA 58N40 processor and a PC using the software Floware for data acquisition. A lens of 0.125 m focal length was used and the system was operated in backscattering mode.

### 2.2 *Sensor conductivity probe methodology*

The four- sensor probe is basically a phase identifier. It consists of two sensors made of stainless steel, coated with gold, with a diameter of 0.22 mm. The vertical distance between both tips was about 1.5 mm. Each sensor is insulated using a insulating varnish except its tips. If the probe is connected to a power supply with a fixed voltage, due to the large difference in conductivity between the liquid phase and the gas phase, the impedance signal acquired rises sharply when a bubble passes through one of the sensor tips, obtaining a more or less square signal. With a suitable signal processing methodology is possible extract precise information from that raw signal.

From the time lag, between the impedance signals of the front and back tips, we can know the time that needs the front of the bubble to travel from one tip to the other that is far away a distance, S. Then a measurable value of the bubble velocity, Vm, can be easily obtained. If the bubble moves with its velocity vector parallel to the conductivity probe orientation then the measurable value Vm of the velocity match the true value of the bubble speed. However, as the bubble velocity fluctuates in response to the turbulence of the liquid phase then the bubble's lateral motion along with the finite value of the distance

Table 1. Experimental flow condition.

| jf = 0.5 m/s | | | jf [m/s] = 1.0 m/s | | | jf = 2.0 m/s | | | jf = 3.0 m/s | | |
|---|---|---|---|---|---|---|---|---|---|---|---|
| | jg [m/s] | <α> | | jg [m/s] | <α> | | jg [m/s] | <α> | | jg [m/s] | <α> |
| F01G00 | 0 | 0 | F02G00 | 0 | 0 | F03G00 | 0 | 0 | F04G00 | 0 | 0 |
| F01G01 | 0.035 | 5.14 | F02G01 | 0.058 | 4.99 | F03G01 | 0.097 | 4.5 | F04G01 | 0.166 | 3.12 |
| F01G02 | 0.077 | 10.03 | F02G02 | 0.142 | 10.3 | F03G02 | 0.233 | 9.73 | F04G02 | 0.389 | 4.72 |
| F01G03 | 0.125 | 15.11 | F02G03 | 0.235 | 14.32 | F03G03 | 0.47 | 12.39 | F04G03 | 0.662 | 7.56 |
| F01G04 | 0.176 | 19.95 | F02G04 | 0.396 | 18.57 | F03G04 | 0.72 | 19.66 | F04G04 | 1.023 | 9.03 |
| F01G05 | 0.257 | 21.7 | F02G05 | 0.67 | 23.96 | F03G05 | 1.181 | 21.8 | F04G05 | 1.695 | 9.51 |
| F01G06 | 0.338 | 24.38 | | | | | | | | | |

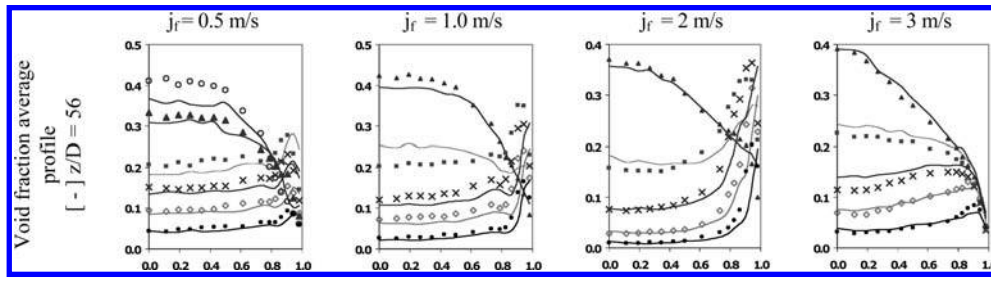


Figure 3. Results: Average profile (r/R) for void fraction for z/D = 56 axial position. Solid symbol correspond to F0A probe configuration, and without symbol for F0. The legend for the graphs are as follow: Black (●) G01, Red (◇) G02, Blue (X) G03, Green(■) G04, Violet (▲) G05, light Violet (○) G06.

between both tips of the probe, and the bubble curvature can cause problems in the measurement of the true value of the bubble velocity. To quantify this difference it is possible to define a calibration factor as the ratio between the mean value and the measured value of the bubble including the missing bubbles. In this work we have chosen the methodology carried out by Muñoz-Cobo et al.[5]to determine the calibration factor. In his study the effects of bubble motions, and probe spacing have been included. The value measured is related to the local bubble interface velocity in the surface normal direction. The probability density function of each variable is identified with the suitable coordinate transformation. Two theoretical calibration factors are defined to relate the mean measurable parameter to the interfacial area concentrations obtained and the measured bubbles, including the missed bubbles. These calibration factors have been obtained through analytical and numerical method, using a Monte Carlo approach. The results of these calculations show that the total interfacial area correction factor is very close to 2, and depends very weakly on the velocity fluctuation, and the relative distance between tips. For the velocity calibration factor, the Monte-Carlo results show that for moderate values of the relative bubble velocity fluctuation and values of the relative distance between tips not too small, the correction velocity factor for the bubble sensor conductivity probe is close to unity.

## 3 EXPERIMENT RESULTS

The flow conditions have been chosen measuring the superficial liquid and air velocity and the average void fraction on z/D = 56 in each condition. All the conditions (Table 1) are in the bubbly flow regime, and only in the highest void fractions appears some large cups, near the transition. For each liquid velocity conditions we have at least five gas conditions from 5% to up 25% . That void fraction was measured by a pressure sensors at z/D = 56. For the probe sensors, two different configurations were used, in order to study the best configuration, mainly near the wall. Details about the experiments and the facility can be found in[6].

Figure 3 shows an example of the results obtained by the experimental facility for the average void fraction profile at z/D = 56. In the paper all the results obtained are presented.

The radial distribution of the bubble, gas phase, depends on the diameter, and the liquid velocity gradient. Small bubbles tend to move toward the wall, while large bubble migrate preferable to the center. This lateral movement is determinate by the lift force, and its sign change as function of the bubble diameter. The balance, from those two forces, produces the peak near the wall. Figure 3, shows the void fraction behavior. We can observe the three typical profiles, wall-peak, transitional and core-peak. The Sauter mean diameter, gas interfacial velocity and interfacial area concentration are showed in reference[6], together the liquid velocity and the turbulence intensity.

## 4 CFD MODELLING

As we commented at the beginning of the paper, a CFD code, ANSYS-CFX has been used in order to modeling some of the experiments performed. In this code a closure laws are needed for the qualification of interfacial forces acting in the two-phase flows. For bubbly flow, forces acting on the bubbles are modeled through the momentum transfer between the phases. Those forces depend on the liquid flow field as well as on the size and the shape of the bubbles. We have used a Tomiyama model for Drag, Lift force and Wall Lubrication force, a Sato model for the turbulence induced by the bubbles and a Favre averaged turbulent dispersion force. We have considered a set of 10 different bubble size classes, (the Multiple Size Group (MUSIG)

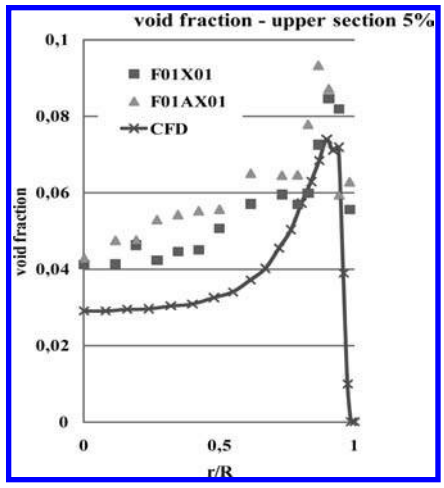


Figure 4. Void Fraction profile for jf = 1 m/s at z/D = 56 for a void fraction average 5%, F02G01. Experimental data vs. CFD calculations.

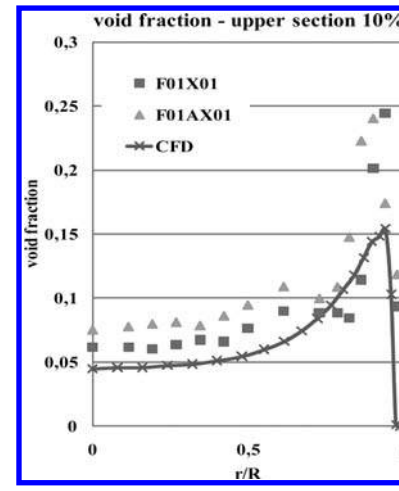


Figure 5. Void Fraction profile for jf = 1m/s at z/D = 56 for a void fraction average 10%, F02G02. Experimental data vs. CFD calculations.

model) and the participation of the break-up (Prince and Blanch model) and coalescence (Prince and Blanch model) of the bubbles In Figure 4 and 5 are showed a typical example of the CFD calculation compared with the experimental data for the void fraction profile. The results obtained have been quite good, mainly for void fraction profiles less than 20% and liquid velocity below 2 m/s.

## ACKNOWLEDGMENTS

This research was supported by the Plan Nacional de I + D + I. Project EXPERTISER ENE2007-68085-C02-02

## REFERENCES

[1] Shen X, Y. Saito, K. Mishima, H. Nakamura, (2005), Methodological improvement of an intrusive four-sensor probe for the multi-dimensional two-phase flow measurement, International Journal of Multiphase Flow, Vol. 31, pp. 593–617

[2] Delhaye J.P., P. Bricard, (1994), Interfacial area in bubbly flow: experimental data and correlations, Journal of Nuclear Engineering Design, Vol. 151, pp. 65–77

[3] Ishii M., 1975, Thermo-fluid Dynamic Theory of Two-phase flow, Eyrolles Pari

[4] Kataoka I., M. Ishii, A. Serizawa, (1986), Local formulation and measurement of interfacial area concentration in two-phase flow, International Journal of Multiphase Flow, Vol. 12, pp. 505–529

[5] Muñoz-Cobo J.L., J. Peña, S. Chiva, S. Mendez, (2007) Monte-Carlo calculation of the calibration factors for the interfacial area concentration and the velocity of the bubbles for double sensor conductivity probe, Nuclear Engineering and Design, Volume 237, Issue 5, Pages 484–496

[6] Mendez Diaz, Santos, Medida Experimental De La Concentración De Area Interfacial (2008), PhD Thesis, Politechnic University of Valencia, Spain

*Environmental Hydraulics – López-Jiménez et al (eds)*
*© 2010 Taylor & Francis Group, London, ISBN 978-0-415-56697-1*

# Heavy metal (Cd, Pb, Cu and Zn) distribution in marine sediments of the Bay of Cullera, Valencia (Western Mediterranean Sea)

Angela María Jaramillo Londoño & Vicent Benedito Durà
*D.I.H.M.A. Laboratorio de Ecología, Universidad Politécnica de Valencia, Valencia, España*

Andrea Tombari
*Laboratorio de vertebrados, Departamento de Biodiversidad y Biología Experimental, Facultad de Ciencias Exactas y Naturales, Universidad de Buenos Aires, Argentina*

Agustín Pastor García
*Departamento de Química Analítica, Universidad de Valencia, Burjassot, España*

ABSTRACT: Concentrations of four metals (Cd, Pb, Cu, and Zn) were determined in sediments collected from Bay of Cullera. Total metal concentration in sediments varied, in general in a short range and showed similar distribution. The highest metal concentrations were presented around the offshore sewage outfall. The metal concentration was bigger in winter than in summer. Metal concentrations were greatest in the bottom of sediment core (10–15 cm). Metal concentrations were compared with those found by several authors in sediments from different areas of Mediterranean Sea and we can state that the concentration levels on this coast are comparable to those found in marine sediments in unpolluted areas.

*Keywords*: Metals, Sediments, Cadmium, Lead, Copper, Zinc

## 1 INTRODUCTION

The Jucar River is one of the most important rivers in the Valencia region. This river flows into Bay of Cullera together with an offshore sewage outfall and it makes some specific areas of the bay could be affected by domestic and industrial waste water discharge and also by agricultural activities. The Bay of Cullera is sheltered from the east and northeast winds that are prevalent in that coast. For this reasons the Bay of Cullera is an interesting place for studying the effects of discharges into marine ecosystem and to determine the chemical quality of the marine sediments particularly the content of trace metals. The aim of this study is to determine concentrations of Cadmium (Cd), Lead (Pb), Copper (Cu), and Zinc (Zn) in sediments collected from the Bay of Cullera.

## 2 MATERIALS AND METHODS

Sediment samples were obtained from Cullera Bay during July 2002 and February 2003. The samples were collected from 15 sites in that area (Figure 1). Samples were collected from a boat by hand coring in immersion with a precleaned plastic core tube of 10 cm diameter and about 30 cm long. There were collected two samples in each site, one to determine sediment grain-size and organic matter, and the other one for metal analysis.

The sediment was brought to the laboratory on ice. ediment cores were sliced in three layers of 5 cm each one, and then frozen at $-18°C$.

Sediment grain-size distributions were determined in sediment by dry sieving. The content of organic matter in sediments was estimated as loss of weight on ignition. Total metal content analyses were performed on the fraction of 250 μm. All samples were freeze-dried. The samples were crushed to uniform particle size before metal analysis. The resulting powder then underwent acid digestion ($HNO_3 - H_2O_2$) in an automatic microwave digestion system. After digestion, the samples were diluted to 25 ml and kept in polyethylene bottles for storage.

Following acid digestion, all the samples were analysed for 4 elements by atomic absorption spectrometry (AAS). Cd, Pb, and Cu were determined in a graphite furnace (Perkin-Elmer 4100 ZL with Zeeman background corrector) with an autosampler. Zn was analysed in an air-acetylene flame (UNICAM, with double beam and deuterium background corrector). The standard addition method was used to correct for matrix effects. A procedural blank was run with each set of samples in order to correct for spurious signals. Nitric and perchloric acids were analytical grade. Water used for all dilutions was Milli-Q deionized. Metal concentrations are reported on a dry weight basis. The heavy metal analyses were recorded as mean ± standard deviation (S.D.) of duplicate measurements. The results are showed in micrograms per gram of dry weight (μg/g d.w.). In each one of the measurement sessions, the equipment was calibrated. During a measurement session, three or two calibrated process were made depending on the number of samples, and to make the calculations the mean values of all the calibrated ones were used. The detection limit for each one of metals were: Cd (0.07 μg/g), Pb (0.16 μg/g), Cu (0.6 μg/g), and Zn (2.9 μg/g). Recovery essays checked data accuracy and precision. Recovery was over 98%.

Statistical analysis of data was carried out using SPSS statistical package programs. Data used here were plotted on graphs to see their distributions. In all cases, the level of significance was set at $P < 0.05$. Data showed mostly normal distribution and therefore, no transformation was done for statistical analysis.

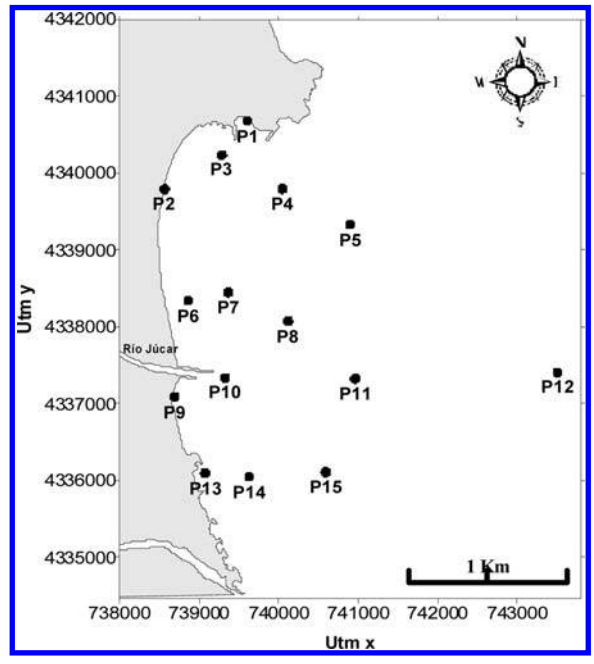


Figure 1. Bay of Cullera location map showing sampling sites.

Table 1. Sediment grain-size and content of organic matter

| Sampling site | Organic matter % | Sediment grain-size (%) | | |
|---|---|---|---|---|
| | | Gravel >250 μm | Sand 0,063–250 μm | Clay – Silt <0,063 μm |
| P1 | 1.4 | 1.05 | 98.87 | 0.09 |
| P2 | 1.0 | 2.23 | 97.78 | 0.03 |
| P3 | 2.2 | 1.44 | 98.08 | 0.49 |
| P4 | 1.3 | 0.50 | 99.09 | 0.42 |
| P5 | 2.4 | 1.14 | 97.64 | 1.23 |
| P6 | 1.1 | 0.69 | 99.26 | 0.06 |
| P7 | 2.3 | 5.98 | 92.30 | 1.73 |
| P8 | 2.4 | 0.63 | 97.73 | 1.67 |
| P9 | 1.3 | 1.53 | 98.46 | 0.03 |
| P10 | 1.5 | 0.45 | 95.87 | 3.69 |
| P11 | 4.8 | 63.13 | 36.73 | 0.15 |
| P12 | 3.6 | 0.32 | 73.41 | 26.28 |
| P13 | 2.3 | 0.73 | 99.20 | 0.10 |
| P14 | 1.9 | 1.07 | 95.51 | 3.42 |
| P15 | 3.0 | 0.56 | 97.13 | 2.35 |

## 3 RESULTS AND DISCUSSION

High proportions of gravel and sand were found. Both fractions have a mean value of 97,2% of the total weight in samples. Clay and silt were 2,8%. Organic matter content was low in the samples (2,2%). The values for each sampling site are shown in Table 1.

Total metal concentration in samples varied, in general, in a short range for all metals. They showed similar distributions along the bay in summer. There was not significant differences in Cadmium concentrations ($F_{14,29} = 0.39$; $P = 0.97$), which was homogenous within the bay. There was significant differences in Lead ($F_{14,29} = 9.54$; $P < 0.001$), Copper ($F_{14,29} = 3.83$; $P < 0.05$) and Zinc concentrations ($F_{14,29} = 6.22$; $P < 0.001$), with the highest levels around the offshore sewage outfall (P11 and P12). The lowest concentrations were presented near shoreline. The highest level was for Zinc, followed by Lead, Copper and Cadmium. The last one was below the detection limits. The metal contents of sediments in summer are shown in Figure 2.

When compare the results between summer and winter seasons, we found significant differences in Cadmium ($F_{1,28} = 10.87$; $P < 0.05$), Copper ($F_{1,28} = 28.08$; $P < 0.05$), and Zinc ($F_{1,28} = 10.20$; $P < 0.05$) levels, with the highest concentrations in winter. In Lead, the concentrations in winter were higher than summer but the differences between seasons were not statistically significant ($F_{1,28} = 0.09$; $P = 0.76$). In winter the trend of distribution was similar to summer with the highest concentrations around the offshore sewage outfall (Figure 3).

The Cadmium concentrations in winter increased with respect to those of summer. The Lead concentrations in winter were smaller in some sampling sites, although an increase pattern towards the sampling site P12 was observed. The Copper concentrations were greater in winter than in summer and the distribution pattern demonstrates a greater extension of high concentrations by the whole bay and not only in the zone of the offshore sewage outfall. Finally, the distribution pattern of Zinc was similar in both seasons, being the concentrations in winter higher than in summer.

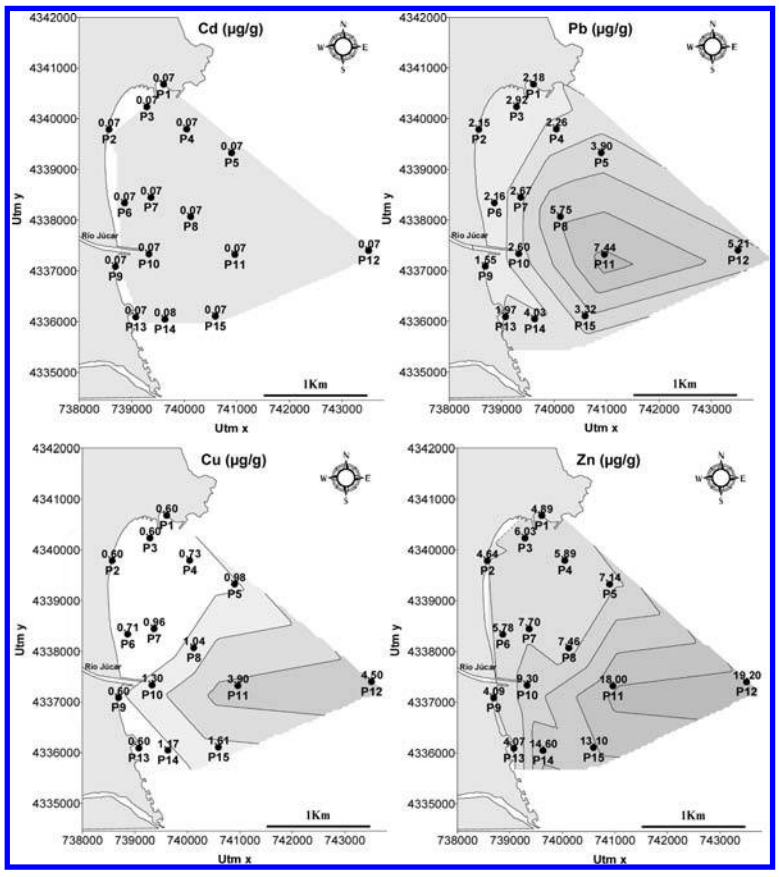


Figure 2. Total metal distribution in marine sediments of the Bay of Cullera in summer.

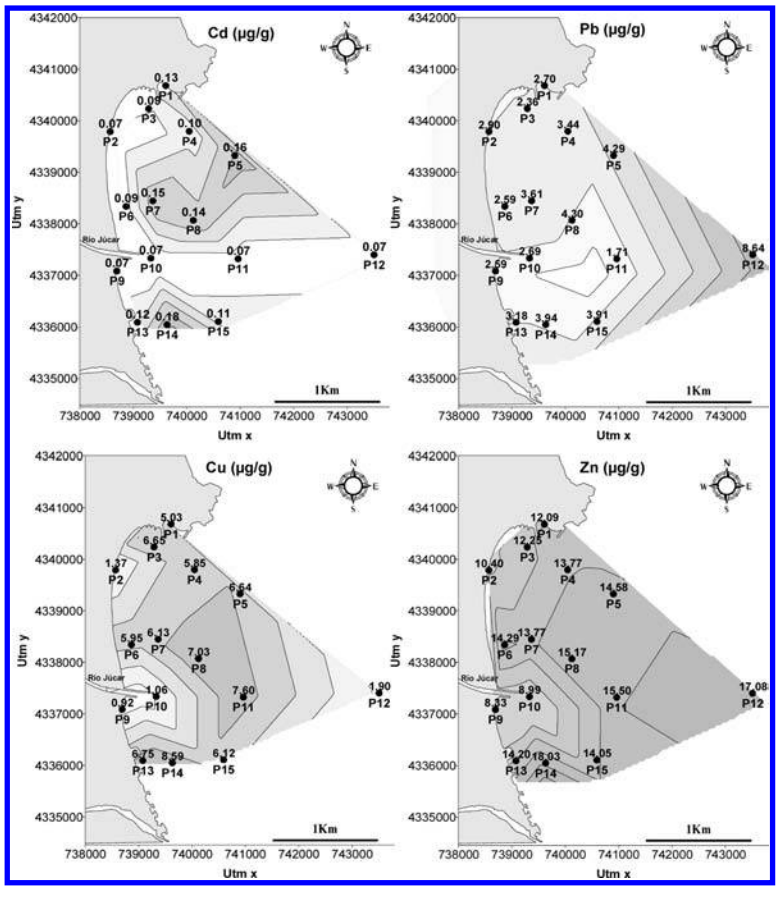


Figure 3. Total metal distribution in marine sediments of the Bay of Cullera in winter.

From the metal levels observed in the sediment of the bay of Cullera, we can indicate that in general they were distributed in a quite homogenous form in all the studied area. The Cadmium concentrations always displayed very low levels, and Copper, Lead and Zinc could have certain influence of the mouth of the river and the offshore sewage outfall. In our opinion, this influence must be due to the finest fraction of sediments since the texture that presented in the sampling stations P11 and P12 included a greater percentage of this fraction.

However, we did not detect contamination by these heavy metals within the bay, because the sediment metal concentration was distributed of a quite homogenous form in the studied area. In general, the more superficial stations showed the smaller concentrations of all metals.

The analysis of the sediment column showed that the vertical metal distribution was very variable. There was not significant differences in vertical distribution of Cadmium ($F_{2,41} = 2.3$; $P = 0.11$) and Copper ($F_{2,41} = 0.86$; $P = 0.43$) found in the three sections, while for Lead ($F_{2,41} = 12.06$; $P < 0.001$) and Zinc ($F_{2,41} = 5.14$; $P < 0.05$) the differences between the sections were significant. We stated a predominant pattern by which it seems that a slight increase existed towards the deepest sections. Is widely cited an increase in the metal concentration in the finest fractions of the sediment.

The four metals showed similar temporal patterns, even though there were higher concentrations of Copper over the winter period. These results are similar to those of Benedito (1996)[1] in coastal sediments in the Valencian Community, nevertheless, unlike our results the metal levels were superior in summer with respect to winter. The results clearly demonstrate that there isn't any heavy metal pollution in marine sediments of the bay of Cullera, and the levels that we found are very low. In agreement with our results, we considered that in studies of control of the contamination by heavy metals, it would be interesting to study at least two annual samples of superficial sediments (summer and winter). In order to study last conditions or to see effects of the environmental conditions of the sediment, it is possible to analyze the deepest sections. The concentrations that we have found for metals in sediments of the bay of Cullera, are the lowest of those cited by other authors for the Mediterranean Sea.

The average levels of Cadmium in sediments of bay of Cullera were of 0.07 μg/g D.W., which are lower than 0.39–1.59 μg/g D.W. found by Ballester *et al*. (1980)[2] in Coast of Catalonia; 0.15 μg/g D.W. obtained by Whitehead *et al.* (1984)[3] in Mediterranean coastal sediments; 0.07–0.22 μg/g D.W. of Hernández *et al*. (1985)[4] in Coast of Valencia; and, 0.1–0.2 μg/g D.W. obtained by Benedito (1996)[1] in bay of Altea.

The Zinc concentrations that we have obtained were between 8.3 and 19.20 μg/g D.W., which are lower than 20–60 μg/g D.W. obtained by Benedito (1996)[1] in bay of Altea. Martincic *et al*., (1990 a,b)[5,6], found 23–30 μg/g D.W., in an unpolluted place of the Central Adriatic. Our results also are below the 50 μg/g D.W., proposed as baseline levels of Zinc for coastal sediments of the Mediterranean (Whitehead *et al*., 1984)[3], and in the lower range (10 y 152 μg/g D.W.) of those encountered by Chabert *et al*. (1983)[7], in Port Cros (France).

We found levels of Copper between 0.92 a 8.59 μg/g D.W., which are similar to Benedito (1996)[1] in bay of Altea (5–9 μg/g D.W)., and lower than Ballester *et al*. (1980)[2], in the coast of Cataluña. These values are slightly below the 15 μg/g D.W. proposed by Whitehead *et al.* (1984)[3], as Mediterranean baseline, and these values are lower to Martincic *et al*. (1990 a, b)[5,6], in an unpolluted place of the Central Adriatic. Our concentrations are similar to Chabert *et al*. (1983)[7], in Port Cros.

The Lead levels in sediments of bay of Cullera were between 1.5 a 8.6 μg/g D.W. Benedito (1996)[1] encountered in bay of Altea lead levels between 20 y 40 μg/g D.W. and Hernández *et al.* (1985)[4], encountered 19.5 μg/g D.W. in superficial sediment of coast of Valencia and Castellon, and these values are considered as baseline for these authors. Ballester *et al.* (1980)[2], obtain lead levels in sediments of the same order of magnitude that ours.

Whitehead *et al.* (1984)[3], propose 25 μg/g D.W. as lead baseline for the coastal Mediterranean sediments. Martincic *et al.* (1990 a, b)[5,6] in Kornati Islands (Greek) encountered 12.4 μg/g D.W. in sediment fraction of <463 μm. The lower values than Chabert et al. (1983)[7] encountered in Port Cros, were between 6.5–19 μg/g D.W., and the highest between 37.5 and 108, and they affirm that there are a lead pollution proceeding from the fuels of the boats that travel by the zone. In the same way, Cristiani (1980)[8] found lead concentrations between 26 a 40.9 μg/g D.W. in French Mediterranean coasts.

We can conclude that the bay of Cullera is an area with very low metal concentrations that can be considered like baseline levels for coastal areas of the Mediterranean Sea; and the river and the sewage outfall don't produce any contamination effect in this area.

## REFERENCES


[1] Benedito, V. (1996), *Fenología vegetativa y dinámica de acumulación de metales pesados en Posidonia oceanica (L.) Delile.* Thesis. University of Valencia. Department of Animal Biology. Valencia, Spain.

[2] Ballester, A.; Miller, J.; Dunyach, M. (1980), "Some pollutants in marine sediments, animals and plants in the coastal waters of Catalonia, Spain", Thalassia Jugosl., Vol.16 (2–4), pp. 275–288.

[3] Whitehead, N.E.; Oregioni, B.; Fukai, R.(1984), "Background levels of trace metals in Mediterranean sediments", Journees Etud Pollutions, CIESM'VII, Luceme, pp. 233–240.

[4] Hernández, F.; Pastor, A.; Medina, J.; Beferull, J.B.; Barbera, J.C. (1985), "Heavy metal distribution in the marine sediments of the Valencia – Castellón Coasts. Spain", Thalassographica, Vol. 8, pp.71–82.

[5] Martincic, D.; Kwokal, Z.; Branica, M. (1990 a), "Distribution of zinc, lead, cadmium and copper between different size fractions of sediments. I: The Limski Kanal (North Adriatic Sea)", The Science of the Total Environment, Vol. 95, pp. 201–215.

[6] Martincic, D.; Kwokal, Z.; Branica, M. (1990b), "Distribution of zinc, lead, cadmium and copper between different size fractions of sediments. II: The Krka river estuary and the Kornati islands (Central Adriatic Sea)", The Science of the Total Environment, Vol. 95, pp. 217–225.

[7] Chabert, D.; Vicente, N.; Huang, W. (1983), "La pollution par métaux lourds dans les rades du Parc National de Port Cros. II. Control pluriannuel". Trav. Sci. Parc. Nat. Port Cros, Vol. 9, pp. 17–34.

[8] Cristiani, G. (1980), *Biomasse et repartition de l'herbier de Posidonia oceanica de la Côte Bleue (Bouches du Rhône, France) et pollution marine par les métaux lourds*. Thèse Doct. Univ. Aix-Marseille III: 150pp.

*Environmental Hydraulics – López-Jiménez et al (eds)*
*© 2010 Taylor & Francis Group, London, ISBN 978-0-415-56697-1*

# Quantification of uncertainties in a 2D hydraulic model for the Dutch river Rhine using expert opinions

Jord J. Warmink
*Department of Civil Engineering, University of Twente, Enschede, The Netherlands*

Hanneke van der Klis
*Deltares, Delft, The Netherlands*

Martijn J. Booij & Suzanne J.M.H Hulscher
*Department of Civil Engineering, University of Twente, Enschede, The Netherlands*

ABSTRACT: Hydraulic–morphological river models are applied to design and evaluate measures for purposes such as safety against flooding. These numerical models are all based on a deterministic approach. However, the modeling of river processes involves numerous uncertainties. The aim of this study is to identify the sources of uncertainty that induce the largest uncertainties in the model outcomes and quantify this uncertainty using expert opinions. Experts have been selected based on a Pedigree matrix. The selected experts are asked to list and quantify the most important uncertainty sources for two situations: (1) the computation of design water levels (DWL) and (2) the computation of the hydraulic effect of a change in the river bed. The experts stated that the sources of uncertainty are different for the computation of the DWL and effect studies. The experts agreed that for DWL, the upstream discharge and the roughness predictor for the main channel have the largest uncertainty. For effect studies, no clear dominant source could be identified. The quantification of the uncertainty sources showed a significant effect on the predicted water levels under design discharge conditions.

*Keywords*: Uncertainty analysis, Uncertainty identification, Water management, Hydraulic modeling, Pedigree, Expert opinions.

## 1 INTRODUCTION

Hydraulic–morphological river models are applied to design and evaluate measures for purposes such as safety against flooding. These numerical models are all based on a deterministic approach. However, the modeling of river processes involves numerous uncertainties, resulting in uncertain model results. Uncertainty is defined as any deviation from the unachievable ideal of complete determinism [1]. Uncertainty in models comprises (1) the difference between a model outcome and a measurement and (2) the possible variation around a computed value. According to Morgan and Henrion [2], decision makers make less than optimal decisions without information on the uncertainties in outcomes. Knowledge of the type and magnitude of these uncertainties is crucial for a meaningful interpretation of the model results. Therefore, there is a need for structured analysis of the uncertainties in environmental management practice.

Most studies about uncertainty analysis of hydrodynamic models only take uncertainties in input and model parameters (e.g. [3] and [4]) into account. However, uncertainty also resides in the model structure, computational characteristics, for example, discretizations and grid type, and in the model context. A structured approach is required to identify the uncertainties in all these locations in a model. Also, not all these uncertainties can be quantified. To get insight in the sources of uncertainty that influence the model outcomes, expert opinion elicitation is used as the method to identify the key uncertainties. The aim of this study is to identify the sources of uncertainty that induce the largest uncertainties in the model outcomes and quantify this uncertainty.

## 2 METHOD

### 2.1 *Study area*

In this study, the two-dimensional WAQUA model for the River Waal is used for the identification of sources of uncertainty. Shortly after the Rhine enters the Netherlands, it splits (by two subsequent bifurcations) into three main branches. The largest of these branches is the River Waal, which discharges about 2/3 of the total Rhine discharge. Flood protection and navigation are the main issues in the river Waal region. Every 5 years the safety of the primary dikes is evaluated against a design discharge. This design discharge is based on the statistical analysis of historical discharge series. In 1999 a new policy for flood protection was adopted, the Room for the Rivers policy. This policy implies that instead of raising the dikes, if possible, other measures are taken to increase the discharge capacity of the river [5].

The WAQUA model is used to compute the design water levels (DWL) based on the design discharge and to compute the effects of the Room for the River (RfR) measures. The results of this model are used for the decision, which leads to a set of measures in the river bed to ensure safety against flooding in the Netherlands. However, the uncertainty in the model outcomes are not explicitly considered in the decision making process.

The uncertainties in the outcomes of this model are a result of the uncertainties in all parts of the model, called the sources of uncertainty. Figure 1 shows a sketch of a general model. Uncertainties are present in the model input, parameters, computational characteristics and model structure [1].

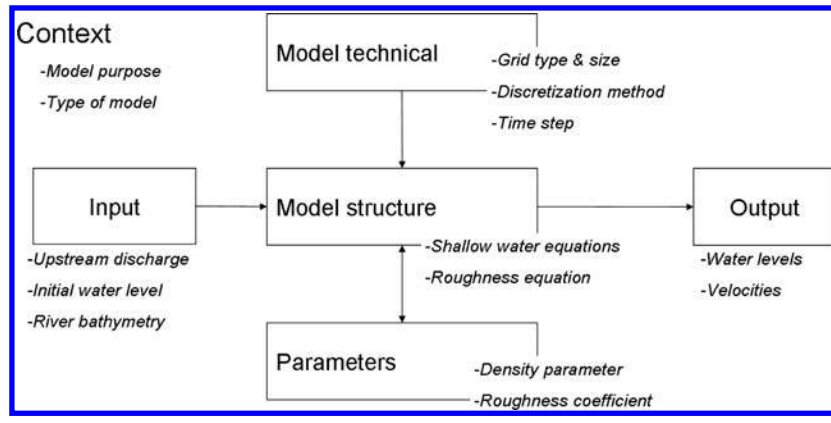


Figure 1. Locations of some major sources of uncertainty in a model that contribute to the model output uncertainty (based on Walker et al. [1]).

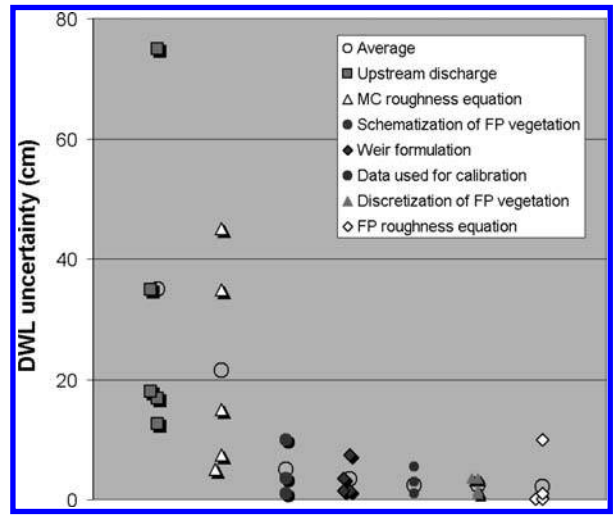


Figure 2. Uncertainty in the computed design water level (DWL), due to different uncertainty sources. The average uncertainty for each source (open circle) and the individual opinions of the experts are given for each uncertainty source. (MC is main channel; FP is floodplain.)

### 2.2 *Expert selection*

At first 30 experts are asked for their experience with the WAQUA model. From these 30 experts, 16 are selected based on a Pedigree matrix[6] with 4 criteria: 1) experience with code development, 2) experience with WAQUA projects, 3) number of years of 'hands-on' experience with WAQUA, and 4) number and type of publications about WAQUA. On each criterion a score between 0 and 4 has been given, based on the information given by the expert. Subsequently, the scores have been normalized and a weight factor is used for each criterion from 4 to 1 respectively. The 16 experts with the highest Pedigree scores have been invited for an interview. Interviews are held with 11 of these experts.

### 2.3 *Expert interviews*

The experts are asked to list the most important uncertainty sources. These are defined as the sources with the largest contribution to the model outcome uncertainties, which means that both the sources are highly uncertain and they have a large influence on the model outcomes. The experts are asked to consider the following two situations: (1) the computation of design water levels (DWL), based on a design discharge wave and (2) the computation of the hydraulic effect of a measure in the river bed, which is computed using a constant discharge as input. To compare the different experts, the experts are asked to comment on the sources of uncertainty on the same level of detail. Subsequently, the experts are asked to indicate the effect of a source of uncertainty on the computed water levels.

## 3 RESULTS

The experts stated that the sources of uncertainty are different for the computation of the DWL and effect studies. In case of effect studies, the experts agreed that the sources of uncertainty that do not change between the computation with and without a measure have little influence on the uncertainty in the computed effect. In case of DWL computations, the uncertainties are dominated by the sources that are not compensated during calibration.

### 3.1 *Uncertainties in design water levels*

The uncertainty in the DWL computations for different sources is shown in figure 2. Only the seven largest sources of uncertainty in the DWL are shown. Clearly, the upstream discharge, that is derived from the extrapolation of the historical

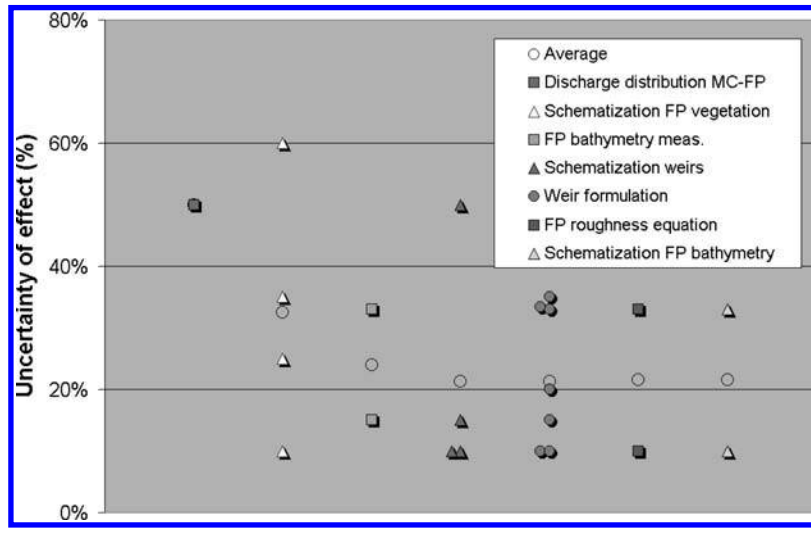


Figure 3. Sources of uncertainty for effect studies, expressed as a percentage of the computed effect. Also the mean (open circle) and the range of 1 standard deviation around the mean are given for each source of uncertainty.

discharge series, and the main channel roughness equation have a large uncertainty according to the experts. The other sources have an uncertainty in the order of magnitude of 5–10 cm. Besides the large values given for the order of magnitude of the uncertainty, also a large scatter is shown in the experts' opinions.

### 3.2 *Uncertainties in effect studies*

Regarding the uncertainties in effect studies (figure 3), less experts were able to quantify the sources of uncertainty and the effect of uncertainty sources on model outcomes. This is mainly caused by the large dependency of the uncertainty on the location in the river bed. In general, the uncertainty in an effect study is important if it is different in the situation with a measure compared to the reference situation. If, for example, many weirs are changed, the uncertainty due to weirs has a relatively large influence. Due to this large dependency on (and interaction with) the local flow characteristics, uncertainty quantification becomes complicated. However for the Waal region several uncertainties are dominant. These uncertainties are the schematization of the vegetation, weirs and bathymetry in the floodplain area, the formulations of roughness due to vegetation and weirs, and the measurements of the floodplain bathymetry (figure 3).

## 4 DISCUSSION

According to the experts many uncertainties are reduced by calibration. This effect is taken into account in the estimation of the uncertainties. The uncertainties that are influenced by calibration are uncertainties in the measurement data, uncertainties in the discretization of this data onto a grid and the uncertainties in the computational parameters. This assumes that these parts of the model do not change between the situation used during calibration and the design conditions.

Other uncertainties that are not compensated for during calibration are valued by the experts to have a large effect on the uncertainty in the model outcomes. These uncertainties comprise the upstream discharge and the main channel roughness formulation. Furthermore, some experts state that the extrapolation to design conditions also introduces uncertainty in other parts of the model. This uncertainty mainly comes from the difference in water levels between the calibration conditions and the design conditions. This difference is especially large in the floodplain area and becomes apparent in the roughness formulations. Therefore, the formulation of the floodplain roughness formulation and the weir formulation is also stated as uncertain. For example, some experts question the validity of the weir formulation in case a large water level is present above the top of the weir.

The major difficulty in the determination of the main uncertainties is that all uncertainties are correlated. Therefore, many experts state that the discharge distribution between the floodplain and the main channel is of main importance. The ratio between both discharges expresses the ratio between the aggregated roughness of the main channel and the aggregated roughness of the floodplain area. In future studies, this characteristic should be taken into account in the calibration and validation of 2D hydrodynamic models. The uncertainty in this characteristic also expresses the uncertainty in the aggregated roughnesses.

The experts are also asked for the uncertainty sources for other models than the WAQUA model for the Waal. They stated that the dominant source of uncertainty is determined by the characteristics of the flow field and river geometry. For example, the uncertainty in the main channel roughness is much larger than the uncertainty in the vegetation roughness. However, for the IJssel River, the model outcome uncertainty is more dominated by uncertainty in vegetation roughness than for main channel roughness, because the floodplain areas are relatively large compared to the main channel.

## 5 CONCLUSIONS

The aim of this study is to identify the sources of uncertainty that induce the largest uncertainties in the model outcomes and quantify this uncertainty using expert opinions. The experts stated that the sources of uncertainty are different for the computation of the DWL and effect studies. In case of DWL computations, the uncertainties are dominated by the sources that do not change between the calibration and the prediction. The experts agreed that the imposed discharge and the empirical

roughness equation for the main channel have a relatively large uncertainty. For effect studies, the floodplain topography, weir formulation and discretization of floodplain topography induces the largest uncertainty. Next to the large values given for the order of magnitude of the uncertainty, also a large scatter is shown in the experts' opinions. Finally, the effect of the uncertainty sources on the model outcomes showed that the uncertainty sources have a significant effect on the predicted water levels under design discharge conditions. Future research focuses on the quantification of these main sources of uncertainty.

## ACKNOWLEDGEMENTS

This research is supported by the Technology Foundation STW, and the technology program of the Ministry of Economic Affairs. The authors thank all experts for their time and constructive input in the preparation stage and during the interviews.

## REFERENCES

[1] Walker, W.E., Harremoës, P., Rotmans, J., Van der Sluijs, J.P., Van Asselt, M.B.A., Janssen, P.H.M. and Krayer von Kraus, M.P. (2003) "Defining uncertainty, a conceptual basis for uncertainty management in model-based decision support" Integrated Assessment, Vol. 4 (1), pp. 5–17

[2] Morgan, M.G., Henrion, M. (1990) "Uncertainty: a guide to dealing with uncertainty in quantitative risk and policy analysis" Cambridge University Press, New York

[3] Hall, J.W., Tarantola, S., Bates, P.D. and Horritt, M.S. (2005) "Distributed sensitivity analysis of flood inundation model calibration" Journal of Hydraulic Engineering, Vol. 131 (2), pp. 117–126

[4] Bates, P.D., Horritt, M.S., Aronica, G., Beven, K.J. (2004) "Bayesian updating of flood inundation likelihoods conditioned on flood extent data" Hydrological Processes, Vol. 18 (17), pp. 3347–3370

[5] Van Stokkom, H.T., Smits, A.J., Leuven, R.S. (2005) "Flood defence in the Netherlands: a new era a new approach" Water International, Vol. 30 (1), pp. 76–87

[6] Funtowicz, S.O. and Ravetz, J.R. (1990) "Uncertainty and Quality in Science for Policy", Kluwer, Dordrecht. ISBN 0-7923-0799-2

*Environmental Hydraulics – López-Jiménez et al (eds)*
*© 2010 Taylor & Francis Group, London, ISBN 978-0-415-56697-1*

# Evolutive techniques applied to water quality models calibration

P. Amparo López-Jiménez, F. Javier Martínez-Solano, Gonzalo López-Patiño & Vicente S. Fuertes-Miquel
*Centro Multidisciplinar de Modelación de Fuidos, Universidad Politécnica de Valencia, Valencia, España*

ABSTRACT: In this paper we present a methodology to calibrate water quality models. This methodology is based on defining two sort of parameters involved in calibration. On one hand, internal parameters appear in the equations from semi empirical estimations and they can be found within some intervals. We propose the use of Genetic Algorithms to estimate them. On the other hand, experimental measurement comes into equations as external parameters. They affect the accuracy of the final solutions; therefore an uncertainty analysis has to be performed. Finally, a termination criterion for calibration has been proposed based on the overlapping between the confidence intervals of predicted and reference values.

*Keywords*: receiving waters quality, DO model, calibration, Genetic Algorithm, Uncertainty.

## 1 INTRODUCTION

Receiving waters quality models are broadly used in representing the environmental problem of streams and, in general, receiving water pollutant dispersion processes. But the reliable use of the model is exposed to a correct and systematic calibration and validation process. Calibration is the process of identifying appropriate values for model parameters [1]. This is a difficult task because of uncertainty in the model structure and the identification between reality and the model equations. Therefore, the developing of a proper calibration methodology is extremely important because it assures the reliability of the mathematical model.

Many calibration methods have been proposed, but calibration presents some problems that arise when trying to validate the model: there is no such thing as general validity (the model can be sufficiently validated for one purpose but not for another); there may be no such real world or experimental results to compare with; the real world is neither accurate enough, nor are there sufficient time or resources to validate or verify everything. So, with these problems the calibration method must usually resort to a manual trial and error curve fitting. Such procedures can lead to unrealistic and time-wasting parameter sets.

In this paper we maintain that parameters should be considered in two categories: Firstly internal parameters are the coefficients present in the equations, (those which appear in the model equations and they come from semi empirical databases, for example the reareation velocity coefficient). Secondly, we consider the external parameters, those involved in the model from some experimental measurement procedure (for example the incoming flow values).

## 2 PROBLEM STATEMENT

The Dissolved Oxygen (DO) concentration is the main parameter historically used to identify the quality of the receiving water. Therefore, there have been many different sorts of models[2] used to represent such a concentration as well as others involved in the DO evolution.

The DO model represents DO concentration and other process and concentrations governing DO evolution in receiving waters: decomposition of organic matter, reareation, nitrogen cycle, algae and sediment interactions. Therefore, the main results of the model simulation are DO concentrations. These values, considered as the objective of the modelling process, are intended to fit with some measurement taken from the modelled case, representing reality. The calibration procedure modifies the value of some model parameters in order to obtain an optimal agreement between model calculations and data set.

The mathematical model will represent the evolution of DO by solving some equations. These equations, when solved, will provide the concentration of compounds considered in the process.

In summary, we depict the equations involved in the one-dimensional complete DO model.

The main equation that will lead to evaluate DO concentration is:

$$\frac{\partial c}{\partial t} + U\frac{\partial C}{\partial x} = K_1\frac{\partial^2 C}{\partial x^2} \quad k_1 L_c + k_2(C_s \quad C) \quad r_{oa}k_{ai}N_a \quad r_{oi}k_{in}N_i \quad \frac{1}{h}k_b L_b + (\alpha_f \mu \quad \alpha_r \rho)A_1 + Tf_C \tag{1}$$

This equation will be solved with the expressions that define the other concentrations considered in the model. They are:

Suspended BOD:

$$\frac{\partial L_c}{\partial t} + U\frac{\partial L_c}{\partial x} = K_1\frac{\partial^2 L_c}{\partial x^2} \quad k_1 L_c + Tf_{Lc} \tag{2}$$

Organic Nitrogen to Ammonia:

$$\frac{\partial N_o}{\partial t} + U\frac{\partial N_o}{\partial x} = K_1\frac{\partial^2 N_o}{\partial x^2} \quad k_{oa}N_o + Tf_{No} \tag{3}$$

Ammonia to nitrite transformation:

$$\frac{\partial N_a}{\partial t} + U\frac{\partial N_a}{\partial x} = K_1\frac{\partial^2 N_a}{\partial x^2} + k_{oa}N_o \quad k_{ai}N_a + Tf_{Na} \tag{4}$$

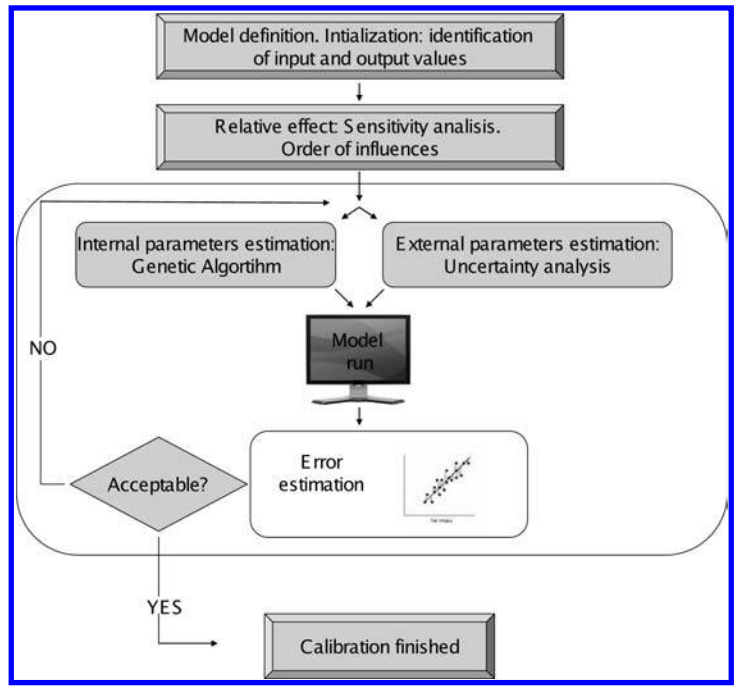


Figure 1. Calibration strategy.

Nitrite to Nitrate transformation

$$\frac{\partial N_i}{\partial t} + U\frac{\partial N_i}{\partial x} = K_1\frac{\partial^2 N_i}{\partial x^2} + k_{ai}N_a \quad k_{in}N_i + Tf_{Ni} \tag{5}$$

Appearance of Nitrate

$$\frac{dN_n}{dt} = k_{in}N_i \tag{6}$$

Sedimentable BOD fraction

$$\frac{\partial L_b}{\partial t} = hk_sL_s \quad k_bL_b \quad k_rL_b \tag{7}$$

Algae concentration:

$$\frac{\partial A_l}{\partial t} + U\frac{\partial A_l}{\partial x} = K_l\frac{\partial^2 A_l}{\partial x^2} + \mu \quad \rho \quad \frac{\sigma}{h}A_l + Tf_{Al} \tag{8}$$

Previous equations have to be solved by some numerical techniques in order to obtain the desired concentrations. Normally, they are solved in the computer. The numerical method will be chosen to generate sufficiently stable and accurate solutions with the minimum computational effort. In this case, a finite differences method (McCormack's method) was used to avoid problems with numerical dispersion[3].

## 3 CALIBRATION STRATEGY

No model is 100% accurate. Indeed, a model (as a reality representation), will not be exactly the same as the represented problem, but we can focus our efforts in order to achieve a good concordance between model and reality.

Nevertheless, some actions can be performed in order to ascertain the value of the parameters considered in the equations. The objective of the model calibration methodology, depicted in this paper, is to determine the parameters most affecting the results of the water quality model, and finding their values to reach the best agreement between results and measurements.

Figure 1 presents this methodology. The first step is to initialise the model in order to identify input and output variables. To do so, we can use default values for parameters provided from references or previous estimations. This is a conceptual phase and should be done at the same time as the problem statement.

The process continues by ordering parameters according to the influence in the model results, determined by a sensitivity analysis, and after that making the parameters estimation. This sensitivity analysis is a way to understand the behaviour of the model. In this case we implement a parameter perturbation sensitivity analysis[3] and, as a result, we obtain the value of the Relative Effect (RE) defined as:

$$RE = \frac{C(k+\Delta k) \quad \overline{C(k \quad \Delta k)}}{\frac{\overline{C(k)}}{\frac{2\Delta k}{k}}} \tag{9}$$

When arranging these effects, the modeller is able to understand the most important parameters that influence the solution, for future estimation parameters strategies.

When a sensitivity analysis is done, it is time for the fitting process. In this phase the value of parameters has to be known and we distinguish between the two kinds of considered variables in order to adjust the predicted results of the model to some reference data. These reference data can be taken from reality, laboratory or other model.

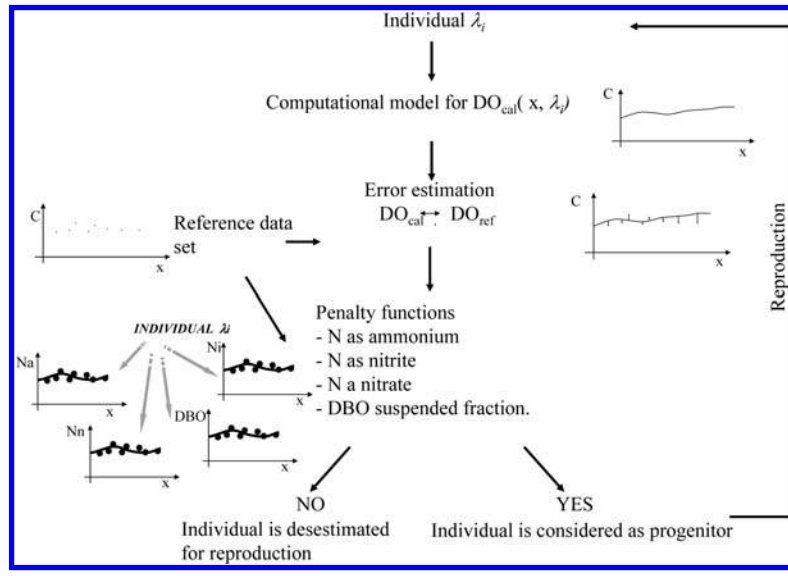


Figure 2. Genetic Algorithm and calibration of DO model.

For internal parameters, estimations can be done with the aid of Genetic Algorithms (GA)[1] in order to speed up the searching process. Genetic Algorithms are an evolutive searching technique capable of providing the value for variables present in the model equations by matching them to reference values, while minimizing the error function, considered as an objective. This technique has been used to evaluate internal parameters.

On the other hand, the influence of the external parameters in the accuracy of results can be considered by an uncertainty analysis. This procedure, combined with the value of internal models provided by the Genetic Algorithms, leads to the best adjust between the model and the reference data set. Also, we will be informed of the reliability of predictions by means of the confidence intervals appearing around the model results. This information will let the modeller know when the calibration process has finished and an acceptable accuracy level has been achieved.

### 3.1 *Using Genetic Algorithm (GA) to estimate internal parameters*

GA is an optimisation technique that simulates the process of evolution based on natural selection and genetic inheritance. This have been proven to be a powerful method even in non-linear problem parameters estimation, especially in engineering problems as considered here[3,4]

In GA numerical optimisation, a problem is defined by biological analogies: the parameters to be estimated play the role of the individual as potential solutions of the problem; and these individuals evolve within the environment in order to fit the objective function to some external reference values.

### 3.2 *Uncertainty analysis in calibration methodology*

As it has been noted, calibration objective is the definition of the best value of parameters involved in the model equations in order to adjust to some reference set of values. The precision of the estimation must be known and understood. Unfortunately, this aspect of the job is often overlooked. The precision of estimated parameters (in a linear o non linear model) is indicated by the size (amplitude) of their joint confidence region[4]. "Joint" indicates that all the parameters in the model are considered simultaneously (even the imprecision in reference values). The confidence regions of both (predicted and reference values) should overlap to consider that calibration is finished; in this way, this uncertainty analysis is the tool for defining criteria for an acceptable level of adjustments between model and references.

When observations that contain measurements are used to calculate other values, errors are transmitted, to a greater or lesser degree, into the calculated (modelled) values. It is very useful to know whether errors in estimation of some values present in model equations will be transmitted into predicted values. These errors can be magnified or suppressed, depending on the relative effect of the parameters, into the final concentration.

The problem is to know exactly how the measurement errors will be transmitted into the calculations, and the definition of the predicted concentration variance solves this. Lets consider concentration Cj and parameter $k_i$. If we know the variance of this parameter, and the relative effect of the variation of this parameter in this concentration; we can establish the value of the variance and typical deviation of calculated values[5,6]

$$\mathrm{Var}(C_j) = \sum_i \mathrm{Var}(k_i)\ \mathrm{ER}_{ij}^{\ 2} \qquad \sigma_R(C_j) = \frac{\sigma(C_j)}{C_j} = \sqrt{\sum_i [\sigma_R(k_i)]^2 \mathrm{ER}_{ij}^{\ 2}} \tag{10}$$

When these statistical parameters are known, we can define the 95% confidence interval (or confidence region) as $C_j \pm 2\sigma_R(C_j)$. Therefore, at all times we know the confidence region for predictions and we can compare it with references. When they overlap in more than 90% of measurements we consider that calibration is finished.

To apply all this, we have used the previously described methodology in a case study for predicting DO concentration. This case study was conducted to confirm the match with field data. A quality model solving the previous equations was used to represent the dynamic of Dissolved Oxygen in a receiving waters channel in Valencia, Spain. This is an irrigation canal but

there are some water flows coming from specific pollution sources. Consequently, we can find a very low initial concentration of Dissolved Oxygen. This concentration increases as a consequence of clean waters coming along the channel.

As well as the DO concentration, we have studied the BOD, Organic Nitrogen, Ammonia, Nitrite and Nitrate concentrations along the modelled channel and they were all calibrated to adjust the predicted concentrations to the measured ones. QUAL2[7] model has been also used to evaluate the concentrations of pollutants in the represented channel.

Depicted methodology has been implemented in the modelling of concentrations in the channel by using GA for searching internal parameters and uncertainty analysis for confidence interval. As DO concentration has been used as objective function, this concentration matches quickly the reference values. When applying the depicted methodology for calibrating the model, error between predictions and measurements decreased 74% over the initial values without implementing the proposed strategy.

## 4 CONCLUSIONS

We have presented a methodology for calibrating DO models. This methodology is based on the consideration of parameters to be estimated in two categories: internal and external ones.

Genetic Algorithms have been investigated for their potential use as a calibration tool in water quality modelling for estimating the value of the so-called internal parameters (appearing in the equations coming from semi empirical studies). To use them, we require an explicit objective and penalty functions. Based on DO model equations GA has also proven to be capable of finding optimum parameters set in constrained and multi response systems such as the DO complete set of equations. On the other hand, GA provides additional information about the searching space, such as sensitivity of some parameters over objective function. These results agree with other sensitivity analysis techniques used in previous phases of the proposed methodology.

This study demonstrates the capability of GA to obtain optimal estimations in constrained systems with a very big number of parameters (more than 14 simultaneously) such as the DO model. Furthermore, the GA population can be used to learn more about model sensitivity and parameter correlation. The presented uncertainty analysis is able to predict the variance of modelled results and it can be considered to determine confidence intervals. Within them, we can define a criterion to finish the calibration process considering both inaccuracies: predicted and reference values. When both confidence interval overlap in more than 90% of occasions, calibration is finished.

## REFERENCES


[1] Mulligan, A., Brown, L. (1998). “Genetic Algorithms for calibrating water quality models”. Journal of Environmental Engineering. ASCE 1998. Vol 3 pp 202–211.

[2] Streeter H.W. y Phelps, E.B. (1925). “A Study of the Pollution and Natural Purification of the Ohio River. III. Factors concerning the Phenomena of Oxidation and Reaireation”. U.S. Public Health Bulletin. No 146.

[3] Chapra, S.C. (1997) *Surface Water Quality modelling.* Mc Graw-Hill. ISBN 0-07-011364-5.

[4] Golberg, D.E; (1987). “Genetic Algorithms in Pipeline Optimization”. Journal of Computing in Civil Engineering, Vol. 1, n° 2, 148–141.

[5] Sumer, D. and Lansey, K. (2009) Effect of Uncertainty on Water Distribution System Model Design Decisions. Journal of Water Resources Planning and Management, Vol. 134, No. 1, January/February 2009, pp. 38–47.

[6] López-Jiménez P. A. (2001). *Metodología para la calibración de modelos matemáticos de dispersion de contaminantes incluyendo regimenes no permanentes.* PhD Thesis. Universidad Politécnica de Valencia.

[7] *QUAL2K model manua*l. http://www.epa.gov/athens/wwqtsc/html/qual2k.html

*Environmental Hydraulics – López-Jiménez et al (eds)*
*© 2010 Taylor & Francis Group, London, ISBN 978-0-415-56697-1*

# Direct sensitivity computation for the shallow water equations with discontinuous solution

Carole Delenne, Vincent Guinot & Bernard Cappelaere
*UMR HydroSciences Montpellier, Université Montpellier 2, Montpellier, France*

ABSTRACT: An approximate Riemann solver is proposed for direct sensitivity computation for the shallow water equations with discontinuous solutions. An extra source term is needed to restore sensitivity balance across the shocks. The sensitivity equations are derived, the numerical technique is given and applied on the dam-break problem with bottom slope.

*Keywords*: shallow water, sensitivity, Riemann solver, shocks, dam-break.

## 1 INTRODUCTION

Sensitivity analysis is widely used in engineering problems (model calibration, geometry optimization, data assimilation, uncertainty analysis, etc). Classical sensitivity analysis methods meet problems when the model output becomes discontinuous, leading to locally infinite sensitivity values[1]. The purpose of this contribution is to present a finite volume-based numerical technique for the computation of the sensitivity of the solutions of the one-dimensional Shallow Water Equations in presence of discontinuous solutions. An application to the dam-break problem is given as example.

## 2 SENSITIVITY EQUATIONS FOR DISCONTINUOUS FLOW PROBLEM

The one-dimensional shallow water equations can be written in vector form as

$$\frac{\partial \mathbf{U}}{\partial t}+\frac{\partial \mathbf{F}}{\partial x}=\mathbf{S}$$
$$\mathbf{U}=\begin{pmatrix} h \\ q \end{pmatrix},\ \mathbf{F}=\begin{pmatrix} q \\ q^2/h+gh^2/2 \end{pmatrix},\ \mathbf{S}=\begin{pmatrix} 0 \\ gh\left(S_0-S_f\right) \end{pmatrix} \tag{1}$$

where $h$ is the water depth, $q$ the unit-discharge, $S_0=-\partial z_b/\partial x$ the bottom slope (with $z_b$ the bottom elevation) and $S_f$ the friction slope, which is assumed to obey a classical Manning-Strickler law under the wide channel approximation

$$S_f=\begin{pmatrix} 0 \\ n_M^2 q|q|h^{-10/3} \end{pmatrix} \tag{2}$$

A sensitivity analysis consists in studying the influence of a small variation in a given parameter $\varphi$, on the solution of the flow equation. The sensitivity equations are obtained by differentiating (1) with respect to $\varphi$

$$\frac{\partial \mathbf{s}}{\partial t}+\frac{\partial \mathbf{G}}{\partial x}=\mathbf{Q}$$
$$\mathbf{s}=\begin{pmatrix} \eta \\ \theta \end{pmatrix}=\begin{pmatrix} \partial h/\partial\varphi \\ \partial q/\partial\varphi \end{pmatrix},\ \mathbf{G}=\frac{\partial \mathbf{F}}{\partial \mathbf{U}}\mathbf{s}=\begin{pmatrix} \theta \\ \left(c^2-u^2\right)\eta+2u\theta \end{pmatrix},\ \mathbf{Q}=\frac{\partial \mathbf{S}}{\partial \mathbf{U}}\mathbf{s}+\frac{\partial \mathbf{S}}{\partial \varphi}\varepsilon-\frac{\partial}{\partial x}\left(\frac{\partial \mathbf{F}}{\partial \varphi}\varepsilon\right) \tag{3}$$

where $\eta$ and $\theta$ are the sensitivities of $h$ and $q$ with respect to $\varphi$; $c=\sqrt{gh}$ is the sound speed (i.e. the propagation speed of the pressure waves in the fluid at rest); $u$ is the flow velocity defined as $q/h$; and $\varepsilon$ is the so-called perturbation index, with $\varepsilon=0$ in the region where the parameter is to be left unchanged and $\varepsilon=1$ in the regions where $\varphi$ is perturbed for the purpose of the sensitivity analysis. These sensitivity equations are obtained using the implicit assumption that the flow solution is continuous and differentiable with respect to $\varphi$ over the domain. In the presence of discontinuous flow solutions (shocks such as hydraulic jumps, moving bores, etc.) differentiability is not guaranteed in the general case and the governing sensitivity equations must be modified so as to account for extra terms in the balance equation (2). In the case of the solution of the Riemann problem, where $\mathbf{U}$ and $\mathbf{F}$ are constant on both sides of the discontinuity and where the perturbation index $\varepsilon$ is assumed to be zero every where for $t>0$, the complete jump relationships (or Rankine-Hugoniot conditions) for the sensitivity are given by[3].

$$\left(\mathbf{s}_\mathrm{L}-\mathbf{s}_\mathrm{R}\right)c_s=\mathbf{G}_\mathrm{L}-\mathbf{G}_\mathrm{R}+\mathbf{R}\quad\text{with}\quad\mathbf{R}=\frac{\partial c_s}{\partial\varphi}\left(\mathbf{U}_\mathrm{L}-\mathbf{U}_\mathrm{R}\right) \tag{4}$$

This source term **R** being non zero only where **U** is discontinuous, (3) can be rewritten for the general case as

$$\frac{\partial \mathbf{s}}{\partial t}+\frac{\partial \mathbf{G}}{\partial x}=\mathbf{Q}+\mathbf{R}\delta_s \tag{5}$$

## 3 NUMERICAL TECHNIQUE

### 3.1 *Finite volume discretization*

The flow and sensitivity equations are discretized using the following finite volume formulation

$$\mathbf{U}_i^{n+1}=\mathbf{U}_i^n+\frac{\Delta t}{\Delta x_i}\left(\mathbf{F}_{i-1/2}^{n+1/2}-\mathbf{F}_{i+1/2}^{n+1/2}\right)+\Delta t\mathbf{S}_i^{n+1/2} \tag{6}$$

$$\mathbf{s}_i^{n+1}=\mathbf{s}_i^n+\frac{\Delta t}{\Delta x_i}\left(\mathbf{G}_{i-1/2}^{n+1/2}-\mathbf{G}_{i+1/2}^{n+1/2}\right)+\Delta t\mathbf{Q}_i^{n+1/2} \tag{7}$$

where $\mathbf{U}_i^n$ and $\mathbf{s}_i^n$ denote respectively the average value of **U** and **s** over the cell $i$ at the time level $n$, $\mathbf{F}_{i-1/2}^{n+1/2}$ and $\mathbf{G}_{i-1/2}^{n+1/2}$ are the average values of **F** and **G** at the interface $i-1/2$ between the cells $i-1$ and $i$ between the time levels $n$ and $n+1$, $\mathbf{S}_i^{n+1/2}$ and $\mathbf{Q}_i^{n+1/2}$ are the average values of **S** and **Q** over the cell $i$ between the time levels $n$ and $n+1$, $\Delta t$ is the computational time step and $\Delta x_i$ is the width of the cell $i$.

### 3.2 *Flux calculation*

A single Riemann problem is defined for the hyperbolic part of the governing equations (1) and (5) at a given interface located at $x_{i-1/2}$ between the cells $i-1$ and $i$

$$\begin{aligned}&\frac{\partial \mathbf{U}}{\partial t}+\frac{\partial \mathbf{F}}{\partial x}=0\\&\frac{\partial \mathbf{s}}{\partial t}+\frac{\partial \mathbf{G}}{\partial x}=0\\&(\mathbf{U},\mathbf{s})(x,0)=\begin{cases}(\mathbf{U}_\mathrm{L},\mathbf{s}_\mathrm{L}) & \text{for} \quad x<x_{i-1/2}\\(\mathbf{U}_\mathrm{R},\mathbf{s}_\mathrm{R}) & \text{for} \quad x\geq x_{i-1/2}\end{cases}\end{aligned} \tag{8}$$

The fluxes are computed using the HLL Riemann solver, with a modification for the sensitivity problem. The two waves separating the intermediate region of constant state from the left and right states of the Riemann problem are assumed to be discontinuities[4]. Here, the discontinuities heading to the left and right respectively have the following celerities

$$\begin{pmatrix}\lambda^-\\ \lambda^+\end{pmatrix}=\begin{pmatrix}u-c\\ u+c\end{pmatrix} \tag{9}$$

and are computed as [5]

$$\begin{aligned}\lambda^- &= \min\left(u_\mathrm{L}-c_\mathrm{L},u_\mathrm{R}-c_\mathrm{R},0\right)\\ \lambda^+ &= \max\left(u_\mathrm{L}+c_\mathrm{L},u_\mathrm{R}+c_\mathrm{R},0\right)\end{aligned} \tag{10}$$

The Rankine-Hugoniot conditions can then be written as

$$\begin{aligned}\left(\mathbf{U}_\mathrm{L}-\mathbf{U}_*\right)\lambda^- &= \mathbf{F}_\mathrm{L}-\mathbf{F}_*\\ \left(\mathbf{U}_\mathrm{R}-\mathbf{U}_*\right)\lambda^+ &= \mathbf{F}_\mathrm{R}-\mathbf{F}_*\end{aligned} \tag{11}$$

where the subscript * indicates the value of the variable in the intermediate region of constant state. Solving Eq (11) for **U** and **F** yields

$$\mathbf{U}_*=\frac{-\lambda^-\mathbf{U}_\mathrm{L}+\lambda^+\mathbf{U}_\mathrm{R}+\mathbf{F}_\mathrm{L}-\mathbf{F}_\mathrm{R}}{\lambda^+-\lambda^-} \tag{12}$$

$$\mathbf{F}_*=\frac{\lambda^+\mathbf{F}_\mathrm{L}-\lambda^-\mathbf{F}_\mathrm{R}-\lambda^-\lambda^+\left(\mathbf{U}_\mathrm{L}-\mathbf{U}_\mathrm{R}\right)}{\lambda^+-\lambda^-} \tag{13}$$

The sensitivity flux $\mathbf{G}_*$ is obtained by extending (13) to the sensitivity balance

$$\mathbf{G}_*=\frac{\lambda^+\mathbf{G}_\mathrm{L}-\lambda^-\mathbf{G}_\mathrm{R}-\lambda^-\lambda^+\left(\mathbf{s}_\mathrm{L}-\mathbf{s}_\mathrm{R}\right)}{\lambda^+-\lambda^-} \tag{14}$$

### 3.3 *Source term calculation*

The source term S in (6) is discretized using a classical source term upwinding procedure[6]

$$\mathbf{S}_i^{n+1/2} = \begin{bmatrix} 0 \\ gh\left(S_0 - S_f\right) \end{bmatrix}_{i,\mathrm{L}}^{n+1/2} + \begin{bmatrix} 0 \\ gh\left(S_0 - S_f\right) \end{bmatrix}_{i,\mathrm{R}}^{n+1/2} \tag{15}$$

where the subscripts L and R denote the respective contributions of the left and right interface of the cell $i$ to the total source term. The contributions of the interface $i-1/2$ to the cells $i-1$ and $i$ are given by

$$\begin{aligned} \left[gh\left(S_0 - S_f\right)\right]_{i,\mathrm{L}}^{n+1/2} &= \frac{-\lambda^-}{\lambda^+ - \lambda^-} gh_{i-1/2}^n \left( \frac{z_{bi-1} - z_{bi}}{\Delta x_i} - n_M^2 \left(h_{i-1/2}^n\right)^{-10/3} q_{i-1/2}^n \left| q_{i-1/2}^n \right| \right) \\ \left[gh\left(S_0 - S_f\right)\right]_{i-1,\mathrm{R}}^{n+1/2} &= \frac{+\lambda^+}{\lambda^+ - \lambda^-} gh_{i-1/2}^n \left( \frac{z_{bi-1} - z_{bi}}{\Delta x_i} - n_M^2 \left(h_{i-1/2}^n\right)^{-10/3} q_{i-1/2}^n \left| q_{i-1/2}^n \right| \right) \end{aligned} \tag{16}$$

where the subscript $i-1/2$ denotes the mean of the variable values in cells $i-1$ and $i$.

The source term **Q** for the sensitivity is discretized using the same procedure as **S** and computed as

$$\mathbf{Q}_i^{n+1/2} = \begin{pmatrix} 0 \\ \left(S_0 + \frac{7}{3} S_f\right) g\eta - 2\frac{S_f}{q} g\theta - 2gh\frac{S_f}{n_M} \varepsilon_n \end{pmatrix}_i^{n+1/2} \tag{17}$$

where $\varepsilon_n = 1$ if the sensitivity analysis is performed with respect to the Manning's friction coefficient.

The point source term **R** is split into two contributions, using (4) and the two wave celerities

$$\begin{aligned} \mathbf{R}^- &= -\frac{\partial \lambda^-}{\partial \varphi}\left(\mathbf{U}_\mathrm{L} - \mathbf{U}_*\right) \\ \mathbf{R}^+ &= -\frac{\partial \lambda^+}{\partial \varphi}\left(\mathbf{U}_* - \mathbf{U}_\mathrm{R}\right) \end{aligned} \tag{18}$$

Noticing that the wave speeds depend on $\mathbf{U}_L$ and $\mathbf{U}_R$ only in the conservation part of the equations and that $\partial \mathbf{U}/\partial \varphi = \mathbf{s}$, (18) can be rewritten as

$$\begin{aligned} \mathbf{R}^- &= -\left(\frac{\partial \lambda^-}{\partial \mathbf{U}_\mathrm{L}} \mathbf{s}_\mathrm{L} + \frac{\partial \lambda^-}{\partial \mathbf{U}_\mathrm{R}} \mathbf{s}_\mathrm{R}\right)\left(\mathbf{U}_\mathrm{L} - \mathbf{U}_*\right) \\ \mathbf{R}^+ &= -\left(\frac{\partial \lambda^+}{\partial \mathbf{U}_\mathrm{L}} \mathbf{s}_\mathrm{L} + \frac{\partial \lambda^+}{\partial \mathbf{U}_\mathrm{R}} \mathbf{s}_\mathrm{R}\right)\left(\mathbf{U}_* - \mathbf{U}_\mathrm{R}\right) \end{aligned} \tag{19}$$

The source term **R** is computed only if a shock is detected, that is, for the wave $\lambda^-$, if the following conditions are satisfied [3]

$$\begin{aligned} u_\mathrm{L} - c_\mathrm{L} &> u_* - c_* \\ u_\mathrm{L} + c_\mathrm{L} &> u_* + c_* \end{aligned} \tag{20}$$

while a shock is detected for the wave $\lambda^+$ if

$$\begin{aligned} u_* - c_* &> u_\mathrm{R} - c_\mathrm{R} \\ u_* + c_* &> u_\mathrm{R} + c_\mathrm{R} \end{aligned} \tag{21}$$

## 4 COMPUTATIONAL EXAMPLE: DAM-BREAK PROBLEM ON A SLOPING BED

The purpose of the dam-break problem is to study the sensitivity of the flow solution to the initial water depth in the reservoir (e.g. $h_\mathrm{L}$). It is a Riemann problem defined as follow

$$\begin{aligned} h(x,0) &= \begin{cases} h_\mathrm{L} & \text{for} \quad x < x_0 \\ h_\mathrm{R} & \text{for} \quad x \geq x_0 \end{cases} \\ q(x,0) &= 0 \end{aligned} \tag{22}$$

This definition implies that the initial free surface has the same slope as the bottom one. Although it does not correspond to equilibrium conditions, it gives the advantage that the analytical solution is easy to compute[3]. The analytical, numerical and

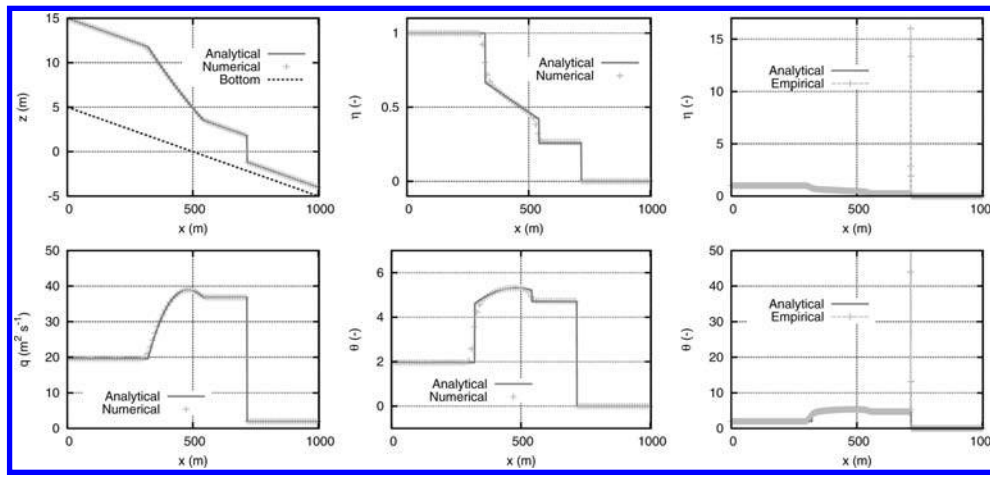


Figure 1. Dam-break problem: flow solution (left), numerical (middle) and empirical (right) sensitivities.

Table 1. Parameters used for the dam-break problem.

| Symbol | Meaning | Value |
|---|---|---|
| $g$ | Gravitational acceleration | $9.81\,\mathrm{m\,s^{-2}}$ |
| L | Length of the simulation domain | 1000 m |
| $S_0$ | Bottom slope | 0.01 |
| $x_0$ | Abscissa of the initial discontinuity | 500 m |
| $h_\mathrm{L}$ | Water depth on the left-hand side of the initial discontinuity | 10 m |
| $h_\mathrm{R}$ | Water depth on the right-hand side of the initial discontinuity | 1 m |
| $\eta_\mathrm{L}$ | Depth sensitivity on the left-hand side of the initial discontinuity | 1 |
| $\eta_\mathrm{R}$ | Depth sensitivity on the right-hand side of the initial discontinuity | 0 |
| $\theta$ | Sensitivity of the unit-discharge on both sides of the discontinuity | 0 |
| $n_\mathrm{M}$ | Manning's friction coefficient | $0\,\mathrm{m^{-1/3}\,s}$ |
| $\Delta x$ | Cell width | 1 m |
| $t$ | Computational time | 20 s |

empirical solutions are plotted in Figure 1 for a positive slope with the parameters given in Table 1. The computational time step is automatically computed to ensure the stability constraint

$$\Delta t_{\max} = \min_i \frac{\Delta x_i}{\left|u_i^n\right| + c_i^n} \tag{23}$$

The empirical sensitivity profiles have been obtained using two slightly different values for $h_\mathrm{L}$ (i.e. 10 m and 10.01 m). The numerical solution is seen to allow for a correct location of the discontinuities in the sensitivity profiles and the empirical approach is invalid in the neighborhood of shocks, with a strong, artificial overshoot.

## 5 CONCLUSION

A numerical technique has been presented for the one-dimensional shallow water sensitivity equations in the presence of discontinuous solutions and applied on the dam-break problem, i.e. a Riemann problem with discontinuous initial conditions. Supplementary Numerical experiments indicate that the proposed approach gives satisfactory results for discontinuous boundary conditions problems or to perform uncertainty analysis with respect to a given parameter such as the Manning's friction coefficient. Ongoing researches focus on the generalization of the present technique to the solution of the two-dimensional shallow water equations on unstructured grids, or the development of higher-order schemes for the solution of the sensitivity equations.

## REFERENCES

[1] Gunzburger, M.D. (1999), "Sensitivities, adjoints and flow optimization", International Journal for Numerical Methods in Fluids, Vol. 3, pp. 53–78.
[2] Bardos, C. and Pironneau, O. (2002), "A formalism for the differentiation of conservation laws", Comptes Rendus de l'Académie des Sciences Paris, Ser. I, Vol. 335, pp. 839–845.
[3] Guinot, V., Delenne, C. and Cappelaere, B. (2009), "An approximate-state Riemann solver for sensitivity equations with discontinuous solutions", Advances in Water Resources, Vol. 31 (1), pp. 61–77.
[4] Harten, A., Lax, P.D. and Van-Leer, B. (1983), "On upstream differencing and Godunov-type schemes for hyperbolic conservation laws", SIAM Review, Vol. 25, pp. 35–61.
[5] Davis, S. F. (1988), "Simplified second-order Godunov-type methods", SIAM Journal on Scientific and Statistical Computing, Vol. 9, pp. 455–473.
[6] Vasquez-Cendon, M.E. (1999), "Improved treatment of source terms in upwind schemes for the shallow water equations in channels with irregular geometry", Journal of Computational Physics, Vol 148, pp. 497–526.

*Environmental Hydraulics – López-Jiménez et al (eds)*
*© 2010 Taylor & Francis Group, London, ISBN 978-0-415-56697-1*

# Filtering and validation of velocities obtained with ADV equipment inside of hydraulic jumps

Luis G. Castillo
*Departamento de Ingeniería Térmica y de Fluidos – Grupo I+D+i Hidr@m, Universidad Politécnica de Cartagena, Cartagena, España*

ABSTRACT: Measurement of instantaneous velocities with ADV equipment, are very reliable in laminar and turbulent flows without the air presence. However, in two-phase flows (water-air), for example inside of a hydraulic jump, the register measurements can be wrong when air bubbles pass through the measurement volume, because in this instant the sound echo is not correctly transmitted. In this paper are analyzed some digital filters and applied to the registers of instantaneous velocities measurements inside of some configurations of free and submerged hydraulic jump.

*Keywords*: Digital Filtering, Acoustic Doppler Velocimeter, Turbulent High Two-Phase Flow.

## 1 INTRODUCTION

Acoustic Doppler Velocimeter (ADV) measure the velocity of acoustic targets moving with the fluid, rather than directly the fluid velocity. Since these acoustics targets follow the fluid motion with negligible inertial lag, their velocity is assumed to be identical to the fluid velocity. ADVs are able to measure the time-averaged flow field with an accuracy that is better than 4%. However, the signal suffers parasitical noise contributions and this noise has the following characteristics (Blanckaert and Lemmin[1]):

- Its energy content is uniformly distributed over the investigated frequency domain (white noise).
- It is unbiased: $\overline{\sigma}_i = 0$.Therefore, it does not affect the estimates of the time-averaged velocity $\overline{u}$.
- It is statistically independent of the corresponding true Doppler frequency: $\overline{\sigma_i f_{D,i}} = 0$ if $i \neq j$.
- The noise of the different receivers is statistically independent: $\overline{\sigma_i \sigma_j} = 0$. Noise-free estimates of the turbulent shear stress are obtained if $\overline{\sigma}_i^2 = \overline{\sigma}_j^2 = \overline{\sigma}^2$. However, the estimates of the turbulent normal stress, are affected by noise.

The spikes in ADV time series can be caused by many factors, including high turbulent intensities, aerated flows that have undesirable acoustic properties, and phase difference ambiguities that occur when the velocities exceed the upper limits of ADV probe velocity range. Although spikes can be reduced or eliminated in many cases by adjustment of probe operational parameters, there are some situations in which spikes cannot be entirely avoided (Wahl[2]).

A hydraulic jump is characterized by a sudden rise of the free-surface, with strong energy dissipation and mixing, large-scale turbulence, air entrainment, waves and spray. So, it is necessary a digital filtering of the information, in order to eliminate and/or correct the anomalous data but maintaining the continuity of the register.

## 2 METHODS

Despiking involves two steps: (1) detecting the spike and (2) replacing the spike. There are some spikes detection algorithms. In this paper we apply the following ones:

- Acceleration Thresholding Method (Goring and Nikora[3]) and modified in this paper.
- Progressive cut of the lower and upper limits in function of 5 and 95% statistical (Castillo[4]).
- Phase-Space Thresholding Method[3] with the modified version[2] and in this paper.

### 2.1 Acceleration Thresholding Method (ATM + C)

In order to a point be a spike, the acceleration must exceed a threshold $\lambda_a g$ and the absolute deviation from the mean velocity of the point must exceed $k\sigma$, where $\lambda_a$ is a relative acceleration threshold, $\sigma$ is the standard deviation and $k$ is a factor to be determined. The acceleration is calculated from $a_i = (u_i - u_{i-1})/\Delta t$, where $u_i$ is discrete velocity time series and $\Delta t$ the sampling interval. This method is a detection and replacement procedure with two phases: one for negative accelerations and the second for positive accelerations. In each phase, numerous passes through the data are made until all data points conform to the acceleration criterion $\lambda_a g$ and the magnitude threshold $k\sigma$. Goring and Nikora[3] indicate that good choices for the parameters are: $\lambda_a = 1 - 1.5$ and $k = 1.5$. However, we have observed that for hydraulic jump cases the $\lambda_a$ value must be calculated in function of the $j$ section position ($d_j$) inside of hydraulic jump and its corresponding Froude number, $Fr_j$. Then the acceleration $a_j$ in function of Froude number is:

$$a_j = \frac{u_j}{\Delta t} = \frac{Fr_j \sqrt{g y_j}}{\Delta t} = \lambda_{aj} g \qquad (1)$$

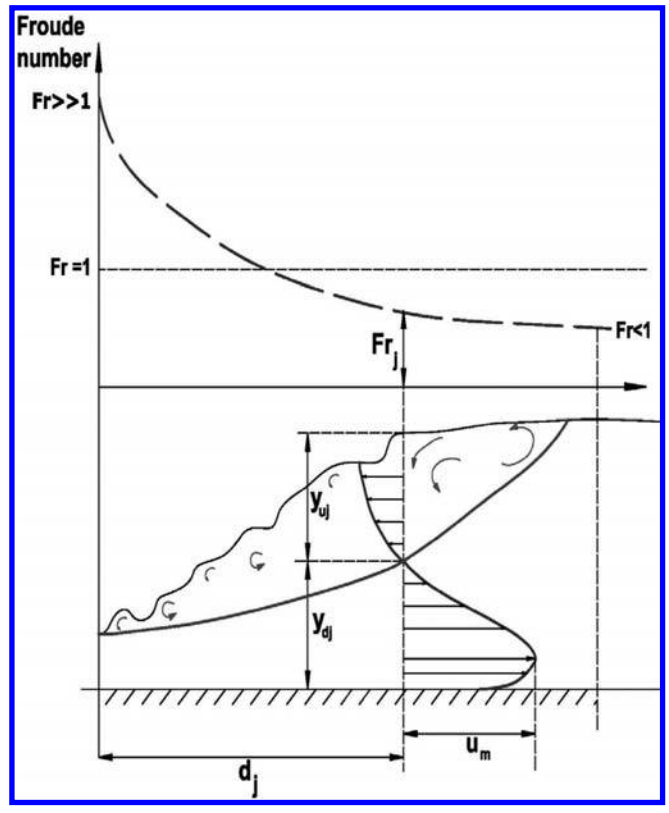


Figure 1. Froude number variation and principal parameters inside of hydraulic jump.

Where $\lambda_{aj} = Fr_j\sqrt{y_j}/(\Delta t\sqrt{g})$, $\Delta t$ is time interval between data points, $y_j$ takes the depth value $y_{dj}$ when the flow is downstream and $y_{uj}$ when the flow is upstream (see Figure 1). In this way, the parameter $\lambda_{aj}$ is established by the flow specific characteristics in each section of measurement.

The threshold $k$ that is usually applied arises from a theoretical result from normal probability distribution theory which says that for $n$ independent, identically distributed, standard, normal, random variable $\xi_i$, the expected absolute maximum is $\mathrm{E}(|\xi_i|_{\max}) = \sqrt{2\ln n} = \lambda_U$, where $\lambda_U$ is denominated the Universal threshold. For a normal, random variable whose standard deviation is estimated by $\sigma$ and the mean zero, the expected absolute maximum is $\lambda_U\sigma = \sqrt{2\ln n}\sigma$. However, this threshold can result very wide when the time distribution is not normal, as in the case of the velocities distribution inside of a hydraulic jump.

### 2.2 *Progressive cut of the lower and upper limits in function of 5% and 95% statistical (PCLU)*

The method is based on the above conclusions. So, because the velocity time distribution does not fit a normal distribution, then it is better to estimate a threshold trends to the upper limit really registered in the signal. The data filtering is based on progressive cut of the lower and upper limits, in function of the 5% and 95% statistical[4]. From the mean, $\overline{u}$ and maximum, $u_{\max}$ values registered in the data series, the first relative amplitude is determined, $A_1 = u_{\max} - \overline{u}$. Next is found the value $u_{mín} = \overline{u} - A_1$ and the general amplitude $A = u_{\max} - u_{mín}$. Finally they are obtained the superior cut value, $X_{máx.c}$ and the lower cut value, $X_{mín.c}$ from the initial series, so that $X_{máx.c} = u_{\max} - (0.05A)$ and $X_{mín.c} = u_{mín} + (0.05A)$.

This process can be repeated if the data series need it. However it is recommended not to do more than two filtering data, so that the initial series to be little altered. In the original method the spike is replaced automatically by the upper or lower value of the corresponding cut. However, in this paper the spike was replaced by the sample median.

### 2.3 *Phase-Space Thersholding Method (PSTM + W)*

The method uses the concept of a three-dimensional Poincaré map or phase-space plot in which the variable and its derivatives are plotted against each other. The points are enclosed by an ellipsoid defined by the Universal criterion and the points outside the ellipsoid are designated as spikes. The method iterates until the number of good data becomes constant. Each iteration has the following steps[3]:

1. Calculate surrogates for the first and second derivatives from central differences algorithm: $\Delta u_i = (u_{i+1} - u_{i-1})/2$ and $\Delta^2 u_i = (\Delta u_{i+1} - \Delta u_{i-1})/2$. Note that is not divided by time step $\Delta t$ to ensure that some equations do not become ill conditioned.
2. Calculate the standard deviations of all three variables $\sigma_u$, $\sigma_{\Delta u}$, and $\sigma_{\Delta 2u}$, and thence the expected maxima using the Universal criterion.
3. Calculate the rotation angle of the principal axis of $\Delta^2 u_i$ versus $u_i$ using the cross correlation $\theta = \tan^{-1}\left(\sum u_i \Delta^2 u_i / \sum u_i^2\right)$.
4. For each pair of variables, calculate the ellipse that has maxima and minima. Thus, for $\Delta u_i$ versus $u_i$ the major axis is $\lambda_U\sigma_u$ and the minor axis is $\lambda_U\sigma_{\Delta u}$; for $\Delta^2 u_i$ versus $\Delta u_i$ the major axis is $\lambda_U\sigma_{\Delta u}$ and the minor axis is $\lambda_U\sigma_{\Delta 2u}$; and for $\Delta^2 u_i$ versus $u_i$ the major and minor axes, $a$ and $b$, respectively, are the solutions of $(\lambda_U\sigma_U)^2 = a^2\cos^2\theta + b^2\sin^2\theta$ and $(\lambda_U\sigma_{\Delta 2u})^2 = a^2\sin^2\theta + b^2\cos^2\theta$.

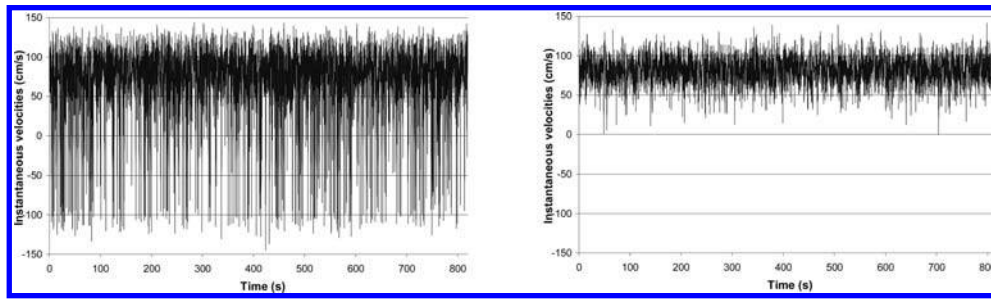


Figure 2. Types of velocity registers. Left: pathological register. Right: clean register.

Table 1. Comparison of results obtained by the application of different filtering methods.

| | Pathological register | Clean register |
|---|---|---|
| Length of time series: | 4504 | 4504 |
| Time interval between data point (s): | 0.20 | 0.20 |
| Sample mean (cm/s): | 69.56 | 81.56 |
| Standard deviation (cm/s): | 52.73 | 18.63 |
| ATM+C method | | |
| Spikes identified: | 1238 | 98 |
| Sample mean after of filtering (cm/s): | 82.2 | 82.01 |
| Standard deviation after of filtering (cm/s): | 25.96 | 17.78 |
| PSTM+W method | | |
| Spikes identified: | 581 | 44 |
| Sample mean after of filtering (cm/s): | 80.91 | 81.81 |
| Standard deviation after of filtering (cm/s): | 18.25 | 18.28 |
| ATM+C and PSTM+W methods | | |
| Spikes identified: | 1323 | 120 |
| Sample mean after of filtering (cm/s): | 83.24 | 82.08 |
| Standard deviation after of filtering (cm/s): | 24.68 | 17.70 |
| ATM+C and PCLU methods | | |
| Spikes identified: | 697 | 30 |
| Sample mean after of filtering (cm/s): | 79.81 | 81.66 |
| Standard deviation after of filtering (cm/s): | 27.59 | 18.56 |

However, it can be demonstrated that an equations system more precise obeys to the following expressions:

$$(\lambda_U \sigma_U)^2 = a^2 \cos^2(\theta/2) + b^2 (\lambda_U \sigma_u / \lambda_U \sigma_{\Delta 2u})^2 \sin^2(\theta/2) \quad (2)$$

$$(\lambda_U \sigma_{\Delta 2u})^2 = a^2 (\lambda_U \sigma_{\Delta 2u} / \lambda_U \sigma_u)^2 \sin^2(\theta/2) + b^2 \cos^2(\theta/2)\,. \quad (3)$$

5. For each projection in phase space, identify the points that lie outside of the ellipse and replace them.

At each iteration, replacement of the spikes reduces the standard deviation and thus the size of the ellipsoid. This despiking algorithm uses the mean and standard deviation, the classic estimators for locations and scale, respectively. However, a single outlier of extraordinary magnitude can corrupt both parameters and affect significantly the performance. Wahl[2] proposed the sample median as an estimator of location and, the median of the absolute deviations from the sample median, as estimator of scale. He added to the WinADV computer program[5] the modified algorithm. The program incorporates too the Chauvenet's criterion to define the rejection probability and exclusions thresholds and, the position of the $u$, $\Delta u$ and $\Delta_u^2$ data point is expressed in spherical coordinates.

## 3 APPLICATION AND CONCLUSIONS

Figure 2 shows two horizontal velocity register obtained inside of a hydraulic jump in identical conditions of position and flow. The registers were obtained with a rate of data acquisition of 5 points per second and, the unique difference consisted in that the velocity range of the left register was +/−100 cm/s (theoretical horizontal maximum velocity +/−300 cm/s) and, for the right register, +/−250 cm/s (horizontal maximum velocity of +/−360 cm/s).

In the case of the clean register, all the methods give similar results in the sample mean after of filtering and, are a bit higher than the mean value of the original series. However, the standard deviations are reduced over the five percent after of filtering. This circumstance indicates that the turbulence normal stress is not correct and, we would be able to discriminate the real stress from the white noise. It is interesting to note that for the case of velocities registered inside of hydraulic jump, the combination ATM+C and PCLU methods constitute the more robust procedure of filtering. We can observe that the mean value and the standard deviation are the most similar to the original series values and, is the only procedure that let us obtain the mean value from the pathological register, with an error lower that 3% (Table 1). From systematic application of the ATM+C and PCLU

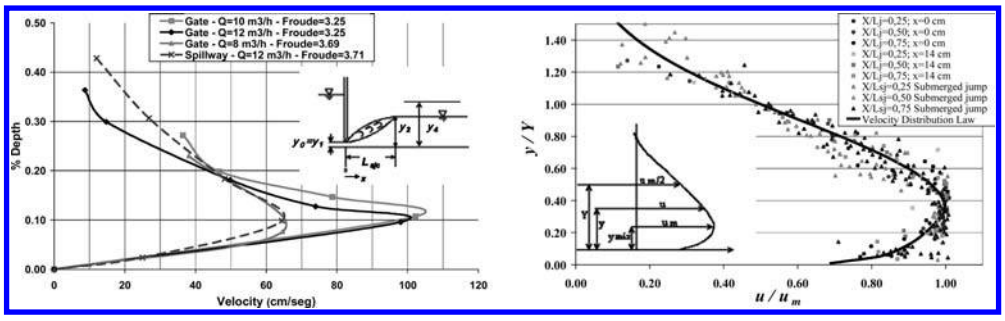


Figure 3. (a) Velocity distributions in the middle of hydraulic jump. (b) Velocity distribution law inside of free and submerged hydraulic jumps. Validities ranges: $2.5 \leq F_{r1} \leq 5$; $0.25 \leq x/L_{sjc} \leq 0.75$; $4 \leq y_4/y_0 \leq 10$.

methods to the time registers of velocities in different sections inside of free and submerged hydraulic jumps (Figure 3a) and, from analysis of the mean velocity experimental distribution, it was obtained a universal velocity distribution law[4], in the range $[0.2 \leq x/L_{sjc} \leq 0.7]$ (see Figure 3b).

## REFERENCES


[1] Blanckaert, K. and Lemmin, U. (2006), "Means of noise reduction in acoustic turbulence measurements", J. Hydraulic Research Vol. 44, No. 1, pp. 3–17.

[2] Wahl, T. L. (2003), Discussion of "Despiking acoustic Doppler velocimeter data" by Derek G. Goring and Vladimir I. Nikora. January 2002, Vol. 128, No 1, pp. 117–126, J. Hydraulic Engineering, June 1. pp. 484–488.

[3] Goring, G. and Nikora, V.(2002), "Despiking acoustic Doppler velocimeter data, J. Hydraulic Engineering, Vol. 128, Nº 1, January 1. pp. 117–126.

[4] Castillo, L. (2008), "Validation of instantaneous velocities measurements with ADV equipment in turbulent high two-phase flows". *Proceedings of The Eight Int. Conference on Hydro-Science and Engineering (ICHE 2008). Nagoya, Japan, Sep 8–12.*

[5] Wahl, T. L. (2000), "Analyzing ADV data using WinADV", *Proceedings of Joint Conference on Water Resources Engineering and Water Resources Planning and Management, ASCE, Minnneapolis, July 30–August 2.*

*Environmental Hydraulics – López-Jiménez et al (eds)*
*© 2010 Taylor & Francis Group, London, ISBN 978-0-415-56697-1*

# Lessons for the calibration of hydraulic transient simulators

Nelson J.G. Carriço & Dídia I.C. Covas
*Instituto Superior Técnico, Technical University of Lisbon, Lisbon, Portugal*

Alexandre K. Soares
*Department of Environmental and Sanitary Engineering, Federal University of Mato Grosso, Cuiabá, Brazil*

*Keywords*: calibration, transient simulator, viscoelasticity, unsteady friction.

## 1 INTRODUCTION

The current paper aims at the presentation of guidelines for the calibration of hydraulic transient models taking into account different dynamic effects (i.e., unsteady friction and pipe non-elastic behaviour) and applied to different types of pipe systems. A hydraulic transient simulator has been developed, which incorporates different numerical schemes for steady state friction, unsteady friction and the pipe wall rheological behaviour. A data collection programme has been carried out in an experimental facility at Instituto Superior Técnico, collecting pressure data during simulated transient events; the facility has a reservoir-pipe-valve configuration; the pipe is made of high density polyethylene (HDPE), is 203 m long and has 50 mm inner diameter. Calibration guidelines that are divided in steady state calibration and transient state calibration, are presented. The developed simulator is calibrated and validated by following the proposed methodology and by using physical data collected in laboratory conditions. The main conclusions of the research work and suggestions for future studies are presented.

## 2 HYDRAULIC TRANSIENT SIMULATOR

### 2.1 *Classic solver*

Equations that describe 1-D transient flow in pressurised pipes are a set of two differential equations (Chaudhry, 1987):

$$\frac{\partial H}{\partial x}+\frac{1}{gS}\frac{\partial Q}{\partial t}+h_f=0 \tag{1}$$

$$\frac{\partial H}{\partial t}+\frac{a^2}{gS}\frac{\partial Q}{\partial x}=0 \tag{2}$$

where $Q$ = flow rate; $H$ = piezometric head; $g$ = gravity acceleration; $S$ = pipe cross-sectional area; $x$ = coordinate along the pipeline axis; $t$ = time; $a$ = elastic wave speed; $h_f$ = slope of the energy line. These principles take into account simplifying assumptions as (i) pseudo-uniform velocity profile, (ii) linear-elastic rheological behaviour of pipe wall, (iii) fluid is one-phase, homogenous and compressible; and (iv) uniform and constrained pipe. These equations are quasi-linear and hyperbolic, valid at intermediate sections of the pipe.

### 2.2 *Linear-viscoelastic model*

Eq. (1) and (2) presuppose that the pipe material is linear-elastic, which is valid for concrete and metal pipes, but incorrect for plastic pipes. In order to take into account the pipe rheological behavior, the continuity equation must be derived from the Reynolds Theorem assuming that linear viscoelasticity of pipe material for small strains and that the pipe material has a constant Poisson's ratio, $\nu$, so that the mechanical behaviour depends only on the creep function, $J(t)$. Decomposing total strain in the sum of an elastic strain, $\varepsilon_e$, and a retarded strain, $\varepsilon_r$, the continuity equation yields:

$$\frac{\partial H}{\partial t}+\frac{a^2}{gS}\frac{\partial Q}{\partial x}+\frac{2a^2}{g}\frac{\partial \varepsilon_r}{\partial t}=0 \tag{3}$$

The third term of Eq.(3) represents the retarded strain and the instantaneous-elastic strain is included in the piezometric-head time derivative and in the elastic wave speed, $a$.

### 2.3 *Unsteady friction model*

The friction term, $h_f$, can be decomposed into two terms, a steady-state component $h_{fs}$, and an unsteady-state component, $h_f$ [1]. The steady-state component $h_{fs}$, can be determined using steady-state formulations, if the flow is a turbulent regime than the Colebrook-White equation can be used or if the flow is a laminar regime the Hagen-Poiseuille equation can be applied.

The unsteady-state component $h_{fu}$, can be calculated by using different formulations, such as Vardy[6] or Vitkovsky *et al.*[7] formulations Eqs. (4–5) and (6), respectively, which have been implemented in the transient solver.

$$h_{fu} \approx \frac{16\nu'}{gD^2} \sum_{i=A,B} Y_i(t) \quad \text{where} \quad Y_i(t) = Y_i(t-\Delta t)e^{-B_i \frac{4\nu'}{D^2}\Delta t} + A_i\left[U(t) - U(t-\Delta t)\right] \tag{4}$$

$$h_{fu} = \frac{k_3}{g}\left(\frac{\partial V}{\partial t} + a \cdot SGN(V)\left|\frac{\partial V}{\partial x}\right|\right) \tag{5}$$

### 2.4 *Method of characteristics*

The Method of Characteristics (MOC) is a numerical method which converts the first order partial differential equations (PDE) into ordinary differential equations (ODE) along certain curves in the x-t plane (called characteristic lines $C^+$ and $C^-$), that can be solved, after being expressed in terms of finite differences. The friction and piezometric-head terms may be included in the equations and can handle up complex systems of pipes. This method is not the only one that can be used to solve the equations, but is increasingly used for the study of water hammer problems. The result of MOC's application to equations (3) and (2) is the following set of equations:

$$C^{\pm}: \frac{dH}{dt} \pm \frac{a}{gS}\frac{dQ}{dt} \pm ah_f + \frac{2a^2}{g}\left(\frac{\partial \varepsilon_r}{\partial t}\right) = 0 \tag{6}$$

valid along $dx/dt = V \pm a$. Generally, the fluid velocity is negligible when compared to the wave speed propagation, leading to approximately straight characteristic lines. These equations have two terms that cannot be directly calculated and need further numerical discretization: the slope of the energy line, $h_f$, and retarded strain time derivative, $\partial\varepsilon_r/\partial t$. Several mechanical models can be used combining springs and dashpots, connected in series or in parallel, to describe the behaviour of simple systems, to numerically describe the viscoelastic behaviour of materials. Polyethylene pipes are viscoelastic solids, being described by the generalized Kelvin-Voigt model[4].

## 3 EXPERIMENTAL SET-UP

A data collection programme was carried out in an experimental facility at the Laboratory of Hydraulic and Water Resources from the Instituto Superior Técnico, Lisbon (Portugal). The experimental facility works in a closed circuit in which a centrifugal pump injects water from a tank into a hydropneumatic vessel. The pipe is made of high-density polyethylene (HDPE) with a nominal diameter of 50 mm, a wall thickness of 3 mm and a nominal pressure of 10 kgf/cm$^2$. The pipe was installed in a coil, with 1 m of radius of curvature. The HDPE pipe has a total length of 199 m. The installation from the hydropneumatic vessel to the downstream valve has a total length of 203.37 m. The downstream boundary condition of the experimental facility is an atmosphere-valve. This valve is a ball valve type and is manually operated and closed and opened as fast as possible to simulate instantaneous valve manoeuvres. The inflow is controlled by another ball valve at the upstream of the tank with two-compartments. The configuration of the experimental facility and a collected data set are depicted in Figure 1.

## 4 CALIBRATION GUIDELINES

Calibrate approach is divided into two main stages: the steady state calibration of the regime and the transient state calibration. Each stage is divided into steps (1–8). This methodology is particular to "Tank-Pipe-Valve" type system, but can be extended to other pipe system configuration (Figure 2).

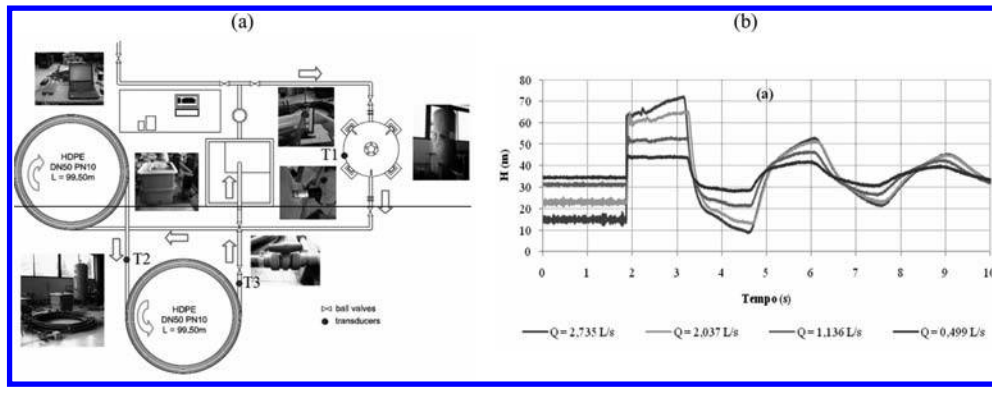


Figure 1. (a) Schematic configuration of the experimental facility and (b) example of collected data.

## 5 RESULTS OF CALIBRATION

*Steady-State Calibration (Steps 1–3)*

The steady state calibration depends on the flow regime and on the flow resistance equations. For smooth pipes with high Reynolds numbers (Re > 4000), the von Karman-Prandtl formulation may be use; for rough pipes and high Reynolds numbers, Colebrook-White formula may be use the; for the laminar regime, Hagen-Poiseuille equation should be use (Step 1). For turbulent flow, calibrated parameters are the roughness coefficient, $k$. The absolute roughness varies proportionally with the flow being average values of roughness 0.06 mm (Step 2). The last step of calibration of the steady state (Step 3) focuses on the valve opening. The calibration of this parameter can be carried out by inverting the equations to obtain a reference value or by a trial-and-error procedure.

*Valve manoeuvre and wave speed (Step 4)*

The calibration of the valve manoeuvre requires (i) the initial time of closure based on a preliminary analysis of measurements, (ii) the total time of closure (corresponding to the inflection point of the first wave), and (iii) the manoeuvre. The valve manoeuvre may be linear, bilinear, or composed of linear stretches.

*Range of wave speed values (Step 5)*

A range of wave speed values should be estimated using maximum and minimum values of dynamic modulus of elasticity, Poisson coefficient and axial constraints. Wave speed can be estimated by theoretical formulae. For plastic pipes the dynamic modulos of elasticitity should be used $E_d$ which is approximately 1.5–2.0 times the static modulus of elasticity ($E_0$) provided by manufactures for HDPE (Covas, 2003), and, 1.0–1.5 $E_0$ for PVC[5]. For non plastic pipes, $E_0$ can be used. In this case $E_0$ varies between 0.7 and 1.0 GPa; accordingly, the estimated range of wave speed is between 270 and 380 m/s.

*Case (a): the use of a linear elastic solver with unsteady friction modelling in a viscoelastic pipe (Step 6)*

This corresponds either to a linear elastic pipe (which is not the case), or to the use of a linear elastic transient model incorporating unsteady friction in a plastic pipe (the current case). In the latter, if the unsteady friction formulation has parameters, these have to be calibrated simultaneously with the wave speed. The example shown corresponds to the use of Vistkovsky's formulation and the calibration of the empirical coefficient, $k_3$, for wave speed, $a$. A maximum of 100 iterations was used. The analysis of the results shows that: (i) the optimal values occur at different wave speeds for each experimental test; (ii) the OF decreases for each experimental test (*i.e.* the OF decreases directly with flow); (ii) the OF decreases until it reaches a minimum value and then increase it. Figure 3(a) presents an example of the best fitted solution for Q = 2.735 L/s; a general discrepancy between numerical results and the measurements is observed due to the fact of using a linear-elastic solver (thought with unsteady friction modelling) to describe the behaviour of a viscoelastic pipe.

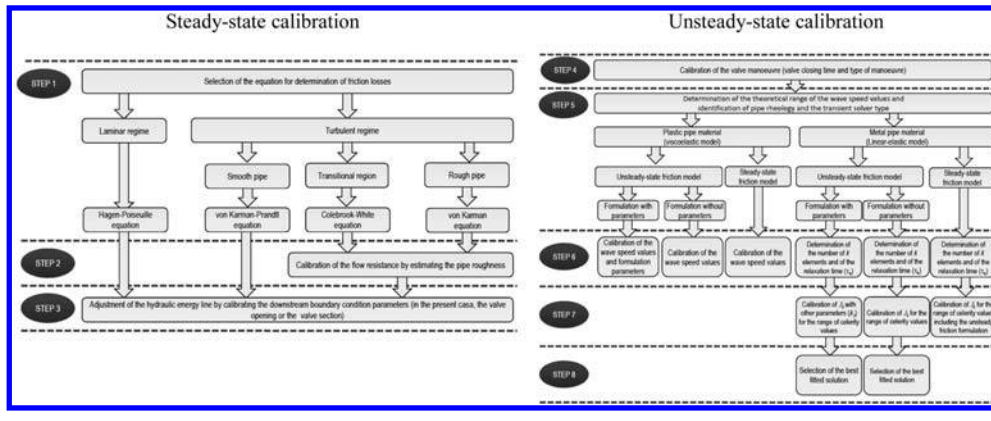


Figure 2. Calibration steps.

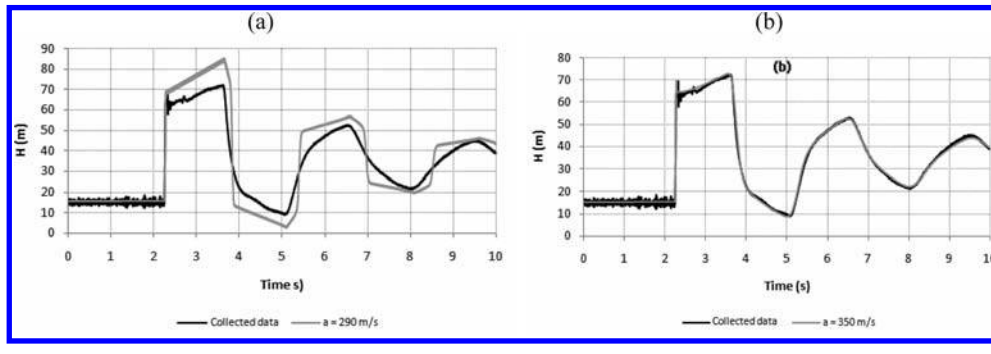


Figure 3. Best fitted solution for Q = 2.735 L/s (a) for the calibration of the empirical coefficient, $k_3$, and (b) for the calibration of the viscoelasticity incorporating unsteady-friction.

*Cases (b): the use of a viscoelastic solver in a viscoelastic pipe (Steps 6–8)*

A viscoelastic solver is calibrated incorporating unsteady friction and pipe-wall viscoelasticity. Vardy's (1992) unsteady friction formulation was used. The creep function coefficients $J_k$ (for a pre-set of $\tau_k$) are be calibrated simultaneously with the wave speed, $a$. The number of Kelvin-Voigt (K-V) elements to consider in the mathematical model depends essentially on the type of the pipe material. For HDPE pipes at least three elements of the K-V model are required to obtain a good calibration (Covas et al., 2004, 2005), whereas, for PVC pipes only one element is needed (Soares et al., 2008). Thus, 3 K-V elements were used (Step 6). Relaxation times, $\tau_k$, can be estimated for each K-V element as follows: (i) the 1st element is equal to half of the valve closure time, $t_c$; (ii) the second element is equal to 1/2 period of the pressure wave, $T$; (iii) the 3rd element is equal to 1/3 of the simulation time, $t$. (Step 6). Obtained results show that: (i) values of the elastic wave speed above 300 m/s do not change the creep function; (ii) for the experimental test Q = 0499 L/s the component $J_3$ is null, meaning that only two elements are required to represent the creep function for low flow; (iii) the values of each element of $J_k$ decrease with the flow increase; (iv) the value of $J_1$ raises almost linearly with the wave speed increase; (v) the values of $J_2$ and $J_3$ stabilize with as the wave speed increases. Figure 3(b) depicts the best fitted solution for Q = 2.735 L/s; an excellent agreement between numerical results and the measurements is observed which shows the importance of using accurately calibrated linear viscoelastic solvers to describe the transient behaviour of fluids in plastic pipes, particularly for fast transient events.

## SUMMARY

This research work aimed at the presentation of calibration guidelines for different hydraulic transient solvers incorporating unsteady friction formulations and pipe wall linear elastic and linear viscoelastic behaviours. To support and test this methodology, a hydraulic transient solver was developed incorporating Vitkovsky's[7] and Vardy's[6] unsteady friction formulations and the above two rheological behaviours. The mathematical model was calibrated using data collected in a laboratory facility made of HDPE, with approximately 200 m. Further research can be carried out to extend this methodology to more complex pipe system with different boundary conditions and other unconventional dynamic effects (e.g., cavitation, pipe movement, dissolved air).

## REFERENCES


[1] Covas, D. (2003) – Inverse Transient Analysis for Leak Detection and Calibration of Water Pipe Systems – Modelling Special Dynamic Effects. Imperial College London, UK.

[2] Covas, D., Stoianov, I., Mano, J., Ramos, H., Graham, N., Maksimovic, C. (2004a). "The Dynamic Effect of Pipe-Wall Viscoelast. in Hydr. Transients. Part I – Exper.Analysis and Creep Charact.." Jour. of Hydr. Research, 42(5), 516–530.

[3] Covas, D., Stoianov, I., Graham, N., Maksimovic, C., Ramos, H., Butler, D. (2004b). "Water hammer in pressurized polyethylene pipes: conceptual model and experimental analysis." Urban Water Journal, 1(2), 177–197.

[4] Covas, D., Stoianov, I., Mano, J., Ramos, H., Graham, N., Maksimovic, C. (2005). "The Dynamic Effect of Pipe-Wall Viscoelast. in Hydr. Transients. Part II – Model Develop., Calibrat and Verific." Journ. of Hydr. Res., 43(1), 56–70.

[5] Soares, A. K., Covas, D. & Reis, L. F. (2008). Analysis of PVC pipe-wall viscoelasticity during water hammer. Journal of Hydraulic Engineering 143 (9), 1389–1394.

[6] Vardy, A. E. (1992). Approximating Unsteady friction at High Reynolds Numbers. Proceedings of the International Conference on Unsteady Flow and Fluid Transients. 21–29. Balkema, Rotterdam, The Netherlands, Bettess & Watts.

[7] Vitkovsky, J. P., Lambert, M. F. & Simpson, A. R. (2000) – Advances in unsteady friction modelling in transient pipe flow. 8th Inter. Confe. on Pressure Surges – Safe Design and Operation of Industrial Pipe Systems. Anderson, A. (eds.) Suffolk, UK, BHR Group Ltd., Pub. No. 39, 471–498.

[8] Wylie, E. B. & Streeter, V. L. (1993) – Fluid Transients in Systems. Prentice Hall, Englewood Cliffs, N. J.

*Environmental Hydraulics – López-Jiménez et al (eds)*
*© 2010 Taylor & Francis Group, London, ISBN 978-0-415-56697-1*

# Two dimensional experimental and numerical analyses of flow and pollutant transport in meandering channel

Il Won Seo, Sung Won Park & Chang Geun Song
*Department of Civil and Environmental Engineering, Seoul National University, Seoul, South Korea*

ABSTRACT: Pollutant mixing based on hydraulics in rivers have been recently analyzed and developed via various numerical models. Numerical approaches should be analyzed simultaneously with the experimental researches due to uncertainties of geometries and effects of hydraulic mechanisms such as secondary current, water level fluctuation, and so on.

To reveal flow and mixing behaviors in meandering channel, a laboratory channel has been set up with two S-curved parts. Data of 3D velocity profiles and tracer tests have been compared with flow and concentration fields of 2D simulation under same hydraulic conditions. As the results, it was clearly noticed about primary flow profiles and secondary flow cells in 12 measuring sections. Experimental results showed that mixing of solute tracer is significantly affected by the complex mechanisms of un-uniform primary and secondary flow cell. Shortly the primary flow separates the tracer clouds in the longitudinal direction, and the secondary flow cell further separates retarding tracer clouds in the transverse direction respectively.

Secondly 2D numerical modeling (SMS and RAMS) have been applied with same experimental conditions. According to velocity profiles, Widely-known primary flows have been visualized adequately. From the contour maps of pollutant behaviors illustrated from the results of numerical methods with instantaneous and centered injection of solute tracer, separation, superposition and stagnation could be deduced outwards of two meandering sections.

*Keywords*: meandering channel, two-dimensional numerical models (SMS, RAMS), primary and secondary flows, pollutant clouds.

## 1 INTRODUCTION

General inflows and spreading of various toxic pollutants in inland waters have been happened by continuous population growth and industrial development and have threatened the balance of environment of human life and ecosystem. It is necessary to maintain and control the water pollution problems with accurate researches and continuous efforts to predict losses and damages from them using numerical analysis verified with experiments or field researches. To simulate complex flow and pollutant transport in meandering channel, a 3D hydrodynamic model is required. However, for a practical engineering problem, a 2D model can be used over a 3D model, greatly reducing computational efforts and experimental expenses.

## 2 BACKGROUNDS

Fischer [5], for the first time, suggested flow features to the transverse dispersion coefficient considered bend effects. Chang (1971) conducted laboratory experiments with the S-curved channel to obtain the transverse dispersion coefficient considering the secondary flow effects. A theoretical approach which in another methodology for evaluating the transverse dispersion coefficient in cases of having no concentration data was proposed, for the first time, by Fischer[5] using the transverse velocity equation of Rozovskii (1957). Recently, Boxall and Guymer[2] suggested new theoretical equation which is derived from the method of Chickendu (1986). Summary of assumptions and results of previous studies which has been involved with this study have been represented in Table 1.

Numerical models have been developed for describing circulation phenomena and the solute transport in the meandering open channel flows. McGuirk and Rodi[7] developed a depth-averaged model for the near field calculations of the flow and concentration distribution by side discharges of the pollutant into open-channel flow. Duan [3] derived the dispersion term for

Table 1. Experimental analysis with channel mixing.

| Researcher | Channel | Results |
|---|---|---|
| Elder (1959) | Straight | $e_y/HU_* = 0.23$ |
| Fischer (1969) | Meander | Theoretical form Derived |
| Chang (1971) | Meander | Developed |
| Miller & Richardson (1974) | Straight | $D_L/e_y > 100$ |
| Krisnappan & Lau (1977) | Meander | $0.222 < D_T/WU_*$<br>$0.416 > D_T/WU_*$ |
| Lau & Krisnappan (1977) | Straight | Instead of, $D_T/WU_*$ using $D_T/HU_*$ |
| Webel & Schatzmann (1984) | Straight | Criticized results of Lau & Krisnappan (1977) |
| Almquist & Holley (1985) | Meander | Transverse dispersion coefficient increasing in natural cross section |
| Noke & Wood (1988) | Straight | Transverse dispersion coefficient dependent of a friction factor |
| Boxall & Guymer (2003) | Meander | Conducted with setups natural cross-section |
| Boxall et al. (2003) | Meander | Transverse dispersion coefficient varied in direction of channel curvature |

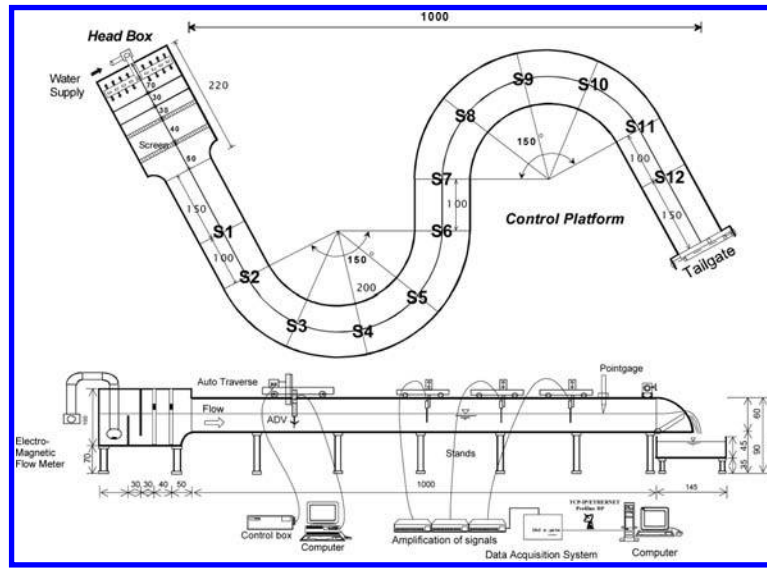


Figure 1. Sketches of S-curved Laboratory Channel Setup.

the depth-averaged 2D model in Cartesian coordinates and used the Schmidt number as a calibration parameter to simulate mass dispersion in meandering channels.

The model by Duan [3] was applied to the experiments of Chang (1971) to test the capability of the model to simulate mass transport in meandering channels.

## 3 EXPERIMENTAL SETTINGS

In this study, 3D-flow profiles were conducted in the S-curved meandering laboratory channel with a rectangular cross-section which is 16.5 m long, 1 m wide, and 0.6 m deep. It consists of circular arcs connected by straight sections, as shown in Figure 3. The radius of curvature of the arc region is 2.0 m, the wavelength is 7.5 m, and the arc angle is 150°. Velocity data was measured by ADV (Acoustic Doppler Velocimetry).

## 4 NUMERICAL METHODS

### 4.1 *SMS (Surface water Modeling Sytem)*

RMA-2 is a two-dimensional depth-averaged finite element hydrodynamic numerical model of commercial software SMS (Surface-water modeling system). It computes water surface elevations and horizontal velocity components for subcritical , free-surface two-dimensional flow fields.

RMA-2 computes a finite element solution of the Reynolds form of the Navier-Stokes equations for turbulent flow. Friction is calculated with the Manning's or Chezy equation, and eddy viscosity coefficients are used to define turbulent characteristics. Both steady and unsteady (dynamic) problems can be analyzed. The generalized computer program RMA-2 solves the depth-integrated equations of fluid mass and momentum conservation in two horizontal directions.

$$\frac{\partial h}{\partial t}+h\left(\frac{\partial u}{\partial x}+\frac{\partial v}{\partial y}\right)+u\frac{\partial h}{\partial x}+v\frac{\partial h}{\partial y}=0 \tag{1}$$

$$h\frac{\partial u}{\partial t}+hu\frac{\partial u}{\partial x}+hv\frac{\partial u}{\partial y}-\frac{h}{\rho}\left[E_{xx}\frac{\partial^2 u}{\partial x^2}+E_{xy}\frac{\partial^2 u}{\partial y^2}\right]+gh\left[\frac{\partial a}{\partial x}+\frac{\partial h}{\partial x}\right]+\frac{gun^2}{h^{1/3}}\left(u^2+v^2\right)^{1/2}=0 \tag{2}$$

$$h\frac{\partial v}{\partial t}+hu\frac{\partial v}{\partial x}+hv\frac{\partial v}{\partial y}-\frac{h}{\rho}\left[E_{yx}\frac{\partial^2 v}{\partial x^2}+E_{yy}\frac{\partial^2 v}{\partial y^2}\right]+gh\left[\frac{\partial a}{\partial y}+\frac{\partial h}{\partial y}\right]+\frac{gvn^2}{h^{1/3}}\left(u^2+v^2\right)^{1/2}=0 \tag{3}$$

RMA-4 is a finite element water quality transport numerical model in which the depth concentration distribution is assumed uniform. It computes concentrations for up to constituents, either conservative or non-conservative, within the one-and/or two-dimensional computational mesh domain. The CEWES version of RMA-4 is a revised version of RMA-4 as developed by King (1989). The generalized computer program solves the depths-integrated equations of the transport and mixing process. The form of the depth averaged transport equation is:

$$h\left(\frac{\partial c}{\partial t}+u\frac{\partial c}{\partial x}+v\frac{\partial c}{\partial y}-\frac{\partial}{\partial x}D_x\frac{\partial c}{\partial x}-\frac{\partial}{\partial y}D_y\frac{\partial c}{\partial y}-\sigma+kc+\frac{R(c)}{h}\right)=0 \tag{4}$$

### 4.2 *RAMS (River Analysis Modeling System)*

RAMS (River Analysis and Modeling System) is consist of river flow analysis model (RAM2), pollutant transport model (RAM4), bed elevation change model (RAM6), and graphic user interface (RAMS-GUI) is combined with above numerical programs to develop commercial package. This software can simulate physical phenomena in natural rivers with complex topography by 2D finite element numerical calculations with underlying consistency and generality which would provide

Table 2. Properties of geometries (RMA-2, RAM2).

| | RMA-2 | RAM2 |
|---|---|---|
| **Number of nodes** | 7729 | 2625 |
| **Number of element** | 2480 | 2480 |
| **Type of element** | Rectangular (quadratic basis element) | Rectangular (linear basis element) |

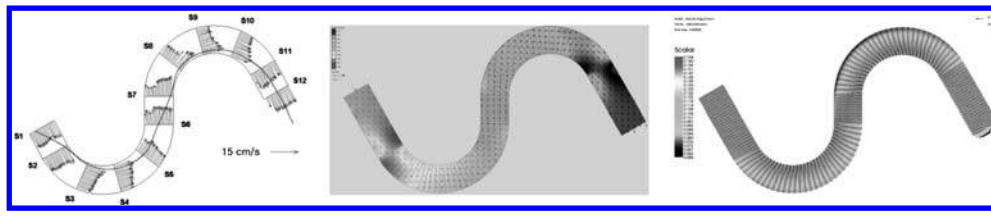


Figure 2. 2D-Velocity Profiles and Velocity Contour Maps: Left (RMA-2); Right (RAM2).

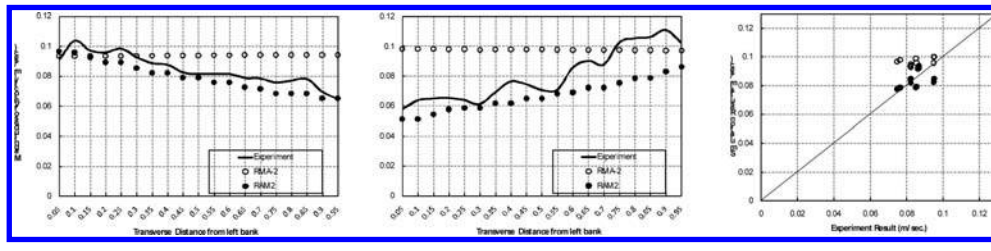


Figure 3. Comparison of primary flows in 2 meandering part(S4, S9) & Simulated vs. Observed.

accurate and stable solutions to open channel flow equation, and mass transport equation for various types of problems. Details about governing equations of RAMS package can be confirmed in website (www.rams.or.kr).

Flow model, RAM2 is an finite element model based on Streamline Upwind/Petrov-Galerkin(SU/PG) scheme for analyzing and simulating two-dimensional flow characteristics of irregular natural rivers with complex geometries. The type of elements in a mesh can be a triangular, quadrilateral or mixed one. A triangular element could have either 3-nodes or 6-nodes and a quadrilateral element either 4–nodes or 8-nodes. This mesh can constructed from DEM and TIN format in the tools of GIS.

$$\frac{\partial h}{\partial t}+\frac{\partial (uh)}{\partial x}+\frac{\partial (vh)}{\partial y}+i=0 \tag{5}$$

$$\frac{\partial (uh)}{\partial t}+\frac{\partial (u^2h)}{\partial x}+\frac{\partial (uvh)}{\partial y}+g\frac{\partial (h^2/2a)}{\partial x}=gh(S_{ax}-S_{fx}) \tag{6}$$

$$\frac{\partial (vh)}{\partial t}+\frac{\partial (v^2h)}{\partial y}+\frac{\partial (uvh)}{\partial x}+g\frac{\partial (h^2/2a)}{\partial y}=gh(S_{ay}-S_{fy}) \tag{7}$$

RAM4 is a FEM model for pollutant transport analysis in two-dimensional flow fields and it is developed based on the depth-averaged mass transport equation. It can calculate the advection and dispersion of injected substances in a two-dimensional flow field. This engine can treat the conservative or non-conservative substances as pollutant tracers.

$$\frac{\partial c}{\partial t}+\nabla\cdot(qc)-\nabla\cdot(D\cdot\nabla c)=0,\ x\in\Omega,\ t\in[0,T] \tag{8}$$

## 5 RESULTS

Velocity data detected in this S-curved channel are expressed with two dimensional vector profiles and contour maps at the test sections (S1∼S12). Transverse distribution of the primary velocity skews toward the inner bank at the bends and at the crossovers, almost symmetric. Additionally, maximum velocities in each transverse sections, has been detected taking the shortest course. The reason of this discrepancy in the flow pattern is that experiments were conducted on the rectangular cross-section channel, whereas, the cross-sectional shape of the natural stream is usually triangular, and skewed to the outer bank with fixed or mobile beds (Figure 2).

## 6 CONCLUSIONS AND FUTURE WORKS

In this research, velocity profiles of experiment method and numerical simulation have been compared and analyzed with same hydraulic condition. From the observed data, specific behaviors can be founded; the first bend region without secondary current effect and the second bend region which was divided again into entrance, apex, and exit. Asymmetry velocity profiles can make spatial re-arrangements of pollutant clouds with regional stabilities. Furthermore numerical simulation data can make expectation of the similar developments such as separation, stagnation, and superposition of pollutant clouds.

In the future, characteristics of solute transport in the channel can be compared with 2-D numerical analysis using quantitative analysis methods of plotting. For the longitudinal progress, transverse spatial distribution, and dimensional hydraulic index can be estimated with the further researches.

## ACKNOWLEDGEMENTS

This research was financially supported by the Construction Technology Innovation Program(08-Tech-Inovation-F01) through the Research Center of Flood Defense Technology for Next Generation in Korea Institute of Construction & Transportation Technology Evaluation and Planning(KICTEP) of Ministry of Land, Transport and Maritime Affairs(MLTM), 21C Frontier project "Application of RAMS" of the Ministry of the Science and Technology, and SNU SIR Group of the BK21 research Program funded by Ministry of Education & Human Resources Development.

## REFERENCES

[1] Almquist, C. W., and Holley, E. R. (1985). "Transverse mixing in meandering laboratory channels with rectangular and naturally varying cross sections," Technical Report CRWR-205, Univ. of Texas, Austin, Texas.
[2] Boxall, J. B., Guymer, I., and Marion, A. (2003). "Analysis and prediction of transverse mixing coefficients in natural channels." Journal of Hydraulic Engineering, ASCE, 129(2), 129–139.
[3] Duan, G. (2004). "Simulation of flow and mass dispersion in meandering channels." J. Hydr. Engrg., ASCE, 130(10), 964–976.
[4] Fischer, H. B. (1966). "Longitudinal dispersion in laboratory and natural streams." Technical Report KH-R-12, Caltech, Pasadena, California.
[5] Fischer, H. B. (1969). "The effect of bends on dispersion in streams." Water Resour. Res., 5(2), 496–506.
[6] Guymer, I. (1998). "Longitudinal dispersion in sinuous channel with changes in shapes." Journal of Hydraulic Engineering, ASCE, 124(1), 33–40.
[7] McGuirk, J. J., and Rodi, W. (1978). "A depth-averaged mathematical model for the near field of side discharges into open channel flow." J. Fluid Mech., 86(4), 761–781.
[8] Seo, I. W., and Baek, K. O. (2000). "Predicting velocity profiles and longitudinal dispersion coefficient in natural streams." *Proceedings of 12th Congress of the Asia and Pacific Division of the IAHR*, Bangkok, Thailand.

*Water and environmental engineering and hydroinformatics*

*Environmental Hydraulics – López-Jiménez et al (eds)*
*© 2010 Taylor & Francis Group, London, ISBN 978-0-415-56697-1*

# A process based model applied to morphodynamic evolution for long-term climate change studies

Patrícia Laginha Silva, Selma Gabriel & Flávio Martins
*University of Algarve – Centro de Investigação Marinha e Ambiental, Faro, Portugal*

ABSTRACT: The sea level changes observed in coastal zones are a direct consequence of several processes that act in global, regional and local scales. This work intends to contribute to the reconstruction of the physical-geological processes in estuarine environments, derived from climate changes since the last glacial-interglacial transition to the present. With this objective the process-based MOHID model was implemented to simulate the sedimentary infilling process and the sediment spacial distribution inside a conceptual estuary in temporal scales of thousands of years associated to climate changes impacts. The model was modified to enable extrapolation of the riverbed evolution. Initially the model was compared against linearized equilibrium model results obtained from literature. Next, several bed evolution extrapolation schemes were tested to reduce computational time. At last the combined effect of tide, sea level rise and river discharges was investigated. The results demonstrate the feasibility of using process based models to perform studies in scales of $10^4$ years. This is an advance relative to the use of conceptual models, enabling the use of variable forcing.

*Keywords*: Morphodynamic Modeling, Basin Filling, Sediment Dynamics, Time Extrapolation

## 1 INTRODUCTION

The first attempts for a quantitative description and simulation of basin filling in geological times started in the late 60's of the last century [1,2]. Most of the models presently used to study fluvial basin filling are of the "diffusion type" [3]. It must be noted that this models do not assume that the sediment transport is performed by a physical diffusive process. Rather they are synthetic models based on mass conservation. Other very stringent assumption for the applicability of the diffusion equation in real situations is that boundary conditions such as sediment supply and river flow must be constant. The simulation of time dependent processes such as the impact of climate change is thus difficult to accomplish with such models.

In this article a process-based hydrodynamic, sediment transport and morphodynamic model, solving explicitly the mass and momentum conservation equations is used to perform river basin evolutions simulations traditional studied with synthetic models. As these evolutions occur in timescales of $10^3$ to $10^4$ years computer power is a relevant issue.

## 2 METHODS

The implementation of the process-based morphodynamic model will be based on the finite volume MOHID modeling system. It is an open access code developed over the last 30 years in the IST (Technical University of Lisbon, Portugal). It has originally been developed for present time short time studies (days to years) and is now being applied for the first time in geologic timescale studies. It is a modular system that includes, among others, models for hydrodynamics, sediment transport and sediment bed evolution. The hydrodynamic and sediment transport modules of MOHID were kept to implement several simplified sediment transport and bottom shear stress formulations.

The system architecture is object oriented[4]. The velocity fields are computed in the hydrodynamic module, using a 3D formulation with hydrostatic and Boussinesq approximations[5]. The equations are solved using the finite volume method with an ADI (Alternate Direction Implicit) discretization. The resulting equations are obtained by integration of the Navier-Stokes equations over the cells. At the open boundaries both imposed values and radiative conditions can be set[7]. In tidal flats a moving boundary condition is implemented enabling the drying and flooding of cells as a function of the water level. The bottom stress is implemented implicitly using a quadratic law.

The transport of properties (including suspended sediments) uses an advection-diffusion equation with the same formulation used for momentum. The bed evolution is computed solving the mass balance equation:

$$(1-n)\frac{\partial \eta}{\partial t} + div\overrightarrow{q_s} = \frac{\Theta_s}{\rho_s} \quad (1)$$

Where $n$ is the sediment porosity $(-)$, $\Theta s$ is the sediment flux between the water column and the bed (Kg/(m$^2$ s)) and $\rho s$ is the dry sediment density (Kg/m$^3$). The sediment fluxes are computed using the Meyer-Peter & Muller[8] formulation for the bed load and the Ackers-White[9] formulation for the suspended load.

The MOHID results were obtained computing the hydrodynamics, the sediment transport and bed evolution processes. The hydrodynamic fields drive the sediment transport model interacting with the bottom. These models are well tested for short term simulations. They are however computationally quite demanding and cannot be used directly to long term simulations (order of centuries). The computational time is thus a relevant issue in this type of models. Several extrapolation options were investigated to allow longer and more elaborate simulation. A first order local extrapolation was used in each cell to compute

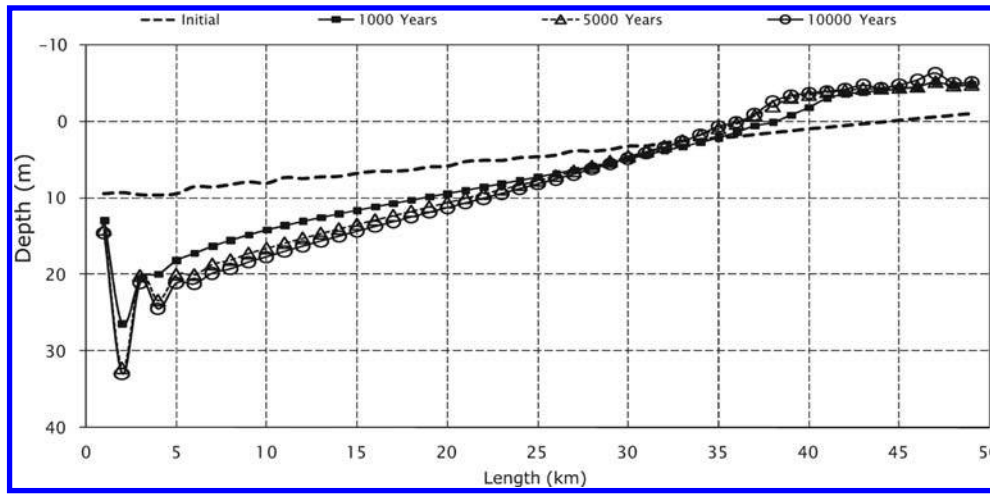


Figure 1. Evolution of the bed depth during $10^3$ years using the MOHID model. (Mouth of the river on the left of the figure).

the depth at time $t_3$ using the depths at times $t_1$ and $t_2$:

$$\eta^{t3} = \eta^{t1} + (t_3 - t_1)\,\frac{\eta^{t2} - \eta^{t1}}{t_2 - t_1} \tag{2}$$

A second order extrapolation was also tested using:

$$\eta^{t4} = \eta^{t1} + (t_4 - t_1)\,\frac{\eta^{t2} - \eta^{t1}}{t_2 - t_1} + (t_4 - t_1)(t_4 - t_2)\,\frac{\dfrac{\eta^{t3} - \eta^{t2}}{t_3 - t_2} - \dfrac{\eta^{t2} - \eta^{t1}}{t_2 - t_1}}{t_3 - t_1} \tag{3}$$

Several MOHID simulations were performed with the intention to test the sensitivity and behavior of the model. With this objective a schematic 1D basins were chosen and several time interpolation schemes were tested. Therefore a 1D constant width bathymetry with 50 Km length by 1 Km width and 50 cells was used in all the simulations at this point. Even thought the assumptions are different the results obtained are compared with similar simulations of synthetic models and with what can be called “intermediate models”.

The initial bed depth was imposed with a linear variation from 0 m at the head of the estuary to 10 m at the mouth. By convention the depth values are assumed to be positive. The system was forced in the open boundary by a single $M_2$ tide with constant amplitude of 1.75 m. In this first approach, no river flow or sediment flux was considered. Noncohesive sediments with $d_{35}$, $d_{50}$ and $d_{90}$ values of 250, 200 and 100 μm respectively were used.

At the open boundary the 10 m depth is held constant over time. The sediment concentration at the open boundary during ebb is equal to the interior concentration adjacent to the boundary. During flood the concentration of sediment entering the system is obtained from a first order relaxation equation to a fixed exterior value with an infinitely large decay time.

## 3 RESULTS AND DISCUSSION

Several morphodynamic simulations were performed for periods ranging from $10^3$ to $10^4$ years. A first $10^4$years run was performed to investigate the stability of the method and the achievement of equilibrium conditions. In Figure 1 the evolution of the bed profile during $10^4$ years is shown.

The evolution of the bed profile during $10^4$years shows that after a rapid change during the first 2000 years the bed profile stabilizes toward an equilibrium profile. Next the bed evolution during the first 750 years is compared with the equilibrium profile obtained by Schuttelaars and Swart[11] and with an intermediate, process-based, linearized model[10]. These simulations were carried out for the original 50 km bathymetry and for an extended 100 Km bathymetry. Hibma and her coworkers[10] have compared the Schuttelaars and Swart[11] idealized model with a linearized “intermediate” model for the same geometry and conditions in a simulation with a duration of 750 years. The results obtained and the comparisons are presented in Figure 2. The results are not expected to be identical because different assumptions are made in each of the models. Nonetheless the general trend of the profiles in the three models is very similar. It’s also possible to verify that the simulations are not yet stabilized.

Several different schemes were tested to extrapolate the bed profile evolution with the objective of saving computational power. If the errors prove to be small this will enable the achievement of longer and more complex runs. In Figure 3 the bed profiles after 900 years simulations using the various extrapolation schemes are presented.

It was shown that second order extrapolations produce severe instability of the solution. From the first order arrangements tested an extrapolation with the same period of the simulation time has shown to produce the best results with a 50% savings in computer time and an overall RMSE of 0.55 m when compared with the continuous run simulation. The extrapolation methods tested are able to reduce computational load to one third with losses of accuracy lower than 10%. However the “blind” extrapolation poses some problems: The extrapolation in a cell with sedimentation characteristics can produce sedimentation above the surface water level. This is physically unrealistic. The “blind” extrapolation also does not take into consideration the energy spectrum of the boundary conditions. It means that computations are being performed during periods of little

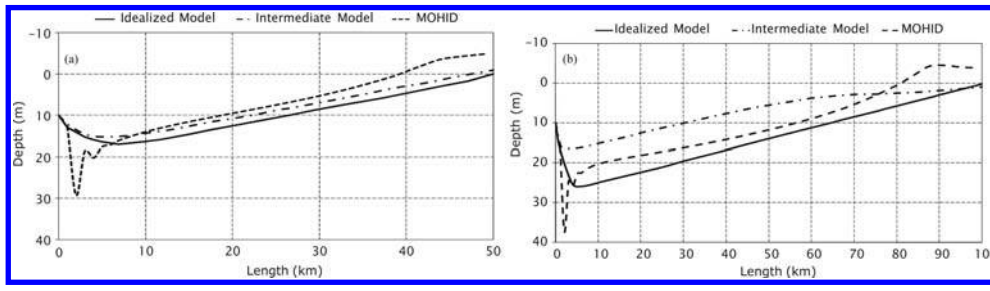


Figure 2. Equilibrium profile after 750 years for a 50 Km (a) and a 100 Km (b) long basin obtained with the idealized model of Schuttelaars and Swart[11]; the linearized model of Hibma[10] and the MOHID model.

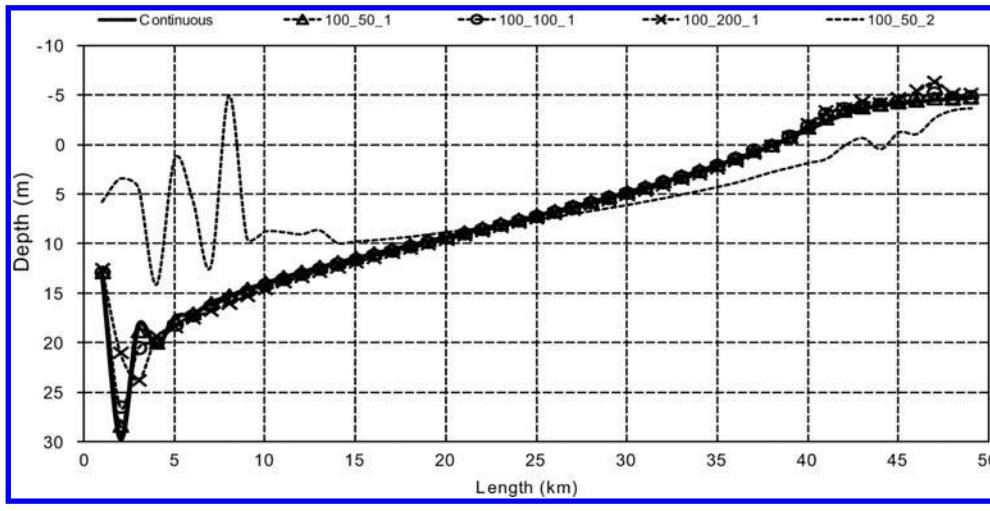


Figure 3. Equilibrium profile after 900 years for a 50 Km long basin obtained with the MOHID model running continuously and using different extrapolation schemes.

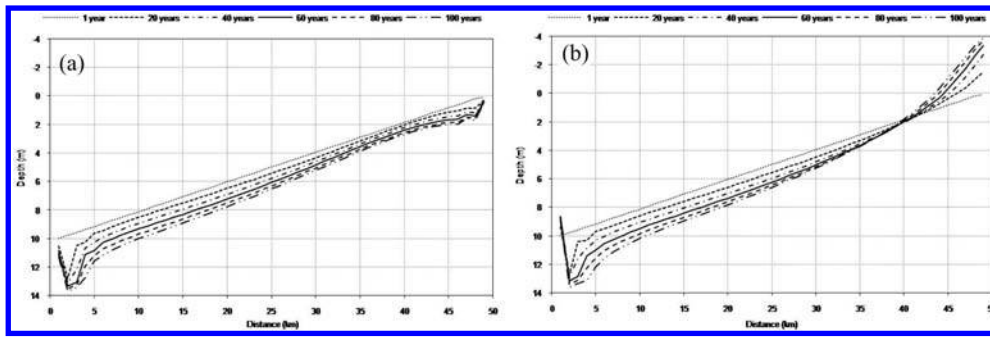


Figure 4. Evolution of the bed depth for the period of 100 years with (a) and without (b) addition of a water and sediment discharge at the head of the river. The color palette represents the year of sediment deposition (mouth of the river on the left of the figure).

morphodynamic activity and extrapolations are being performed during periods of high morphodynamic activity. These two aspects of the extrapolation process must be improved in the future.

The above set of simulations has helped the understanding of model behavior and sensitivity to parameters. The model response to different tidal and river forcing was then investigated in another type of approach where several simulations were performed, changing both the river input and the open boundary condition to analyze the behavior and sensitivity of the model to those conditions. The objective is to understand how river forcing modifies the morphodynamic evolution. A constant river discharge with a flow of 332.17 $m^3/s$ and a sediment concentration of 1 $kg/m^3$ was used. These values were selected as the mean flow and the highest sediment concentration observed on this basin. Data was obtained from the hydrometric and sedimentologic station at *Pulo do Lobo* on the Guadiana basin[12].

The results (Figure 4a) present the expected erosion at the head of the river when compared with the run only with tidal forcing (Figure 4b). The existence of a river discharge with water and sediments fluxes promotes a better result than only with tidal forcing on the mouth of the river. Only with tidal forcing (Figure 4b), is visible a pronounced sediment accretion on the head of the river and erosion on the mouth of the river.

The effect of sea level rise was then investigated including a sea level rise of 0.88 m per century to the M2 tidal wave of the ocean boundary. The river discharge of water and sediment was maintained constant. The results obtained in this simulation can be observed on the Figure 5a. The results obtained show that the sea level rise produces globally a much smaller erosion when compared with the constant level situation (Figure 4). Several sediment accretion zones could also be identified. This behavior is confirmed by classic infilling models that show a strong correlation between basin infilling and sea level rise[13].

The previous simulation was repeated including a variable annual flow distribution at the head of the river and a tidal forcing without the addition of the sea level rise. The results for this simulation can be observed in Figure 5b.

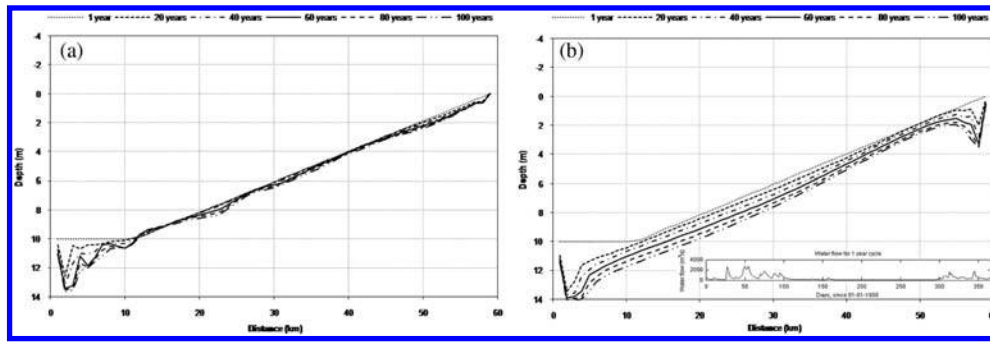


Figure 5. Same as Figure 4 but with the addition of a tidal component M2 plus a sea level rise of 88 cm per century (a) and with the addition of a variable annual flow distribution at the head of the river (b).

The database used for the annual flow distribution was acquired in the INAG online database[12]. This database does not have a full 100 years extent time series of the daily mean flow because the registries only started after October 1940. For this reason, the temporal flow distribution used in this simulation consists in a replication during 100 years of one year record in the station *Pulo do Lobo* (reference 27L/01H). The year selected was 1960 as a representative flow distribution in this area during a heterogeneous year with two main annual events of higher flows.

The SNIRH database do not possess for the *Pulo do Lobo* station a correspondent sediment distribution only a group of scattered measurements of sediment concentrations during a four years period of February 1982 to February 1985. To construct a temporal series of sediment concentration the higher sediment concentration was chose and a direct relationship between sediment concentration and flow was performed. With a variable annual flow, the results show a remarkable erosion process on the head of the river, resultant from the increasing of the river flow from the direct discharge on this area. Immediately after this area, the river bed equilibrates with the sediment inflow and the erosion process acts in a smaller scale. Downstream the river originates higher erosion processes along the river bed similar to the results already achieved in the previous simulation, with a simple tidal wave and a constant river discharge.

## 4 CONCLUSION

The results demonstrate the feasibility of using process based models to perform studies on the scales of $10^4$ years. This is an advance relative to the use of conceptual models, enabling the use of variable forcing (e.g. sea level rise). These results are somewhat contrary to the common experience that indicates flood periods as main events of sediment input to the basin. That effect is not happening in the model because the simulation is 1D and thus do not include flood plains that inundate and capture the sediments. This is an important conclusion and show that the use of 2D models with inundation plains is important to obtain physically realistic results.

The main conclusion from this series of simulations is that sea level rise promotes an important sedimentation behavior in the estuary. It was also possible to see the effect of variable river and sediment flows. However the main effect of extreme river flows in sedimentation occurs over the river banks. These processes cannot be simulated with a 1D configuration. In the future 2D meshes will be used to include these processes. The simulations were also performed during the first hundreds of years. It is now clear that the results are still not stabilized and longer runs are needed.

## REFERENCES

[1] Briggs, L.I. and Pollack, H.N. (1967) – "Digital model of evaporate sedimentation". *Science*, 155, 453–456.
[2] Schwarzacher, W., 1966. Sedimentation in a subsiding basin. *Nature*, 5043, 1349–1350.
[3] Flemmings, P.B. and Jordan, T.E. (1989) – "A synthetic stratigraphic model of foreland basin development". *J. Geophys. Res.*, 94, 3851–3866.
[4] Miranda, R., Braunschweig, F., Leitão, P., Neves, R., Martins, F. & Santos A. (2000) – "MOHID 2000 - A coastal integrated object oriented model". Proc. Hydraulic Engineering Software VIII, Lisbon, 2000, 393-401, Ed. W.R. Blain & C.A. Brebbia, WITpress.
[5] Martins, F., Neves, R. and Leitão, P. (1998) – "A three-dimensional hydrodynamic model with generic vertical coordinate". Proceedings de Hydroinformatics'98, Vol. 2, pp. 1403–1410, Ed. V. Babovic & L.C. Larsen, Balkema, Rotterdam.
[6] Martins, F., Neves, R., Leitão, P. & Silva, A. (2001) – "3D modeling in the Sado estuary using a new generic coordinate approach". *Oceanologica Acta*, 24, S51–S62.
[7] Coelho, H., Neves, R., White, M., Leitão P. & Santos, A. (2002) – "A Model for Ocean Circulation on the Iberian Coast", *Journal of Marine Systems*, 32(1–3), 153–179.
[8] Meyer-Peter, E., and Muller, R. (1948) – "Formulas for Bed-Load Transport". Report on Second Meeting of International Association for Hydraulic Research.
[9] Ackers, P. and White, W.R. (1973) – "Sediment Transport: New Approach and Analysis". *Journal of the Hydraulics Division*, ASCE, 99(HY11)
[10] Hibma, A., Schuttelaars, H.M., and Wang, Z.B. (2003) – "Comparison of longitudinal equilibrium profiles of estuaries in idealized and process-based models". *Ocean Dynamics*, 53, 252–269.
[11] Schuttelaars, H.M., and Swart, H.E. (2000) – "Multiple morphodynamic equilibria in tidal embayments". *J Geophys Res*, 105, 24105–24118.
[12] SNIRH (2009) – "INAG online database SNIRH (*Sistema Nacional de Informação de Recursos Hídricos*)" at http://snirh.pt/.
[13] Paola, C., Parker, G., Mohrig, D.C. and Whipple, K.X. (1999) – "The large-scale dynamics of grain-size variation in alluvial basins". 1: Theory. *Basin Res.*, 4, 73–90.

*Environmental Hydraulics – López-Jiménez et al (eds)*
*© 2010 Taylor & Francis Group, London, ISBN 978-0-415-56697-1*

# WiMMed, a distributed physically-based watershed model (I): Description and validation

María José Polo
*Grupo de Hidrología e Hidráulica Agrícola, Universidad de Córdoba, Córdoba, España*

Javier Herrero
*Grupo de Dinámica de Flujos Ambientales, Universidad de Granada, CEAMA, Granada, España*

Cristina Aguilar
*Grupo de Hidrología e Hidráulica Agrícola, Universidad de Córdoba, Córdoba, España*

Agustín Millares, Antonio Moñino, Sergio Nieto & Miguel Á. Losada
*Grupo de Dinámica de Flujos Ambientales, Universidad de Granada, CEAMA, Granada, España*

ABSTRACT: WiMMed (**W**ater **I**ntegrated **M**anagement for **Med**iterranean Watersheds) is a physically based and distributed model at watershed scale developed for integrated management of water resources. This work presents the first user version which includes all processes that determine water flows along the watershed, carefully considering characteristic aspects of Mediterranean watersheds with influence on the spatial and temporal variability, as well as processes where topography may substantially affect the results. WiMMed focuses on the distributed modelling at the cell scale of the digital elevation model and the resolution at different temporal scales in the same calculation sequence in order to better reproduce physical simulated processes. To this purpose, the model was developed and validated in the Guadalfeo river watershed (Granada, Southern Spain), where the topographic gradient between the high mountains of Sierra Nevada and the coast in less than 70 km distance has led to a wide heterogeneity of climate, soil, meteorological conditions (snow occurrence every year), vegetation, water sources, soil uses, and water demand. The topographic algorithms pose a great potential for the study of ungauged watersheds by means of computer techniques from a digital elevation model, and constitute a useful tool for water planning and management that can be technically applied in any other watershed.

*Keywords*: WiMMed, watershed, distributed model, hydrological analysis.

## 1 INTRODUCTION

The planning and management of water resources, with both quality and quantity criteria, including the global environment and its conservation among the aims of such planning, require models,

- That describe the integral response of the watershed and how they relate to the processes that determine the amount and quality of water.
- That reproduce the behaviour of all processes involved. Thus, models that determine not only the outputs under a certain input to the system but also the most probable response as well as all the possible responses and their associated probability, must be developed. Moreover, physically-based models are preferred – as these are not subject to wholly empirical calibration – in order to allow the development of methodologies applicable to non-monitored areas or under different management conditions to those with the model was calibrated.
- That consider spatial and temporal scale effects in all the processes involved. The possibility to obtain data relative to broad surfaces with relatively high frequency together with the capacity of computers nowadays enables the calculation on large spatial units in reasonable execution time. However, the original models for each process were not obtained under such conditions, so the parameterization at certain spatial and temporal scales is of major concern. Scale effects especially take place when the processes are spatially auto-correlated, as most hydrologic processes scale nonlinearly. Terrestrial water balance is known to be a highly nonlinear and spatially variable process, especially because of the key role of soil moisture and its spatial and temporal variability due to variability in soil properties[1][2].

The development of GIS and the increase in processing speed and storage capacity of computers, together with the opportunity for the acquisition of spatially distributed data through remote sensing techniques, have led to the application of semi-distributed models. These models are applied over each spatial unit in which the system is divided and route the response of each unit towards the outlet, combining these responses both in time and space in order to produce watershed scale outputs[3]. In this way, analytical models can be applied over highly extensive systems, but the rigorousness and accuracy of the results will depend on the quality of the spatially-distributed inputs available to the model and the suitability of the global and/or analytical model to the spatial and temporal scale of the research[4].

Spatial and temporal quantification of water flows in a watershed constitute the first step in the determination of sediment fluxes and associated substances[5]. Thus, scale effects in the first ones will determine scale effects in the latter's. On the other hand scale effects are especially important in heterogeneous watersheds where spatial variability of parameters and inputs, processes determining intermediate variables, and the heterogeneous temporal frequency of datasets for model calibration, make even bigger such effects. The Guadalfeo River watershed, southern Spain (Fig. 1), is a very clear example of multiple heterogeneity. Elevations in the model area range from 3480 m to sea level in 70 km length in a 1300 km$^2$ area. The combination of such altitudinal gradients together with the large number of vegetation, landforms and soil types produces a complex mountainous territory with variable hydrological behaviour. The main part of the watershed, in terms of hydrology, is comprised of

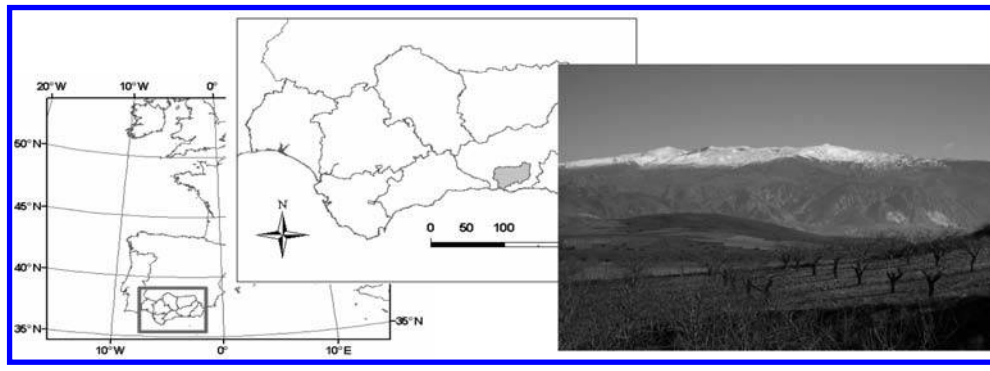


Figure 1. The Guadalfeo River watershed.

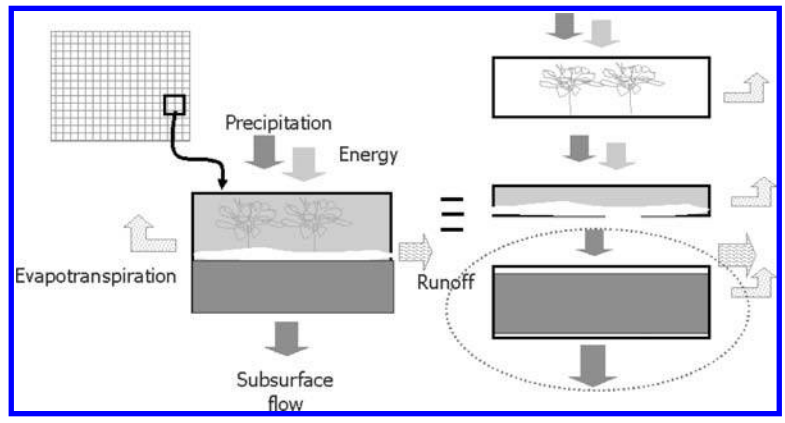


Figure 2. Water and energy balance cascade reservoirs at a cell.

the southern hillside of Sierra Nevada, however, deep valleys with characteristic south orientation lead to important differences in terms of height, slope, aspect (Fig. 1).

This study is part of the Guadalfeo Project (2007), financed by the Andalusian Water Agency, whose aim was the development of an integrated water management model that covers the three main issues in classical planning and management: how much, where and when as well as how and the associated uncertainty. Particularly, the watershed model tries to solve some gaps in hydrological models available nowadays: (1) Watersheds with the same degree of agricultural and non-agricultural uses; (2) Mediterranean watersheds where processes characterizing dry periods, which are sometimes very prolonged, determine to a great extent the evolution of water flows as drought periods, or periods between rainfall events, involve processes in which delay in the output is more modulated and continuous in contrast with runoff generation as the output to a pulse of rainfall, which follows a cause-effect pattern; (3)rainfall models based on storm evolution as the first time steps inputs; (4) runoff generation models based on the morphology of the watershed; (5) inputs to the models from wide variety of sources, remote sensing imagery, gauges, field data, etc.; (6) littoral models, especially important in Mediterranean watersheds flowing into the sea with high elevations where the boundary conditions are not just the closure to the system.

The watershed model, WiMMed, is implemented in a user-interface whose first version, related to water fluxes, is presented in this work together with the results for the Guadalfeo River watershed.

## 2 WIMMED DESCRIPTION

### 2.1 *Hydrological model structure*

Two different situations in terms of the occurrence of rainfall are defined in the watershed: event, associated with storms (when it rains somewhere in the watershed) and non-events (periods between events). A distributed water and energy balance model is implemented as a cascade of reservoirs (vegetation cover, snow cover, and vadose zone of the soil) at each cell of the Digital Elevation Model of the watershed, as figure 2 describes. Calculation is made on a time step of 1 hour under event situations, or 1 day under non-event situations; however, the time step can be reduced to minutes or seconds at the cells with snow, independently of the event/non-event situation, due to the energy balance submodel requirements[6]. The spatial variability of meteorological variables is approximated by interpolation algorithms, including corrections with height for both rainfall and temperature, topographic corrections for solar radiation[7][8]. Interception by the vegetation is included[9] from Landsat TM data analysis of cover fraction and forest and crop cartography. The snowmelt/accumulation dynamics is included by a 1D thermodynamic model of energy and water balance in the snow cover, with a correction of emissivity derived by experimental field data in Sierra Nevada mountains[6]. During events (rainfall/snowmelt), and non-events (snowmelt) infiltration flux is calculated by Green and Ampt equation, and redistribution approximated after a lag time[8]. During non-events, slow drying of each reservoir is calculated. Detailed information about input parameters and algorithms is presented in the references[7][8].Water excess is routed as runoff along the hillslope by means of a travel time distribution for each cell calculated from an effective velocity field estimated from topography characteristics. The resulting hydrographs were calibrated from water flow measurements at different sub-watershed monitoring points[8]. These hydrographs constitute the input data for the flow routing along the main river channel in the watershed (in this work, the Guadalfeo river). Muskingum routing or a 1D high resolution hydrodynamic

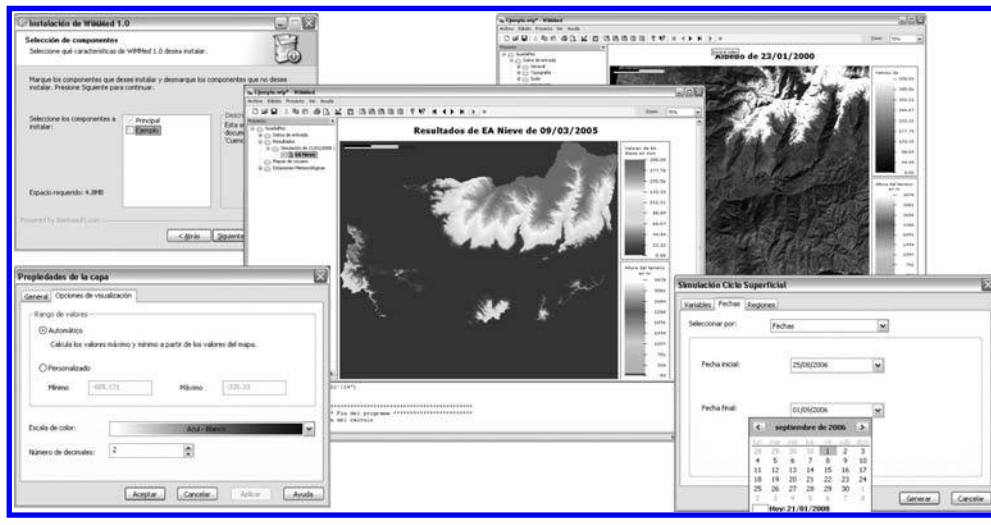


Figure 3. Selected examples of WiMMed displays.

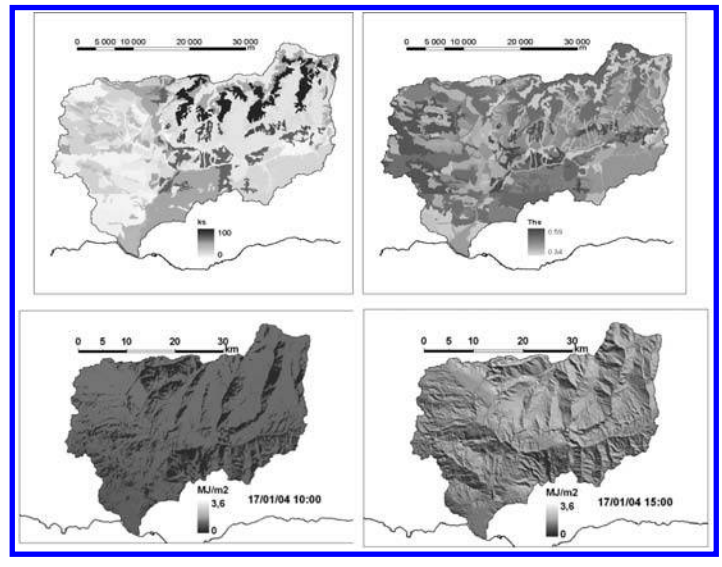


Figure 4. Examples of soil parameters and hourly solar radiation.

model[10] can be selected depending on the desired results. Baseflow contribution is included from recession pre-analysis and slow water release through fractured materials[11].

## 2.2 *The WiMMed user interface*

Due to the characteristics of input data to the watershed model, together with the desirable exportable formats of the pursued results, an user interface has been developed under a Window format. Different kinds of simulations can be selected, as well as different groups of resulting variables in terms of their spatial and temporal resolution. The aspect of the designed screens and menus follows a pattern familiar to GIS software users, and special attention has been paid to data input and output, including visualization and figure options. An assistant tool for installation has been developed. The following figure show some examples of WiMMed displays. An English language version will be soon available.

# 3 SELECTED RESULTS FROM GUADALFEO WATERSHED VALIDATED SIMULATIONS

The extension of this document does not allow a detailed description of WiMMed results; further analysis and information of these results at the Guadalfeo watershed can be found in the listed references, and here selected examples have been included to illustrate the model capabilities. Figure 4 shows some examples of distributed input parameters (saturated hydraulic conductivity) and meteorological variables (hourly solar radiation), and figure 5, some examples of distributed and aggregated results for the water and energy balance at watershed scale for a certain time period. Soil characteristics were estimated from available field data belonging to the LUCDEME Project in Spain, and pedotransfer functions included in the Rosetta model. The topographic influence can be easily seen from figure 4 solar radiation values.

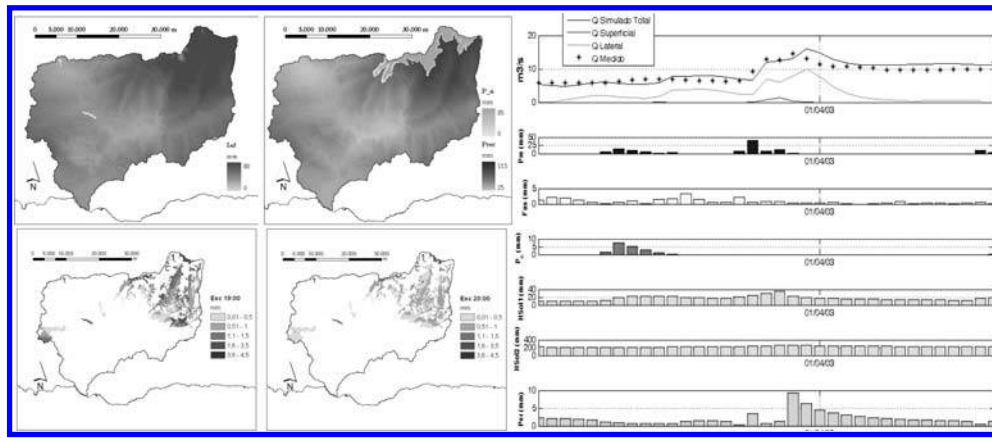

Figure 5. Selected results for the rainfall event from March, 26th to 30th, 2003.

## 4 CONCLUSIONS

The criteria to develop a hydrological distributed model especially focused on spatial and temporal variability of Mediterranean watershed have resulted in a first user version of WiMMed, and the validated results in the Guadalfeo river watershed have been shown. WiMMed potential to estimate the hydrological response under situations of non-availability of measured water flow data is derived from its physical basis, GIS-based structure and specific interpolation algorithms included, together with the variable time step resolution which provides a high, flexible capability of appliance. Several examples of further applications are shown in another work in this edition.

## REFERENCES


[1] Wood, E.F. (1998), *Scale analyses for land-surface hydrology*. In: *Scale Dependence and Scale Invariance*, G. Sposito (ed.), Cambridge UP, New York.

[2] Rodríguez-Iturbe I., Porporato, A., Laio, F. and Ridolfi, L. (2001). "Plants in water-controlled ecosystems: active role in hydrologic processes and response to water stress. I. Scope and general outline". Adv. Water Resour. Vol. 24, pp. 695–705.

[3] Beven, K.J. (2000). "On the future of distributed modeling in hydrology". Hydrol. Processes. Vol. 14, pp. 3183–3184.

[4] Blöschl G. and Sivapalan, M. (1995). "Scale issues in hydrological modelling-a review". Hydrol. Processes. Vol. 9, pp. 251–290.

[5] Merritt, W.S., Letcher, R.A. and Jakeman, A.J. (2003). "A review of erosion and sediment transport models". Envir. Model. & Soft. Vol. 18, pp. 761–799.

[6] Herrero, J., Polo, M.J., Moñino, A. and Losada, M.A. (2009). "An energy balance snowmelt model in a Mediterranean site", J. Hydrol. Vol. 371, pp. 98–107.

[7] Herrero, J. (2007), *Physical model of snowmelt. Application at Sierra Nevada (Spain)*. Ph. D. Thesis, University of Granada. (In Spanish). Available at www.cuencaguadalfeo.com

[8] Aguilar, C. (2008), *Scale effects on hydrological processes. Application at Guadalfeo River watershed (Granada)*. Ph.D. Thesis, University of Cordoba. (In Spanish). Available at www.cuencaguadalfeo.com

[9] Díaz-Gutiérrez (2007), *Temporal series for vegetation oriented to a distributed hydrological model*. Master Degree, University of Cordoba. (In Spanish). Available at www.cuencaguadalfeo.com

[10] Ávila, A. (2007), *Multiple scale processes in coastline evolution*. Ph. D. Thesis. University of Granada. (In Spanish). Available at www.cuencaguadalfeo.com

[11] Millares, A., Polo, M.J. and Losada, M.A. (2009). "The hydrological response of baseflow in fractured mountain areas". Hydrol. Earth Syst. Sci. Discuss. Vol. 6, pp. 1–26.

*Environmental Hydraulics – López-Jiménez et al (eds)*
*© 2010 Taylor & Francis Group, London, ISBN 978-0-415-56697-1*

# WiMMed, a distributed physically-based watershed model (II): Application examples

Marta Egüen, Cristina Aguilar & María José Polo
*Grupo de Hidrología e Hidráulica Agrícola, Universidad de Córdoba, Córdoba, España*

Isabel Moreno, Javier Herrero, Agustín Millares & Miguel Á. Losada
*Grupo de Dinámica de Flujos Ambientales, Universidad de Granada, CEAMA, Granada, España*

ABSTRACT: WiMMed (**W**ater **I**ntegrated **M**anagement for **M**editerranean Watersheds) is a physically based and distributed model at watershed scale developed for integrated management of water resources. This work presents some applications of the model for situations with lacking data. The selected examples correspond to 1) the main contributing watershed to the Mar Menor coastal lagoon (Murcia, Eastern Spain) with no available gauging records and located in a semiarid Mediterranean area, and 2) the simulation of the effects on climate change on water balance and water flow in the river in the Guadalfeo River watershed (Granada, Southern Spain), with high altitudes and snow presence every year especially affected by such previsible trends. The results show the potential of distributed physically based hydrological modeling under such situations and, particularly, its usefulness in Mediterranean catchments.

*Keywords*: WiMMed, watershed, distributed model, hydrological analysis.

## 1 INTRODUCTION

Physically based models allow the simulation of non-monitored systems, with increasing goodness of results as measurements and good-quality input data provide a closer approximation to the main processes governing changes. Despite their sounder basis, over-parameterization is sometimes adduced as a major constraint for their use, since a huge number of parameters always leads to an effective solution close enough to experimental data. However, such models are usually the only option under situations of lacking data, that is, the non-existence of a (good) monitoring network, and also the need for analyzing how the system would behave under conditions and/or actions different from the current or past sequences. Future sceneries of soil uses, sudden catastrophes such as fires or earthquakes, short-term variability of climate conditions, and medium and long term climate are representative examples of situations where empiric or statistic approaches are of limited appliance. Previous work presented in this forum[1] has shown a proposal for a distributed physically-based hydrological model at watershed scale, WiMMed, together with its suitability to capture the spatial variability inherent to Mediterranean areas by means of the results obtained at the Guadalfeo River watershed, in Southern Spain, after calibration and validation from data in gauged points of the fluvial network. The present work completes such results and show how WiMMed can be used in situations as described above. In particular, two additional examples have been selected from on-going research work: the hydrological modeling of the contributing area to the Mar Menor coastal lagoon in Eastern Spain, and a hypothetical simulation of the effects of climate change scenery on snow evolution and water flow in the Guadalfeo River watershed (south face of Sierra Nevada, in Southern Spain).

## 2 WiMMed APPLICATION EXAMPLE 1: MAR MENOR CONTRIBUTING AREA

### 2.1 *Study site description*

The Mar Menor is a saltwater coastal lagoon of approximately 135 km$^2$ located at Eastern Spain in Murcia. With a semicircular shape, it is partially isolated from the Mediterranean Sea by a long (24 km) but narrow (100 to 1200 m) sand bar (figure 1). With a higher water salinity than the Mediterranean Sea, their internal borders are contoured by a series of littoral wetlands that, together with the lagoon ecosystem, provide the whole system with singular ecological features that have deserved the recognition of legal protection figures, not only on a national but also international background. The contributing watershed to the lagoon consists of a mainly semiarid plain that drains agricultural areas together with semiarid areas, by the action of highly torrential storm episodes. The Albunjon Rambla is the main course in the fluvial network, with recently quasi-continuous water flow due to the irrigation systems that have increasingly substituting other crop uses. Together with water drainage, nutrient excess and herbicides residues are being loaded to the lagoon. Since the 60's, an increasing tourists population concentrates on the borders of the lagoon including the bar.

Despite the increasing stress on water resources by both agriculture and intense tourism, in terms of water demand and pollution loads to the lagoon, no monitoring permanent network of water flow exists in the watershed. The ephemeral character of runoff to the lagoon before the agricultural changes and the low amount of annual rainfall (up to 300 mm per year) registered could be the main causes for that.

The main water and pollutant loads correspond to the Albunjon Rambla (figure 2) and this study focuses on this subwatershed.

### 2.2 *WiMMed simulation of the Albunjon Rambla contribution to the lagoon*

The following results were part[2] of a wider study financed by the Coasts General Division of the Environment Ministry of Spain in 2006. Meteorological data series from the regional government together with the Digital Elevation Model (30 m), soil data from the LUCDEME Project and soil uses cartography from the regional government were used as input data for

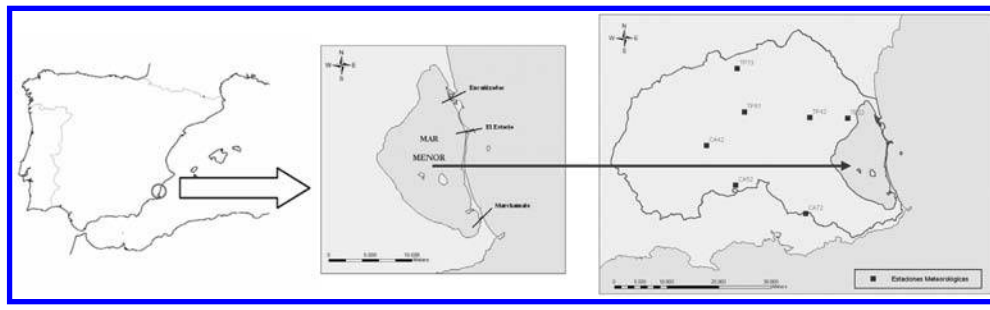


Figure 1. (From left to right) Mar Menor lagoon location in Spain, and contributing watershed with meteorological stations.


Figure 2. The Albunjon Rambla contributing watershed and fluvial network, and outfall to the lagoon (picture).

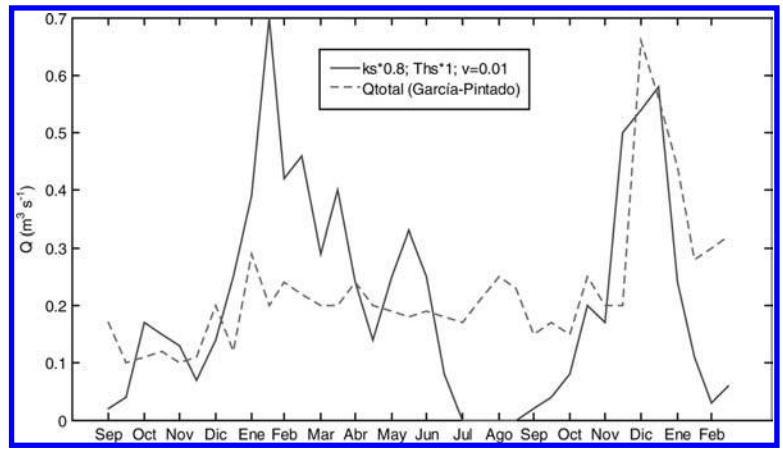


Figure 3. Simulated and measured water flow in the outlet.

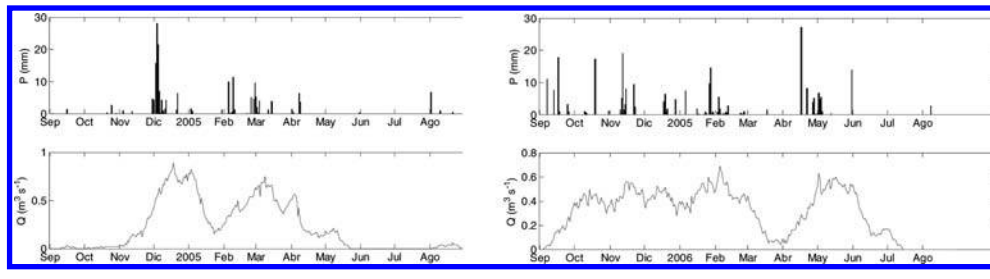


Figure 4. 2004/05 (left) and 2005/06 (right) simulations of daily water flow through the Albunjon Rambla.

WiMMed. The simulation period shown in this work is 2002/2004 since some field data[3] from a scientific project in the area were available to compare results. Figure 3 shows simulated (under natural regime) and measured data (including irrigation influence on water flows and sewage discharges) for water flow at the outlet to the lagoon. Differences correspond sufficiently well to the estimated water derived for horticultural irrigation during 2003 winter-spring period, and estimated sewage loads in 2003 summer period due to the huge tourism population increase (up to a 100% in some locations).

Figure 4 shows further additional simulations which constitute a good estimation of water loads to the lagoon through the Albunjon Rambla under natural conditions. A monitoring gauged point at this oulet together with data from the sewage plants in the area and irrigation demands would constitute a necessary advance to better characterize the hydrological contributions and estimate the associated inputs, such as sediments and excess nutrients and herbicides.

## 3 WiMMed APPLICATION EXAMPLE 2: CLIMATE CHANGE SCENERIES EFFECTS IN SOUTHERN SIERRA NEVADA (SPAIN)

To illustrate WiMMed potential as a tool for future sceneries, the simulated effects of climate change on snow distribution and water flow in the Guadalfeo River watershed are presented by incorporating one of the future sceneries published[4] by of

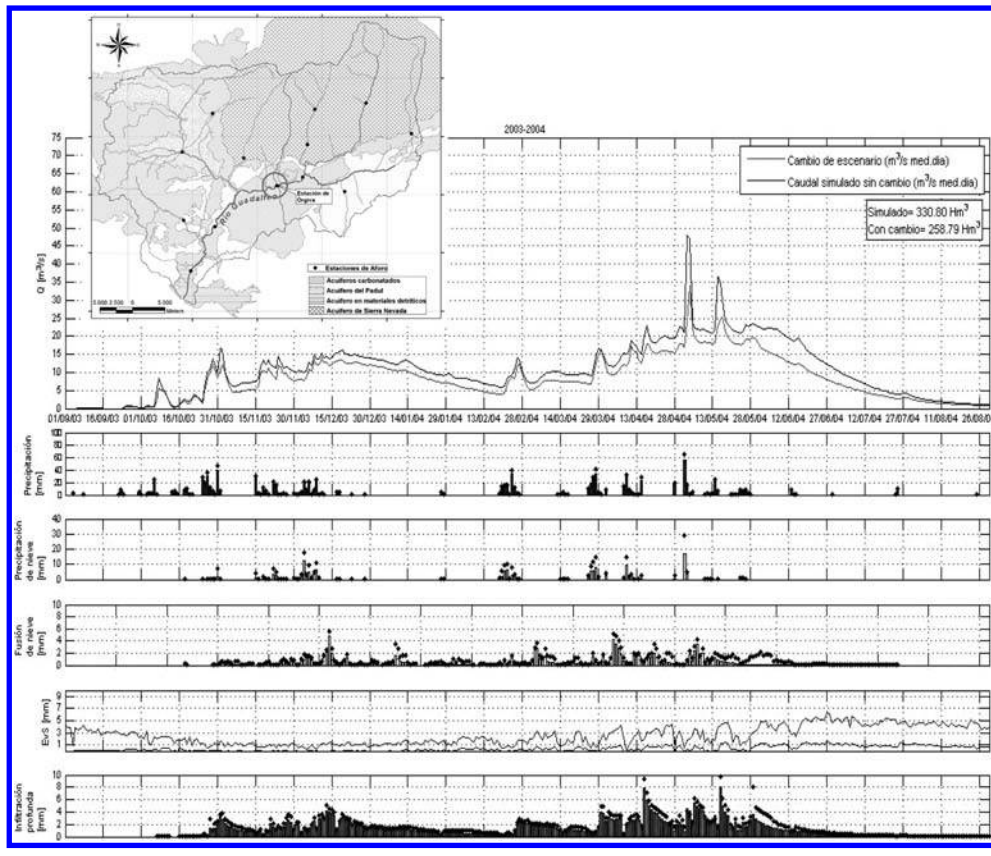


Figure 5. Measured and simulated under changing conditions daily water flow at Orgiva in the Guadalfeo River, together with other interest variables.

an increase of 2°C of medium temperature and a decrease of 15% of total rainfall for 2050 in the Mediterranean area. These values are taken just as reference examples, and are applied uniformly to 2003/04 meteorological series in the watershed as a first estimation of their impact on water flow at the gauged section in Orgiva (red circle in figure 5 map) in the main course of the river. The results[5] estimate in 72 $hm^3$ the decrease in the annual discharge at the gauged section (up to a 26% of the registered values).

## 4 CONCLUSIONS AND ONGOING WORK

This work presents further results from WiMMed as examples of its suitability under non-data situations. The selected study sites and sceneries show the model capability to capture the spatial heterogeneity of both meteorological and soil conditions, and the distributed modeling of future scenaries. WiMMed is being currently used in a wide set of ongoing work supported by the Andalusian Water Agency, such as some Atlantic watersheds in Western Andalusia, semiarid environments as the Adra and Almanzora River in Eastern Andalusia, and in joint projects included in the VII Framework European Program. Future results will provide with better knowledge of hydrological processes characterization in Mediterranean environments and their evolution.

## REFERENCES

[1] Polo, M.J., Herrero, J., Aguilar, C., Millares, A., Moñino, A., Nieto, S. and Losada, M.A. (2009). "WiMMed, a distributed physically-based watershed model (I): description and validation", *IWEH 2009, Valencia, 29–30 de octubre de 2009*.
[2] Egüen, M. (2008), *Water and nutrient loads to the Mar Menor lagoon (Murcia)*, Graduate Thesis, University of Cordoba. (In Spanish).
[3] García-Pintado, J., Martínez-Mena, M., Barberá, G.G., Alvadalejo, J., Castillo, V.M. (2007) "Anthropogenic nutrient sources and loads from a Mediterranean catchment into a coastal lagoon: Mar Menor, Spain", Sci. of the Total Environ., Vol. 373, pp. 220–239.
[4] European Environmental Agency (2008), *Impacts of Europe's changing climate-2008*.
[5] Millares, A. (2008), *Baseflow modelling in a distributed model at watershed scale. Groundwater contribution in mountain rivers*, Ph.D. Thesis, University of Granada. (In Spanish). Available at www.cuencaguadalfeo.com.

*Environmental Hydraulics – López-Jiménez et al (eds)*
*© 2010 Taylor & Francis Group, London, ISBN 978-0-415-56697-1*

# Impact of urban growth in pluvial runoff in the city of Chihuahua, Mexico

José Santos García, Guadalupe Estrada Gutiérrez, Benito Aguirre Sáenz &
Rodrigo Ruiz Santos
*Facultad de Ingeniería, Universidad Autónoma de Chihuahua, Chihuahua, México*

ABSTRACT: Evaluate the changing conditions of hydrological parameters under natural and artificial conditions of runoff according to the official guidelines for the growth of urban areas to determine the impact that has on one river basin.

*Keywords*: Urban basin, modeling, floodplain, risks.

## 1 INTRODUCTION

The dramatic urban growth that is present in the city of Chihuahua, Mexico in recent years has generated changes in land use in watersheds of streams that cross it. From a hydrological point of view, change in land use is reflected in the response of a watershed to extreme precipitation events such as occurred in September 1990 where it fell in an hour, approximately 30% of rain annual average. These extraordinary events generate serious problems of flooding, accompanied by severe economic damage and occasionally loss of life.

Prior to urbanization, a large proportion of the total rainfall contributes to soil moisture and groundwater recharge through infiltration or storage is retained in surface depressions and artificial nature. These changes in natural or rural to urban use means that areas with soil become an impermeable surface where the retention of water from rainfall is almost zero (Weng, 2001, Dow and De Walle, 2000). This increase in impervious surfaces combined with extreme precipitation is reflected in increased flood flows and reduction of peak time and concentration, affecting in different ways, including flooding in topographically lower areas of the basin.

An analysis of the behavior of urban growth in the last 30 years on one of the major watersheds that drain to the south-east of the city of Chihuahua is the watershed of Arroyo Los Nogales (Figure 1) to determine the variation land use at the time considered as this affects the runoff for a return period of 1000 years.

In the city of Chihuahua city and suburban growth has varied from 5.054 ha in 1975 to 18.850 ha in 2004, representing an annual growth of 3.45% and predicted a growth of 29.784 ha for 2020 (IMPLAN, 2007), which represents a 6.25% per annum. The rapid change in land use in the whole periphery of the city, but mainly in the lower parts of the basin under study, a condition of low natural vegetation cover, low transpiration in the upper watershed and farming area in the low, the use of high-density residential land (45 to 65 buildings per hectare), which is causing increased flood risk caused by extreme precipitation events.

## 2 OBJECTIVE

Analyze the impact of urbanization in the watershed above, through data obtained from hydrologic studies conducted in the watershed of Los Nogales, and through an analysis of the behavior over time of the urban area (Weng, 2002), using Geographic Information Systems (GIS), interpretation of satellite images (LANDSAT) and cartographic analysis. The flow evaluation was performed using empirical methods like unit hydrograph, Chow hydrograph and the use of HEC-HMS software from Corps of Engineers United States.

## 3 MATERIALS AND METHODS

Delimited area of the drainage basin of the Los Nogales, which has an area of 251.32 $km^2$, closed at coordinates 105° 58′ 20095″ W 28° 40′ 4836″ N. Using aerial photographs and satellite images made a comparative analysis of urban sprawl and the 1975 forecast for 2020 (Figures 2 and 3).

It's was define the different runoff coefficients according to geology, vegetation types and density and impermeability of the soil under the Urban Master Plan of the City of Chihuahua, 2008.

With information of precipitation in the study area, the curves were designed ID-Tr, and the storm was generated for the design return period of 1000 years, to estimate the flood flows and the subsequent evaluation of flood plains by HEC-RAS model.

The multitemporal analysis of urban growth, obtaining hydrological parameters and output results was performed by applying a GIS.

### 3.1 *Impact of land use change in the rate of runoff into the stream The Nogales*

According to Kliber (1982), quoted by Azócar and Henríquez (2006), at different stages of urban growth can be seen various impacts of the hydrological cycle. The removal of natural vegetation in the first stage of urban development reduces the

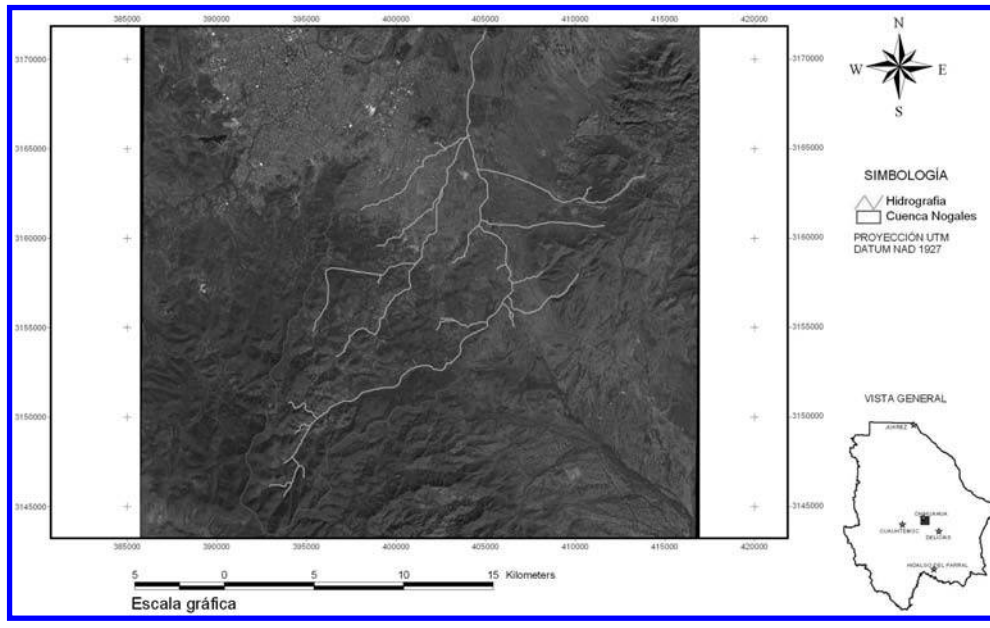


Figure 1. Basin Los Nogales.

Figure 2. Urban area of the city of Chihuahua for the year of 1975 (IMPLAN, 2007).

interception of rainfall by the foliage. Later, when it begins construction of houses and streets to reduce groundwater recharge and increased surface runoff. The third stage, when they are fully developed residential and commercial areas, increasing the absorption times of reduced concentration and peak runoff and increased peak flows. The last step is generated when the flood runoff are concentrated in low-lying areas beyond the capability of conducting channels and culverts.

The surfaces of the lower basin of the Los Nogales and downstream from the point of closure of the basin, are in the second stage of growth, considering that by 2020, as planned growth in the Master Plan for Urban City Chihuahua, they are at greater risk of flooding, as shown in Figure 4.

## 4 CONCLUSION

To study the basin was estimated at a rate of 495.00 $m^3/s$, which will be passed to generate a flood zone with a deep up to 3.40 m in the southern part of the stream, and this floodplain is spreading to affect the fractional areas have reached up to 0.80 m straps in proximity to the road to the airport. At present, the urban sprawl in the Los Nogales watershed covers an area of 13.89% of the basin and further progress towards the urban area the highest parts of the same change in the coefficients of runoff will increase dramatically causing increase in peak flow rate and decreasing time of concentration of runoff.

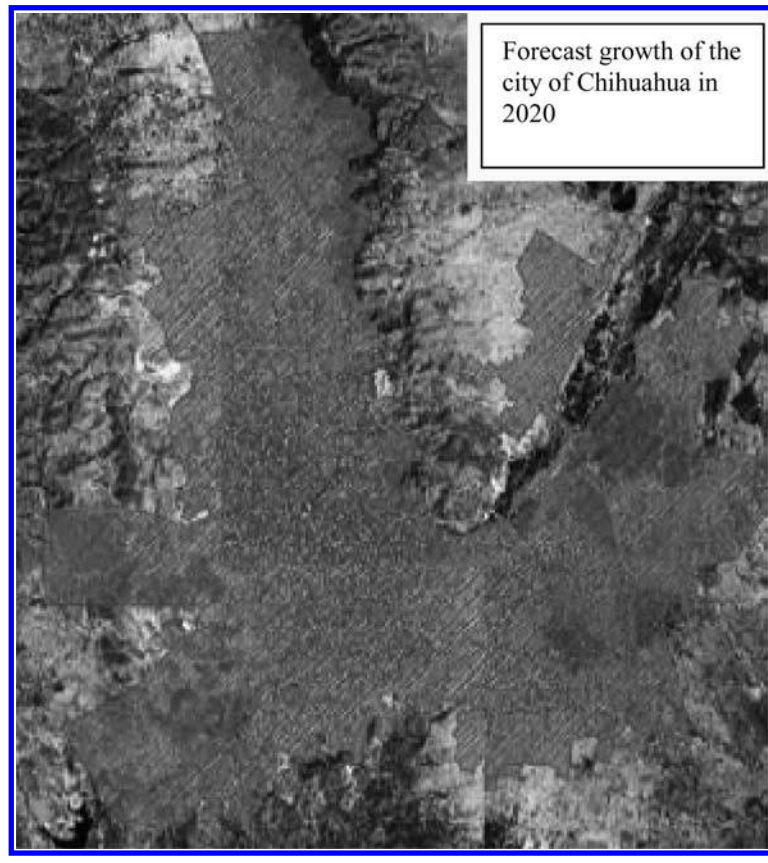


Figure 3. Urban area of the city of Chihuahua for the year of 2020 (IMPLAN, 2007).

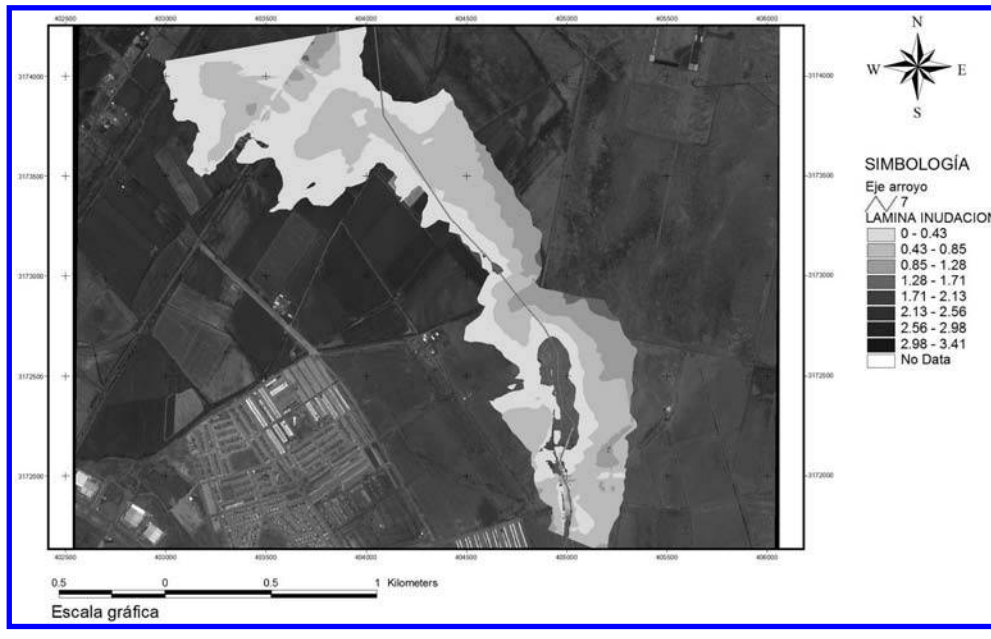


Figure 4. Area of flooding in the valley The Concorde-Airport, downstream the river basin of Los Nogales.

## REFERENCES

[1] Instituto Municipal de Planeación Chihuahua, (IMPLAN), 2007, Urban Master Plan of the City of Chihuahua.
[2] Dow, C., & De Walle, D., Trends in evaporation and Browen ratio on urbanizing watersheds in eastern United States. Water Resources Research, 2000, No. 36, Vol. 7, p. 1835–1844.
[3] Henríquez, C. y Azocar, G., Changing land use and runoff: application of a spatial simulation model in Los Angeles, VIII Region Biobío, Chile. *Rev. Geografía Norte Grande*, dic. 2006, No.36, p.61–74.
[4] Stanuikynas, T. y D. Van Abs (2000). *Impervious surface methodology. A methodology for defining and assessing impervious surfaces in the Raritan River basin*. New Jersey: New Jersey Water Supply Authority.
[5] Weng, Q., Modeling Urban Growth Effects on surface Runoff with the integration of Remote Sensing and GIS. Journal of Environmental Management, 2001. No. 28, p. 737–748.
[6] Weng, Q., Land use change analysis in the Zhujiang Delta of China using satellite remote sensing, GIS, and stochastic modeling. Journal of Environmental Management, 2002. No. 64, p. 273–284.

*Environmental Hydraulics – López-Jiménez et al (eds)*
*© 2010 Taylor & Francis Group, London, ISBN 978-0-415-56697-1*

# Linking urban drainage to surface water management models

D. Bertram
*Department of Civil Engineering, University of Glasgow, Glasgow, UK*

M. Roberts
*Water and Environment Group, Capita Symonds Ltd., East Grinstead, UK*

H. Haynes
*Department of Civil Engineering, University of Glasgow, Glasgow, UK*

ABSTRACT: United Kingdom Flood Risk Assessments (FRAs) and Surface Water Management Models (SWMMs) increasingly employ surface 2D hydraulic models that dynamically integrate 1D subsurface models representing local urban drainage infrastructure; IUD models. A generic SWMM of short road section, modelled using British Standards and TUFLOW 2D hydraulic modelling software, is used to address some of the deficiencies in IUD modelling by analysing the configuration and representation of the element linking model surface and subsurface domains. Data indicate that model sensitivities were >30% for the drainage network inlet configuration, showing kerb-side link elements representing gutter channel flow capture to be the optimal setup. Inlet link type data proves less conclusive, indicating both orifice and weir based elements perform similarly, displaying <15% in result variation.

*Keywords*: 1D/2D urban flood modelling, Hydraulic modelling, Integrated Urban Drainage (IUD), Surface Water Management Models (SWMM), TUFLOW

## 1 INTRODUCTION

The inclusion of urban drainage infrastructure within Surface Water Management Models (SWMM) is increasingly undertaken as a key component of developing integrated urban flood risk assessments. As such, the use of integrated 1D/2D hydraulic models has seen a significant increase for analysis of urban environments[1],[2]. These often employ a strategic approach and link the surface and subsurface models to form an Integrated Urban Drainage (IUD) model[2],[3],[4]. A critical component is therefore correct representation of inter-model boundaries and the link elements. However, information on the IUD component is both limited and generally software or case-study dependent.

In United Kingdom road surface water drainage infrastructure, kerbside gully inlets transfer surface flood water from gutter channels into a subsurface network of piped storm water sewers[5],[6]. Surface topography models of grid resolutions varying from 2.0 m to 5.0 m [4],[7],[8] are used to model surface flow paths; yet these scales do not readily permit identification and representation of the kerbside gutter channels or gully inlets. As a result, current modelling practice [2] commonly ignores both features and directly links the surface and subsurface models via drainage network manholes. However, this oversimplification of the road drainage system leads to inaccuracy in IUD model output because, in reality, it is the gully inlets that are designed to accept the majority of surface flow in normal drainage operation. It therefore follows that accurate representation of surface water drainage infrastructure requires that both gully inlets (the linking elements) and their associated topography must be featured in any IUD model. In response, this paper seeks to support IUD modelling and benchmarking by detailed performance analysis of a range of road drainage network inlet configuration options and link element representations within a generic street SWMM modelled using TUFLOW/ESTRY[9].

## 2 METHODOLOGY OF MODEL DEVELOPMENT

### 2.1 *Surface topography and drainage infrastructure model development*

A simple surface topography model representing a straight section of single-carriageway road, designed to United Kingdom engineering standards[10,11] was constructed. Surface topography characteristics included a 7.3 m road width bordered by 2 m wide footpaths with a cross-fall 1 in 40 (2.5%); 5.0 m high buildings were modelled bounding the footpaths. The longitudinal road gradient was 6% (1 in 16) with lateral road camber of 2.5% (1 in 40). Kerbs (height 0.125 m) and buildings (height 5.0 m) were represented as continuous walls to reduce localised flow circulation and limit indirect surface flows. From an upstream surface boundary, the test section allowed a clear length for flow development. The IUD model connects the surface model to the subsurface storm-water pipe at gutter channel gully inlets and at manholes (Figure 1), modelled in accordance with the relevant British Standards[10,12].

For a 6% road gradient and 2.5% road camber, gully inlet spacing was 14.14 m. Gully pot inlets were sited in 0.5 m wide kerbside gutter channels and offset 50 mm from the kerb edge. Gully inlet outflow pipes were of 0.15 m diameter and connected to either manhole chambers or directly to the sewer. Manholes were spaced at 30 m intervals, as specified for a 0.3 m diameter main sewer line. Manhole aperture was modelled at 0.6 m and a storage factor applied to represent the chamber below. The surface roughness value uniformly applied to both topography and drainage infrastructure was Manning's $n = 0.017$[13].

### 2.2 *TUFLOW SWMM and IUD model development*

In developing the SWMM, TUFLOW hydraulic software[9] was employed to simulate the free surface, depth-averaged, 2D and 1D channel flows. The surface street topography was discretised by a regular grid of 1.0 m resolution forming the Digital

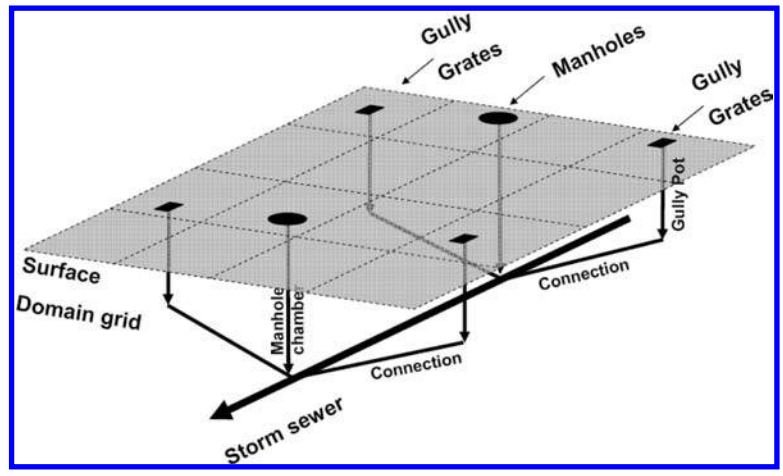


Figure 1. Schematic of 2D surface domain linked to subsurface 1D pipe network.

Table 1. Drainage network configuration outflow and variation.

| | Gully Design Flow Conditions | | Larger 2 $m^3/s$ Inflow Conditions | |
|---|---|---|---|---|
| Network Configuration Options | Flow Captured ($m^3/s$) | Variation (%) | Flow Captured ($m^3/s$) | Variation (%) |
| Closed Manholes & open Gully inlets | 0.00092 | Baseline | 0.16279 | Baseline |
| Open Manholes only | 0.00000 | −100.0% | 0.02665 | −83.63% |
| Open Gully inlets only | 0.00092 | 0.0% | 0.16279 | 0.00% |
| Open Manholes and Gully inlets | 0.00092 | 0.0% | 0.19493 | 19.74% |
| Open Manhole with increased surface area* | 0.00000 | −100.0% | 0.08446 | −48.12% |

* No gully inlets, manhole surface area increased to compensate.

Terrain Model (DTM) and the model grid was orientated parallel to the road centreline. For each grid cell, TUFLOW defines the DTM topography by attributing an elevation value to nine discrete points, Zpts, located at the cell centre (ZC), mid sides and corners. Linear elevation features (kerbs, buildings) are reinforced by Zlines that translate elevations onto the proximate Zpts. The spatial discretisation resolution influences the representation of surface model topography, such as longitudinal gradient and lateral camber, and may lead to some features being located and labelled incorrectly. For example, using a 1.0 m model grid discretisation causes the 7.3 m road to exhibit gully elevation asymmetry of 129 mm between left and right sides, a reduction in left-side camber and left-side kerb faces to be sloping.

TUFLOW[9] links the 2D surface and 1D subsurface ESTRY models via the grid cell within which the 1D/2D link element is depicted in GIS. Link element elevation and position are taken from the cell centre (ZC); for this reason the 1.0 m grid model located the link cell ZC 300 mm from the right-side kerb and 390 mm from the left-side kerb, rather than the 50 mm offset prescribed in the DRMB[12]. Similarly, the cell ZC elevations are inconsistent with the low-relief road gutter channel, which indicates an average DTM variation of 54 mm from the original surface topography elevations. Weir equations were used to model flow through gully link elements; to maximise inflow, a weir length of 0.31 m was employed to represent the upstream face of a gully grate[10] and a weir coefficient 1.7 of applied[14]. Model performance was assessed through two constant flow scenarios applied at the upper boundary of each gutter: the Gully Design Flow, GDF, ($1.5 \times 10^{-3}$m/s) and a larger flow event (1 $m^3/s$).

## 3 RESULTS

### 3.1 *Baseline model result*

Using a 1.0 m grid discretisation, the generic baseline model road drainage system comprised both sealed manholes and open gully inlets. Each individual gully inlet is designed to capture at least 80% of the GDF[12]; yet, results show that the modelled series of six gully pots in each gutter channel permitted only 30.6% capture of the surface flow. This was partly attributed to poor model representation. The weir inlet (0.31 m length) covered only a small section of the 1.0 m wide cell, permitting flow bypass at each gully grate inlet. Equally, the hydraulic parameters applied (e.g. weir coefficients) and inlet cell ZC elevations can influence flow capture and reduce effect. The observed elevation difference between left and right-side gutter channels (129 mm) results in increased flow capture in the gutters of lower elevation; right-side gully inlets pass 62% of the flow of the less accurately defined left-side gullies (38%).

### 3.2 *Drainage network inlets configuration variation*

Four configurations of drainage network inlets were simulated and compared to that of the baseline model with results strongly indicating that inlet configuration plays a critical role in surface water capture. During GDF flow conditions (Table 1) only drainage network configurations including kerbside gully inlets captured surface water. At these conditions, gutter channels carry the whole surface flow component with no lateral transfer across the road camber (Figure 2a). Thus, any representation

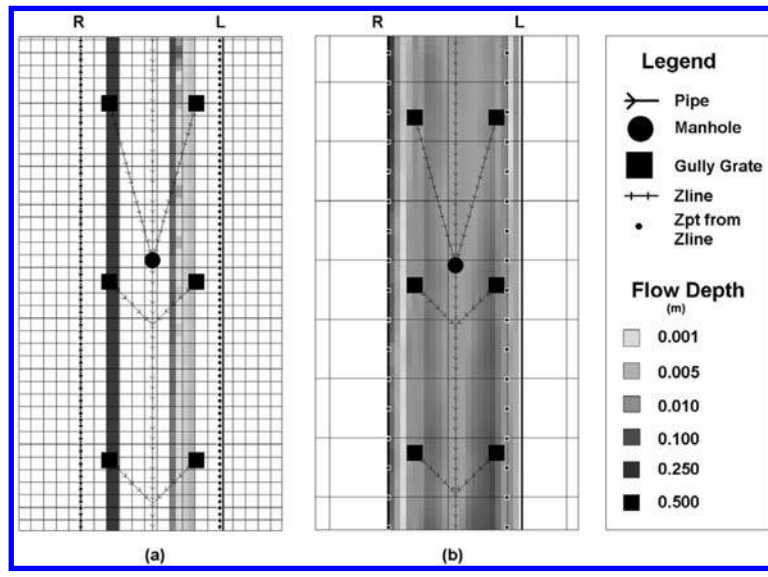


Figure 2. Flow result plots for (a) low flow GDF conditions and (b) 2 $m^3$/s inflows.

Table 2. Drainage network inlet link type element analysis outflow and variation.

| | Gully Design Flow Conditions | | Larger 2$m^3$/s Inflow Conditions | |
|---|---|---|---|---|
| Inlet Type | Flow Captured ($m^3$/s) | Variation (%) | Flow Captured ($m^3$/s) | Variation (%) |
| Weir inlet | 0.00092 | Baseline | 0.16279 | Baseline |
| Rectangular orifice | 0.00079 | −14.13% | 0.15839 | −2.78% |

Table 3. Single inlet link element analysis outflow and variation results

| | Gully Design Flow Conditions | | Larger 2$m^3$/s Inflow Conditions | |
|---|---|---|---|---|
| Inlet Type | Flow Captured ($m^3$/s) | Variation (%) | Flow Captured ($m^3$/s) | Variation (%) |
| Weir inlet | 0.00012 | Baseline | 0.03705 | Baseline |
| Rectangular orifice | 0.00011 | −8.33% | 0.03688 | −0.45% |

of manholes (i.e. permitting inflow) centrally located along the camber apex, or road centreline, is redundant. This highlights the importance of including open kerbside gully pots in IUD model set-up for analysis at low flow conditions. This has a direct application to rainfall event scenarios, in addition to large scale surface flood event modelling.

In contrast, during higher inflow conditions (2 $m^3$/s, Table 1) the most efficient drainage network inlets configuration includes both open manholes and gully inlets. At these conditions, higher water depths, in excess of road camber apex (Figure 2b), permit surface flows to access open central manholes, capturing nearly 20% more surface flow than a network of kerbside gully inlets alone. However, an open manhole inlet configuration is unrealistic because in normal drainage operation, manholes would be closed and unable to accept inflows[12]. Unless a flood event occurred at the same time as a period of maintenance, road centreline manhole covers would only open in the event of the sewer network's surcharging. In this case it is likely that the drainage network would add to the flood risk, rather than mitigate it. Data also indicate the common IUD modelling technique of using manholes enlarged to include a gully-equivalent area is a poor assumption, significantly underestimating surface flow capture by −48% (Table 1). Overall, a key finding of this paper is the demonstrated importance of realistic drainage network configuration for accurate flow capture simulation; i.e. IUD models should be configured with kerbside gully grate inlets and closed central manholes.

### 3.3 *Inlet link element type*

Within TUFLOW modelling there are two methods of representing the link: weir or orifice-based elements. The baseline model employs weirs representing the upstream gully grate face as the link elements; this is based on the viable assumption that overland flow in a gutter may be considered as having an infinite crest length, commensurate with the broad-crested weir definition with a ratio of crest length to upstream head being greater than 1.5 to 3[13]. Comparison data represented the link element as an orifice with rectangular geometry defined from British Standards[10]. It is important to note that defining either type of inlet requires detailed calibration, particularly at low flow conditions; this can lead to model uncertainty that may differ in degree for each inlet type. Specifically, the uncertainty associated with the weir, considered to be a single factor element, is greatly reduced when compared to the uncertainty associated to multi-factor element, such as orifices. This is demonstrated as, in addition to geometry definitions, weir elements require only a weir coefficient to control flow whereas orifice based elements require consideration of parameters such as flow area, constriction, hydraulic losses and discharge coefficients. As such, the generic model developed for the present paper represented these elements using TUFLOW default[9] coefficients and parameter values.

Table 2 indicates a 14% relative under-performance of the orifice element at GDF flow conditions compared to that of the weir inlet element. This resulted from lower upstream head conditions (30∼40% difference) generating a lower flow through

the orifice than for a broad crested weir. Comparison of the element's head-discharge relationships, Equations (1) and (2) explicitly shows that for given upstream head conditions the flow over a weir element will be greater.

$$Q = CLH^{3/2} \tag{1}$$

$$Q = KAH^{1/2} \tag{2}$$

where: $Q$ is the flow rate ($m^3/s$), $H$ is the energy head upstream relative to the weir crest[15] or the center of the orifice, L = the weir length (m), $A$ = the orifice area ($m^2$), C = the weir coefficient (taking into account the coefficients of discharge and submergence factor) and K = the orifice coefficient[16]. At higher flow conditions, a −3% variation on inlet type performance is recorded showing the influence of inlet type decreases significantly (Table 2). This is a direct result of upstream head values at the inlet elements recording 1∼5% differences in value. Results suggest that inlet type influence on flow capture at the higher flow conditions is largely insignificant, providing that specified geometries and hydraulic parameters are correctly applied in representing the same gully inflow path.

Further review (Table 3) of the inlet link element types in a simple model consisting of one inlet element within a simple gutter channel (i.e. no camber and gutter is grid aligned) revealed that model topography and discretisation play a more significant influence. Considering only the inlet elements themselves, at low flows the variation between orifices and the weir is reduced to 8.33%; at higher flows, the variation recorded reduces to 0.45%. However, in both analyses it is noted that the actual proportion of surface flow captured at the inlets is significantly lower than expected, representing only approximately 5% of the applied upstream boundary inflow in both scenarios. This suggests that the hydraulic methods applied to modelling inlets in TUFLOW under perform in surface flow capture. This is likely related to the modelling approximation that flows entering an inlet node or "pit channel"[9] are calculated for a horizontal 1D structure (orifice or weir) of the geometries and properties specified and then inflows are assumed to then translate vertically into the 1D pipe network. Clearly the data suggest this assumption is weak and requires further consideration and review, potentially with comparison to physical and experimental modelling of surface water drainage mechanisms.

## 4 CONCLUSIONS

This study demonstrates that realistic configurations of kerbside gutter channel gully inlets and closed centreline manholes can be readily integrated into a SWMM to more accurately represent the local urban storm water drainage network. Accurate link element elevations interpretation underpins model performance; representing kerbside gully inlets as a weir-based link element was shown to successfully link the two domains and out-perform orifice based inlets. TUFLOW's hydraulic methods of linking drainage networks to surface flows were shown to require further review.

## ACKNOWLEDGMENTS

This research is part of a wider study into IUD modelling has been funded as part of CASE award from the Engineering and Physical Sciences Research Council *(Ref: CAN/06/05)* and Capita Symonds Ltd. Data from this study is currently under review in the UK's CIWEM Journal of Flood Risk Management. The authors acknowledge the contributions and support of J. Minto in early-stage modelling of the surface topography models.

## REFERENCES

[1] Bamford, T., Balmforth, D., Lai, R.H.H., Martin, M. (2007) *Using Integrated Modelling to Drive Effective Flooding Solutions*, WaPUG Autumn Conference, 2007.
[2] Bozhko, A., Cotton, A. (2008) *Benchmarking Integrated Urban Drainage Modelling Methods*. WaPUG Spring Conference, Coventry, UK, 3rd June 2008.
[3] Phillips, B. C., Yu, S., Thompson, G. R., De Silva, N. (2005) *1D and 2D Modelling of Urban Drainage Systems using XP-SWMM and TUFLOW,* 10th International Conference on Urban Drainage, Copenhagen/Denmark, 21–26 August 2005.
[4] Hunter, N.M., Bates, P.D., Neelz, S., Pender, G., Villaneuva, I., Wright, N.G., Liang, D., Falconer, R.A., Lin, B., Waller, S., Crossley, A.J., Mason, D.C. (2007) "Benchmarking 2d hydraulic models for urban flooding", Water Management 161, Issue WM1, Proceedings of the Institution of Civil Engineers, February 2008.
[5] Butler, D., Davies, J.W. (2004) *Urban Drainage,* Second Edition, London and New York: E & FN Spon.
[6] Small, I. (2008) IUD *Methodologies including Gulley Modelling*, Technical Paper, Atkins, March 2008.
[7] Syme, W. J. (2008) *Flooding in Urban Areas – 2D Modelling Approaches for Buildings and Fences, Engineers Australia*, 9th National Conference of Hydraulics in Water Engineering, Darwin, 23–26 September 2008.
[8] Mark, O., Weesakul, S., Apirumanekul, C., Aroonnet, S.B. and Djordjević, S. (2004) "Potential and limitations of 1D modelling of urban flooding", Journal of Hydrology, 299, 284–299.
[9] TUFLOW (2007) *TUFLOW User Manual*, Build 2007-07-AF, July 2007, BMT WBM Ltd, Brisbane, Australia.
[10] British Standards (1998) BS EN 752-4, *Drain and sewer systems outside buildings – Part 4: Hydraulic design and environmental considerations*. 15/06/98, BSI Group.
[11] Highways Agency (1999) DMRB Volume 5 Section 1 Part 3 TA 79/99 Traffic Capacity of Urban Roads, http://www.standardsforhighways.co.uk/
[12] Highways Agency (2000) DMRB Volume 4 Section 2 Part 3 HA 102/00 Spacing of Road Gullies, http://www.standardsforhighways.co.uk/
[13] Chow, V. T. (1973) Open Channel Hydraulics, New York: McGraw-Hill.
[14] Dyhouse, G., Hatchett, J., Benn, J., Ford, D., Rhee, H. (2003) Floodplain Modelling Using HEC-RAS, Haestad Methods, http://www.haestad.com/library/books/fmras/
[15] Henderson, F. M. (1966) Open Channel Flow, New York: Macmillan.
[16] FHA (1973) U.S. Department of Transportation, Federal Highway Administration Hydraulics of Bridge Waterways, Hydraulic Design Series No. 1, Second Edition.

*Environmental Hydraulics – López-Jiménez et al (eds)*
*© 2010 Taylor & Francis Group, London, ISBN 978-0-415-56697-1*

# A methodology for the calculation of hydrological risk in areas to integrate to urban development

Carlos E. Rodriguez, Guadalupe I. Estrada & Rogelio A. Orozco
*Facultad de Ingeniería, Universidad Autónoma de Chihuahua, Chihuahua, México*

ABSTRACT: In Mexico, the use of hydrological studies as a tool for urban development planning has been limited because it merely looks for construction permits for small channels and gain land from rivers and streams. The most of these studies focus on methodologies to determine maximum flows for channeling natural flows. Some use statistical tools such as frequency analysis, or the determination of the hydrograph, curves of intensity-duration-return period, up to calculation of the flood routing. This paper is based on graphical comparison of the probabilities obtained from the application of several methods for calculating the frequency distribution, to validate a methodology to estimate the maximum storm and flood routing, that allow determine the flood plains which should be exempted from building in the development of a residential area. The results show that, from the rainfall data for a given return period can be known the flow of floodwaters and the delimitation of potential flooding areas.

*Keywords*: Methodology, Hydrological Risk, Urban Development

## 1 INTRODUCTION

In Mexico the initial founding of population nuclei has been developed on the banks of rivers and in the lower watersheds, this to ensure water supply for economic activities and domestic use. The growth of urban development until a few years ago, was so disorganized, lacks any planning, without considering that a further development of upstream impervious areas and towards extreme rainfall, building invasions in flood plains, as well as of channels of rivers and streams, would be reclaimed by the great and unusual runoff, causing human and material losses.

This research aimed to demonstrate and validate a sequence to estimate the maximum storm and flood through channels, to allow determine the floodplain that should be exempted from building in the development of residential areas.

The area where the investigation was conducted, is a territorial reserve for urban development, owned by the State Government of Chihuahua, in the city of the same name, located in the Hydrological Region RH-24 called Bravo – Conchos, Rio Conchos – Presa El Granero Basin and Chuviscar River sub-basin, whose runoff drains into this river.

## 2 LOCATION

The city of Chihuahua is located in south-central portion of the State of Chihuahua, Mexico, and at the south of this city the study area is located. The territorial reserve for urban development is limited by the UTM coordinates 396.000 W – 400.000 W and 3.170.000 N – 3.175.000 N[1], in an area of 20 square kilometers, lined by fourteen streams all parallel to each other and tributaries of the Rio Chuviscar. One of these streams was taken for study purposes, and has a drainage area of 2.03 square kilometers, as shown in Figure 1.

## 3 OBJECTIVES

Propose a sequence of calculations for hydrologic studies, focusing on the applicability of models of frequency distributions to estimate the maximum storm in 24 hours per channel, to urban development plans.

## 4 GEOLOGY AND GEOMORPHOLOGY

The study area is located east of the city of Chihuahua on the south side of the Sierra de Nombre de Dios, near the confluence of Chuviscar and Sacramento rivers, within the Ranges and Basins province; its topomorphic expression is narrow and elongated, with an elevation of 1,700 meters above sea level. The area consists predominantly of heavily eroded volcanic rocks on the southern edge of the mountain range, whose morphological expression is a soft and low range of hills. To a lesser extent, are sedimentary rocks[1].

## 5 GENERAL ASPECTS OF THE NATURAL ENVIRONMENT

### 5.1 *Climatology*

The climate of the study area is the type $BS_0$hw (w)[1], this is dry weather with summer rains and scarce throughout the year, and the semi-dry subtype, with summer rainfall, winter rainfall less than 5 mm and cool winter. Annual average temperature for the reserve is 16°C, at an average altitude of 1,550 m above sea level[1].

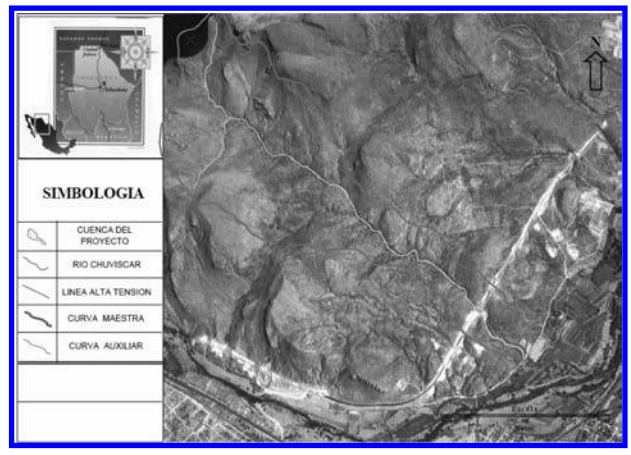


Figure 1. Location and land use in the basin.

Table 1. Maximum precipitation in 24 hr for Observatorio station.

| Año | Lluvia Max en 24 hr | Año | Lluvia Max en 24 hr | Año | Lluvia Max en 24 hr | Año | Lluvia Max en 24 hr | Año | Lluvia Max en 24 hr | Año | Lluvia Max en 24 hr |
|---|---|---|---|---|---|---|---|---|---|---|---|
| **1951** | 18.00 | **1961** | 20.00 | **1971** | 26.20 | **1981** | 35.00 | **1991** | 42.20 | **2001** | 63.20 |
| **1952** | 34.70 | **1962** | 23.00 | **1972** | 34.90 | **1982** | 43.00 | **1992** | 46.00 | **2002** | 12.70 |
| **1953** | 11.00 | **1963** | 62.00 | **1973** | 64.50 | **1983** | 34.00 | **1993** | 28.20 | | |
| **1954** | 70.00 | **1964** | 19.00 | **1974** | 51.00 | **1984** | 23.00 | **1994** | 46.70 | | |
| **1955** | 48.00 | **1965** | 42.50 | **1975** | 38.00 | **1985** | 55.30 | **1995** | 112.90 | | |
| **1956** | 30.60 | **1966** | 70.00 | **1976** | 80.60 | **1986** | 57.60 | **1996** | 57.70 | | |
| **1957** | 23.60 | **1967** | 43.00 | **1977** | 31.80 | **1987** | 48.00 | **1997** | 33.00 | | |
| **1958** | 31.50 | **1968** | 60.30 | **1978** | 67.20 | **1988** | 36.00 | **1998** | 27.10 | | |
| **1959** | 24.60 | **1969** | 49.00 | **1979** | 71.50 | **1989** | 56.00 | **1999** | 54.00 | | |
| **1960** | 25.60 | **1970** | 30.50 | **1980** | 64.00 | **1990** | 70.50 | **2000** | 60.00 | | |

### 5.2 *Soils*

The main type of soil in the area is a Regosol of Eutric type[1], characteristic in arid and semi-arid climates in mountainous areas to ranges of hills, supporting a natural vegetation of grassland and scrub. Its origin is volcanic ashes; these soils are colored from light gray to white. This type of soil present carbonates or gypsum crystals, high salinity, low sodicity, low permeability and are susceptible to erosion.

### 5.3 *Vegetation*

In the project area there are two types of vegetation, from lowest to highest presence, microphilic desert scrub (Dm) and rosetophilous desert scrub (Dr)[2]. The first is characterized by the dominance of shrub species of small leaves, but not always thorny. Ephemeral summer and winter shrubs and bushes stark, with substrates ranging from 0.7 to 3.0 m. Dominated by grass species such as Z. Escoba (*tridens grandiflorus*), Z. Navaja (*boutelova gracilis*), which usually develops at the shrubs base, while the Ocotillo (*fouqueiria splendens*) and Gatuño (*acacia gregii*) increases their density in runoff areas to become co-dominant. In the rosetophilous desert scrub, shrub species of long and narrow leaves are distinctive, growing in limestone type substrate and strata ranging from 0.2 to 1.5 m.

## 6 METHODOLOGY

For this research, information of maximum rainfall in 24 hours was available from the National Weather Service of the National Water Commission (CNA)[1], for the Observatorio weather station, which is presented in Table 1. For the area under study, the annual average rainfall is 406.6 mm.

### 6.1 *Processing data of rain in 24 hours*

From the INEGI topographic chart H13C66, scale 1:50 000 and using AUTOCAD, geomorphologic characteristics were obtained: $A = 2.63\,km^2$, $L = 3859.4\,m$. To calculate the slope of the main channel, the Taylor and Schwarz and equivalent straight line methods were used (Figure 2). To calculate the concentration time the Kirpich[3] formula was applied from the length and average slope of the channel data, yielding a value of $Tc = 0.619$ hr

According to geology, soil use and vegetation cover in the area, was estimated the runoff number, N (Table 2)

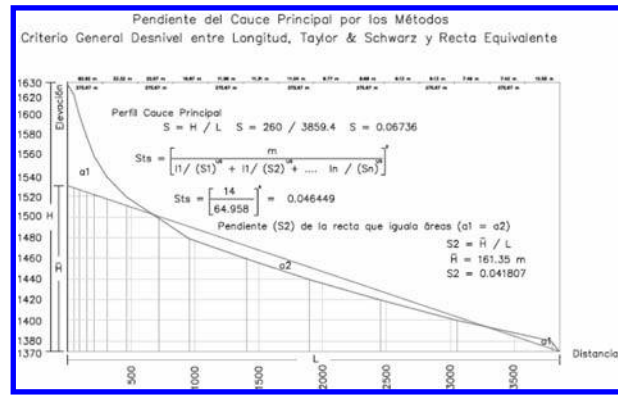


Figure 2. Main channel slope, method of equivalent straight line.

Table 2. Runoff number (N)

| | | Grupo hidrológico de suelo | | | | | | | | | Valor de N para Icuenca | | |
|---|---|---|---|---|---|---|---|---|---|---|---|---|---|
| | | A | | | B | | | D | | | A (N) (Área) | B (N) (Área) | D (N) (Área) |
| | | Sup | % Área | N | Sup | % Área | N | Sup | % Área | N | | | |
| Pastiz | Pobre | | | | 18.708 | 0.093 | 79 | 116.436 | 0.578 | 89 | | 7.339 | 51.457 |
| | Regular | | | | 24.999 | 0.124 | 69 | 28.490 | 0.141 | 84 | | 8.565 | 11.883 |
| | Bueno | 8.254 | 0.041 | 39 | | | | | | | 1.598 | | |
| Legum | Surco Pobre | 1.100 | 0.005 | 66 | | | | | | | 0.361 | | |
| | Surco Bueno | 1.651 | 0.008 | 55 | | | | | | | 0.451 | | |
| Camino | Tierra | | | | 0.092 | 0.000 | 82 | 0.33895 | 0.002 | 89 | | 0.038 | 0.150 |
| | Pavimento | | | | 1.321 | 0.007 | 84 | | | | | 0.551 | |
| | | | | | | | | | | N | 2.410 | 16.492 | 63.489 |

N para la subcuenca = 82.3915

Table 3. Calculation of C for the basin, considering the percentage of urban soil usage built and to be build, according to figure 1.

| | | Grupo hidrológico de suelo | | | | | | | | | Valor de N para Icuenca | | |
|---|---|---|---|---|---|---|---|---|---|---|---|---|---|
| | | A | | | B | | | D | | | A (C) (Área) | B (C) (Área) | D (C) (Área) |
| | | Sup | % Área | C | Sup | % Área | C | Sup | % Área | C | | | |
| Pastiz | Pobre | | | | 17.000 | 0.09290 | 0.63 | 105.804 | 0.57816 | 0.84 | | 0.059 | 0.486 |
| | Regular | | | | 22.716 | 0.12413 | 0.25 | 25.888 | 0.14146 | 0.65 | | 0.031 | 0.092 |
| | Bueno | 7.500 | 0.04098 | 0.07 | | | | | | | 0.003 | | |
| Legum | Surco Pobre | 1.100 | 0.00546 | 0.49 | | | | | | | 0.003 | | |
| | Surco Bueno | 1.500 | 0.00820 | 0.27 | | | | | | | 0.002 | | |
| Camino | Tierra | | | | 0.084 | 0.00046 | 0.69 | 0.308 | 0.00168 | 0.84 | | 0.000 | 0.001 |
| | Pavimento | | | | 1.200 | 0.00656 | 0.99 | | | | | 0.006 | |
| | | | | | | | | | | | 0.008 | 0.096 | 0.579 |

**C para le cuenca = 0.6832**

### 6.2 *Runoff* **C** *calculation of the hydrological – soil – coverage complex*

To calculate this parameter the method of the U. S. Soil Conservation Service[4] requires the classification of soil types, coverings and uses. (Table 3)

| | |
|---|---|
| Cuando **k ‹ 0.15** | **C = k ((P- 250)/ 2,000)** |
| Cuando **k › 0.15** | **C = k ((P-250)/ 2,000) + (k – 0.15)/1.5** |

where, **C** is the Annual Runoff Coefficient, non dimensional; **P** is the annual rainfall, mm; **k** is a type, usage or covering of soil depending parameter.

Table 4. Maximum rainfall in 24hr obtained from the different distributions applied.

| P(X <= x) % | Tr Años | Normal X mm | Log Normal X mm | Pearson Tipo III X mm | Log Pearson Tipo III X mm | Weibull X mm | Gamma Incompleta X mm | Gumbel Simple X mm |
|---|---|---|---|---|---|---|---|---|
| 99.90 | 1000 | 106.172 | 177.977 | | | 110.107 | 132.335 | 153.607 |
| 99.80 | 500 | 101.934 | 160.632 | 121.360 | 120.451 | | | |
| 99.00 | 100 | 90.903 | 123.006 | 102.190 | 102.781 | 94.124 | 103.749 | 113.978 |
| 98.00 | 50 | 85.454 | 107.812 | 93.434 | 94.302 | | | |
| 96.00 | 25 | 1.993 | | 84.239 | 85.195 | | | |
| 95.00 | 20 | 77.280 | 88.466 | | | 79.917 | 81.760 | 85.981 |
| 90.00 | 10 | 70.018 | 74.210 | 71.105 | 71.892 | 71.037 | 71.565 | 73.617 |
| 80.00 | 5 | 61.222 | 59.984 | 59.990 | 60.404 | | 60.171 | 60.727 |
| 50.00 | 2 | 44.400 | 39.930 | 41.759 | 41.562 | 43.510 | 41.780 | 41.258 |
| 30.00 | | | | | | 31.967 | 32.380 | 31.774 |
| 20.00 | 1.25 | 27.750 | 26.580 | 27.290 | 27.010 | | | |
| 10.00 | 1.111 | 18.780 | 21.480 | 21.090 | 21.060 | 20.867 | 21.790 | 20.637 |

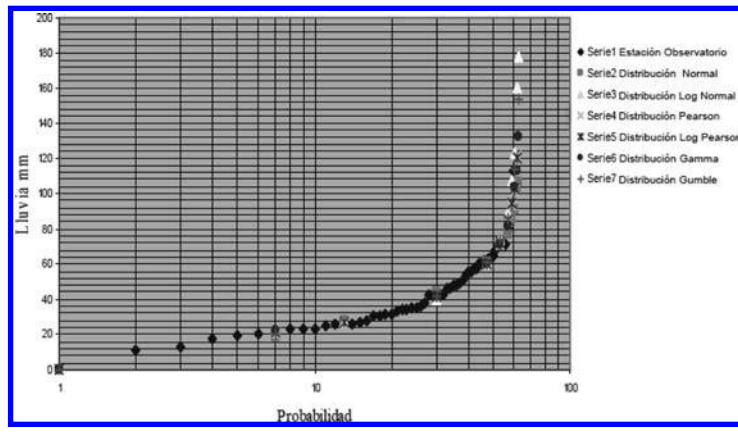


Figure 3. Comparison of frequency distribution data adjustment.

Table 5. Data of flow or rainfall-runoff ratio, calculated with the Rational Method formula.

| | | | | Qp ($m^3/s$) | | |
|---|---|---|---|---|---|---|
| DATOS BASICOS | | Tr (años) | i (mm/hr) | Natural | Urbano 1 | Incremento |
| Ac | 2.0344337 $km^2$ | 1000.00 | 177.98 | 68.77 | 74.34 | 5.57 |
| Lc | 3.8594 km | 500.00 | 160.63 | 62.07 | 67.09 | 5.02 |
| H | 260.00 m | 100.00 | 123.01 | 47.53 | 51.38 | 3.85 |
| | | 50.00 | 107.81 | 41.66 | 45.03 | 3.37 |
| S | 0.067360 | 20.00 | 88.47 | 34.18 | 36.95 | 2.77 |
| Sts | 0.067360 | 10.00 | 74.21 | 28.67 | 31.00 | 2.32 |
| Sreq | 0.041807 | 5.00 | 59.98 | 23.18 | 25.05 | 1.88 |
| C | 0.6832 Natural | 2.00 | 39.93 | 15.43 | 16.68 | 1.25 |
| C | 0.7385 Urabo 1 | 1.25 | 26.58 | 10.27 | 11.10 | 0.83 |
| Tc | 0.3459 hr | 1.11 | 21.48 | 8.30 | 8.97 | 0.67 |

### 6.3 *Frequency distributions and algorithms of their parameters*

Planning and design concerns future events, whose occurrence time or magnitude can not be predicted, relying on the probability or frequency in which a flow can be exceeded[5,6]. The U. S. Geological Survey[4] recommends as the most appropriate probability distributions of annual runoff, the Normal, Log-Normal and Weibull methods. The maximum hourly or daily rainfall is consistent with the distribution of extreme values type I or Gumbel, the Pearson III and Gamma incomplete.

### 6.4 *Normal and log-normal distribution*

The normal distribution is symmetrical, bell-shaped, theoretically represents the distribution of accidental errors around their mean. The log-normal distribution is asymmetric with bias to the right, corresponding to a normal distribution in which the variable is replaced by its logarithmic value. Like normal distribution, the log-normal is function only of two statistical parameters, mean and standard deviation.

Table 6. Precipitation data for Observatorio station, obtained from the Log-normal distribution.

| Probabilidad | Tr años | X mm Observatorio |
|---|---|---|
| 99.9 | 1000 | 177.98 |
| 99.8 | 500 | 160.63 |
| 99.0 | 100 | 123.01 |
| 98.0 | 50 | 107.81 |
| 95.0 | 20 | 88.47 |
| 90.0 | 10 | 74.21 |
| 80.0 | 5 | 59.98 |
| 50.0 | 2 | 39.93 |
| 20.0 | 1.250 | 26.58 |
| 10.0 | 1.111 | 21.48 |

### 6.5 *Pearson Type III distribution*

This is a special case of Gamma distribution; is asymmetric and generally bell-shaped, depends on three statistical parameters and therefore it is quite flexible, if the asymmetry coefficient (Cs) is zero, is reduced to a normal distribution.

### 6.6 *Weibull distribution*

This methodology requires the calculation of the variation coefficient (Cv) and the arithmetic mean (x) of annual rainfall or runoff. The Cv value is used to determine values of X related to its mean, for non exceedence probability.

### 6.7 *Incomplete Gamma distribution*

Also called the two parameters a and b positive, is quite flexible.

### 6.8 *Simple Gumbel distribution*

This distribution is of exponential type, because when x grows, it converges to an exponential function, also known as Type I extreme values distribution.

### 6.9 *Derivation of adjusted data for each frequency distribution*

Table 4 shows the values of maximum rainfall for 24 hours produced by various distributions methods.

To determine which of the functions of probability distribution is more representative about the tendency of maximum rainfall records under study, it was considered the following values: Coefficient of Variation = 0.450, Coefficient of Obliqueness = −0.4877, and Asymmetry Coefficient = 0.7762.

### 6.10 *Statistical validation of data adjustment for each frequency distribution*

It was chosen to compare graphically the probability distribution obtained from the Weibull calculation method with the results obtained from the different probability distribution functions studied, because it represents more accurately the tendency of Maximum rainfall records in terms of their probability. (Figure 3).

## 7 CONCLUSION

The calculation of the flow of floodwaters and the delimitation of potential flooding areas, once the behavior of the precipitation is known for a given return period, as shown in Tables 5 and 6, ceases to have complexity. According to Figure 3 it is determined that the most representative probability function of the tendency in the Observatorio station records, is the log-normal distribution. The equation of the rational formula proved to be the most recommended method for small basins, as in compliance with the rainfall intensity is constant throughout the area[3].

## REFERENCES


[1] INEGI. Instituto Nacional de Estadística y Geografía. Web page: http://www.inegi.org.mx

[2] Modesto, C. (2000), *Estudio técnico justificado para cambio de utilización del suelo forestal*, Cementos de Chihuahua, S. A. de C. V., SEMARNAP, México.

[3] Estrada, G. G. (2008), *Conceptos básicos de hidrología*, Colección Textos Universitarios, Universidad Autónoma de Chihuahua. México.

[4] U. S. Department of the Interior Bureau of Reclamation, (1966), *Diseño de Presas pequeñas*, Editorial Continental, E. U. A.

[5] Dingman, S., (1984), *Fluvial Hydrology*, W. H. Freeman & Co., U. S. A.

[6] Chow, V. T. et al, (1993), *Hidrología Aplicada*, McGraw-Hill, Colombia

*Environmental Hydraulics – López-Jiménez et al (eds)*
*© 2010 Taylor & Francis Group, London, ISBN 978-0-415-56697-1*

# Vulnerability of the aquifer "El Sáuz-Encinillas", Chihuahua, México

R. Licón Rubio & A. Pinales Munguia
*Universidad Autónoma de Chihuahua, México*

J. Gómez-Hernández, G. Llerar Meza & L. Salas Lechuga
*Grupo de Hidrogeología, Universidad Politécnica de Valencia, Valencia, España*

H.O. Rubio Arias, L. Villalba, M. Royo Ochoa & R. de la Garza Aguilar
*Universidad Autónoma de Chihuahua, México*

ABSTRACT: When there is insufficient information available, the determination of vulnerability is uncertain and highly subjective. Yet, it is a measure that can be applied in the decision making process while protecting groundwater resources. The objective of this research was to determine the vulnerability of the aquifer known as El Sáuz-Encinillas, located in the state of Chihuahua, in northern México. The SINTACS and AVI methods were utilized. These methods take into account the aquifer properties to assess the level of vulnerability. The SINTACS method uses seven parameters while the AVI method is calculated as a function of just one parameter. The SINTACS method showed that 38% of the aquifer area presents a vulnerability level ranging from moderate to very high. In contrast, the AVI method determines that 62% of the aquifer area presents that level of vulnerability.

*Keywords*: vulnerability, SINTACS, AVI, aquifer.

## 1 INTRODUCTION

Presently, aquifers are facing a pollution problem mostly due to anthropogenic activities. Therefore, it is crucial to know which zones are the most vulnerable to environmental pollution and try to protect them. The contamination vulnerability of any aquifer is a characteristic that depends on the interaction of several factors like depth to water, net recharge, aquifer and soil media, impact of the vadose zone and hydraulic conductivity, among others. The vulnerability terminology in relation to groundwater was introduced by a French hydrogeologist named Margat, in the late 1960s[1]. Margat hypothesized that the physical characteristics of the soil environment protect the aquifer from contaminants that can be infiltrated from higher levels. Thus, the vulnerability can be defined as the level of penetration of any contaminant in the aquifer, after its introduction in some position of the unsaturated zone. The risk to any contaminant is determined by aquifer characteristics and the existence of potential anthropogenic contaminants[2].

The vulnerability index is used when the groundwater contamination risk of is evaluated. It affects the contaminants discharge levels that are occurring in the soil profile. The use of maps then allows the classification and identity of those zones with the highest vulnerability. It also allows economic activities according to zone, the planning of urban and other areas to improve aquifer water quality and the management of this natural resource in a sustainable way.

In recent years, several countries have experienced contamination problems in the groundwater environment. Consequently, some methodologies have been designed to identify the transport mechanism of the contaminants; to determine the aquifer's vulnerability level[3]. The objective of this research was to determine the vulnerability of the aquifer known as El Sáuz-Encinillas, located in the state of Chihuahua, in northern México. These results will establish the basis for planning more detailed studies in order to diminish the risk of aquifer pollution and to serve as planning data.

### *Study area*

The El Sáuz-Encinillas aquifer is located in central Chihuahua in the polygon: latitude 28°52′07″–29°40′ 29″ N; longitude 106°02′19″–106° 44′ 35″ W. This aquifer is one of the main sources of drinking water in Chihuahua supplying about 16 $hm^3 year^{-1}$. The lowest elevation in the area is approximately 1,500 m while the highest elevation is about 2,850 m. The area has an estimated surface of 2,743 $km^2$. The soils of this watershed are nearly level to gently sloping and moderately well drained to well drained.

The aquifer is unconfined, where the major part is constituted of soil, silt, lime or gravel, unsaturated or partially saturated. Then there are granular materials like gravel or conglomerates, uncemented and cemented at times. The materials in general had good permeability but the volcanic rock could be fracturated and in deep layers could be considered as impermeable. In this region, the main industries are irrigating agriculture using mostly groundwater and cattle production systems[4].

The vulnerability maps were developed with data from field samples, measuring water depth and utilizing 95 vertical electric probes, 29 pumping wells, and temperature data and precipitation coming from eight meteorological stations in the study area. In addition, geological sections and edaphic maps were also used[4].

## 2 METHODOLOGY

The SINTACS method is based on the evaluation of seven aquifer parameters in a given cell[5]. A score for each parameter is then assigned to each cell. The scores are then over imposed, summing up the parameter indices to obtain a value which is a function of the vulnerability level.

Table 1. Parameters of SINTACS model.

| No. Parameter | Acronym | Parameter | |
|---|---|---|---|
| 1 | S | Soggiacenza | Depth to groundwater |
| 2 | I | Infiltrazione efficaze | Effective infiltration |
| 3 | N | Nan-saturo | Unsaturated zone |
| 4 | T | Tipologuadella copertura | Soil type |
| 5 | A | Acquifero | Hydrogeologic characteristics of the |
| 6 | C | Conducibilitá | Hydraulic conductivity range of the aquifer |
| 7 | S | Superficie topografica | topographic slope |

The AVI method requires the vertical hydraulic conductivity of the geological layers located above the unsaturated zone and their thickness.[6].

The vulnerability index of the aquifer is then obtained. Finally, the aquifer characteristics are converted to numerical values through different graphs and equations.

## 2.1 *Sintacs*

This is a DRASTIC type method[7]. Table 1 shows the seven parameters and the acronym SINTACS is explained for the parameters of the natural system. We will use the methodology proposed by Cavita to use SINTACS and to define the hydrogeologic units and the weight of each parameter[8].

The SINTACS vulnerability index ($I_{SINTACS}$), is calculated with the following equation:

where:

$$I_{SINTACS} = \sum_{i=1}^{7} P_i W_i \tag{1}$$

$P_i$ = The rating of each of the seven parameters used.

$W_i$ = The weight in each class, which can vary from 1 to n.

In this study, each parameter was calculated utilizing graphs proposed by Cavita[8], with the exception of the following parameters; depth water, effective infiltration, hydraulic conductivity and topographic slope. The calculus of these four parameters was established using the following analytical relations. Our starting point is the following relationship:

**Depth to groundwater:**

$$I_1 = 18.7333154 P_1^{(0.6028258)} \tag{2}$$

Where: $I_1$ = vulnerability index of this parameter. $P_1$ = depth of the groundwater in meters.

**Effective infiltration:**

$$\begin{aligned} I_2 = {} & 2.80796225885854X10^{14} P_2^6 + 4.68713210783183X10^{11} P_2^5 \quad 2.83566266892671X10^{8} P_2^4 \\ & + 7.567213879914934X10^{6} P_2^3 \quad 9.75057316681318X10^{4} P_2^2 + 9.89609609464785X10^{2} P_2^2 \\ & 8.19059759579049X10^{1} \end{aligned} \tag{3}$$

Where: $I_2$ = vulnerability index of this parameter. $P_2$ = net recharge in mm/year.

**Hydraulic conductivity:**

$$I_6 = 0.00607130 P_6^4 + 0.09484264 P_6^3 + 0.26539844 P_6^2 + 0.1017187 P_6 + 9.82211133 \tag{4}$$

Where: $I_6$ = Vulnerability index of this parameter. $P_6$ = exponent of the hydraulic conductivity value 1E (m/s).

**Topographic slope**

$$I_7 = 8.98450145X10^{5} P_7^3 + 7.78391408X10^{3} P_7^2 \quad 4.93005055X10^{1} P_7 + 9.95047264 \tag{5}$$

Where: $I_7$ = Vulnerability index of this parameter. $P_7$ = Topographic slope in%.

Equations 2 to 4 were obtained from an exponential or polynomial approximation considering the curve type proposed by Cavita[8].

## 2.2 *AVI*

The AVI method is useful in quantifying the natural vulnerability of the aquifer. It uses the vertical hydraulic resistance of the water in passing from one soil layer to another in the aquifer. The hydraulic resistance is a factor that indicates the amount of time it takes for the water to move from one zone to another and is calculated by the equation:

$$C_T = \sum_{i=1}^{n} \frac{d_i}{K_{vi}} \tag{6}$$

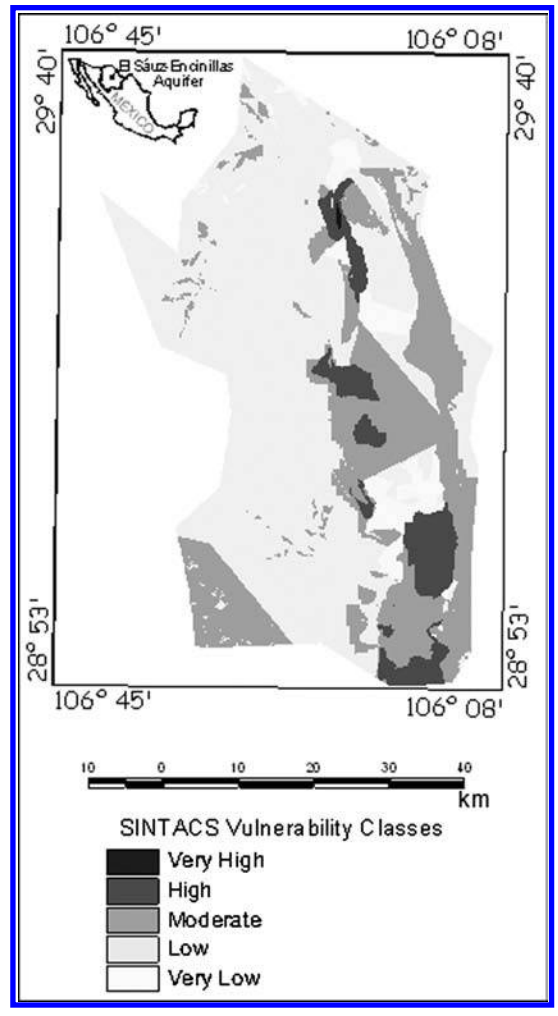


Figure 1. SINTACS vulnerability map for the study area.

Table 2. SINTACS Classification of the Vulnerability.

| Vulnerability Classes | SINTACS | Area km$^2$ | Area % |
|---|---|---|---|
| Very High | 187–210 | 1.8 | 0.1 |
| High | 141–186 | 116.8 | 4.3 |
| Moderate | 106–140 | 915.8 | 33.4 |
| Low | 81–105 | 1595.9 | 58.2 |
| Very Low | 23–80 | 112.7 | 4.1 |

Where:
$C_T$: Hydraulic resistance (years).
$d_i$: Thickness of the homogeneous layer "i" that is above the saturated area (cm).
$K_{vi}$: Vertical hydraulic conductivity of the homogeneous layer "i" that is above the saturated area (cm/year).

The result is hydraulic resistance zones that are related to vulnerability. Therefore, in the same way that higher hydraulic resistance is noted, lesser vulnerability of the system is observed. The vulnerability map was elaborated through the interpolation of the values of total hydraulic resistance in years C in Log C.

## 3 RESULTS AND DISCUSSION

The management of the information and the results were obtained using the geographic information system (GIS). Maps were designed for each parameter using the SINTACS and AVI methods and finally, the maps of the vulnerability indexes.

### 3.1 *SINTACS method*

Figure 1 shows the distribution of the vulnerability of the El Sáuz-Encinillas aquifer using the SINTACS method. In addition, Table 2 specifies the percentages of each vulnerability level of the aquifer. It is noted that about 92% of the aquifer presents a low to moderate vulnerability level.

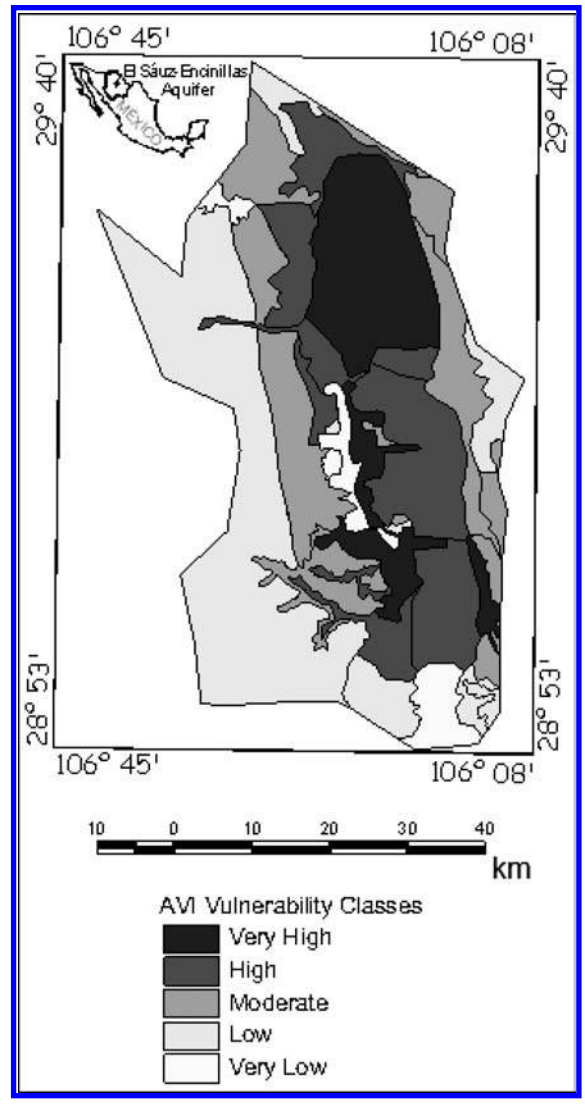


Figure 2. AVI vulnerability map for the study area.

Table 3. AVI Classification of the Vulnerability.

| Vulnerability Classes | Hydraulic resistance | Log (c) | Area km$^2$ | Area % |
|---|---|---|---|---|
| Very High | <10 | <1 | 464.67 | 16.6 |
| High | 10–100 | 1a$^2$ | 632.01 | 23.0 |
| Moderate | 100–1,000 | 2a$^3$ | 606.69 | 22.1 |
| Low | 1,000-10,000 | 3a$^4$ | 908.7 | 33.1 |
| Very Low | >10,000 | <4 | 131.03 | 4.8 |

### 3.2 *AVI method*

Figure 2 and Table 3 show the results using the AVI method. One can observe that about 62% of the aquifer presents a vulnerability level from moderate to very high while the rest of the aquifer is considered to be at a low vulnerability level.

The different methods to calculate the vulnerability of any aquifer requires significant amount of data that at times is not available. So, the use of interpolations is necessary and therefore, the level of uncertainty is high. We recommend the estimation of this level of uncertainty using a parameter estimation procedure to improve this type of study.

## 4 CONCLUSIONS

The vulnerability results using the SINTACS and AVI methods disagree. With the SINTACS method, about 38% of the aquifer's zone presented a vulnerability level varying from moderate to very high when compared to AVI, where almost 62% of the aquifer's zone presented that level of vulnerability. The recommendation is to continue an evaluation of this aquifer in a long-term susceptibility and environmental pollution plan.

ACKNOWLEDGMENTS

The authors express their thanks to the Program for Faculty Improvement (PROMEP) of the Secretary of Public Education México, for the partial funding of this study. We also extend our appreciation to Oscar Raul Herrera Lagunas, director of the Faculty of Engineering of the Autonomous University of Chihuahua for their personal support.

REFERENCES

[1] Margat, J. (1968), Groundwater vulnerability to contamination. BRGM, 68 sgl 198, HYD, Orleans, France.
[2] Ferreira, J. P., Oliveira M. M. (2004), Groundwater Vulnerability Assessment in Portugal. Geophysical International, v.43 No. 4. México
[3] Reynoso, L., Sasal C., Portela S., and Andriulo A. (2005), Vulnerabilidad del acuífero Pampeano a la contaminación en el norte de la provincia de Buenos Aires. Aplicación de la metodología DRASTIC. Revista de Investigaciones Agropecuarias, v.34 No. 1. Argentina.
[4] Pinales, A., L. Villalba, M. Royo, B. Aguirre, R. Chávez, R. de la Garza, and G. Llerar. (2008), Disminución del error en calibración y predicción de modelos hidrodinámicos, caso de aplicación: acuífero El Sáuz – Encinillas. PROMEP/103./07/3577. Posgrado en Hidrología Subterránea, Chihuahua, Chihuahua, México.
[5] Civita, M. (1990), La valutazione della vulnerabilità degli acquiferi. Atti 1º Conv. Naz. “Protezione e Gestione delle Acque Sotterranee: Mettodologie, Technologie e Obiettivi”. Marano sul Panaro, v-3, p. 39-86.
[6] Van Stempvoort, D., L. Ewert and L. Wassenaarl. (1992), AVI: A method for groundwater protection mapping in the Prairie, Provinces of Canada. PPWB Report No. 114. National Hydrology Research Institute, Saskatoon Saskatchewan, Canada.
[7] Aller, L., T. Bennet, J. H. Lehr, R. J. Petty and G. Hackett. (1987), DRASTIC: A Standardized system for evaluating groundwater pollution potential using hydrogeologic setting. National Water Well Association/EPA, Ser., EPA-600/287035. 455 pp. USA.
[8] CIVITA, M. 1994, Le Carte della vulnerabilità degli acquiferi all’inquinamento: Teoria and Pratica. Pitagora Edittrice, Bologna, 325 pp.

*Environmental Hydraulics – López-Jiménez et al (eds)*
*© 2010 Taylor & Francis Group, London, ISBN 978-0-415-56697-1*

# Estimation of aquifer recharge in "El Sáuz-Encinillas"

A. Pinales Munguia
*Facultad de Ingeniería, Universidad Autónoma de Chihuahua, México*

J. Gómez-Hernández, G. Llerar Meza & L. Salas Lechuga
*Grupo de Hidrogeología, Universidad Politécnica de Valencia, Valencia, España*

L. Villalba
*Facultad de Ingeniería, Universidad Autónoma de Chihuahua, México*

ABSTRACT: In this paper we quantified the recharge to the "El Sáuz-Encinillas" aquifer through the mountain area and through the mountain front using two different models: a hydroclimatic model and a groundwater flow model. For the hydroclimatic model, the study area was divided into three zones: the mountain area, the mountain front and the valley. In the groundwater model, recharge is applied to the entire area as a function of the spatial distribution of. The net recharge to the aquifer obtained using the hydroclimatic model was 86.1 $hm^3$/yaer, whereas using the groundwater flow model was 69.4 $hm^3$/year. These values represent 8% and 6.5% of the average precipitation in the watershed, respectively.

*Keywords*: mountain front, rainfall, linear recharge, diffuse recharge.

## 1 INTRODUCTION

The two main mechanisms of natural recharge to regional aquifers in arid and semiarid areas are stream recharge and mountain front recharge[1]. Estimates of the recharge to regional aquifer are important for management purposes. However, data on groundwater in regional aquifer zones are limited. This shortage of information associated with uncertainties inherent in the data and calculations, may lead to discrepancies in the estimated recharge depending on the method used to compute it[1].

In this work, we present the estimation of the net recharge to the El Sáuz-Encinillas aquifer using a hydroclimatic model and a groundwater flow model. El Sáuz-Encinillas aquifer is located in the center of the Chihuahua state, México, and is bounded by latitudes 28° 52' 07" N and 29° 40′ 29″ N and by longitudes 106° 02′ 19″ W and 106° 44′ 35″ W. The extension of the aquifer is 2743 $km^2$, divided into a mountain area of 946.7 $km^2$, a mountain front area of 170,6 $km^2$ and a valley area of 1625.7 $km^2$ [2].

In the study area there are eight climatological stations: Parritas, Cañón del Álamo, Majalca, casco La Campana, rancho El Retiro, Huerta San Antonio, El Olivo de Abajo and rancho La Esperanza. Precipitation data obtained from climatological stations display higher precipitation over the period July – October, as compared to that in the period November – June. The average annual precipitation is 388 mm/year, while the average annual temperature is 15.5° C. El Sáuz-Encinillas aquifer is a major source of water supply to Chihuahua city with 16 $hm^3$withdrawn per year. The aquifer is unconfined and the surface materials consist of clay soil, silt, sand, gravel and pebble. Underlying the above are granular materials such as sand, gravel, and conglomerate pebble that may or may not be cemented. Non-compacted materials have good permeabilities. Underlying the above is the riolitic, which in its upper part can be fractured, but that can be considered impermeable at depth[2]. The main productive activities in the region of study are irrigated agriculture with ground water, and livestock.

## 2 METHODOLOGY

### 2.1 *Estimation of recharge by hydroclimatological balance*

Diffuse recharge in the mountainous area of the basin surrounding the aquifer was calculated using a hydroclimatological balance. For a period of any number of full years, during which the change of water storage in the basin is close to zero, the water balance equation is:

$$P = ET + Y \tag{1}$$

where P is precipitation, *ET* is evapotranspiration, and *Y* is the watershed yield (surface runoff + underground runoff). Therefore, *Y* from equation (1), is:

$$Y = P - ET \tag{2}$$

To estimate the evapotranspiration, *ET*, we used the empirical formula by Turc, which only requires the precipitation data and the average annual temperature as shown in equation (3):

$$ET = \frac{P}{\sqrt{0.90 + \frac{P^2}{L^2}}} \tag{3}$$

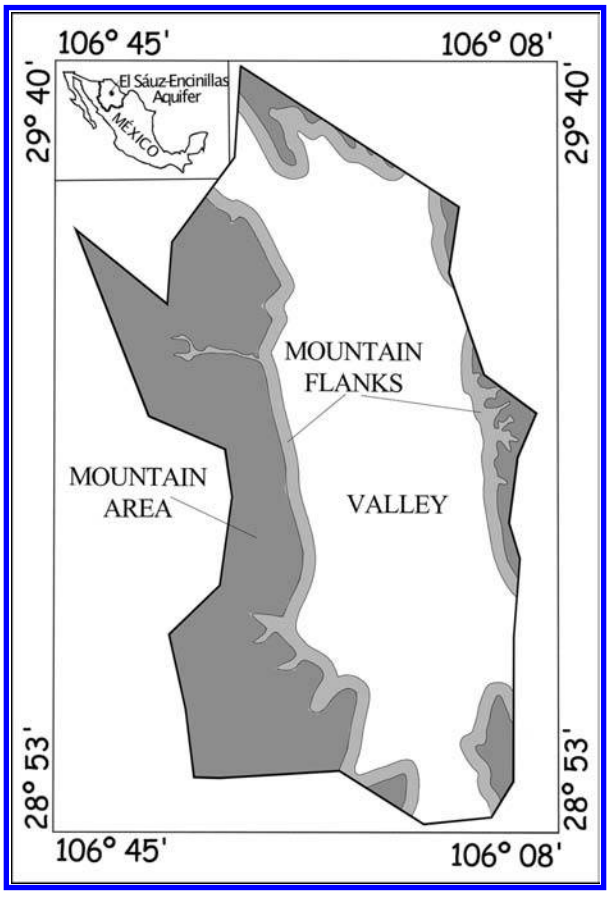


Figure 1. Mountain area, mountain front area and valley area.

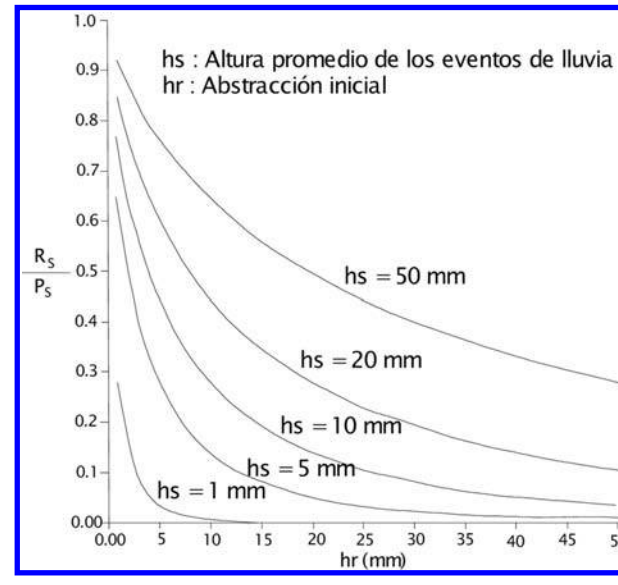


Figure 2. Rainfall-runoff relationship of average annual (or seasonal) in mountain areas[4].

where: $L = 300 + 25T + 0.05T^3$, with P and $ET$ in millimeters, and $T$ in °C.

Considering that rainfall increases with elevation topographical we will make a linear approximation for precipitation considering the stations of Majalca and El rancho Retiro. However, it is important to consider that in the basin the mountain ranges are of very low permeability, so that the recharge from mountain blocks is negligible. Water drains off the mountain block through the creeks and streams[3]. In the mountain flanks a portion of runoff is lost through evaporation in the channel and adjacent riparian strips, and another portion is eventually recharged to the aquifer.

### 2.1.1 *Estimation of mountain front recharge*

In semi arid areas of central and north of México, and in those mountains where the rocks are volcanic, such as the mountains surrounding the aquifer, we considered what is called mountain front recharge. The mechanism consists of water draining to the bottom of the mountain and then infiltrating through the mountain flanks. We distinguish between diffuse recharge (RDF) and linear recharge (RLF). The RDF is a direct infiltration of rainwater. The RFL is the infiltration that occurs along streams and creeks that drain the mountains and hills surrounding the aquifer. Thus, mountain front recharge (MFR) is the sum of the previous two and can be expressed as (Figure 1):

$$MFR = RLF + RDF \tag{4}$$

Linear recharge is calculated using equation (5), which considers that the water runoff generated in the upper parts of the mountains flows on the surface to the mountain flanks[4].

$$\frac{\overline{R}}{\overline{P}} = 2\left(\frac{h_r}{\overline{h_s}}\right)^{1/2} K_1\left(2\left(\frac{h_r}{\overline{h_s}}\right)^{1/2}\right) \tag{5}$$

Where $\overline{R}$ is the average annual runoff, $\overline{P}$ is the average annual rainfall, $h_r$ is the effective initial abstraction, $\overline{h_s}$ is the height of average rain events, and $K_1[]$ is the modified Bessel function of first order.

Equation (5) is represented in Figure 2 for selected values, $\overline{h_s}$ it is estimated in practice from the daily record of precipitation assuming that there is a single rain event per day.

Initial abstraction, $h_r$, was taken as 20 mm, which is a typical value for areas with low vegetation of xerophytic semi-arid areas[4]. The average height of the rain events, $\overline{h_s}$, was calculated from daily records of precipitation from the weather stations. The ratio of precipitation/runoff is determined using equation (5), which multiplied by the average annual precipitaion and by the mountainous area gives the volume that drains to the mountain front.

The rate of recharge by infiltration along ephemeral in the mountains and basins providence, is 30% of the flow of runoff[5][6].

As for the RDF, according to the method of Maxey-Eaking, is estimated as 15% of the average annual precipitation for rainfall values between 381 to 508 mm/*year*[7]. This high percentage is in agreement with more recent studies[8]. Then, the RDF is equal to 15% of the average annual precipitation falling on the mountain front area.

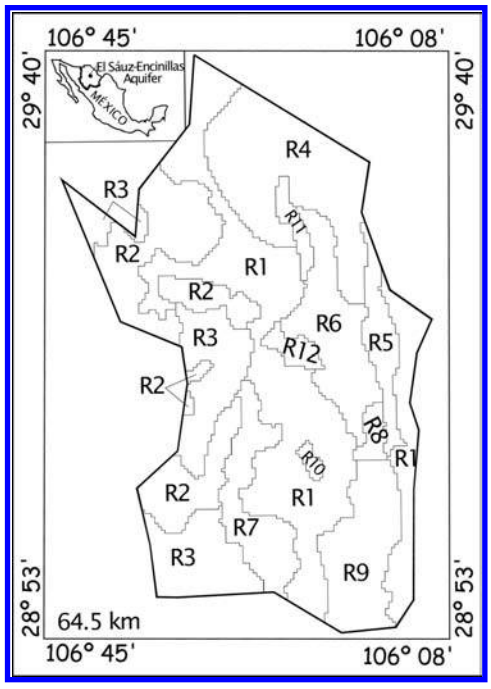


Figure 3. Zoning diffuse recharge.

Table 1. Values of recharge obtain through PEST.

| Zonas de recarga | Recarga (mm/a) |
|---|---|
| R1 | 31.7 |
| R2 | 26.5 |
| R3 | 15.2 |
| R4 | 24 |
| R5 | 0 |
| R6 | 5 |
| R7 | 15.7 |
| R8 | 6.3 |
| R9 | 44.9 |
| R10 | 4.3 |
| R11 | 24.9 |
| R12 | 26.3 |

#### 2.1.2 *Recharge in the valley estimation*

Diffuse recharge in the valley can be by rainfall and irrigation return. Diffuse recharge from direct precipitation in the valley (RV) was calculated using the water balance equation (equation 1), where P = 388 mm, T = 15.5°C, and L = 873.7, and ETR = 370.4 mm, resulting in a direct recharge by precipitation on the surface of the valley of 17.6 mm/year.

The recharge by irrigation returns is highly uncertain. We have used a value equal to 30% of the extractions by agricultural pumping, a percentage close to that reported by the Arizona Water Commission for many agricultural areas of their state[9]. Extraction pumps for agricultural use in the aquifer El Sáuz-Encinillas is 110.2 $hm^3/year$.

### 2.2 *Estimation of recharge using an aquifer model*

The groundwater flow model MODFLOW was used to simulated regional El Sáuz-Encinillas aquifer. The active area of model is 2743 $km^2$ and is bounded by latitudes 3'194,500 N and 3'283,000 N and by longitudes 330,000 E and 399,500 E. The groundwater flow problem was resolved using a finite difference grid consisting of 177 rows and 139 columns of 500 m square cells. Figure 1, display the domain of model.

Recharge values were estimated by model calibration for transient conditions between years 1978 and 2008 with 880 observations of hydraulic heads. The parameters estimated in the calibration process include the hydraulic conductivity, storage parameters and recharge zones. Figure 3 illustrates the spatial distribution of recharge, defined into 12 zones. The inverse problem was solved combining trial and error and automatic calibration. The automatic calibration was performance using the PEST code [10]. The prior estimates for each recharge zone obtained from the balance water equation were used as initial values for each zone in the calibration.

## 3 RESULTS AND DISCUSSION

Average annual rainfall in the area of the mountain aquifer El Sáuz-Encinillas is $P = 531$ mm, mean annual temperature at 13.8°C, the yield of the watershed is 77 mm which corresponds to a volume of $Y = 72.9\ hm^3/year$. The average height of the rain events, $\overline{h}_s$, is 7.5 mm. The ratio of precipitation to runoff resulted in 0.096, i.e. 9.6% of average annual precipitation in the mountains drains to the mountain front, it corresponds to a volume of 48.3 $hm^3$/year, from this runoff we obtain RLF as 14.5 $hm^3$/year and 9.9 for RDF. Therefore, mountain front recharge (MFR) is equal to 24.4 $hm^3/year$. Recharge in the valley on direct precipitation is RV = 28.6 $hm^3/year$, and recharge for the return of irrigation resulted in RRR = 33.1 $hm^3/year$. Therefore the total recharge (RT), using a balance approach to El Sáuz-Encinillas aquifer is 86.1 $hm^3$/year.

Figure 3 and Table 1 show the different types of vegetation and recharge zones (mm/year), estimated using PEST and MODFLOW. In this case, the recharges from the mountain area, the mountain front and the valley are 21.4, 10.3 and 37.7 $hm^3$/year, respectively. Therefore, the total estimated recharge calculated using numerical models was of 69.4 $hm^3$/year.

The estimation of recharge in the mountain area and mountain front using hydroclimatic equation resulted in 24.4 $hm^3$/year, while in the case of numerical model this recharge result of 31.7 $hm^3$/year. In the case of recharge that occur in the valley, recharge estimated through the hydroclimatic model is 61.7 $hm^3$/year, and numerical model calculated a value of 37.3 model $hm^3$/yaer. We observe an important difference between the results from both models.

## 4 CONCLUSIONS

Two models were developed to estimate the net recharge to a regional aquifer. The first model is a hydroclimatic equation and the second is a groundwater flow model. The net recharge was divided into recharge in the mountain area, in the mountain front

and diffuse recharge in the valley area. Model results represented 8% and 6.5% of the average precipitation in the watershed, respectively.

Yet, we note that the results obtained are an approximation based on the information available of precipitation and thereby further analysis is needed.

## ACKNOWLEDGMENTS

The authors express their thanks to the Program for Faculty Improvement (PROMEP) of the Secretary of Public Education México, for the partial funding of this study. We also extend our appreciation to Oscar Raul Herrera Lagunas, director of the Faculty of Engineering of the Autonomous University of Chihuahua for their personal support.

## REFERENCES

[1] Chávez, A., S. Sorooshian, and S.N. Davis. (1994), Estimation of mountain front recharge to regional aquifers: 1. Development of an analytical hydroclimatic model, Water Resources Research, 30(7), 2157–2167.

[2] Pinales, A., L. Villalba, M. Royo, B. Aguirre, R. Chávez, R. de la Garza, and G. Llerar. (2008), Disminución del error en calibración y predicción de modelos hidrodinámicos, caso de aplicación: acuífero El Sáuz - Encinillas. PROMEP/103./07/3577. Posgrado en Hidrología Subterránea, Chihuahua, Chihuahua, México.

[3] Rantz, S. E. and T. E. Eakin. (1971), A summary of methods for the collection and analysis of basic hydrologic data for arid regions. U.S. Geological Survey. California, USA.

[4] Chávez, A., S. Sorooshian, and S.N. Davis. (1994), Estimation of mountain front recharge to regional aquifers: 2. A maximum likelihood approach incorporating prior information, Water Resources Research, 30(7), 2169–2181.

[5] Burkham, D.E. (1970), A method for relating infiltration rates to streamflow rates in perched streams, U.S. Geological Survey Professional Paper 700-D, p. D266–D271.

[6] Goodrich, D. C., D. G. Williams, C. L. Unkrich, R. L. Scott, K. Hultine, D. R. Pool, A. Coes and J. Hogan. (2003), Multiple approaches to estimating ephemeral channel recharge. Proceedings First Interagency Conference on Research in the Watersheds. Benson, AZ., pp. 118–124.

[7] Maxey, G. B., and T. B. Eakin. (1949), Ground water in White River Valley, White Pine, Nye, and Lincoln counties, Nevada. State of Nevada, Office of the State Engineer, Water Resources Bulletin no. 8.

[8] Hilton, J., and A. C. Lewis, (2007), Estimating recharge in New Mexico water planning regions. Ground Water Summit, Albuquerque, New México.

[9] Arizona Water Commission. (1975), Phase 1, Arizona State Water Plan: Inventory of resources and uses, Phoenix, AZ, U.S.A., 224 p.

[10] Doherty, J. (2001), PEST-ASP Users' manual. Watermark Numerical Computing, Brisbane, Australia.

*Environmental Hydraulics – López-Jiménez et al (eds)*
*© 2010 Taylor & Francis Group, London, ISBN 978-0-415-56697-1*

# Radium presence on spring water from San Diego De Alcala, Chihuahua, México

Lourdes Villalba
*Facultad de Ingeniería, Universidad Autónoma de Chihuahua, Chihuahua, México*

Luis Colmenero
*Instituto Tecnológico de Chihuahua II (ITECH II), Chihuahua, México*

Guillermo Manjon
*Departamento de Física Aplicada I. E.U.I.T.A, Universidad de Sevilla, Sevilla, Sevilla, Spain*
*Departamento de Física Aplicada II. E.T.S.A, Sevilla, Spain (FAMN)*

Rafael Chávez, Miguel Royo, Adan Pinales, Benito Aguirre & Miguel Royo-León
*Facultad de Ingeniería. Universidad Autónoma de Chihuahua, Chihuahua, México*

Fernando Mireles & Ignacio Dávila
*Centro Regional de Estudios Nucleares, Universidad Autónoma de Zacatecas, Zacatecas, México*

ABSTRACT: The San Diego de Alcala (SDA) thermal springs, are situated toward the eastern margin of an extensive tectonic valley, filled by a great thickness of alluvial sediments from the Tertiary-Quaternary. The valley is limited by mountain ranges mainly formed by Tertiary rhyolitic volcanic rocks that lie over Mesozoic limestone. In this paper we report radium concentrations in samples collected from the SDA springs water. The obtained results are above the maximum permissible levels for radioactivity in water, recommended by the Official Mexican Norm NOM-127-SSA1-1994 and by the USEPA.

*Keywords*: radium, spring water, Chihuahua, México.

## 1 INTRODUCTION

The geothermic studies on thermal springs in Mexico have focused preferently towards evaluating their potential for electricity generation. Nevertheless, springs have recently acquired an unusual notoriety on the tourist-therapeutic field, as shown by the development of many thermal water spas in different points of the Mexican Volcanic Belt[1].

The state of Chihuahua has 34 geothermal zones [2], being the spring at San Diego de Alcala (SDA) one of the more visited because of the thermal baths used regularly as therapeutics treatments for several illness of the motor system, dermatological problems, and other treatments based on ingesting mineral water. It is important to point that spring water contains a great amount of chemical compounds, even radioactive elements. These elements and other compounds, found on the rocks, are dissolved and carried by water when it flows from the interior to Earth's surface [3].

Studies realized around the world have determined that the majority of the spring waters have high concentrations of Radium [4]. It comes from the disintegration of Uranium or Thorium isotopes and forms part of the so called natural disintegration series; Radium is generated from disintegration of Uranium and Thorium, which are present in the majority of rocks, soil and water. Radium is considered one of the most important radionuclides from all isotopes, because it has chemical properties similar to Calcium, which is absorbed in the bloodstream and distributed to the soft tissues and bones. When deposited on bone, Radium substitutes Calcium, which triggers the risk of developing osseous cancer [4].

## 2 MATERIALS AND METHODS

### 2.1 *Sample recollection – sampling*

Eight spring water samples where collected during August (boreal summer) at SDA, in the entrance of the thermal baths. The amount of Radium was determined by these methods: four samples by means of (electreto) ion chamber, three by the radiochemical extraction procedure using liquid scintillation counting (LSC), and the last one was sent to the Department of Physics of the Universidad de Sevilla, España to determine Radium with a LB770 proportional gas flow detector for inter comparing results.

Conductivity, temperature and total dissolved solids where determined at the moment of the sampling. The samples presented similar conductivity and TDS values of 200 μs/cm and 670 ppm respectively. The temperature values ranged from 46 to 48°C.

A chemical analysis of the samples was done to determine the concentrations of the elements Ba, Ca, Mg, K, Mn and Na. Table 1 shows the average of the concentrations on mg/l of these elements in the water of San Diego de Alcalá's springs.

### 2.2 *E-PERM Electret Ion Chamber*

The determination of the amount of Radium on water consisted on taking a 67 ml sample from the SDA spring, proceeding with the elimination of Radon by passing it through a constant air flow for one hour. Once the water sample was free of Radon, the method of Electret Ion Chamber to measure the Radon dissolved on water, as described by [5].

Table 1. Average concentration (mg/l) on spring water samples from San Diego de Alcala.

| Element | Average (mg/1) |
|---|---|
| Ba | <2,0 |
| Ca | 35,76 |
| Mg | 8,09 |
| K | 1,69 |
| Mn | <0,1 |
| Na | 195,12 |

The sample was exposed during a 5 days period. Under these conditions, the Radon content generated when reaching radioactive equilibrium is the same as the amount of Radium found in the sample.

The specific activity of the Radium obtained from the spring water samples from SDA was calculated with the following equation:

$$A_{Ra}(Bq/l) = (A_{Rn}) * C_1 * C_2 \quad (1)$$

Where: $A_{Rn}$ = Specific activity for Radon, determined by the equation (2):

$$A_{Rn}(Bq/l) = \left[(V_i \quad V_f)/FC * TA\right] \quad (2)$$

Where: $V_i$ is the starting voltage (volts) of the electret, $V_f$ is the final voltage (volts) of the electret measured after the 5 day exposition time, FC is the calibration factor ($FC = 1.6978 + 5.742 \times 10^{-4}[(Vi + Vf)/2]$), TA is the time of exposure of the sample in days, C is the equivalence of the gamma radiation dose (1 μR/h = 0.087 pCi/L), M is the dose of environmental gamma radiation from the lab where the Radium determination was done (0.5 μR/h). $C_1$ is the time since the Radon emanation until the activity recount, which is calculated by equation (3):

$$C_1 = e^{\lambda T} = e^{0.1814\,TD} \quad (3)$$

λ is the semi disintegration period of $^{222}$Rn in days, TD is the time in seconds until the sample is placed on the electrets ionization chambers method [4], until the beginning of the activity recount. $C_2$ is the time during the activity recount, equation (4):

$$C_2 = 55.55 * \lambda T / \left(1 - e^{\lambda T}\right) = 55.55 * 0.1814 * TA / \left(1 \quad e^{\,0.1814\,TA}\right) \quad (4)$$

TA is the time in days in which the analysis takes place.

### 2.3 *Liquid Scintillation Counting*

Five liters of water where taken on a polyethylene container, acidified to a pH of 2 with concentrated nitric acid, evaporated one liter and proceeding with the radiochemical method for separation of Radium isotopes [6].

This procedure is based on using $BaCl_2$ as carrier[7], and dividing in two parts, the first part of the methods consists on the precipitation of Radium isotopes in the form of sulfates found in the sample due to the addition of $Ba^{+2}$. This precipitate is deposited on a Millipore filter of 47 mm diameter and 0.4 mm previously weighted. The second part of the method consists on the dissolution of the precipitate obtained on the filter adding NH4OH, adding also EDTA to obtain a pH between 8 and 9, then rinsing and shaking vigorously until the precipitate is completely dissolved[8]. The resulting mixture is evaporated until 7 ml. Finally, the solution is placed on a glass vial of 20 ml with low potassium content and adding the liquid scintillation cocktail Optiphase Hisafe (EG&G Wallac) until filling the vial completely. Mix vigorously until a homogeneous mix is obtained. The measurement was realized on a Thiathler Hidex portable liquid scintillation detector for a 60 minute period.

To the quantitative analysis a $^{226}$Ra prepared reference solution was used, based on the standard reference material SRM 4965 certified by NIST in the United States. This was mixed with Optiphase Hisafe resulting an activity of 7.864 ($\sigma = 0.5$ %) Bq. The presence of $^{222}$Rn, $^{218}$Po and $^{214}$Po in equilibrium with the $^{226}$Ra was considered to obtain the efficiency of alpha counting, whose value was $\varepsilon = 0.68$.

The specific activity of the extracted Radium from the spring water samples at SDA was determined with equation (5):

$$A_{Ra}(Bq/l) = \frac{cps\ \alpha}{4\,t\,V\,\varepsilon} \quad (5)$$

Where V is the volume in liters of the water samples, t is the counting time and 4 is the disintegration factor considering radioactive equilibrium. On each measuring section the alpha counting was determined on a target by means of a vial with Optiphase Hisafe cocktail in pure state. The statistic relation obtained for the Radium activity was of 5%.

## 3 RESULTS AND DISCUSSION

The results obtained by the applied methods to determine the specific activity of Radium (Bq/l) on the spring water samples at SDA are on Table 2.

Table 2. Results of the radio activities (Bq/l) in samples of Water of the Spring SDA.

| Clave | Applied method | Radium concentrations (Bq\l) | Standard deviation |
|---|---|---|---|
| 1 | Electreto | 5.55 | 0.67 |
| 2 | Electreto | 5.61 | 0.67 |
| 3 | Electreto | 5.27 | 0.63 |
| 4 | Electreto | 6 | 0.72 |
| 5 | LSC | 5.83 | 0.85 |
| 6 | LSC | 6.12 | 0.54 |
| 7 | LSC | 5.97 | 0.52 |

The four samples analyzed by the ionization chambers method gave a Radium average concentration of $5.6 \pm 0.3$ Bq/l while the samples analyzed by Radium radiochemical extraction using liquid scintillation had an average value of $5.9 \pm 0.6$ Bq/l. The results for the sample sent to Universidad de Sevilla, España, as inter comparison, had a value of $5.6 \pm 0.4$ Bq/l. The averages show us the Radium content present of the spring water of SDA.

On some springs considered as radioactive, the reported Radium concentrations happen to be minor than those found on the SDA springs, such as the springs at Tuwa, India, with values of 0.4–0.9 Bq/l. In other cases, such as some springs at Iran, concentrations as high as 146 Bq/l [9], have been found; this value exceeds by far the values found at SDA. So, because of the average values obtained, we can think that SDA springs could be considered for medium radioactivity [9],[6].

Because the possible origin of the spring water from SDA could be infiltration of meteoric waters on the recharge zones placed in the adjacent ranges, which when descending to deeper levels through a fractures or faults systems, increase their temperature by means of geothermic gradient and by the presence of a possible geothermal source and residual heat of magmatic bodies placed during the tectonic distention period, facilitating the high temperatures and the dissolution of radioactive elements such as Radium [6].

Considering the spring water chemical analysis results; those compiled from previous works [11], [12], and those obtained for this study (Table 1); the water is classified as mixed sodic bicarbonated, with important contents of sulfates and chlorides, with values from 670 to 900 ppm of total dissolved solids.

Also taking into account, from the contents of Ca and Na can be inferred that this spring ground water has flowed in the deep through a basement made by a majority of carbonated rocks and that the sedimentary sequences must contain evaporitic members. It is also considered that the filling alluvial deposits of the valley, which rest over this basement, can contribute in the increase of the STD that has already been deposited under highly evaporitic – desertic conditions. It's been suggested that when bicarbonated groundwater surpasses the 600 ppm of STD, it has already gone through evaporites, mainly gypsum[13].

To support the latter comment, it must be noted that at a short distance NE from the thermal springs area is found the San Diego range, compound by an important sequence of calcareous sedimentary rocks of Cretaceous age, correlated with similar sequences which appear in nearer localities, like the ones exposed on the zone of the *El Granero* dam ($\pm$ 38 km NE from the area of study) where the base of the calcareous sequence is compound by great gypsum layers thickness, correspondent to the *Las Vigas* and *Cuchillo* formations, deposited on mixed or transition environments. Considering that to a certain point they constitute part of the basement in the area of study, it's clear that the groundwater which proceeds from the recharge zone at San Diego range has gone through deeply through this sequence, which has originated the high STD contents and other elements like Ca, Na and Mg[14]. Castany [15], on this aspect, points that spring water which has gone through calcareous grounds show the following amounts: Ca = 47.5 ppm, Mg = 13.9 ppm, $HCO_3$ = 183 ppm, and a pH of 7.37, which are very similar to the values obtained from the spring water samples at SDA; and of course, these contents increase when the calcareous sequence is intercalated by gypsum and halite stratum.

Spring water's high temperature comes normally from the geothermic gradient when infiltration water flows at increasing depths. This way, temperatures measured on the surface, at a well's mouth or on a spring, reflect the temperature at the minimum flowing depth[15], [16]. This means that the minimum flowing depth temperature can be estimated as an approximation, taking the water temperature at the mouth of a well or in a spring, subtract the average isotherm temperature of the region and dividing the result with the average geothermic gradient which, for practical means, is considered 3°C/100 m. If considered that thermal spring water at SDA has an average temperature of 47°C and the annual average isotherm of the area of study is approximately 19.4°C, we have that: (47°C – 19.4°C)/(3°C/100 m) = 920 m. Of course this depth is approximate. This result can be seen affected by other geological or even chemical factors generated during the movement and interaction between groundwater and the rocky environment.

## 4 CONCLUSIONS

The obtained results for Radium concentrations range between 5.6 and 5.9 Bq/l, which is above the maximum allowable limit for radioactivity in water, implemented in the Official Mexican Norm NOM-127-SSA1-1994 of 0.56 Bq/l of $\alpha$ and $\beta$ totals, and the North American norm by EPA for Radium of 0.188 Bq/l[17].

These values are relevant due to the usage of the water as part of therapeutic treatments (thermal baths) to cure dermatological and motor illnesses which combine water ingest. This is important, because together with the Radium ingest is the potential effects of Radon gas inhalation from the water and breath on closed rooms (badly ventilated) where there are small pools for thermal baths.

As a health measure it must be avoided to ingest this water, because Radium deposits on soft tissues and bones, and triggers cancer risk by this mean.

About the Radium concentration on spring water at SDA there must be considered several statements supported by the geological-geo hydrological context.

Radium acquisition happens when thermal waters flow through the geological medium, which constitutes the basement and/or the upper levels of the alluvial filling of the valley, where ancient calcrete horizons could have fixed the radioactive elements, in areas such as the radiometric anomalies at *Chilicote* and *Los Pozos*[17].

The water flow can pick up radioactive elements of undiscovered or discovered mineralized zones on the environment close to the SDA valley, to mention an example of these, the anomalous areas of the *Santa Eulalia* and *La Gloria* ranges.

The tectonic valley where the SDA area is found forms part of a uraniferous mineralization province already identified with exploited deposits found NW of SDA ($\pm$ 60 km), on the superior part of the geohydrological basin, on the *Peña Blanca* and *Gómez* ranges.

ACKNOWLEDGEMENTS

The authors appreciate the collaboration and help of M.I. Oscar Raul Herrera Lagunas director of the Facultad de Ingenieria (UACH), for the accomplishment of this investigation.

REFERENCES

[1] Pantoja-Alor, J. y Gómez-Caballero, A. (2000), Géiseres y manantiales termales en México. Ciencias, No. 59, 23–25.
[2] Prol-Ledesma, R. M. and Juárez, M. G. (1986), Geothermal map of Mexico, Journal of Volcanology and Geothermal Research, 28, 351–362.
[3] Lawrie, W.C, Desmond, J.A, Spence, D., Anderson, S. and Edmondson, C. (2000), Determination of radium-226 in environmental and personal monitoring samples, Applied Radiation and Isotopes, 53, 133–137.
[4] Oliveira, J., Mazzilli, P., B., Nisti, B. M., and Sampa H.O M. (2002), Natural radioactivity in a Brazilian termal spa, *Memoria del Congreso Internacional de Radiactividad en el Medio Ambiente*, Monaco.
[5] Kotrappa, P. and Jester, W.A. (1993), Electret ion chamber radon monitor measure dissolvent 222 Rn in water, Health Physics Society, No. 64, 397–405.
[6] Villalba, M. L. (2003), *Análisis y dosimetría de radionúclidos en agua del Estado de Chihuahua,* Tesis doctoral, CIMAV, Chihuahua, México.
[7] Moron, M.C., García Tenorio, R., García-Montaño, E., García Leon, M. and Madurga, G. (1986), An Easy Method for the Determination of Ra Isotopes and Actinide Alpha Emitters From the Same Water Sample. Int. J. Rad. Appl. Instrum. Part A 37, 383–390.
[8] Manjón G, Vioque I., Moreno H., García Tenorio R and García Leon M. (1997), Determination of Ra226 y Ra 224 in drinking water by liquid scintillation counting. Appl. Radiat. Isot. Vol. 48 No. 4, 535–540.
[9] Sohrabi, M, Beitollahi M, Hafezi S, Asefi M and Bolourch M. (1998), Effective dose to the public from Ra 226 in drinking water supplies of Iran. Health Physics Society. Vol. 77. No. 2, 150–153.
[10] Segovia, N., Tamez E., Peña, P., Carrillo, J., Acosta, E., Armienta, M.A., iturbe J.L. (1999). Groundwater flow system in the Valley of Toluca, Mexico: An assay of natural radionuclide specific activities. Applied Radiation and Isotopes, Vol. 50, 589–598.
[11] Graniel-Castro, E. H. (1989), *Estudio geohidrológico del área de San Diego de Alcalá en el Estado de Chihuahua*, Tesis de maestría, Facultad de Ingeniería, U.A.CH., Chihuahua, México.
[12] Quijano,L. J. L. (1983), Estudio Isotópico del agua subterránea en la región Chihuahua-Aldama-Delicias, Bol. Investigación Geohidrológica, No. 2, Facultad de Ingeniería, U.A.CH., pp. 8–17.
[13] Mazor, E. (1991), *Applied Chemical and isotopic groundwater hydrology*, Halsted Press a division of John Wiley & Sons, New York.
[14] Lee, K. and Fetter, C. W. (1994), Hydrogeology, Laboratory Manual, Prentice -Hall, New Jersey.
[15] Castany, G. (1971), *Tratado práctico de las aguas subterráneas. Primera parte. Elementos de Hidrología de superficie.* Omega. Barcelona, 672 pp.
[16] Bebout, D. G. and Gutierrez, D. R. (1981), Geopressured geothermal resources in Texas and Louisiana, Geological Constraint, Proc. 5th. *Conf. Geopressured Geothermal Energy,* Baton Rouge, Louisiana.
[17] EPA Environmental Protection Agency. (2006), Executive Summary Es. 1 Legislative Mandate. Summary of High-End Inhalation Cancer Risk.
[18] GEOCA-CNEN.(1968), *Informe de avance mensual de exploración aereoradiométrica en el Valle de Aldama, Chih.*

*Environmental Hydraulics – López-Jiménez et al (eds)*
*© 2010 Taylor & Francis Group, London, ISBN 978-0-415-56697-1*

# Comparison of evolutionary algorithms for design of sewer systems

Daniel Mora-Meliá, Pedro L. Iglesias-Rey, Vicente S. Fuertes-Miquel &
Francisco J. Martinez-Solano
*Centro Multidisciplinar de Modelación de Fuidos, Universidad Politécnica de Valencia, Valencia, España*

ABSTRACT: The evolutionary algorithms are methods of search of solutions that are based in the natural beginning of the evolution. Inside the evolutionary algorithms, we can find both the AG (Genetic Algorithms) and PSO (Particle Swarm Optimization), being one of many applications that present these algorithms the design of sewer systems.

The work presents the application of these methods to the design of sewer systems. The design of these networks with evolutionary algorithms is of great interest if there is had present that allows us to choose a solution between the different alternatives that verify the conditions imposed for the pipes and the slope of the area. Finally, we realize an analysis of the obtained results, comparing both methods and extracting the possible advantages and disadvantages of applying each of these methods in the design of water sewer systems.

*Keywords*: Genetic Algorithms, Particle Swarm Optimization, Sewer systems, Water systems design

## 1 INTRODUCTION

The design of sewer systems is extremely complex. It is well-known that when the diameters of the conductions are chosen as decision variables, the restrictions are implied functions of these variables of decision, so the space's region of solutions is a no convex type and the objective function becomes multimodal. The application of a stochastic technique allows the search beyond these local minimums, which generally ample the field search and with it the capacity to obtain better solutions.

This work shows a comparison between two evolutionary algorithms applied to optimal design of water sewer systems: Genetic Algorithms (GA) and Particle Swarm Optimization (PSO). The aim is to minimize the necessary costs of investment for the implantation of a certain system, starting from the topological layout and the contribution of each junction.

Genetics algorithms (GA) are a searching method based on Darwin's evolution theory (Holland[1]). It works identically to the evolution of a population that is put under similar random actions to which they act in the biological evolution (mutations and genetic recombination). The individuals best adapted survive and the less ones are discarded, based in some stablished criteria.

PSO was initially proposed by J. Kennedy and R. Eberhart[2]. This technique is based on the behavior of the swarms (populations) of birds (particles) when they migrate to destinies unknown in search of food. The swarms are particle populations that represent potential solutions of a certain problem. The search towards new solutions is guided reason why we could denominate "social pressure", that is to say, one is based on the knowledge of the other individuals. The members of the swarm of birds communicate to each other where to direct the search, emulating the exploration techniques that the insects or birds use.

## 2 METHODOLOGY

Traditionally, GA and PSO have been methods adapted for problems formulated in binary variables but not advisable for other searching methods. However, in the present work a formulation of the problem is introduced based on a numerical codification, non binary, of the solution.

In the techniques based on evolutionary algorithms, it is necessary to have a discrete set of possible solutions to solve the optimization problem (chromosomes in GA, birds in PSO). This set of solutions is what also forms a generic chain $X^i$ constituted by an equal number of variables to the number of decision variables ($N_{VD}$), so that generic chain i of a P population is defined as a vector of numerical values.

$$X^i = \left\{X_1^i, X_2^i, \ldots, X_{N_{VD}}^i\right\} \tag{1}$$

In Genetic Algorithms each element $X^i$ is a generic chain that codifies in each one of the variables of the element the value of the diameters or slopes of the different conductions. In Particle Swarm Optimization each bird has coordinates that codify the solution that the particle represents. These coordinates are the values of the diameters and slopes.

The characteristic that measures "kindness" or capacity of a certain chain's survival regarding the others is known like aptitude. The aptitude of a certain generic chain is identified through the value that adopts the objective function for the codified solution. The objective function proposed for design of sewer systems is defined as:

$$\begin{aligned} F(X^i) = &\sum_{j=1}^{N_C} C_j\left(X^i\right)\cdot L_j + \lambda_v \cdot \sum_{k=1}^{N_C} \delta_{k,v_{máx}} \cdot \left|v_{k,s} - v_{máx;k}\right| + \\ &+\lambda_v \cdot \sum_{k=1}^{N_C} \delta_{k,v_{mín}} \cdot \left|v_{k,s} - v_{mín;k}\right| + \lambda_y \cdot \sum_{k=1}^{N_P} \delta_{k,s} \cdot \left|y_{k,s} - y_{máx;k}\right| + \lambda_{top} \end{aligned} \tag{2}$$

The objective function has two differentiated parts. First it is relative to the cost associated with the installation and the construction of the cleaning system. We calculate this cost from the unit cost Cj associated to the pipe j of the $N_C$ conductions

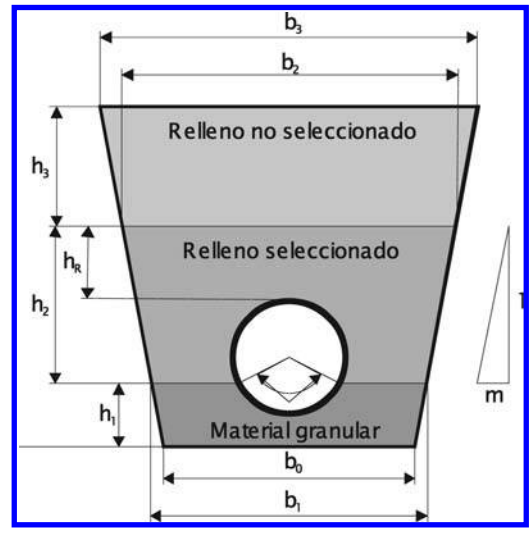


Figure 1. Standard trench used for optimization.

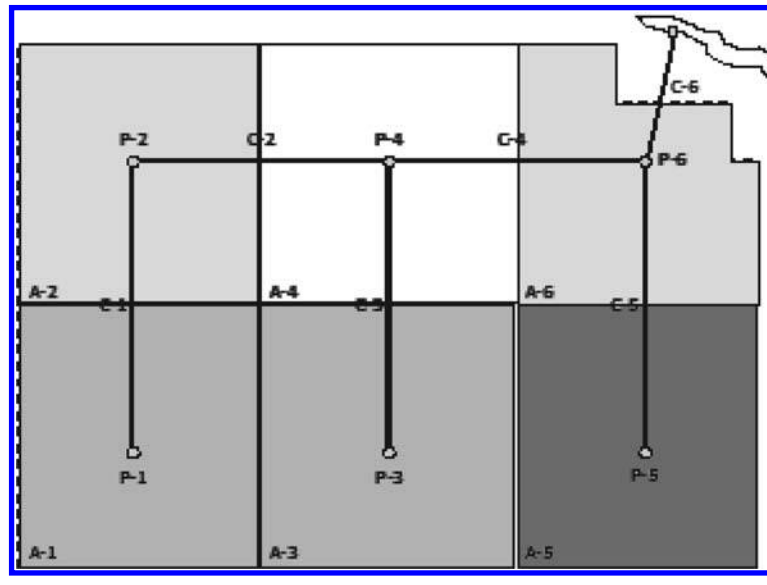


Figure 2. Study case. Example Network.

that there are. This cost not only includes the costs of the pipe, but also the costs associated to the installation of the same, that directly are related to the depths of excavation and slopes of the terrain. In order to introduce these costs we have used a standard trench (to see figure 1), in that each parameter is directly related to the diameter of the pipe and the average depth of the terrain, obtained like the semisum of the depths in extreme manholes of the pipe.

The second part of the objective function represents the penalties that settle down when some of the restrictions is not fulfilled. Thus three penalties are considered: $\lambda_v$ for the excess or defect of speed, $\lambda_y$ for the excess of depth, and $\lambda_{top}$ for the cases in that solution $X^i$ is not compatible with the topology of the system. These penalties require the definition of a series of variables:

- $\delta_{k,x}$ is a function that adopts value 1 if a penalty of type x exists whereas it adopts value 0 in the case of not breaking this restriction. In the same way we considered the functions $\delta_{k,vmáx}$ for cases in which the maximum velocity is exceeded and $\delta_{k,y}$ for cases of excess of depth.
- $v_{max,k}$ is the maximum allowable velocity in the pipe k.
- $v_{min,k}$ is the minimum allowable velocity in the pipe k.
- $y_{max,k}$ is the maximum depth of conduit k.
- $N_C$ is the number of pipes.
- $N_P$ is the number of manholes.

## 3 CASE STUDY

The comparative analysis of the two analyzed techniques of optimization has been done on a basic network that in its simplified form consist of 6 pipes, 6 manholes and an outfall.

The reduced size of the network allows certain agility of calculation. A series of restrictions prevails, as maximum slope of the conduits, maximum and minimum velocity in the pipes and maximum filling degree of the conduits.

Table 1. Analysis of the results.

| | GA (205 075 €) | | PSO (203 921 €) | | |
|---|---|---|---|---|---|
| Tubo | D (mm) | S (‰) | D (mm) | S (‰) | Desv. s (%) |
| C-1 | 500 | 7.92 | 500 | 7.85 | 0.82 |
| C-2 | 600 | 7.42 | 600 | 7.25 | 2.19 |
| C-3 | 600 | 2.97 | 600 | 2.77 | 6.45 |
| C-4 | 800 | 7.42 | 800 | 7.13 | 3.93 |
| C-5 | 600 | 12.37 | 600 | 11.67 | 5.58 |
| C-6 | 1000 | 9.90 | 1000 | 11.20 | 13.16 |

Table 2. Number of iterations.

| Cost (€) | AG | PSO | Difference (%) |
|---|---|---|---|
| ≤205 075 € | 771 | 1669 | 216 |
| ≤207 125 € (+1%) | 656 | 1335 | 203 |
| ≤209 176 € (+2%) | – | 996 | – |
| ≤211 227 € (+3%) | – | 913 | – |
| ≤213 278 € (+4%) | 420 | 1209 | 288 |
| ≤215 328 € (+5%) | – | 874 | |

One of the main characteristics of this type of methods is that they work in a random way. The characteristics of the heuristic methods do not guarantee with certainty the obtaining of the optimal value of the system. For that reason the minimum value of obtained cost is analyzed. In the same way a "good solution" is defined with whose cost is over the minimum cost until in a 1%.

The comparative analysis of the two techniques of optimization was realised with more than 6000 different simulations with each one of the two methods. The results of the best solutions obtained with each one of the methods are in Table 1. Also in Table 2 is the average number of iterations used by each one of the methods.

Table 2 shows like in all the cases the number of iterations that needs the optimization PSO to find the final solution is more of the double which it needs GA. on the other hand, in both methods the number of iterations realised in each simulation is greater whichever better is the obtained result.

## 4 CONCLUSIONS

Of the analysis of the results with both methods it is possible to emphasize the following conclusions:

- The convergence towards feasible solutions is greater in the case of the GA. The GA practically find a solution in the 100% of the cases. On the other hand, in optimization PSO almost a 30% of the solutions do not converge towards a feasible solution.
- If we analyzed the solutions that converge to a feasible solution, optimization PSO owns a greater probability of obtaining a solution of smaller cost.
- Optimization PSO allows to design the slope of the terrain like a continuous variable. The GA only can work with discontinuous variables. For the design of sewer systems it is an advantage to be able to work with continuous variables.
- The number of iterations that need the GA to find the final solution is much smaller in average term than the one that needs optimization PSO.
- Really, both models seem valid for the water sewer systems. Maybe GA has greater speed and robustness, PSO seems to obtain better results in the cost of design.

## 5 ACKNOWLEDGEMENTS

This article has been possible inside the actions developed by the researchers of CMMF involved in the project "Integración de la caracterización dinámica de elementos y consumos en modelos de redes de abastecimiento de agua utilizando sistemas de información geográfica y algoritmos genéticos (CADAGIAS)". The number reference of the project is DPI2006-13113.

## REFERENCES

[1] Holland, J. (1992). *"Algoritmos Genéticos. Investigación y Ciencia". Septiembre 1992. 38–45*.

[2] J. Kennedy, R.C Eberhart (1995). "Particle swarm optimization" Proc. IEEE Internat. Conf. on Neural Networks, Perth, Australia, vol IV, IEEE Service Center, Piscataway, NJ, pp 1942–1948.

*Environmental Hydraulics – López-Jiménez et al (eds)*
*© 2010 Taylor & Francis Group, London, ISBN 978-0-415-56697-1*

# Application of the harmony search algorithm to water distribution networks design

Daniel Mora-Meliá, Pedro L. Iglesias-Rey, Gonzalo Lopez-Patiño & Vicente S. Fuertes-Miquel
*Centro Multidisciplinar de Modelación de Fuidos, Universidad Politécnica de Valencia, Valencia, España*

ABSTRACT: The meta-heuristic techniques are optimization methods that allow the search beyond local minimums, which extends in many occasions the search field, and therefore, the capacity to obtain good solutions. The Harmony Search (HS) is a heuristic technique of optimization used for water distribution networks design.

Initially, the work displays the results of the HS on a water network studied in the literature (network of Hanoi). The results show the kindness of the method. Also is made a statistical analysis of the obtained solutions. This analysis allows verifying the values of the harmony parameters more suitable for the proposed method. The second part analyzes the influence of harmony parameters in the velocity of the algorithm. The aim is to find the most suitable configuration of the problem, so that good solutions are obtained in the less time.

*Keywords*: Water distribution network, design, harmony search, IWEH09.

## 1 INTRODUCTION

The design of water distribution networks is extremely complex. It is well-known that when the diameters of the conductions are chosen as decision variables, the restrictions are implied functions of these variables of decision, so the space's region of solutions is a no convex type and the objective function becomes multimodal. Traditionally, water distribution network design, upgrade, or rehabilitation has been based on engineering judgement. Traditionally, water distribution network design, upgrade, or rehabilitation has been based on engineering judgement.

Howewer, in the last three decades a significant amount of research has focused on the optimal design of water distribution networks. Initially, researchers have used linear programming to optimize a design of a pipe network (Alperovits and Shamir[1]). Later studies applied nonlinear programming to the network design problems. Some examples are Su et al[9] that used non linear programming to optimize looped pipe networks or Lansey and Mays[4], whose model was able to simulate pumps, tanks and multiple loading cases.

The application of heuristic techniques of optimization allows the search beyond these local minimums, which generally ample the field search and with it the capacity to obtain better solutions. The evolutionary algorithms are methods of search of solutions that are based in the natural beginning of the evolution. Inside the evolutionary algorithms, we can find Genetic Algorithms (GA), Particle Swarm Optimization (PSO), Ant Colony, Harmony Search (HS) and so on.

Some investigators have compared these techniques to each other (Zecchin[10]), but it is difficult to say that one of them is clearly better than the others.

The Harmony Search Algorithm imitate the process of a band's improvisation searching the perfect state of "harmony" (Geem[2]). The Harmony Search has been applied successfully in many optimization problems (Lee[5]; Mahdavi[6]). In this case we apply the method to water distribution design, and the final solution will correspond to the combination of diameters that provides the smaller cost in a network. Previous works like those of Geem[2] demonstrate the utility of the method for this kind of problems.

In the same way, other authors have tried to do improvements in the original algorithm, increasing the efficiency in the search minimums or in the speed. For example, Omran and Mahdavi[8] present modifications on the original algorithm (Global-best HS). These modifications try to obtain a more efficient work of the algorithm in continuous and discreet problems.

The aim is to minimize the necessary costs of investment for the implantation of a certain system, starting from the topological layout and the demands and requirements of pressure in the nodes. This cost is associated to a goal function that will be evaluated in each algorithm iteration. Thus, each one of the possible diameters will represent a musical note and each one of the network conductions will be represented by an instrument. The combination of instruments and musical notes will provide a music sheet (solution) in each iteration.

Initially, the work show the kindness of HS method on the network of Hanoi. Also is made a statistical analysis of the obtained solutions. As it is a water network of important size and with a real layout, there is a wide range of solutions obtained with different models of design in the literature, which has allowed us to compare the results of the different models of design.

The statistical analysis of the solutions allows to optimize the HS parameters, so that we can establish the most suitable for the proposed method. A suitable combination of parameters not only provides better results in the cost of the network, but allows to make a smaller number of iterations until reaching the final solution. In this way the influence in the method of the parameters Harmony Memory Size (HMS), Harmony Memoy Considering Rate (HMCR) and Pitch Adjusting Rate is analyzed (PAR).

## 2 METHODOLOGY

Most of heuristic techniques are based on the imitation of natural processes. HS tries to imitate the improvisation process of a music band. The process consists of finding every time a better music sheet, which is represented by an objective function that there is to minimize. The notes of every musical instrument determine the quality of the music sheet and the value of the objective function is the combination from all the musical notes that represent values of the decision variables.

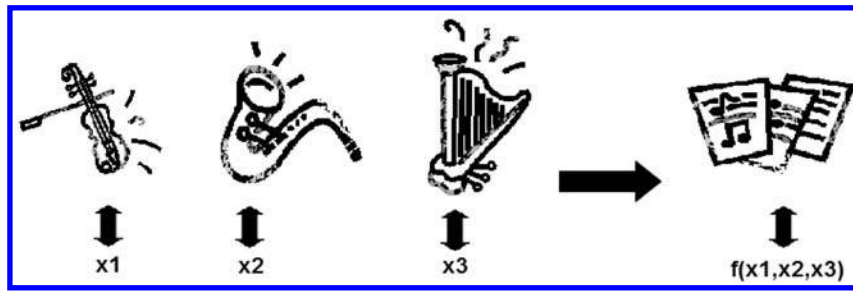


Figure 1. Composition of a music sheet.

The random character of the method does not guarantee a complete exploration of the space of solutions, nor supposes guarantee to reach a minimum of the objective function. However, the method offers a set of good solutions that try to improve.

In the method each one of the decision variables can have a rank of possible different solutions, which is represented with an alphanumerical variable (music note). The combination of these notes (variables of decision) composes a music sheet, that will be improved in the next iteration (to see figure 1). A music sheet represents a solution to the problem. This solution is constituted by a serial of notes that defines a unique solution of the optimization process.

In the design of water distribution networks, each gene is represented with a number or a letter, that identifies the diameter of each one of the lines. In this paper the only network components that are considered are the pipes, but it is possible incorporate elements as pumps, tanks, valves and reservoirs without invalidating the algorithms.

In order to solve the optimization problem it is necessary to have a discrete set of possible solutions (musical sheet). This set of musical sheets is what also forms the harmony memory size. In HS a generic music sheet X is constituted by an equal number of notes to the number of decision variables (NVD), so that generic sheet i of a memory is defined as a vector of numerical values.

$$X^i = \left\{X_1^i, X_2^i, \ldots, X_{N_{VD}}^i\right\}$$

The characteristic that measures "kindness" or capacity of a certain music sheet's survival regarding the others is known like aptitude. The aptitude of a certain generic sheet is identified through the value that adopts the objective function for the codified solution. In the case of the algorithm proposed for design and extension of distribution networks this objective function is defined as

$$F(X^i) = \sum_{j=1}^{N_{VD}} C_j\left(X_j^i\right) \quad L_j + \lambda \quad \sum_{s=1}^{N_s}\sum_{k=1}^{N_n} \delta_{k,s} \quad \left(H_{min,k} \quad H_{k,s}\right)$$

where Cj is the associated unit cost to the decision variable's value contained in link j of music sheet i; and Li is the length of conduction of pipe j. Moreover, they are NR imposed restrictions that must achieve the possible solutions of the problem. These restrictions have been including through a penalty in the total cost of the solution that later affects the aptitude of the music sheet. The restrictions that must be fulfilled are the derived ones to satisfy the restrictions with minimum pressure height (Hmin,k) in each node k. These restrictions must be verified in all the analyzed scenes NS, that usually are the on-speed operation of the system and its operation under the scene of failure of some of the conductions. The function penalty represents the difference between the head height of the node k in scene s (Hk,s) and the required minimum height (Hmin,k). In order to compute this penalty two variables are defined. One of them ($\delta$k,s) is a binary variable that adopts value 1 if Hk,s < Hmin,k, and it adopts null value in opposite case. The parameter $\lambda$ represents a weight function that establishes the penalty's value for not verifying the restrictions of minimum pressure in the nodes. Pressure is considered as a hard constraint, and $\lambda$ is big enough (107) for reject all solutions that violates the constraint.

The proposed method tries the evolution of a random population throught a parallelism similar to the improvisation process of a band in the search of a perfect music sheet. All the parameters of adjustment for HS will be specified from the beginning of the problem. For it an adjustment of three parameters of extreme importance is possible, as they are the harmony memory size (number of musical instruments), the Harmony Memory Considering Rate (HMCR) and the Pitch Adjustment Rate (PAR).

HS works with a sequential form. Thus, once given the value of the different parameters from optimization an assembly of scores is created of random way. Each one of these music sheets is composed by so many notes as variable of decision we have in the problem. A complete musical sheet provides a solution for the problem, with a certain value for the objective function.

The following iteration of the algorithm improvises a new music sheet Xi from the previous, considering HMCR and PAR. HMCR is the probability of choosing one value from the historic values stored in the harmony memory, and (1-HMCR) is the probability of randomly choosing one feasible value not limited to those stored in the harmony memory. An HMCR value of 1 is not recommended because of the possibility that the solution may be improved by values not stored in the harmony memory.

Every component of the new sheet is examined to determine whether it should be pitch-adjusted. This procedure uses the PAR parameter that sets the rate of adjustment for the note Xij. PAR is the probability of a note Xij changes it value. Thus, if the note is modified, the pitch adjust will be:

$$X_j^i \rightarrow X_j^i \pm \alpha$$

where based on the value of $\alpha$ the Xij note will increase ($\alpha = 1$) or will decrease ($\alpha = -1$).

This way, the harmony memory size will have to be enough in order to guarantee the diversity of solutions, and, in addition, it must grow with the number of music sheet's bits. The main problem that is generated when using high memories is that convergence time of the algorithm is bigger. Therefore it is necessary to reach a commitment solution depending on the approach of the problem.

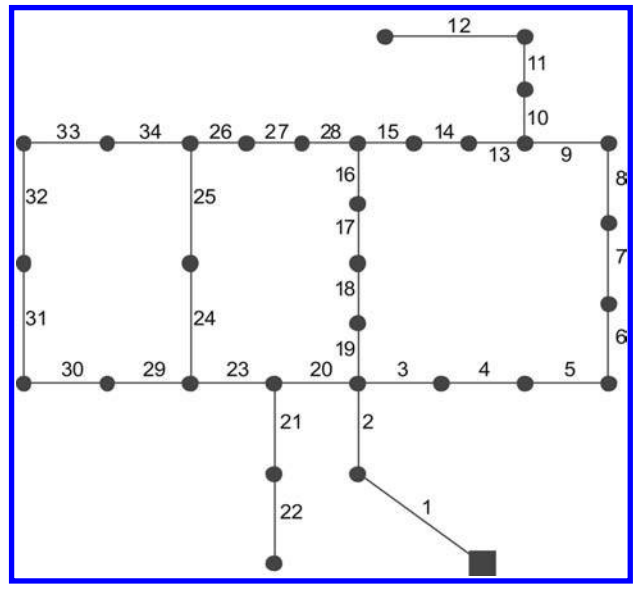


Figure 2. Network of Hanoi.

Table 1. Range of diameters used for the design of the water distribution network.

| | Original range | |
|---|---|---|
| N° Diameter | Diameter (mm) | Cost (um/m) |
| A | 304′8 | 45′73 |
| B | 406′4 | 70′40 |
| C | 508′0 | 98′39 |
| D | 609′6 | 129′33 |
| E | 762′0 | 180′75 |
| F | 1016′0 | 278′28 |

The following sections analyze the capacity of the proposed HS method to obtain equal or better solutions to the existing ones in the references. It has been analyzed the Hanoi network, determining the minimum cost of design them. Thus, working on the network of Hanoi, the influence of the different parameters has been analyzed on the final solution, dividing the work in two phases: First stage where the best combination of parameters in the obtaining of the minimum cost for the network is analyzed, and one second phase, where the influence of the parameters in the number of iterations is analyzed until reaching the final solution.

## 3 APPLICATION EXAMPLE

The analysis of the proposed model has been made on the network of Hanoi (to see Figure 4), proposed by Fujiwara and Khang (1990). As it is a water network of important size and with a real layout, there is a wide range of solutions obtained with different models of design in the bibliography, which has allowed us to compare the results of the different models of design.

One of the characteristics that contribute to define the optimal solution of the network is the range of diameters used. For the study we used the original range of the bibliography.

The table 2 shows the solution's variation obtained by some researchers, as well as its corresponding total cost.

If we rely on the obtained minimum value, we observe that the HS improves those of all his competitors but the one of Savic[2], in terms of the used heuristic method does not fulfill the pressure specifications. HS obtains like minimum cost 6.081 thousands of um. The rest of solutions that shows the table fulfills these specifications, consisting of which all the nodes have a pressure over 30 mca.

## 4 ANALYSIS OF THE RESULTS

One of the main characteristics of HS is that it works in a random way. The characteristics of the method do not guarantee with certainty the obtaining of the optimal value of the system. In addition, the obtained result can suffer sometimes certain variations. In order to analyze this randomness it is necessary to make statistical analyses that will study the influence that have the different parameters from the HS algorithm proposed in the solution of the analyzed network, with the purpose of optimizing them to increase the probability of obtaining the minimum.

In a first study, the harmony memory size, HMCR and PAR were modified were modified to study the influence of parameters. For it they have been made 54000 simulations altogether. For the calculation of these simulations we use a computer system in parallel with 23 computers AMD Duron to 1400 MHz and 128 MB of ram. The initial values are the recommended ones by

Table 2. Comparison of diameters (mm) obtained as solution for the network of Hanoi.

| | Bibliography solutions | | | Obtained solutions | | | |
|---|---|---|---|---|---|---|---|
| Líne | Matías[1] | Savic1[2] | Savic2[3] | Sol Genetic[4] | Sol PSO[5] | Sol annealing 2[6] | Sol HS[7] |
| 1 | 1016 | 1016 | 1016 | 1016 | 1016 | 1016 | 1016 |
| 2 | 1016 | 1016 | 1016 | 1016 | 1016 | 1016 | 1016 |
| 3 | 1016 | 1016 | 1016 | 1016 | 1016 | 1016 | 1016 |
| 4 | 1016 | 1016 | 1016 | 1016 | 1016 | 1016 | 1016 |
| 5 | 1016 | 1016 | 1016 | 1016 | 1016 | 1016 | 1016 |
| 6 | 1016 | 1016 | 1016 | 1016 | 1016 | 1016 | 1016 |
| 7 | 1016 | 1016 | 1016 | 1016 | 1016 | 1016 | 1016 |
| 8 | 1016 | 1016 | 1016 | 1016 | 1016 | 1016 | 1016 |
| 9 | 1016 | 762 | 1016 | 1016 | 1016 | 762 | 1016 |
| 10 | 762 | 762 | 762 | 762 | 762 | 762 | 762 |
| 11 | 609,6 | 762 | 609,6 | 609,6 | 609,6 | 762 | 609,6 |
| 12 | 609,6 | 609,6 | 609,6 | 609,6 | 609,6 | 609,6 | 609,6 |
| 13 | 508 | 406,4 | 508 | 508 | 508 | 406,4 | 508 |
| 14 | 406,4 | 406,4 | 406,4 | 406,4 | 406,4 | 406,4 | 406,4 |
| 15 | 304,8 | 304,8 | 304,8 | 304,8 | 304,8 | 304,8 | 304,8 |
| 16 | 304,8 | 406,4 | 304,8 | 304,8 | 304,8 | 304,8 | 304,8 |
| 17 | 406,4 | 508 | 406,4 | 406,4 | 406,4 | 406,4 | 406,4 |
| 18 | 609,6 | 609,6 | 508 | 609,6 | 609,6 | 609,6 | 609,6 |
| 19 | 609,6 | 609,6 | 508 | 508 | 508 | 508 | 508 |
| 20 | 1016 | 1016 | 1016 | 1016 | 1016 | 1016 | 1016 |
| 21 | 508 | 508 | 508 | 508 | 508 | 508 | 508 |
| 22 | 304,8 | 304,8 | 304,8 | 304,8 | 304,8 | 304,8 | 304,8 |
| 23 | 1016 | 1016 | 1016 | 1016 | 1016 | 1016 | 1016 |
| 24 | 762 | 762 | 762 | 762 | 762 | 762 | 762 |
| 25 | 762 | 762 | 762 | 762 | 762 | 762 | 762 |
| 26 | 508 | 508 | 508 | 508 | 508 | 609,6 | 508 |
| 27 | 304,8 | 304,8 | 304,8 | 304,8 | 304,8 | 406,4 | 304,8 |
| 28 | 304,8 | 304,8 | 304,8 | 304,8 | 304,8 | 304,8 | 304,8 |
| 29 | 406,4 | 406,4 | 406,4 | 406,4 | 406,4 | 406,4 | 406,4 |
| 30 | 304,8 | 406,4 | 406,4 | 304,8 | 304,8 | 406,4 | 304,8 |
| 31 | 304,8 | 304,8 | 304,8 | 304,8 | 304,8 | 304,8 | 304,8 |
| 32 | 406,4 | 304,8 | 304,8 | 406,4 | 406,4 | 406,4 | 406,4 |
| 33 | 406,4 | 406,4 | 406,4 | 406,4 | 406,4 | 406,4 | 406,4 |
| 34 | 609,6 | 508 | 508 | 609,6 | 609,6 | 609,6 | 609,6 |
| Coste (miles um) | 6.093 | 6.187 | 6.073 | 6.081 | 6.081 | 6.125 | 6.081 |

[1]Obtained solution by Matías[7](2003).
[2]Obtained solution by Savic y Walters (1997).
[3]Obtained solution by Savic (1997), no pressure restrictions acomplished.
[4]Obtained solution with Pseudo Genetic algorithm[3].
[5]Obtained solution with Particle Swarm Optimization.
[6]Obtained solution with Simulated Snnealing.
[7]Obtained solution with Harmony Search.
Highlighted in grey the diameters that are different from the proposed solution of Savic & Walters, that verifies the restrictions of pressure in the nodes.

Geem (2001). The harmony memory size go from 15 to 135 individuals, varying the HMCR between 0.88 and 0.92, and PAR between 0.05 and 0.015.

The histogram of figure 3 represents the total of simulations. This graph incorporates the accumulated probability of the obtained solutions. The graph allows to detect the more frequent solutions, as well as to determine the probability of obtaining a given solution better to one given. It is important to consider that the histogram represents the totality of obtained costs, and so they are including all the possible combinations of size of memory, HMCR and pitchrate, those that worse work, reason why it is even logical that the number of values corresponding to the minimum cost is not very high.

In order to determine the influence of the different parameters in the obtaining of the minimum cost value, we adopted the solution corresponding to 6081 thousands of monetary units. This minimum was considered the optimal value of design. The optimal value of design is obtained only four times in the 54000 simulations that were realised. The concept of “good solution” is introduced now. One of the characteristics of the heuristics methods in general is the capacity to obtain not only one single optimal value, but to obtain a set of “good solutions” on the design problem. In this work “good solution” is defined with whose cost is over the minimum cost until in a 3%.

Figure 4 indicates the probability of obtaining a “good solution” for each combination of memory size and HMCR.

Figure 4 shows that sizes of memory over 45 and below 120 are those that provide better results. In the same way, these memory sizes, combined with values HMCR of 0.89 and 0.90 give rates of success over 25%. This shows the capacity of the method not only to obtain minimum values, but also to obtain with relative frequency values very near the optimal one defined. Thus, Figure 5 indicates the probability of obtaining a “good solution” for each combination of memory size and PAR.

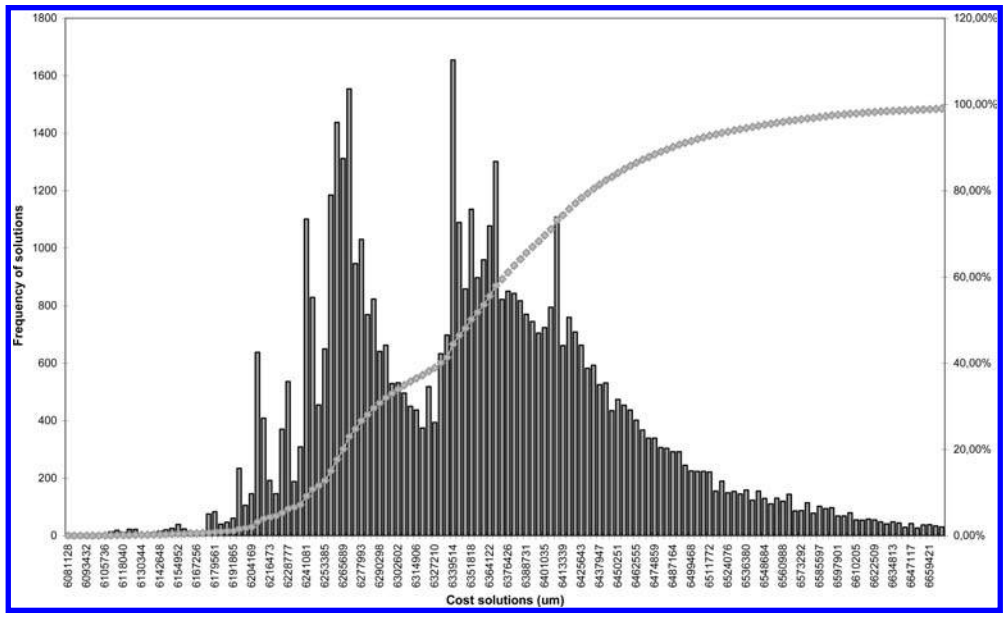


Figure 3. Histogram.

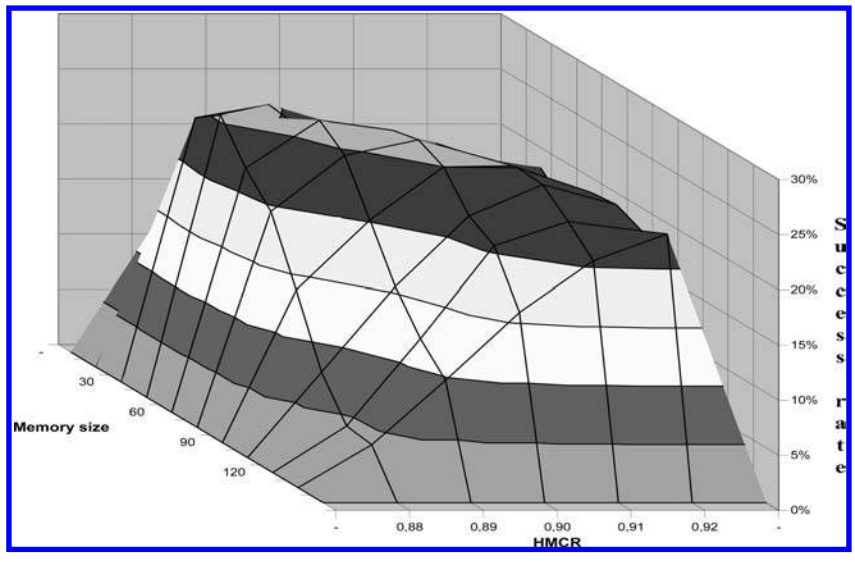


Figure 4. Probability of obtain a “good solution” (Memory Size vs HMCR).

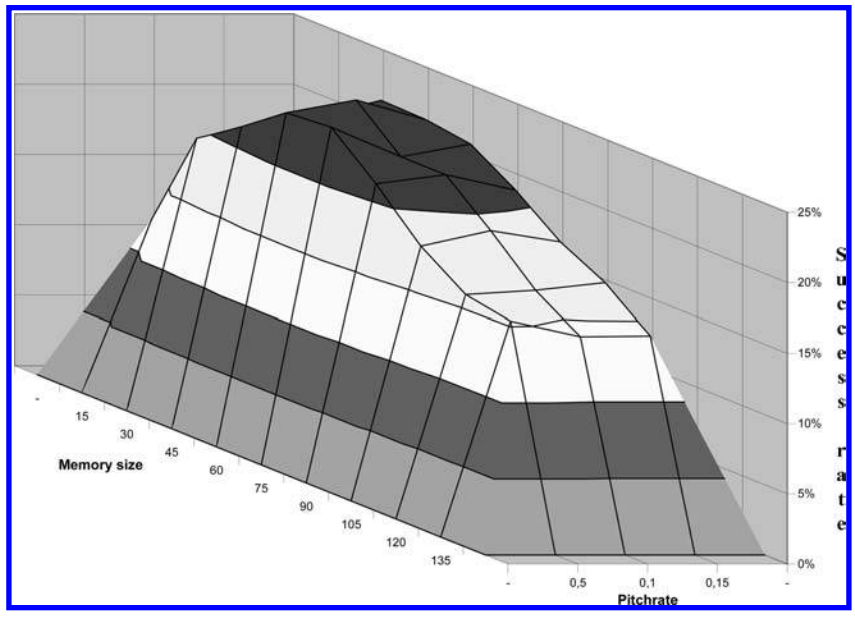


Figure 5. Probability of obtain a “good solution” (Memory Size vs PAR).

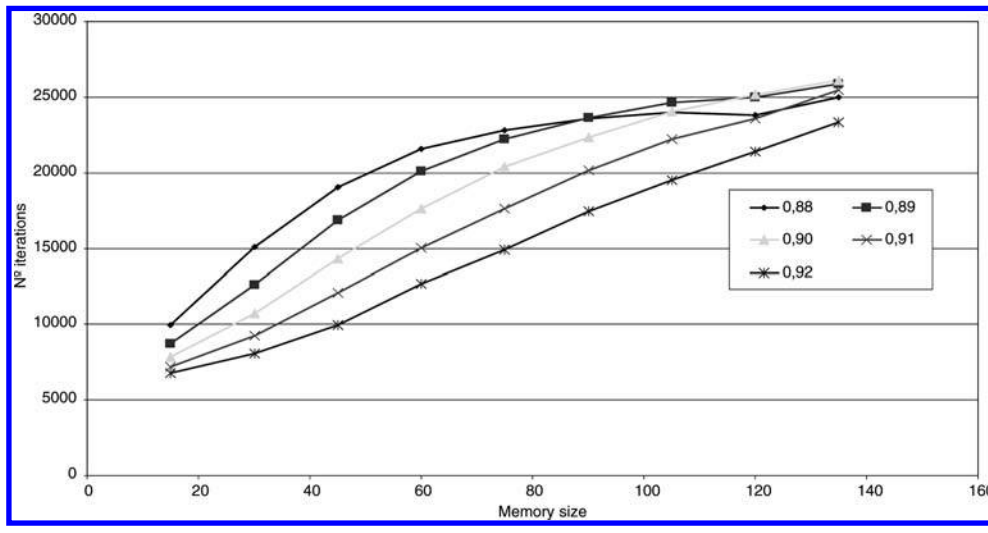


Figure 6. Number of iterations according to HMCR.

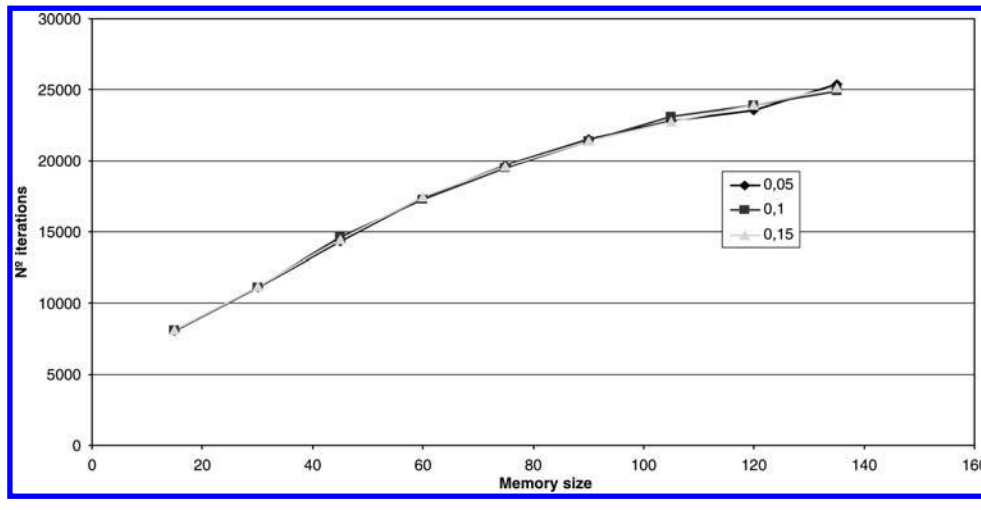


Figure 7. Number of iterations according to pitch rate.

Figure 5 shows that the used values of PAR do not have a great influence on the result of the simulation. In the other way, the results confirm that harmony memory size has a great influence in the final result of the simulation, since in the analyzed network sizes of memory between 45 and 90 provide higher probabilities of success.

Another factor to consider when the optimal parameters of the method are chosen is the speed with which it calculates HS, since to choose values or others it influences in the number of total iterations that HS makes before reaching the final solution. The graphs 6 and 7 represent the number of iterations that the algorithm realises in each case.

Figure 6 shows that at the most great is the used size of memory greater number of iterations realise the algorithm before finding the final solution, and so the HS is slower. Thus, higher values of HMCR bring about an increase of the number of realised iterations in every simulation.

Figure 7 confirms the increase of the number of iterations realised by the algorithm when the size of memory is greater. Nevertheless, pitchrate in the studied values have not any type of influence in the number of made iterations, since the three series studied are superposed.

## 5 CONCLUSIONS

The economic design in the Water Distribution Networks is of great interest, as it allows us to choose a solution between the different alternatives that verify the imposed hydraulic conditions. In this work, the main objective consists of making the design of a water distribution network, using for it a method based on HS.

The objective of the economic design is to find the minimum cost for the analyzed network. However, it is possible to define the concept of “good solution”. The statistical analysis for the different parameters from HS allows to conclude that:

- The size of the memory has a key influence in the obtaining of good solutions, because harmony memory sizes too high or too low make worse the yield of the algorithm.
- Thus, whichever greater is the memory size, greater is the number of iterations that the algorithm realises until finding the minimum, which makes the process slowly.
- For the studied values, PAR does not represent a great influence in the optimization process.

- In the studied network, values around 0.90 HMCR are the most suitable if the objective considers only to obtain good solutions of design. In the other way, whichever minor is HMCR greater number of iterations realises the algorithm, which makes the calculation slowest.

The results are valid in the network of Hanoi. It is necessary the verification of these hypotheses in other models.

## ACKNOWLEDGEMENTS

This article has been possible inside the actions developed by the researchers of CMMF involved in the project “Integración de la caracterización dinámica de elementos y consumos en modelos de redes de abastecimiento de agua utilizando sistemas de información geográfica y algoritmos genéticos (CADAGIAS)”. The number reference of the project is DPI2006-13113.

## REFERENCES

[1] Alperovits, E; Shamir, U (1977). “Design of Optimal Water Distribution Systems”. Water Resource Research, Vol 12, n° 6, 885–900.
[2] Geem, Zong Woo (2001). “Optimal cost design of water distribution networks using harmony search”. Environmental Planning and Management Program. John Hopkins University.
[3] Iglesias, P.L; Mora, D; Fuertes, V; Martinez, F.J (2006). “Análisis estadístico de soluciones de diseño de Redes de Abastecimiento de Agua mediante Algoritmos Genéticos”. XXII Congreso Latinoamericano de Hidráulica. Ciudad Guayana. Venezuela.
[4] Lansey, K.E; Mays, L.W (1989). “Optimization model for water distribution system design.” J. Hydr. Engrg., ASCE, Vol 115, n° 10, 1401–1418.
[5] Lee, K.G; Geem, Z (2005). “A new meta-heuristic algorithm for continuous engineering optimization: harmony search theory and practice”. Computer methods in applied mechanics and engineering, 194, pp 3902–3933.
[6] Mahdavi, M; Fesanghary, M; Damangir, E (2007) “An improved harmony search algorithm for solving optimizatin problems”. Applied Mathematics and Computation, 188, pp 1567–1579.
[7] Matías, A (2003). “Diseño de redes de distribución de agua contemplando la fiabilidad mediante algoritmos genéticos”. Tesis Doctoral – Dpto. Ingeniería Hidráulica y Medio Ambiente. Universidad Politécnica de Valencia
[8] Mahamed G.H. Omran, Mehrdad Mahdavi (2008). “Global-best harmony search”. Applied Mathematics and Computation, 198, pp 643–656.
[9] Su, Y.C; Mays, L.W; Duan, N.; Lansey, K.E. (1987). “Reliability-based optimization model for water distribution Systems”. J. Hydr. Engrg., ASCE, Vol 114, n°12, 1539–1556.
[10] Zecchin, A.C; Maier, H.R; Simpson, A.R; Leonard, M; Nixon, J.B (2007). “Ant colony optimization applied to water distribution system design: Comparative Study of Five Algorithms”. Journal of Water Resources Planning and Management, ASCE, Vol 133, n° 1, 87–92.

*Environmental Hydraulics – López-Jiménez et al (eds)*
*© 2010 Taylor & Francis Group, London, ISBN 978-0-415-56697-1*

# Evaluation of the front leakage flow in a low-specific-speed centrifugal pump

Marc Pelegrí, Jordi Armengol, Josep Ramon González, Toni Pujol & Lino Montoro
*Àrea de Mecànica de Fluids, Departament d'Enginyeria Mecànica i de la Construcció Industrial, Universitat de Girona, Girona, Spain*

Pere Tubert
*ESPA GROUP, Banyoles, España*

ABSTRACT: In low-specific-speed pumps, losses due to recirculation of flow and friction become a big issue to deal with. The overall pump efficiency of those turbomachines is usually low, hardly reaching 40 percent. This study tries to build a better understanding of the effect of recirculating flows through the leakage seals of a low-specific-speed multistage centrifugal pump. Different models of recirculating flows have been taken in account and pressure measurements on the seal location have been made to check their predictions; in addition, complete 3D CFD simulations of the whole stage have been performed. Finally, improvements on the seal geometry have been tested in order to reduce the recirculating flows and improve the overall efficiency.

*Keywords*: Turbomachinery, hydraulic losses, CFD.

## 1 INTRODUCTION

Pumps are the single largest user of electricity in industry in the European Union, consuming 160 TWhpa[1] of electricity, accounting for 79 Mton $CO_2$. This represents 20% of energy consumed by electric motors. This is equivalent to 14% of the total electricity consumed in industry and commerce. Centrifugal pumps in the EU use 117 TWhpa of electricity. This represents 73% of all pump energy consumption.

It is estimated that if users select higher rather than lower efficiency pumps, energy savings of 3% can be made. It is expected that it will not be until the year 2020 that all less efficient pumps will be replaced, due to their estimated 20 year lifetimes. Using these assumptions, calculations were undertaken showing the possible future energy saving. This shows that savings of 1.1 TWhpa could be made in 2015 from the use of higher efficiency centrifugal pumps. This would give a cumulative saving of 8.35 TWh by 2015. If this was inclusive of all pumps the cumulative energy saving value is expected to at least double. Further reductions in emissions could be made through improved system design and the reduction of system losses.

The value of the practically attainable overall pump efficiency is mainly influenced by factors such as surface roughness of parts which are in contact with the flow as well as the internal leakage flows through the sealing gaps. Computing these leakage flows through a front cavity leakage seal can be done with simple modeling. A relationship between the velocity and pressure at the impeller tip and the seal location can be written in terms of the total relative pressure. This is the incompressible equivalent of rothalpy for a compressible fluid.

Nevertheless, it is necessary to obtain the velocity at the impeller tip and at the seal location and this is difficult to do. Consequently, a sensible approximation has been done. The relative velocity at each location has been approximated as some fraction F of the local wheel speed ($W = F \cdot U$). It is possible to use different fractions at the impeller tip and at the seal location, but this pressupposes a knowledge far beyond any available data. Hence it is assumed that the relative velocity at the impeller tip and at the seal location is some fixed fraction of the local wheel speed. This simplification yields a static pressure difference across the seal that can be solved and related to a pressure loss coefficient in the usual manner as some fraction of the dynamic head through the seal, and finally a simple relationship is obtained for the velocity or the leakage mass flow rate through the seal and the F factor assumed for the velocity field in the cavity area.

This method permits to evaluate the leakage flow rate through an arbitrary seal. Contributions from Egli[1] made possible to calculate the flow through a labyrinth seal, and Stepanoff[5] and Winn[6] have contributed to set forth the theory of leakage flow through annular rings.

To quantify the effects of these internal recirculating flows through the shroud leakage, the following investigation on a low specific speed, multiple stage centrifugal pump was carried out. Pressure measurements were made at the seal location to check the predictions of the above mentioned models. Detailed 3D CFD simulations were performed to verify the results. The addition of gap surfaces with circumferential notches in the seal geometry have been tested to study its influence on the recirculating flow. Finally, the design modifications have yielded a more efficient pumping system.

## 2 TESTED GEOMETRIES

Experimental measurements have been done on a multistage centrifugal pump. Impeller and return channel geometries have been designed with the help of Concepts NREC software, a suite of turbomachinery design. Once designed, the impeller 3D geometry has been used to obtain a rapid prototype with stereolitography. The return channel has been forged on aluminium.

[1] All data concerning energy consumption of pumps on this abstract comes from [4].

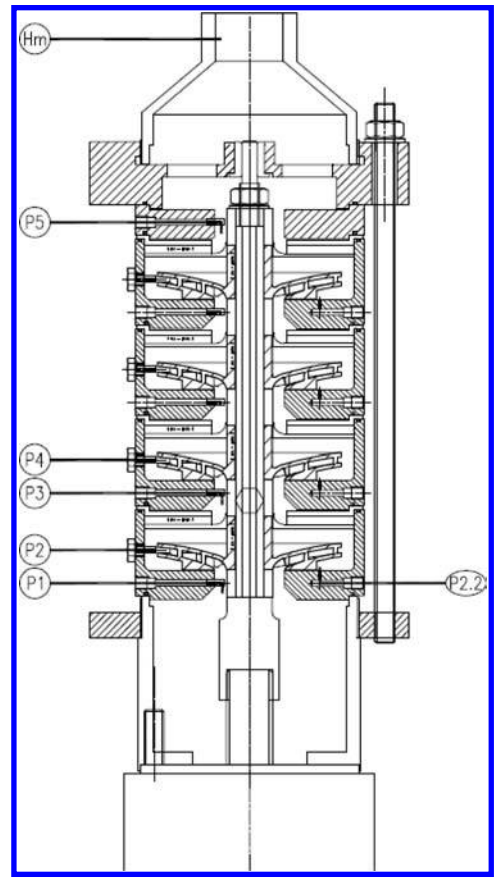


Figure 1. Layout of the tested multistage pump with the measuring points.

There are seven points of static pressure measurement, as shown in Figure 1. The transducers used on the experimental testings are the following:

P1: Digital transducer LEO (-1/30 bar)
P2: Digital transducer WIKA (0/2.5 bar) EA-229
P2.2: Analogic manometer NUOVA FIMA (0/2.5 bar) EA-175
P3: Analogic manometer NUOVA FIMA (0/6 bar) EA-174
P4: Analogic manometer NUOVA FIMA (0/10 bar) EP-2
P5: Digital transducer GASLI (0/10 bar)
Hm: Digital transducer WIKA (0/10 bar) EA-204

According to[4], the reduction of the clearance from 0.6 mm to 0.3 mm on the seal geometry can improve pump efficiency about 3 per cent points, and possible additional reductions of recirculating flows can be achieved by the addition of gap surfaces with circumferential notches.

Three different types of seal geometries have been tested on our pump. The first one is with a smooth gap surface, and the others have one and two circumferential notches of 1 mm deep and 1.5 mm wide, as shown in Figure 2.

## 3 NUMERICAL METHOD AND BOUNDARY CONDITIONS

A complete 3D CFD simulation has been performed on a single stage of the pump. The real geometry has been accurately represented, with the inclusion of the chamber inlet, the seal clearance and the pump inlet clearance and the exit chamber.

A first non-structured tetrahedral mesh was built with a total number of 2.5 million nodes. This initial mesh was then rearranged and converted to a polyhedral mesh maintaining the same number of nodes but reducing the total number of mesh elements.

Following the guidelines appeared in[3], the best options for the solver and boundary conditions have been applied in order to achieve faster convergence and better results.

The following boundary conditions were applied:

- Mass flow inlet on the impeller inlet.
- Pressure outlet on the outlet.
- Moving walls on the walls corresponding to those of the impeller and the axis.
- Stationary walls on the rest of the pump walls.

The following solver conditions were applied:

- Incompressible fluid, without thermal solver.
- Pressure based, implicit formulation: Segregated solver.

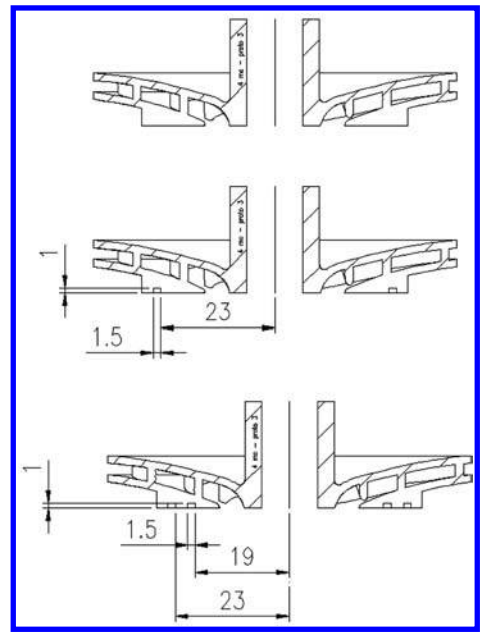


Figure 2. Details of the three seal geometries tested.

- Stationary solution.
- Absolute velocity formulation.
- Gradient option: Green-Gauss node based (the best option for non-structured meshes).
- Second order discretization.
- Turbulence model: RANS (Reynolds-Averaged Navier-Stokes), k-$\varepsilon$ realizable.

## 4 CONCLUSIONS

In multistage centrifugal pumps, the improvement of seal geometries in order to avoid recirculations is a helpful design technique. This improvement can be done by reducing the gap between surfaces in the seal, and also by the addition of notches. The latter case has been studied in this paper, with a result of an improvement of efficiency of nearly 3%.

The CFD simulations performed on the complete impeller and seal geometries have yielded a nearly perfect accordance (less than 3% difference) with the experimental results.

## REFERENCES

[1] Egli, A. (1935), *The leakage of steam through labyrinth seals*. Trans. ASME 115–122.
[2] Japikse, D., Marscher, W.D. and Furst, R.B. (2006), *Centrifugal Pump Design and Performance*. Concepts ETI.
[3] Kelecy, F. (2006), *Best Practices for Rotating Machinery*. ANSYS, Inc. Publication.
[4] *SAVE Pumps Final Report* (European Commission, 2003)
[5] Stepanoff, A.J. (1957), *Centrifugal and axial flow pumps: Theory, design and application*. John Wiley & Sons, Inc. New York.
[6] Winn, L.W. (1984), *Basic seal design - A review of the state of the art*. Mechanical Technology Incorporated, Latham, NY.

*Environmental Hydraulics – López-Jiménez et al (eds)*
*© 2010 Taylor & Francis Group, London, ISBN 978-0-415-56697-1*

# Energy production in water supply systems based on renewable sources: Neural networks

Fábio Veríssimo Gonçalves & Helena M. Ramos
*Civil Engineering Department, Instituto Superior Técnico, Technical University of Lisbon, Lisbon, Portugal*

Luisa Fernanda R. Reis
*Universidade de São Paulo, EESC/USP, Departamento de Hidráulica e Saneamento, São Carlos-SP, Brasil*

ABSTRACT: Water supply systems are large consumers of energy and the use of hybrid systems for green energy production is this new proposal. This work presents a computational model based on neural networks to determine the best configuration of a hybrid system to generate energy in water supply systems. In this study the energy sources to make this hybrid system can be the national power grid, micro-hydro and wind turbines. The artificial neural network is composed of six layers, trained to use data generated by a model of hybrid configuration and an economic simulator – CES. The reason for the development of an advanced model of forecasting based on neural networks is to allow rapid simulation and proper interaction with hydraulic and power model simulator – HPS. The results show that this computational model is useful as advanced decision support system in the design of configurations of hybrid power systems applied to water supply systems, improving the solutions in the development of its global energy efficiency.

*Keywords*: Water Distribution System, Artificial Neural Networks, Hybrid Energy Systems.

## 1 INTRODUCTION

In the last decades, the managers of such water supply systems have been concerned with the reduction of energy consumption, as well as the strong influence of climate changes on water patterns. The re-cent crises in oil prices has made the search for alternatives to generate energy using renewable sources, becoming renewable energy systems as valuable energy resource, in particular through the use of hybrid energy solutions.

Hybrid energy solutions for power generation are feasible applications for water supply systems that need to decrease their costs with the electrical component. These solutions take the advantage of power production based on its own available hydraulic energy as well as on local available renewable sources, saving on the purchase of energy produced by fossil sources contributing for the reduction of $CO_2$ emissions.

The best hybrid solution to be adopted, taking the energy efficiency as the main goal, is a complex and arduous task, besides requiring complex optimization models, where the development of additional tools can become difficult.

This work aims to present a neural artificial network that simulates an optimization model to obtain the best hybrid system configuration for a typical water supply system.

## 2 STATE-OF-THE-ART REVIEW

### 2.1 *Basic concepts*

Unlike a conventional power generation system, a hybrid system by definition is one, which uses an alternative arrangement of technologies to achieve similar objectives i.e. a constant and reliable source of power. Renewable energy takes on many varying forms, when combined could configure an integrated solution to achieve the energy efficiency improvement [1]. To achieve that, energy for pumping to deliver water to populations is needed, representing the main cost for water companies[2].

### 2.2 *Hybrid energy systems*

In recent years the hybrid energy system has received much attention and it is a viable alternative solution as compared to systems based entirely on hydrocarbon fuel, given flexibility to the system and a longer life cycle.

Commonly the hybrid system works with the national energy grid, but during the peak hours when are the higher costs in the electricity tariff, the system could be supplied by renewable sources, such as wind turbines, photovoltaic (PV) or micro turbines integrated installed within the conveyance system to power the system for pumping or turbine the flow between reservoirs, and to sell surplus energy[2].

### 2.3 *Modelling conditions*

In[3] the literature review reveals that the modelling of hybrid energy systems and their application in decentralized mode are quite limited. The models currently applied, are based on one of the available resources while in the literature is found applications with one or two available re-sources. Application of models for matching the projected energy demand with a complementary combination of sources at decentralized level is the main subject. Software models (such as HOMER, PVSYST) have been used by various researchers [2,4], for design and research of alternative energy systems. The need of a model for optimizing the energy management of hybrid type systems with specific operational controls is imperative. In other hand MATLAB can be used for modelling optimization to manage the water and energy in WSS. In [2] linear programming was

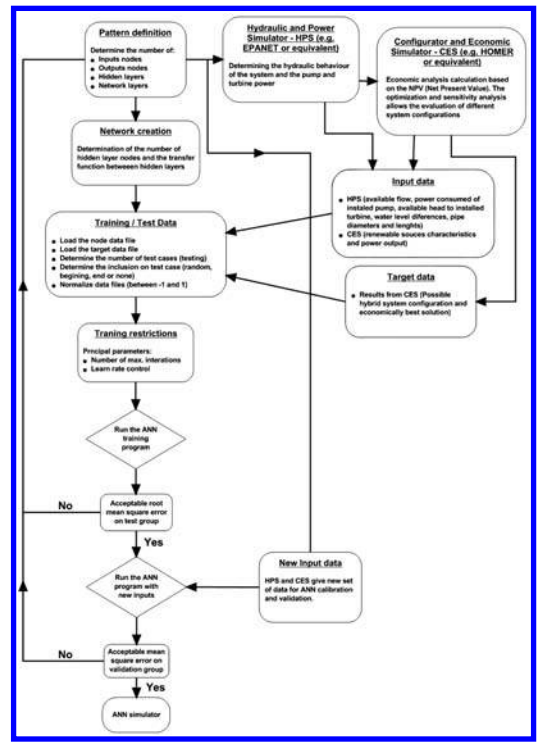


Figure 1. Flowchart of the developed artificial neural network.

used to develop an optimization tool to obtain the best hourly operation, according to the electricity tariff, for a pumped storage system supplied by wind energy, with water consumption and inlet discharge. Others authors use different conditions e.g. based on non-linear programming, Genetic Algorithms [2,5–7].

### 2.4 *Artificial neural networks*

Artificial neural networks (ANN) have been used in water distribution systems to model the degradation of water [5]. The research has been considered promising, providing a strong base for the development of a financial-economical model, which applied with the degradation model, is able to give an integrated approach for optimizing intervention strategies in water distribution systems. Even the limitations identified in this algorithm, their prediction performance has proven to be rather good in the short and medium term.

## 3 METHODOLOGY

### 3.1 *Neural conception*

The neural network was made on Qnet2000, a commercial neural network package has been used for training algorithms, giving the advantage of rapid network development through flexible choices, output functions and other training parameters, thereby enhancing the accuracy solutions.

The conception of a new neural network hybrid energy model which can be compared with an energy configuration model and economical simulator – CES (e.g. HOMER simulator) for limited conditions will adopt the following procedures: use CES to obtain data that may be used in training process and in a reliable neural network tests together with an hydraulic and power simulator model – HPS (e.g. EPANET simulator), alternating flow rates, diameters and pipe lengths and roughness as well as differences levels of water in tanks or reservoirs, characteristic pumping parameters per energy consumption and power evaluation per pumping and turbining procedures. Those data has been available on Ramos and Ramos (2009) research that uses the HPS to hydraulically balance the water supply system, determining the hydraulic behaviour of all system including the most suitable pump and turbine power for each condition. Before starting the creation and implementation of the neural algorithms, it is necessary the creation of a complete database for the input and output data for the training and validation of the network for each system characteristics. The input data come from HPS (e.g. power of installed pump, available head to the turbine to be installed, pipe length, flow, pipe diameters, available head, mean output power, water demand pattern and power consumption of the pump and difference water levels between reservoirs) and CES (e.g. mean output power of wind/hydro generator and mean head discharge/wind velocities).

These data are implemented in CES model and are useful for the economic analysis calculation based on the NPV (Net Present Value) indicator for each hybrid system studied, thus giving the most profitable economic solution. Other economic values are used for the economic such as the prices of installed equipment, energy selling prices for the national electric grid and the limitation of the number of equipment to be used in the simulation, which would bring associated errors in the training process and in the ANN validation.

The optimization algorithms and sensitivity analysis allows to simplify the evaluation of different system-configurations. Inputting technology options, component costs and resource availability, CES tests all combinations creating a list of feasible configurations sorted by net present costs (NPC). In order to take into account the benefits (which are positive indicators), NPC are assumed negative values and are transformed into net present values (NPV) or cash flows in order to use then on the ANN model. A flowchart describing the procedures of design the ANN applied for energy efficiency evaluation in water supply systems is shown in Figure 1.

Table 1. Solution configurations used to obtain the best hybrid configuration.

| Solution configuration | Wind velocity m/s | Stream flow 1/s |
|---|---|---|
| 1 | 4,70 | 19,00 |
| 2 | 4,70 | 48,00 |
| 3 | 4,70 | 106,00 |
| 4 | 5,90 | 19,00 |
| 5 | 5,90 | 48,00 |
| 6 | 5,90 | 106,00 |

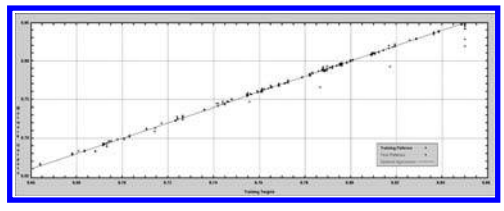

Figure 2. Scatter comparison of normalized targets set.

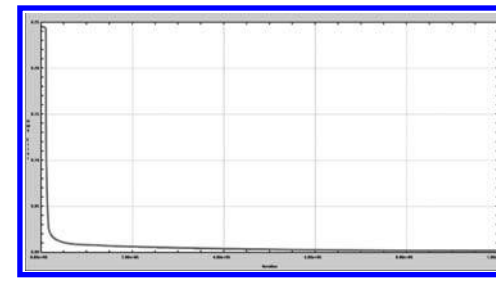

Figure 3. Root Mean Square Error of training versus net outputs.

### 3.2 *Neural network*

The initially proposed method for the basic ANN to be used in this research is the MLP (Multilayer Perceptron), in which the neurons are disposed in successive layers (feed-forward). Preliminary tests are made to determine the ANN parameters that provide the best results. After the initial analysis, networks with just one layer presented very high mean square errors, and then after several attempts more than one hidden layer with various configurations of neurons are implemented.

There are 9 input neurons that correspond [i] to the length of pipe system, [ii] the water levels differences between reservoirs, [iii] the pipe diameters, [iv] the annual average power produced by the wind turbine, [v] the annual average wind velocity, [vi] the flow of the system, [vii] the head available on the system, [viii] the annual average power produced by the micro-hydro and [x] the power consumed by the pump station.

On the output layer is used 5 neurons representing the optimization and sensitivity analysis of different system configurations corresponding to data used by CES simulator, where the neurons are represented by NPV of national

## 4 RESULTS AND DISCUSSION

In the end of training, the neural network adopted is that gives the less root mean square error (RMSE) with a good correlation. After several attempts, modifying the network topology and the number of neurons and hidden layers, the resulted network with the topology adopted was the 9 neurons for input, 40, 30, 20, and 10 neurons for the 4 hidden layers and 5 neurons for the output layer. In Figure 2 the scatter comparison of normalized targets versus net outputs shows a good approach to the optimal agreement and in Figure 3 the root mean square error of training and test settings demonstrate that at the interaction 6.00e+5 the neural network starts to became stable and use higher interactions just bring to the model more computing time, not desired at all.

The back propagation training paradigm uses two controllable factors that affect the algorithm's rate of learning. The two factors are the learning rate coefficient (eta), and the momentum factor, alpha. To optimize the rate at which a network learns, these factors must be set and/or adjusted properly during the training process. Just as there are limits to how fast a brain can learn ideas and concepts, there are also limits to the rate at which a network can learn. If a network is forced to learn at a rate that is too fast, instabilities develop that can lead to training divergence.

On the ANN training, the eta was instable until the 6.00e+5 interactions, at the same point when the ANN start to reach lower RMS value and it's shown on Figure 4.

The best hybrid energy solution demonstrated by CES is a system based on the use of the national electric grid in conjunction with wind-powered generators and hydro turbines, for variables of wind speed and flow of 5,9 m/s and 19 l/s, respectively, with a value of NPV 1,26 millions of Euros with 3 wind-powered generators installed.

The first stage of the study concerned in the composition of all results from CES with the ANN solution (Figure 5), demonstrating a good overlapping for different system configuration. The best energy system configuration is witch has the higher NPV value, resulting for NG+Wind+Hydro solution with the solution configuration 4.

The solution from ANN model has a relative error of 1.19% comparing to CES solution. To determine the number of wind turbines for the best con-figuration, the neuron with the number of wind turbines on the winner configuration set is 3, the same achieved by CES software.

A comparison between CES and ANN results on the energy system configuration (NG + Wind + Hydro) among the all data configurations is described in Figure 6, which confirm that the best solution correspond to the configuration 4. When the comparison is made between the neural network errors and the input sequence values demonstrate the system configuration solution output neuron 5 (NG + Wind + Hydro) present a good approach and is describing in Figure 7.

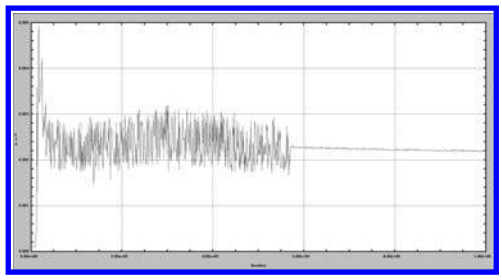

Figure 4. Learning rate coefficient adjustment.

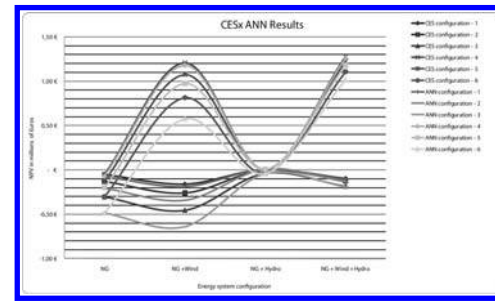


Figure 5. CES versus ANN results.

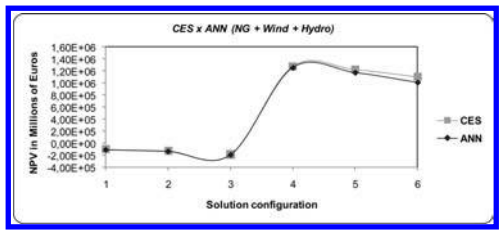


Figure 6. Comparison between CES and ANN results for different solution configuration of (NPV NG + Wind + Hydro).

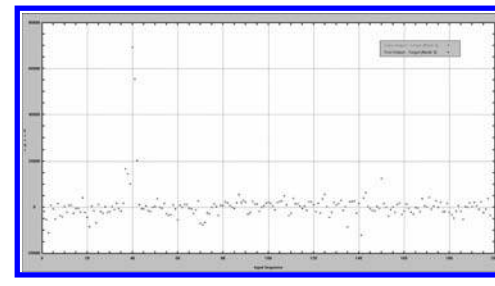

Figure 7. Network output error vs. Input sequence on output node 5 (NPV NG + Wind + Hydro solution).

## 5 CONCLUSIONS AND RECOMMENDATIONS

The best hybrid solution to be adopted in a particular supply system is a complex task, requiring the optimization of several objective functions subjected to multi-criteria analysis of penalty functions, which require advanced computational models where the development of additional tools presents some complexity.

It can be concluded by the results found in this study that the developed neural network behaves accordingly to the results obtained in CES, showing acceptable reliability in terms of possible solutions. For future work a larger number of characteristics of the system are intended to be analysed as well as including extended hybrid solutions, so that the model can be even more robust and comprehensive.

## ACKNOWLEDGEMENTS

The authors wish to thank to FCT through the project PTDC/ECM/65731/2006, as well as CEHIDRO, the Hydro-systems research centre from the Department of Civil Engineering, at Instituto Superior Técnico, Portugal.

## REFERENCES

[1] Seare, K.D.R. (1999), *Grid connecting a hybrid energy system*. in *IEE Colloquium on Protection and Connection of Renewable Energy Systems*.

[2] Vieira, F. and Ramos, H.M. (2008), *Hybrid Solution and Pump-Storage Optimization in Water Supply System Efficiency: A Case Study.* Energy Policy. **36**(11): p. 4142–4148.

[3] Gupta, A., Saini, R.P., and Sharma, M.P. (2006), *Modelling of Hybrid Energy System for Off Grid Electrification of Clusters of Villages*. in *Power Electronics, Drives and Energy Systems, 2006 - PEDES '06.*

[4] Barsoum, N.N. and Vacent, P. (2007), *Balancing Cost, Operation and Performance in Integrated Hydrogen Hybrid Energy System*. in *First Asia International Conference on Modelling & Simulation, 2007. AMS '07.* .

[5] Sakarya, A.B.A. and Mays, L.W. (2000), *Optimal Operation of Water Distribution Pumps Considering Water Quality.* Journal of Water Resources Planning and Management. **126**(4): p. 210–220.

[6] Turgeon, A. (2005), *Daily Operation of Reservoir Subject to Yearly Probabilistic Constraints.* Journal of Water Resources Planning and Management. **131**(5): p. 342–350.

[7] Vieira, F. and Ramos, H.M. (2009), *Optimization of operational planning for wind / hydro hybrid Water Supply Systems.* Renewable Energy. **34**(3): p. 928–936.

*Environmental Hydraulics – López-Jiménez et al (eds)*
*© 2010 Taylor & Francis Group, London, ISBN 978-0-415-56697-1*

# New high head pumped-storage power station design to increase the wind power penetration in island autonomous power systems

Carlos A. Platero & Francisco Blazquez
*Escuela Técnica Superior de Ingenieros Industriales, Universidad Politécnica de Madrid, Madrid, España*

Manuel Álvarez & Carlos Romero
*ENDESA Generación S.A., Subdirección de Ingeniería e I+D, Madrid, España*

ABSTRACT: The integration of wind power into the power systems represents reductions in the greenhouse gases emissions and has a positive environmental impact, although it is very complicated due to the unpredictable behavior of the wind. In the case of isolated power systems, this problem is even more difficult and in order to increase the wind power penetration in a reliable way is essential to have an energy storage system. In case of high wind power penetration, thanks to its larger capacity, the hydro storage is the most suitable energy storage system.

This paper presents an innovative design of a wind-pumped-store high head power plant to supply all the energy from wind power to an island autonomous small power system, El Hierro (Canary Islands), in a reliable and efficient way with a very high wind power penetration. This power plant will be commissioning during the next year 2010 and its aim is to replace the existing diesel power plant in the future, supplying all the island energy from renewable sources.

*Keywords*: Pumped storage power generation, Dispersed storage and generation, Energy storage, Power stations, Wind power generation.

## 1 INTRODUCTION

In all power system, the frequency regulation should be done by the system operator through the balance between the power generation and the power consumption. For this purpose it is mandatory to have power plants that are easily adaptable to the demand requirements. In the case of isolated power systems, the frequency regulation is a very difficult problem due to the small number of generators.

Moreover, in case of renewable power sources, as wind power, it is not possible to supply all the power demand in a reliable way due to the unpredictable behavior of this type of energy sources and, frequently, the wind power penetration is limited to prevent networks incidents. To increase the wind power penetration in a reliable way in such isolated power systems is essential to have energy storage systems, which allow to match the generation and the demand. In some small scale cases, batteries and flywheel are used as energy storage systems. However, thanks to its larger capacity, the hydro storage is more suitable for this type of applications, in the case of high wind power penetration, like the power station presented in this paper.

## 2 DESIGN REQUIREMENTS

The island, called El Hierro, has a population of 10,600 and a surface of 278 $km^2$. The peak demand is 6,3 MW, while the valley hour consumption is 2,9 MW. The island volcanic origin orography makes it possible to build an upper and a lower reservoir. In the Figure 1, it is shown a possible layout based on the information of the reference[3].

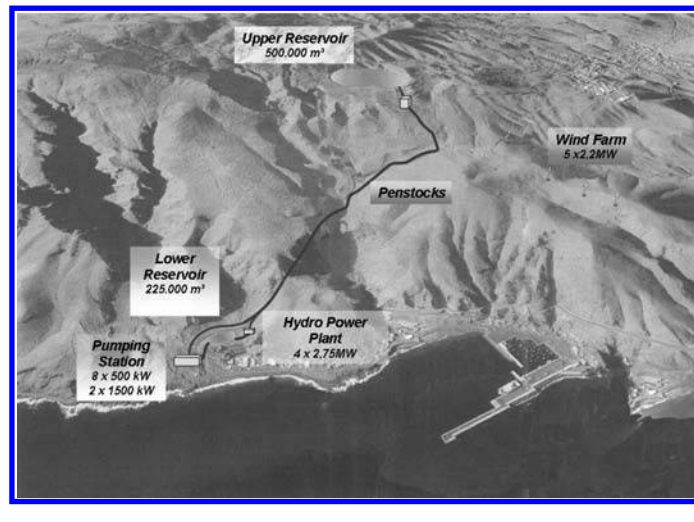


Figure 1. El Hierro wind pumped-storage hydro power plant layout.

The final objective of this wind-pumped storage power plant is to provide all the energy to this island from wind power. For what it is necessary to integrate an 11 MW wind farm in a power system with a maximum power consumption of 6,3 MW as stated before. So the wind farm represents in some cases a power generation of the double of the power consumption. This level of wind penetration has never been reached in any island in the world. There are some remarkable projects in island autonomous power systems [4,5].

For the presented project, with enormously high wind power penetration, it is mandatory to use an energy storage system. This power plant should be able to regulate the frequency fluctuations of the power system, producing the power demanded by the consumers or consuming the exceeding power of the wind farm, in steady state and in transient state. Thus, in case of lack of wind, the power plant should operate in turbine mode, generating power, or in case of high wind, the power plant should operate in pump mode with continuous power regulation, consuming power. Additionally the power plant must have the possibility to change over from pump mode to turbine mode or vice versa, in a fast way, because it is the unique power station of the power system.

To summarize, the main requirements for this project are the maintaining of the frequency within the power quality limits according to the regulations[6], and the withstanding of the trip of the biggest generator without a load shedding, injecting power in a fast way.

## 3 STATE OF THE ART

Compared to a conventional storage pumped station, the main additional features of this installation are the continuous power regulation in pump mode, the possibility to change from pump mode to turbine mode or vice versa in the minimum time and the fast power injection, in order to do not discontinue the power delivery to the consumers.

On one hand, the conventional storage pumped station do not have possibility of fine regulation of the power, because to control the power in pump mode, they vary the number of units connected on the line.

On the other hand, conventional pump turbine units need to change the rotation sense to change from pump mode to turbine mode or vice versa, this process take several minutes, and during this time the unit is out of service and consequently it do not permit to keep an autonomous power system in service. Then another configuration should be use. There are mainly two existing techniques, the 3-machines type, and the variable speed operation.

The 3 machine type combines an electrical machine, a pump and a turbine in the same shaft with the same rotation sense. This configuration allows a continuous regulation of the power in pump mode and very short change over times.

The use of variable speed only allows the active power control in pump mode, and an increased efficiency in pump and turbine mode, but requires electronic converters and in some configuration special electrical machines.

The combination of the two above technologies presents some advantages[7].

## 4 NEW HIGH HEAD PUMPED-STORAGE POWER STATION DESIGN

The pumped-storage power station is divided in a hydro power station, based on Pelton turbines and a pumping station based on multistage centrifugal pumps. The gross head is 690 m.

The fact of having separate electrical machines for the turbine (synchronous generators) and pumps (asynchronous motors) allow a more flexible operation of the power plant.

### 4.1 *Hydro power plant*

The rated power of the hydro power plant is 11 MW, and it is composed by four identical units ($4 \times 2{,}75$ MW).

Pelton turbines have been selected because of their excellent efficiency at partial load. Moreover, for this turbine size there are not commercial high head pump turbine available, and it would be necessary a special design.

The generators are three phases salient poles brushless synchronous generators. The units (turbine and generator) have been designed with extra inertia to withstand during a lack of energy without a significant frequency decrease.

Another important feature of these Pelton units is the reduced time to increase their power.

### 4.2 *Pumping station*

The main goal of the pumping station, during the period when the wind power is higher than the grid load, is to consume the exceeding power, balancing the generation and the loads. The conventional pumped-store hydro plants do not have continuous power regulation in pump mode. But in this project is essential to have a continuous power regulation in order to keep the frequency within the power quality standard limits. There will be installed two different types of pumps, fix speed ($8 \times 500$ kW) and variable speed ($2 \times 1500$ kW) driven pumps, the combination of this two technologies permits to have a discrete and continuous power regulation. In this way the consumption of the pumping station would be adapted by increasing or decreasing the speed of the variable speed driven pumps and the number of fix speed pumps connected to the power system.

In case of excess of power in the grid, the pumping station should increase its power consumption, then the speed set point of the variable speed pumps would be increased to regulate the frequency, until the variable speed pumps reach the maximum flow, then an additional fix speed pump will start. On the contrary, if the wind power decreases, the power consumption of the pumping station should decrease, then the speed set point of the variable speed drive pumps would be decreased, and in case of reaching the minimum flow point, a fix speed pump would be stopped. The minimum flow for the variable speed driven pumps has been selected to operate at a reasonable efficiency.

The main advantages are the optimal efficiency operation of the fix speed pumps, and the reduced harmonics in the power system due to the reduced size of the power converters, only required for the variable speed driven pumps.

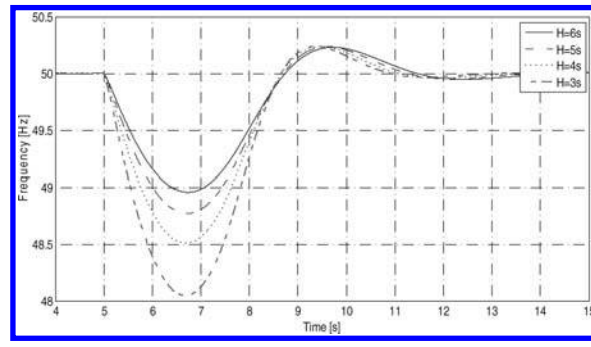


Figure 2. Frequency evolution during a wind generator trip for different hydro generator inertia coefficient H.

## 5 STEADY STATE OPERATION

The wind farm would operate at maximum power production, it means that for every wind speed the wind generators will supply the maximum possible electric power.

Then during steady state operation there are mainly two different scenarios, if the wind power is higher or lower than the grid load, the pumped storage power station would work in pump or turbine mode respectively.

There are other scenarios related with the reservoirs filling, in case of upper reservoir completely filled or completely empty, it is not possible the pump or turbine operation.

Another useful tool to operate the power station in a reliable way is the wind forecast systems, in order to manage the hydro resources.

## 6 TRANSIENT STATE OPERATION

This power station will continuously change its load, in pump mode or turbine mode, according to the wind and grid load power, in order to regulate the system frequency.

Hence, the usual operation would be transient state operation. But there are some special cases to be considered in the power station design.

The worst case is the tripping of the biggest generator of the system, at maximum load, in that situation the power plant should be able to supply the loosen power without a load shedding.

Several computer simulations have been done to calculate the generators inertia coefficient (H) to withstand the trip of the biggest generator. The results of the power system frequency evolution for different inertia coefficients are shown in the Figure 2.

## 7 EFFICIENCY

The maximum efficiency is reached if the grid load is supply directly from the wind power, without any additional energy transformation. So the power plant should work as a consumer or producer according to the wind conditions and load requirements, permitting the flow of the wind power through the consumers. An efficiency study has been done in several scenarios. The global efficiency of the power plant could be increased from 63% to 81%, depending on the operating conditions. The worth case 63% corresponds to a conventional pumped station, in contrast to the best efficiency, which corresponds to the supply of the complete peak power with wind energy and store only the exceeding.

In order to supply the load directly from wind power is essential to have an alternative source in case of lack of wind. As stated before, this power plant can integrate the wind power in steady and transient state.

In addition, the efficiency in turbine and pump modes is also important. In turbine mode the efficiency is enlarged by the use of Pelton turbines. On the other hand, in pump mode the combination of fix speed pumps with variable speed pumps allows the fine regulation of the power with a notable efficiency.

## 8 CONCLUSIONS

A new wind-pumped storage power plant design has been presented in this paper. The final purpose of this new power station is to supply all the electrical energy in a small island, called El Hierro, in Canary Archipelago.

To summarize, the new design pumped-storage power plant main advantages are:

- Excellent operation time response (minimum change over time between pump and turbine mode or vice versa).
- Continuous power regulation in pumping mode, combining fix speed and variable speed driven pumps.
- Increased efficiency in pumping mode.
- Instantaneous power injection in case of power system requirement.
- Reduced harmonics in the power system. (reduced power capacity required in electronics variable speed drives)
- Standard equipment with no special design.
- Maximum wind power penetration in the power systems.

In addition to the innovative design, this power plant will have an important environmental role, reducing the diesel oil consumption by 6000 ton/year, the $CO_2$ emission by 18700 ton/year, the $SO_2$ emission by 100 ton/year and the $NO_X$ emission by 400 ton/year[3].

REFERENCES

[1] P. Kundur. “Power System Stability and Control”. 1994 Mcgraw-Hill. Palo-Alto, California.
[2] B.C. Ummels, E. Pelgrum and W.L. Kling. “Integration of large-scale wind power and use of energy store in the netherlands’electricity supply”. IET Renewable Power Generation. Special Issue Papers from EWEC 2007.
[3] Ministerio de Medio Ambiente. “El Hierro, en el camino hacía la autosuficienca energética”. www.mma.es/secciones/biblioteca 12/12/2008.
[4] J.A.Suul, K. Uhlen and T. Undeland, “Wind Power Integration in Isolated Grids enabled by Variable Speed Pumped Storage Hydropower Plant”, *ICSET 2008.978-1-4244-1888-6/08 ©2008 IEEE*.
[5] P. Theodoropoulos, A. Zervos and G. Betzios. “Hybrid systems using pump-store implementation in Ikaria Island” PROC OPET, 2001.
[6] European standard EN 50160:2007. “Voltage characteristics of electricity supplied by public distribution networks”.
[7] R. Bucher. “Enhanced energy balancing and grid stabilization through 3-machine-type variable-speed pumped-storage units”. The International Journal on Hydropower & Dams. Hydro 2007 15–17 October 2007, Granada (Spain).

*Environmental Hydraulics – López-Jiménez et al (eds)*
*© 2010 Taylor & Francis Group, London, ISBN 978-0-415-56697-1*

# Iterative method for least-cost design and operation of pumping water distribution systems

Heber P. Gomes, Saulo de Tarso M. Bezerra, Paulo Sergio O. Carvalho & Moisés M. Salvino
*Laboratory of Power and Hydraulics Efficiency in Water Supply, Federal University of Paraíba, João Pessoa, Brazil*

ABSTRACT: This study is aimed at developing an economical dimensioning model for a water distribution system. The optimal solution minimises the system's total cost, which comprises the hydraulic network investment, plus the capitalised cost of pumping energy. The developed model, called Lenhsnet, may also be used to economically dimension projects to expand existing hydraulic networks. The methodology developed includes an iterative dynamic calculation process as well as a hydraulic simulation model. This model was tested in WDS The R-9 Network. The results obtained show the feasibility of this model, presenting it as a viable alternative for water distribution systems. The method is easily used, once it is performed under EPANET2 software interface.

*Keywords*: Lenhsnet, economic optimization, energy, EPANET2.

## 1 INTRODUCTION

Water distribution systems (WDS) design optimization have been receiving special attention from researchers of water resources and others related areas, due to the high implementation and operational costs of such systems. Generally, the variables which determine WDS conception and expansion project optimization are the hydraulic network pipeline diameters and pumping head.

WDS dimensioning is mathematically undetermined, thus allowing for innumerable solutions. Throughout history several dimensioning methods have been proposed. The first of them, namely classical ones, were restricted to choosing network diameters which provided the hydraulic balance of system. However, the scientific community has been looking to minimise WDS cost for decades.

In the late 1960s, the consolidation of micro-computing in global research centers enabled the development of techniques focusing on water network dimensioning; therefore the first optimization systems appeared based on mathematical linear programming models (LP)[1], as well as nonlinear programming (NLP)[2]. and dynamic programming (DP)[3].

More recently, brought models based on Genetic Algorithms (GA)[4], which are known as Evolutionary Algorithms (EA). Some researchers have been using methods based on the organization and/or evolution of others living species. Eusuff and Lansey (2003)[5] proposed Shuffled Frog Leaping Algorithms (SFLA), a meta-heuristic algorithm works based on the transformation of frogs and information exchange among the population. Maier et al. (2003)[6] used a new technique called Ant Colony Optimization (ACO) to WDS optimization, based on the analogy of the foraging behavior of a colony of searching ants, and their ability to determine the shortest route between their nest and a food source. Suribabu and Neelakantan (2006)[7] and Montalvo et al. (2008)[8] applied the Particle Swarm Optimization (PSO). PSO is an EA which utilises swarm intelligence to achieve the goal of optimizing a specified objective function. This algorithm uses the cognition of individuals and social behavior in the optimization process.

Numerous algorithms are being tested on distribution systems by researchers to get the most reliable solutions, using the shortest possible computational time[9]. EA methods presented good results, but they require much more computer time. Cui and Kuczera (2003)[10] highlight the problem of long computation times of some models and propose that such analyses be handled by super computers or by parallel computation. This makes their application by technicians difficult.

Abebe and Solomatine (1998)[11] implemented optimization algorithms in GLOBE, Adaptive Cluster Covering with Local Search (ACCOL) and GA, enabling a choice between accuracy and required computer time. Liong and Atiquzzaman (2004)[12] applied a powerful optimization algorithm, Shuffled Complex Evolution (SCE), in order to find solutions with low processing time. SCE deals with a set of population points and searches in all directions within the feasible space based on objective function. Gomes et al. (2008)[13] proposed an iterative method with a relatively short processing time for the optimization of the total costs for the expansion and rehabilitation of WDS.

However, in spite of considerable developments as detailed in literature, these techniques have not been accepted in practice[14]. Dimensioning of new networks and trial and error analysis for extensions are frequent. Jimenez et al. (2007)[15] states that optimization of water networks is not a rule in engineering yet and programs with a user friendly interface have only just begun appearing. This study aims at presenting an optimization model called Lenhsnet, which is designed to obtain an optimal solution of WDS and provide a friendly interface for engineers. This model, which is connected to EPANET 2.00.12[16], provides network pipelines diameters and pumping head as a response to dimensioning so as to find the total minimum cost of the system (implementation cost plus energy cost).

## 2 METHODOLOGY

The methodology includes an iterative process, based on an initial solution, in which the distribution network is made, according to minimum accepted diameters in the project. Such an initial solution has the minimum cost of network implementation, once it is made of the minimum diameters. However, such solution is not a feasible option, once it provides excessive head losses in network pipelines, resulting in high pumping head in the origin of the system.

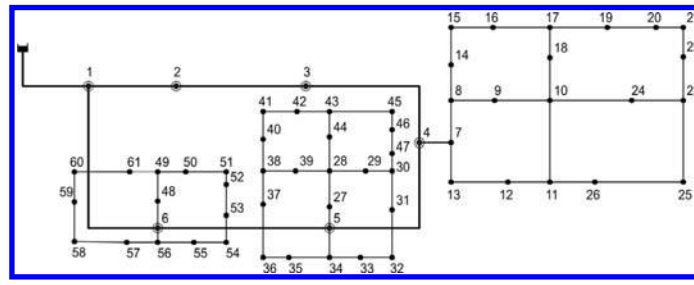


Figure 1. Layout for the R-9 Network.

Based on the initial solution, the calculation process develops iteratively, in a way in which each consequent solution depends on the previous one. The following solutions will be obtained by increasing, in each iteration, the diameter of one of the pipeline, in a way which will keep the additional cost as low as possible. The itterative process finishes when the configurations of network diameters comply with the restrictions imposed by the project (maximum velocity in pipes and the minimum pressure at nodes).

The algorithm method is associated with a hydraulic simulator, which will provide, at each iteration, the hydraulic balance of the system and the values of the variables of the outflow status of the network water flow. EPANET2 was chosen as simulator as it is widely accepted as the world standard in hydraulic and water quality modelling of WDS[9]. Most of the existing WDS have been modelled within EPANET2.

Once the initial solution is established, the simulation of network outflow is done in order to obtain the pressure in all nodes. Once the most unfavourable node is detected, the optimisation process begins. In each iteration, several diameter configurations will be tested. The effective diameter change, in one iteration, will be defined according to the lowest additional network cost in relation to pressure relief given to the network. The pipeline whose change is confirmed will be the one which provides the lowest pressure gradient. The Pressure Gradient (Pg) related to a certain pipeline is given through Eq. (1). It represents the marginal cost of the additional pressure of the most unfavourable node, brought by the change of diameter of the network pipeline by its superior adjacent.

$$Pg = (C_2 - C_1)/\Delta p \tag{1}$$

Where Pg is the pressure gradient value ($/m); $C_1$ is initial cost, related to current diameter ($); $C_2$ is cost of the diameter which is immediately larger than the diameter related to $C_1$($); and $\Delta p$ is the pressure gain in the most unfavourable node (m).

In each iteration there will be “i” pressure gradients, corresponding to “i” configurations of diameter changes in the “i” network pipelines; the optimum value of the pressure gradient (Pg*) will be the lowest one among all those calculated. The pipeline corresponding to Pg* will be called potential section (s*). s* will have a new configuration, in which the diameter will be the one which is immediately higher (tested). This last configuration will be the start configuration for the following iteration. The iterative optimisation process follows the aforementioned methodology until the optimal solution objective is obtained.

Once the dimensioning solution is obtained, the next step is to check if the velocities are within the acceptable maximum limit. If the velocity is greater than the maximum permitted, a new diameter is calculated based on the flow of the pipeline. After the diameter is defined, in case it is available, the initial solution for the model will be changed, and such part will be configured with the new diameter and the other ones with minimum diameters. Dimensioning will finish when the iterative process solution does not present any pipeline with a velocity greater than the maximum established one.

In the system dimensioning, in which the network is pressurised through a pumping station, this method takes the pumping energy cost during the project service life into account. The total cost of the distribution system (objective function) is the network implementation cost plus energy cost, Eq. (2).

$$C(D,Q,H) = \sum_{i=1}^{n} Li \times C(Di) + Cp \times H \times PWF \tag{2}$$

Where C(D,Q,H) is the total cost of the distribution system ($); Li is the length of ist pipeline; D is the internal diameter of the pipe; n is the number of the pipeline; Cp is the annual cost of electrical power ($); H is the pumping head (m); and PWF is the present worth factor.

The dimensioning optimisation system takes into account the energetic cost through the unit called energy cost gradient (Eg). The Eg represents the updated cost of water pressurisation per elevation meter and is provided by the Eq. (3).

$$Eg = \frac{9{,}81 \times Q}{\eta} \times Ec \times np \times PWF \tag{3}$$

Where Q is the pipeline flow rate ($m^3/s$); $\eta$ is the efficiency of the pump-motor unit; Ec is the unit cost of electrical energy ($/kWh); and np is the number of the hours of pumping per annum.

The iterative process is executed; at the end of each process iteration the Pg* is compared to the calculated Eg. In case the Pg* is lower than the Eg, the investment cost to reduce energy losses in network pipelines – and consequently to increase the pressure in the most unfavourable node – will be lower than the energy cost to increase its load in the network. The iterative process will continue increasing the diameters of the portions until the Pg* value exceeds the Eg value. Once the latter is obtained, the pumping head is determined in a way which the minimum pressure of the system is equal to the required minimum pressure.

Table 1. Solution for design of the R-19 Network – Diameters and flows.

| Pipeline | D (mm) | Flow (L/s) | Pipeline | D (mm) | Flow (L/s) | Pipeline | D (mm) | Flow (L/s) | Pipeline | D (mm) | Flow (L/s) |
|---|---|---|---|---|---|---|---|---|---|---|---|
| [1] | 600 | 456.20 | [19] | 100 | 2.27 | [37] | 100 | 1.77 | [55] | 100 | 3.64 |
| [2] | 600 | 395.08 | [20] | 100 | 1.38 | [38] | 100 | 5.86 | [56] | 150 | 10.15 |
| [3] | 600 | 351.01 | [21] | 100 | 4.98 | [39] | 100 | 9.54 | [57] | 150 | 27.01 |
| [4] | 600 | 309.77 | [22] | 100 | 0.40 | [40] | 150 | 21.68 | [58] | 150 | 22.04 |
| [5] | 450 | 86.56 | [23] | 100 | 4.44 | [41] | 100 | 8.10 | [59] | 100 | 10.85 |
| [6] | 100 | 3.23 | [24] | 150 | 8.94 | [42] | 100 | 4.88 | [60] | 100 | 9.05 |
| [7] | 300 | 58.61 | [25] | 150 | 11.74 | [43] | 100 | 2.35 | [61] | 100 | 6.09 |
| [8] | 400 | 222.17 | [26] | 150 | 17.20 | [44] | 100 | 0.04 | [62] | 100 | 1.43 |
| [9] | 200 | 38.62 | [27] | 100 | 6.93 | [45] | 100 | 6.35 | [63] | 100 | 3.11 |
| [10] | 100 | 10.25 | [28] | 100 | 1.26 | [46] | 100 | 9.24 | [64] | 100 | 11.91 |
| [11] | 100 | 3.84 | [29] | 300 | 86.58 | [47] | 100 | 3.89 | [65] | 150 | 16.17 |
| [12] | 100 | 8.46 | [30] | 400 | 145.46 | [48] | 100 | 1.40 | [66] | 150 | 27.05 |
| [13] | 400 | 162.13 | [31] | 400 | 148.72 | [49] | 100 | 3.20 | [67] | 100 | 7.90 |
| [14] | 400 | 170.51 | [32] | 250 | 67.24 | [50] | 100 | 6.67 | [68] | 100 | 3.99 |
| [15] | 400 | 182.21 | [33] | 250 | 62.88 | [51] | 150 | 18.02 | [69] | 100 | 0.29 |
| [16] | 150 | 19.78 | [34] | 150 | 26.19 | [52] | 150 | 23.20 | [70] | 100 | 1.58 |
| [17] | 150 | 14.14 | [35] | 150 | 21.63 | [53] | 100 | 7.74 | [71] | 100 | 4.70 |
| [18] | 100 | 8.57 | [36] | 100 | 3.17 | [54] | 100 | 1.26 | [72] | 100 | 8.22 |

## 3 EXAMPLE OF APPLICATION

The example (see Figure 1) is the R-9 Network, a medium-size municipal network in Joao Pessoa city – Brazil, implanted by urban water company in 1982, which consists of 53 nodes connected via 72 pipes and a reservoir. The input data for this problem are given in FORMIGA (2005)[17].

The costs and pumping conditions are: number of pumping hours per day, $np = 18$, efficiency of the motor-pump unit, $\eta = 0.75$, expected period of service for the network, $t = 20$ years, the average pumping discharge, equal to 456.2 L/s, power tariff, Ec = Cr$ 7/kWh (Current Brazilian currency in 1982, € 1,00 = Cr$ 65,00), annual rate of increase in the tariff of electrical power, $e = 6\%$, and annual discount rate, $i = 12\%$, captation water level = 30 m. The network data, in EPANET2 solver format, are available from http://www.lenhs.ct.ufpb.br/html/benchmarks.html. This network has been used previously by some researchers[17][18][19].

Once the stop condition is established, this method calculates the final pumping head, which was 13.74 m. When the pumping head is multiplied by the Eg, the current cost of electrical power of the system is determined: Cr$ 41,99 million. Pipeline network capital cost is Cr$ 215, 02 million. Consequently, the optimum solution of Cr$ 257,02 million cost units is obtained if the pipes as listed in Table 1 are used resulting in a minimum pressure in the system at node 19 being 15.00 m.

## 4 CONCLUSIONS

The method presented in this study, based on a dynamic programming process, enables engineers to follow several dimensioning alternatives through the developed program.

For various reasons, it is important to point out that it is not reasonable to expect that a WDS project be solved in a totally automatised way. Optimisation should be seen as a decision support tool. It is within such a paradigm that Lenhsnet is presented as an attractive and practical alternative for WDS dimensioning. The computer process time which is necessary for the method is very low and the inclusion and obtaining interface is easier, once the method runs in the EPANET2 program.

## REFERENCES


[1] Karmeli D., Gadish Y. and Meyers S. (1968), "Design of optimal water distribution networks", J. of Pipeline Division Vol. 94 (10), pp. 1–10.

[2] Jacoby S. (1968), "Design of optimal hydraulic networks", J. of Hydraul. Division, Vol. 94 (KY3), pp. 641–661.

[3] Liang T. (1971), "Design of conduit system by dynamic programming", J. of Hydraul. Division, Vol. 97, pp. 383–393.

[4] Dandy G.C., Simpson A.R. and Murphy L.J. (1996), "An improved genetic algorithm for pipe network optimization", Water Resour. Res., Vol. 32 (2), pp. 449–458.

[5] Eusuff M.M. and Lansey K.E. (2003), "Optimization of Water Distribution Network Design Using the Shuffled Frog Leaping Algorithm", J. Water Resour. Plng. Mgmt., Vol. 129 (3), pp. 210–225

[6] Maier H.R., Simpson A.R., Zecchin A.C., Foong W.K., Phang K.Y., Seah H.Y. and Tan C.L. (2003), "Ant Colony Optimization for the design of water distribution systems", J. Water Resour. Plng. Mgmt., Vol. 129 (3), pp. 200–209.

[7] Suribabu C.R. and Neelakantan T.R. (2006), "Design of water distribution networks using particle swarm optimization", Urban Water, Vol. 3 (2), pp. 111–120.

[8] Montalvo I., Izquierdo J., Perez R. and Tung M.M. (2008), "Particle Swarm Optimization applied to the design of water supply systems", Computers and Mathematics with Applications. Vol. 53 (3), pp. 769–776.

[9] Biscos C., Mulholland M., Le Lann M.V., Buckley C.A. and Brouckaert C.J. (2003), "Optimal operation of water distribution networks by predictive control using MINLP", Water SA, Vol. 29 (4), pp. 393–404.

[10] Cui L. and Kuczera G. (2003), "Optimizing urban water supply headworks using probabilistic search methods", J. Water Resour. Plng. Mgmt., Vol. 129 (5), pp. 380–387.

[11] Abebe A.J. and Solomatine D.P. (1998), "Application of global optimization to the design of pipe networks", *Proceedings of 3rd International Conferences on Hydroinformatics, Copenhagen, Balkema, Rotterdam, August*, pp. 1–8.

[12] Liong S.Y. and Atiquzzaman M. (2004), “Optimal design of water distribution network using shuffled complex evolution”, J. Institution Engineers., Vol. 44, pp. 93–107.
[13] Gomes H.P., Bezerra S.T.M. and Srinivasan V.S. (2008), “An iterative optimisation procedure for the rehabilitation of water supply pipe networks”, Water SA, Vol. 34 (2), pp. 225–236.
[14] SAVIC D.A. (2002), “Single-objective vs. multiobjective optimisation for integrated decision support”, Rizzoli A.E. and Jakeman A.J. (Eds.) *Integrated Assessment and Decision Support, Proceedings of the First Biennial Meeting of the International Environmental Modelling and Software Society, Lugano, Switzerland*, pp. 7–12.
[15] Jiménez M.R., Rodríguez K., Fuentes A.O. and De Luna F. (2007), Diseño óptimo de redes utilizando um algoritmo genético. In: Gomes H., Garcia R. and Rey L.I. (Org.). *Abastecimento de Água – O Estado da Arte e Técnicas Avançadas*. 1 ed. João Pessoa: Editora Universitária da UFPB.
[16] Rossman L.A. (2008), *EPANET 2.00.12. U. S.* Environment Protection Agency, Cincinnati, Ohio, USA.
[17] Formiga K.T.M. (2005), *Otimização multiobjetivo de projetos de redes de distribuição de água*. D.Sc. Thesis. University of São Paulo, São Paulo, Brazil.
[18] Leal A.F. (1995), *Estudo comparativo de métodos de otimização de redes malhadas pressurizadas*. M.Sc. Dissertation. Federal University of Campina Grande, Campina Grande, Brazil.
[19] Lopes A.V. (2003), *Otimização do dimensionamento e análise de confiabilidade de redes de distribuição de água*. M.Sc. Dissertation. University of Brasília, Brasília, Brazil.

*Environmental Hydraulics – López-Jiménez et al (eds)*
*© 2010 Taylor & Francis Group, London, ISBN 978-0-415-56697-1*

# Classical renewable hydro-energy devices: The case of an ancient Spanish watermill

Lino Montoro, Toni Pujol, Marc Pelegrí, Josep Ramon González & Joaquim Velayos
*Àrea de Mecànica de Fluids, Departament d'Enginyeria Mecànica i de la Construcció Industrial, Universitat de Girona, Girona, Spain*

ABSTRACT: We report here a recent study that obtains the hydraulic performance of an ancient Spanish horizontal watermill[1]. Previous studies of similar devices have focused on qualitative descriptions of their technical functioning, providing efficiency curves based on two-dimensional analytical approximations. In contrast, here we perform three-dimensional computational fluid dynamics (CFD) simulations that allow us to obtain quantitative values for both the hydraulic torque and the power. The results here found reveal how previous studies clearly overestimated the efficiency of these devices.

*Keywords*: Industrial heritage, Watermill, CFD.

## 1 INTRODUCTION

Spanish watermills were of small dimensions and their primarily use was milling flour and other cereal grains, although other applications such as making paper, powder, etc., are known[2]. At the end of XIX c., the arrival of steam power as a more efficient, affordable and reliable energy for industrial needs led to the abandonment of watermills.

The interest of recovery industrial heritage has promoted the reconstruction of the watermill located at Besalú, a medieval town in northeastern Spain. This watermill follows the general specifications of Spanish watermills, and it was abandoned on 1965, when a sudden flood destroyed part of the building.

Although several authors have analyzed the performance of similar ancient devices[3,4], here we make use of state-of-the-art computational fluid dynamics (CFD) tools, which has been successfully applied in modelling the details of complex flow fields in turbomachinery. Thus, the main novelty of the present work is the simulation of the system by using a commercial CFD code, which allows us to obtain the power extracted from the water fall as a function of the angular velocity of the waterwheel without assuming any of the approximations inherent in previous analytical calculations (that were expected to over-estimate the hydraulic performance)[3]. We would like to stress that here we provide a quantitative analysis by simulating the fluid dynamics in a three-dimensional (3-D) virtual model of the watermill, which contrasts with recent studies of watermills focused on a qualitative description of this ancient technology based on engineering graphics[3,5–6].

## 2 BASICS OF WATERILL FUNCTIONING

We have virtually designed the watermill from information provided by old photographs, semi-perdurable pieces made by stone or iron that are still in good conditions, critical examination of its ruins and direct interviewing of contemporary inhabitants (see Figure 1).

The upper chamber in Figure 1 is named the milling chamber, where the miller controls the whole process. In contrast, the lower chamber in Figure 1 is devoted to convert the hydraulic kinetic energy into mechanical energy. Thus, the water coming from an external conduit reaches the lock gate, which, once open, releases a waterfall that finally impacts with the horizontal waterwheel. The waterwheel contained 30 equally spaced cast iron blades and it was fixed to the drive shaft. At the lower end, the drive shaft contains a metallic pin that turns over a small squared copper piece, named dice. The dice is located above an horizontal wooden beam that supports the weight of the entire mechanism (drive shaft, waterwheel and, eventually, the runner millstone). Through a screw jack located at the very end (i.e., in the upper chamber) of the vertical bar shown in Figure 1, the miller is free to vertically move the horizontal wooden beam.

Once the runner millstone has sped up, the wooden beam is moved downwards slowly with the purpose of reaching a contact between the runner millstone and the static one. At this moment, the miller puts the grain into the upper central orifice of the runner millstone. The product, once milled, leaves the interface between the two millstones through the periphery, where a

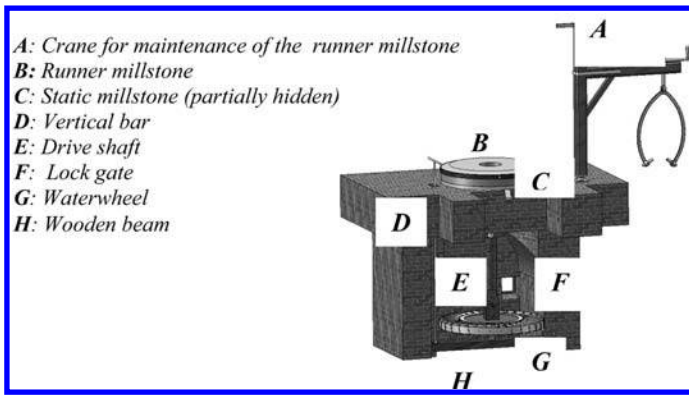


Figure 1. Isometric half section view of the virtual reconstruction of the Besalú watermill.

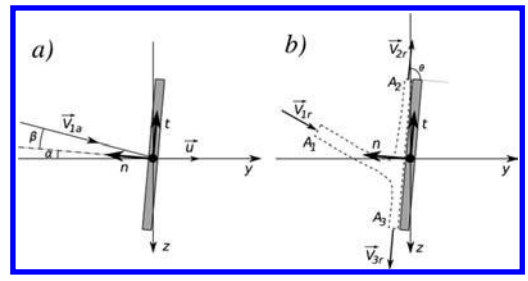


Figure 2. Two-dimensional approximation of the blade profile (a) and its corresponding control volume and surfaces for analytical calculations (b) (see text for details).

tank collects it once passed by a tiny filter in order to retain stone particles that could have been released during the abrasive process. It is important to note that the miller regulates the grain mass rate that entries into the runner millstone in order to achieve a regular functioning of the system (of the order of 75 rpm).

## 3 ANALYTICAL ANALYSIS

### 3.1 *Exit speed of the waterjet*

The exit speed of the waterjet into the lower chamber v is obtained by applying the generalized version of the Bernoulli equation from one point A in the external pond to another point B at the lock gate. By doing this we obtain

$$v = \sqrt{\frac{2gH}{1+fL/(4R_H)+\zeta}}\,, \tag{1}$$

where $H = z_A - z_B = 5.2$ m, $R_H$ is the hydraulic radius of the rectangular channel ($=4.1 \times 10^{-2}$ m) with a friction factor $f = 0.079$ and L ($=1.8$ m) its length. $\zeta$ is the minor loss coefficient here taken equal to 1 since the boundaries of the lock gate are sharp. Eq. (1) with these values gives an exit speed $v = 6.0$ m s$^{-1}$, from which we can assure that the regime is turbulent.

### 3.2 *Hydraulic torque and power*

The hydraulic torque T and power P obtained by the waterwheel is deduced by assuming a 2-D approximation of the actual blade profile that in its midpoint is inclined an angle $\alpha = 5°$ (see Fig. 2). The absolute velocity of the mean flow that impacts the midpoint of the blade in Fig. 2a is $V_{1a} = 6.23$ m s$^{-1}$ and its incidence angle $\beta = 10.7°$ with respect to the surface normal.

From the reference system attached to the blade, the n-t components of the relative flow velocity $V_{1r}$ (which is normal to area $A_1$) are

$$(V_{1rn}; V_{1rt}) = (\ V_{1a}\cos\beta + u_y\cos\alpha;\ V_{1a}\sin\beta\ \ u_y\cos\alpha), \tag{2}$$

where $u_y = r\omega$ is the linear waterwheel speed, with $\omega$ the angular velocity and $r = 0.560$ m the waterwheel radius.

From the Reynolds Transport Equation applied 1) to the mass balance and 2) to the conservation equation of momentum on the control volume, we derive the hydraulic torque in the z direction Tz ($=rF_y$), being

$$T_z = r\left(V_{1a}\cos\beta - u_y\cos\alpha - V_{1r}\cos\theta\right)\rho Q\cos\alpha\ , \tag{3}$$

since we assume a non-viscous fluid unable to exert shear forces on the blade (i.e., $F_y = F_n\cos\alpha$ since $F_t = 0$) and a non-planar blade (i.e., $\theta \neq 90°$). Eq. (3) with $\beta = 0$ and $\alpha = 0$ gives us the classical result for an impulse turbine (i.e., Pelton turbine). In Eq. (3), $\rho$ is the fluid density and Q the volumetric flow.

Finally, the power P extracted from the fluid is

$$P = \omega T_z\,. \tag{4}$$

## 4 CFD SIMULATION

### 4.1 *Model set up*

We use the STAR-CCM+ code, a CFD software from the CD-Adapco company. The virtual domain consists of a rectangular chamber 0.72 m high (z direction), 1.90 m wide (x direction) and 2.00 m long (y direction). The lock gate has the same dimensions as the actual one and its center is located at 0.3 m from the left wall. The 30 blades equally spaced 12° are surfaces that exactly follow the shape of the actual ones.

Surfaces are subdivided into small triangles. This discretization procedure is much more refined on the blades, where each one contains 450 triangles approximately with a value for the maximum length of the edge of the surface element equal to 10 mm. The volume is subdivided into tetrahedral elements with variable size. Volume elements between blades in the waterwheel have edges with a maximum length equal to 10 mm. On the other hand, the maximum length of the edge of volume elements is chosen equal to 15 mm in the density region whose boundaries approximately follow the water fall path. The final grid contains a total amount of $1.7 \times 10^6$ volume elements (tetrahedra) and $10^5$ surface elements (triangles), approximately. We have also performed few calculations with both coarser ($1.2 \times 10^6$ volume elements) and finer ($2.9 \times 10^6$ volume elements) grids in order to test the accuracy of our CFD simulation.

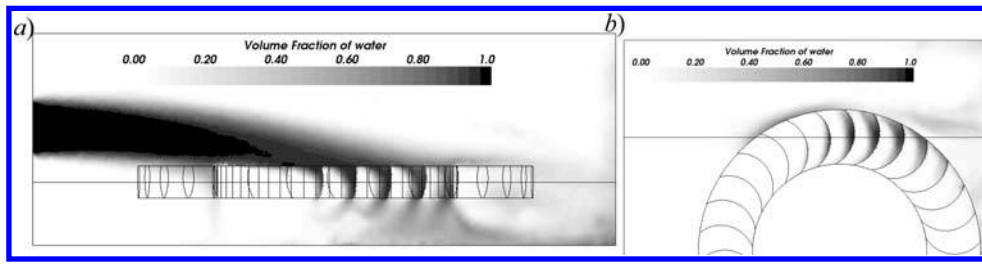


Figure 3. CFD simulation of the volume fraction of water in the y-z vertical plane (a) and in the x-y horizontal plane (b) that intersects the midpoint of the whaterwheel. This corresponds to the ancient waterwheel design rotating at 60 rpm at time t = 0.57 s after the waterjet exits the lock gate.

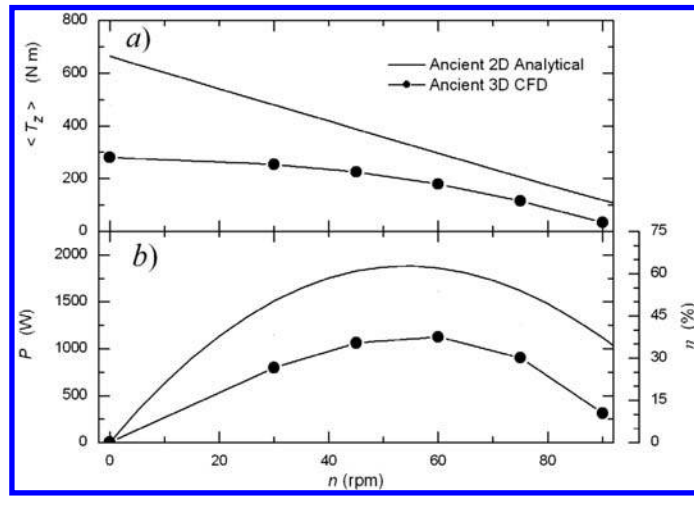


Figure 4. Simulated mean torque $<T_z>$ (a) and hydraulic power P (b) as a function of the waterwheel angular speed (in rpm) from CFD results. For comparison purposes, solid lines show the results from the analytical 2-D approximations. The right axis in panel (b) refers to the hydraulic efficiency with respect to the power of the flow that exits the lock gate $P_a$ (see text).

Turbulence has been modelled by means of the shear-stress transport (SST) k-ω model developed by Menter. We have performed several simulations for the same inlet mass flow rate with the waterwheel turning at different speeds (from n = 0 rpm until n = 90 rpm), which is intended to reproduce the effect of having different loads applied to the drive shaft. The time step chosen for the unsteady simulation is set to 0.002 s (or less) which implies a turn of the waterwheel of 1° at n = 90 rpm.

### 4.2 *Results*

Figure 3a-b shows the volume fraction of water at time t = 0.57 s at two perpendicular planes for the n = 60 rpm case. The vertical y-z plane (Fig. 3a) is located at the center of the lock gate. Note the strong effect of the external surface (i.e., the outer metallic ring) since it clearly divides the falling water into two main flows. The horizontal x-y plane (Figure 3b) located at the center of the waterwheel (rotates clockwise) clearly reveals the effect of the exterior metallic ring. Also note in Fig. 3b the small interaction of water on the rear surface of some blades, which would reduce the overall hydraulic efficiency.

In cylindrical coordinates (σ, φ, z), each cell i at the waterwheel surface develops a torque $T_{zi} = \sigma_i F_{\varphi i}$ where $\sigma_i$ is the radial distance of the center of cell i with respect to the waterwheel axis and $F_{\varphi i}$ is the hydraulic force exerted at cell i on the angular direction φ. The total torque $T_z$ at a given time step follows by adding the values of $T_{zi}$ for all the cell surfaces i on the waterwheel (blades, outer ring, etc.). The value of the mean torque $<T_z>$ is obtained by time averaging $T_z$ over 100 time steps (i.e., over 0.2 s) once the system has reached a regular functioning. Coarser and finer grids have been also used for analysing the n = 45, 60 and 75 rpm cases with results varying less than 4.7% for each case.

Figure 4a-b shows the mean torque $<T_z>$ and the hydraulic power P ($=\omega <T_z>$) obtained from the CFD simulation as a function of the turning velocity (in rpm). The right vertical axis in Fig. 4b shows the hydraulic efficiency with respect to the power available from the incoming water $P_a = \frac{1}{2}\rho v^3 S_c = 3024$ W, where $S_c$ corresponds to the surface area of the lock gate and v ($=6.0$ m s$^{-1}$) is the absolute value for the inlet water velocity at the lower chamber of the watermill.

Figure 4a-b also shows the analytical results that follow from Eqs. (3)–(4) with $\theta = 110^o$. The analytical values clearly overestimate the actual hydraulic torque $< T_z >$ and power P. At the expected nominal regime (75 rpm), the CFD analysis predicts a value for the hydraulic torque of only 56% that deduced from Eq. (3). Thus, the maximum power obtained by the original design is equal to 1125 W at 60 rpm, with an efficiency with respect to the total power available $P_a$ of only 37%.

## 5 CONCLUSIONS

We have analyzed the hydraulic performance of an ancient watermill located in the N-E\ region of Spain. The main feature of this watermill is its horizontal waterwheel with cast iron blades.

Here we first develop simple analytical expressions for both hydraulic torque and power based on a 2-D approximation for the blade geometry in terms of the waterwheel speed. This generalizes the expression used by Ref.[3] in the analysis of the hydraulic performance of an ancient watermill.

We have performed a 3-D CFD simulation of the full system. It is the first time that such a complex simulation (transient turbulent regime, liquid and gas phases, solid parts moving at fixed rpm, etc.) is carried out in the analysis of an ancient watermill. The simulated values for both the hydraulic torque and power are well below those obtained from the 2-D analytical approximations. This is because the actual problem is essentially 3-D and the blade shape becomes a key parameter for determining the hydraulic efficiency. Thus, in comparison with the hydraulic power of the incoming waterfall, the classical waterwheel reaches a maximum efficiency of only 37% at 60 rpm approximately. Such low efficiency values in comparison with usual figures for hydraulic turbines was the main reason why most of Spanish watermills did change the entire waterwheels for turbines (see, e.g.,[6]) or simply disappeared.

## ACKNOWLEDGMENTS

This work has been partially funded by the Generalitat de Catalunya under grant SGR-2005-00087, the MEC-FEDER under grant FIS 2006-12296-C02-02, and the European Commission under grant NEST-28192-FEPRE.

## REFERENCES

[1] Pujol, T., Solà, J., Montoro. L., and Pelegrí, M. (2009), "Hydraulic performance of an ancient Spanish watermill", Renew energy (in press).
[2] Molins fariners d'aigua. Centre d'Estudis del Maestrat, Benicarlo; 2001.
[3] Rojas-sola, J.I. and Domenech-Garcia, J. (2002), "Engineering and computer-aided design: study of watermills in southeastern Spain", Interciencia, vol. 12, pp. 745–751.
[4] Denny, M. (2005), "The efficiency of overshot and undershot waterwheels", Eur. J. Phys., Vol. 25, pp. 193–202.
[5] Rojas-Sola, J.I. and Lopez-Garcia, R. (2007), "Computer-aided design in the recovery and analysis of industrial heritage: Application to a watermill", Int. J. Engng Ed., Vol. 1, pp. 192–198.
[6] Rojas-Sola , J.I. and Lopez-Garcia, R. (2007), "Engineering graphics and watermills: Ancient technology in Spain", Renew energy, Vol. 32, pp. 2019–2033.

*Environmental Hydraulics – López-Jiménez et al (eds)*
*© 2010 Taylor & Francis Group, London, ISBN 978-0-415-56697-1*

# Air valves behavior. Comparison between compressible and incompressible flow

Vicente S. Fuertes-Miquel, Pedro L. Iglesias-Rey, Francisco J. García-Mares &
Daniel Mora-Meliá
*Centro Multidisciplinar de Modelación de Fluidos, Universidad Politécnica de Valencia, Valencia, España*

ABSTRACT: The flow through an air valve usually is considered adiabatic, since the required time so that the fluid crosses the air valve is too short to allow that great heat transference takes place. In addition, it seems logical to suppose that the analysis of the air valves behavior must be done considering a model of compressible flow. Indeed, when the operation pressures are important is necessary to go to models of compressible flow to characterize the behavior of the air inside the air valve. What happens is that the work pressures of the air valves of great orifice, used for the filling and emptying of the conductions, are very small (normally they work with pressures in the pipe below 0.3 bar relative). In these conditions, one verifies that the results provided by both models (compressible or incompressible flow) are very similar.

*Keywords*: Air valves, entrapped air, hydraulic transients, water supply systems.

## 1 INTRODUCTION

There are many causes that lead to the presence of air inside the pipeline: filling and emptying system operations, transient interruptions in the supply, vortex creation in the pump groups, depressurization occurring in the air valves due to transient operations, deliverance of dissolved air, etc. Whatever the origin of air in the pipes, it is an undisputed fact that its presence creates, in the majority of cases, unwanted problems. One of the most important problems is overpressure generation. Other problems include section reduction inside the pipe (which may cause collapse), additional generation head losses causing an increase in electricity consumption, problems with noise and vibrations, interior corrosion due to the oxygen transported by the air, failures in the measurement instrumentation, etc.

A possible solution for these problems is the use of air valves, which are devices than regulate the entrance or escape of air. Nevertheless, air valves are not always a guarantee of good system performance; some problematic circumstances can be generated due to its presence. An inappropriate valve selection, an inaccurate performance measurement, or inadequate maintenance may cause system problems.

Air inside the pipes must be released. This action must be done slowly in order to avoid forcing a water hammer inside the system. Their release capacity must be alto large enough, although this air release must be performed in a controlled way. Otherwise, if the air release is too sharp, undesirable processes might appear in the piping system (Campbell[1], Funk et al.[2], Stephenson[3], Leow and Lee[4], Fuertes[5], etc.).

Therefore, it is important to have the possible most realistic knowledge of the air valve behavior. Air valve behavior comes determined by its characteristic curve, that is to say, the relation between the mass flow expelled or admitted by the air valve and the existing pressure inside the pipe. In order to determine the characteristic curve of the air valve diverse models can be used.

## 2 AIR VALVES MODELING

For the modeling of air valves behavior it is common to make an analogy between the air flow through an air valve and the isentropic flow in nozzles (Wylie and Streeter[6], Chaudhry[7], Fuertes[5], etc.).

The flow of any gas or steam by a nozzle is practically adiabatic, since the required time so that each element of fluid happens through the nozzle is too short to allow that great heat transference takes place. If the flow did not have friction either the expansion that undergoes the fluid it would produce isentropic. From this hypothesis, it is possible to determine of analytical way the characteristic equations that they model the operation of the air valves.

Indeed, supposing the behavior of the air like perfect gas, an isentropic evolution, and considering insignificant the difference in elevation, the energy equation is simplified of the following form:

$$\frac{kR}{k-1}\cdot dT + v\cdot dv = 0 \tag{1}$$

being $k$ = specific-heat ratio ($k = 1.4$ for air), $R$ = gas constant, $T$ = temperature and $v$ = velocity.

Calculating the integral of this equation between the inflow section and the outflow orifice, and considering insignificant the kinetic term to the inflow section, it is obtained:

$$\frac{dm}{dt} = p_0^* A \sqrt{\frac{2k}{k-1}\frac{1}{RT_0}\left[\left(\frac{p^*}{p_0^*}\right)^{\frac{2}{k}} - \left(\frac{p^*}{p_0^*}\right)^{\frac{k+1}{k}}\right]} \tag{2}$$

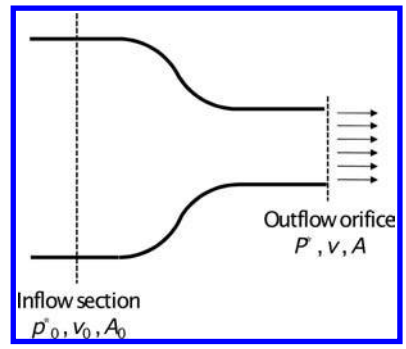


Figure 1. Convergent nozzle.

in which $dm/dt$ = mass flow rate, $p_0^*$ = entrance absolute pressure, $A$ = orifice section, $T_0$ = entrance temperature and $p^*$ = orifice absolute pressure.

This expression provides values corresponding to an "upper limit", since it considers that the isentropic evolution of the air is completely reversible. In fact, due to the friction and to the turbulence, the process is not reversible and the real mass flow is inferior. If $C_{exp}$ is the relation between the "real" mass flow and the "theoretical" mass flow expelled by the air valve (value that must be obtained by means of laboratory test) and distinguishing for an air valve in the phase of expulsion, it is obtained:

$$\left(\frac{dm}{dt}\right)_{\exp} = C_{\exp} p_t^* A_{\exp} \sqrt{\frac{2k}{k-1}\frac{1}{RT_t}\left[\left(\frac{p_{atm}^*}{p_t^*}\right)^{\frac{2}{k}} - \left(\frac{p_{atm}^*}{p_t^*}\right)^{\frac{k+1}{k}}\right]} \tag{3}$$

with $p_t^*$ = pipe absolute pressure, $A_{exp}$ = orifice section of air valve, $T_t$ = pipe temperature and $p_{atm}^*$ = atmospheric absolute pressure.

The previous expression is valid only when the flow through the air valve is subsonic, that is to say, when the absolute pressure inside the pipe is inferior to 1.92 bar. When this pressure is exceeded, the sonic conditions are reached in the outflow orifice and the velocity of the air stays constant (phenomenon known as "sonic blockade"), since supersonic flow cannot exist in a convergent nozzle.

If we integrate the energy equation considering the kinetic term in the inflow section is obtained:

$$\left(\frac{dm}{dt}\right)_{\exp} = \frac{C_{\exp} p_t^* A_{\exp}}{\sqrt{1-\left(\frac{p_{atm}^*}{p_t^*}\right)^{\frac{2}{k}}\left(\frac{A_{\exp}}{A_t}\right)^2}} \sqrt{\frac{2k}{k-1}\frac{1}{RT_t}\left[\left(\frac{p_{atm}^*}{p_t^*}\right)^{\frac{2}{k}} - \left(\frac{p_{atm}^*}{p_t^*}\right)^{\frac{k+1}{k}}\right]} \tag{4}$$

in which $A_t$ = entrance section.

## 3 INCOMPRESSIBLE MODEL

Supposing incompressible flow to model the air behavior in the nozzle, and considering insignificant the kinetic term in the inflow section, it is obtained:

$$\frac{dm}{dt} = A\sqrt{2\left(p_0^* - p^*\right)\rho_{ref}} \tag{5}$$

being $\rho_{ref}$ = constant density.

As density of reference can take the density to the inflow section ($\rho_t$ = airdensity inside the pipe), the density to the outflow section ($\rho_{atm}$ = air density in atmospheric conditions) or an average density ($\rho_{ref} = \frac{\rho_t + \rho_{atm}}{2}$).

Considering the coefficient $C_{exp}$ and distinguishing for an air valve in the phase of expulsion, the expression that allows calculating the expelled mass flow is:

$$\left(\frac{dm}{dt}\right)_{\exp} = C_{\exp} A_{\exp} \sqrt{2\left(p_t^* - p_{atm}^*\right)\rho_{ref}} \tag{6}$$

When we consider the kinetic term in the inflow section, the obtained expression is:

$$\left(\frac{dm}{dt}\right)_{\exp} = \frac{C_{\exp} A_{\exp}}{\sqrt{1-\left(\frac{A_{\exp}}{A_t}\right)^2}} \sqrt{2\left(p_t^* - p_{atm}^*\right)\rho_{ref}} \tag{7}$$

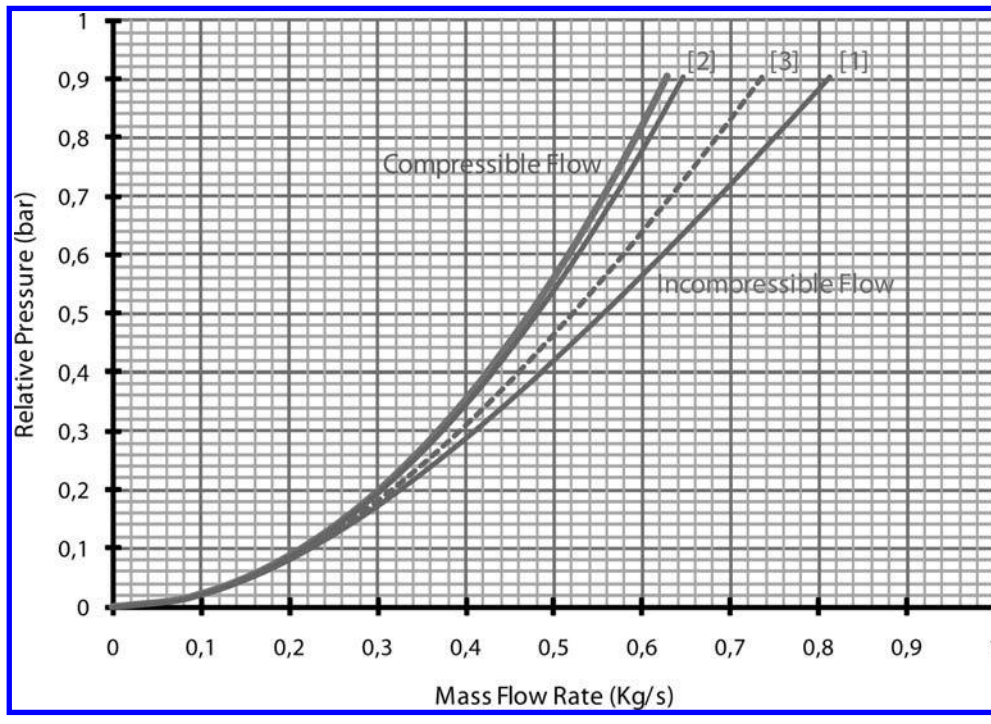


Figure 2. Comparison between compressible and incompressible flow ($D_{exp} = 50$ mm and $C_{exp} = 0{,}7$).

Table 1. Values of coefficient $C_{exp}$ for different models.

| | |
|---|---|
| Compressible Flow | $C_{exp} = 0.616$ |
| Incompressible Flow (atmospheric density) | $C_{exp} = 0.610$ |
| Incompressible Flow (air density inside the pipe) | $C_{exp} = 0.520$ |
| Incompressible Flow (average density) | $C_{exp} = 0.562$ |

In the graph of figure 2 we compared the expression (3), corresponding to a model of compressible flow where the velocity in the entrance section has not considered, with the expression (6), that it corresponds to a model of incompressible flow where the velocity in the inflow section has not considered and where we considered as density of reference the density to the inflow section [1], the density to the outflow section [2] and the average density between inflow and outflow sections [3].

As it can be observed in the graph, the differences between both models are small. Considering that the air valves usually are designed for a relative pressure of 0.3 bar and that really they work even with lower pressures, the results obtained with the models of compressible and incompressible flow can be considered equally valid.

In addition, in the previous graph all the curves are shown with the same $C_{exp}$ coefficient. By definition, this coefficient is the relation between the "real" mass flow and the "theoretical" mass flow, reason why it will be different for each one of the used expressions. Next we analyzed the obtained real results by means of the test of an air valve and the $C_{exp}$ coefficients corresponding to the different models are obtained to be able to compare them.

## 4 CASE STUDY

An air valve of 50 mm nominal diameter has practiced in the laboratory. In figure 3 the experimental results can be seen. From the data collected in the test we have calculated the $C_{exp}$ coefficients corresponding to each one of the models (table 1) and we have represented the corresponding curves (figure 3).

As it is observed, anyone of the presented models adjusts the obtained experimental results in laboratory rather well. Therefore, all of them are perfectly valid.

## 5 CONCLUSIONS

In order to be able to analyze the air valves behavior it is necessary to know its characteristic curve (relation between the difference in pressure and the mass flow expelled or admitted by the air valve). Like it happens to the pumps and other hydraulic elements, the unique form to obtain its characteristic curve is by laboratory testing.

Generally, a model of compressible flow is used to study the air valve behavior. Nevertheless, the results that a model of incompressible flow provides (much more simple) are also perfectly valid when the work pressures are small (air valve working in subsonic conditions).

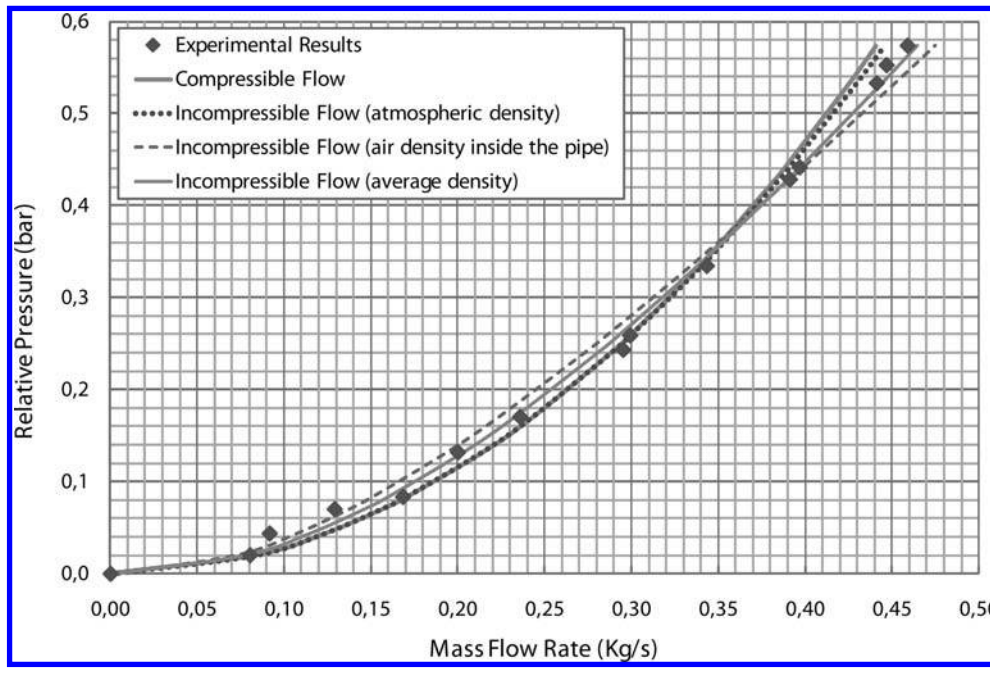


Figure 3. Comparison between experimental results and different models (air valve DN50).

## REFERENCES


[1] Campbell, A. (1983), "The effect of air valves on surge in pipelines", *Proceedings of the 4th International Conference on Pressure Surges (Bath, UK)*, pp. 89–102.

[2] Funk, J.E., Wood, D.J., Reddy, L.S. and Denger, D.C. (1992), "Pressure surges due to rapid expulsion of air", *Proceedings of the International Conference on Unsteady Flow and Fluid Transients (Durham, UK)*, pp. 313–319.

[3] Stephenson, D. (1997), "Effects of air valves and pipework on water hammer pressures", Journal of Transportation Engineering, ASCE, Vol. 123, pp. 101–106.

[4] Leow, L.C. and Lee, T.S. (1998), "Effects of air valve on pressure surges during pumping trip in pumping station", *Proceedings of the XIX Symposium on Hydraulic Machinery and Cavitation, IAHR (Singapur)*, pp. 556–563.

[5] Fuertes, V.S. (2001), *Transitorios hidráulicos con aire atrapado*, PhD Thesis, Universidad Politécnica de Valencia, Spain.

[6] Wylie, E.B. and Streeter, V.L. (1993), *Fluid transients in systems*, Prentice Hall, Englewood Cliffs, New Jersey, USA.

[7] Chaudhry, M.H. (1987), *Applied hydraulic transients*, Van Nostrand Reinhold Company, New York, USA.

*Environmental Hydraulics – López-Jiménez et al (eds)*
*© 2010 Taylor & Francis Group, London, ISBN 978-0-415-56697-1*

# Pipelines with entrapped air pockets. Comparison between adiabatic and isothermal flow

Vicente S. Fuertes-Miquel, Pedro L. Iglesias-Rey, P. Amparo López-Jiménez & Daniel Mora-Meliá
*Centro Multidisciplinar de Modelación de Fluidos, Universidad Politécnica de Valencia, Valencia, España*

ABSTRACT: This work tries to study the behavior of the air inside the pipe when air through air valves is being expelled. Normally, usually one admits that the air has an isothermal behavior. Nevertheless, when transient is very fast, the adiabatic behavior adjusts much more to the reality. Obvious, in a real installation an intermediate evolution between these two extreme conditions will take place. Of the made analysis, it is verified that the results vary of significant form according to the adopted hypothesis (isothermal or adiabatic). From the point of view of the pressure reached about air pocket usually it is adopted the most unfavorable hypothesis (isothermal behavior). Nevertheless, from the perspective of the water hammer that takes place when the water column arrives at the air valve and an abrupt closing takes place, the most unfavorable hypothesis is the opposite (adiabatic behavior). In this case, the residual velocity with which the water arrives at the air valve is higher and consequently, the generated water hammer is greater.

*Keywords*: Air valves, entrapped air, hydraulic transients, water supply systems.

## 1 INTRODUCTION

In the water distribution networks under pressure, mainly in those of irregular profile, the installation of air valves is necessary. Air valves allow the air admission when the pipe enters depression (avoiding in this way its collapse), and in addition they facilitate the expulsion of the air (avoiding the appearance of high overpressures). Of the two situations, the phase of air expulsion is most critical (Fuertes[1]). When the air valve works expelling air, it must allow a volume of outflow sufficiently great like so that the pressure of the air inside the pipe does not exceed a certain value. The exit must be controlled (the outflow does not have to be excessive), because in very fast expulsions the water column advances at a high velocity and, when it arrives at the position of the air valve and the abrupt closing of the same takes place, the generated water hammer can be very problematic. Therefore, it is very important to analyze the behavior of the air valves in the phase of expulsion, since it is fundamental to be able to realise a correct selection.

The classic texts (Wylie and Streeter[2], Chaudhry[3], and so on) deal with analogous way these conditions of contour. On the one hand, they suppose an isothermal behavior for the air inside the pipe. Nevertheless, to calculate the amount of air that leaves through the air valve they consider the expressions of the isentropic flow, characteristic of a fast transient without heat interchange (adiabatic behaviour).

Indeed, in the case of the air to get out by the air valve, the required time so that the air crosses the air valve is too short to allow that significant heat transference takes place. Thus, the adopted hypothesis (adiabatic evolution) seems quite suitable. Nevertheless, to analyze the behavior of the air inside the pipe, the validity of the hypothesis that normally is used (isothermal evolution) is not so evident. The transient velocity can determine the behavior of the air inside the pipe, reason why its evolution can be adiabatic (quickly transient), isotherm (slower transient) or any intermediate situation (surely this option is nearest the reality). As it will be seen in the present work, the obtained results show important differences according to the considered hypothesis.

The analysis of the evolution of the air inside the pipes usually is done always supposing an isothermal behavior, whereas the evolution of the air in other elements, like for example air vessels, it has been always an aspect widely discussed. In air vessels, the analysis of the behavior of the air has deserved the interest of numerous researchers, who have considered all the possible options: adiabatic behavior ($k = 1.4$), isothermal behavior ($k = 1$), and even any intermediate situation, what is called polytropic evolution ($1 < k < 1.4$).

The behavior of the entrapped air in pipes has not studied in depth. In this case, as already it has commented, usually one considers a behavior isothermal. Nevertheless, exists some works (Martin[4], Izquierdo et al.[5], Fuertes et al.[6]) that has analyzed the evolution of the air for different values from the explaining $k$.On the other hand, it has been demonstrated that the majors pressure peaks are reached after isothermal evolutions (Abreu et al.[7], Fuertes[1]), although there are criteria no established on the quick that must be the hydraulic transient to not to have consider the heat interchange and to consider an adiabatic behavior. The experimental datas available in the literature (Lee and Martin[8], Fuertes et al.[9], Fuertes[1]), given the reduced dimensions of the facilities where the measurements are made, they correspond to very fast transient. In these cases, the exponent that better adjust the experimental results is $k = 1.4$ (adiabatic behavior).

The object of the present work is to evaluate and compare the greater peak of pressure generated in the process of air expulsion through an air valve for extreme behaviors (isothermal and adiabatic) of the air inside the pipe. The flow through the air valve is admitted adiabatic. Comparing the two analyzed options, it is verified that the obtained results are very different according to is the used hypothesis. In order to determine the grade of validity of the extreme models and the conditions of intermediate behavior (polytropic evolution), we require additional investigations that will have to lean in experimental measures.

## 2 MATHEMATICAL MODEL

It is tried to compare the results derived from extreme behaviors of the air inside the pipe. For it, an installation with an entrapped air pocket is considered (figure 1), that it must be evacuated through an air valve located in the edge of the pipe. In order to realise the proposed analysis, the installation is simplified supposing that after the air valve there is a closed edge.

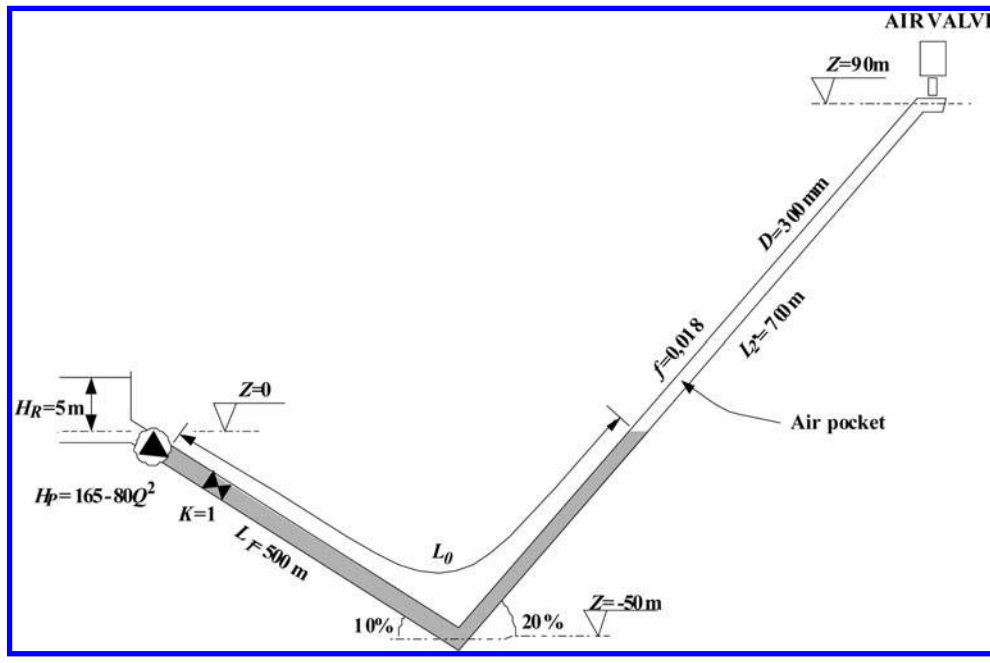


Figure 1. Analyzed system.

The system is fed by a pump whose characteristic curve ($H_P - Q$) is well-known. In order to simulate slower or faster transients, different cases are analyzed, varying the size of the air valve, the initial lenght of the water column and the opening time of the valve.

Admitting that the movement of the liquid column can study without considering the elastic effects (Fuertes[1]), the equations that model the behavior of the system are:

a) Filling water column dynamics. Mass oscillation equation:

$$\frac{dv}{dt} = \frac{p_0^* - p_a^*}{\rho L} - g\frac{\Delta z}{L} - \frac{f\, v|v|}{2D} \tag{1}$$

being $v$ = water column velocity, $t$ = time, $p_0^*$ = upstream pressure, $p_a^*$ = entrapped air pressure, $\rho$ = water density, $L$ = water column length, $g$ = gravity factor, $\Delta z$ = geometric head between the extremes of the water column, $f$ = Darcy-Weisbach factor and $D$ = pipe diameter, (* means absolute pressure).

b) Filling water column dynamics. Interface position:

$$L = L_0 + \int_0^t v\, dt \qquad \left(\frac{dL}{dt} = v\right) \tag{2}$$

in which $L_0$ = initial water column length.

c) Mass balance of the entrapped air pocket:

$$m_a(t) = m_a(t_0) + \int_0^t m_a dt \tag{3}$$

with $m_a$ = mass of the air inside the pipe.

d) Air pocket behavior (Zhou et al.[10]):

Case d1.- Isothermal

$$p_a^* \forall = p_a^*(L_T - L)A = m_a RT \tag{4}$$

Case d2.- Adiabatic

$$\frac{dp_a^*}{dt} = -k\frac{p_a^*}{\forall}\frac{d\forall}{dt} - \frac{p_a^*}{\forall}\frac{k}{\rho_a}\frac{dm_a}{dt} \tag{5}$$

in which $\forall$ = air volume, $L_T$ = total length, $A$ = pipe area, $R$ = universal gas constant, $T$ = air temperature and $\rho_a$ = air density.

e) Upstream boundary condition. A pump is the energy source (see figure 1), then $p_0^*$ is given by:

$$H_R + \frac{p_{atm}^*}{g\rho} + H_P = \frac{p_0^*}{g\rho} + \frac{v^2}{2g} + \varsigma\frac{v^2}{2g} \tag{6}$$

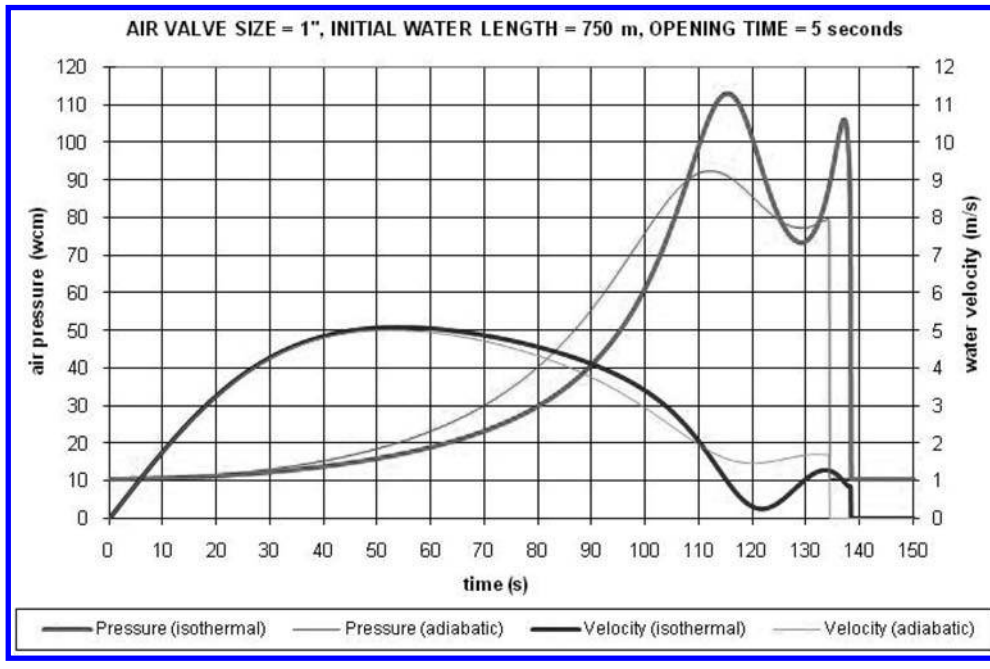


Figure 2. Evolution of pressure and velocity corresponding to air valve size 1″, $L_0 = 750$ m, $T_{open} = 5$ seconds.

being $H_R$ = reservoir elevation, $p^*_{atm}$ = atmospheric pressure, $H_P$ = pump head and $\varsigma$ = valve losses coefficient.

f) Downstream boundary condition (Fuertes[1]):

Case f1.- Subsonic air velocity through the valve ($p^*_{atm} < p^*_a < 1.893 \cdot p^*_{atm}$)

$$\frac{dm_a}{dt} = C_d A_v p^*_a \sqrt{\frac{7}{RT}\left[\left(\frac{p^*_{atm}}{p^*_a}\right)^{1.4286} - \left(\frac{p^*_{atm}}{p^*_a}\right)^{1.7143}\right]} \tag{7}$$

Case f2.- Sonic air velocity through the valve ($p^*_a > 1.893 \cdot p^*_{atm}$)

$$\frac{dm_a}{dt} = C_d A_v \frac{0.6847}{\sqrt{RT}} p^*_a \tag{8}$$

with $C_d$ = air valve discharge coefficient and $A_v$ = air valve area.

This set of equations determines six unknown variables: the motor and resistant pressures ($p^*_0$ y $p^*_a$), the two variables characteristic of the liquid column ($L$ y $v$) and the two variables that define entrapped air pocket ($\rho_a$ y $m_a$).We have eight equations, of which four are common ((1), (2), (3) and (6)), while the other four ((4)–(5) and (7)–(8)) are used of alternative form based on the considered hypothesis. Therefore, in anyone of the possible cases, one has a system with six independent equations and six unknown variables. Its resolution provides the results.

## 3 CASE STUDY AND RESULTS

We consider the installation shown in figure 1, where the most important characteristics of the system are included. The transient begins, once the pump has reached its velocity of regime, with the opening of the valve (different manipulation times of the valve are considered). The variables of greater interest are the maximum pressure that reaches the air pocket and the residual velocity of the water when the air is expelled totally. The value of this residual velocity is important since it determines the water hammer that is generated when the water column arrives at the edge of the pipe and the abrupt closing of the air valve takes place.

Varying some parameters of the system, we have studied twelve different cases. In particular:

a) Size of the air valve: Diameters of 1″ and 2″.
b) Inicial lenght of the water column: 1 m and 750 m.
c) Opening time: Instantaneous opening ($T_{open} = 0$), linear opening in 5 and 20 seconds.

For each one of the twelve analyzed systems we have both considered extreme behaviors of the air inside the pipe (isothermal and adiabatic). Figure 2 shows the evolution of the most significant variables (pressure of the air and velocity of the water) for the case of an air valve of 1″ of diameter, an initial length of the water column of 750 ms ($L_0 = 750$ m) and supposing a linear opening of the valve in 5 seconds ($T_{open} = 5$ seconds).

The results shown in figure 2 show the significant differences that there is between the two considered hypotheses (isothermal or adiabatic behavior). The peak of pressure in isothermal conditions (113.1 wcm) is remarkably superior to the maximum

Table 1. Main results corresponding to air valve size 1″ and initial water length 1 m.

| | | Opening time $T_{open} = 0$ | Opening time $T_{open} = 5$ seconds | Opening time $T_{open} = 20$ seconds |
|---|---|---|---|---|
| Maximum pressure | Isothermal | 110.0 m | 109.4 m | 105.2 m |
| | Adiabatic | 106.1 m | 104.9 m | 98.5 m |
| Residual water velocity | Isothermal | 0.94 m/s | 0.94 m/s | 0.94 m/s |
| | Adiabatic | 1.68 m/s | 1.68 m/s | 1.67 m/s |
| Transient duration | Isothermal | 229.7 s | 275.2 s | 356.5 s |
| | Adiabatic | 214.7 s | 260.1 s | 341.4 s |
| Maximum air temperature | Isothermal | 15°C | 15°C | 15°C |
| | Adiabatic | 287.3°C | 285.5°C | 275.6°C |

Table 2. Main results corresponding to air valve size 1″ and initial water length 750 m.

| | | Opening time $T_{open} = 0$ | Opening time $T_{open} = 5$ seconds | Opening time $T_{open} = 20$ seconds |
|---|---|---|---|---|
| Maximum pressure | Isothermal | 116.0 m | 113.1 m | 101.0 m |
| | Adiabatic | 95.5 m | 92.5 m | 81.0 m |
| Residual water velocity | Isothermal | 0.83 m/s | 0.84 m/s | 0.95 m/s |
| | Adiabatic | 1.68 m/s | 1.69 m/s | 1.64 m/s |
| Transient duration | Isothermal | 109.9 s | 138.3 s | 195.7 s |
| | Adiabatic | 106.0 s | 134.3 s | 191.8 s |
| Maximum air temperature | Isothermal | 15°C | 15°C | 15°C |
| | Adiabatic | 270.8°C | 265.9°C | 245.8°C |

Table 3. Main results corresponding to air valve size 2″ and initial water length 1 m.

| | | Opening time $T_{open} = 0$ | Opening time $T_{open} = 5$ seconds | Opening time $T_{open} = 20$ seconds |
|---|---|---|---|---|
| Maximum pressure | Isothermal | 48.5 m | 47.2 m | 39.4 m |
| | Adiabatic | 37.9 m | 36.2 m | 30.1 m |
| Residual water velocity | Isothermal | 3.34 m/s | 3.35 m/s | 3.28 m/s |
| | Adiabatic | 3.93 m/s | 3.91 m/s | 3.66 m/s |
| Transient duration | Isothermal | 153.3 s | 199.8 s | 285.3 s |
| | Adiabatic | 152.4 s | 198.9 s | 284.4 s |
| Maximum air temperature | Isothermal | 15°C | 15°C | 15°C |
| | Adiabatic | 144.6°C | 139.0°C | 118.0°C |

pressure in adiabatic conditions (92.5 wcm). On the other hand, in isothermal conditions the opposition that offers entrapped air pocket to the advance of the water column is greater and, as a result of it, the residual velocity of the water is smaller and also the water hammer when the air valve closes.

It can seem that the hypothesis that habitually is adopted (isothermal behavior) is more conservative, but in fact this is not thus. From the perspective of the maximum pressure of air pocket during the phase of expulsion, the hypothesis of isothermal evolution gives rise to an upper pressure (113.1 wcm against 92.5 wcm). Nevertheless, if we paid attention to the water hammer that generates the residual velocity when the water column arrives at the air valve and this one closes abruptly, the obtained result is right the opposite. In fact, supposing a velocity of the pressure wave $a = 1000$ m/s, the calculated residual velocities (0.84 m/s in isothermal case and 1.69 m/s in the adiabatic case) will generate important pressure peaks (85.6 wcm and 172.3 wcm respectively). Therefore, unlike which it can initially seem the adiabatic behaviour is most unfavorable (the peak of pressure in entrapped air pocket is 92.5 wcm, but the water hammer is 172.3 wcm when the air valve closes).

Tables 1 to 4 show the most significant results of all the analyzed cases. The main conclusions that are derived from the analysis are:

- The maximum pressure that reaches air pocket inside the pipe is always greater when the hypothesis of isothermal behavior is considered, whereas with the residual velocity of the liquid column it happens right the opposite. Therefore, if we paid attention only to the pressure of entrapped air pocket, the isothermal case is most unfavorable. On the other hand, if we consider the produced water hammer when the air valve is closed the adiabatic behavior is more critical (against which usually it is assumed).
- Pressure peaks of the air inside the pipe depend, by this order: the air valve size, the considered hypothesis (isothermal or adiabatic behavior), the air pocket size, and finally, the time of valve manipulation.
- The residual velocity of the water column when it arrives at the position of the air valve and this one is closed (really, this it is the most critical factor) shows a very similar tendency. In this case, also the most influential factor is the air valve size.
- In the transient duration a different tendency is only appraised. Logically, the most influential variable now is the initial length of the water column, followed as large as the air valve and the time of valve manipulation. It is necessary to emphasize that

Table 4. Main results corresponding to air valve size 2″ and initial water length 750 m.

| | | Opening time $T_{open} = 0$ | Opening time $T_{open} = 5$ seconds | Opening time $T_{open} = 20$ seconds |
|---|---|---|---|---|
| Maximum pressure | Isothermal | 49.7 m | 44.9 m | 29.4 m |
| | Adiabatic | 29.9 m | 27.5 m | 21.0 m |
| Residual water velocity | Isothermal | 3.56 m/s | 3.52 m/s | 3.13 m/s |
| | Adiabatic | 3.96 m/s | 3.85 m/s | 3.27 m/s |
| Transient duration | Isothermal | 82.0 s | 111.3 s | 171.6 s |
| | Adiabatic | 82.0 s | 111.3 s | 171.4 s |
| Maximum air temperature | Isothermal | 15°C | 15°C | 15°C |
| | Adiabatic | 117.2°C | 108.1°C | 79.9°C |

the transient duration practically is not affected by the behavior (isothermal or adiabatic) supposed to model the evolution of the air inside the pipe.

The air valve size has great importance. For the installation that we studied, and due to the relevance that has the residual velocity, it would be advisable to install the smaller air valve (1" of diameter). With the small air valve, the maximum pressure that would have to support the installation would be approximately two or three times smaller compared with the case of installing the 2" air valve. It is appraised, once again, that when the air valves are selected, is very problematic undersizing (the expulsion capacity would not be sufficient) and also oversizing (the water hammer when the air valve closes is important).

It is interesting to observe that when reducing the size of the air valve diverse peaks of pressure can appear (in figure 2 two peaks are observed). This is because the air valve is too small and it is not able to expel the sufficient amount from air during the filling of the pipe. Consequently, inside the pipe it remains an entrapped air pocket that is compressed and it expands repeated times while the air is leaving slowly to the outside.

In the analyzed system, for the air valve of 1″ diameter, and for a velocity of pressure wave around the 1000 m/s, the order of magnitude of the maximum pressure of entrapped air pocket is similar to the water hammer induced by the residual velocity when the air valve closes. Nevertheless, when the air valve is greater (2″ in the example), the pressure generated by the water hammer is greater beyond the one that is reached during the evolution of air pocket inside the pipe. Therefore, from a certain size of the air valve, the most unfavorable hypothesis is to suppose an adiabatic behavior of the entrapped air pocket.

Really, so and as it has been insisted on this work, it is not trivial the question relative to the behavior, isothermal or adiabatic, of the air inside the pipe. The evolution of the air (isothermal or adiabatic) remarkably determines the value of the maximum pressure that is generated in the process of air expulsion during the filling of the pipe.

In the analyzed system, given the transient duration (a few minutes), it seems that both hypotheses are, a priori, possible. In any case, it must be clear that they are values in extreme conditions. In reality, the behavior of the air will follow an intermediate evolution ($1 < k < 1.4$), depending essentially on the transient velocity.

## 4 CONCLUSIONS

The present work shows the remarkable influence that has the behavior of the air (isothermal or adiabatic) concerning the maximum pressure that will have to support the installation. Therefore, the necessity of a deeply investigation is evident on the field of validity of each model of behavior. This investigation would have to include, based in experimental measures, an exhaustive energy balance of the hydraulic transient.

The process is easy to understand. In adiabatic conditions, the greater heating of the air supposes an investment higher in thermal energy instead of elastic energy. Consequently, the pressure of entrapped air pocket is smaller, the opposition to the water column is smaller, the residual velocity is greater and the water hammer induced by the abrupt closing of the air valve is greater. If the behavior were isothermal, the process would be the opposite (it increases the pressure of entrapped air pocket, it stops the water column, the residual velocity is smaller and the water hammer is reduced).

It is advisable to emphasize that the normally adopted hypothesis (isothermal behavior) does not provide the maximum values of pressure. The pressure that reaches the air during its evolution inside the pipe is greater when an isothermal behavior is considered. However, this it is not the most unfavorable case. The critical situation causes the water hammer that takes place when the air valve is closed and, in this case, the adiabatic behavior provides greater peaks of pressure.

Finally, the great importance is evident that has a suitable selection of air valve size, to reduce the maximum values of pressure. If the air valve is too small, the air pocket will be compressed excessively and the reached pressure will be very high. If the air valve is too great, the air pocket will be expelled without problems, but the velocity reached about the water column will be very important and, when the closing of the air valve takes place, a very dangerous water hammer will be generated. Unlike which it could seem a priori, the most adverse situations take place by the shock of the water column against the air valve. In the same way it is certain that, in a real installation, it is not habitual to be with a closed edge. Following which there is downstream the air valve, the situation will be more or less critical. If, for example, downstream there is a water column of great dimensions, the situation could be similar to the considered one in the analyzed system.

## ACKNOWLEDGEMENTS

This article has been made possible through actions of the CMMF researchers, involved in the following projects: *DANAIDES: Desarrollo de herramientas de simulación para la caracterización hidráulica de redes de abastecimiento a través de indicadores de calidad del agua. REF. DPI2007-63424. Ministerio de Educación y Ciencia de España.*

REFERENCES


[1] Fuertes, V.S. (2001), *Transitorios hidráulicos con aire atrapado*, PhD Thesis, Universidad Politécnica de Valencia, Spain.

[2] Wylie, E.B. and Streeter, V.L. (1993), *Fluid transients in systems*, Prentice Hall, Englewood Cliffs, New Jersey, USA.

[3] Chaudhry, M.H. (1987), *Applied hydraulic transients*, Van Nostrand Reinhold Company, New York, USA.

[4] Martin, C.S. (1976), "Entrapped air in pipelines", *Proceedings of the 2nd International Conference on Pressure Surges (London, UK).*

[5] Izquierdo, J., Fuertes, V.S., Cabrera, E., Iglesias, P.L. and García-Serra, J. (1999), "Pipeline start-up with entrapped air", Journal of Hydraulic Research, IAHR, Vol. 37, pp. 579-590.

[6] Fuertes, V.S., Cabrera, E., Izquierdo, J. and Iglesias, P.L. (1999), "Peak pressure evaluation in pipelines with entrapped air pockets", *Proceedings of the 3rd ASME/JSME Joint Fluids Engineering Conference (San Francisco, USA).*

[7] Abreu, J.M., Cabrera, E., García-Serra, J. and Izquierdo, J. (1991), "Boundary between elastic and inelastic models in hydraulic transients with entrapped air pockets", *Proceedings of the International Meeting on Hydraulic Transients with Water Column Separation (Valencia, Spain)*, pp. 159–181.

[8] Lee, N.H. and Martin, C.S. (1999), "Experimental and analytical investigation of entrapped air in a horizontal pipe", *Proceedings of the 3rd ASME/JSME Joint Fluids Engineering Conference (San Francisco, USA).*

[9] Fuertes, V.S., Arregui, F., Cabrera, E. and Iglesias, P.L. (2000), "Experimental setup for entrapped air pockets model validation", *Proceedings of the 8th International Conference on Pressure Surges (The Hague, Holland)*, pp. 133–146.

[10] Zhou, F., Hicks, F.E. and Steffler, P.M. (2002), "Transient flow in a rapidly filling horizontal pipe containing trapped air", Journal of Hydraulic Engineering, ASCE, Vol. 128, pp. 625–634.

*Environmental Hydraulics – López-Jiménez et al (eds)*
*© 2010 Taylor & Francis Group, London, ISBN 978-0-415-56697-1*

# Parameters determination for a mixing model in storage facilities in water distribution systems

Fco. Javier Martínez-Solano, José de Jesús Mora-Rodríguez,
Pedro L. Iglesias-Rey & Gonzalo López-Patiño
*Centro Multidisciplinar de Modelación de Fluidos, Universidad Politécnica de Valencia, Valencia, España*

ABSTRACT: In the interior of tanks of drinking water, the dispersion of substances is one of the most complex aspects of any model of drinking water quality in the network. Storage facilities are often failure in different zones according to its behaviour related with the disinfectant dispersion and its subproducts. In this paper we used a computational fluid dynamics (CFD) program to determine the parameters that represent the evolution of concentrations in the interior of these tanks. As a result, it has established a protocol to develop CFD models in order to analysis the mixture on tanks considering different patterns of interchange flows and it has verified the CFD model as a tool to support the hydraulic simulation models when elements have a complex behavior to represent equations on one dimension. The case analyzed in this paper presents a scenario which the monitoring is done on a conservative substance, ignoring the effects of chemical reaction.

*Keywords*: Water quality models, water supply, tanks, computational fluid dynamics (CFD).

## 1 INTRODUCTION

Nowadays the use of the mathematical models in order to study the hydraulic network through is commonly, the study and monitoring of water quality along the distribution network is an issue that is still under development. In part this is due to the difficulty to determine the effect of water quality on the networks. Situations such as the presence of different points of injection, leakages that can deteriorate suddenly the water quality or the progressive age of mains make more complex the problem.

However the storage facilities are presented before of those problems on the distribution networks. During the hydraulic model, the tanks are complex systems, because the inherent complexity in terms of connections (inlets, outlets, control valves, etc.). If the study considers the evolution of quality in it, the problem is even bigger, because the tanks behave like chemical and biological reactors.

Several authors have developed algorithms to address the issue of water quality in tanks. The objective is that a three-dimensional model of fluid dynamics will be consistent with softwares of one dimension simulation of pipeline networks basically.

The mixture model most used is certainly one which incorporates the EPANET program, developed by the USEPA. This model is based on multiple compartments and precise parameters for calculating dimensions of each compartment.

The aim of this work is to use a computational fluid dynamics (CFD) program to determine the value of these parameters and finally to improve a routine for water quality model of drinking water distribution network.

## 2 METODOLOGY

The EPANET program allows to use four different models (Figure 1) to characterize the mixture into tanks[1]:

- (A) Model of Completely Mixed. It Assumes that all water that enters a tank is instantaneously and completely mixed with the water already in the tank. It is the simplest form of mixing behavior to assume, requires no extra parameters to describe it, and seems to apply quite well to a large number of facilities that operate in fill-and-draw fashion.
- (B) Model of Two-Compartment Mixing. It divides the available storage volume in a tank into two compartments, both of which are assumed completely mixed. The inlet/outlet pipes of the tank are assumed to be located in the first compartment. New water that enters the tank mixes with the water in the first compartment. If this compartment is full, then it sends its overflow to the second compartment where it completely mixes with the water already stored there. When water leaves the tank, it exits from the first compartment, which if full, receives an equivalent amount of water from the second compartment to make up the difference. The first compartment is capable of simulating short-circuiting between inflow and outflow while the second compartment can represent dead zones. The user must supply a single parameter, which is the fraction of the total tank volume devoted to the first compartment.
- (C) Model of Plug Flow (also known as FIFO, *First In, First Out*). This model assumes that there is no mixing of water at all during its residence time in a tank. Water parcels move through the tank in a segregated fashion where the first parcel to enter is also the first to leave. Physically speaking, this model is most appropriate for baffled tanks that operate with simultaneous inflow and outflow. There are no additional parameters needed to describe this mixing model.
- (D) Model of Stacked Plug Flow (also known as LIFO, *Last In, First Out*). It also assumes that there is no mixing between parcels of water that enter a tank. However in contrast to FIFO Plug Flow, the water parcels stack up one on top of another, where water enters and leaves the tank on the bottom. This type of model might apply to a tall, narrow standpipe with an inlet/outlet pipe at the bottom and a low momentum inflow. It requires no additional parameters be provided.

Considering those models, the completely mixed one is widely studied from chemical engineering area. Therefore, the proposition is to model a tank in three-dimensional with two possible connections: the first one is considering the short-circuiting (model D) and the second one that favors the renewal.

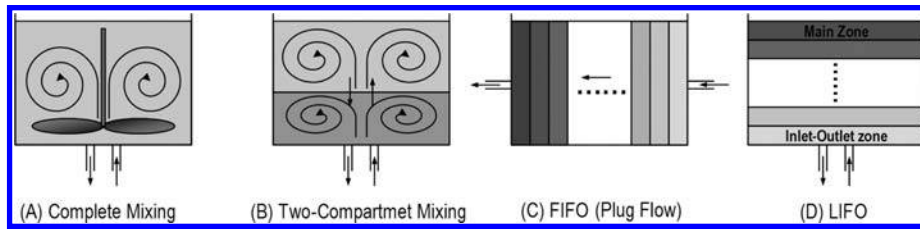


Figure 1. Mixing Models from Epanet.

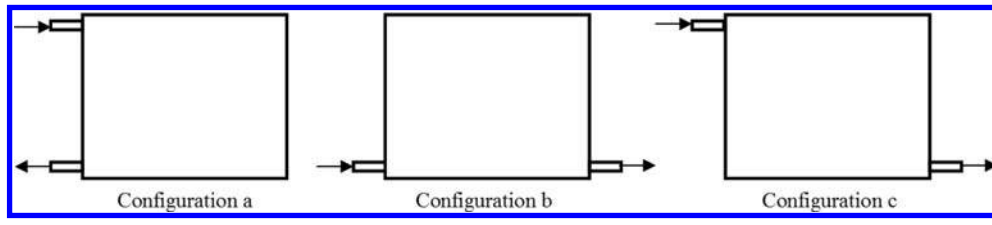


Figure 2. Cases analyzed by the CFD model.

In the first case (Figure 2) is going to determine the concentration gradient inside the tank, besides the concentration in the flow outlet in order to compare with the results obtained with EPANET.

In the second case will be the same analysis, but the objective will be to determine which of the two possible models (B, two compartment mixing, or C, plug flow) is the most appropriate to making a quality model (Figure 2). The results are also compared with those provided by the program EPANET on the same conditions.

For the development of the calculations has been used FLUENT®, that is a CFD based on a finite volume method that allows combines three-dimensional equations of a flow (Reynolds Average – Navier-Stokes equations) with mass transport models and monitoring of concentrations. In order to define the mesh for the discretization of these equations it was used the Gambit®program.

## 3 RESULTS

After simulate each one of the three scenarios proposed, it was obtained the Figure 3 that shows the magnitudes, one of the results relate to the velocity. The magnitude of the velocity indicates the effect of every scheme of the tanks. On the same way was analyzed the vector and direction of the flow.

The first configuration (Figure 2, configuration a) is the case where the inlet and the outlet are closer each to other one, it could shows that it does not produced the phenomenon of short circuiting. On the graphic results it could observe that the main flow tends to pass near the entire perimeter of the tank but with velocities even higher than the value that was set in the inlet boundary. In the interior it could observe a large stationary area with very low velocities (Figure 4). This model simulates the model of two-compartment presented in EPANET.

In the second configuration (Figure 2, configuration b) is presented a short circuiting that would suggest an area almost equivalent that connects directly the entrance and the outlet sections (Figure 4). Besides, there is presented a secondary flow around the perimeter of the tank and it could makes possible the mixing of different sources. Finally, in the center of the tank (not at the far zone from the short circuiting) present small velocities (less than 0,2 m/s) that generate a stationary area. Therefore, this configuration provides the three compartments mentioned earlier and it could not be represents considering the alternatives available on EPANET.

Finally, in the configuration c (Figure 2) presents a better proposed of the pipelines position considering that the goal is to avoid differences in the concentration of substances. Firstly it appears a principal flux that joins the inlet and outlet by a main flow around the border next to the walls of the tank (Figure 4). Moreover, a secondary flow that causes a high eddy in the center of the tank which results in large velocity and, therefore a high mixing capacity. As a result of this eddy, it is not any form of stationary zone. This configuration could be represented by the completely mixed model from EPANET.

## 4 CONCLUSIONS

The conclusions from this work are following described:

- It was developed a CFD model protocol for the mixing analysis in the interior of tanks with different behavior of interchange flows (Figure 4).
- It was obtained the required parameters to monitor the water quality in water distribution networks, mainly in the interior of the storage tanks.
- It was checked the validity of the CFD model as a tool to support the hydraulic simulation models where the elements have a complex behavior in order to represent dimensional equations.

This paper presents the results on a scenario which the monitoring is made on a conservative parameter (it does not present any kind of chemical reaction), considering that the CFD is a tool that will be a greater factor when the inclusion of kinetics reaction from typical problem of water quality, such as the consumption of chlorine or the generation of disinfection products.

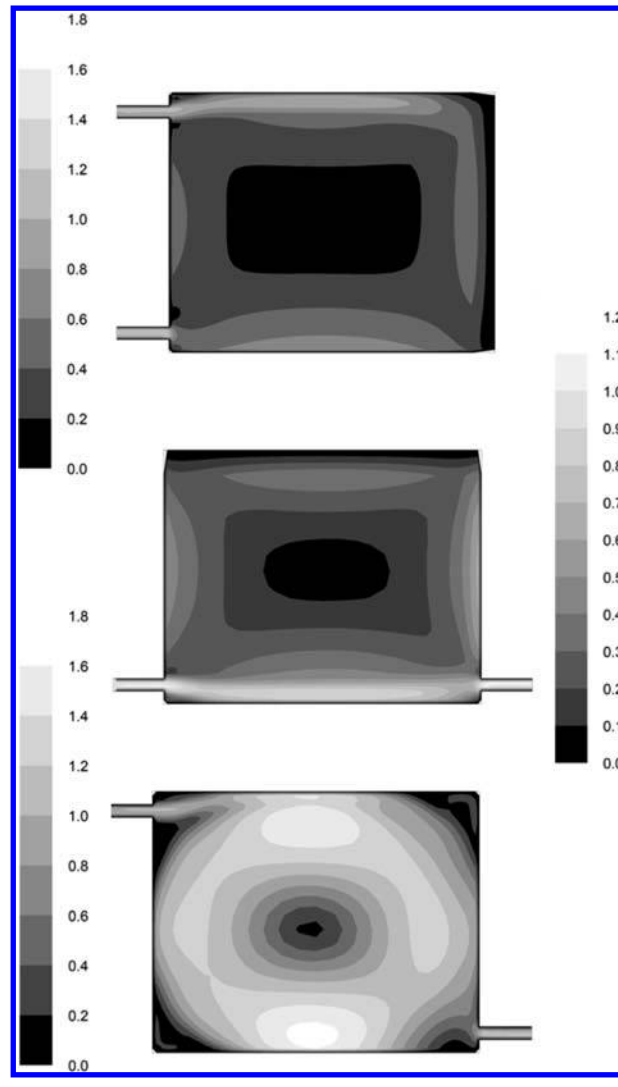


Figure 3. Velocity (m/s) Configurations from the CFD model.

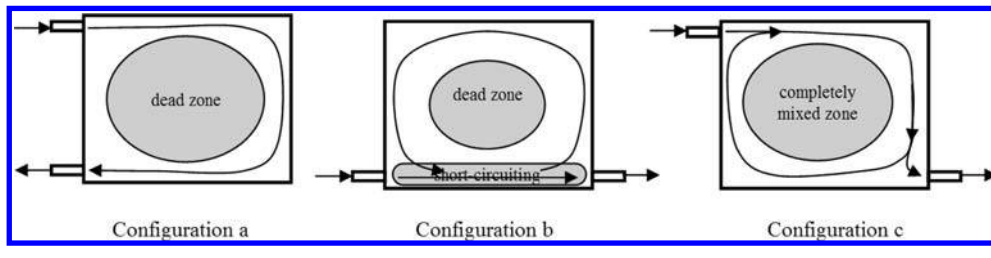


Figure 4. Analysis from the model results.

ACKNOWLEDGEMENTS

This article has been possible inside the actions developed by the researchers of CMMF involved in the project “Integración de la caracterización dinámica de elementos y consumos en modelos de redes de abastecimiento de agua utilizando sistemas de información geográfica y algoritmos genéticos (CADAGIAS)”. The number reference of the project is DPI2006-13113 and DANAIDES: Desarrollo de herramientas de simulación para la caracterización hidráulica de redes de abastecimiento a través de indicadores de calidad del agua. REF. DPI2007-63424. Ministerio de Educación y Ciencia de España.

REFERENCES

[1] Rossman, L.A. (2000). *EPANET 2 User’s Manual*. Water Supply and Water Resources Division. U.S. Environmental Protection Agency. Cincinnati, EE.UU. <http://www.epa.gov/ORD/NRMRL/wswrd/epanet.html)>

*Environmental Hydraulics – López-Jiménez et al (eds)*
*© 2010 Taylor & Francis Group, London, ISBN 978-0-415-56697-1*

# Analysis of transient vaporous cavitation in polyethylene pipes

Alexandre K. Soares
*Department of Environmental and Sanitary Engineering, Federal University of Mato Grosso, Cuiabá, Brazil*

Dídia I.C. Covas & Helena M. Ramos
*Instituto Superior Técnico Technical, University of Lisbon, Lisbon, Portugal*

Luisa F.R. Reis
*São Carlos School of Engineering, University of São Paulo, São Carlos, Brazil*

*Keywords*: Water hammer, Cavitation, Experimental data, Polyethylene pipes.

## 1 INTRODUCTION

The aim of the current paper is to present the results of the combination of different dynamic effects (i.e., pipe-wall viscoelasticity and cavitation) in hydraulic transient calculations as well as to discuss the importance of these phenomena in the analysis of each particular situation. For this purpose, physical data were collected from an experimental polyethylene (PE) pipeline, assembled in the Hydraulic Laboratory of Civil Engineering Department of Instituto Superior Técnico (Lisbon, Portugal). A series of transient tests were carried out collecting pressure at four different locations. A hydraulic transient solver incorporating the description of different phenomena (e.g., unsteady friction, pipe-wall viscoelasticity, distributed cavitation) has been developed and used to analyse these case studies. An inverse transient solver has been used to calibrate several parameters. Collected data are compared with the results of numerical simulations. Conclusions are drawn concerning the importance of considering these effects in design and during the system operation.

## 2 MATHEMATICAL MODELS

### 2.1 *Viscoelastic model*

Equations that describe the one-dimensional transient-state flows in viscoelastic closed conduits are the momentum and continuity equations (Eq. 1 and 2, respectively). Since the flow velocity and pressure (dependent variables) in transient flows are functions of time and space (independent variables), these equations are a set of two hyperbolic partial differential equations[1,2,3,4]:

$$\frac{1}{A}\frac{dQ}{dt} + g\frac{\partial H}{\partial x} + gh_f = 0 \tag{1}$$

$$\frac{dH}{dt} + \frac{a_0^2}{gA}\frac{\partial Q}{\partial x} + \frac{2a_0^2}{g}\frac{d\varepsilon_r}{dt} = 0 \tag{2}$$

where $x$ = coordinate along the pipe axis; $t$ = time; $H$ = piezometric head; $Q$ = flow rate; $a_0$ = celerity or elastic wave speed (dependent on the fluid compressibility, and on the physical properties and external constraints of the pipe); $g$ = gravity acceleration; $A$ = pipe cross-sectional area; $\varepsilon_r$ = retarded strain component (in viscoelastic pipes the total strain can be decomposed into an instantaneous-elastic strain and a retarded strain); and $h_f$ = head loss per unit length ($h_f = fQ|Q|/2DA^2$ in turbulent conditions, in which $f$ = Darcy-Weisbach friction factor and $D$ = pipe inner diameter). These equations assume: pseudo-uniform velocity profile; linear viscoelastic rheological behaviour of the pipe-wall; one-phase, homogenous and compressible fluid, though with negligible changes in density and temperature; uniform and completely constrained from axial or lateral movement pipe.

In this paper, the set of differential Eqs. (1) and (2) together with the strain-stress equation has been solved by the Method of Characteristics (MOC).

### 2.2 *Discrete vapour cavity model*

The discrete vapour cavity model (DVCM) is widely used in standard water hammer software packages for column separation and distributed cavitation analyses[5]. This model is based on the column separation hypothesis that the flow of liquid in the tube is instantaneously and completely separated by its vapour phase when the cavity is formed. Cavities are allowed to form at any of the computational sections if the pressure is computed to be below the vapour pressure. Pure liquid with a constant wave speed is assumed to occupy the reach in between two computational sections. The absolute pressure in a cavity is set equal to the vapour pressure ($p* = p_v*$). The upstream and downstream discharges $Q_{Pu}$ and $Q_P$ at a cavity are computed from the compatibility relations, and, ignoring mass transfer during cavitation, its volume follows then from:

$$\frac{d\forall}{dt} = Q_P \quad Q_{Pu} \tag{3}$$

which is numerically approximated in the Method of Characteristics with a staggered grid by:

$$\forall_P^t = \forall_P^{t-2\Delta t} + \left[\psi\left(Q_P^t - Q_{Pu}^t\right) + (1-\psi)\left(Q_P^{t-2\Delta t} - Q_{Pu}^{t-2\Delta t}\right)\right]2\Delta t \tag{4}$$

in which $\forall_P^t$ and $\forall_P^{t-2\Delta t}$ are the volumes at the current time and at $2\Delta t$ earlier, and $\psi$ is a numerical weighting factor. The cavity collapses when its calculated volume becomes less than zero. The liquid phase is re-established and the standard water hammer procedure is valid again.

### 2.3 *Discrete gas cavity model*

Transient flow of a homogeneous gas-liquid mixture can be described by the classical water hammer equations in which the liquid wave speed a is replaced by the wave speed $a_m$[6]:

$$a_m = a_0 / \sqrt{1 + \frac{\alpha_g \rho a_0^2}{p^*}} \tag{5}$$

where $\alpha_g$ = gas void fraction; and $\rho$ = liquid mass density.

An alternative to modelling free gas distributed throughout the liquid in a homogeneous mix can be achieved by lumping the mass of free gas at computing sections leading to the discrete gas cavity model (DGCM). Each isolated small volume of gas expands and contracts isothermally as the pressure varies, in accordance with the perfect gas law[4]:

$$\left(p^* - p_v^*\right)\forall = \left(p_0^* - p_v^*\right)\forall_0 = C_3 \tag{6}$$

An isothermal volume versus head relationship is assumed at a gas cavity:

$$\forall_P^t = C_3 / \left(H_P^t - z - H_v\right) \tag{7}$$

in which the constant $C_3$ can be computed from:

$$C_3 = \frac{p_0^* \alpha_0 \Delta x A}{\rho g} \tag{8}$$

where $p_0^*$ = a reference absolute pressure; $\alpha_0$ = void fraction at $p_0$ (ratio of volume of free gas to the mixture volume); $z$ = elevation of the pipe; and $H_v$ = gauge vapour pressure head of the liquid.

As in the DVCM, between each computing section, and concentrated gas volume, pure liquid with a constant wave speed is assumed without free gas. The DGCM is also able to simulate vaporous cavitation by utilizing a low initial gas void fraction ($\alpha_0 \leq 10^{-7}$) at all computational sections[6,7].

## 3 RESULTS

An extensive experimental programme has been carried out in an experimental set-up composed of high-density polyethylene (HDPE) pipes, assembled at Instituto Superior Técnico of Lisbon, Portugal (Figure 1). The experimental facility is composed of a single transmission pipeline with a total length of 203 m and inner diameter of 44 mm. This pipeline is connected to an air vessel at the upstream end and to a free discharge outlet into a constant water level at the downstream end. A ball valve is installed immediately downstream the air vessel and it is used to interrupt the flow in order to perform a fast closing manoeuvre. The air vessel was used to keep the upstream pressure constant as an elevated reservoir. Transient pressure data have been collected using pressure transducers located at four pipe sections with a frequency of 500 Hz (at the air vessel; downstream the ball valve at upstream end of the pipeline – Section 1; at the middle of the pipeline – Section 5; and at downstream end of the pipeline – Section 6).

Transient tests were carried out by closing the upstream end ball valve to originate cavitating pipe flow in the system. Initially, the creep function calibrated for non-cavitation tests was used in order to describe the system mechanical behaviour. Actually, when pressure decreases and reaches the vapour pressure, a gas cavity is formed and consequently decreases the wave speed. In this way, a new set of viscoelastic parameters was determined and it has been assumed that unsteady friction losses, pipe-wall viscoelasticity and wave speed variation due to localised gas cavities were described by the creep function.

Elastic wave speed was estimated as 250 m/s. The discrete vapour cavity model (DVCM) and the discrete gas cavity model (DGCM) developed in this study were used in order to describe the cavitating flow in the system. In the later, a small void fraction was adopted ($\alpha_0 \leq 10^{-7}$), since the flow did not exhibit distributed air bubbles at the beginning of the tests.

Numerical results obtained by using the DVCM and the linear viscoelastic transient solver are presented for two locations of the pipe rig: Section 1 (upstream end of the pipeline and immediately downstream the ball valve – Figure 2a) and Section 5 (middle pipe section – Figure 2b).

The use of DVCM taking into account pipe-wall viscoelasticity has shown that the attenuation and dispersion in the transient pressures were not described. In addition to the deficiencies pointed out by Shu [8], this is due to the assumption of the absolute pressure in the gas cavities being set equal to the vapour pressure and the energy dissipation during the expansion and contraction of the gas cavities being neglected. In this way, the DGCM has been used in order to describe the system behaviour, considering a small initial void fraction ($\alpha_0 \leq 10^{-7}$). Numerical results obtained by using the DGCM and the linear viscoelastic transient solver are presented for two locations of the pipe rig: Section 1 (upstream end of the pipeline and immediately downstream the ball valve – Figure 3a) and Section 5 (middle pipe section – Figure 3b).

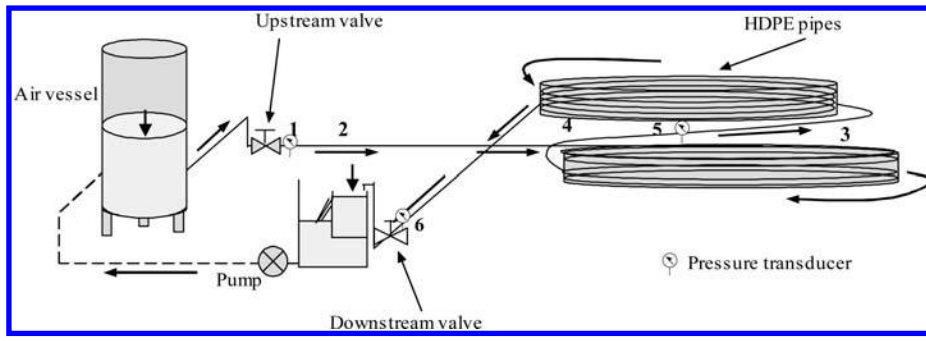


Figure 1. Experimental set-up with high-density polyethylene pipes.

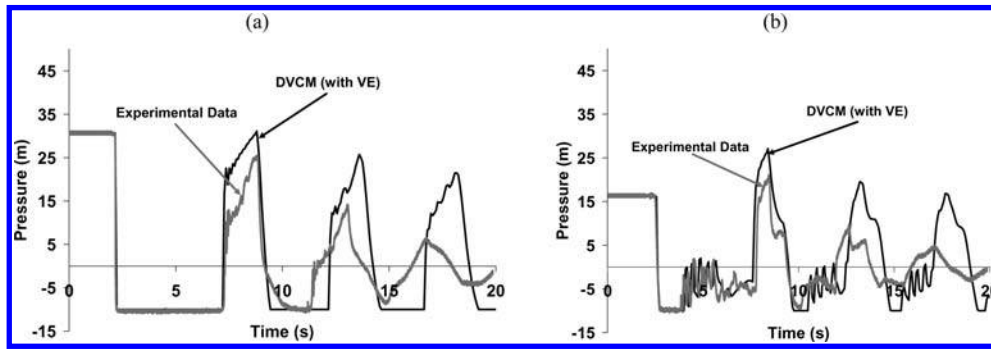


Figure 2. DVCM numerical results taking into account pipe-wall viscoelasticity versus experimental data at (a) Section 1 and (b) Section 5 ($Q_0 = 4.0$ L/s; R $\approx$ 120,000).

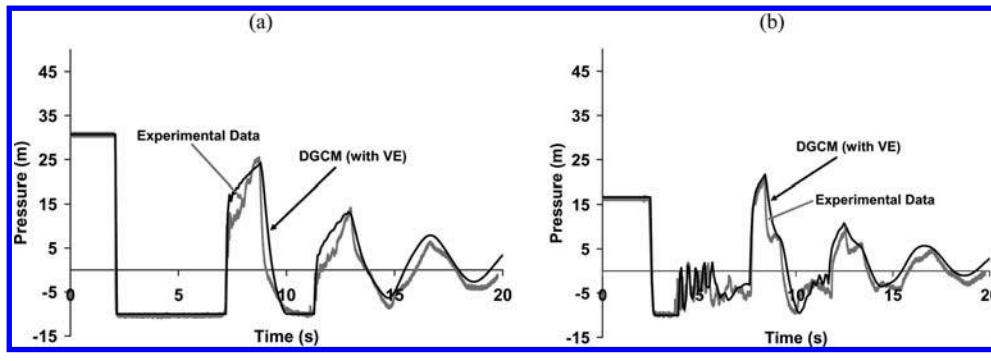


Figure 3. DGCM numerical results taking into account pipe-wall viscoelasticity versus experimental data at (a) Section 1 and (b) Section 5 ($Q_0 = 4.0$ L/s; R $\approx$ 120,000).

The use of DGCM taking into account pipe-wall viscoelasticity has shown that:

- a better adjustment to the experimental data was obtained by DGCM than those one when utilizing the DVCM;
- the assumption of the ideal gas law is more appropriate than the simple adoption of vapour pressure when pressure reaches vapour pressure (DVCM) – this influences the energy dissipation during the expansion and contraction of gas cavities. In DGCM formulation, the exponent of the polytropic gas is assumed to be equal to 1.0 in order to obtain explicit equations and considering that the free gas is assumed to behave isothermally, which is valid for tiny bubbles. In this study, large bubbles were formed on the upper part of the pipe cross-section and growth along the pipe axis. Large bubbles and column separations tend to behave adiabatically. It is recommended further analyses of the exponent of the polytropic gas and of the implicit formulation;
- some features of the HDPE pipe rig during the transient tests, such as pipe displacement and a free discharge outlet at the downstream end of the pipeline, lead to more uncertainties on the system behaviour.

## 4 CONCLUSIONS

The current paper presented experimental tests and numerical analyses of water hammer with cavitation in a pressurised single transmission pipeline composed of high-density polyethylene pipes. Pressure data in turbulent conditions were collected during transient events caused by valve closure. A hydraulic transient solver that takes into account pipe-wall viscoelasticity mechanical behaviour has been developed. Such measured data were used to calibrate and verify two developed mathematical models to the description of cavitating pipe flow: discrete vapour cavity model (DVCM) and discrete gas cavity model (DGCM).

Obtained numerical results showed that DVCM is imprecise for the description of hydraulic system behaviour. Whilst such model is on the safest side for design purposes as it predicts higher overpressures, it is not accurate for calibration purposes due to the neglecting of the energy dissipation during the expansion and contraction of the gas cavities. The assumption of the

ideal gas law (DGCM) is more appropriate than the simple adoption of vapour pressure when pressure reaches vapour pressure (DVCM) and induces more attenuation and dispersion of transient pressures. For cavitating flows, a new set of viscoelastic parameters was determined and it was assumed that unsteady friction losses, pipe-wall viscoelasticity and wave speed variation due to the formation of localised gas cavities were described by the creep function.

Considering the analysis carried out in this work, cavitation flows in pressurised systems composed of plastic pipes have to be better analyzed. The study of new numerical methods, such as two-dimensional (2D) methods, can be the solution for the description of pressure transients during cavitation.

## REFERENCES


[1] Almeida, A.B., Koelle, E. (1992), *Fluid Transients in Pipe Networks*, Computational Mechanics Publications, Elsevier Applied Science, Southampton, UK.

[2] Chaudhry, M.H. (1987), *Applied Hydraulic Transients*, Litton Educational Publishing Inc., Van Nostrand Reinhold Co, New York, USA.

[3] Covas, D., Stoianov, I., Mano, J., Ramos, H., Graham, N., Maksimovic, C. (2005), "The Dynamic Effect of Pipe-Wall Viscoelasticity in Hydraulic Transients. Part II – Model Development, Calibration and Verification", Journal of Hydraulic Research, Vol. 43, N. 1, PP. 56–70.

[4] Wylie, E.B., Streeter, V.L. (1993), *Fluid Transients in Systems*, Prentice Hall, Englewood Cliffs, N.J.

[5] Bergant, A., Simpson, A.R., Tijsseling, A. (2006), "Water Hammer with Column Separation: A Historical Review", Journal of Fluids and Structures, Vol. 22, PP. 135–171.

[6] Wylie, E.B. (1984), "Simulation of Vaporous and Gaseous Cavitation", Journal of Fluids Engineering, Vol. 106, N. 3, pp. 307–311.

[7] Simpson, A.R., Bergant, A. (1994), "Numerical Comparison of Pipe-Column-Separation Models", Journal of Hydraulic Engineering, Vol. 120, n. 3, pp. 361–377.

[8] Shu, J.J. (2003), "Modelling Vaporous Cavitation on Fluid Transients", International Journal of Pressure Vessels and Piping, Vol. 80, pp. 187–195.

*Environmental Hydraulics – López-Jiménez et al (eds)*
*© 2010 Taylor & Francis Group, London, ISBN 978-0-415-56697-1*

# A method for sizing first flush water diverters tanks in rainwater harvesting systems

Gonzalo López-Patiño, F. Javier Martínez-Solano, P. Amparo López-Jiménez & Vicente S. Fuertes-Miquel
*Centro Multidisciplinar de Modelación de Fluidos, Universidad Politécnica de Valencia, Valencia, España*

ABSTRACT: In this contribution, a theoretical formulation is presented to size first flush rain water diverters, based on the traditional catchment expressions. The applicability of the proposed formulation is considered in order to optimize the volume stored based on environmental criteria. Finally an application to Valencia case study is presented.

*Keywords*: rainwater, rainwater harvesting, water diverter

## 1 INTRODUCTION

As part of the rainwater harvesting system, a device must be located to prevent the first rain, most contaminated, from entering the tank. This equipment diverts polluted water to the sewage. Once rainwater is clean, it is automatically directed along the pipe system to the tank.

The pollution of rain water is produced by the drag of some substances deposited on the catchment area: sediments, chemical pollutants, leaves, insects, etc.. The problem is to determine when the rainwater is clean enough to be directed to the tank.

There are different devices that diverts first flush rain water. One of them is a valve that diverts water to sewage while flow is low, what happens on the rain starts. As rainfall continues, the flow grows up and the valve shuts diverting water to the main tank.

Another one is a little container which stores water while it is polluted. When this container is filled, the rainwater is directed to the principal rain harvesting system tank.

Manufacturers of water diverters show, on its technical information, the volume to divert. This value depends on: the catchment area and a pollution factor[1] that takes in count the vegetation surrounding this area, or the rainfall intensity[2]. Pollution is greater when the water harvesting system is located in an area with vegetation than if located in the open field, and when rain flow is lower than when it is greater.

For diversion valve, the flow-rate that shuts the valve is between 10-20 l/min[2]. For diversion container, the volume of the tank is[1] 0.5 l per $m^2$ of catchment surface if it can be seen as "clean"; i.e. free of vegetation around, without bird droppings, etc. If the catchment surface contains litter or droppings or insects, then the ratio increases to 2 l/$m^2$.

The rain fall intensity, use to calculate flow-rate with the diversion valve system, and the pollution factor, use for the diversion container, are estimated according to the experience of manufacturers, with no scientific basis. As no relationship is establish with other parameters, such as: intensity of rainfall; rainfall duration; type, material and area of the catchment surface, etc., it is difficult to apply this methods when the conditions are not the ones experienced by the manufacturers.

The objective of this paper is to establish a procedure, with a scientific base, to calculate the volume to divert when is used a container device.

The method estimates the time a rainwater drop inverts to get, from any point in the catchment, to the diverter. The volume of the diverter is the rain water fall during this period.

## 2 METHODOLOGY

The purposed methodology consists on:

- Determine the time invested by the rain from the more unfavourable point until the diverter: Tc
- Determine the rainfall occurred since the rain began until the previous considered time: Tc
- Considering geometrical limitations of the facility, establish the diverter diameter and length

The determination of the time spent by the rainfall in arriving from the farthest point in the catchment until a precise point is a known hydrologic concept known as time of concentration, $T_C$. This is a very documented parameter and many formulation proposal can be found in references [3], [4], [5], and [6]. In the building engineering applications, the sizes of catchments are very big, so we recommend the use of the plan flow formula from Soil Conservation Service (USDA NRCS, 1986).

$$T_C = 5.476 \frac{(nL)^{0.8}}{\sqrt{p_2 S^{0.4}}} \quad (1)$$

Where $T_C$ is the time of concentration, expressed in minutes, n is the Manning's coefficient in the catchment surface, L is the maximum length expressed in m, $p_2$ is the maximum precipitation in 24 hours for a return period of 2 years expressed in mm; and S is the medium slope expressed in mm.

The next step in the procedure consists of determining the rainfall from the rain beginning until the farthest drops reaches the diverter. The simpler solution enables us to consider a project reference pluviograph to know the time evolution for a typical rain and take the y-coordinate at the corresponding abscise $T_C$ in the pluviograph.

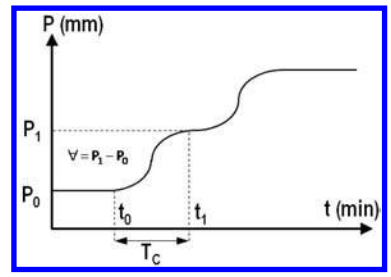


Figure 1. Methodology proposed for size diverter calculation.

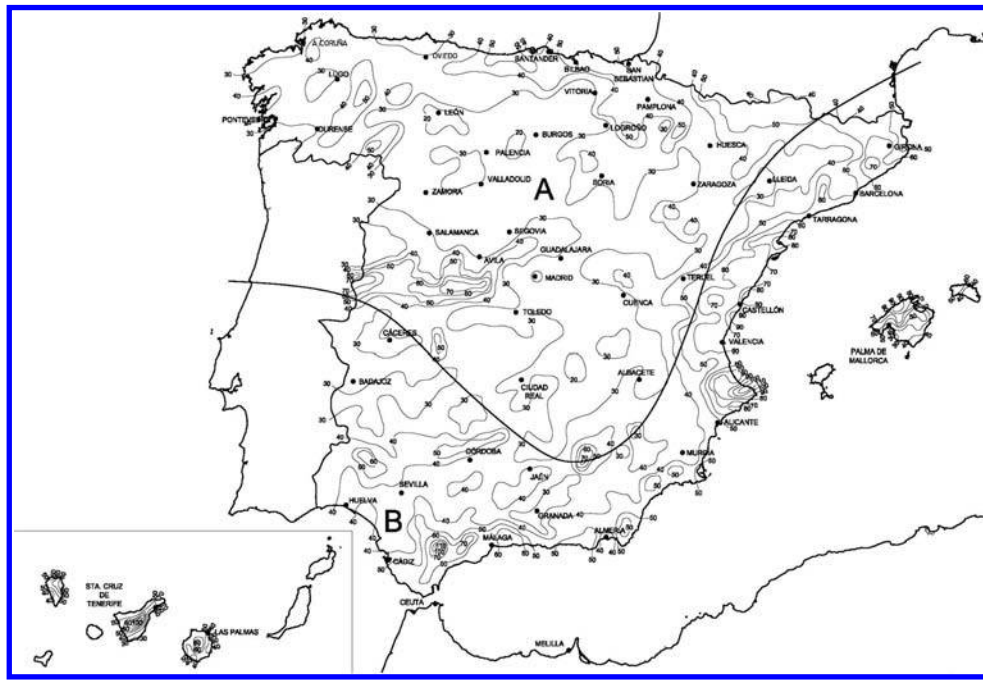


Figure 2. Maximum isoyetas map for 1 hour and T = 10 years. Source: Codigo Técnico de la Edificación [7].

Table 1. Adjust parameters for IDF curve.

| City | $\alpha$ | $\beta$ | $\gamma$ | ‘$\Delta$t | IM |
|---|---|---|---|---|---|
| Valencia | 2593,13 | 21 | −0,83 | min | mm/h |
| Alicante | 3532,55 | 24 | −0,98 | min | mm/h |

Nevertheless, we do not usually have hystorical information about pluviogrames for an especific location. This makes more difficoult the calculation porcess. This is the reason that encourages us to adapt the methodology to the available information.

IDF curves are the usually more available information about a determined location. The way to obtain such curves using hystorical data is defined in [5].

The proposed expression for the IDF curve can be adjusted to an exponential such as:

$$I_M = r_T\, \alpha(\Delta t + \beta)^{\gamma} \tag{2}$$

Where:

- ‘$r_T$’ is a coefficient depending on the return period considered for a precise rainfall,
- ‘$\Delta$t’ is the interval duration to calculate the medium intensity
- ‘$\alpha$’, ‘$\beta$’, and ‘$\gamma$’ are characteristic parameters related to the location.

In the reference [5] some adjust for IDF curves can be found for short duration rains, as it is shown in Tables 1 and 2.

The use of the IDF curves for the volume calculation of the diverter located in a particular position, when the coefficients $\alpha$, $\beta$, and $\gamma$ are fixed, depends only on $r_T$ and therefore on the return period. The selection of the most suitable return period must be done in terms of an economic analysis of the solution. The bigger periods used, the bigger value of maximum medium intensity will be achieved and thus the size of the diverter. If the diverter is too big the cost will increase. Opposite, a return period too small will induce to a higher probability of exceeding the values of medium maximum intensity calculated in the project, undersizing then the diverter. In this last situation, more pollution can be produced, with a failure risk related to the

Table 2. Correction for the IDF curve related to the return period.

| City | Return Period | $r_T$ |
|---|---|---|
| Valencia | 2 | 0.50 |
| | 5 | 0.80 |
| | 10 | 1.00 |
| | 20 | 1.19 |
| | 30 | 1.30 |
| | 50 | 1.44 |
| Alicante | 2 | 0.56 |
| | 5 | 0.82 |
| | 10 | 1.00 |
| | 20 | 1.17 |
| | 30 | 1.26 |
| | 50 | 1.39 |

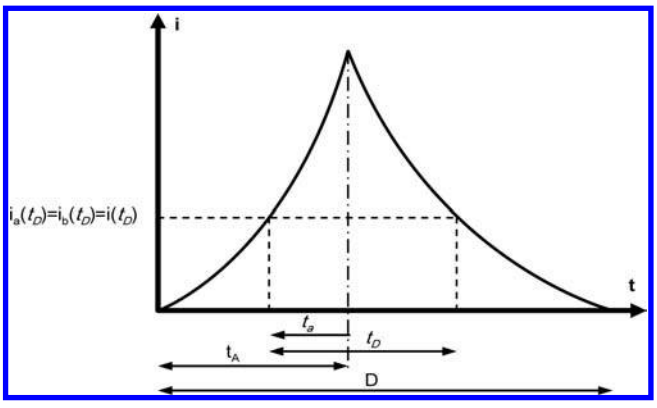


Figure 3. Project storm using instantaneous intensity method.

return period defined in[3]. If the designer has not more precise information, a value of risk related to the return period of 10% and 5 years of non failure performance are suggested in the references. This implies a return period of 50 years.

A synthetic hyetograph will be obtained from the IDF curves. The intensity function integration gives the values in the synthetic pluviograph, required from the retention volume. To estimate the synthetic hyetograph the instantaneous method is proposed in[4]: the intensity function will be obtained from the maximum intensity and the time-to-peak ratio:

$$r = \frac{t_A}{D} \tag{3}$$

Where $t_A$ is the meantime from the initial instant to the maximum intensity moment and D the total duration of the rainfall.

As indicated in Chow[6], the value for 'r' will be found between 0.4 y 0.5 and can be considered constant along the rainfall duration. In any time instant the relation (4) can be established :

$$r = \frac{t_a}{t_D} \tag{4}$$

Considering the medium intensity for a determined duration of rainfall is proportioned by expression (2), the instantaneous intensity in terms of $t_D$ will be as indicated in (5):

$$i_a(t_D) = i(t_D) = r_T \alpha \left(t_D + \beta\right)^{\gamma} \quad 1 \quad (\gamma) \frac{t_D}{t_D + \beta} \tag{5}$$

Considering that in the initial moment: $t = t_A$:

$$t_a = t_A - t \tag{6}$$

$t_D$ can be considered time dependent

$$t_D = D \quad \frac{t}{r} \tag{7}$$

This will enable us to consider the intensity function for any time, particularly for the instant "time of concentration, $t_C$" when the more polluted fraction of water is arriving to the diverter

$$i_a(t_C) = i(t_C) = r_T \alpha \quad D\frac{t_C}{r} + \beta^{\gamma} \quad 1 \quad (\gamma)\frac{D\frac{t_C}{r}}{D\frac{t_C}{r} + \beta} \tag{8}$$

The water stored until this moment could be obtained by integration of the instantaneous intensity function from the initial moment until time '$t_C$'. Nevertheless, considering the proposed simplifications and the adjust uncertainty, it is convenient to average the medium intensity during the interval 0-tC to the value of this intensity in the instant '$t_C$'. Thus, the precipitation storage in the interval will be:

$$p(mm) = i(t_C) \times t_C \tag{9}$$

And the volume in the first rain diverters will be obtained by the expression 10, considering the catchment surface.

$$\forall(l) = p(mm) \times A(m^2) \tag{10}$$

## 3 VALENCIA CASE STUDY

Applying the previously described methodology to Valencia city case study, the catchment surface o consider will be 100 $m^2$, with a squared morphology 10 × 10, with a slope 0.5%. This will be collected in a single sink located in the surface corner, with a high Manning coefficient due to possible dirt drag, with value 0.03. In this situation the evaluated time of concentration is 3.63 minutes. Assuming that the time-to-peak ratio is 0.45, the minimum value for the diverter is 117 litters.

Comparing this value with those provided by Rain Harvesting (0.5 l/$m^2$ – 2 l/$m^2$) we can see that the value is insider the expected range (50 l-200 l.). The applicability of the method partially depends on the catchment surface treatment and the assigned value for the Manning coefficient in this surface. For clean surfaces, Manning coefficients will be small and therefore also will be small the volume of the diverter. Surface with abundant leaves, Manning coefficients will be greater and thus the volume of the diverter.

## ACKNOWLEDGMENTS

This article has been made possible through actions of the CMMF researchers, involved in the following projects: *DANAIDES: Desarrollo de herramientas de simulación para la caracterización hidráulica de redes de abastecimiento a través de indicadores de calidad del agua. REF. DPI2007-63424. Ministerio de Educación y Ciencia de España.*

## REFERENCES

[1] Rain Harvesting Pty Ltd. (2009). *How does a first flush water diverter work?* [on-line]. Quensland, Australia. http://www.rainharvesting.com. au/FileLibrary/rh_water_diverters_lores_1.12.05.pdf [ref. 2009, 10th June]

[2] Safe rain (2009). *First flush diversion valve* [on-line]. Australia. http://www.saferain.com.au/reverse-flow_valve.html [ref. 2009, 10th June]

[3] Martínez-Solano, F.J.; et al. (2005). *Interpretación del concepto de tiempo de concentración en modelos hidrológicos basados en métodos de depósito. Aplicación al módulo de cálculo hidrológico del programa SWMM 5. V SEREA. Seminario sobre planificación, proyecto y operación de sistemas de abastecimiento de agua*. Valencia (España). 2005

[4] USDA NRCS (1986). *Urban hydrology for small watersheds.* Technical Release 55 (SCS), Washington D.C., USA. http://www.ce.ufl.edu/~markn/CWR4306/tr55.pdf [ref. 2009, 6th July]

[5] Catalá Moreno, F. (1989). *Cálculo de caudales en las redes de saneamiento*. Paraninfo. Madrid. 1989

[6] Chow, V.T., (1994). *Hidrología Aplicada*. McGrawHill. Santa Fé de Bogotá.1994

[7] Ministerio de la Vivienda. R.D. 314/2006, por el que se aprueba el Código Técnico de la Edificación. Ministerio de Vivienda (Gobierno de España). Boletín Oficial del Estado, de 28 de marzo de 2006, pp 11816-11831. http://www.boe.es/boe/dias/2006/03/28/pdfs/A11816-11831.pdf

*Environmental Hydraulics – López-Jiménez et al (eds)*
*© 2010 Taylor & Francis Group, London, ISBN 978-0-415-56697-1*

# Water intrusion in pipes due to a transient event

L. Salas-Lechuga & J.J. Gómez-Hernández
*Grupo de Hidrogeología, Universidad Politécnica de Valencia, Valencia, España*

P.L. Iglesias-Rey, V. Fuertes-Miquel & P.A. López-Jiménez
*Centro Multidisciplinar de Modelación de Fluidos, Universidad Politécnica de Valencia, Valencia, España*

ABSTRACT: Infrastructure systems for water distribution may be old and deteriorating, especially in big and old cities. Water systems with its many pumps, valves and tanks is susceptible to hydraulic transients resulting in high and low pressure waves thought the network. While both kinds of pressures stress an already weak system, there is evidence that intrusion of contaminants into the drinking water pipes occurs during the low-pressure episodes. These contaminants will end up into the home plumbing or in water tanks. An understanding of the pressure and flow patterns within a piping system should lead to safer in-house designs and better municipality maintenance practices. In this paper, we address the problem of contaminated water intrusion and backflow into the distribution piping.

*Keywords*: Transient flow, pressure, contaminant intrusion, water hammer.

## 1 INTRODUCTION

The growth of bottled water consumption, and the use of in-house water treatment systems, such as filters, distillation, ion exchange, or reverse osmosis, indicates that citizens are concerned with the quality of water supply. However, the low cost of tap water, the maintenance problems related with in-house treatment and the relatively low improvement in water quality that these treatments imply are in favor of public water supply. In this paper, we address the problem of intrusion of contaminated water into the distribution piping through fracture cracks, leaky joints, faulty seals, submerged air vacuum valves, and cross connections. It was widely believed that because a drinking water distribution system is pressurized the water can only come out; however, there is evidence that pump operation, the opening and closing of fire hydrants, valve maneuvering, pipe breaks, sudden changes in water demand, and valve malfunctioning can induce significant transients that lead to a lowering of the pressure within the piping thus allowing the possibility of contaminated water intrusion from the environment. Tests of surrounding soil and pipe specimens from repair locations show the presence of pathogens.

Le Chevallier et al.[1] defines intrusion as the specialized backflow situation in which non potable/contaminated water from the environmental outside of the distribution piping flows into the pipe through available openings. Kirmeyer et al.[2] and Friedman et al.[3] point out different physical mechanisms: such as transitory contamination due to low pressure in the system permitting a push-through of contaminants from the exterior; connection between a potable water system and a contaminated source; and pipe break, repair and installation that expose the distribution system to potential contamination. Additional sources for pathogen intrusion are the storage facilities, both covered and uncovered, purposeful contamination, and the growth and suspension of pathogens. Karim et al [4] reported bacteria and viruses in 66 soil and water samples collected next to drinking water pipelines in eight public utilities in six states. Friedman et al[3] documented intrusion and low pressures of the order of negative 10 psi. They also emphasize that the intruded contaminant is not re-extruded out of the pipe but a portion of it is carried downstream. Distribution conducts downstream of pumps, pipes in high elevation areas and/or low static pressure zones, areas far away from tanks, and segments of pipes upstream and downstream of active valves in high flow areas are most susceptible for low or negative pressures. Locations with frequent leaks and breaks, high water table regions, flooded air vacuum valve vaults, and high risk cross connections have the highest potential for intrusion. Gullick et al.[5] observed most surge events as the result of pump operations and outages.

Some conditions must exist for contamination to occur. First, there must be a connection from the water inside the pipe to the exterior. Kinmeyer et al[2] states that leakage rates in water systems range up to 32 percent, which indicates that there is a significant connection between the water in the pipe and the ground outside. Second, the pressure of the ground water surrounding the pipe must be greater than the water pressure inside the pipe. This is called an adverse gradient. Third, there must be contaminants in the ground water. Normally the pressure of the water distribution system can be triggered by the closing of a valve, the power failure of a pump, or the sudden release of flow such when a fire hydrant opens. Batterton[7] suggests that during water hammer events, low pressure waves develop in the system. If the pressure inside the pipeline drops below the pressure of the fluid surrounding the pipeline, an adverse pressure gradient is created and this creates a pathway for the fluid from outside of the pipe to get into the water distribution system. Intrusion is especially important if there are harmful contaminants in the surrounding area which could be potentially brought into the drinking water system. In a study by Karim et al[4], it was shown that significant levels of microorganism contaminants exist immediately adjacent to main water drinking lines.

## 2 GOVERNING EQUATION

The water hammer is a transient flow phenomenon introduced in pipe flow systems by suddenly obstructing the flow. As a consequence, there is a pressure rise and fall and the pattern is repeated until transient decay. For completeness, we present the

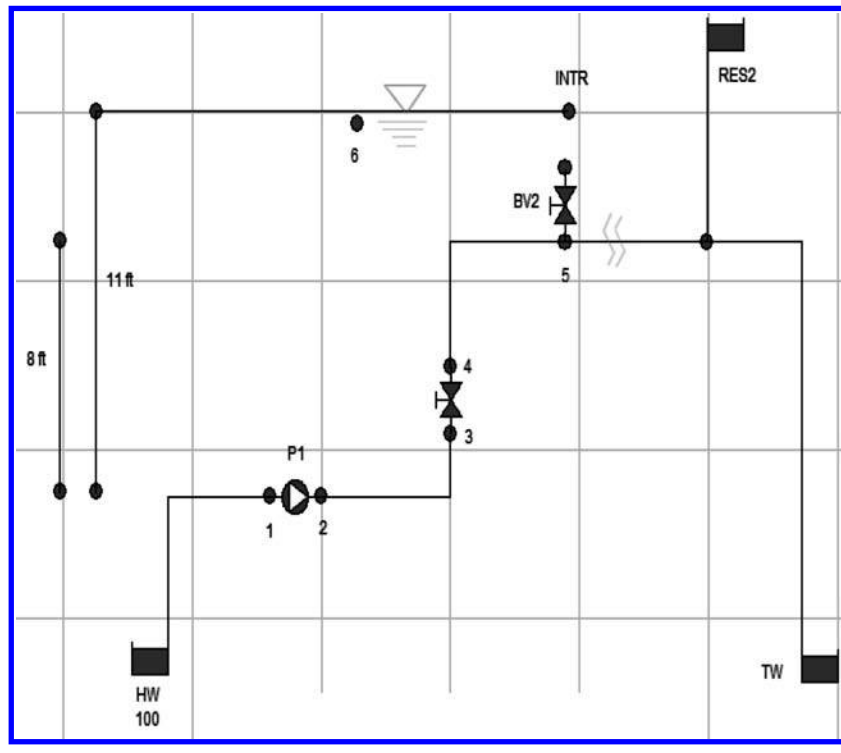


Figure 1. System schematic.

water hammer equations here as
for continuity

$$\frac{\partial p}{\partial t} + \frac{\partial p}{\partial x} + c^2 \rho \frac{\partial V}{\partial x} = 0 \tag{1}$$

for momentum

$$\frac{\partial V}{\partial t} + V\frac{\partial V}{\partial x} + \frac{1}{\rho}\frac{\partial p}{\partial x} + g \sin\alpha + \frac{f}{2D} V|V| = 0 \tag{2}$$

in which: p = pressure, V = velocity, c = wave speed, $\infty$ = density, g = acceleration due to gravity, $\alpha$ = angle of inclination of pipe, f = friction factor, D = diameter, x = spatial dimension, t = time. These equations have to be solved for a network with suitable interior boundary condition for such accessories as valves, pumps, and junctions where several pipes join and external boundary conditions for street level, tanks, and faucets.

Wylie and Streeter[6] provide detailed accounts of the solution methodology. The solution of these equations yields the pressure, p(x,t) and velocity, V(x,t) as functions of distance x along the length of the pipe. The pressure can be positive or negative and the velocity can also be positive or negative, in this later case indicating flow reversal.

We are using the WHAMO package from the U.S. Army Corps of Engineers that can solve the transient flow problem. WHAMO (Water Hammer and Mass Oscillation) is designed for hydropower systems to analyze transients induced by pumps, turbines, and turbine pumps involving valves, governors, reservoirs and surge tanks. In this study we are solving for pressure and flow patterns in networks involving several valves, a pump, and a tank.

The purpose of WHAMO application is to improve the unsteady phase design of piping before we actually construct it. In addition to the unsteady phase, it is also crucial to have an understanding of the steady state of the system.

## 3 EXPERIMENTAL DESIGN

An experimental set up was constructed in the Tulane Hydraulics lab to test for intrusion into the system events by Wang[8]. A similar system is modeled in this paper and using WHAMO code we test for intrusion in different scenarios.

The system starts with a reservoir at elevation zero with zero head at node 100. A vertical conduit joints this reservoir to a pump. After the pump (P1), there is a ball valve (BV1), which is used to trigger transient flow. Then the pipes rise to an elevation of 8 feet above the pump and to a static reservoir. At the high point of the line, it has a junction (node 5) that leads to a valve reservoir.

This valve (BV2) represents a crack or hole in the pipe providing a potential pathway for intrusion to occur. The reservoir represents the groundwater table (INTR). Then the pipes branch and continue on.

The remainder of the network is represented by two more reservoirs that model the heads downstream in the water distribution. A scheme of the system is given in Figure 1.

## 4 NUMERICAL SIMULATIONS

In the first simulation, the upstream reservoir (HW) has a head of zero feet. The pump provides the additional energy to move the water through the system. There is a point of leakage in the pipe at node 5. The opening is a quarter inch in diameter and is

Table 1. Parameter definitions.

| Read Head | Inertia | Valve time | Celerity | Orifice | K-valve | Intrusion Head | T Shutoff |
|---|---|---|---|---|---|---|---|
| 40 | 1.03 | 1 | 4000 | ¼″ | 0.16 | 3 | 6 |

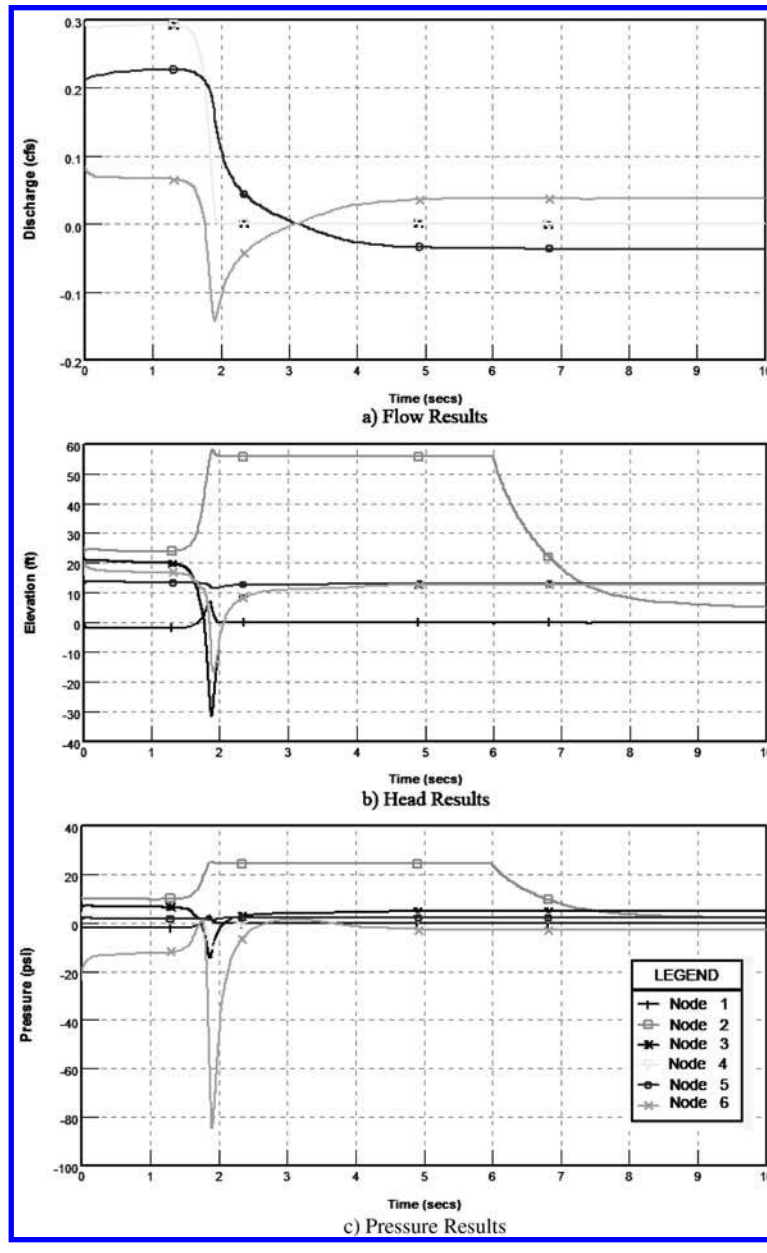


Figure 2. Simulation results.

represented by a ¼″ valve with a loss coefficient of 0.16. The groundwater table has an elevation of 11 feet above the opening in the pipe. The orifice coefficient is that of an open gate vale.

Additional resistance would be expected as the groundwater flows through porous media surrounding the pipe. There are two reservoirs at the end of the systems that have heads of 13 feet and 0 feet. The initial conditions for the pipeline pressures before any transients are trigged are very low. Since they are very low, they have a greater chance for the pressure to drop below the external pressure during water hammer events. The input parameters for the first simulation are summarized in Table 1.

## 5 RESULTS AND DISCUSSIONS

In this simulation there is a negative (suction) pressure at the intake for the pump at node 1 before the valve is closed. The dominant factor is the valve closure between nodes 3 and 4. The steady state head is 23.1 feet at node 4 and then the head rises to 61.8 feet on the upstream side of the valve and drops to −31.4 feet on the downstream side (see Figure 2b). The pressure (negative) corresponding to this head is −14.6 psi which is approximately vapor pressure for water at room temperature. In this case the velocity is high at 13.2 feet per second which is the main factor for the large head change. Water distribution systems are typically designed with a maximum velocity of 8 feet per second.

Table 2. Simulation Results.

| Node | Max Head (feed) | Time (sec) | Min Head (feet) | Time (sec) | Max Q (cfs) | Time (sec) | Min Q (cfs) | Time (sec) |
|---|---|---|---|---|---|---|---|---|
| 100 | 0 | 0 | 0 | 0 | 0.3 | 0 | 0 | 7.4 |
| 1 | 7.2 | 1.9 | −2.1 | 0 | 0.3 | 0 | 0 | 7.4 |
| 2 | 58.1 | 1.9 | 5.2 | 10 | 0.3 | 0 | 0 | 7.4 |
| | 58.1 | 1.9 | 5.2 | 10 | 0.3 | 0 | 0 | 7.4 |
| 3 | 61.8 | 1.9 | 5.2 | 10 | 0.3 | 0 | 0 | 7.4 |
| | 61.8 | 1.9 | 5.2 | 10 | 0.3 | 0 | 0 | 7.4 |
| 4 | 25.8 | 0 | −31.3 | 1.9 | 0.3 | 0 | 0 | 7.4 |
| 5 | 20.8 | 0 | −16.3 | 1.9 | 0.3 | 0 | 0 | 7.4 |
| | 20.8 | 0 | −16.3 | 1.9 | 0.1 | 0 | −1.1 | 1.9 |
| | 20.8 | 0 | −16.3 | 1.9 | 0.2 | 1.30 | 0 | 10 |
| 6 | 20.8 | 0 | −16.3 | 1.9 | 0.1 | 0 | 0.1 | 1.9 |

The WHAMO code does not handle phase change so it will output negative pressures that exceed vapor pressure and only give a warning about possible column separation. The negative energy wave produces an adverse gradient and flow intrudes from the outside for about 1.2 seconds. Node 4 experiences a minimum head of −13.6 feet and the energy difference between the intrusion reservoir representing the outside water table and energy inside the pipe cause the water to flow into the pipe, reaching a maximum rate of −.14 cfs.

The extreme negative pressure at the intrusion valve is due to the fact that the velocity head is very large as the flow passes through the small diameter of the intrusion opening (Figure 2c). The power failure to the pump after the valve is closed has little impact on the simulation.

Table 2 provides a summary of the maximum and minimum heads and their respective times as well as the maximum and minimum flows and their times of occurrence. Figure 2a), is important because it shows the flow rate at node 6. A negative flow at node 6 indicates that the outside groundwater is being drawn into the system.

## 6 SUMMARY & CONCLUSION

In this test, we have observed when and how intrusion occurs. The intrusion flow rate is relatively large due to the large difference between the internal and external head and the small entrance loss coefficient. The head difference between nodes 5 and the ground water elevation reach a maximum of 27.3 feet. The difference is found by subtracting the minimum energy elevation for node 4 as shown in Table 2 from the constant elevation of the ground water table. We know from the energy equation that flow is driven by the energy gradient so the initial head boundaries can be changed to a constant value and the flow would be the same. In this case, adding 27.3 feet of head to each of the head boundaries would bring the system to the point where no intrusion would occur.

## ACKNOWLEDGEMENTS

Thanks are due to the group of Hydrogeology of the Universidad Politécnica de Valencia for the financial aid to the first author.

## REFERENCES

[1] LeChevallier, M., R. Gullick, M. Karim, M. Friedman, and J. Funk. (2003), “The potential for health risks from intrusion of contaminants into the distribution system from pressure transients”. Journal of Water and Health, 1(1): 3–14.

[2] Kirmeyer, G., M. Friedman, K. Martel, D. Howie, M. LeChevallier, M. Abbaszadegan, M. Karim, J. Funk, and J. Harbour. (2001). “Pathogen Intrusion into the Distribution System”. American Water Works Association Research Foundation. Denver CO.

[3] Fiedman, M., L. Readeer, S. Harrison, D. Howie, M. Britton, G. Boyd, H. Wang, R. Gullick, M. LeChevallier, D. Wood, and Funk. (2004). “Verification and Control of Pressure Transients and Intrusion in Distribution Systems”. Report 91001F. AWWA Research Foundation. Denver CO.

[4] Karim, M., M. Abbaszadegan, and M. LeChevallier. (2003). “Potential for pathogen intrusion during pressure transients”. Journal of the American Water Works Association 95(5): 134–146.

[5] Gullick, R. M. LeChevallier, R. Svindland, and M. Friedman. (2004). “Occurrence of transient low and negative pressures in distribution systems”. Journal of the American Water Works Association 96(11): 52–66.

[6] Wylie and Streeter (1993), Fluid Transients in Systems, Prentice Hall, Englewood Cliffs, NJ 07632.

[7] Batterton, S. 2005, Water Hammer: An Analysis of Plumbing Systems, Intrusion, and Pump Operation. MS Thesis. Virginia Tech. Blacksburg, VA.

[8] Wang, Hua, (2002), Master´s thesis. Tulane University, Laboratory verification of Intrusion during pressure transients in a simulated water distribution system.

*Environmental Hydraulics – López-Jiménez et al (eds)*
*© 2010 Taylor & Francis Group, London, ISBN 978-0-415-56697-1*

# Comparison of air valve behaviour by using CFD techniques

F.J. García-Mares, P.L. Iglesias-Rey, V.S. Fuertes-Miquel, D. Mora-Meliá & P.A. López-Jiménez
*Centro Multidisciplinar de Modelación de Fluidos, Universidad Politécnica de Valencia, Valencia, España*

ABSTRACT: The characterization of air valves during the processes of air admission and air expulsion is fundamental for the design of systems of water supply. The Lab testing for the characterization of air valves are expensive, essentially by the enormous necessary amounts of air and the size of the required air compressors. This work presents an alternative methodology for the characterization of air valves by means of techniques CFD. The analysis by means of CFD is verified by Lab testing. Also we analyze the influence that can have the used model of turbulence. The developed methodology can be extrapolated for another type of air valves, even for another type of elements whose experimental characterization is complex.

*Keywords*: CFD techniques, air valve, entrapped air.

## 1 INTRODUCTION

The air presence in the pipes of supplying and water transport is linked directly to the tasks of operation, maintenance and put into operation. There are many causes by which the air can be within the conductions: filling and emptying operations, temporary interruptions of the supply, vortex formation in the suction of the pumping groups, operation of the air valves by appearance of negatives pressures in the system, fissures in points in which pressure is negative, appearance of breakages in some point of the conduction, release of the dissolved air that takes the water when moving, etc. Whatever its origin, the air presence generates in many occasions problems unwanted.

The air valves or valves of admission and air expulsion settle to control the input and output processes of air. The aim of this type of elements is to avoid the appearance of uncontrolled air pockets. To choose the suitable size of the air valve implies to know its behavior. For that reason the characterization of the air valve is a necessity without which the design process cannot be realized.

The vast majority of the manufacturers of air valves offer characteristic curves such as the shown ones in Figure 1. Previous studies[5] show discrepancies between the data technician-deals contributed by the manufacturer and the data to them collected by Lab test. Its experimental verification is not simple since the tests require of enormous air volumes previously stored. Figure 2 shows a photography of the installation used for the tests. This installation has a great deposit that stores the air and later a series of pressure reductions generates the controlled exit of pressure for the carrying out of the tests.

The work verifies the validity to use techniques CFD (Computational Fluid Dynamics) like alternative for the characterization of air valves. The displayed methodology will be verified later by Lab tests.

## 2 AIR VALVES CHARACTERIZATION

The characteristic of an air valve glass is the relation that exists between the mass volume G that can expel or admit and the pressure $p_t$ inside the pipe. Traditionally obtained expressions of the studies of the compressible flow have been used considering that the flow through an air valve is similar to the isentropic flow in a convergent nozzle (Chaudhry[1]; Wylie and

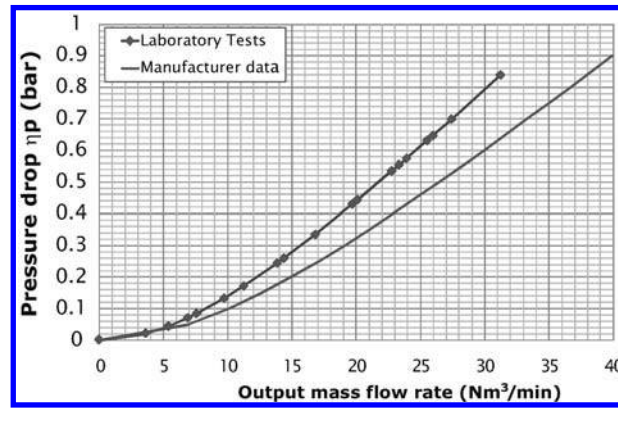


Figure 1. Manufacturer vs. experimental data of an air valve.

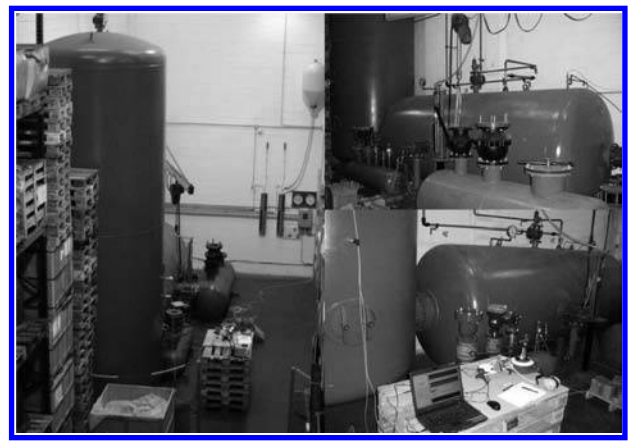

Figure 2. Air valve testing installation.

Streeter[6]). Thus, the complete equations of an air valve in phase of expulsion are:

$$G = C_{exp} A_{exp} p_t^* \sqrt{\frac{7}{RT_t}\left[\left(\frac{p_{atm}^*}{p_t^*}\right)^{1,4286} - \left(\frac{p_{atm}^*}{p_t^*}\right)^{1,714}\right]} \quad \text{if } p_t^* \le 1.8929 \cdot p_{atm}^*$$
$$G = C_{exp} A_{exp} \frac{0,686}{\sqrt{RT_t}} p_t^* \quad \text{if } p_t^* > 1.8929 \cdot p_{atm}^* \tag{1}$$

where $A_{exp}$ is the cross-section of the air valve, $C_{exp}$ its coefficient of expulsion, R the constant characteristic of the air and $T_t$ the temperature inside the pipe. The previous equations have been simplified[2], being this simplification sufficiently reasonable (Fuertes et al.[3]). Mathematically, the equation simplified for the expulsion flow and subsonic flow comes given by the expression:

$$G = C_{exp}\sqrt{\Delta p \cdot p_t^*} \tag{2}$$

where $\Delta p$ is the pressure drop that undergoes to the air between the input and the output. As we can see, the fundamental advantage that presents the simplified formulation (2) is the necessity to have to determine a unique characteristic coefficient. Obviously, a similar expression for the flow of air admission can consider.

## 3 CFD MODEL OF AN AIR VALVE

The equations that describe the movement of a fluid are obtained by application of the continuity and angular momentum equations (equations of Navier-Stokes). These equations are:

$$\frac{\partial \rho}{\partial t} + \nabla \cdot \left(\rho \vec{V}\right) = 0 \tag{3}$$

$$\rho \frac{\partial \vec{V}}{\partial t} + \rho\left(\vec{V} \cdot \nabla\right)\vec{V} = -\nabla p + \rho \vec{g} + \nabla \cdot \tau_{ij} \tag{4}$$

where $\rho$ is the density of the fluid, V the speeds field, p the pressures field, g the forces by volume unit which the fluid is put under, and $\tau_{ij}$ is the voltage tensor.

In order to be able to solve the previous system of equations it is necessary to turn the system (3) and (4) into algebraic expressions by means of a discretization process. This discretization implies dividing the system in smaller volumes. In this case we use a mesh like defined in the Figure 3a. In this figure some of the obtained results can be seen.

In the CFD analysis, one of the basic aspects that are necessary to establish is the turbulence model. The more used model for air and water flows with highly turbulent regimes is the model k-$\varepsilon$ proposed by Launder and Spalding[4]. In this model, the turbulent kinetic energy k, and their ratio of dissipation $\varepsilon$ is obtained from the following equations

$$\frac{\partial}{\partial t}(\rho k) + \frac{\partial}{\partial x_i}(\rho k u_i) = \frac{\partial}{\partial x_j}\left[\left(\mu + \frac{\mu_t}{\sigma_k}\right)\frac{\partial k}{\partial x_j}\right] + G_k + G_b - \rho\varepsilon - Y_M + S_k \tag{5}$$

$$\frac{\partial}{\partial t}(\rho \varepsilon) + \frac{\partial}{\partial x_i}(\rho \varepsilon u_i) = \frac{\partial}{\partial x_j}\left[\left(\mu + \frac{\mu_t}{\sigma_\varepsilon}\right)\frac{\partial \varepsilon}{\partial x_j}\right] + C_{1\varepsilon}\frac{\varepsilon}{k}\left(G_k + C_{3\varepsilon}G_b\right) - C_{2\varepsilon}\rho\frac{\varepsilon^2}{k} + S_\varepsilon \tag{6}$$

In these equations, $G_k$ represents the generation of turbulent kinetic energy originated by the variations of the components of the average speed of the flow; $G_b$ represents the kinetic energy generated by boundary push; $Y_M$ is the contribution of the pulsatile expansion associated to the compressible turbulence; $C_{1\varepsilon}$, $C_{2\varepsilon}$ y $C_{3\varepsilon}$are constants; $\sigma_k$ y $\sigma_e$ are the Prandl numbers for k and $\varepsilon$ respectively; and $S_k$ y $S_\varepsilon$ respectively represent a global variation in the time of parameters k and $\varepsilon$ that can be defined of independent form of the rest of variables. On the other hand, turbulent viscosity $\mu_t$ calculates by means of a combination

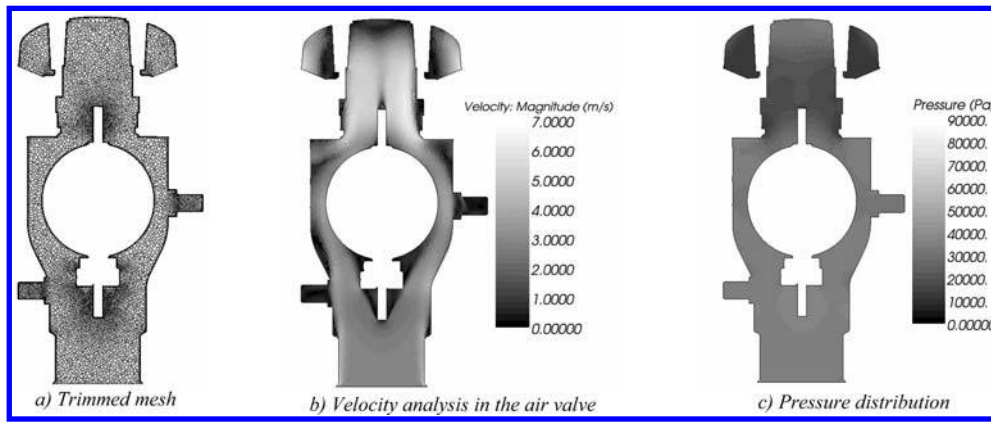


Figure 3. Analysis with the CFD. Mesh and results.

Table 1. Results of different k-$\varepsilon$ models.

| | Model options | | CFD results | Error |
|---|---|---|---|---|
| Turbulence model | Viscous Heating | Bouyancy effects | G (kg/s) | $\Delta$G (%) |
| Experimental results | – | – | – | – |
| Standard k-$\varepsilon$ model | SI | SI | 0.04% | 0.04% |
| | NO | SI | 0.17% | 0.17% |
| | NO | NO | 0.15% | 0.15% |
| | SI | NO | 0.17% | 0.17% |
| RNG k-$\varepsilon$ model | SI | SI | 0.58% | 0.58% |
| | NO | SI | 0.65% | 0.65% |
| | NO | NO | 0.69% | 0.69% |
| | SI | NO | 0.71% | 0.71% |
| Full k-$\varepsilon$ model | SI | SI | 0.06% | 0.06% |
| | NO | SI | 0.11% | 0.11% |
| | NO | NO | 0.13% | 0.13% |
| | SI | NO | 0.11% | 0.11% |

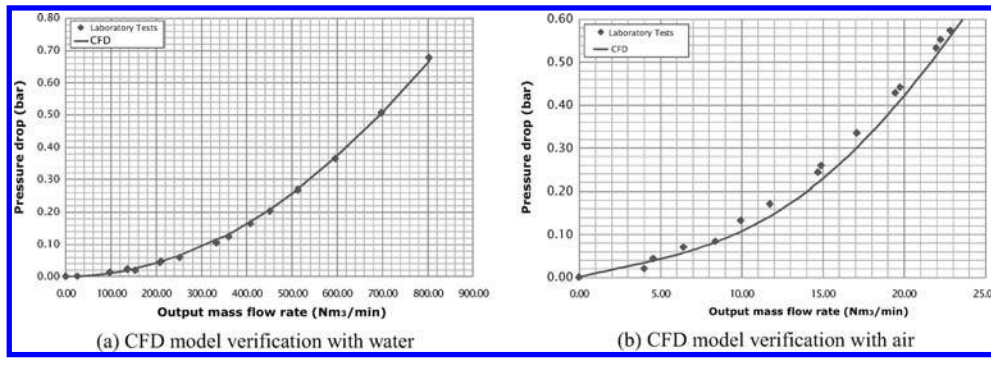


Figure 4. Comparison of results obtained with CFD model and experimental tests.

of the values of k and $\varepsilon$. The constants $C_{1\varepsilon}$, $C\varepsilon$, $\sigma_k$ and $\sigma_\varepsilon$ adjust from the obtained results of experimental form. However, the values contributed by Launder and Spalding[4] have been very effective with turbulent air flows and turbulent water flows.

During the development of the present work we have studied the influence that can have the model of turbulence used in the final results. For it we have considered the model k-e defined by means of Launder and Spalding[4] and two variations of the same: the model RNG k-$\varepsilon$ proponed by Yakhot and Orszag[7] and the complete model k-$\varepsilon$ proposed by Shih et al[5]. The comparative results of the realized study of sensitivity are shown in Table 1. Also we have studied in each case the effect that has the consideration of two factors: the energetic dissipation due to the viscous efforts, and the effects that it has on the equation characteristic of the ratio of dissipation to consider the effects of the drag of the fluid.

The validation of the results of Table 1 has been realized comparing the obtained results of mass volume expelled by the air valve for a certain differential of pressure between its ends.

During the analysis of air valves by means of CFD two different computer models have been used: ANSYS Fluent and STAR-CCM+. Both models practically offer equal results when the size of the mesh and the calculation options are the same. In any case, the definitive verification of the used model is realized comparing the results obtained by means of CFD with Lab tests.

Since the objective was the hydraulic characterization of the behavior of the air valve, the realized lab tests have concentrated in determining the volume of flow that is able to expel the air valve glass for each fall in differential pressure. Also to determine the validity of the used model of turbulence we have realized tests as much with air as with water.

The obtained comparative results of the analysis by means of CFDs are shown in Figure 4. Figure 4.a. shows the goodness of fit of the results obtained in tests realised with water. Figure 4.b. shows the obtained results with air. As it can be seen, the results obtained with CFD and experimentally have a good goodness of fit.

## 4 CONCLUSIONS

To conclude, after analyzing the results obtained by means of the analysis with CFD of the air valves the following conclusions can be obtained:

- The modeling of the air flow by means of CFD allows to predict the characteristic lines of the air valves without needing to perform the tests.
- The model k-$\varepsilon$ of turbulence has been extremely adapted to represent the behavior of the flow inside the air valve.
- The different alternatives from the model k-$\varepsilon$ analyzed have not been significantly important when calculating the mass volume admitted or expelled for each one of the pressures in the connection from the air valve with the pipe. These differences are more significant in the case of analyzing the drag force on the floater of the air valve.
- The validity of the model developed by means of CFD has been demonstrated so much in the case of circulating air as in the case of circulating water. Without a doubt, the adjustment with water is much more precise, since during the development of the models with air it is necessary to fit the characteristic parameters of the compressible flow.

In conclusion, the propose methodology can be extrapolated for other types of air valves and including for other types of device. It can even constitute a suitable methodology to avoid great infrastructures for the characterization of air valves of great dimensions.

## ACKNOWLEDGEMENTS

This article has been possible inside the actions developed by the researchers of CMMF involved in the project “Integración de la caracterización dinámica de elementos y consumos en modelos de redes de abastecimiento de agua utilizando sistemas de información geográfica y algoritmos genéticos (CADAGIAS)”. The number reference of the project is DPI2006-13113. And DANAIDES: Desarrollo de herramientas de simulación para la caracterización hidráulica de redes de abastecimiento a través de indicadores de calidad del agua. REF. DPI2007-63424.

## REFERENCES

[1] Chaudhry, M.H. (1987). *Applied hydraulic transients*. Ed. Van Nostrand Reinhold Company, New York, USA.
[2] Fuertes-Miquel, V.S. (2001). *Transitorios hidráulicos con aire atrapado*. PHD Thesis. Universidad Politécnica de Valencia.
[3] Fuertes-Miquel, V.S., Iglesias-Rey, P.L., García-Mares, F.J. & Mora-Meliá, D. (2009). “Air valves behavior. Comparison between compressible and incompressible modelling”, *International Workshop on Environmental Hydraulics: Theoretical, experimental & computational solutions, IWEH09, Valencia, Spain, 29–30 October.*
[4] Launder, B.E. & Spalding, D.B. (1972). *Lectures in Mathematical Models of Turbulence*. Academic Press, London, England.
[5] Shih, T.H., Liou, W.W., Shabbir, A., Yang, Z. & Zhu, J. (1995). “A New k-e Eddy-Viscosity Model for High Reynolds Number Turbulent Flows – Model Development and Validation". Computers Fluids, 24(3):227–238.
[6] Wylie, E.B.; Streeter, V.L. (1993). *Fluid transients in systems*. Ed. Prentice Hall, Englewood Cliffs, New Jersey, USA.
[7] Yakhot, V.y Orszag, S.A (1986). “Renormalization Group Analysis of Turbulence: I. Basic Theory”. Journal of Scientic Computing, 1(1):1–51.

*Environmental Hydraulics – López-Jiménez et al (eds)*
*© 2010 Taylor & Francis Group, London, ISBN 978-0-415-56697-1*

# Fuzzy model in the vulnerability multi-criteria assessment in water supply systems

Veruska Zidko & Helena M. Ramos
*DECivil, Instituto Superior Técnico, Lisboa, Portugal*

ABSTRACT: Water supply systems are strategic infrastructures and are continuously subject to various situations which can threaten its good functioning. The occurrence of ruptures, leaks, or even service interruption, are in a general way, the result combination between the physical properties of the hydraulic circuit and the aspects related to the system operation, in particular the occurrence of pressure variations. These aspects reflect the susceptibility of such infrastructures, whose vulnerability must be carefully evaluated and constantly monitored. In this work is presented a multi-criteria analysis associated to the vulnerability on water supply infrastructures, as well as, the develop of a methodology for ordered intervention planning (e.g. rehabilitation), of preventive and emergency maintenance on water supply systems, through the application of Fuzzy Logic. For that, it is identified the vulnerabilities of the hydraulic circuit, considering the physical properties and its dynamic behaviour due to variation of consumption or on hydro-mechanical equipment. This analysis allows identifying elementary zones of distribution network that present a greater vulnerability index.

*Keywords*: supplying infrastructures, pressure variation, vulnerability evaluation, fuzzy logic.

## 1 INTRODUCTION

During lifetime, water supply infrastructures become more vulnerable to the actions that provoke structural integrity degradation of mains and accessories, resulting, so many times, in rupture of such systems. It is in this way essential, measures of prevention and mitigation, which assure on one hand, the safety of routine operations, the system response capacity in emergency cases[3] , the damages containment in catastrophe situations and on the other hand, improve the performance in a fast and efficient way, both from responsible technician and from protection services in abnormal, emergency and catastrophe situations[10].

Many mathematical models uses historical data on faults and ruptures occurred in the past, supposing its continuation, in order to foresee the probable occurrence of ruptures in the future, as the work of [2][6][7][8][17][18][19]. The methods of study developed by these authors consider that the tax of rupture of infrastructures dependent on the installation, the material, the involving conditions, the thickness and the quality, in function of the time.

Almeida and Ramos [1] had verified that the occurrence of extreme pressures, even if of short period, can induce pressure variation values in the system, being able to cause ruptures on pipes and accessories and to the collapse of pipe walls by crushing. Pressure alterations cause critical stress on the entire hydraulic system, for these reasons mechanical structures in a system must not be neglected neither when dimensioning nor when usage [11][12][13][14].

In the present study is developed a method of analysis of vulnerabilities that considers, stops beyond static variables (e.g., age, type and dimensions of the behaviours and accessories), relative variables to the functioning of a supplying system, such as variations of the pressure of service and the velocity of draining. The relative variables to the functioning of the system had been analysed having for base the results gotten in the study developed for Ramos et al.[15][16]

The fuzzy hierarchy model used in this work, for vulnerability analysis, follows in general way the methodology presented by Nobre[9], although with modifications to adjust itself to the characteristics of the supplying systems. The model is based on the matrices that represent demand and supply are the kind of $A = (a_{ij})_{hxn}$ and $B = (b_{jk})_{nxm}$, respectively, where *n* are attributes and *m* the various components of the hydraulic system. Variable *h* is identified as the performance.

## 2 VULNERABILITY ANALYSIS

### 2.1 *Brief description of the system to be analyzed*

The main system that is proposed to analysis corresponds to the network example net3.inp, which comes with program EPANET 2.0. The system is composed of two main water supply systems that start in the reservoirs called “River” and “Lake”. The mains material type in analysis is Casting Iron. The Figure 1 is presented a system layout.

### 2.2 *Infrastructures characteristics*

Studied the following vulnerability orientated to hydraulic system: (i) Structural property: material type, length and diameter; (ii) Internal loads: service pressure and velocity; (iii) Degradation of structural integrity: age associated with material type. The classifications of associated vulnerability values related are done based on the study ma**d**e by Godfrey[4][5].

### 2.3 *Characteristics of system operation*

The vulnerability analysis of a water supply system that operates under pressure develops based on three conditional stages: (1) Determination of penalty curve, which traces the vulnerability value attributed to the network conditional variable; (2) Application of generalization function, which allows calculating global aggregate values to the system or subsystem in analysis and (3) Evaluation of system behaviour during its normal operational period.

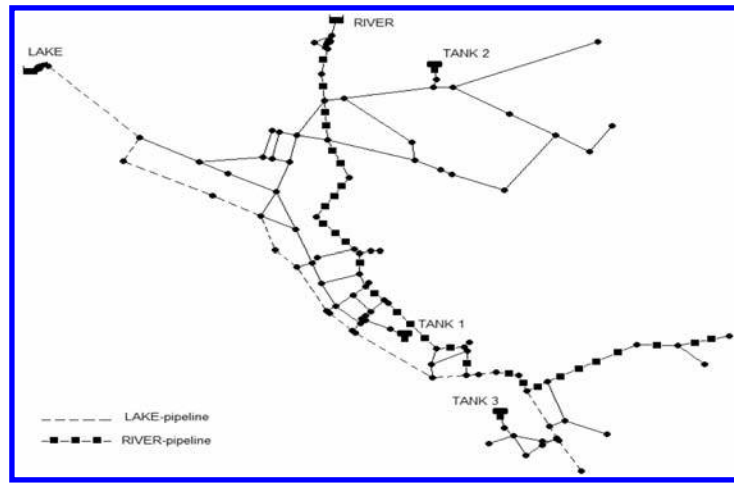


Figure 1. System to be analyzed.

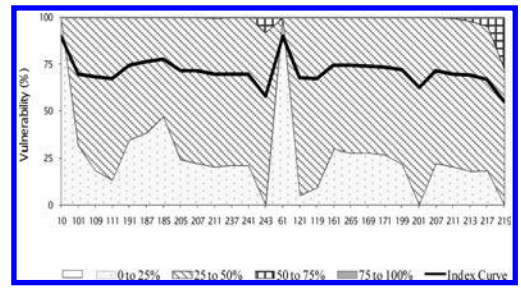


Figure 2. Vulnerability to pressure variation.

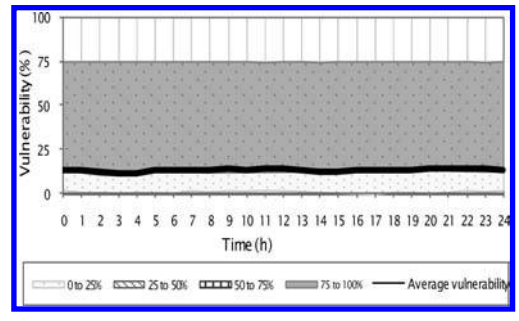


Figure 3. Network vulnerability to global velocities.

Is considered the vulnerability analysis for the system during draining dynamic conditions, for what the velocity in the system that can be significant throughout the day (under conditions of quasi-permanent draining regime) and of extreme pressure variations induced by the occurrence of manoeuvres in hydro-mechanical equipment (transitory regime).

According to pressure variation diagram (Figure 2) average vulnerability reaches levels around 75%, confirming the high vulnerability of system due to dynamic conditions of operation (transitory regime).

Figure 3 shows that the average vulnerability curve develops within the optimal situation (0entire period of simulation.

## 3 APPLICATION OF FUZZY LOGIC

### 3.1 *Attributes definition and model parameters*

The model attributes have been defined in accordance with vulnerability factors of mains and fittings: type of material (f1), length (f2), diameter (f3), pressure of service (f4), draining velocity (f5) and mains and accessories degradation (f6)

### 3.2 *Matrices definition*

The *demand matrix* is defined by the attributes above referred and by the network vulnerability index to the risk of fail. For each attribute of demand matrix a weight is attributed, according to its importance in network performance of water supply network regarding the risk of fail occurrence during a normal system operation. The *supply matrix* is defined by supplied classifications to each attribute in relation to vulnerability situations. The *resultant matrix* is calculated through a Fuzzy mathematical Operator definite with the definition of four classes to the index of network performance for each vulnerability situation verified. The *results matrix* has been got from divide the results provide for the product matrix by the demand factor (FD), which results in the sum of the numerical values of the weights given to the matrix elements.

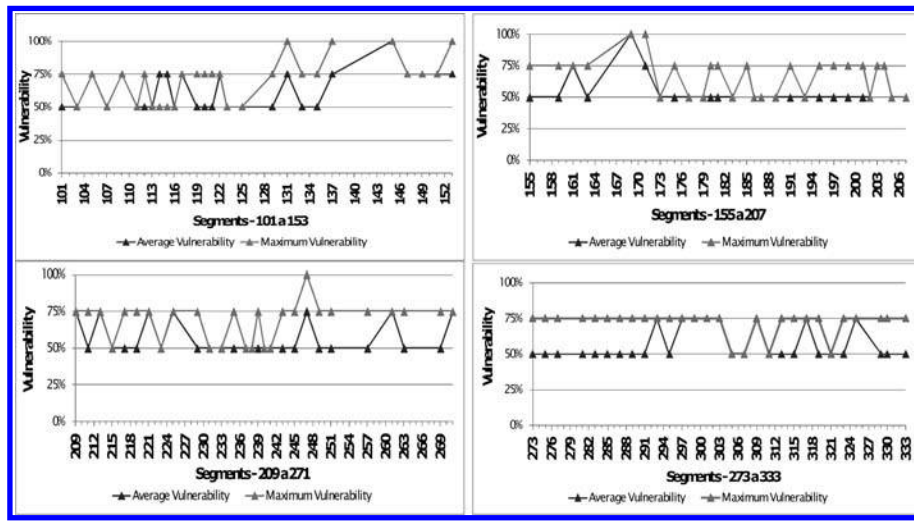


Figure 4. Vulnerability index hierarchy of the network segments (transitory regime).

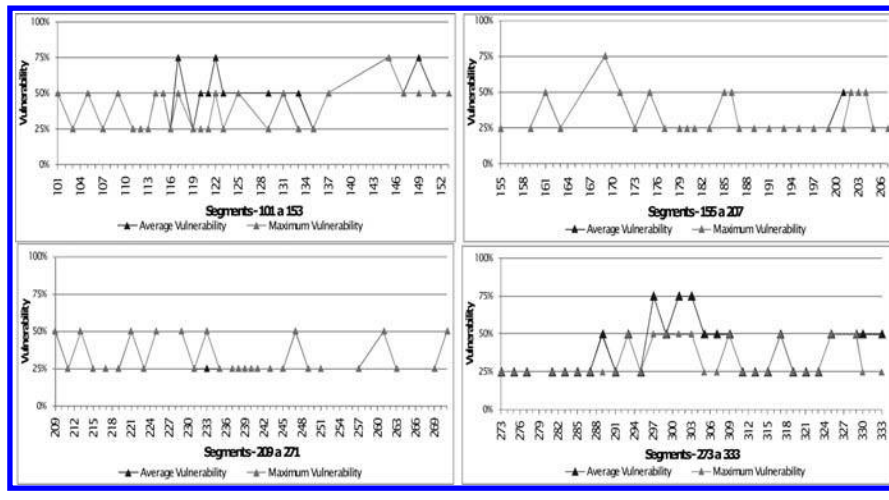


Figure 5. Vulnerability index hierarchy of the network segments (permanent regimen).

The matrices elements of demand and supply have four categories in accordance with the importance degree of each factor attributed, related to the element vulnerability degree, as follow:
$a_{ij}$ = ■, □, ■, □, If the demand of attribute *i* is crucial, conditioned, partially conditioned or irrelevant, respectively
$b_{ij}$ = ■, □, ■, □, If the supply of attribute *i* of vulnerability *j* is excellent, good, reasonable or unsatisfactory, respectively.

### 3.3 *Analysis of results – FUZZY HIERARCHY*

The vulnerability index hierarchy of the network in study is presented separately for two distinct conditions of operation: during the occurrence of transitory draining regime situations – presented in Figure 4, and during the occurrence of situations corresponding to quasi-permanent draining regimes, whose hierarchy can be visualized in Figure 5. In both situations it is analyzed the average vulnerability and the maximum vulnerability associated to the parameter relative to pressure (f4).

As it can be analyzed on Figure 4, during a transitory regime the system presents a vulnerability index variation between minimum acceptable performance grade (50%) and service interruption (100%). Whereas, in case of quasi-permanent regime, the variation of such index is 25%, adequate performance degree, up to 75%, unacceptable performance degree (Figure 5). In both Figures can be verified the hierarchy of vulnerability index for each segment in the system. It is verified that (Figure 4) there are seven segments (131, 137, 145, 153, 169, 171 and 247) that present a maximum vulnerability grade. Two of these segments also present a maximum vulnerability grade, when analyzing pressure average vulnerability (145 and 169). To these segments is conferred a conjugation of attributes/parameters that present less protection to vulnerability, such as, length (f2), diameter (f3) and pressure (f4).

## 4 CONCLUSION

From the hydraulic point of view, for the good operation of a supply system, the service pressure and the draining velocity in the mains will have to be within a lower limit and an upper limit, in order to guarantee a comfort level to consumers and acceptable values of water quality.

The fuzzy hierarchy model developed in this research work allows identifying system zones that present greater vulnerability indices, as well as the identification of possible problems associated with the different attributes studied in the problem. This

model applied to operational management on supply systems can be considered as innovative and actuate as an instrument of great utility in the identification and the evaluation of system components and zones that present high sensitivity to the occurrence of an operational fault.

## ACKNOWLEDGEMENTS

The authors wish to thank to FCT through the projects PTDC/ECM/64821/2006 and PTDC/ECM/65731/2006, as well as CEHIDRO, the Hydro-systems' Research Centre from the Department of Civil Engineering, at Instituto Superior Técnico (Lisbon, Portugal).

## REFERENCES

[1] Almeida A.B., e Ramos H. (2008), Water supply safety: diagnosis of an abnormal accident in a main Lisbon pumping system – Reliability Engineering & System Safety.
[2] Clark R. M., Stafford C. L., and Goodrich J. A. (1982), Water distribution systems: A spatial and cost evaluation – J. Water Resources Planning and Management Division, ASCE, 108(3), 243–256.
[3] Cruz A.M. (2005) – Engineering Contribution to the Field of Emergency Management – Emergency Administration and Planning Department of Public Administration – University of North Texas. Denton.
[4] Godfrey S., Niwagaba C., Howard G., Tibatemwa S. (2005), Water Safety Plans for Utilities in Developing Countries – A case study from Kampala, Uganda.
[5] Godfrey S. and Howard G. (2004), Water Safety Plans (WSP) for Urban Piped Water Supplies in Developing Countries – WEDC, Loughborough University, UK. http:www.lboro.ac.uk/wedc/projects/iram/ index.htm
[6] Jacobs P., and Karney B. (1994), GIS development with application to cast iron water main breakage rate – 2nd Int. Conf. on Water Pipeline Systems – BHR Group Ltd., Edinburgh, Scotland.
[7] Jon Rostum (2000), Statistical Modelling of Pipe Failures in Water Networks – Dissertation for the degree of Doctor Engineer – Norwegian University of Science and Technology, Trondheim, Norway
[8] Kleiner Y., e Rajani, B.B. (2000), Considering time-dependent factors in the statistical prediction of water main breaks – American Water Works Association: Infrastructure Conference, Baltimore, Maryland- March 12–15, 2000, pp. pp. 1–12.
[9] Nobre, R. (2006), Avaliação de Risco para o Uso e Protecção de Aquíferos. Estudo de Caso: Região Metropolitana de Maceió-Alagoas, PhD thesis – UFRJ, Universidade Federal do Rio de Janeiro, Brasil.
[10] Pan American Health Organization (1998), Natural Disaster Mitigation in Drinking Water and Sewerage Systems – Guidelines for Vulnerability Analysis- Regional Office of the World Health Organization, Disaster Mitigation Series, Washington D. C.
[11] Ramos H. (2006), Escoamentos Variáveis – Vulnerabilidade dos sistemas hídricos, DFA em Hidráulica e Recursos Hídricos. Instituto Superior Técnico, Lisboa.
[12] Ramos, H. (2004), Efeitos Dinâmicos não Convencionais para Sistemas Hidráulicos em Pressão – Folhas de apoio às disciplinas de Escoamentos Variáveis e de Sistemas elevatórios e hidroeléctricos – Mestrado em Hidráulica e Recursos Hídricos. IST – DECivil.
[13] Ramos, H. (2003), Folhas de apoio à disciplina de Sistemas elevatórios e hidroeléctricos do Mestrado em Hidráulica e Recursos Hídricos. IST, DECivil.
[14] Ramos, H. (2002), Transitórios Hidráulicos em Pressão – Textos de apoio às aulas de Mestrado na disciplina de Escoamentos Variáveis, IST, DECivil.
[15] Ramos H., Tamminen S., e Covas D. (2008), Water Supply System Performance for Different Pipe Materials – Part I: Water Quality Analysis, Water Resources Management, DOI 10.1007/s11269-008-9244-x.
[16] Ramos H., Tamminen S., Covas D. (2008), Water Supply System Performance for Different Pipe Materials – Part II: Sensitivity Analysis to Pressure Variation, Water Resources Management, DOI 10.1007/s11269-008-9279-z.
[17] Rajani B., Kleiner Y. (2000), Considering time-dependent factors in the statistical prediction of water main breaks – American Water Works Association: Infrastructure Conference, Baltimore, Maryland, pp. pp. 1–12
[18] Rajani B., Kleiner Y. (2000), Comprehensive review of structural deterioration of water mains: physically based models – Urban Water, Vol. 3, n.º 3, pp. 151–164.
[19] Shamir U., and Howard C.D.D. (1979), An analytic approach to scheduling pipe replacement – J. AWWA, 71(5), 248–258.

*Environmental Hydraulics – López-Jiménez et al (eds)*
*© 2010 Taylor & Francis Group, London, ISBN 978-0-415-56697-1*

# Statistical analysis of water distribution networks design using Shuffled Frog Leaping Algorithm

Daniel Mora-Meliá, Pedro L. Iglesias-Rey, Gabriel Bosque-Chacón & P. Amparo López-Jiménez
*Centro Multidisciplinar de Modelación de Fuidos, Universidad Politécnica de Valencia, Valencia, España*

ABSTRACT: The evolutionary algorithms are methods of search of solutions that are based on the natural principles of the evolution. Shuffled Frog Leaping Algorithm is one of them. Here it is applied to determine optimal design in a water distribution network.

The work demonstrates the kindness of the method on the Hanoi Towers network and in the New York supply network, widely studied in the bibliography. Moreover, starting with random values for the different parameters of the method, the influence of these parameters is analyzed in the final solutions. The aim is to find the most suitable configuration of the problem, so that good solutions are obtained in the less time.

*Keywords*: Water distribution design, SFLA, Heuristic methods

## 1 INTRODUCTION

Water distribution networks are systems that communicate reservoirs of water with discharge points through a group of pipes. These reservoirs can be lakes, tanks, ponds, etc. Water is going inside the pipes from maximum pressure points to lower pressure areas. However, simulation of hydraulic and physic behaviour in a pressurized and looped network is not an easy task. The solution process involves simultaneous considerations of the continuity and energy equations and the head-loss function (Savic and Walters[3]).

The design of water distribution networks consist in selecting the cheapest combination of pipe diameters for the network provided some established restrictions (minimum pressure). Solving this problem is extremely complex. It is well-known that when the diameters of the conductions are chosen as decision variables, the restrictions are implied functions of these variables of decision, so the space's region of solutions is a no convex type and the objective function becomes multimodal.

That is due to in a looped network, if any of the diameters is changed, the entire network is affected. A network made up by branches and no loops can be solved branch by branch until the entire network, but a looped network has to be solved at the same time. There are many techniques to try to solve this kind of problem. One of the most important families of methods to attack these problems is meta-heuristics. Inside the heuristics, we can find the evolutionary algorithms, and the Shuffled Frog Leaping Algorithm (SFLA) is one of them.

The technique studied in this work, called Shuffled Frog Leaping Algortihm (Eusuff and Lansey[1,2]) is a method created mixing Memetic Algorithms and Particle Swarm Optimization principles. In SFLA, individuals are called "frogs". Each frog contains one solution, which is changing over the time. Each solution is formed by a group of variables (in this case, a specific combination of diameters in a water distribution network).

In a first step, every frog has a random solution. Then, the frogs are divided in Memeplexes (group of frogs) depending on their fitness. In this case, the fitness function represents the cost of the network. In each memeplex, frogs exchange information (best frogs inform to worst frog), changing and improving their fitness. This process, called evolutionary step, is very similar to the "local search" of PSO algorithms. After several evolutionary steps in each Memeplex, all frogs are put together again. They are put in order by their fitness again (shuffling process) and they are divided again into Memeplexes. The process is repeated as many times as needed until the convergence criteria is carried out.

## 2 METHODOLOGY

SFLA contains five variable parameters, which have an influence on the ability of the algorithm to solve the water networks. Some combinations of parameters provide better solutions than others, but the best value of each parameter is unknown.

In order to establish as they are the best combinations of parameters, the studied networks are attacked trying some possible combinations of the different parameters. Then, the results are analysed depending on the success of rate. SFLA has five different parameters to optimize:

- m: Number of memeplexes
- n: Number of Frogs per Memeplex
- N: Number of Evolutionary Steps per Memeplex per Loop
- q: Number of Frogs per Submemeplex

In order to choose a rank of study for the different parameters we have considered orientative values given by other researchers. The most interesting procedure is to study the widest range possible. So, for an initial study of the method, it was necessary to reduce the size of the range of parameters to speed up the calculations. The rank of values studied for each parameter is the

following one:

Table 1. Variation range of SFLA characteristic parameters.

| Parameters | | Variation range | Range size |
|---|---|---|---|
| Memeplexes | *m* | 10, 20, 30 | 3 |
| Frogs per Memeplex | *n* | 10, 20, 30 | 3 |
| Frog per Submemeplex | *q* | 0.25, 0.43, 0.62, 0.81, 1 | 5 |
| Evolutionary Steps | *N* | 5, 11.25, 17.5, 23,75, 30 | 5 |
| Accelerator parameter | *C* | 1, 1.375, 1.75, 2.125, 2.5 | 5 |

Therefore, initially $m = 10$ and $n = 10$ are fixed values. Then, the three parameters left are studied: q, N and C. Totally, there are 125 ($5 \times 5 \times 5$) possible combinations between q, N and C. Two hundred runs of each combination of parameters were done.

Then it was studied the relation between q and N for each value of C. It was done this way because it is very difficult optimize more than two parameters at the same time without handling complex statistical tools, that exceed the objective of the work. After that, the best combination of the group q-N-C is found. The expression "best combination" means the combination that produces a higher percentage of optimum solutions. For example, in the Hanoi network the best result known is 6081 millions um.

When the best combination of parameters q-N-C is fixed, the second part of the optimization method is to find the best combination for the other parameters, m and n. For it 200 runs for each possible combination are calculated. The total number of simulations in this phase ate 1800 runs. In this point the best combination of all parameters for a studied network is already known.

It is probably that using this methodology we can lose some information in the interactions between the parameters because it studies the group q-N-C first and the group m-n later. This was done in order to reduce the number of simulations. This way SFLA does $25000 + 1800 = 26800$ runs per network. If the five parameters were studied at the same time that would require $5 \times 5 \times 5 \times 3 \times 3 \times 200 = 225000$ runs, almost 10 times more calculations.

The characteristic that measures "kindness" or capacity of a certain frog's (solution) survival regarding the others is known like aptitude. The aptitude of a certain generic frog is identified through the value that adopts the objective function for the codified solution. In the case of the SFLA proposed for design and extension of supplying networks this objective function is defined as

$$F(X^i) = \sum_{j=1}^{N_{VD}} C_j\left(X_j^i\right) \; L_j + \lambda \sum_{s=1}^{N_S} \sum_{k=1}^{N_R} \delta_{k,s} \; \left(H_{min,k} \quad H_{k,s}\right) \tag{1}$$

where $C_j$ is the associated unit cost to the decision variable's value contained in link j of frog i; and $L_l$ is the length of conduction of pipe j. Moreover, they are $N_R$ imposed restrictions that must achieve the possible solutions of the problem. These restrictions have been including through a penalty function.

The restrictions that must be fulfilled are the derived ones to satisfy the restrictions with minimum pressure height ($H_{min,k}$) in each node k. These restrictions must be verified in all the analyzed scenes $N_S$, that usually are the on-speed operation of the system and its operation under the scene of failure of some of the conductions. The function penalty represents the difference between the head height of the node k in scene s ($H_{k,s}$) and the required minimum height ($H_{min,k}$). In order to compute this penalty two variables are defined. One of them ($\delta_{k,s}$) is a binary variable that adopts value 1 if $H_{k,s} < H_{min,k}$, and it adopts null value in opposite case. The parameter $\lambda$ represents a weight function that establishes the penalty's value for not verifying the restrictions of minimum pressure in the nodes. Pressure is considered as a hard constraint, and $\lambda$ is big enough ($10^7$) for reject all solutions that violates the constraint.

## 3 APPLICATION EXAMPLE

The two studied networks in this work are completely real. Hanoi network is in Vietnam. This network has been used frequently to test these kind of algorithms due to it exists a lot of information and bibliography available. Since the first 90s every algorithm designed to solve least-cost problem in water distribution networks has been tested in Hanoi network. Therefore, this network provides an excellent point of comparison to researchers all over the world. Hanoi network is shown in the following figure:

The second water distribution network is in New York. It is the New York City water supply tunnel system. Schaake and Lai[4] first studied it in detail in 1969. Unlike the previous network, this one faces a problem a bit different and that is why it is a good complement to study the solving capacity of SFLA. New York network is an expansion design problem. At the beginning of the situation there is already a previous existing network of tunnels that constituted the primary water distributions system of the city of NY. The problem comes out in some nodes in which the pressure is lower than the minimum allowed pressure. So, the objective here is to determine the cheapest design for additions to the previous network.

The complete data of Hanoi and NY networks is shown in the next table:

## 4 RESULTS AND ANALYSIS

This section shows the best combination of diameters found for Hanoi and NY networks. The total budget of the network is calculated multiplying the cost per length unit times the length for each pipe. The cost (in $ million) for Hanoi network is 6.081. NY supply system is an expansion-design problem. The best solution found is 38.64 (in $ million). Both solutions equal the found minimum cost until today by the different researchers.

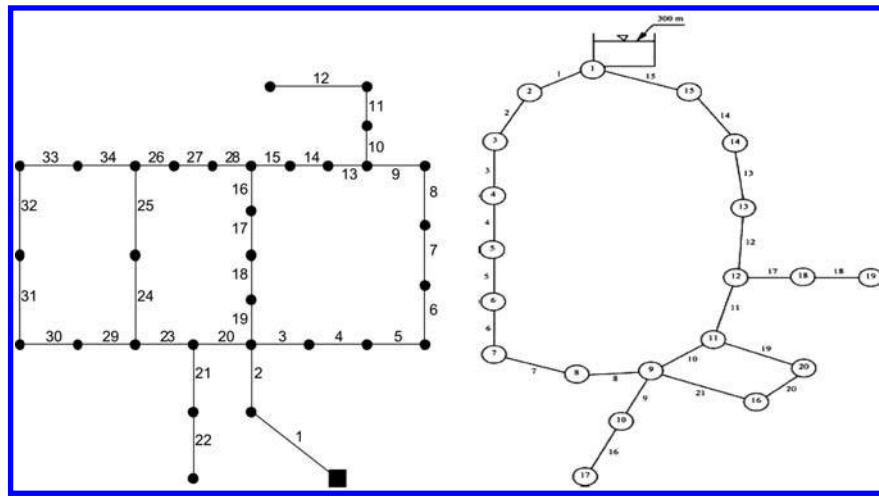

Figure 1. Hanoi water distribution network and New York supply system network.

Table 2. Hanoi and NY network data.

| Network | Hanoi | New York water supply system |
|---|---|---|
| Location | Hanoi, Vietnam | New York, USA |
| No. Pipes | 34 | 21 |
| No. Nodes | 32 | 20 |
| No. Loops | 3 | 2 |
| Set Available Diameters (in inches) | 12, 16, 20, 24, 30, 40 | 36, 48, 60, 72, 84, 96, 108, 120, 132, 144, 156, 168, 180, 192, 204 |
| Corresponding Cost | 45.726, 70.4, 98.378, 129.333, 180.748, 278.28 (in dollar/meter) | 93.5, 134, 176, 221, 267, 316, 365, 417, 469, 522, 577, 632, 689, 746, 804 (in dollar/foot) |
| No. Possible Solutions | $6^{34} = 2.8651*10^{26}$ | $16^{21} = 1.93*10^{25}$ |
| Type of Problem | Design | Expansion-Design |

Generally, SFLA works in a random way. The characteristics of this kind of method do not guarantee with certainty the obtaining of the optimal value of the system. In addition, the obtained result can suffer sometimes certain variations. In order to analyze this randomness it is necessary to make statistical analyses that will study the influence that have the different parameters from the SFLA proposed in the solution of the analyzed network, with the purpose of optimizing them to increase the probability of obtaining the minimum.

Before starting to analyse the data is quite important to clarify some concepts and ideas. Success rate is the ability of one combination of parameters of SFLA of finding the cheapest solution to a network.

The concept of "good solution" is introduced now. One of the characteristics of heuristic methods in general is the capacity to obtain not only one single optimal value, but to obtain a set of "good solutions" on the design problem. In this work "good solution" is defined with whose cost is over the minimum cost until in a 3%. Therefore, with those ideas already clarified it is time to analyse the real influence of each parameter in the entire algorithm.

As we can see in figure 3, Accelerator parameter (C) optimum is around 2 (2,125 for Hanoi network and 1,75 for NY network). That means that allowing bigger jumps between the frogs accelerates the searching speed and improves the found optimums. For low values of C SFL Algorithm has a lot of problems to find minimums and even good solutions. In Hanoi network the first minimum found was for C = 1,75.

The best value for Submemeplex size (q) is 43% of the Memeplex size. Both networks agree in this point. Some others intermediate values work also well (q = 62%). The evolutionary steps (N) is the only parameter with no real influence. Higher values (N = 23.5, N = 30) produces higher success rate but slower searches and lower values (N = 5, N = 11.25 vice versa.

The number of Frogs per memeplex (n) is optimum at 30 individuals, but it is clear that higher values would produce better optimums. In this parameter the range of values taken was wrong. It should have been higher, towards n = 50 or even more. Finally, the number of Memeplexes (m) has been the most problematic parameter. Hanoi set the optimum at m = 20 with worse results for lower and higher values of the parameter. Nevertheless, in NY network the parameter seems not to have a big influence because it produces very similar results for all its values. In this point it will be necessary further researching in order to clarify this point. Finally, the optimal combination of parameters for each network is:

This study was done to clarify the real influence of parameters. From the best values obtained for different parameters another study was made, with the objective to confirm the improvements of the results. A histogram is made (see Figures 3 and 4). This graph incorporates the accumulated probability of the obtained solutions. The graph allows to detect the more frequent solutions, as well as to determine the probability of obtaining a given solution better to one given.

Both previous figures show the importance of choosing the parameters correctly. The best combination of parameters increases the probability of obtaining the minimum cost until a 20% in the case of the network of Hanoi. For, NY problem, the probability of obtaining the minimum increases almost until a 50% with the best parameters.

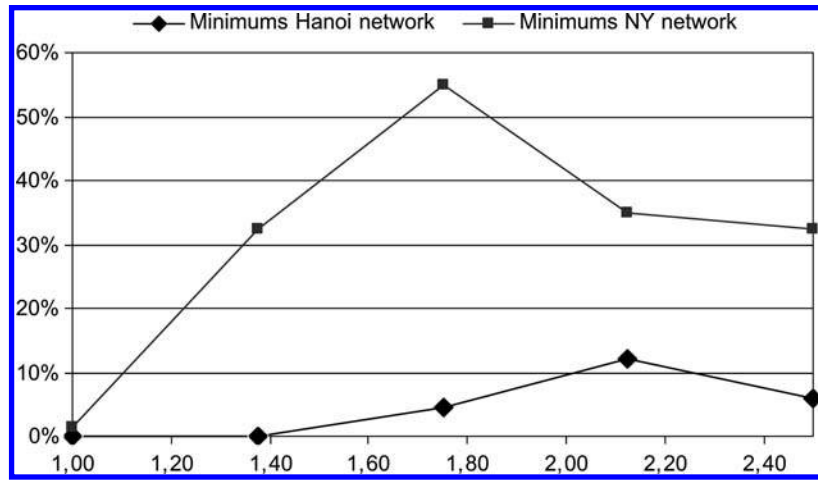


Figure 2. Influence of C in success rate.

Table 3. Final proposed combinations.

| | Network | |
|---|---|---|
| Parameter | Hanoi | NY |
| C | 2.125 | 1.75 |
| q | 0.4375 | 0.4375 |
| N | 30 | 23.75 |
| m | 20 | 10 |
| n | 30 | 30 |

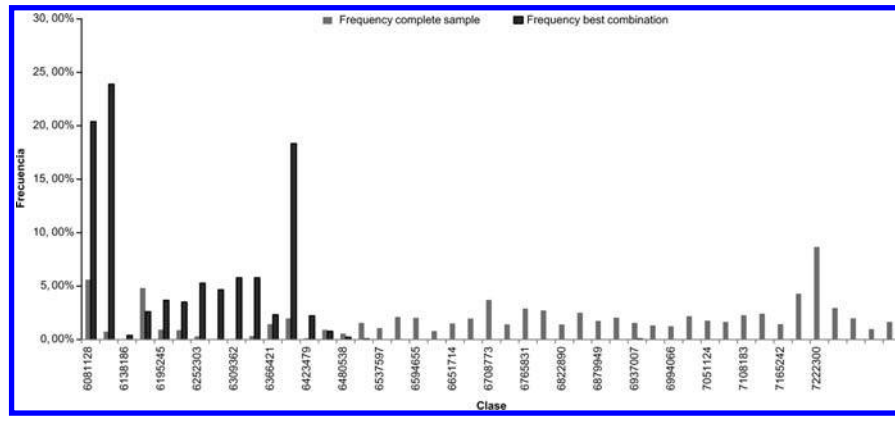


Figure 3. Diagram of frequencies of the obtained solutions in Hanoi network.

## 5 CONCLUSIONS

The economic design in the Water Distribution Networks is of great interest, as it allows us to choose a solution between the different alternatives that verify the imposed hydraulic conditions. SFL Algorithms has been tested in water distribution networks design with good results. Thus, of the results in the proposed model it is possible to emphasize the following conclusions:

- The success rate for find the minimum cost is quite high in both networks, around 20% in Hanoi case and more of a 50% in NY case.
- The best combination of parameters in both networks is quite similar, but these combinations are valid in the studied models. The verification is necessary from the hypotheses raised here with different models.
- If it is not required to find the minimum of the system, but only a set of good solutions, SFLA is a very solid method although we do not study the optimization of the SFLA parameters.

Therefore, as a general conclusion of this work, SFLA seems valid for the water distribution networks design. The adjustment of its parameters has been verified with the statistical analysis.

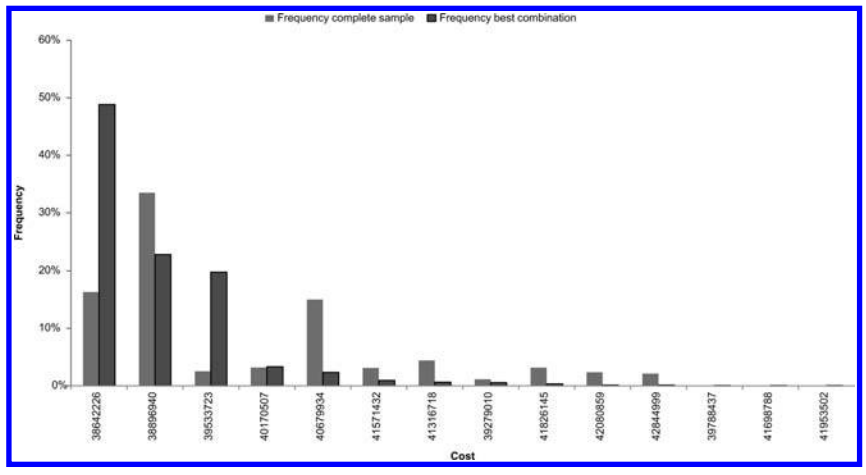


Figure 4. Diagram of frequencies of the obtained solutions in Hanoi network.

ACKNOWLEDGEMENTS

This article has been possible inside the actions developed by the researchers of CMMF involved in the project “Integración de la caracterización dinámica de elementos y consumos en modelos de redes de abastecimiento de agua utilizando sistemas de información geográfica y algoritmos genéticos (CADAGIAS)”. The number reference of the project is DPI2006-13113.

REFERENCES

[1] Eusuff, M.M., Lansey, K.E. (2000). “Shuffled frog leaping algorithm: a memetic meta-heuristic for combinatorial optimization. J. Heuristics, in press.

[2] Eusuff, M.M., Lansey, K.E. (2003). “Optimization of water distribution network design using the shuffled frog leaping algorithm”. Journal Water Resources Planning and Management, 129 (3), 210.225

[3] Savic, D., and Walter, G.A. (1997). “Genetic algorithms for least-cost design of water distribution networks”. *Journal. water resour. plann. manage. div., am. soc. civ. eng.*, 123(2), 67–77.

[4] Schaake, J.C., Lai, D. (1969). “Linear programming and dynamic programming application to water distribution network design”. Rep. 116, Dep. of Civil Engineering, Massachussets Institute of Technology, Cambridge, Massachussets.

*Environmental Hydraulics – López-Jiménez et al (eds)*
*© 2010 Taylor & Francis Group, London, ISBN 978-0-415-56697-1*

# Backward transient analysis: A conceptual method for leak detection in pressurized pipes

A. Haghighi
*Civil Engineering Faculty, K.N. Toosi University of Technology, Tehran, Iran*

D. Covas & H. Ramos
*Civil Engineering Department, Instituto Superior Técnico, Lisbon, Portugal*

ABSTRACT: This work aims to introduce the concept of a new model-based leak detection method in pressurized pipes in which two numerical methods - the method of characteristics and the finite differences method - are used to solve the indeterminacy of leak location and size. This approach is referred as Backward Transient Analysis (BTA). Transient state is generated in the pipe system by closing the downstream end valve and the transient pressure signal is measured only at the valve location. The pipe system is numerically modeled with potential leak locations at all characteristic nodes. Using the pressure signal after the full valve closure, the transient flow is backwardly analyzed by sweeping the pipe, step-by-step, from downstream to the upstream end. In this condition all flow characteristics are directly calculated as well as nodal leak areas. Major uncertainties and basic unknown conditions in real-life pipes modeling have been especially taken into consideration. The new scheme of BTA developed herein for leak detection is completely independent of the valve type and closure maneuver as well as of the upstream boundary conditions. Finally, one theoretical example is presented to show the application and the results of the method in the location and sizing of a very small single leak. The method has been found practical, reliable, fast and easy to be applied.

*Keywords*: Backward Transient Analysis, Method of Characteristics, Finite difference, Leak detection.

## 1 INTRODUCTION

Nowadays, leaks and their economic and environmental costs are well-known problems. Many studies around the world report huge losses of drink water due to leaks in pipelines (Jowitt and Xu 1990, AWWA 1990, Weil 1993). As a consequence, many efforts and investigations are still highly demanded to develop and promote leak detection methods. In recent years, several model-based methods for leak detection have been introduced which can be categorized into two different approaches - time and frequency domain analyses. Most time domain approaches are in the subcategory of Inverse Transient Analysis (ITA) (Liggett and Chen 1994, Vitkovsky et al. 2000 and 2007, Kapelan et al. 2003, Covas et al., 2005a,b, Khomairi 2008, Shamloo and Haghighi 2009). The current work aims to overcome the main uncertainties of ITA by introducing a novel time-domain approach for leak detection in pressurized pipes that is independent of the accurate knowledge of pipe characteristics and boundary conditions. In this method, the main steps of ITA are significantly simplified, as well as many uncertainty resources in modeling are removed. The new method, referred as Backward Transient Analysis (BTA), is only based on measurements and hydraulic numerical methods of characteristics and finite differences. Using BTA, the whole pipe length is backwardly analyzed and leaks are detected from downstream to the upstream end for only a half theoretical wave period of the transient flow. The developed method is independent of the valve type, the valve maneuver and the closure time and does not require posing initial and upstream boundary conditions.

## 2 GOVERNING EQUATION

For most hydraulic engineering applications, the governing equations for transient pipe flow are based on the continuity and momentum principles (Chaudhry 1987):

$$\frac{\partial H}{\partial t}+\frac{a^2}{gA}\frac{\partial Q}{\partial x}=0 \tag{1}$$

$$\frac{\partial Q}{\partial t}+gA\frac{\partial H}{\partial x}+\frac{fQ|Q|}{2DA}=0 \tag{2}$$

where $x$ = distance along pipe, $t$ = time, $a$ = wave speed, $g$ = gravitational acceleration, $A$ = pipe cross-sectional area, $D$ = pipe diameter, $Q$ = instantaneous discharge, $H$ = instantaneous piezometric head, and $f$ = friction factor which can be described by steady, quasi-steady or unsteady state conditions.These equations are typically solved by using the Method of Characteristics (MOC), although other numerical methods can be used (e.g., finite differences and finite volume method). Furthermore, unsteady friction effects are considered herein by using Brunone's model (Brunone *et al.* 1991a, 1995) which has been modified by Vítkovský *et al.* (2000a).

## 3 UNCERTAINTIES OF MODEL-BASED METHODS

The principle of most model-based leak detection methods is to match the calculated transient pressures with the measurements. Accordingly, the numerical modelling should be as precise in the simulation of the transient pipe flow. Besides, there are several uncertainties and undetermined parameters which can have a significant role in model reliability, such as the valve manoeuvre,

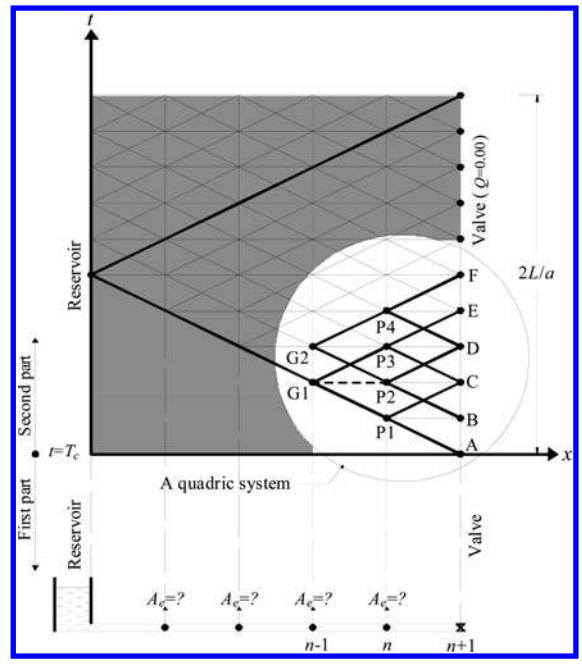


Figure 1. Backward characteristics grid.

unsteady friction losses, initial steady state conditions, upstream boundary conditions and collected transient data. Considering these issues and focusing on remedies to remove and decrease those uncertainties, a novel method of leak detection is developed herein.

## 4 BACKWARD TRANSIENT ANALYSIS (BTA)

Consider a simple pipe without leakage as shown in Fig. 1. By closing the downstream end valve, a transient event is induced in the system and transient pressures are measured at the valve location. For this situation, the induced transient event can be divided into two distinct parts: (i) the first part is during the valve closure (when $t < T_c$) and (ii) the second part is after the full valve closure (when $t \geq T_c$, where $T_c$ is the valve closure time). In the first part (i.e., while the valve is being closed), the flow at the valve decreases from initial flow to zero. The pattern of this variation is dependent on the valve type and maneuver. Numerical modelling of this needs simplifying assumptions and may lead to significant uncertainties in real-life applications. In the second part (i.e., after the valve is fully closed), the flow at the valve location is obviously equal to zero, and the valve behavior can be described as a dead-end. Undesirable issues associated to the valve simulation and to the initial valve position are avoided, when collecting data after the full valve closure. Accordingly, the boundary conditions at the downstream end are perfectly well known since instantaneous pressures are measured and the discharge is null. Based on these boundary values of pressure and flow and considering the pipe wave speed, a regular staggered mesh can be defined for flow analysis in time-space domains (Fig. 1).

In a system without leakage, there are two unknown variables at each node which are instantaneous head and discharge. Accordingly, to calculate these variables two equations based on governing Equations (1) and (2) are needed for each node. Method of Characteristics (MOC) is the most popular technique to analyze transient state in multi-pipe systems. However, the traditional scheme of MOC cannot be applied herein since initial conditions and valve description have been omitted from the modelling. For this purpose, a new scheme of MOC introduced by Shamloo and Haghighi (2009) is applied to backwardly describe the transient state equations in pipes. The final equations are obtained as following:

$$Q_P - Q_C + \frac{gA}{a}(H_P - H_C) - RQ_C|Q_C|\Delta t = 0 \tag{3}$$

$$Q_P - Q_A - \frac{gA}{a}(H_P - H_A) - RQ_A|Q_A|\Delta t = 0 \tag{4}$$

where QC, QA and QP1 are instantaneous discharges, $H_C$, $H_A$ and $H_{P1}$ are instantaneous piezometric heads at points C, A and P1, respectively (Fig. 1), and $R = f/2DA$. Equation (3) is valid along the semi-implicit positive characteristic line P1-C and Equation (4) along the explicit negative characteristic lien P1-A.

Using the proposed scheme with Equations (3) and (4), the transient flow conditions are calculated along the $t$-axis for each node (from downstream) and then along the $x$-axis for all nodes backwardly (i.e., domains of time and space are analyzed, respectively). As presented in Fig. 1, there is also an "Inaccessible Zone" in the characteristic grid. Fortunately, the initial pipe conditions are located in this zone. It is therefore not required to impose the initial conditions in the numerical modeling as well as the valve features simulation. Additionally, there is no need to define upstream boundary conditions, since these are automatically calculated by the model. Accordingly, using BTA not only some major modelling difficulties are removed but also significant uncertainty sources are totally avoided. Furthermore, in this method, calculations can be started from an adequate desirable time after valve closure, where probable errors on measured signal have disappeared.

## 5 LEAK DETECTION METHODOLOGY

In this section, the backward transient analysis is developed for pipes with leaks. Unknowing the number of leaks and their locations, all characteristic nodes are primarily assumed as potential leak locations with unknown effective leak areas, except

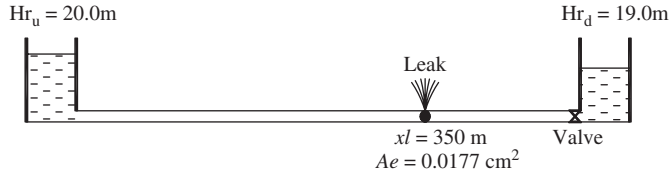


Figure 2. Pipe system of the example.

those at the upstream and downstream ends. After the leak detection is carried out, nodes with non-zero leak area are introduced as leaks. When calculation nodes are considered to be leaky, another unknown variable of effective leak area $Ae$ is added to unknown flow specifications of head $H_P$ and discharge $Q_P$ at each node. In this condition there are three unknown variables at each node with only two positive and negative characteristic equations and this is why the problem of leak detection is underdetermined. This paper presents a numerical scheme to be combined with BTA to put the problem of leak detection in a determined way in which leaks are directly detected through transient analysis. Flow at a leaky node is divided into two parts of left and right side discharges which are related to each other with leak and continuity equations as follows:

$$Q_{Pi}^{L} = Ae\sqrt{2g(H_{Pi} - Z)} + Q_{Pi}^{R} \tag{5}$$

in which $Q_{Pi}^{L}$ and $Q_{Pi}^{R}$ are instantaneous discharges in left and right sides of point Pi (i.e., i = 1,2,3), respectively. $Ae$ is effective leak area and $Z$ is the elevation at the leak location. Equation (5) with the defined positive and negative characteristic equations is developed at leaky nodes. In beginning semi-implicit positive and explicit negative characteristic lines are developed at node $n$ immediately before the valve location $n+1$ (Fig. 1). All transient heads ($H_P$) and discharges at the right side of node $n$($Q_P^R$) can be easily calculated along $t$-axis for the whole modelling time.

Backward analysis is still at node $n$ where the discharge $Q_{Pi}^{L}$ and the leak area $A_e$ are still unknown. It is obviously concluded by analysing Fig.1. that there is no way to find these unknown variables by BTA along the pipe unless node $n$ is connected with its left adjacent node$n$-1. This connection links the left and right sides of leak discontinuity at node $n$ and makes the problem determined. A system of equations and variables are considered and solved instead of node-by-node backward solution. This scheme is shown in Fig. 1 and is called as quadric scheme in which there are four main points P1, P2, P3 and P4, and two aid points G1 and G2, at each calculation node.

Using Equations (3) and (4) for lines P1-C and P1-A respectively, transient head $H_{P1}$ and discharge in the right side $Q_{P1}^{R}$ are calculated at point P1. In the same way for points P2, P3 and P4 values of $H_{P2}$, $H_{P3}$ and $H_{P4}$, $Q_{P2}^{R}$, and $Q_{P4}^{R}$ are also calculated. Based on Equation (5) transient discharges in left side of P1, P2, P3 and P4 are then formulated for node $n$. Backward characteristic lines of G1-P3 and G1-P1 and also G2-P4 and G2-P2 relate G points to P-points in the left side. G1 and G2 add four unknown variables of heads and discharges in their right sides and also four characteristic equations. There is therefore only one unknown variable of leak area ($Ae$) in the quadric scheme considered at node $n$. The problem is still undermined and one equation else is needed to make the problem determined to be directly solved.

G-points give the additional equations developing a finite difference approximation of governing equations around point G1. Using a fully implicit scheme, the partial derivative terms of governing equations are discretized around G1. Based on this discretization both governing equations of continuity and momentum around point G1 can be used as the missing equation in the quadric scheme. For this purpose sensitivity analyses were carried out and have shown that momentum equation is more sensitive to transients and leaks than continuity equation, and it is considered as follows:

$$\frac{\left(Q_{G2}^{R} + Q_{P3}^{L}\right) - \left(Q_{G1}^{R} + Q_{P2}^{L}\right)}{2\Delta t} + gA\frac{H_{P3} - H_{G2}}{\Delta x} + \frac{f}{2DA}Q_{P2}^{L}\left|Q_{G1}^{R}\right| = 0 \tag{6}$$

So, in a quadric scheme, there are four flow unknown variables of heads and discharges at G points and one unknown leak area at P-points ($Ae_n$). Besides, there are four characteristic equations and also one aid Equation (6) between G-points and P-points. Now the quadric scheme is determined and the leak area at node $n$ can be directly calculated as well as flow characteristics at G-points. The quadric scheme equations can be simultaneously solved using Newton-Raphson method or alternatively by optimization techniques. After the leak area at node $n$ is found, all transient features at node $n$ can be calculated along $x$-$t$ plan. Consequently, in this condition, BTA process as described can be moved along the pipe. Whole the pipe length is backwardly analyzed to the upstream end by applying step-by-step the quadric scheme development and solution for each node. Using this method, the whole pipe length is swept and leaks are detected only in the analysis a half of theoretical period ($2L/a$).

## 6 EXAMPLE

This example presents a piping system with $L = 500$ m, $D = 150$ mm, pipe roughness $e = 0.0015$ mm, $a = 1000$ m/s, upstream reservoir head $Hr_u = 20$ m, downstream reservoir head $Hr_d = 19$ m and the fluid viscosity $\nu = 1.25\text{e-}6$ m$^2$/s. A very small leak is located at $x_l = 325$ m from the upstream reservoir with a leak area $Ae = 0.0177$ cm$^2$ corresponding to 0.01% of the cross-sectional pipe area (Fig. 2.).

With the aim of leak detection, a transient state is generated by closing the downstream end valve for $T_c = 4.5$ s. Transient pressures at the valve location are collected with \a sampling frequency $fr_s = 40$ Hz (see Fig. 3). Regarding the sampling frequency and the wave speed, a characteristic grid can be developed with $\Delta t = 0.025$ s and $\Delta x = 25$ m. The problem comprises 19 leaks located on the characteristic nodes except those of upstream reservoir and downstream end valve.Running the proposed method with only one stage backward transient analysis, the whole pipe is analyzed for the first period after full valve closure and for leak detection. The calculated leak areas have been illustrated in Fig. 4 versus calculation nodes along the pipe.

Fig. 4 shows obviously that the leak parameters in the pipe have been successfully detected by the proposed method. There is only one small leak in the pipe located at node 14 which means that the leak location is 325 m from the upstream end and the

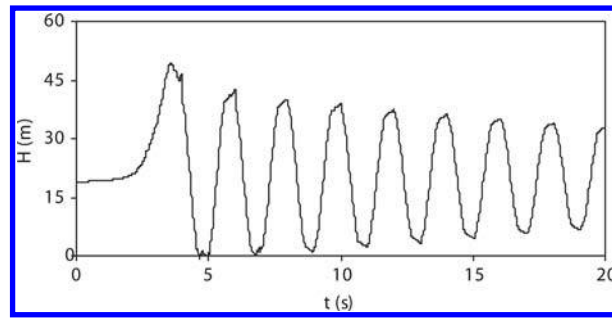


Figure 3. Transient pressures at the valve location.

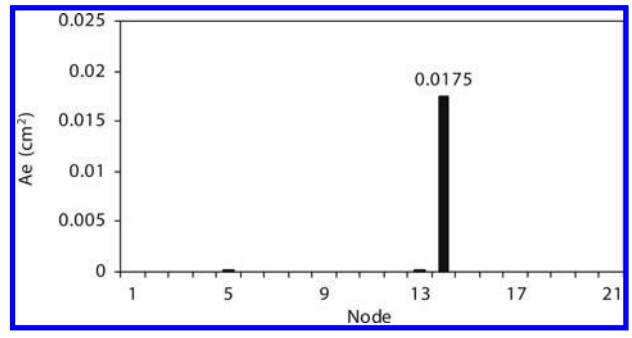


Figure 4. Calculated leak area at the pipe nodes.

leak area is 0.0175 $cm^2$. The upstream reservoir head has been also calculated by the method and equal to 19.91 m. Comparing the results with the precise leak area and also upstream reservoir head results in 1.13% and 0.45% errors, respectively. The leak discharge is also about 1.06% of mean flow in the initial steady condition.

## 7 CONCLUSIONS

A new model-based method has been introduced and developed for leak detection. In gravity single pipe systems, using a few measured data of transient pressures at the end valve a new scheme based on the method of characteristics was considered for backward transient analysis in which some major uncertainty sources are avoided from numerical modelling. With the aim of leak detection in pipes, backward transient analysis was developed to calculate leak parameters directly, as well as the flow parameters. For this purpose numerical method of finite difference was combined with backward transient analysis in a system of equations named quadric scheme. Quadric schemes are developed and solved for each calculation node along the pipe from the downstream to the upstream end step-by-step. Using only a half period of measured data, whole the pipe can be analyzed at once for leakage detection. Finally, leaks are located at the nodes with non-zero value of leak area. Transient analysis using the proposed method is entirely independent of the valve type, the method of maneuver and the time of closure. There is also no need to impose initial flow and upstream conditions which would be a very remarkable advantageous for pipes (e.g. with pumping facilities at upstream end). These benefits not only significantly simplify the modeling but also avoid some major uncertainty sources of the numerical calculations which are very important for leak detection. One stage backward analysis is enough for leak detection. Consequently the method is very fast with very few calculations. Finally based on the mentioned advantages of this method and the presented example, this method of leak detection is found out practice-oriented, reliable and easy to be utilized with no need to specify particular boundaries and method of operation. Besides, the proposed approach is still on papers and no experimental tries have been done yet. Limitations and implementation problems should be addressed and replied to strengthen the method as a practical tool for real-life pipes.

## REFERENCES

[1] Al-Khomairi, A. M., (2008). Leak Detection in Long Pipelines Using The Least Squares Method. *Journal Hydr. Res.* 46(3), 392–401.
[2] Brunone, B., Golia, U.M., Greco, M. (1991a). Some remarks on the momentum equation for fast transients *Proc. Int. Conf. On Hydraulic Transients with Water Column Separation (9th and last round Table of IAHR Group), Valencia, Spain*. 201–209.
[3] Chaudhry, M.H. (1987). Applied hydraulic transients, 2nd ed. Litton Educational/Van Nostrand Reinhold, New York.
[4] Covas, D., Ramos, H., Graham, N., Maksimovic, C. (2005a). "Application of hydraulic transients for leak detection in water supply systems" *Water Science and Technology: Water Supply*, 4 (5–6), 365-374 © IWA Publishing.
[5] Covas, D., Ramos, H., Young, A., Graham, N., Maksimovic, C. (2005b). "Uncertainties of Leak Detection by Means of Hydraulic Transients: from the Lab to the Field." Proc. eighth international conference on Computing and Control for the Water Industry (CCWI 2005). University of Exeter, 5–7 September 2005.
[6] Kapelan, Z.S., Savic, D.A, Walters, G.A (2003). A hybrid inverse transient model for leakage detection and roughness calibration in pipe networks. *Journal Hydr. Res.* 41(1), 481–492.
[7] Liggett, J.A., Chen, L.C. (1994). Inverse transient analysis in pipe networks. *Journal Hydr. Engng*. 120(8), 934–954.
[8] Vitkovsky, J., Lambert, M., Simpson, A., Liggett, J.A. (2007). Experimental observation and analysis of inverse transients for pipeline leak detection. *J. Water Resour. Planning Manage.* 133(6), 519–530.

*Environmental Hydraulics – López-Jiménez et al (eds)*
*© 2010 Taylor & Francis Group, London, ISBN 978-0-415-56697-1*

# Analysis of seismic actions in pipe infrastructures security

Ana Cesteiro & Helena M. Ramos
*DECivil – CEHIDRO, Instituto Superior Técnico, Technical University of Lisbon, Portugal*

ABSTRACT: The current research work aims at analysis of seismic analysis in hydraulic infrastructures. The extreme importance of this subject is the simulation of an abnormal action in a main pipe water drinking system in the Pumping-Station of Telheiras, from Lisbon Water Supply System, which caused pipe displacements and breaks in some supports. To seek the vulnerability of these hydraulic systems (to different typical loads), many case studies were developed by water hammer and structural models. The analysis was developed in order to show the possible consequences in terms of displacements, when the system is submitted to different loads and type of supports. It is equally emphasized the importance of integrated analysis (fluid-structure interaction) and the purpose of supports in water pipe systems in the infrastructures design.

*Keywords*: Hydraulic infrastructures, Seismic, Security, Fluid-structure interaction.

## 1 INTRODUCTION

The current research work aims at the study of instability factors leading to rupture and the security analysis on a hydraulic pressure system that is under subjected to a seismic action. In the domain of fluid-structure interaction, the analysis of various aspects involved in hydraulic pipe systems is confronted with one of the most complex subjects, which in recent decades has been remarkable progresses due to the advent of computers and their evolution, as regards the analysis of transient phenomena. The hydraulic pipe systems are usually under different types of vulnerabilities. The associated hazards when neglected in the different stages of a design [3,4] may put at risk the security of each system.

## 2 WATER HAMMER AND STRUCTURAL DEFORMATION

Changes in pressure caused by changes in flow induce the appearance of inertia forces that interfere on fluid compressibility and on pipe walls deformation. These variations in flow conditions originated from some disturbances impose on the pipe systems dynamic uncontrolled conditions, such as seismic actions. The pipe movement due to the occurrence of these types of actions depends on the mechanical properties, supports' conditions and dynamic forces that act on the fluid, on the pipe wall and on supports. Fluid-structure interaction in piping systems consists on the transfer of momentum and forces between pipes and the fluid during unsteady fluid-structure conditions. The interaction is evident through pipe-structure vibrations. The phenomenon has recently received increased attention because the security and the reliability concerns in hydraulic and structural systems which transport a scarce and essential good to the life as the water is.

The water main systems constitute an essential part of lifelines of urban cities, as all public and private infra-structures which support the human's activities. They are so important that their existence and good operation had so many implications in the politic, as economic level to be able to satisfy the human life quality, in terms of water, gas, oil and electricity distribution. Pipe systems need special attention in terms of hydraulic-structural analysis, because their destruction or damage could bring serial consequences in human lives, as well as in social and environment issues.

The evaluation of seismic action in water mains can be carry out by direct damages' analyses, that are related with the interruption of water supply systems after the earthquake occurrence, or by indirect damages, resulted of some lack of operation system for a long period, with social consequences, economic and environment in the affected areas.

It is known that water supply systems, sewers, gas and fuel networks are usually made by buried pipeline systems. One of the principal characteristic of theses systems that are extended for very large areas is standing to the random earthquake occurrence such as in space, time and intensity. This kind of structures can suffer damages caused by earthquake waves or caused by permanent ground displacements such as, geologic fails, liquefaction, or slips/slides.

Pipelines systems, buried or superficial, continuous or not (fragmented by branches), are important components of lifelines. Their design and implantation rarely obey to performance earthquake conditions. By this omission many damages are being demonstrated in lifelines during the earthquake, as for San Francisco earthquakes (Figure 1).

## 3 COMPUTATIONAL MODELING

### 3.1 *Hydraulic modeling*

It is advisable to use computational modeling in all phases of a design (previous studies, viability studies, projects for tender, final project, and during exploitation – operation and maintenance), just to know the highest and minimum pressure and their evolution in time and along the hydraulic circuit. Only this way is possible to specify the control procedures in terms of dynamic effects that may occur (e.g. pressure and velocity variations) and what is the best way to control them[1,2,3,4]. The hydraulic modeling is based on the following equations derived from Navier-Stockes equations:

Dynamic equation:

$$\frac{\partial Q}{\partial t} + gA\frac{\partial H}{\partial x} + RQ|Q| = 0 \qquad (1)$$

Near Crystal Springs Reservoir in San Mateo County, during the earthquake of 1906 in San Francisco city (font: http://www.sfmuseum.net/1906/photos.html).

Figure 1. Damages verified in water pipelines.

Table 1. Absolute displacements in the node of valve V59.

| | | Ux (cm) | Uy (cm) | Uz (cm) |
|---|---|---|---|---|
| Node of valve V59 | Pipe and Water weights + seismic combination | 10,9583 | 0,0076 | −0,1965 |
| | | −10,8436 | −0,0078 | −0,2123 |

Continuity equation:

$$\frac{\partial H}{\partial t} + \frac{c^2}{gA}\frac{\partial Q}{\partial x} = 0 \tag{2}$$

It is important to refer that in equations (1) and (2) there is no analytical solution known, but by using the Method of Characteristics they can be converted into equations with total derivatives and be used more easily.

### 3.2 *Structural modeling*

Physical phenomenon behind structural problems can be solved by using the same Navier-Stockes equations and consequently in the same conservation principles as the hydraulic modeling adding the specific structural variables (Covas & Ramos, 2006; [5]).The method of finite elements gets the solution by minimizing the functional energy in each element. This solution is based on the virtual work principle, which establishes that if one particle is on balance by a system of forces, so for any motion the virtual work is zero, this is the aim of the basic conservation principle of total mechanical energy of continuous systems[5].

Conservative equation of total energy:

$$\Pi = \frac{1}{2}\int_{\Omega}\sigma^T \varepsilon dV - \int_{\Omega} d^T b dV - \int_{\Gamma} d^T q dV \tag{3}$$

where $\sigma$ and $\varepsilon$ are vectors of stress and strain components in every point, d is the vector of displacements in the same points, b the vector of force in each element per unit of volume, and q the vector of tension applied in the control volume surface. The method of finite elements is the method used in SAP2000, which supported the structural calculus in this research work.

## 4 APPLICATION

### 4.1 *Seismic action in the water pipe system*

In the modulation of a seismic action it was considered the regulation spectral answer of earthquake Type 1, soil Type II, zone A and a damping coefficient of 5%. The described test matches to a seismic analysis to the pipelines system inside the Telheiras Pumping-Station (Figures 2 and 3).

To take into account a seismic analysis of the effect of water inside the pipelines was necessary to add into pipe elements a distribute loads per meter. The only loads that account for this analysis are the pipeline's and water's weights, for the reason that this pipes are above the ground.

Related with supports' conditions (see details in Almeida & Ramos, 2007), the CPC Inferior pipeline, CRD and CRE can have axial movements with the exception of the pipe connection nodes of CRE and CRD to CPC Inferior, where only it is restricted to vertical movement, and CPC Superior pipeline can moved in its axis direction, except in pipe connection node of d = 1 m with CPC Superior, which only allows the rotation.

The absolute displacements in valve V59 are registered in Table1. Observing this table, it is evident that exists a major and a minor value for the same direction movements which is due to the fact of seismic action is an enveloping efforts resulting actions in two directions, being the minor and the major values match with the sense earthquake force in that direction.

The positive and negative signs of displacements presented in Table 1, only represents the fact that these displacements can or cannot turn out into positive direction global axes system. The Ux correspond to the movement in direction X, the Uy in direction Y and Uz describes the movement in direction Z.

For the observation of all displacements the valve V59 reveals to be the conditioning section of the system. Valuing the displacements obtained in this node, it is visible that the axial movement in CPC pipeline is about 11 cm, value a little superior

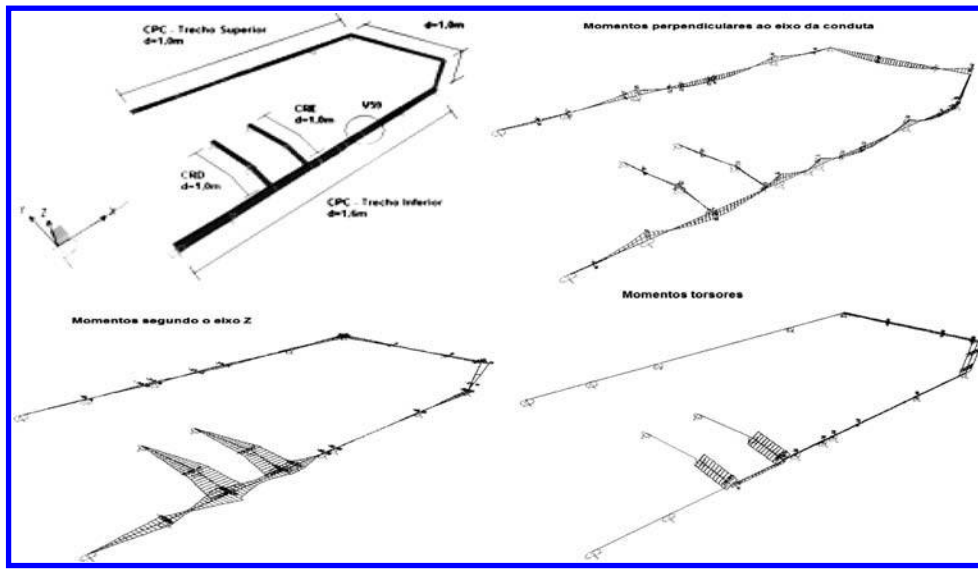


Figure 2. Pipeline system in the Pumping – Station of Telheiras and momentum diagrams due to seismic combination.

Figure 3. Damage in some supports (Almeida & Ramos, 2009).

than the value obtained in the accident by closing the valve when an unbalanced force is observed (8 cm). This aspect is due to the fact that during the occurrence of an earthquake, all the structural components (i.e. pipes and supports) are integrated involved with the hydraulic component. In an isolated analysis of the hydraulic component, only the fluid compressibility and the deformation of the pipe walls may interact, bringing significant pressure waves that propagate along the hydraulic system which can induce, also, pipe displacements.

### 4.2 *Discussion of results*

Concluded several simulations it is important to mention that the introduction of pressure forces in valve V59 demonstrated that the force of about 765 kN, obtained by hydraulic simulation and introduced in structural simulation, that results a final displacement similar to the observed one, is not relevant, because the structural model considers the supports effects while the commercial hydraulic models did not. Hence, it is emphasized the importance to have good correlation of fluid-structure analysis with measurements to give confidence about future results. It is important to say that in this case, it was also developed sensitive analyses for the supports conditions, with the interest to prevent from consequences that might occur, in terms of possible displacements. It was concluded that, in terms of supports restrictions, other pipes can be exposed to possible breaks. This analysis can relate the importance of a correct design for all supports as well as the fluid-structure interaction, such as, showing what can happen if some supports leave their normal functions-duty, resulting problems in new pipes.

## 5 FINAL REMARKS

When the pipe systems are not well anchored may suffer significant displacements due to the occurrence of earthquakes leading to the collapse of the system. On the other hand, these displacements generate pressure waves inducing fluid-structure interaction too, which are always linked to dynamic phenomena that can put at risk the security and the operation of these infrastructures. The effects of a seismic action often neglected in the pipe systems design, could endanger water mains or drainage strategic infrastructures that implicate e.g. interruption of water supply for urban densely populated areas. The actions due to degradation of the pipe and their supports that compose the fluid transport systems, the occurrence of earthquakes or the change in pressure can have similar effects, inducing high levels of vulnerability, which must be considered from the earliest stages of any Civil Engineering project.

## ACKOWLEDGEMENTS

The authors wish to acknowledge the financial support of this research work to the Portuguese foundation for Science and Technology (FCT) for grants reference PTDC/ECM/65731/2006 and PTDC/ECM/64821/2006, as well as CEHIDRO, the Hydro-systems' Research Centre from the Department of Civil Engineering, at Instituto Superior Técnico (Lisbon, Portugal).

REFERENCES

[1] Almeida, A. B. & Ramos, H. (2009). Water supply safety: diagnosis of an abnormal accident in a main Lisbon pumping system. *Under revision at WST – Aqua*, IWA publications.
[2] Ramos, H. (2004). Efeitos dinâmicos não convencionais em sistemas hidráulicos em pressão. *Instituto Superior Técnico*. Lisboa.
[3] Ramos, H. (2006). Escoamentos variáveis: Vulnerabilidade dos sistemas hídricos. Elementos de apoio ao Mestrado e DFA em Hidráulica e Recursos Hídricos. *Instituto Superior Técnico.* Lisboa.
[4] Ramos, H. (2007). Avaliação da vulnerabilidade na gestão operacional de sistemas de abastecimento. Elementos de apoio ao Mestrado de Hidráulica e Recursos Hídricos e DFA em Gestão ARS. *IST*, Lisboa.
[5] Tijsseling, A. S. & Wiggert, D. C. (2001). Fluid transients and fluid-structure interaction in flexible liquid-filled piping. *Applied Mechanics Reviews*. Vol. 54. Issue 5. pp. 455–481.

*Environmental Hydraulics – López-Jiménez et al (eds)*
*© 2010 Taylor & Francis Group, London, ISBN 978-0-415-56697-1*

# Main factors for the damping of pressure waves: The pumping system of the city of Guarda

Nuno A. Melo
*Technical-Scientific Unit of Engineering and Technology, Escola Superior de Tecnologia e Gestão, Instituto Politécnico da Guarda, Guarda, Portugal*

Helena M. Ramos
*Department of Civil Engineering and Architecture, Instituto Superior Técnico, Technical University of Lisbon, Lisbon, Portugal*

ABSTRACT: The factors that influence the damping of the pressure variations are of different kinds, such as the type of pipe material and its roughness, the presence of bubble gas in the flow, and the presence of leaks or ruptures in the system. In the laboratory facilities or in real systems, there are usually, damping effects more significant that those obtained through numerical simulations, specially, if in the modelling, the friction factor was not considered and if the boundary conditions of the system are not properly modelled. These discrepancies do not allow the correct determination of the time from which the new steady regime flow is established and consequently it is not possible to determine the safety time to switch on the hydromechanical equipment again. In this paper the analysis of the influence of different factors in the damping of pressure waves is made, using for that field tests done in a real pumping system.

*Keywords*: damping curves, energy dissipation, dynamic behaviour, leakage.

## 1 INTRODUCTION

In the domain of the transient regimes, the knowledge about the actions that cause the most significant effects on the pressure variation and the prediction of these values is already very good, but the correct prediction of the pressure wave propagation, in particular due to the damping effect, is a field of knowledge in the area of transient regimes that needs more research and validation, especially with real data.

According to the type of system or accuracy of the results, different mathematic formulations can be implemented with the aim of obtaining an answer closer to the reality. In addition, the commercial software of transient regimes does not allow, in general, a correct estimation of the time of complete damping of the pressure oscillations and hence the establishment of a new steady-state regime after the occurrence of a manoeuvre which causes a transient regime. Generally there is a greater damping in the lab experimental facilities or real systems than in computational simulations.

The factors that influence the damping of the peaks of pressure are: the presence of viscoelastic pipe materials (where the rheological behaviour of pipe walls depends on the temperature), gas contained of the liquid; the occurrence of leakage or ruptures; as well as the shear stress in the pipe walls (i.e. unsteady friction losses) [6]. Thus a comprehensive and reliable analysis of the influence of physical phenomena is an important contribution to the understanding of the variability of the damping effect.

## 2 EXPERIMENTAL FACILITY AND TEST EQUIPMENT

The experimental facility which gave support to this work, is a real pumping system which supplies the city of Guarda – Portugal (Figure 1), and which is operated by Águas do Zêzere e Côa.

The system has a total length of 2246.15 m, composed by four sets of pipes: the first (compression pipe) is of cast iron Ø300 mm with a length of 11.38 m; the second (main pipe) is composed by pipes of cast iron Ø500 mm with a total length of 2218.62 m; the third consists of PVC pipes Ø400 mm which has the length of 7.25 m; and the fourth is composed by three pipes which supply the cells of the downstream reservoir, which are of PVC Ø200 mm, and each of them is, in average, 8.9 m long.

The pumping station of Prado is composed by five pump groups with their own a check valve, and in each link of these to the compression pipe, is installed a flow control valve and a gate valve. The system protection against overpressures is done by a relief valve which is preceded by a gate valve.

In the area of the transition of the compression pipe to the main pipe, there is a bottom discharge (B1) and throughout the development of the main pipe, more two bottom discharges and one air valve of triple effect (A1) are installed. Inside IPG reservoir, in the transition from the main pipe to the PVC pipe Ø400 mm, the system has an electromagnetic flow meter (Q2) and in the transition of the PVC pipe Ø400 mm, to the pipes, which supply the reservoir cells of the IPG is made through a crosspiece equipped with gate valves in each way out. The entry of each discharge pipeline in the reservoir cells of IPG is done in a free surface (detail in Figure 1).

The following equipment was used in the field tests: two pressure transducers (pressure range 0–25 bar absolute) (P1, P2); two feeding boxes for the pressure transducers; two oscilloscopes with 4 channels each; an ultrasonic portable flow meter (Q1); signal converters for 4–20 mA to 0–10 V; two laptops and software for data acquisition.

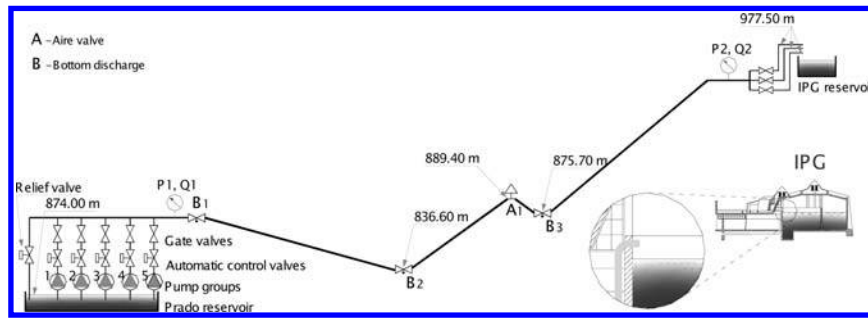


Figure 1. Pumping system Prado – IPG and detail of the entrance to the pipe in the IPG reservoir.

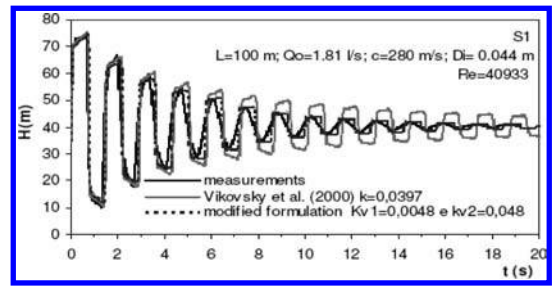


Figure 2. Comparison between piezometric heads: experimental data, formulation of Vítkovský et al. [7]and formulation of Ramos and Loureiro[5] (adapted from Loureiro[3]).

## 3 DAMPING CURVES DEFINED BY THE PRESSURE OSCILLATIONS

### 3.1 *Pipe material effects*

Ramos et al.[6], has presented a technique that aims to characterize the energy dissipation (damping), through the variation of the maximum and minimum piezometric head observed in a transient regime. This dynamic effect can be influenced, on the one hand, by the non elastic behaviour of the pipes, and on the other hand, by the friction effect.

### 3.2 *Estimation of the friction effect in transient regime*

To calculate the energy dissipation in turbulent regime, under transient conditions, different formulations have been proposed. Such formulations are generally composed of a first component based on the quasi-stationary assumption, $J_{qs}$, and a second component that takes into account the unsteady effect, $J_u$, being $J = J_{qs} + J_u$.

Ramos and Loureiro[5] also presented a formulation to calculate the unsteady effect, based on Vítkovský et al.[7], having two new and different empirical decay-coefficients (eq. 1).

$$J_u = \frac{1}{g} \quad k_{V1} \quad \frac{\partial V}{\partial t} + k_{V2} \quad c \quad SGN(V) \quad \left| \frac{\partial V}{\partial x} \right| \tag{1}$$

The use of different heights coefficients ($K_{v1}$ and $K_{v2}$) applied to the convective and local acceleration, to estimate the unsteady friction factor, improves the adjustment between the numerical simulations and tests data[6]. With this formulation is possible to reproduce in a reasonable way the experiments in terms of damping and phase[6].

Figure 2 shows the configuration of the wave propagation simulated, using the formulation proposed by Ramos and Loureiro[5], noting that is more marked than the real one. For long pipelines and high flow values, where the pack effect is much notorious, the results fitted well to the first pressure peaks. It was verified that the term $K_{V1}\partial V/\partial t$ affects the phases shift of the pressure waves and $K_{V2}\partial V/\partial x$ is associated to the damping effect. Therefore, reducing $K_{V1}$, the numerical pressure wave is faster than the experimental wave and when this increases, there is a delay of the numerical wave. According to Ramos et al. [6] the equation (1) allows a better fitting between the numerical simulations and the tests for the damping and phase effects, however, there are some differences, observed in the shape of the pressure waves (i.e. more square than in the real situations). Covas et. al.[1],[2] has been analysing this incompatibility due to the behaviour of the pipe material, focusing in the plastic pipes, with viscoelastic behaviour.

### 3.3 *Formulations of the damping*

In order to understand better the absolute head variation, $H$, depending on the characteristics of systems, Ramos et al.[6] states that the estimate of head for fast manoeuvres should include the following terms: (i) a final head, $H_f$, for which the fluctuation of pressure tend to, what for a complete closure is equivalent to static height of upstream; (ii) the instant overpressure given by the formulation of Joukowsky, $K_1 \times Q$, with $K_1 = c/(g \times S)$, in which $Q$ is the discharge, $c$ is the wave speed propagation, $g$ is the gravity acceleration, $S$ is the cross section flow area; (iii) damping effect, $K_2 \times t$ which depends on system total head losses, which are expressed by an inverse term and the behaviour of the system by an exponential equation. Thus we have, in absolute mode of formulation for systems with elastic or plastic behaviour the following equations:

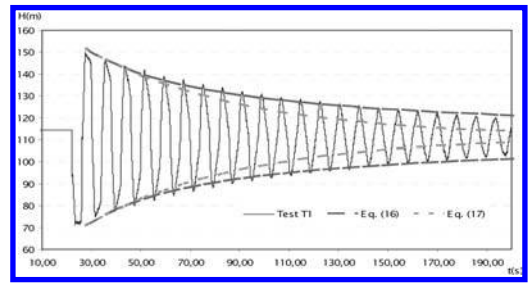


Figure 3. Data from Test 1 and fitting of the damping curves calculated by the equations (2) and (3).

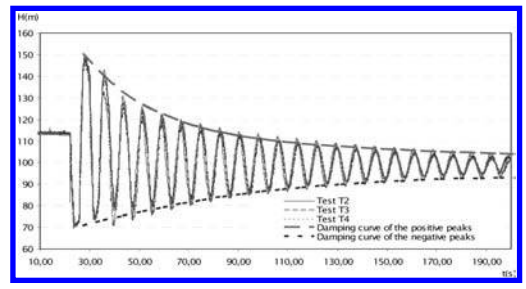


Figure 4. Damping curves in tests T2, T3 and T4. (adapted from Loureiro [3]).

Elastic (e.g. concrete or metal pipes)

$$H = H_f \pm \frac{K_1 \quad Q}{(1 + K_2 \quad t)} \tag{2}$$

Plastic (e.g. presence of bubble air or viscoelasticity of the material)

$$H = H_f \pm K_1 \quad Q \quad e^{K_2 \ t} \tag{3}$$

in which the sign $\pm$ is for a positive or negative peak, respectively.

## 4 DISSIPATIVE EFFECT – COMPARATIVE ANALYSIS

Experimental data were collected in the pumping system of Prado – IPG presented in section 2, with the purpose to analyse the dynamic response of the pipes that compose the system, when a transient regime is made by the stoppage of one pump group, for a situation without leaks and for other three situations with leaks of different flows in each case: Test 1 (T1) – The pipe has no leaks the flow at the way-out of the pumping station is of $Q = 7.147 \times 10^{-2}$ m$^3$/s; Test 2 (T2) – The pipe has a leak in the flow of $Q = 1.111 \times 10^{-2}$ m$^3$/s at 905.29 m in relation to the upstream end and the flow at the way-out of the pumping station is of $Q = 7.215 \times 10^{-2}$ m$^3$/s; Test 3 (T3) – The pipe has a leak of $Q = 2 \times 10^{-2}$ m$^3$/s a 905.29 m in relation to the upstream end and the flow at the way out of the pumping system is of $Q = 7.276 \times 10^{-2}$ m$^3$/s; Test 4 (T4) – The pipe has a leak of $Q = 2.917 \times 10^{-2}$ m$^3$/s at 905.29 m in relation to the upstream end and the flow at the way out of the pumping system is of $Q = 7.346 \times 10^{-2}$ m$^3$/s.

The pumping system, due to the material of its pipes, cast iron in 99,3% of the total length, can be classified as a typically elastic, which is confirmed by the celerity value obtained through the tests data and it is of $c = 1112$ m/s, and this value is characteristic of rigid pipes. Therefore, according to Ramos et al.[6], the equation (2) the one which best represents the damping effect in the system during the occurrence of a transient regime, as it can be observed in Figure 3. This figure also represents the damping curve resulting from the application of the equation (3), which defines a damping curve much more marked (characteristic of systems with plastic behaviour), and not fitting conveniently to systems with rigid pipes[4].

In Figure 4, there is an overlap of the tests data T2, T3 and T4, and the curves which define the damping verified during the tests. From the test overlap analysis, it can be seen that these follow the same behaviour during the transient regimes. Concerning the damping, there are some asymmetries. That means, the damping curve of the positive peaks is more marked than the damping curve of the negative peaks. After analyzing this situation, one can conclude that the fact is due to the characteristics of the facility. This means that, since the pipeline discharges in free surface in the downstream reservoir, when the pump group stop and when there is a leak in the system, the water volume which supplies the leak flow is the one contained inside the pipe, which makes that the free surface downstream decreases throughout the time, giving it that curve damping [4].

Figure 5 presents a comparison between the damping verified in the tests with and without leaks. For that, we had to determine the points which defined the damping curves of the tests with a leak, admitting that the level of the free surface downstream is approximately maintained constant. In this way, the height variation, verified between the maximum and minimum peaks, was determined for each of the instants which define the ends. The average was also determined, which was then added and subtracted to the final head value $H_f$ which would be verified if the downstream level remained constant. The mesh of points shown in Figure 5, with name "symmetric points that define the damping of tests with a leak", was obtained in that way. The equation, which better fits the obtained points was equation (2), in which the coefficient $K_2$ was 0,03, whereas it was 0,018 for the damping curves defined in test T1, a situation without leaks x.

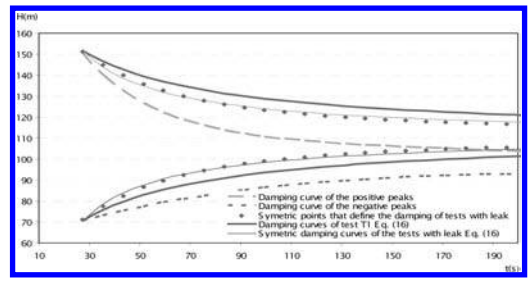


Figure 5. Comparison between the damping verified in the tests with and without leaks.

Comparing the damping curves of test T1 with the symmetrical damping curves of the tests with a leak, it is verified that the presence of the leak in the system induces a greater damping effect.

Comparing the symmetrical damping curves of the tests with a leak with the real damping curves of the tests with leak, it is possible to observe the delay suffered by the latter because of the variation in the level of free surface at the downstream end and the leakage effect at the time of testing.

## 5 CONCLUSIONS

Considering the work developed, the following conclusions can be drawn:

- In a general way, all formulations used to calculate the friction factor in a transient regime allow to estimate the first pressure wave after a fast manoeuvre. Nevertheless, the differences increase the simulation throughout time, depending on the capacity of modelling all the intervenient parameters in the characterization of the system;
- The classic models of water hammer only reproduce elastic effects, being only reasonably adequate to simulate systems with rigid pipes of metal or concrete type;
- The calibration models of the systems composed by pipes of plastic material must take into account the viscoelasticity of it, namely, to detect the leaks or to prevent operational conditions (e.g. starting or stopping of electro-mechanic equipments);
- Considering the operational response of the system, the damping effect can be estimated in an absolute way by the equations (2) or (3), depending on the main behaviour of the system (i.e. elastic or plastic type).

## ACKNOWLEDGEMENTS

The authors thank FCT for the financial support of the projects POCTI/ECM/58375/2004 and PTDC/ECM/65731/2006 as well as Águas do Zêzere e Côa and CEHIDRO for their support to the development of this work.

## REFERENCES

[1] Covas, D.; Stoianov, I.; Graham, N.; Maksimovic, C.; Ramos, H.; Butler, D. (2002). “Hydraulic Transients in Polyethylene Pipes”. In: *Proceedings of 1st Annual Environmental & Water Resources Systems Analysis (EWRSA) Symposium*, ASCE EWRI, Roanoke, Virginia, USA.

[2] Covas, D.; Stoianov, I.; Ramos, H.; Graham, N.; Maksimovic, C.; Butler, D. (2004). “Water hammer in Polyethylene Pipes: Conceptual Model and Experimental Analysis”. Urban Water Journal, v. 1, n. 2, p. 177–197.

[3] Loureiro, D. (2002). “The Influence of Transients in Characteristic Hydraulic and Water Quality Parameters”. MSc Thesis - Instituto Superior Técnico, Technical University of Lisbon, Lisbon, Portugal (in Portuguese).

[4] Melo, N. (2009). “Diagnosis and Monitoring for the Leakage Detection using transients – Application to the main water pipeline system of Guarda city.” MSc Thesis - Instituto Superior Técnico, Technical University of Lisbon, Lisbon, Portugal (in Portuguese).

[5] Ramos, H.; Loureiro, D., (2001). “Evaluation of the influence of transients in the energy dissipation of pipe flows”. Laboratory of Hydraulics Water Resources and Environment, Civil Engineering Department, Instituto Superior Técnico, Technical University of Lisbon Lisbon, Portugal (in Portuguese).

[6] Ramos, H.; Borga, A.;Covas, D.; Loureiro, D. (2004). “Surge Damping Analysis in Pipe Systems: Modelling and Experiments”. Journal of Hydraulic Research, v. 42, n. 4, p. 413–425.

[7] Vítkovský, J.P.; Lambert, M.F.; Simpson, A. R. (2000). “Advances in Unsteady Friction Modelling in Transient Pipe Flow”. In: *Anderson, A. (ed.): VIII International Conference on Pressure Surges: Safe Design and Operation of Industrial Pipe Systems, the Hague, the Netherlands*. BHR Group 2000 Pressure Surges, Publications n. 39, v. 1, p. 471–498.

*Environmental Hydraulics – López-Jiménez et al (eds)*
*© 2010 Taylor & Francis Group, London, ISBN 978-0-415-56697-1*

# Optimal scheduling of the renewal of pipes in a system of urban water supply: Case study

Carlos Alonso, Rafael Pérez, José L. Diáz & Xitlali Delgado
*Centro Multidisciplinar de Modelación de Fluidos, Universidad Politécnica de Valencia, Valencia, España*

ABSTRACT: In this work the main factors influencing pipelines deterioration is analyzed, and an instrument to aid in the decision-making process that allows for the prioritization of needs for water distribution network renewal planning is proposed. To identify these priorities we apply Multicriteria Decision Support Systems (MDSS), Genetic Algorithms. By considering the various influencing factors involved in decision-making, the developed instrument proposes an acceptable sequence of interventions in the water network. It identifies the hierarchy of groups of pipes needing renovation and takes into account all aspects associated with the endogenous and exogenous factors, and the technical constraints of operation of the water network for a given planning horizon. It also considers the yearly available budgets for pipeline rehabilitation.

*Keywords*: Water distribution network, renewal, hierarchy, decision-making.

## 1 INTRODUCTION

Identifying the factors that influence the determination for prioritization in the renewal of the pipes is not an easy task, given that the selection should support the fundamental criteria at the time the pipe is considered for renewal. Age is undoubtedly the first criterion for inclusion in the list, but not the only one. Coupled with age is the availability of financial resources required and the financial resources available to water companies that operate water distribution networks. The aim is to improve the reliability and operation of the network. The emphasis on the renewal of the pipes is done according to a decision-making process that takes into account a number of variables related to the pipes and their environment, the conditions of operation of the network, technical restrictions and of course the financial implications.

## 2 OBJECTIVES AND SCOPE

The main objective is to study the factors of influence on the deteriorating pipes, in order to propose a model for the scheduling of work on the prioritization of the renewal of pipelines. We take into consideration a number of factors in order to prioritize of a group of pipes with similar characteristics including age and type of material. This requires the development of the proposed methodology for the allocation of priorities for renewal of pipes, using the system to support the decision making of the weighted sums, detailing the weighting matrix of alternatives and evaluation of results. Once addressed the methodology referred, it was applied the method of weighted sums for the prioritization of renewal in eight groups of piping within the water distribution network in Celaya City, Mexico.

## 3 ELECTION OF THE CRITERIA

The selection of criteria that can really influence in the decision to replace or not to replace a pipe or to position it on a priority list is not immediate. This is undoubtedly a particular decision of the managers of each network. They must choose the criteria more representatives in their environment and make an assessment in accord with the reality they live, depending of course, on their technical expertise of the business. Based on the above, here is the classification of the eight criteria that in the view of the network manager in Celaya City deserved to be considered. The criteria are classified into groups with different characteristics, but they allow for a quantitative assessment of the item analysis. They are the “Fundamental” group, “Hydraulic” group and the “Specials” group.

## 4 EVALUATION OF PIPES SELECTED ACCORDING TO THE CRITERIA DEFINED

### 4.1 *Fundamental criteria*

*The age of the pipe*. – Is proposed a maximum value of 10 points for a pipe 50 years old and a minimum of 0 in the case of a new pipe (0 years). The rating associated with each age, as expressed in the equation 1 has been made assuming a parabolic relationship between the two ends. It seems logical to penalize in an increasingly proportionate way to the age of the pipe.

*History of each pipe breakage*. – The number of breakages is proportional to the length of the pipe, for this reason the number of breaks is estimated per km., and the year of each pipe as a fundamental value to calculate the penalty. The values of breaking/Km. and year are high, but for various reasons are considered high. We propose a linear interpolation where we assign a value of 10 to the maximum number of breakages and assigned a value 0 for the minimum number of breakage per km per year (Hirner, 1997). This criterion is to assess with the following equation.

$$Value\,(age) = 10 \cdot \left(\frac{t}{60}\right)^2 \tag{1}$$

### 4.2 *Hydraulic criteria*

*Transport capacity of each pipe.* – In this first hydraulic criterion it is desired to value the hydraulic capacity of the pipe regardless of their behavior and real possibilities in the network. Knowing both the pipes diameter and roughness characteristics, and that the roughness of the pipe increases with the passage of time as well as other features such as type of material, conducted water flow quality, etc. it decides the absolute roughness for a given moment of time through the following equation.

$$k_{si}(t) = k_{soi} + a_i(t + g_i) \tag{2}$$

Moreover, the actual diameter of the pipe for a given moment in time is calculated by the equation 3:

$$D_i(t) = D_{oi}(1 - red_i(t + g_i)) \tag{3}$$

With the formulation taken from the previous model posed by Sharp and Walski (1998) operation of a water distribution network can be determined for a given period of time considering the increased roughness of the pipe and obstruction by the same inlay of materials, both linear with respect to time. Based on the above we can calculate the pressure loss per km. of pipe anytime, through a simulation model using EPANET ®.

*Index deficiency nodes.*– This procedure makes it possible to identify the group of affected nodes. Once these nodes are identified, one calculates each pipe cut and prepares the report between the number of non-communicating nodes and the total number of nodes that make up the network. There will be a penalty for the number of pipes that are below the lowest pressure allowed. The penalty was higher when the number of larger pipes fell below the minimum allowable pressure. The sector that had the highest number of "important" pipelines had the greatest penalty. Is assigned a value of 10 for the largest IDN and 0 for the lowest index, which is directly proportional to the value of the IDN. The evaluation was carried out through the expression 4:

$$IDN_j = \frac{Number\ nodes_{low}}{Total\ \ number\ nodes} \tag{4}$$

*Impact flow escaped by the behavior of the network, compared with an optimal level of efficiency.*– This approach influences the consumption of the affected nodes, in addition to the changes incurred in the pipe nodes analyzed where we had the leak. When comparing the simulation of EPANET ®with the 85% efficiency of rating of the physical network, it was considered a satisfactory ratio (AWWA Water Leak Detection and Accountability Committee, 2004).Comparing the simulation results with current actual data. The allocation of leakage is dependent on pressure, the same happens with the 85% efficiency level where the escaped flow in each node is based on the pressure. The evaluation was conducted using the following expression.

$$IIQ_{leak} = \frac{Num.nodes_{lowreal} - Num.nodes_{low85\%}}{Total\ number\ nodes} \tag{5}$$

The score will be the greater value derived from the equation 5 for each group of pipe assigned the value of 10 and for the lower the value of zero, making an interpolation for the intermediate values.

### 4.3 *Special criteria*

*Optimal time to replace the pipe according to Shamir-Howard.*– The statistical methodology proposed here gathers pipes that have the same properties that are considered discriminatory: age (years) and size (diameter). Other factors such as corrosion, material, the method of union between pipes, the conditions of the bed of the pipe, and traffic are considered fairly homogeneous for all pipes in every sector. Using a linear regression "age-size" we obtained for each group, the relationship between the number of breaks and time. For this type of analysis, Shamir and Howard (1979) proposed for the temporary development of breakages per unit length an exponential law as reflected in the following equation, where N (t) is the number of breaks/km in the year (t) and (t0) represents the reference year.

$$N(t)_i = N(t_o)_i * e^{A_i(t+g_i)} \tag{6}$$

N(t)i is the number of breakages per unit length per year in pipe in time t (km-1, year-1), N(t0)i is the N(t)i in the year of installation of the pipe (new pipe); t is the time in years; gi is the age of the pipe in the present (years), and Ai is the ratio of the rate of growth of breakages in the pipe (years). Shamir and Howard (1979) derive an expression (7) to calculate the optimal timing of replacement of a pipe (ts), adding the cost of replacing the pipe (Cs) and the costs of repair (Cr) occurred in the period ts – t0 and derive regarding ts year to obtain the replacement year at the minimum cost. In the following equation the variable (i) represents the annual rate of inflation and (to) the reference year. Now is the time to evaluate this approach. No penalty is given for pipes that have a year of optimal renewal greater than or equal to 25 years, but a penalty of 10 points is given to a value of ts – tc = 0 years. Now is the time to evaluate this approach.

$$t_s = -g_i + \frac{1}{A_i}\ln\left[\frac{C_s + \ln(1+i)}{C_r N(t_o)}\right] \tag{7}$$

*Influence of a water "cut" in different types of user in the water distribution network:*.– We had considered using the JUMAPA classification for consumers called "majors" which are users who consume at least 100 $m^3$ monthly. In the simulated program EPANET ®(EPA, 2000) we cut each pipe by initiating main pipes at the network and analyze the number of affected nodes when the greatest demand occurs. And the degree of influence of this court in each node, By we also measured the original pressure drop, as well as the number of affected nodes are located where the major consumers are located.

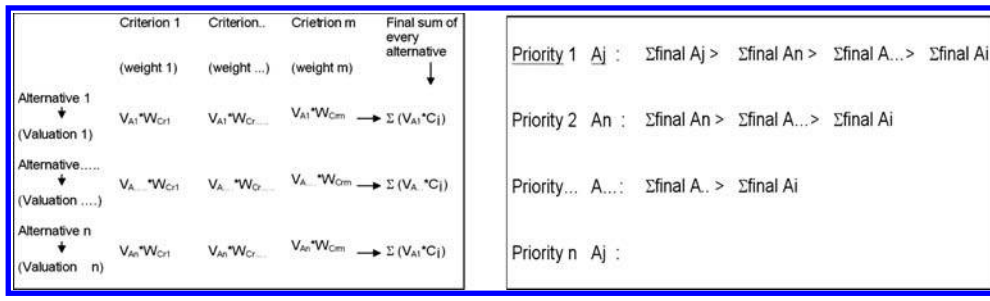


Figure 1. Typical structure of the matrix weighting alternative and prioritization of alternatives.

Table 1. Order of prioritize on 100.

| Order of prioritize | Assessment on 100 | Hierarchy |
|---|---|---|
| 1 | 7.33 | FoGa (C1) |
| 2 | 6.71 | FoGa (C2) |
| 3 | 6.62 | FoFo (C1) |
| 4 | 6.11 | AC (A1) |
| 5 | 5.39 | AC (A2) |
| 6 | 4.8 | PVC20 |
| 7 | 4.52 | Polythene |
| 8 | 4.48 | PVC30 |

*Impact of a break in the environment.*– This factor will be the score with a valuation of 10 for a density of extreme traffic, 6 for a strong density, 3 in the case of a moderate density and 0 for a low density of traffic. A relative weight of 60% is considered for each of the 4 factors analyzed. The same set of values is applied to the density of buildings and/or historic monuments, obtaining the score of each pipe.

## 5 METHODOLOGY

### 5.1 *Matrix weighing alternatives*

Method for prioritization pipelines renewal using-Decision Support System of the weighted sums. Of the different approaches used to generate the set of efficient solutions, this was the first to develop. Zadeh in 1963 was the one who suggested this method. Its basic idea is to combine all the criteria in a unique role. To that end, you associate a weight or ratio of consideration to each criterion, at which time you add the value of an alternative to each criterion (adjusting these by the weights of these criteria), to generate and achieve a global solution of this alternative. Each alternative depending on the criteria evaluated, reaches a (VAJ) valuation, which is affected by the weight assigned to this criterion, (WCrI). Having said that, and given a set of criteria m and n alternatives, the alternative J will add m products as (VAJ * WCrI) represented in a summation. The matrix includes n amounts for n alternative as shown in Figure 1.

### 5.2 *Assessment final results*

In the specific case of keeping a list of prioritized pipes ready to renew with greater urgency, given that the evaluation of each criterion implies greater need to renew when the score is higher in each case, we immediately conclude that greater sum of these products involves a greater need, and at the global level, to renew the pipe which is associated with the product. As a result, the final step in the process is to organize, from highest to lowest, each of the final results achieved by the alternatives (see figure 1), in order to know the final order for renewal.

*Implementation of the decision support system about weighted amounts for prioritization, renewal in eight groups pipelines network Celaya City, Mexico.*– We need to make some clarifications regarding the composition of the water distribution network on the diameters referred to on the majority of the pipes that make up the network, which range between 75 mm and 200 mm. The age of the pipes in the downtown sector are older (50 years) and there are different materials in the five areas such as: Fo-Fo, Fo-Ga, PVC and polyethylene. The eight groups of pipes selected were homogeneous in terms of the type of material and age.

*Association of partial ratings of each pipe with respect to each of the criteria considered.*– Once you evaluate the pipes for each criterion and all receive a value qualifier between 0 and 10 for each criterion, it is time to add these values, and average the weight of each criterion as described in the matrix above to achieve a final outcome for each alternative, which allows you to establish as a last step, the order of priority for renewal. Finally partial and weighted scoring of each pipe is shown in Table 1.

Once prioritization is done in the group of pipes, galvanized iron pipes can be seen first; that are 50 years old, followed by galvanized iron pipes 40 years old, which are older than the cast iron pipes FoFo (C1). The same is true for PVC pipes which are younger but are higher priority on this list. (i.e. PVC piping 20 years old get ratings higher than those pipes PVC30 in hydraulic and fundamental criteria.) Another significant data obtained are the very close values between the following pipes in the downtown sector: FoGa (C2) FoFo (C1), AC (A1) except the Asbestos Cement pipes AC (A2). This tells us what the homogeneous characteristics are in terms of the age and the material, and furthermore, their behavior so far. Proof of this is the hydraulic behavior.

Table 2. Result of the sensibility analysis.

| Order of prioritize | Assessment on 100 | Hierarchy |
|---|---|---|
| 1 | 7.36 | FoGa (C1) |
| 2 | 7.07 | FoFo (C1) |
| 3 | 6.67 | FoGa (C2) |
| 4 | 6.11 | AC (A1) |
| 5 | 4.71 | AC (A2) |
| 6 | 4 | PVC30 |
| 7 | 3.74 | PVC20 |
| 8 | 3.54 | Polythene |

*Sensitivity analysis of the results to changes in the consideration of the values on weights the criteria*.– If the relative weight in the key considerations were interspersed values, (i.e. were rated 30% age and 20% at breakage history (original values were 20% age, 30% breakage history), another change is QIIbreak from 10% to 5%, and the special criteria that was rated at 10% optimal renewal, is now 5%. The system after these changes is reflected in table 2. Clearly, the first group of pipes to be considered for renewal is the group that corresponds to the galvanized iron pipes (FoGa1). With the two assessments that have been made, we note that the prioritization changes considerably by changing the weight the ratings.

## 6 CONCLUSIONS

Managers who make decisions on prioritization for the renewal of the pipes is have a complicated task, because there are several factors of influence involved. For this reason, we believe that the method developed here can be a good tool for decision making in its simplicity. The results obtained in this study show us that the first group of pipelines on the prioritization is the group of pipe FoGa1 even with the sensitivity analysis. We note that this group of pipes score highest with established methods of scoring, Given that the factors for groups of the “fundamental” and “hydraulic” criteria obtained high values for both because of their characteristics of age and the number of breaks by the length, there is no doubt that it is the first group of pipes that should be considered for renewal. For the second and third place we will support the results of indexing and base the decision on the criteria JUMAPA decides.

## REFERENCES


[1] Grablutz, F. and S. Hanneken, (2000). “Economic Modeling for prioritizing pipe replacement Programs”. Presented at the AWWA Infrastructure Conference and Exhibition. Baltimore, MD, 14 March.

[2] Kleiner Y.; Adams; Rogers, (2001). “Water network renewal planning”. Journal of Computing in Civil Engineering. Vol. 15, No. 1.

[3] Laky, Dora, (2003). “Water network reconstruction in Hungary to reduce number of pipe bursts. Rehabilitation management of urban infrastructure networks”. Vol. December, ISBN 3 86005 430 1.

[4] Shamir U., and C.D.D Howard (1979), “An Analytic approach to scheduling pipe replacement”, Journal of AWWA, Vol. 71, No 5, May, pp. 248–258.

[5] Sharp, W. and Walski, W, (1998). Predicting Internal roughness in water mains. Journal of American Water Works Association, Vol. 80, No. 11.

*Environmental Hydraulics – López-Jiménez et al (eds)*
*© 2010 Taylor & Francis Group, London, ISBN 978-0-415-56697-1*

# Author index